

Pertanika Journal of  
**SCIENCE &  
TECHNOLOGY**

**JST**

**VOL. 32 (2) MAR. 2024**



PERTANIKA  
JOURNALS

A scientific journal published by Universiti Putra Malaysia Press

# PERTANIKA JOURNAL OF SCIENCE & TECHNOLOGY

## About the Journal

### Overview

Pertanika Journal of Science & Technology is an official journal of Universiti Putra Malaysia. It is an open-access online scientific journal. It publishes original scientific outputs. It neither accepts nor commissions third party content.

Recognised internationally as the leading peer-reviewed interdisciplinary journal devoted to the publication of original papers, it serves as a forum for practical approaches to improve quality on issues pertaining to science and engineering and its related fields.

Pertanika Journal of Science & Technology currently publishes 6 issues a year (*January, March, April, July, August, and October*). It is considered for publication of original articles as per its scope. The journal publishes in **English** and it is open for submission by authors from all over the world.

The journal is available world-wide.

### Aims and scope

Pertanika Journal of Science & Technology aims to provide a forum for high quality research related to science and engineering research. Areas relevant to the scope of the journal include: bioinformatics, bioscience, biotechnology and bio-molecular sciences, chemistry, computer science, ecology, engineering, engineering design, environmental control and management, mathematics and statistics, medicine and health sciences, nanotechnology, physics, safety and emergency management, and related fields of study.

### History

Pertanika Journal of Science & Technology was founded in 1993 and focuses on research in science and engineering and its related fields.

### Vision

To publish a journal of international repute.

### Mission

Our goal is to bring the highest quality research to the widest possible audience.

### Quality

We aim for excellence, sustained by a responsible and professional approach to journal publishing. Submissions can expect to receive a decision within 90 days. The elapsed time from submission to publication for the articles averages 180 days. We are working towards decreasing the processing time with the help of our editors and the reviewers.

### Abstracting and indexing of Pertanika

Pertanika Journal of Science & Technology is now over 27 years old; this accumulated knowledge and experience has resulted the journal being abstracted and indexed in SCOPUS (Elsevier), Clarivate Web of Science (ESCI), EBSCO, ASEAN CITATION INDEX, Microsoft Academic, Google Scholar, and MyCite.

### Citing journal articles

The abbreviation for Pertanika Journal of Science & Technology is *Pertanika J. Sci. & Technol.*

### Publication policy

*Pertanika* policy prohibits an author from submitting the same manuscript for concurrent consideration by two or more publications. It prohibits as well publication of any manuscript that has already been published either in whole or substantial part elsewhere. It also does not permit publication of manuscript that has been published in full in proceedings.

### Code of Ethics

The *Pertanika* journals and Universiti Putra Malaysia take seriously the responsibility of all of its journal publications to reflect the highest in publication ethics. Thus, all journals and journal editors are expected to abide by the journal's codes of ethics. Refer to *Pertanika's Code of Ethics* for full details, or visit the journal's web link at [http://www.pertanika.upm.edu.my/code\\_of\\_ethics.php](http://www.pertanika.upm.edu.my/code_of_ethics.php)

### Originality

The author must ensure that when a manuscript is submitted to *Pertanika*, the manuscript must be an original work. The author should check the manuscript for any possible plagiarism using any program such as Turn-It-In or any other software before submitting the manuscripts to the *Pertanika* Editorial Office, Journal Division.

All submitted manuscripts must be in the journal's acceptable similarity index range:  
**≤ 20% – PASS; > 20% – REJECT.**

### International Standard Serial Number (ISSN)

An ISSN is an 8-digit code used to identify periodicals such as journals of all kinds and on all media—print and electronic.

Pertanika Journal of Science & Technology: e-ISSN 2231-8526 (Online).

### Lag time

A decision on acceptance or rejection of a manuscript is reached in 90 days (average). The elapsed time from submission to publication for the articles averages 180 days.

### Authorship

Authors are not permitted to add or remove any names from the authorship provided at the time of initial submission without the consent of the journal's Chief Executive Editor.

### Manuscript preparation

For manuscript preparation, authors may refer to *Pertanika*'s **INSTRUCTION TO AUTHORS**, available on the official website of *Pertanika*.

### Editorial process

Authors who complete any submission are notified with an acknowledgement containing a manuscript ID on receipt of a manuscript, and upon the editorial decision regarding publication.

*Pertanika* follows a **double-blind peer-review** process. Manuscripts deemed suitable for publication are sent to reviewers. Authors are encouraged to suggest names of at least 3 potential reviewers at the time of submission of their manuscripts to *Pertanika*, but the editors will make the final selection and are not, however, bound by these suggestions.

Notification of the editorial decision is usually provided within 90 days from the receipt of manuscript. Publication of solicited manuscripts is not guaranteed. In most cases, manuscripts are accepted conditionally, pending an author's revision of the material.

### The journal's peer review

In the peer-review process, 2 to 3 referees independently evaluate the scientific quality of the submitted manuscripts. At least 2 referee reports are required to help make a decision.

Peer reviewers are experts chosen by journal editors to provide written assessment of the **strengths** and **weaknesses** of written research, with the aim of improving the reporting of research and identifying the most appropriate and highest quality material for the journal.

### Operating and review process

What happens to a manuscript once it is submitted to *Pertanika*? Typically, there are 7 steps to the editorial review process:

1. The journal's Chief Executive Editor and the Editor-in-Chief examine the paper to determine whether it is relevance to journal needs in terms of novelty, impact, design, procedure, language as well as presentation and allow it to proceed to the reviewing process. If not appropriate, the manuscript is rejected outright and the author is informed.
2. The Chief Executive Editor sends the article-identifying information having been removed, to 2 to 3 reviewers. They are specialists in the subject matter of the article. The Chief Executive Editor requests that they complete the review within 3 weeks.

Comments to authors are about the appropriateness and adequacy of the theoretical or conceptual framework, literature review, method, results and discussion, and conclusions. Reviewers often include suggestions for strengthening of the manuscript. Comments to the editor are in the nature of the significance of the work and its potential contribution to the research field.

3. The Editor-in-Chief examines the review reports and decides whether to accept or reject the manuscript, invite the authors to revise and resubmit the manuscript, or seek additional review reports. In rare instances, the manuscript is accepted with almost no revision. Almost without exception, reviewers' comments (to the authors) are forwarded to the authors. If a revision is indicated, the editor provides guidelines for attending to the reviewers' suggestions and perhaps additional advice about revising the manuscript.
4. The authors decide whether and how to address the reviewers' comments and criticisms and the editor's concerns. The authors return a revised version of the paper to the Chief Executive Editor along with specific information describing how they have addressed' the concerns of the reviewers and the editor, usually in a tabular form. The authors may also submit a rebuttal if there is a need especially when the authors disagree with certain comments provided by reviewers.
5. The Chief Executive Editor sends the revised manuscript out for re-review. Typically, at least 1 of the original reviewers will be asked to examine the article.
6. When the reviewers have completed their work, the Editor-in-Chief examines their comments and decides whether the manuscript is ready to be published, needs another round of revisions, or should be rejected. If the decision is to accept, the Chief Executive Editor is notified.
7. The Chief Executive Editor reserves the final right to accept or reject any material for publication, if the processing of a particular manuscript is deemed not to be in compliance with the S.O.P. of *Pertanika*. An acceptance letter is sent to all the authors.

The editorial office ensures that the manuscript adheres to the correct style (in-text citations, the reference list, and tables are typical areas of concern, clarity, and grammar). The authors are asked to respond to any minor queries by the editorial office. Following these corrections, page proofs are mailed to the corresponding authors for their final approval. At this point, **only essential changes are accepted**. Finally, the manuscript appears in the pages of the journal and is posted on-line.

Pertanika Journal of  
**SCIENCE  
& TECHNOLOGY**

**Vol. 32 (2) Mar. 2024**



A scientific journal published by Universiti Putra Malaysia Press



## EDITOR-IN-CHIEF

**Luqman Chuah Abdullah**  
*Chemical Engineering*

## CHIEF EXECUTIVE EDITOR

**Mohd Sapuan Salit**

## UNIVERSITY PUBLICATIONS COMMITTEE

### CHAIRMAN

**Zamberi Sekawi**

### EDITORIAL STAFF

#### Journal Officers:

Ellyianur Puteri Zainal  
Kanagamalar Silvarajoo  
Siti Zuhaila Abd Wahid  
Tee Syin Ying

#### Editorial Assistants:

Ku Ida Mastura Ku Baharom  
Siti Juridah Mat Arip  
Zulinaardawati Kamarudin

#### English Editor:

Norhanizah Ismail

### PRODUCTION STAFF

#### Pre-press Officers:

Nur Farrah Dila Ismail  
Wong Lih Jiu

### WEBMASTER

#### IT Officer:

Illi Najwa Mohamad Sakri

### EDITORIAL OFFICE

#### JOURNAL DIVISION

Putra Science Park  
1<sup>st</sup> Floor, IDEA Tower II  
UPM-IMTDC Technology Centre  
Universiti Putra Malaysia  
43400 Serdang, Selangor Malaysia.

#### General Enquiry

Tel. No: +603 9769 1622 | 1616

#### E-mail:

[executive\\_editor.pertanika@upm.edu.my](mailto:executive_editor.pertanika@upm.edu.my)

URL: [www.journals-jd.upm.edu.my](http://www.journals-jd.upm.edu.my)

### PUBLISHER

#### UPM Press

Universiti Putra Malaysia  
43400 UPM, Serdang, Selangor, Malaysia.  
Tel: +603 9769 8851  
E-mail: [penerbit@putra.upm.edu.my](mailto:penerbit@putra.upm.edu.my)  
URL: <http://penerbit.upm.edu.my>



### ASSOCIATE EDITOR

#### 2023-2024

#### Adem Kilicman

Mathematical Sciences  
Universiti Putra Malaysia, Malaysia

#### Miss Laiha Mat Kiah

Security Services Sn: Digital Forensic,  
Steganography, Network Security,  
Information Security, Communication  
Protocols, Security Protocols  
Universiti Malaya, Malaysia

#### Saidur Rahman

Renewable Energy, Nanofluids, Energy  
Efficiency, Heat Transfer, Energy Policy  
Sunway University, Malaysia

### EDITORIAL BOARD

#### 2022-2024

#### Abdul Latif Ahmad

Chemical Engineering  
Universiti Sains Malaysia, Malaysia

#### Ho Yuh-Shan

Water research, Chemical Engineering  
and Environmental Studies  
Asia University, Taiwan

#### Mohd Zulkifly Abdullah

Fluid Mechanics, Heat Transfer,  
Computational Fluid Dynamics (CFD)  
Universiti Sains Malaysia, Malaysia

#### Ahmad Zaharin Aris

Hydrochemistry, Environmental  
Chemistry, Environmental Forensics,  
Heavy Metals  
Universiti Putra Malaysia, Malaysia

#### Hsiu-Po Kuo

Chemical Engineering  
National Taiwan University, Taiwan

#### Mohd. Ali Hassan

Bioprocess Engineering, Environmental  
Biotechnology  
Universiti Putra Malaysia, Malaysia

#### Azlina Harun@Kamaruddin

Enzyme Technology, Fermentation  
Technology  
Universiti Sains Malaysia, Malaysia

#### Ivan D. Rukhlenko

Nonlinear Optics, Silicon Photonics,  
Plasmonics and Nanotechnology  
The University of Sydney, Australia

#### Nor Azah Yusof

Biosensors, Chemical Sensor, Functional  
Material  
Universiti Putra Malaysia, Malaysia

#### Bassim H. Hameed

Chemical Engineering: Reaction  
Engineering, Environmental Catalysis &  
Adsorption  
Qatar University, Qatar

#### Lee Keat Teong

Energy Environment, Reaction  
Engineering, Waste Utilization,  
Renewable Energy  
Universiti Sains Malaysia, Malaysia

#### Norbahiah Misran

Communication Engineering  
Universiti Kebangsaan Malaysia,  
Malaysia

#### Biswajeet Pradhan

Digital image processing, Geographical  
Information System (GIS), Remote  
Sensing  
University of Technology Sydney,  
Australia

#### Mohamed Othman

Communication Technology and  
Network, Scientific Computing  
Universiti Putra Malaysia, Malaysia

#### Roslan Abd-Shukur

Physics & Materials Physics,  
Superconducting Materials  
Universiti Kebangsaan Malaysia,  
Malaysia

#### Daud Ahmad Israf Ali

Cell Biology, Biochemical, Pharmacology  
Universiti Putra Malaysia, Malaysia

#### Mohd Shukry Abdul Majid

Polymer Composites, Composite  
Pipes, Natural Fibre Composites,  
Biodegradable Composites, Bio-  
Composites  
Universiti Malaysia Perlis, Malaysia

#### Wing Keong Ng

Aquaculture, Aquatic Animal Nutrition,  
Aqua Feed Technology  
Universiti Sains Malaysia, Malaysia

### INTERNATIONAL ADVISORY BOARD

#### 2021-2024

#### CHUNG, Neal Tai-Shung

Polymer Science, Composite and  
Materials Science  
National University of Singapore,  
Singapore

#### Mohamed Pourkashanian

Mechanical Engineering, Energy, CFD  
and Combustion Processes  
Sheffield University, United Kingdom

#### Yulong Ding

Particle Science & Thermal Engineering  
University of Birmingham, United  
Kingdom

#### Hiroshi Uyama

Polymer Chemistry, Organic  
Compounds, Coating, Chemical  
Engineering  
Osaka University, Japan

#### Mohini Sain

Material Science, Biocomposites,  
Biomaterials  
University of Toronto, Canada

### ABSTRACTING AND INDEXING OF PERTANIKA JOURNALS

The journal is indexed in SCOPUS (Elsevier), Clarivate-Emerging Sources Citation Index (ESCI), BIOSIS, National Agricultural Science (NAL), Google Scholar, MyCite, ISC. In addition, Pertanika JSSH is recipient of "CREAM" Award conferred by Ministry of Higher Education (MoHE), Malaysia.

The publisher of Pertanika will not be responsible for the statements made by the authors in any articles published in the journal. Under no circumstances will the publisher of this publication be liable for any loss or damage caused by your reliance on the advice, opinion or information obtained either explicitly or implied through the contents of this publication.

All rights of reproduction are reserved in respect of all papers, articles, illustrations, etc., published in Pertanika. Pertanika provides free access to the full text of research articles for anyone, web-wide. It does not charge either its authors or author-institution for refereeing/publishing outgoing articles or user-institution for accessing incoming articles.

No material published in Pertanika may be reproduced or stored on microfilm or in electronic, optical or magnetic form without the written authorization of the Publisher.

Copyright © 2021 Universiti Putra Malaysia Press. All Rights Reserved.





**Pertanika Journal of Science & Technology**  
**Vol. 32 (2) Mar. 2024**

**Contents**

Foreword <i>Mohd Sapuan Salit</i>	i
Analysis Study of Thermal and Exergy Efficiency in Double-Layers Porous Media Combustion Using Different Sizes of Burner: A Comparison <i>Nazmi Che Ismail, Mohd Zulkifly Abdullah, Nurul Musfirah Mazlan, Khairil Faizi Mustafa, Mohd Syakirin Rusdi and Roslan Kamarudin</i>	481
<i>Review Article</i> Bacterial Secondary Metabolite Activation Through Epigenetic Modifiers: A Systematic Review <i>Joana Noor Rashidah Rosli, Sharifah Aminah Syed Mohamad, Anis Low Muhammad Low and Suhaidi Ariffin</i>	495
Baby Weight and Length Measurement System with Data Storage Using MySQL Database <i>Rifqi Kamaddin Sholeh Lubis, Rahmat Rasyid and Meqorry Yusfi</i>	509
<i>Review Article</i> Integration of Unmanned Aerial Vehicle and Multispectral Sensor for Paddy Growth Monitoring Application: A Review <i>Nur Adibah Mohidem, Suhami Jaafar and Nik Norasma Che'Ya</i>	521
A Comparison of Results from Two Multi-Criteria Decision-Making Methods for Solar Photovoltaic Plant Site Location: Case Study Rio De Janeiro <i>Marco Pereira de Souza, Luis Claudio Bernardo Moura, Carlos Alberto Nunes Cosenza, Silvio de Macedo Amaral, Rodrigo Pestana Cunha Telles, Manuel Oliveira Lemos Alexandre, Silvio Barbosa, Bruno de Sousa Elia, Maria Fernanda Zelaya Correia, Antonio Carlos de Lemos Oliveira, Rodrigo Ventura da Silva and Thais Rodrigues Pinheiro</i>	551
Modelling and Optimisation of Cooling-Slope Parameters of Magnesium AZ91D Using Improvement Multi-Objective Jaya Approach for Predicted Feedstock Performance <i>Rahaini Mohd Said, Roselina Salleh@Sallehuddin, Norhaizan Mohamed Radzi, Wan Fahmin Faiz Wan Ali and Mohamad Ridzuan Mohamad Kamal</i>	573

Microencapsulation of <i>Citrus Hystrix</i> Essential Oil by Gelatin B/Chitosan Complex Coacervation Technique	599
<i>Siti Afiqah 'Aisyah Murtadza, Nurul Asyikin Md Zaki, Junaidah Jai, Fazlena Hamzah, Nur Suhanawati Ashaari, Dewi Selvia Fardhyanti, Megawati and Nadya Alfa Cahaya Imani</i>	
<i>Review Article</i>	
Current Insight on <i>Siraitia grosvenorii</i> Flavonoids Extraction Process and its Bioactivity Characteristic: A Review	623
<i>Zhao Jing, Douglas Law, Ahmed Najm, Cheah Yew Hoong and Shazrul Fazry</i>	
Loss-of-Life Analyses Based on Modified Arrhenius and Relative Aging Rate for Non-Thermally Upgraded Paper in Oil-Immersed Transformer	647
<i>Najiyah Saleh, Norhafiz Azis, Jasronita Jasni, Mohd Zainal Abidin Ab Kadir and Mohd Aizam Talib</i>	
Performance of Waste Cooking Oil Esterification for Biodiesel Production Using Various Catalysts	669
<i>Indah Thuraya Herman, Khairuddin Md Isa, Naimah Ibrahim, Saiful Azhar Saad, Tuan Amran Tuan Abdullah, Mohd Aizudin Abd Aziz and Muhammad Auni Hairunnaja</i>	
Smart Hydroponic Farming System Integrated with LED Grow Lights	685
<i>Primadiyanti Nirbita, Kah-Yoong Chan, Gregory Soon How Thien and Chu-Liang Lee</i>	
Biochemical and Agronomic Responses of Soybean ( <i>Glycine max</i> L. Merrill) to Spent and Deoiled Bleaching Earth of NPK Fertilization on Filler Basis	703
<i>Muhammad Parikesit Wisnubroto, Eka Tarwaca Susila Putra and Budiastuti Kurniasih</i>	
Physical Properties of Full-ripe Dabai ( <i>Canarium odontophyllum</i> miq. Variety Song) at Different Fractions	725
<i>Nur Afiqah Hani Abdul Rashid, Rosnah Shamsudin, Siti Hajar Ariffin, Wan Nor Zanariah Zainol@Abdullah and Puteri Nurain Megat Ahmad Azman</i>	
Microencapsulation of <i>Acalypha indica</i> Linn. Extracts Using Chitosan-Polycaprolactone Blends	741
<i>Maizatul Akmal Johari, Fathilah Ali, Azlin Suhaida Azmi, Hazleen Anuar, Jamarosliza Jamaluddin and Rosnani Hasham</i>	

Utilization of Aluminum Dross as a Cement Replacement Material for Sustainable Concrete Development <i>Nur Hidayah Mohd Zahari, Ali Salmiaton, Shafreeza Sobri, Noor Azline Mohd Nasir and Nor Shafizah Ishak</i>	761
Structural Deformation and Displacement of a Disc Winding due to Standard Switching Impulse Voltage via Finite Element Method <i>Nurul Farahwahida Md Yasid, Norhafiz Azis, Jasronita Jasni, Mohd Fairouz Mohd Yousof, Mohd Aizam Talib and Avinash Srikanta Murthy</i>	781
Integrating Fuzzy Logic and Brute Force Algorithm in Optimizing Energy Management Systems for Battery Electric Vehicles <i>Abdulhadi Abdulsalam Abulifa, Azura Che Soh, Mohd Khair Hassan, Raja Kamil and Mohd Amran Mohd Radzi</i>	797
Mechanical Properties of Virgin and Recycled Polymer for Construction Pile Application <i>Hoo Tien Nicholas Kuan, Yee Yong Lee, Sim Nee Ting, Chee Khoon Ng and Mohd Khairul Afiq</i>	819
Thermal Decomposition and Combustion Analysis of Malaysian Peat Soil Samples Using Coats Redfern Model-free Method <i>Dayang Nur Sakinah Musa, Hamidah Jamil, Mohd Zahirasri Mohd Tohir, Syafie Syam and Ridwan Yahaya</i>	839
<i>Review Article</i>	
Employment of Artificial Intelligence (AI) Techniques in Battery Management System (BMS) for Electric Vehicles (EV): Issues and Challenges <i>Marwan Atef Badran and Siti Fauziah Toha</i>	859
Optimal Constrained Groove Pressing Process Parameters Applying Modified Taguchi Technique and Multi-Objective Optimization <i>Muni Tanuja Anantha, Sireesha Koneru, Saritha Pyatla, Parameshwaran Pillai Thiruvambalam Pillai, Tanya Buddi and Nageswara Rao Boggarapu</i>	883
Inorganic Material of Magnesium Nitrate $Mg(NO_3)_2$ Film as Q-Switcher in the C-Band Region <i>Noor Ummi Hazirah Hani Zalkepali, Muwafaq Mohammed Bakr Alsaady, Mustafa Mudhafar, Nik Noor Haryatul Eleena Nik Mahmud, Nur Ainnaa Mardhiah Muhammad, Ain Zamira Muhammad Zamri and Noor Azura Awang</i>	901

<i>Review Article</i>	
Bead Geometry Control in Wire Arc Additive Manufactured Profile — A Review	917
<i>Zarirah Karrim Wani and Ahmad Baharuddin Abdullah</i>	
Application of the Ultrasonic Method to Produce Starch Nanoparticles from Cassava Starch	943
<i>Beni Hidayat, Vida Elsyana and Sheniah Glori Simorangkir</i>	
<i>Review Article</i>	
A Review: Current Trend of Immersive Technologies for Indoor Navigation and the Algorithms	955
<i>Muhammad Shazmin Sariman, Maisara Othman, Rohaida Mat Akir, Abd Kadir Mahamad and Munirah Ab Rahman</i>	

# Foreword

Welcome to the second issue of 2024 for the *Pertanika Journal of Science and Technology (PJST)*!

PJST is an open-access journal for studies in Science and Technology published by Universiti Putra Malaysia Press. It is independently owned and managed by the university for the benefit of the world-wide science community.

This issue contains 25 articles; six review articles and the rest are regular articles. The authors of these articles come from different countries namely Brazil, India, Indonesia, Iraq, Kingdom of Saudi Arabia and Malaysia.

Marco Pereira de Souza et al. presented an article titled “A comparison of results from two multi-criteria decision-making methods for solar photovoltaic plant site location: Case study Rio De Janeiro” from Brazil. Their study compares the results of two studies on the optimal site selection of PV in the Brazilian state of Rio de Janeiro. This comparison was carried out by map analysis and applying different correlation coefficients. The map comparison showed a high similarity of results; 83% of the best sites were identical in studies 01 and 02. It is relevant because the intersections of this study show great potential for PV plants as different methods validated them. The four coefficients used had a very high degree of correlation, with all of them above 0.9. Thus, the consistency of all the ranks also validates the results of both studies since they gave similar results, although they were tested in different ways. Therefore, the consistency of the results of the analysed studies indicates the potential for installing photovoltaic solar power plants in Rio de Janeiro and validates the methods used and the results themselves. The detailed information of this study is available on page 551.

Another article we wish to highlight is “Integrating Fuzzy Logic and Brute Force Algorithm in Optimizing Energy Management Systems for Battery Electric Vehicles” by Abdulhadi Abdulsalam Abulifa and colleagues from Universiti Putra Malaysia, Malaysia. This research proposes a solution to achieve more efficient control of heating, ventilation, and air conditioning consumption by integrating fuzzy logic techniques with brute-force algorithms to optimise the energy management system in battery electric vehicles. The model was based on actual parameters, implemented using MATLAB-Simulink and ADVISOR software, and configured using a backwards-facing design incorporating the technical specifications of a Malaysian electric car, the PROTON IRIZ. An optimal solution was proposed based on the Satisfaction ratio and state of charge metrics to achieve the best system optimisation. The results demonstrate that the optimised fuzzy energy management system improved power consumption by 23.2% to 26.6% compared to a basic fuzzy energy management system. Further details of the investigation can be found on page 797.

The next article uses the Coats Redfern model-free method to investigate the thermal decomposition and combustion analysis of Malaysian peat soil samples. The sample analyses include virgin peat from a forest reserve and agricultural peat from a cultivated area. Virgin peat experiences a 43% mass loss during pyrolysis, while agricultural peat shows a 46% mass loss, emphasising insights into thermal behaviour and consistent decomposition patterns across peat types. Furthermore, the study determines average activation energy trends, measuring 14.87 kJ/mol for virgin peat and 5.37 kJ/mol for agricultural peat under an inert atmosphere, and 28.89 kJ/mol for virgin peat and 36.66 kJ/mol for agricultural peat under an oxidative atmosphere. The study underscores the higher flammability of virgin peat due to its elevated carbon content, impacting ignition points and decomposition rates, emphasising the need for tailored management strategies based on peat type to mitigate fire risks. Details of this study are available on page 839.

We anticipate that you will find the evidence presented in this issue to be intriguing, thought-provoking and useful in reaching new milestones in your own research. Please recommend the journal to your colleagues and students to make this endeavour meaningful.

All the papers published in this edition underwent Pertanika's stringent peer-review process involving a minimum of two reviewers comprising internal as well as external referees. This was to ensure that the quality of the papers justified the high ranking of the journal, which is renowned as a heavily-cited journal not only by authors and researchers in Malaysia but by those in other countries around the world as well.

We would also like to express our gratitude to all the contributors, namely the authors, reviewers, Editor-in-Chief and Editorial Board Members of PJST, who have made this issue possible.

PJST is currently accepting manuscripts for upcoming issues based on original qualitative or quantitative research that opens new areas of inquiry and investigation.

**Chief Executive Editor**

**Mohd Sapuan Salit**

[executive\\_editor.pertanika@upm.edu.my](mailto:executive_editor.pertanika@upm.edu.my)

## Analysis Study of Thermal and Exergy Efficiency in Double-Layers Porous Media Combustion Using Different Sizes of Burner: A Comparison

Nazmi Che Ismail<sup>1</sup>, Mohd Zulkifly Abdullah<sup>1\*</sup>, Nurul Musfirah Mazlan<sup>2</sup>, Khairil Faizi Mustafa<sup>1</sup>, Mohd Syakirin Rusdi<sup>1</sup> and Roslan Kamarudin<sup>1</sup>

<sup>1</sup>*School of Mechanical Engineering, Universiti Sains Malaysia, Engineering Campus, 14300 Nibong Tebal, Penang, Malaysia*

<sup>2</sup>*School of Aerospace Engineering, Universiti Sains Malaysia, Engineering Campus, 14300 Nibong Tebal, Penang, Malaysia*

### ABSTRACT

Experimental investigations are currently exploring the impact of adding porous layers within burner housing on thermal and exergy efficiency. Specifically, the focus is on understanding the significance of double layers on porous media combustion and how it can improve fuel mixing and flame stability. Premixed butane-air combustion in rich conditions was examined using three different sizes of burners (i.e., 23 mm, 31 mm, and 44 mm) porous media with equivalence ratios ranging from  $\phi = 1.3$  to 2.0. The experimental findings revealed a substantial improvement in performance efficiency (thermal and exergy) as the equivalence ratio increased. This study reveals that smaller burner diameters (ID, inner diameter = 23 mm) provide greater efficiency than larger ones (ID = 31 mm and 44 mm). The maximum flame temperature and porous wall temperature are found to decrease as the equivalence ratio increases. The highest temperature measured was 924.82°C for 23 mm, 910.23°C for 31 mm, and 850.76°C for 44 mm at  $\phi = 1.3$ . Lastly, the

thermal and exergy efficiency in a 23 mm porous media burner (PMB) is higher at  $\phi = 2.0$  at 84.30% and 83.47%, respectively. It can be concluded that the diameter size of the burner and equivalence ratio for double-layer porous material influence the performance (efficiency) of PMB.

**Keywords:** Burner, exergy efficiency, porous media, rich combustion, surface flame, thermal efficiency

### ARTICLE INFO

#### Article history:

Received: 29 January 2023

Accepted: 14 June 2023

Published: 23 February 2024

DOI: <https://doi.org/10.47836/pjst.32.2.01>

#### E-mail addresses:

[nazmi@student.usm.my](mailto:nazmi@student.usm.my) (Nazmi Che Ismail)

[mezul@usm.my](mailto:mezul@usm.my) (Mohd Zulkifly Abdullah)

[nmusfirah@usm.my](mailto:nmusfirah@usm.my) (Nurul Musfirah Mazlan)

[mekhairil@usm.my](mailto:mekhairil@usm.my) (Khairil Faizi Mustafa)

[syakirin@usm.my](mailto:syakirin@usm.my) (Mohd Syakirin Rusdi)

[roslan\\_k@usm.my](mailto:roslan_k@usm.my) (Roslan Kamarudin)

\*Corresponding author

## INTRODUCTION

In recent years, the use of fossil fuels has intensified global warming and pollution. These fossil fuels threaten the nation and will impact the economy in the future due to depletion. This issue has impacted the demand for crude oil and has been increasing the price until today, which cannot be overlooked. A free flame from a combustion burner commonly generates higher pollution emissions and less efficiency, leading to high fuel consumption and environmental problems due to improper air-fuel mixing inside the burner.

Home burners like portable butane stoves are now widely recognized and used for domestic and commercial applications. In a normal household burner, combustion is a free flame, with heat transmission primarily by conduction. Porous media combustion (PMC) has grown more popular in residential burners in recent years due to its superior features over free flame combustion (Mujeebu et al., 2009; Javier et al., 2003). Indeed, double-layer porous media are becoming increasingly attractive to researchers because of their flame stability, high thermal efficiency, and decreased pollutant emissions (Zeng et al., 2017; Hashemi & Hashemi, 2017; Chen et al., 2019).

Many scholars have attempted to study double-layer PMC with various types of characteristics such as porous media materials (Liu et al., 2016), porosity (Yu et al., 2013), diameter size and thickness (Janvekar et al., 2017), and layers of pores (Dai et al., 2018) to enhance porous medium combustion's efficiency and performance. Furthermore, premixed fuel-air combustion is more likely to be acceptable for domestic burner stoves because it may improve performance while operating with flame control, provide minimal emission, and shorten the residence time of the gas mixture. Mishra and Muthukumar (2018) conducted an experimental study on fabricating and developing a self-aspirating liquefied petroleum gas (LPG) cooking stove with a two-layer porous radiant burner and three different types of orifice diameters. The results reveal that the maximum thermal efficiency of the porous radiant burner is 75.1% in the power range of 1–3 kW, whereas the traditional burner is only 65%. At the same time, Fan et al. (2019) numerically studied the combustion efficiency of microburners with single-layered and double-layered walls. The SiC inner wall significantly improves the heat recirculation effect of a double-layered micro burner compared to a quartz burner. Furthermore, compared to the SiC burner, the heat loss rate can be reduced by utilizing quartz exterior walls. Ghorashi et al. (2018) studied experimentally pollution emission of the burners with the effect of diameter hole on silicon carbide (SiC) and alumina oxide ( $Al_2O_3$ ) with three different pore densities (i.e., 10, 20, and 30 pores per inch). Their results indicated that CO concentration decreases in the  $Al_2O_3$  porous medium compared to that of the SiC porous medium.

Various studies of the characteristics of the PMB have been conducted due to the variation of equivalence ratio in the combustion. To maintain steady flame operation, the influence of the equivalence ratio on PMB stability becomes crucial in terms of



sustainability and performance. The implementation of porous media inside burners also plays an important role in temperature distribution (Wang et al., 2014; Li et al., 2019) and thermal efficiency (Sharma et al., 2009). In fuel-rich combustion, Dhamrat and Ellzey (2006) investigated a porous media reactor with rich equivalence ratios ranging from 1.5 to 5.0 and discovered that the initial fuel-air mixture intake velocity increases with conversion efficiency. In addition, a study made by Ismail et al. (2013) found that the thermal efficiency of the porous media burner improved with the rise in fuel-air mixture ratio as fuel mass fraction increased to create higher heating value in alumina foam ( $\text{Al}_2\text{O}_3$ ) in fuel-rich equivalence ratio at  $\phi = 1.3$  to  $\phi = 1.6$ . Qu et al. (2015) studied the combustion of premixed methane air in a two-zone alumina pellets burner, and the findings revealed that raising the equivalence ratio and pellet diameter enhanced the flame stability limits.

In the last few years, most researchers have focused on studying an alternative method to improve thermal and exergy efficiency inside a burner's combustion. Mohseni et al. (2021) examined the effect of inserted porous media, perforated fins, and 8-tube and 24-tube outlets on the geometry model at the outlet micro-combustor to improve the thermal efficiency and performance of exergy. Meanwhile, Cai et al. (2021) examined the effect of inserting a bluff body in a hydrogen-fueled meso-combustor by optimizing thermal performance and exergy efficiency. They observed that the exergy efficiency of the bluff-body combustor is higher than that of the conventional combustor. Different studies by Johar et al. (2017) focus on analyzing thermal storage's energy and exergy efficiency integrated with a micro-cogeneration system. Also, Nadimi and Jafarmadar (2019) used a micro-combustor for thermophotovoltaic systems to investigate energy conversion and exergy efficiency to improve thermal performance.

In similar work, Sharma et al. (2016) conducted an experimental study on the thermodynamics performance of a double-layered porous burner made of alumina and silicon carbide. According to the findings, the highest efficiency of the porous media stove is determined to be  $\sim 10\%$  greater than that of a standard conventional stove. Since it affects the distribution of heat and reactants inside the porous medium, burner diameter is essential in PMC. This study could use porous media materials to monitor flame characteristics and combustion efficiency, and the findings could be examined to determine the optimal burner diameter, which might provide valuable insight into the design and optimization of PMC systems for enhanced combustion performance.

As a result, investigations on the thermal management (performances) of double-layer PMB in premixed butane-air combustion with varied burner sizes remain insufficient. This study aims to investigate the influence of burner diameter size on thermodynamic efficiencies, such as thermal and exergy of PMB performance and flame characteristics for double-layer porous media configurations using premixed butane-air combustion under rich conditions.

## EXPERIMENTAL SETUP

Figure 1 (a) depicts a schematic design of the experimental setup used to examine the combustion of double-layer porous media with varied equivalence ratios. The burner housing comprises mild steel with a constant length of 100 mm and an inner diameter (ID) of 23 mm, 31 mm, and 44 mm. On the top of the burner are two porous media stacks with large pore sizes (alumina foam) for the reaction zone and small pore sizes (porcelain foam) for the pre-heat zone (Figure 2).

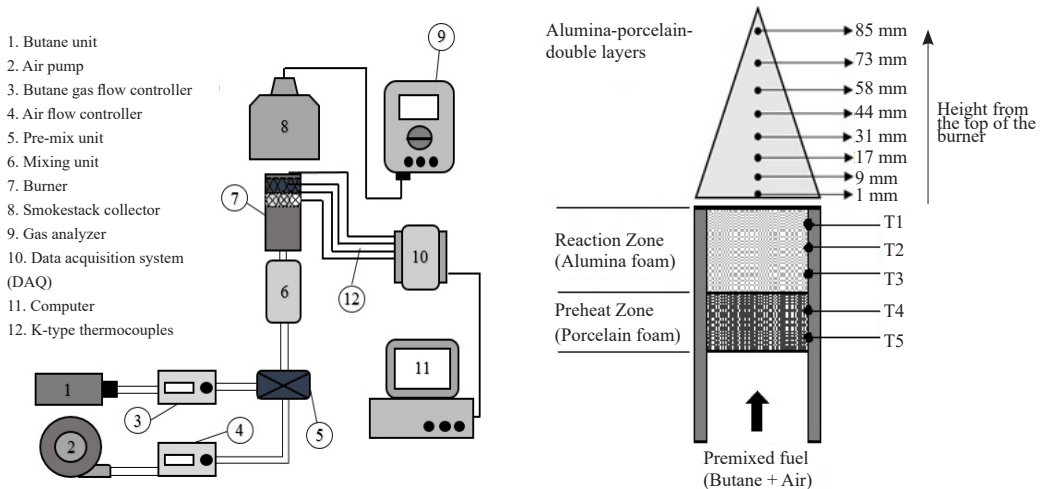


Figure 1. Schematic diagram of the experimental setup and layout, (a) the porous media combustion (PMC) system, and (b) the double layers porous configuration with thermocouples placement.

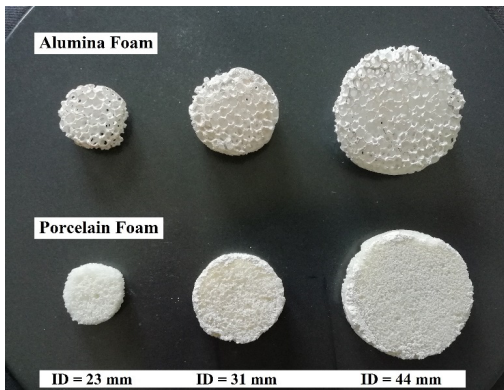


Figure 2. Photographic image of the alumina and porcelain foam in different sizes of burner (i.e., 23 mm, 31 mm, and 44 mm)

The alumina and porcelain foam utilized in this study were fabricated and modified in diameters (ID) of 23 mm, 31 mm, and 44 mm, respectively. The properties of the porous media materials employed in this experiment are shown in Table 1. Two digital flow meters with a control valve (Vögtlin instrument) measure the butane fuel ( $C_4H_{10}$ ) and airflow rates. Both digital flow meters display the value in liters per minute (L/min) for measuring flow rate.

The temperature readings were monitored using a K-type thermocouple

and recorded using Advantech DAQ (Data acquisition) devices (Model: USB-4718) with 8 thermocouple input channels at a sampling rate of one data (temperature) per second.

Temperature measurements were collected, analyzed, and saved on a personal computer. All eight thermocouples were mounted on the top of the PMB at varying heights [Figure 1 (b)] to evaluate the flame temperature distributions. Meanwhile, the thermocouple indicates T1, T2, and T3, which were used to determine the average porous wall temperature of alumina foam and T4 and T5 of porcelain foam. For the initial conditions, the experiments were carried out at room temperature.

Table 1  
*Porous media materials specifications for porcelain and alumina foam*

Specifications	Porcelain	Alumina
Pore size	26 ppcm	8 ppcm
Porosity	86%	84%
Made by	School of Materials and Mineral Resources Engineering, Universiti Sains Malaysia	Goodfellow Cambridge Limited (LS 3699006/1), England
Type	Foam	Foam

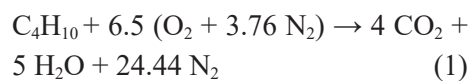
*Note.* ppcm - pore per centimeter

The difference between air-fuel ratios is used to supply air and butane fuel, which is then routed to the burner through a rubber tube. The experiments were carried out using a fuel source with a butane cartridge manufactured by Milux Sdn. Bhd. (Malaysia). A commercial aquarium air pump manufactured by Atman Co. Ltd. (China) provided natural air. Before entering the burner, air and butane fuel were mixed in the box. The images representing the outside wall burner housing temperature were captured using the FLUKE Thermal Imager (Ti27 Industrial Commercial model). Carbon monoxide (CO) and nitric oxide (NO) pollution emissions in part per million (ppm) are measured using a handheld flue gas analyzer type (Kane 251 Combustion Analyzer). The equivalent ratio,  $\phi$ , was determined for each experiment based on the air and fuel flow rates. Table 2 shows the detailed mass flow rate of butane fuel and air used, including the relevant equivalence ratios.

Table 2  
*The specification of mass flow rate for butane fuel and air at various equivalence ratios*

Equivalence Ratio, $\phi$	1.3	1.5	1.8	2.0
Air (liters/min)	3.10			
Butane fuel (liters/min)	0.13	0.15	0.18	0.20

Porous media porosity and configurations are important factors that affect the flame stability and temperature distributions inside the burner. For complete combustion, the chemical formula for butane gas and natural air is as Equation 1.



where,

O<sub>2</sub> - Oxygen

N<sub>2</sub> - Nitrogen

CO<sub>2</sub> - carbon dioxide

The assessment of thermal efficiency,  $\eta_{\text{Thermal}}$  of the burner performance for heating purposes based on the water boiling test, the energy provided,  $Q_{\text{actu}}$  [Energy generated from combustion (J/s)], is equal to the energy generated,  $Q_{\text{total}}$  [total energy (J/s)] by combustion as in Equation 2.

$$Q_{\text{total}} = \dot{m} \times C_v \quad (2)$$

where  $\dot{m}$  is the mass flow rate of the butane fuel and  $C_v$  [Calorific value of butane fuel (J/kg)] is the calorific value of the butane fuel. Furthermore, the energy generated by the combustion burner is denoted by  $Q_{\text{actu}}$  (Equation 3):

$$Q_{\text{actu}} = [(M_w C_w + M_c C_p) \times (50^\circ\text{C} - T_o)] / \text{time} \quad (3)$$

where,

$M_w$  - Mass of water (kg)

$C_w$  - Specific heat of water (kJ/kg.K)

$M_c$  - Mass of container (kg)

$C_p$  - Specific heat of container (kJ/kg.K)

$M_w$  and  $M_c$  are the masses of water and container, respectively. The water's and the container's standard specific heat values are 4.1826 kJ/kg.K for the water and 0.5024 kJ/kg.K for the container. Another thing is the ambient temperature of the room, 302 K (Equation 4).

Hence, the total exergy in the combustion burner is:

$$Q_{\text{exergy}} [\text{Total exergy (J/s)}] = (Q_{\text{actu}} / \dot{m}) - T_o (S_{\text{max}} - S_{\text{amb}}) \quad (4)$$

where  $S_{\text{amb}}$  [Specific entropy at ambient temperature (J/kg.K)] is the total entropy at room temperature, whereas  $S_{\text{max}}$  [Specific entropy at maximum temperature (J/kg.K)] represents the total entropy at the highest flame temperature.

While exergy efficiency,  $\eta_{\text{Exergy}}$  based on basic thermodynamics fundamentals from the second law allows for the direct derivation of exergy analysis. The procedure for calculating these parameters was the same as in prior research (Equations 5 & 6) (Ismail et al., 2020).

$$\eta_{\text{Thermal}} = (Q_{\text{actu}} / Q_{\text{total}}) \times 100\% \quad (5)$$

$$\eta_{\text{Exergy}} = (Q_{\text{exergy}} / Q_{\text{total}}) \times 100\% \quad (6)$$

where  $Q_{\text{actu}}$  is the energy produced by the combustion,  $Q_{\text{exergy}}$  is the overall exergy in the combustion, and  $Q_{\text{total}}$  is the energy provided by the combustion.

## RESULTS AND DISCUSSION

Experiments were conducted to investigate the thermal and exergy efficiency of porous medium combustion double layers. In these experiments, the equivalence ratio is measured from 1.3 to 2.0. The effect of the equivalence ratio on flame stability and emissions is a factor that influences the performance of PMB. Figure 3 illustrates a photographic picture of the surface flame characteristics for burner diameter, ID = 23 mm double-layer configurations ranging from  $\phi = 1.3$  to 2.0 taken with a Nikon J1 digital camera. Based on the findings, the surface flame is stable at  $\phi = 1.3$  and 1.5 with a predominance of blue flame but unstable at  $\phi = 1.8$  and 2.0 with an orange flame. Furthermore, the surface flame images reveal that the flame length increases when the equivalence ratio rises from 1.3 to 2.0 as the butane fuel mass flow rate rises.

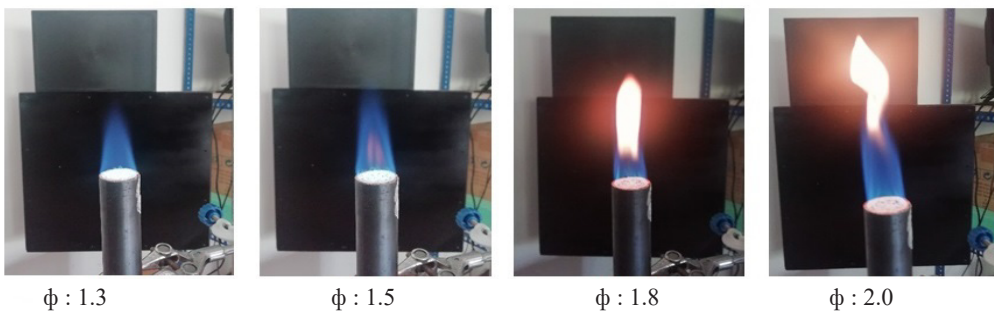


Figure 3. Photographic images of the surface flame stability with the double-layer configuration using a digital camera

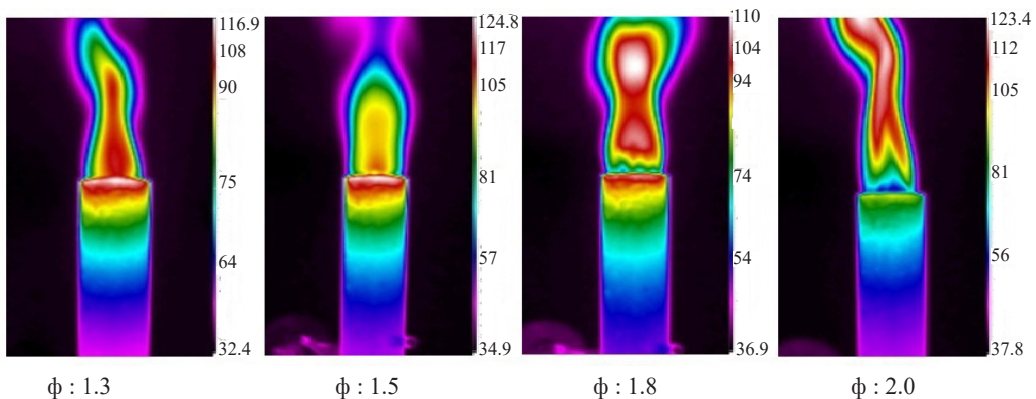


Figure 4. Thermal images of the porous media burner (PMB) with varied equivalence ratio

Figure 4 depicts the thermal pictures as the equivalence ratio fluctuates based on the temperature wall of the PMB. The thermal pictures are characterized by porous wall

temperature, indicating the location of the thermocouples and porous medium. The porous wall temperature of double layers PMB decreases substantially as the equivalence ratio increases (from  $\phi = 1.3$  to 2.0), as seen in the picture, where the red contour color gradually disappears. Heat radiation from the porous burner housing is stronger at  $\phi = 1.3$  and diminishes at  $\phi = 2.0$  (see the contour color of purple around the burner housing). It is due to the propagation of the flame speed combustion when the butane fuel mass flow increases.

The CO emission in double layers PMB measured with a portable flue gas analyzer was within the 12–67 ppm range for all equivalence ratios. While NO emission measurements were taken, they were within the 5–14 ppm range. It has been shown that emissions concentrations are still at a low pollution level and below an acceptable limit for human health (Ghorashi et al., 2018).

For the temperature distribution, Figures 5 (a), (b), and (c) show the maximum flame temperature of the PMB as well as the average porous wall temperature of the pre-heat and reaction zones with variations in equivalence ratio. The highest temperature measured by eight thermocouples positioned on top of the burner at different equivalence ratios is the maximum flame temperature (Gao et al., 2012). It is also noted that the maximum flame temperature reduces when the equivalence ratio increases from  $\phi = 1.3$  to 2.0. At PMB ID = 23 mm, maximum flame temperature is recorded at 924.37°C at  $\phi = 1.3$ , followed by 887.43°C at  $\phi = 1.5$ , 840.35°C at  $\phi = 1.8$ , and 825.17°C at  $\phi = 2.0$ . The same trend happens to PMB ID = 31 mm, where the maximum flame temperature is recorded at 910.23°C at  $\phi = 1.3$ , followed by 850.34°C at  $\phi = 1.5$ , 830.73°C at  $\phi = 1.8$ , and 820.11°C at  $\phi = 2.0$ . Also, at PMB ID = 44 mm, the maximum flame temperature is recorded at 850.76°C at  $\phi = 1.3$ , followed by 824.68°C at  $\phi = 1.5$ , 817.68°C at  $\phi = 1.8$ , and 810.66°C at  $\phi = 2.0$ .

The findings reveal that porous materials aided the burner in improving heat recirculation and retention within the burner. This phenomenon arises owing to flame stability in double layers PMB at  $\phi = 1.3$  and 1.5 but becomes unstable as the mass flow fuel mixture increases ( $\phi = 1.8$  and 2.0). The maximum flame temperature decreased significantly with increased equivalence ratios owing to the lower power output generated from the combustion for three different PMB IDs. Thus, as shown in Figure 4, double-layer porous media increased internal heat recirculation in the pre-heat zone, and the heat was transferred from the reaction zone to the pre-heat zone via radiation heat.

The average temperature of the burner wall is another critical element in assessing the efficiency of porous medium combustion. It illustrates a declining trend in average wall burner temperature as equivalence ratios rise from  $\phi = 1.3$  to 2.0 for pre-heat and reaction zones for all three different PMB ID. From Figure 5 (a), (b), and (c), the highest average wall temperature achieved at  $\phi = 1.3$  is 95.43°C (reaction zone) and 85.52°C (pre-heat zone) for PMB ID = 23 mm. Then, it starts to reduce the highest average temperature porous wall as the PMB ID = 31 mm at 93.42°C (reaction zone) and 84.75°C (pre-heat

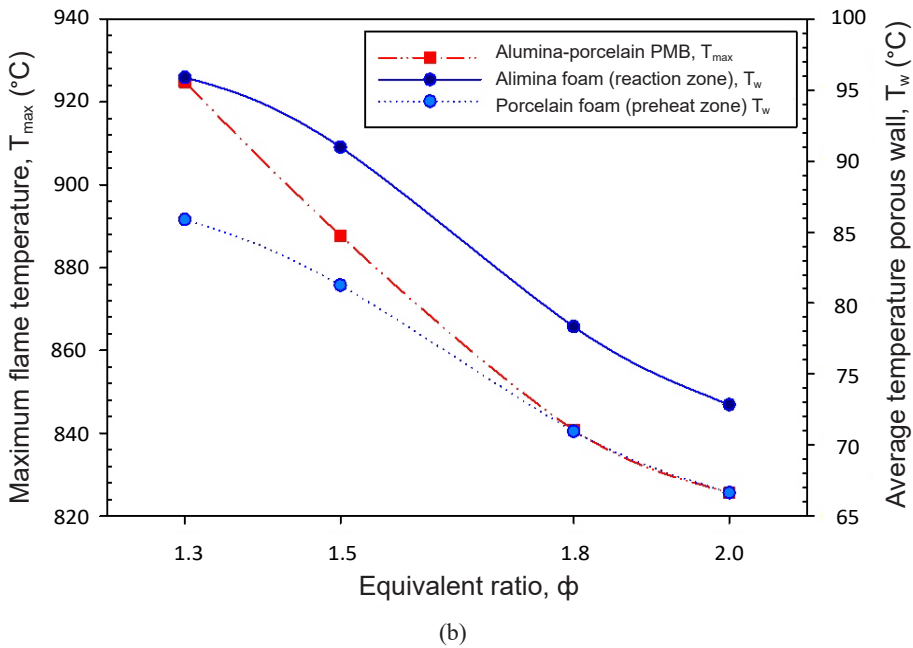
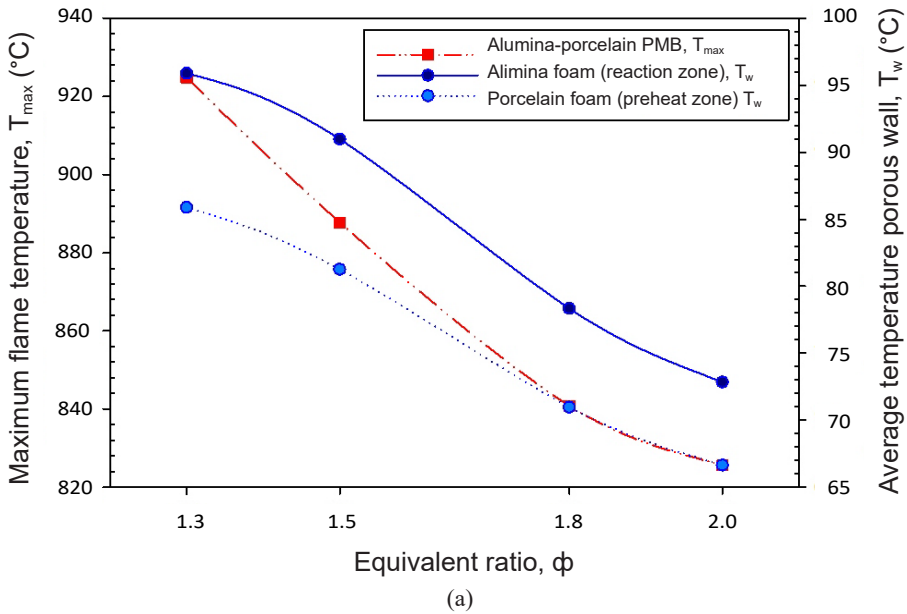
zone), and then PMB ID = 44 mm at 90.68°C (reaction zone) and 35.86°C (pre-heat zone), respectively. According to the results, the temperature decreases significantly at small burner diameters (PMB ID = 23 mm) but only slightly at large burner diameters (PMB ID = 44 mm), implying that the different burner sizes in PMC have a significant impact on controlling the temperature of double-layer porous walls. Surprisingly, the average porcelain foam porous wall temperature (pre-heat zone) appears to be almost consistent with an increase in the equivalence ratios (from  $\phi = 1.3$  to  $\phi = 2.0$ ) in larger diameter burners (PMB ID = 44 mm) compared to the others (PMB ID = 23 mm and 31 mm) due to the quenching effect that occurs inside porcelain foam, which prevents the flame from propagating far enough to reach the burner wall in bigger PMBs.

From Equations 2 and 3, the thermal efficiency,  $\eta_{\text{Thermal}}$ , and exergy efficiency,  $\eta_{\text{Exergy}}$  achieved for double-layer porous medium design with various equivalence ratios for three different PMB IDs are shown in Figure 6 (a), (b), and (c). PMB ID's thermal and exergy efficiency = 23 mm, 31 mm, and 44 mm double layers PMB improved as the premixed butane-air equivalence ratios increased from 1.3 to 2.0. Besides, at PMB ID = 23 mm, the results also show the percentage performance efficiency is higher at  $\phi = 2.0$  with  $\eta_{\text{Thermal}} = 84.30\%$  and  $\eta_{\text{Exergy}} = 83.47\%$ , respectively. While the lowest percentage efficiency performance at  $\phi = 1.3$  with  $\eta_{\text{Thermal}} = 71.80\%$  and  $\eta_{\text{Exergy}} = 70.95\%$ . Then, the thermal and exergy efficiency starts to reduce as the burner diameter size (PMB ID) increases from 23mm to 31 mm and 44 mm. At PMB ID = 31 mm, the highest thermal and exergy efficiency happen at  $\phi = 2.0$  with  $\eta_{\text{Thermal}} = 78.90\%$  and  $\eta_{\text{Exergy}} = 78.07\%$ , while the lowest thermal and exergy efficiency happen at  $\phi = 1.3$  with  $\eta_{\text{Thermal}} = 68.80\%$  and  $\eta_{\text{Exergy}} = 65.91\%$ . Moreover, at PMB ID = 44 mm, the highest thermal and exergy efficiency happen at  $\phi = 2.0$  with  $\eta_{\text{Thermal}} = 75.00\%$  and  $\eta_{\text{Exergy}} = 74.18\%$ , while the lowest thermal and exergy efficiency happen at  $\phi = 1.3$  with  $\eta_{\text{Thermal}} = 63.40\%$  and  $\eta_{\text{Exergy}} = 62.55\%$ , respectively.

The thermal and exergy efficiency rises as the fuel mass flow rates (butane fuel) improve with increases in equivalence ratios, indicating that it substantially impacts both thermal and exergy performances. The increase in thermal efficiency with a higher fuel flow rate is related to lower convective and radiative heat losses, whereas increased exergy efficiency implies better heat energy utilization inside PMBs.

Moreover, the amount of exergy the system destroys is determined by the difference in efficiency between thermal and exergy. Exergy destroyed is the amount of energy that could have been used for useful work but was wasted due to irreversibilities (Dincer & Bicer, 2020). The exergy destroyed is determined to be 0.83% for PMB ID = 23 mm at  $\phi = 1.5$  and 2.0, followed by  $\phi = 1.3$  at 0.85% and  $\phi = 1.8$  at 0.88%. On the other hand, for PMB ID = 31 mm, the amount of exergy destroyed is 2.89% at  $\phi = 1.3$ , 0.85% at  $\phi = 1.5$ , 0.84% at  $\phi = 1.8$ , and 0.83% at  $\phi = 2.0$ . Additionally, the exergy destroyed for PMB ID = 44 mm at  $\phi = 1.3$  is 0.85%, followed by  $\phi = 1.5$  and 1.8 at 0.83% and  $\phi = 2.0$  is

0.82%, respectively. According to the findings, the highest amount of exergy destroyed occurred inside PMB ID = 31 mm at  $\phi = 1.3$  and was wasted on the environment, which cannot be recovered.





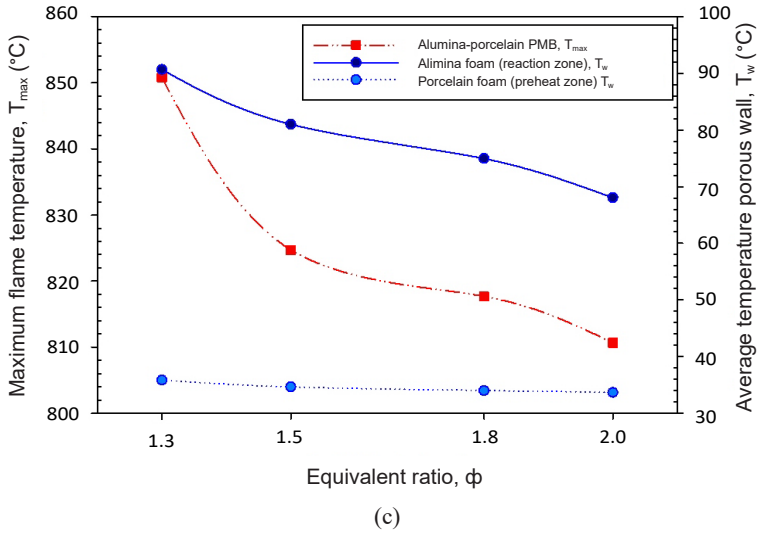


Figure 5. Maximum flame temperature and average temperature porous wall varies with equivalence ratio: (a) 23 mm, (b) 31 mm, and (c) 44 mm

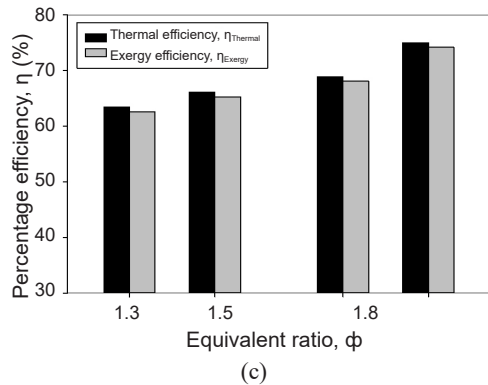
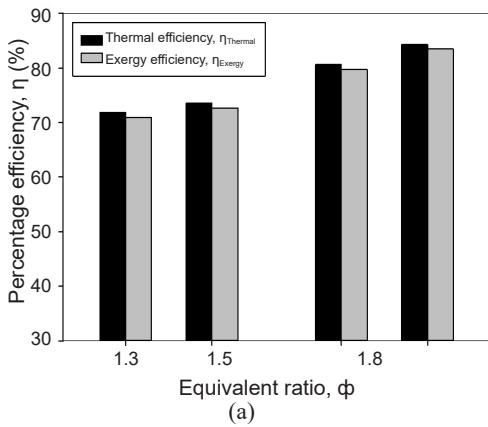
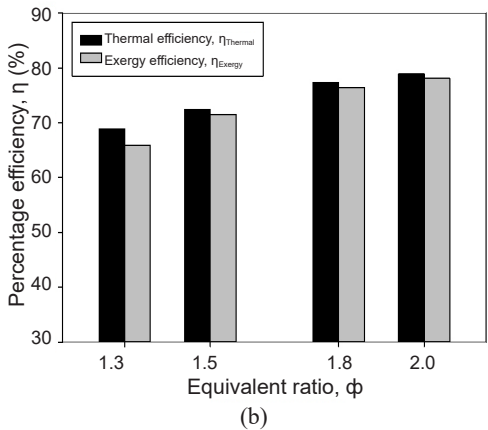


Figure 6. Thermal efficiency,  $\eta_{Thermal}$ , and exergy efficiency,  $\eta_{Exergy}$  with varies equivalence ratios: (a) 23 mm, (b) 31 mm, and (c) 44 mm



The impact of improving PMB performance efficiency is attributed to reduced radiation heat transfer from the porous media burner wall as fuel mass flow rates in premixed combustions increase. It can be concluded that the mass flow input of the mixture significantly affects the thermal performance of the PMB's (Ismail et al.,

2013). Overall, it can be said that the double-layer designs and equivalence ratio affect the thermal and energy efficiency characteristics.

## CONCLUSION

In this research, a double-layer porous media combustion with varied burner diameters was constructed and experimentally tested for thermal and exergy efficiency. Studies were carried out with three different sizes of burner, PMB ID = 23 mm, 31 mm, and 44 mm, at equivalence ratios,  $\phi = 1.3, 1.5, 1.8,$  and  $2.0$ . The following are the study's primary findings:

1. The highest flame temperature was found in PMB ID = 23 mm,  $T_{\max}$  [maximum temperature ( $^{\circ}\text{C}$ )] =  $924.37^{\circ}\text{C}$  at  $\phi = 1.3$  for various equivalence ratios, while the lowest flame temperature was obtained in PMB ID = 44 mm,  $T_{\max} = 810.66^{\circ}\text{C}$  at  $\phi = 2.0$ .
2. In addition, for both pre-heat and reaction zones for three different PMB IDs, the wall porous temperature decreases as the equivalence ratio increases.
3. The highest thermal and exergy efficiency were observed in PMB ID = 23 mm at  $\phi = 2.0$  with 84.30% and 83.47%, respectively.
4. The exergy destroyed,  $e_{\text{des}}$  [Exergy destroyed (W)] in all the experiments in the range of 0.82% to 0.88% except for the PMB ID = 31 mm at  $\phi = 1.3$  is 2.89%, which is higher.

The results demonstrate that the temperature distribution, thermal efficiency, and exergy efficiency analyses show that the equivalence ratio significantly defines the PMB characteristics. This study reveals that the advantages of utilizing porous media materials and smaller diameter burners produced better performances are related to the thermal and exergy efficiency using double-layer configurations. Therefore, this study indicates to other researchers the advantages of varying burner sizes for improving PMB performance in the future.

## ACKNOWLEDGEMENTS

This project was financially supported by the Ministry of Higher Education, Malaysia, and Universiti Sains Malaysia via FRGS (203.PMEKANIK.6071391) and Research University (1001.PAERO.8014089) Grants, respectively.

## REFERENCES

- Cai, T., Zhao, D., & Karimi, N. (2021). Optimizing thermal performance and exergy efficiency in hydrogen-fueled meso-combustors by applying a bluff-body. *Journal of Cleaner Production*, 311, Article 127573. <https://doi.org/10.1016/j.jclepro.2021.127573>

- Chen, X., Li, J., Feng, M., Zhao, D., Shi, B., & Wang, N. (2019). Flame stability and combustion characteristics of liquid fuel in a meso-scale burner with porous media. *Fuel*, *251*, 249-259. <https://doi.org/10.1016/j.fuel.2019.04.011>
- Dai, H., Zhao, Q., Lin, B., He, S., Chen, X., Zhang, Y., Niu, Y., & Yin, S. (2018). Premixed combustion of low-concentration coal mine methane with water vapor addition in a two-section porous media burner. *Fuel*, *213*, 72-82. <https://doi.org/10.1016/j.fuel.2017.09.123>
- Dhamrat, R. S., & Ellzey, J. L. (2006). Numerical and experimental study of the conversion of methane to hydrogen in a porous media reactor. *Combustion and Flame*, *144*(4), 698-709. <https://doi.org/10.1016/j.combustflame.2005.08.038>
- Dincer, I., & Bicer, Y. (2020). Chapter 2: Fundamentals of energy systems. In I. Dincer & Y. Bicer (Eds.), *Integrated Energy Systems for Multigeneration* (pp. 33-83). Elsevier.
- Fan, A., Li, L., Yang, W., & Yuan, Z. (2019). Comparison of combustion efficiency between micro combustors with single- and double-layered walls: A numerical study. *Chemical Engineering and Processing – Process Intensification*, *137*, 39-47. <https://doi.org/10.1016/j.ccep.2019.02.004>
- Gao, H. B., Qu, Z. G., He, Y. L., & Tao, W. Q. (2012). Experimental study of combustion in a double-layer burner packed with alumina pellets of different diameters. *Applied Energy*, *100*, 295-302. <https://doi.org/10.1016/j.apenergy.2012.05.019>
- Ghorashi, S. A., Hashemi, S. A., Hashemi, S. M., & Mollamahdi, M. (2018). Experimental study on pollutant emissions in the novel combined porous-free flame burner. *Energy*, *162*, 517-525. <https://doi.org/10.1016/j.energy.2018.08.005>
- Hashemi, S. M., & Hashemi, S. A. (2017). Flame stability analysis of the premixed methane-air combustion in a two-layer porous media burner by numerical simulation. *Fuel*, *202*, 56-65. <https://doi.org/10.1016/j.fuel.2017.04.008>
- Ismail, A. K., Abdullah, M. Z., Zubair, M., Ahmad, Z. A., Jamaludin, A. R., Mustafa, K. F., & Abdullah, M. N. (2013). Application of porous medium burner with micro cogeneration system. *Energy*, *50*, 131-142. <https://doi.org/10.1016/j.energy.2012.12.007>
- Ismail, N. C., Abdullah, M. Z., Mazlan, N. M., & Mustafa, K. F. (2020). Entropy generation and exergy analysis of premixed fuel-air combustion in microporous media burner. *Entropy*, *22*(10), Article 1104. <https://doi.org/10.3390/e22101104>
- Janvekar, A. A., Miskam, M. A., Abas, A., Zainal, Z. A., Juntakan, T., & Abdullah, M. Z. (2017). Effects of the preheat layer thickness on surface/submerged flame during porous media combustion of the micro burner. *Energy*, *122*, 103-110. <https://doi.org/10.1016/j.energy.2017.01.056>
- Javier, E. S., Mehta, S. A., & Moore, R. G. (2003). An experimental study of controlled gas-phase combustion in porous media for enhanced recovery of oil and gas. *Journal of Energy Resources Technology*, *125*, 64-71. <https://doi.org/10.1115/1.1510522>
- Johar, D. K., Sharma, D., Soni, S. L., Gupta, P. K., & Goyal, R. (2017). Experimental investigation and exergy analysis on thermal storage integrated micro-cogeneration system. *Energy Conversion and Management*, *131*, 127-134. <https://doi.org/10.1016/j.enconman.2016.10.075>
- Li, Q. Q., Li, J., Shi, J. R., & Guo, Z. L. (2019). Effect of heat transfer on flame stability limits in a planar micro-combustor partially filled with porous medium. *Proceedings of the Combustion Institute*, *37*(4), 5645-5654. <https://doi.org/10.1016/j.proci.2018.06.023>

- Liu, Y., Fan, A., Yao, H., & Liu, W. (2016). A numerical investigation on the effect of wall thermal conductivity on flame stability and combustion efficiency in a mesoscale channel filled with fibrous porous medium. *Applied Thermal Engineering*, *101*, 239-246. <https://doi.org/10.1016/j.applthermaleng.2016.02.099>
- Mishra, N. K., & Muthukumar, P. (2018). Development and testing of energy efficient and environment-friendly porous radiant burner operating on liquefied petroleum gas. *Applied Thermal Engineering*, *129*, 482-489. <https://doi.org/10.1016/j.applthermaleng.2017.10.068>
- Mohseni, S., Nadimi, E., Jafarmadar, S., & Rezaei, R. A. (2021). Enhance the energy and exergy performance of hydrogen combustion by improving the micro-combustor outlet in thermofluidic systems. *International Journal of Hydrogen Energy*, *46*(9), 6915-6927. <https://doi.org/10.1016/j.ijhydene.2020.11.114>
- Mujeebu, M. A., Abdullah, M. Z., Bakar, M. Z. A., Mohamad, A. A., & Abdullah, M. K. (2009). Application of porous media combustion technology – A review. *Applied Energy*, *86*(9), 1365-1375. <https://doi.org/10.1016/j.apenergy.2009.01.017>
- Nadimi, E., & Jafarmadar, S. (2019). The numerical study of the energy and exergy efficiencies of the micro-combustor by the internal micro-fin for thermophotovoltaic systems. *Journal of Cleaner Production*, *235*, 394-403. <https://doi.org/10.1016/j.jclepro.2019.06.303>
- Qu, Z. G., & Feng, X. B. (2015). Catalytic combustion of premixed methane/air in a two-zone perovskite-based alumina pileup-pellets burner with different pellet diameters. *Fuel*, *159*, 128-140. <https://doi.org/10.1016/j.fuel.2015.06.066>
- Sharma, M., Mahanta, P., & Mishra, S. C. (2016). Usability of porous burner in kerosene pressure stove: An experimental investigation aided by energy and exergy analyses. *Energy*, *103*, 251-260. <https://doi.org/10.1016/j.energy.2016.02.100>
- Sharma, M., Mishra, S. C., & Acharjee, P. (2009). Thermal efficiency study of conventional pressure stoves equipped with porous radiant inserts. *International Energy Journal*, *10*(4), 247-254.
- Wang, H., Wei, C., Zhao, P., & Ye, T. (2014). Experimental study on temperature variation in a porous inert media burner for premixed methane-air combustion. *Energy*, *72*, 195-200. <https://doi.org/10.1016/j.energy.2014.05.024>
- Yu, B., Kum, S. M., Lee, C. E., & Lee, S. (2013). Combustion characteristics and thermal efficiency for premixed porous-media types of burners. *Energy*, *53*, 343-350. <https://doi.org/10.1016/j.energy.2013.02.035>
- Zeng, H., Wang, Y., Shi, Y., Ni, M., & Cai, N. (2017). Syngas production from CO<sub>2</sub>/CH<sub>4</sub> rich combustion in a porous media burner: Experimental characterization and elementary reaction model. *Fuel*, *199*, 413-419. <https://doi.org/10.1016/j.fuel.2017.03.003>

*Review Article*

## Bacterial Secondary Metabolite Activation Through Epigenetic Modifiers: A Systematic Review

Joana Noor Rashidah Rosli<sup>1,2</sup>, Sharifah Aminah Syed Mohamad<sup>1,2</sup>, Anis Low Muhammad Low<sup>1,3</sup> and Suhaidi Ariffin<sup>3\*</sup>

<sup>1</sup>Atta-ur-Rahman Institute for Natural Products Discovery (AuRIns), UiTM Puncak Alam Campus, 42300 Puncak Alam, Selangor, Malaysia

<sup>2</sup>Faculty of Applied Sciences, UiTM Shah Alam, 40450 Shah Alam, Selangor, Malaysia

<sup>3</sup>Faculty of Applied Sciences, UiTM Negeri Sembilan Branch, Kuala Pilah Campus, 72000 Kuala Pilah, Negeri Sembilan, Malaysia

### ABSTRACT

Bacteria have produced many important secondary metabolites, especially in the pharmaceutical industry. However, the increase in the rediscovery rate of the known compound has been inconvenient to researchers and the pharmaceutical industry. Nevertheless, genome mining in bacteria has uncovered several cryptic metabolic pathways that may be key to discovering new secondary metabolites. The conventional laboratory environment, however, limits the metabolic pathways of microorganisms, making it impossible for secondary metabolites to be produced. As a result, researchers began using epigenetics to change the expression of the genes that code for secondary metabolites in microorganisms. Using epigenetics modifiers, secondary metabolite gene clusters are activated without altering the bacterial DNA sequence. This review article focuses on

the different epigenetic changes and how they affect gene expression to activate the synthesis of secondary metabolites in bacteria.

### ARTICLE INFO

*Article history:*

Received: 31 January 2023

Accepted: 24 August 2023

Published: 23 February 2024

DOI: <https://doi.org/10.47836/pjst.32.2.02>

*E-mail addresses:*

joanarosli11@gmail.com (Joana Noor Rashidah Rosli)  
sharifah459@uitm.edu.my (Sharifah Aminah Syed Mohamad)  
anislow3085@uitm.edu.my (Anis Low Muhammad Low)  
suhaidi@uitm.edu.my (Suhaidi Ariffin)

\*Corresponding author

*Keywords:* Bacterial, epigenetic modifiers, gene clusters, secondary metabolites

### INTRODUCTION

Microorganisms create a wide range of secondary metabolites with industrial

and medicinal applications. Microbial natural products remain an unrivalled source of pharmacological leads and are essential in modern medicine. Alexander Fleming's ground-breaking discovery of penicillin from the fungus *Penicillium notatum* in 1929 triggered a surge in interest in microorganism-derived natural goods. Microorganisms have produced almost 50,000 natural compounds, with over 10,000 having biological functions (Shah et al., 2017). Natural products contribute to 49% of the 175 small-molecule anticancer medicines authorised since the 1940s (Okada et al., 2017). Natural product derivatives comprised about 80% of commercial medications by the 1990s. Due to the expansion of synthetic combinatorial methods and a rise in the rediscovery rates of natural compounds through classical discovery campaigns, this percentage has fallen over the last few decades. Despite several secondary metabolite biosynthetic gene clusters discovered by genome sequencing, some of these genes are silenced under normal conditions (Scherlach & Hertweck, 2021). As a result, only a small amount of secondary metabolites were discovered. Gene expression can be induced through epigenetic modification methods such as DNA methylation and histone modification.

Several significant challenges exist in discovering novel microbial natural product-derived drug leads, including being unable to cultivate most microorganisms found in environmental samples. Next, there is a general lack of tools that can be used to promote the production of small bioactive molecules from a variety of "silent" pathways in microorganisms that are simple to cultivate in the lab, as well as challenges in identifying and dereplicating unknown metabolites from expressed pathways that typically have unpredictably structured and functional features (Trautman & Crawford, 2016). Most companies, however, have stopped or limited their efforts in natural product screening due to the frequent rediscovery of existing chemicals (Li et al., 2009). Antibiotic resistance, cancer chemotherapeutics, and pesticide resistance are all on the rise, posing a threat to current healthcare and agricultural practices. Many routine surgical operations would be complicated without effective antibiotics, and one-third of agricultural commodities would be destroyed without effective pesticides, according to estimates (Rutledge & Challis, 2015). Previous studies have estimated that the global economic impact of antimicrobial resistance will result in more than 10 million annual deaths by 2050, corresponding to a loss of 2.0–3.5% of the global gross world product (Murray et al., 2022). This rising problem emphasises the importance of natural product discovery, particularly in the search for novel antimicrobials to replace antibiotics that have become abused.

In the last few decades, the research on epigenetic regulation of gene function has become more critical in the sciences. In plants, animals, and microbes, the mechanisms and effects of processes including DNA methylation, histone post-translational modifications, non-coding RNAs, and their impact on chromatin structure and dynamics are all engaged in physiological homeostasis (Poças-Fonseca et al., 2020). One approach to this problem

would be stimulating novel secondary metabolite production via epigenetic modification. Epigenetics was initially described as the addition of changes in genetic sequence. However, the term has now extended to include any processes that alter gene activity without changing the DNA sequence (Weinhold, 2006). Epigenetic processes include methylation, acetylation, phosphorylation, ubiquitylation, and sumoylation. These processes can be essential to modulate gene transcription in secondary metabolite production.

The production of the potential metabolites must be stimulated to obtain access to this untapped reservoir of potentially bioactive molecules. This review article will focus on how epigenetic modifications play a role in biosynthetic pathway silencing and how epigenetic changes allow scientists to access a hidden treasure of natural bacterial products. This article highlights the mechanism of epigenetic modification in bacteria and some of the most recent documented discoveries of secondary metabolites from epigenetic modifications.

### **Biosynthetic Gene Clusters for Secondary Metabolites**

Biosynthesis of natural chemicals happens more frequently inside distinct localised sections of the microorganisms' genome known as biosynthetic gene clusters. The biosynthetic gene clusters often contain all the genes essential for metabolite production, regulation, and transport. Biosynthesis gene clusters are groupings of two or three genes that code for a secondary metabolite biosynthetic pathway (Medema et al., 2015). Non-ribosomal peptide synthetases (NRPS), polyketide synthases (PKS), terpenes, and ribosomally synthesised and post-translationally modified peptides (RiPPs) are all structural classes of biosynthetic gene clusters. NRPS and PKS are well-known for synthesising products with beneficial applications in medicine and science, such as antibiotics, antifungals, and immunosuppressants. They are popular for synthesising natural products (Le Govic et al., 2019). Meanwhile, RiPPs are a significant group of natural products with a wide range of bioactivities and high structural diversity (Zhang et al., 2018).

The size of metabolic gene clusters varies highly depending on the complexity of the end product's pathway. For instance, the production of the glycosylated anthracycline nogalamycin is encoded by a gene cluster that contains 32 enzymes (Baral et al., 2018). From assembly to expression control, many clustered genes perform diverse functions in the synthesis and complexity of a natural substance. Secondary metabolite-producing microbes frequently create various chemicals from a single strain. Cumulative research implies that activating gene clusters can vastly speed up the discovery of novel natural compounds with high pharmaceutical potential.

In bacteria, gene regulation is controlled by operon structures. The activation and repression of biosynthetic gene clusters, secondary metabolite production, and other developmental processes of the organism may be based on the differences in gene cluster mechanisms (Chakraborty, 2022). According to a study by Tanaka et al. (2013),

microorganisms' ability to generate beneficial secondary metabolites has been underestimated due to cryptic gene clusters. Genome data analysis of sequenced *Streptomyces* revealed that a single *Streptomyces* genome generally encodes 25–50 biosynthetic gene clusters, and about 90% of them are silent or cryptic under standard laboratory growth conditions (Liu et al., 2021). It concludes that only a small fraction of the constitutively expressed biosynthetic gene clusters has contributed to the current collection of naturally derived drugs. Methods to access the silent majority would significantly impact drug discovery and increase the collection of bioactive molecules.

According to Jackson et al. (2017), only about 10% of the genes encoding small molecules in bacteria have been found to date. Several Gram-negative bacteria genomes, including *Pseudomonas*, *Burkholderia*, and *Clostridium*, were known to have possible cryptic biosynthetic gene cluster repositories (Gross & Loper, 2009; Klaus et al., 2020; Pahalagedara et al., 2020). According to much more meticulous estimations based on genome sequence data, the genus *Streptomyces* alone can create 150,000 secondary metabolites, with only around 5% being identified thus far (Smanski et al., 2016). A genome mining study by Lebedeva et al. (2021) revealed a higher number of biosynthetic gene clusters in two strains of cave *Paenibacillus* sp. compared to a report in 2019 for *Paenibacillus* sp. indicating that the strains encode additional clusters that may range significantly from strain to strain, thus having the potential for novel secondary metabolites.

Meanwhile, in another study by Belknap et al. (2020), gene clusters in *Streptomyces* bacteria showed a wide range and plenty of biosynthetic gene clusters across the genus *Streptomyces*, with hybrid biosynthetic gene clusters vastly enlarging the supply of secondary metabolites, therefore aiding the novel secondary metabolites discovery. They also reported that biosynthetic gene cluster diversity varies significantly among members of the same species. It implies that strain-level genome sequencing can find significant biosynthetic gene cluster variety levels and potentially valuable derivatives of any compounds.

The studies of full genome sequencing revealed more gene clusters that encode enzymes that are generally engaged in specialised metabolite production (Lee et al., 2020; Little et al., 2020; Lebedeva et al., 2021). Although the metabolic products of these new biosynthetic gene clusters are unknown, bioinformatics-based predictions suggested that some of them may encode novel structures. Potentially intriguing gene clusters that may encode chemicals that increase competitiveness in natural habitats can go undetected in the artificial setting of the microbiology laboratory. According to Trautman and Crawford (2016), many cases of microbes' biosynthetic secondary metabolite gene clusters now exceed the number of natural products synthesised in the lab. These cryptic gene clusters are rich in unique bioactive components that can be exploited to build new drugs. Due to the constraints on secondary metabolite production imposed by these vital regulatory



systems, natural product scientists face unique problems. The fact that many microbes have many secondary-metabolite-encoding biosynthetic pathways, yet only a portion of their small-molecule products are identified in the laboratory, exemplifies this point. As a result, heterologous expression platforms and gene modification technologies *in situ* have been developed to bypass transcriptional barriers and directly access natural products from quiet metabolic processes.

The number of secondary metabolites identified by bacteria and fungi may only be the tip of the iceberg. Homologous and heterologous expression of these mysterious secondary metabolites-biosynthetic genes, which are typically "silent" under standard laboratory fermentation conditions, might facilitate the identification of new secondary metabolites. The discovery and prioritising of relevant biosynthetic genes, their activation, and, ultimately, establishing the link between the genes and the encoded secondary metabolites are all significant challenges in achieving this potential. It has given rise to a new field known as genomics-driven natural product discovery, a strategy for identifying novel microbial metabolites with potential medical and agricultural uses that complement traditional bioactivity-guided methods.

Biosynthetic gene clusters typically respond to various environmental stimuli, although the relationship between the regulators and the stimuli is frequently unclear. Native environmental signals may not be present in the laboratory, rendering biosynthetic gene clusters transcriptionally inactive. Different techniques must be used to awaken these clusters and investigate their potential for biosynthesis because cryptic gene clusters seem silent in lab settings. The epigenetic modification technique is suggested to ensure the discovery of novel bioactive natural products to overcome these issues.

### **Epigenetic Modification and Transcription**

Epigenetics are heritable traits that do not involve changes in the DNA sequence. The term "epi" refers to traits that are "on top of" or "in addition to" inheritance through traditional genetics (Pfannenstiel & Keller, 2019). Epigenetic and post-translational modifications have been suggested to affect gene transcription and are likely to be engaged in secondary and primary metabolism (Yang et al., 2022).

Epigenetic mechanisms include DNA methylation and histone modification, which both use DNA modifications to modulate gene expression. Due to epigenetic regulation, unicellular organisms can adapt quickly to environmental stresses or signals (Xue & Acar, 2018). While some of these changes, such as phosphorylation, ubiquitination, and ADP-ribosylation, have been discovered in the past, methylation and acetylation are the most well-studied and prevalent. DNA methylation involves the covalent attachment of a methyl group to the 5-carbon position of the cytosine ring, resulting in the production of 5-methylcytosine, which extends into the main groove of the DNA and inhibits transcription (Bind et al., 2022). Hypermethylation is linked with the repression of gene expression in

the gene promoter region, while hypomethylation is associated with the activation of gene expression.

Gene expression is influenced by post-translational modifications such as DNA methylation, histone acetylation, and phosphorylation at certain times and locations (Akone et al., 2018). Histone acetylation is frequently associated with transcriptional activation, with enzyme inhibition leading to greater gene activation and secondary metabolite production (Strauss & Reyes-Dominguez, 2011).

DNA methyltransferases, histone acetyltransferases, and histone deacetyltransferases are only a few of the epigenetic modifying enzymes discovered. Small molecule inhibitors and activators are powerful tools for activating cryptic biosynthetic gene clusters to create novel natural products.

### Epigenetic Modification by Small Molecules

Epigenetic modifiers, or epidrugs, are natural or manufactured tiny molecular substances that target epigenetic marks or enzymes with epigenetic activity, causing epigenetic changes (Pillay et al., 2022). Treatment of the microorganism with epigenetic modifiers has proven highly successful in stimulating the activation of silent biosynthetic gene clusters to create unknown secondary compounds. Epigenetic modifiers, histone deacetyltransferases (HDAC), and DNA methyltransferases (DNMT) inhibitors can cause cryptic biosynthetic gene cluster activation (Pettit, 2011). DNMT inhibitors impact developmental and other cellular processes by silencing genes, resulting in unique phenotypic features (Ramesha et al., 2018). Two main epigenetic modifiers induce the expression of silent biosynthetic gene clusters. Table 1 shows the epigenetic modifiers with the example of chemical elicitor and their mode of action.

Table 1  
*Comparisons of epigenetic modifier and their mode of actions*

Group of inhibitors	Target	Chemical elicitor	Mode of actions
HDAC inhibitor	HDAC enzyme	SAHA	Inhibit class I and II HDACs
		Valproic acid	
		Trichostatin A	
		Sodium butyrate	
DNMT inhibitor	DNMT enzyme	Apicidin	Inhibit Class I HDACs
		Nicotinamide	Inhibit Class III HDACs
		Sirtinol	
DNMT inhibitor	DNMT enzyme	5-azacytidine	Inhibit DNMT enzyme
		RG-108	

The first group of epigenetic modifiers would be histone deacetylase inhibitor, which usually targets histone deacetylase enzymes. The chemical inhibitors that have succeeded in boosting the secondary metabolites production target Class I and Class II histone deacetylases are SAHA, valproic acid, trichostatin A, sodium butyrate, and apicidin (Kim & Bae, 2011; Li et al., 2020). Also, Class III histone deacetylase inhibitors can alter strain metabolite profile. The most common Class III histone deacetylase inhibitors are nicotinamide and sirtinol. Most Class I and II enzyme inhibitors interrupt the binding of zinc ions. For example, SAHA has a hydroxylamine group that binds to Zn<sup>2+</sup>, linked by a straight alkyl chain to a hydrophobic group that interacts with the amino acids at the rim of the catalytic site to control the specificity of the inhibitor (Moore et al., 2012).

The second group of inhibitors is DNA methyltransferase inhibitor, which inhibits the enzyme DNA methyltransferases. 5-azacytidine is the most used DNA methyltransferase inhibitor to inhibit DNA methylation when incorporated with DNA. Another DNA methyltransferase inhibitor is RG-108, which can block the active site of DNA methyltransferases and is the only epigenetic modifier capable of direct enzyme inhibition (Ou et al., 2018).

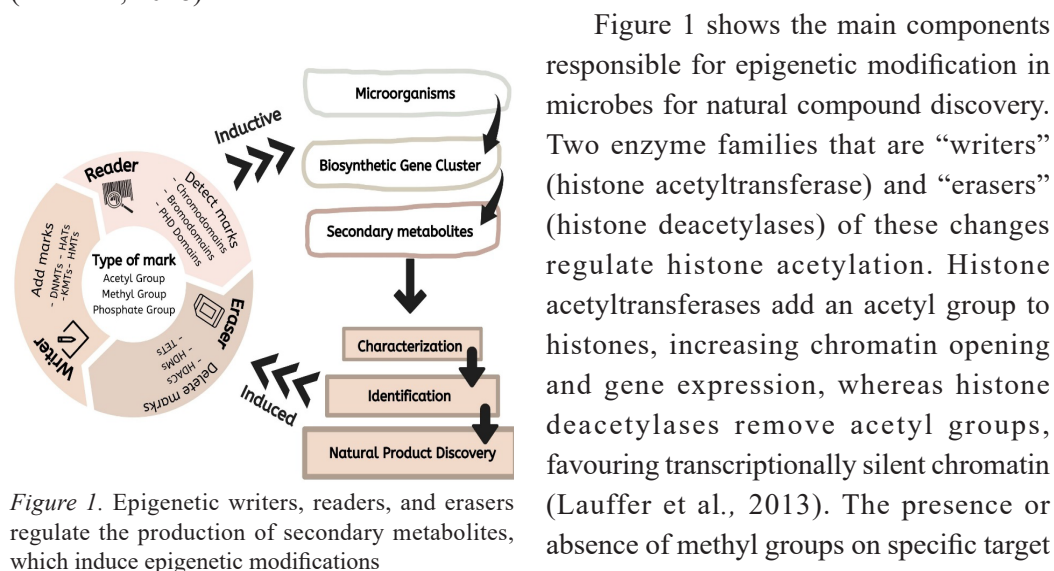


Figure 1. Epigenetic writers, readers, and erasers regulate the production of secondary metabolites, which induce epigenetic modifications

Figure 1 shows the main components responsible for epigenetic modification in microbes for natural compound discovery. Two enzyme families that are “writers” (histone acetyltransferase) and “erasers” (histone deacetylases) of these changes regulate histone acetylation. Histone acetyltransferases add an acetyl group to histones, increasing chromatin opening and gene expression, whereas histone deacetylases remove acetyl groups, favouring transcriptionally silent chromatin (Lauffer et al., 2013). The presence or absence of methyl groups on specific target sites is defined as the methylation pattern of a DNA region. Histone acetyltransferases

(HAT), DNMT, and HDAC are among the epigenetic-modifying enzymes discovered so far. HAT adds acetyl groups to the  $\epsilon$ -amino group of nucleosomal histone lysine residues, whereas HDAC removes them (Fischer et al., 2016). Small molecule inhibitors and activators are used as biological probes and possible therapeutic agents and as effective tools for activating cryptic biosynthetic gene clusters for novel natural product manufacture.

## Epigenetic Modifiers Studies on Bacteria

Epigenetic controls have primarily been investigated in eukaryotes, where they play a role in cell differentiation via various processes, including histone modifications and DNA methylation. However, evidence for epigenetic regulation in prokaryotes is becoming more widespread. Table 2 summarises the results of bacteria being treated with epigenetic modifiers and the compounds obtained. Marisol et al. (1995) studied the effects of sinefungin and 5-azacytidine on the development of *Streptomyces antibioticus*, which later revealed that it specifically affects *Streptomyces antibioticus* sporulation; 5-azacytidine also stimulates antibiotic production in *Streptomyces antibioticus* and *Streptomyces coelicolor*. Moore et al. (2012) used sodium butyrate to stimulate the expression of secondary metabolites in *Streptomyces coelicolor* on two different types of media: minimal agar and R5 agar. The result demonstrated that sodium butyrate influences actinorhodin production, increasing secondary metabolite production under poor nutrient conditions. The qPCR results also demonstrated that sodium butyrate induced five cryptic pathways in *Streptomyces coelicolor*. According to Kumar et al. (2016), *Streptomyces coelicolor* treated with 5-azacytidine showed twelve compounds, whereas untreated *Streptomyces coelicolor* showed five compounds in HPLC analysis. The crude extract from cultures treated with 5-azacytidine was also effective against five human pathogenic bacteria. The crude extract from untreated culture was only effective against three human pathogenic bacteria.

A study by Wang et al. (2013) investigated the plausibility of increasing secondary metabolite production in *Pseudomonas aeruginosa* bacteria through epigenetic modification. This study, however, was inconclusive regarding whether the observed changes in metabolite formation were due to epigenetic modifying modifier treatments or co-culturing. Extracts from neither epigenetic modification-treated nor co-cultured cells showed increased bioactivity in antimicrobial assays, yet co-cultures treated with epigenetic modifiers had more bioactivities. Research by Militello et al. (2016), which incorporated 5-azacytidine to study the DNA methylation in *Escherichia coli*, revealed that 5-azacytidine increased gene expression at the early stationary phase, and 62 gene expressions were detected. Other than that, 5-azacytidine was also reported to influence the structure of the bacterial transcriptome in *Escherichia coli*. Meanwhile, a gene expression study on respiratory tract opportunistic pathogen *Burkholderia cenocepacia* using DNMT inhibitor, sinefungin resulted in overexpression of specific genes, including BCAM0820 and BCAL0079, whose function can be linked to the biofilm and motility observed (Vandenbussche et al., 2020).

As the research demonstrated, epigenetic modifiers are essential in activating the silent gene cluster of secondary metabolites, which can boost the production of various bioactive chemicals. Although epigenetic modification is complex, it is one of the most effective methods for synthesising industrial secondary metabolites with pharmacological applications.

Table 2

*The compound obtained from bacteria treated with epigenetic modifiers*

Bacteria	Epigenetic modifiers	Compound obtained	References
<i>Streptomyces antibioticus</i>	5-azacytidine Sinefungin, 1 mM	Rhodomyacin Actinorhodin	Fernandez et al. (1995)
<i>Streptomyces coelicolor</i>	Sodium butyrate, 25 mM	Actinorhodin	Moore et al. (2012)
<i>Pseudomonas aeruginosa</i>	Manzamine A, kahalalide F, Scepterin, ilimaquinone	1-phenazine-carboxamide 1-phenazine carboxylic acid 1-hydroxy-2-heptyl-4-quinolone 2-Octyl-4(1H)-quinolone 2-nonyl-4(1H)-quinolone 2-(2-nonenyl)-4(1H)-quinolone 2-(1-nonenyl)-4(1H)-quinolone Rhamnolipids D-rhamnose $\alpha$ -hydroxy fatty acid moieties	Wang et al. (2013)
<i>Bacillus pumilus</i>	5-azacytidine,	Amicoumacin	Schumacher (2014)
<i>Streptomyces coelicolor</i>	5-azacytidine, 25 $\mu$ M	- (Twelve compounds present in HPLC analysis)	Kumar et al. (2016)
<i>Escherichia coli</i>	5- azacytidine, 0.5–50 $\mu$ g/mL	-	Militello et al. (2016)
<i>Burkholderia cenocepacia</i>	Sinefungin 50 $\mu$ g/ml	-	Vandenbussche et al. (2020)

## CONCLUSION

The significance of secondary metabolites in numerous sectors increases the desire to regulate them by manipulating their synthesis process. The abundance of cryptic and silent pathways in bacterial genomes offers excellent potential for synthesising a novel compound with significant therapeutic properties. These regulatory mechanisms could be altered to increase the production of secondary metabolites. However, it is not easy to activate the numerous quiet gene clusters. Furthermore, understanding the control of secondary metabolism and the activation or silencing of gene clusters is crucial. This article outlines the several types of epigenetic regulation used in bacteria to increase secondary metabolite synthesis.

On the one hand, the rising need for novel pharmaceuticals raised the demand for alternative epigenetic modifiers, and on the other, innovative technologies for high-

throughput natural product discovery. Nowadays, epigenetics is an emerging tool that is gaining importance in microbial biotechnology for synthesising new bioactive chemicals and their increased concentration in microorganisms. The epigenetic modifiers can be considered an effective tool to stimulate the silent or poorly expressed biosynthetic pathways in bacteria, thus stimulating the production of secondary metabolites. However, learning the impact of epigenetic modifiers on DNA structure via DNA methylation analysis and DNA-protein interaction analysis, as well as the effectiveness of their ability to activate a silent biosynthetic gene cluster must be continued.

## ACKNOWLEDGEMENTS

This study was supported by the Ministry of Higher Education Malaysia under the Fundamental Research Grants Scheme 2019 (FRGS/1/2019/STG05/UITM/02/03). The authors would like to thank the Atta-ur-Rahman Institute for Natural Products Discovery (AuRIns), Universiti Teknologi MARA, Malaysia for providing facilities and the anonymous participants for their cooperation and time in providing the researchers' needs.

## REFERENCES

- Akone, S. H., Pham, C.-D., Chen, H., Ola, A. R., Ntie-Kang, F., & Proksch, P. (2018). Epigenetic modification, co-culture and genomic methods for natural product discovery. *Physical Sciences Reviews*, 4(4), Article 20180118. <https://doi.org/10.1515/psr-2018-0118>
- Baral, B., Akhgari, A., & Metsä-Ketelä, M. (2018). Activation of microbial secondary metabolic pathways: Avenues and challenges. *Synthetic and Systems Biotechnology*, 3(3), 163-178. <https://doi.org/10.1016/j.synbio.2018.09.001>
- Belknap, K., Park, C., Barth, B., & Andam, C. (2020). Genome mining of biosynthetic and chemotherapeutic gene clusters in streptomyces bacteria. *Scientific Reports*, 10, Article 2003. <https://doi.org/10.1038/s41598-020-58904-9>
- Bind, S., Bind, S., Sharma, A. K., & Chaturvedi, P. (2022). Epigenetic modification: A key tool for secondary metabolite production in microorganisms. *Frontiers in Microbiology*, 13, Article 784109. <https://doi.org/10.3389/fmicb.2022.784109>
- Chakraborty, P. (2022). Gene cluster from plant to microbes: Their role in genome architecture, organism's development, specialised metabolism and drug discovery. *Biochimie*, 193, 1-15. <https://doi.org/10.1016/j.biochi.2021.12.001>
- Fernandez, M., Soliveri, J., Novella, I., Yebra, M., Barbés, C., & Sánchez, J. (1995). Effect of 5-azacytidine and sinefungin on streptomyces development. *Gene*, 157(1-2), 221-223. [https://doi.org/10.1016/0378-1119\(94\)00672-F](https://doi.org/10.1016/0378-1119(94)00672-F)
- Fischer, N., Sechet, E., Friedman, R., Amiot, A., Sobhani, I., Nigro, G., Sansonetti, P. J., & Sperandio, B. (2016). Histone deacetylase inhibition enhances antimicrobial peptide but not inflammatory cytokine expression upon bacterial challenge. *Proceedings of the National Academy of Sciences of the United States of America*, 113(21), E2993-E3001. <https://doi.org/10.1073/pnas.1605997113>

- Gross, H., & Loper, J. E. (2009). Genomics of secondary metabolite production by pseudomonas spp. *Natural Product Reports*, 26(11), 1408. <https://doi.org/10.1039/b817075b>
- Jackson, S., Crossman, L., Almeida, E., Margassery, L., Kennedy, J., & Dobson, A. (2018). Diverse and abundant secondary metabolism biosynthetic gene clusters in the genomes of marine sponge derived streptomyces spp. isolates. *Marine Drugs*, 16(2), Article 67. <https://doi.org/10.3390/md16020067>
- Kim, H. J., & Bae, S. C. (2011). Histone deacetylase inhibitors: Molecular mechanisms of action and clinical trials as anticancer drugs. *American Journal of Translational Research*, 3(2), 166-179.
- Klaus, J., Coulon, P., Koirala, P., Seyedsayamdost, M., Déziel, E., & Chandler, J. (2020). Secondary metabolites from the *Burkholderia pseudomallei* complex: Structure, ecology, and evolution. *Journal of Industrial Microbiology and Biotechnology*, 47(9-10), 877-887. <https://doi.org/10.1007/s10295-020-02317-0>
- Kumar, J., Sharma, V. K., Singh, D. K., Mishra, A., Gond, S. K., Verma, S. K., Kumar, A., & Kharwar, R. N. (2016). Epigenetic activation of antibacterial property of an endophytic *Streptomyces coelicolor* strain AZRA 37 and identification of the induced protein using MALDI TOF MS/MS. *PLoS One*, 11(2), Article e0147876. <https://doi.org/10.1371/journal.pone.0147876>
- Lauffer, B. E. L., Mintzer, R., Fong, R., Mukund, S., Tam, C., Zilberleyb, I., Flicke, B., Ritscher, A., Fedorowicz, G., Vallero, R., Ortwine, D. F., Gunzner, J., Modrusan, Z., Neumann, L., Koth, C. M., Lupardus, P. J., Kaminker, J. S., Heise, C. E., & Steiner, P. (2013). Histone deacetylase (HDAC) inhibitor kinetic rate constants correlate with cellular histone acetylation but not transcription and cell viability. *Journal of Biological Chemistry*, 288(37), 26926-26943. <https://doi.org/10.1074/jbc.M113.490706>
- Le Govic, Y., Papon, N., Le Gal, S., Bouchara, J., & Vandeputte, P. (2019). Non-ribosomal peptide synthetase gene clusters in the human pathogenic fungus *Scedosporium apiospermum*. *Frontiers in Microbiology*, 10, Article 2062. <https://doi.org/10.3389/fmicb.2019.02062>
- Lebedeva, J., Juknevičiute, G., Čepaitė, R., Vickackaite, V., Pranckutė, R., & Kuisiėne, N. (2021). Genome mining and characterisation of biosynthetic gene clusters in two cave strains of *Paenibacillus* sp. *Frontiers in Microbiology*, 11, Article 612483. <https://doi.org/10.3389/fmicb.2020.612483>
- Lee, N., Hwang, S., Kim, J., Cho, S., Palsson, B., & Cho, B. K. (2020). Mini review: Genome mining approaches for the identification of secondary metabolite biosynthetic gene clusters in *Streptomyces*. *Computational and Structural Biotechnology Journal*, 18, 1548-1556. <https://doi.org/10.1016/j.csbj.2020.06.024>
- Li, G., Tian, Y., & Zhu, W. (2020). The roles of histone deacetylases and their inhibitors in cancer therapy. *Frontiers in Cell and Developmental Biology*, 8, Article 576946. <https://doi.org/10.3389/fcell.2020.576946>
- Li, J. W., & Vederas, J. C. (2009). Drug discovery and natural products: End of an era or an endless frontier? *Science*, 325(5937), 161-165. <https://doi.org/10.1126/science.1168243>
- Little, R. F., Samborsky, M., & Leadlay, P. F. (2020). The biosynthetic pathway to tetromadurin (SF2487/A80577), a polyether tetronate antibiotic. *PLoS One*, 15(9), Article e0239054. <https://doi.org/10.1371/journal.pone.0239054>
- Liu, Z., Zhao, Y., Huang, C., & Luo, Y. (2021). Recent advances in silent gene cluster activation in streptomyces. *Frontiers in Bioengineering and Biotechnology*, 9, Article 632230. <https://doi.org/10.3389/fbioe.2021.632230>
- Medema, M. H., Kottmann, R., Yilmaz, P., Cummings, M., Biggins, J. B., Blin, K., de Bruijn, I., Chooi, Y. H., Claesen, J., Coates, R. C., Cruz-Morales, P., Duddela, S., Düsterhus, S., Edwards, D. J., Fewer, D.

- P., Garg, N., Geiger, C., Gomez-Escribano, J. P., Greule, A., ... & Glöckner, F. O. (2015). Minimum information about a biosynthetic gene cluster. *Nature Chemical Biology*, *11*(9), 625-631. <https://doi.org/10.1038/nchembio.1890>
- Militello, K. T., Simon, R. D., Mandarano, A. H., DiNatale, A., Hennick, S. M., Lazatin, J. C., & Cantatore, S. (2016). 5-azacytidine induces transcriptome changes in *Escherichia coli* via DNA methylation-dependent and DNA methylation-independent mechanisms. *BMC Microbiology*, *16*, Article 130. <https://doi.org/10.1186/s12866-016-0741-4>
- Moore, J. M., Bradshaw, E., Seipke, R. F., Hutchings, M. I., & McArthur, M. (2012). Use and discovery of chemical elicitors that stimulate biosynthetic gene clusters in *Streptomyces* bacteria. *Methods in Enzymology*, *517*, 367-385. <https://doi.org/10.1016/B978-0-12-404634-4.00018-8>
- Murray, C., Ikuta, K., Sharara, F., Swetschinski, L., Robles Aguilar, G., & Gray, A., Gray, A., Han, C., Bisignano, C., Rao, P., Wool, E., Johnson, S. C., Browne, A. J., Chipeta, M. G., Fell, F., Hackett, S., Haines-Woodhouse, G. Hamadani, B. H. K., Kumaran, E. A. P., McManigal, B., ... & Naghavi, M. (2022). Global burden of bacterial antimicrobial resistance in 2019: A systematic analysis. *The Lancet*, *399*(10325), 629-655. [https://doi.org/10.1016/S0140-6736\(21\)02724-0](https://doi.org/10.1016/S0140-6736(21)02724-0)
- Okada, B. K., & Seyedsayamdost, M. R. (2017). Antibiotic dialogues: Induction of silent biosynthetic gene clusters by exogenous small molecules. *FEMS Microbiology Reviews*, *41*(1), 19-33. <https://doi.org/10.1093/femsre/fuw035>
- Ou, Y., Zhang, Q., Tang, Y., Lu, Z., Lu, X., Zhou, X., & Liu, C. (2018). DNA methylation enzyme inhibitor RG108 suppresses the radioresistance of esophageal cancer. *Oncology Reports*, *39*(3), 993-1002. <https://doi.org/10.3892/or.2018.6210>
- Pahalagedara, A. S. N. W., Flint, S., Palmer, J., Brightwell, G., & Gupta, T. B. (2020). Antimicrobial production by strictly anaerobic clostridium spp. *International Journal of Antimicrobial Agents*, *55*(5), Article 105910. <https://doi.org/10.1016/j.ijantimicag.2020.105910>
- Pettit, R. (2011). Small-molecule elicitation of microbial secondary metabolites. *Microbial Biotechnology*, *4*(4), 471-478. <https://doi.org/10.1111/j.1751-7915.2010.00196.x>
- Pfannenstiel, B. T., & Keller, N. P. (2019). On top of biosynthetic gene clusters: How epigenetic machinery influences secondary metabolism in fungi. *Biotechnology Advances*, *37*(6), Article 107345. <https://doi.org/10.1016/j.biotechadv.2019.02.001>
- Pillay, L. C., Nekati, L., Makhwitine, P. J., & Ndlovu, S. I. (2022). Epigenetic activation of silent biosynthetic gene clusters in endophytic fungi using small molecular modifiers. *Frontiers in Microbiology*, *13*, Article 815008. <https://doi.org/10.3389/fmicb.2022.815008>
- Poças-Fonseca, M. J., Cabral, C. G., & Manfrão-Netto J. H. C. (2020). Epigenetic manipulation of filamentous fungi for biotechnological applications: A systematic review. *Biotechnology Letters*, *42*, 885-904. <https://doi.org/10.1007/s10529-020-02871-8>
- Ramesha, K., Mohana, N., Nuthan, B., Rakshith, D., & Satish, S. (2018). Epigenetic modulations of mycoendophytes for novel bioactive molecules. *Biocatalysis and Agricultural Biotechnology*, *16*, 663-668. <https://doi.org/10.1016/j.bcab.2018.09.025>
- Rutledge, P. J., & Challis, G. L. (2015). Discovery of microbial natural products by activation of silent biosynthetic gene clusters. *Nature Reviews Microbiology*, *13*, 509-523. <https://doi.org/10.1038/nrmicro3496>



- Scherlach, K., & Hertweck, C. (2021). Mining and unearthing hidden biosynthetic potential. *Nature Communication*, 12, Article 3864. <https://doi.org/10.1038/s41467-021-24133-5>
- Schumacher, J. D. (2014). *Epigenetic modification and analysis of natural product gene clusters to enhance drug discovery from bacteria* (Publication no. 309). [Master's thesis]. University of Rhode Island, USA. <https://doi.org/10.23860/thesis-schumacher-justin-2014>
- Shah, A. M., Shakeel-U-Rehman, Hussain, A., Mushtaq, S., Rather, M. A., Shah, A., Ahmad, Z., Khan, I. A., Bhat, K. A., & Hassan, Q. P. (2017). Antimicrobial investigation of selected soil actinomycetes isolated from unexplored regions of Kashmir Himalayas, India. *Microbial Pathogenesis*, 110, 93-99. <https://doi.org/10.1016/j.micpath.2017.06.017>
- Smanski, M., Zhou, H., Claesen, J., Shen, B., Fischbach, M., & Voigt, C. (2016). Synthetic biology to access and expand nature's chemical diversity. *Nature Reviews Microbiology*, 14, 135-149. <https://doi.org/10.1038/nrmicro.2015.24>
- Strauss, J., & Reyes-Dominguez, Y. (2011). Regulation of secondary metabolism by chromatin structure and epigenetic codes. *Fungal Genetics and Biology*, 48(1), 62-69. <https://doi.org/10.1016/j.fgb.2010.07.009>
- Tanaka, Y., Kasahara, K., Hirose, Y., Murakami, K., Kugimiya, R., & Ochi, K. (2013). Activation and products of the cryptic secondary metabolite biosynthetic gene clusters by rifampin resistance (rpoB) mutations in actinomycetes. *Journal of Bacteriology*, 195(13), 2959-2970. <https://doi.org/10.1128/JB.00147-13>
- Trautman, E. P., & Crawford, J. M. (2016). Linking biosynthetic gene clusters to their metabolites via pathway-targeted molecular networking. *Current Topics in Medicinal Chemistry*, 16(15), 1705-1716. <https://doi.org/10.2174/1568026616666151012111046>
- Vandenbussche, I., Sass, A., Pinto-Carbó, M., Mannweiler, O., Eberl, L., & Coenye, T. (2020). DNA methylation epigenetically regulates gene expression in *Burkholderia cenocepacia* and controls biofilm formation, cell aggregation, and motility. *Molecular Biology and Physiology*, 5(4), Article e00455-20. <https://doi.org/10.1128/mSphere.00455-20>
- Wang, B., Waters, A. L., Sims, J. W., Fullmer, A., Ellison, S., & Hamann, M. T. (2013). Complex marine natural products as potential epigenetic and production regulators of antibiotics from a marine *Pseudomonas aeruginosa*. *Microbial Ecology*, 65, 1068-1075. <https://doi.org/10.1007/s00248-013-0213-4>
- Weinhold B. (2006). Epigenetics: The science of change. *Environmental Health Perspectives*, 114(3), A160-A167. <https://doi.org/10.1289/ehp.114-a160>
- Xue, Y., & Acar, M. (2018). Mechanisms for the epigenetic inheritance of stress response in single cells. *Current Genetics*, 64, 1221-1228. <https://doi.org/10.1007/s00294-018-0849-1>
- Yang, K., Tian, J., & Keller, N. P. (2022). Post-translational modifications drive secondary metabolite biosynthesis in aspergillus: A review. *Environmental Microbiology*, 24(7), 2857-2881. <https://doi.org/10.1111/1462-2920.16034>
- Zhang, Y., Chen, M., Bruner, S., & Ding, Y. (2018). Heterologous production of microbial ribosomally synthesised and post-translationally modified peptides. *Frontiers in Microbiology*, 9, Article 1801. <https://doi.org/10.3389/fmicb.2018.01801>



## Baby Weight and Length Measurement System with Data Storage Using MySQL Database

Rifqi Kamaddin Sholeh Lubis, Rahmat Rasyid and Meqorry Yusfi\*

*Department of Physics, Faculty of Mathematics and Natural Sciences, Andalas University, Pauh, Padang 25163, Indonesia*

### ABSTRACT

Baby weight and length measurement system has been designed based on ultrasonic and load cell sensors with data storage using MySQL database and website interface. This research aims to produce a baby weight and length measurement system with microcontroller NodeMCU ESP32. The system is designed with an ultrasonic sensor HC-SR04 and four half-bridge load cells of 50 kg. The ultrasonic sensor works on the piezoelectric and inverse piezoelectric principles, while load cell sensors work on strain gauge principles. An ultrasonic sensor measures body length, while a load cell sensor measures body weight. According to the Ministry of Health of the Republic of Indonesia's regulations, this system also has an LCD 20×4 to display measurement and nutritional status assessment results. The experiment used four doll objects with different lengths and weights. This research shows that the ultrasonic sensor HC-SR04 used in this research has an average error of 0.494% in length measurement. The load cell sensor and HX711 ADC used in this research has an average error of 0.949% in weight measurement. The designed system automatically assesses the nutritional status and stores the measurement result and nutritional status in the database to be displayed on the website.

*Keywords:* Anthropometric, HC-SR04 sensor, load cell, NodeMCU ESP32, website

### ARTICLE INFO

*Article history:*

Received: 01 February 2023

Accepted: 07 September 2023

Published: 23 February 2024

DOI: <https://doi.org/10.47836/pjst.32.2.03>

*E-mail addresses:*

[rifqi.kamaddin@gmail.com](mailto:rifqi.kamaddin@gmail.com) (Rifqi Kamaddin Sholeh Lubis)

[rahmatrasyid@sci.unand.ac.id](mailto:rahmatrasyid@sci.unand.ac.id) (Rahmat Rasyid)

[meqorryyusfi@sci.unand.ac.id](mailto:meqorryyusfi@sci.unand.ac.id) (Meqorry Yusfi)

\* Corresponding author

### INTRODUCTION

Having a healthy child is every parent's dream. Parents can maintain the child's growth from birth until the age of five years old in an optimal range. Children who experience growth and development not in

line with their age may face various consequences, such as hindering brain development, increased susceptibility to illnesses and weakened immune systems, excessive anxiety or fear, inability to control emotions, and cognitive disorders (Merita, 2019). Their weight and length must be maintained within their anthropometric standard range to determine if a child is growing optimally. Generally, anthropometry assesses the human body's size, proportion, and composition (Sari et al., 2017). Child anthropometrics is a collection of data on body size, proportion, and composition to assess infants' nutritional status and growth trends (Kementrian Kesehatan Republik Indonesia, 2020). The baby's growth is usually observed as a body length and weight change.

Body length measurement can be done by measuring from the feet to the baby's head using a ruler, while body weight can be measured using a weight scale. The result of this measurement is then compared with the values in the child anthropometric standard table to see if the child is overweight or underweight (Wahyudi et al., 2021). This process is carried out manually by health workers in public health centres. This process is considered less effective because the result must be compared with table data and graphs from standard anthropometrics, which takes up much time and is prone to mistakes when comparing or human error while conducting the measurement.

Several studies have built measurements of body weight and length systems. Fajri and Wildian (2014) have made a height and weight measurement instrument based on microcontroller ATmega 8535 and used a phototransistor to measure the weight and body length. The built system is only for measurement without storing the measurement result. Akbar and Rachmat (2018) also built a measurement system using an ultrasonic transducer for body length measurement and a strain gauge for body weight measurement, and they displayed the result in LCD. The system sends and stores the result to a personal computer using PLX-DAQ software with a USB cable. The nutritional status assessment system based on Arduino Nano was built by Ardianto et al. (2022). This system measures body weight with a load cell sensor and body length with an ultrasonic sensor. Arduino processes the measurement result and sends it to a smartphone wirelessly using Bluetooth.

Based on the above problem, the body weight and length measurement system was developed using microcontroller NodeMCU ESP32. An ultrasonic HC-SR04 sensor was selected to measure the body length, and a load cell sensor was chosen to measure the body weight. The developed system can store measurement results in the MySQL database and display the data on the website. The website is intended to see changes in body weight and length between the measurements. The data stored in MySQL is transferred using a WiFi connection without any additional device. The system can also display the measured height, weight, and nutritional status on an LCD.

## METHODS

### Tools and Materials

A sensor is a device that converts a physical quantity into a signal that an electronic device can read. Sensors are used in various applications, such as industrial automation, medical diagnostics, and home automation (Wilson, 2005).

The measurement system uses an HC-SR04 ultrasonic sensor for length measurement sensor and a load cell sensor as a weight measurement sensor. The HC-SR04 sensor consists of two ultrasonic transducers, a transmitter, and a receiver. The transmitter side works with inverse piezoelectric effect to create and transmit an ultrasonic sound, while the receiver side works with direct piezoelectric effect to perceive the echo. The immediate piezoelectric effect is when mechanical stress is applied to a piezoelectric material, causing it to generate an electric charge. The inverse piezoelectric effect is when an electric current is applied to a piezoelectric material, causing it to deform (Casini, 2016).

The transmitter creates and emits ultrasonic sound at 40 kHz to the object. These waves travel to the object and are reflected to the receiver. The time it takes for the ultrasonic waves to travel to the objects and back is measured by the sensor and sent to a microcontroller to calculate the distance (Zhmud et al., 2018). Ultrasonic sensors are chosen due to their high object detection capability for the wood material used for the system (Adarsh et al., 2016).

A load cell sensor is a device that measures force and converts it into an electrical signal. It uses strain gauges, small devices that change their resistance when deformed. The strain gauges are arranged in a Wheatstone bridge configuration, a type of electrical circuit that is very sensitive to changes in resistance. When a force is applied to the load cell, it causes the strain gauges to deform, which changes their resistance. This change in resistance is changing the voltage difference in the Wheatstone bridge to be measured (Ajibola et al., 2018).

The voltage difference in the Wheatstone bridge usually has a very small value (in  $\mu\text{V}$ ). An analog-digital converter (ADC) with a high resolution is required to measure the tiny voltage difference (Marcelino et al., 2018). ADC is an electronic circuit used to convert analogue signals to digital signals. It converts continuous voltage signals into discrete signal form, allowing them to be processed by a microcontroller (Fraden, 2016).

LCD or Liquid Crystal Display is a type of display media that utilizes liquid crystals to generate the desired output (Kho, 2018). LCDs do not produce light on their own. Instead, they use a backlight or reflector to provide light. The light is then passed through the liquid crystals, which control how much light can pass through. It allows the LCD to create images by controlling the light that is allowed to pass through the crystals (Gabriel, 2020). The system used LCD to display measurement results and nutritional status results. A personal computer (PC) stores the data in the MySQL database and displays the data on the website. The weight scale is used to compare the load cell reading, and the ruler is used to compare the ultrasonic reading.

### Hardware Design

The system block diagram can be seen in Figure 1. The body weight was measured with a load cell sensor, and the body length was measured with an ultrasonic sensor HC-SR04. The output from the load cell sensor is then sent to the HX711 ADC to be changed from an analogue signal to a digital signal before being sent to NodeMCU ESP32. The ultrasonic HC-SR04 output is sent directly to NodeMCU ESP32 to be processed. The system’s electronic circuit can be seen in Figure 2, and the system’s overall design can be seen in Figure 3.

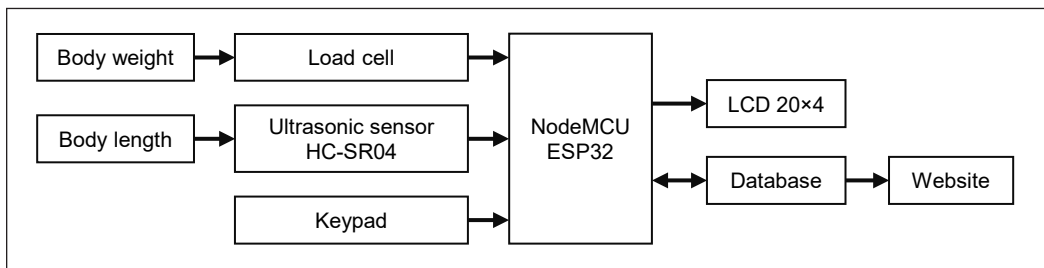


Figure 1. Block diagram of baby weight and length measurement system with data storage using MySQL database

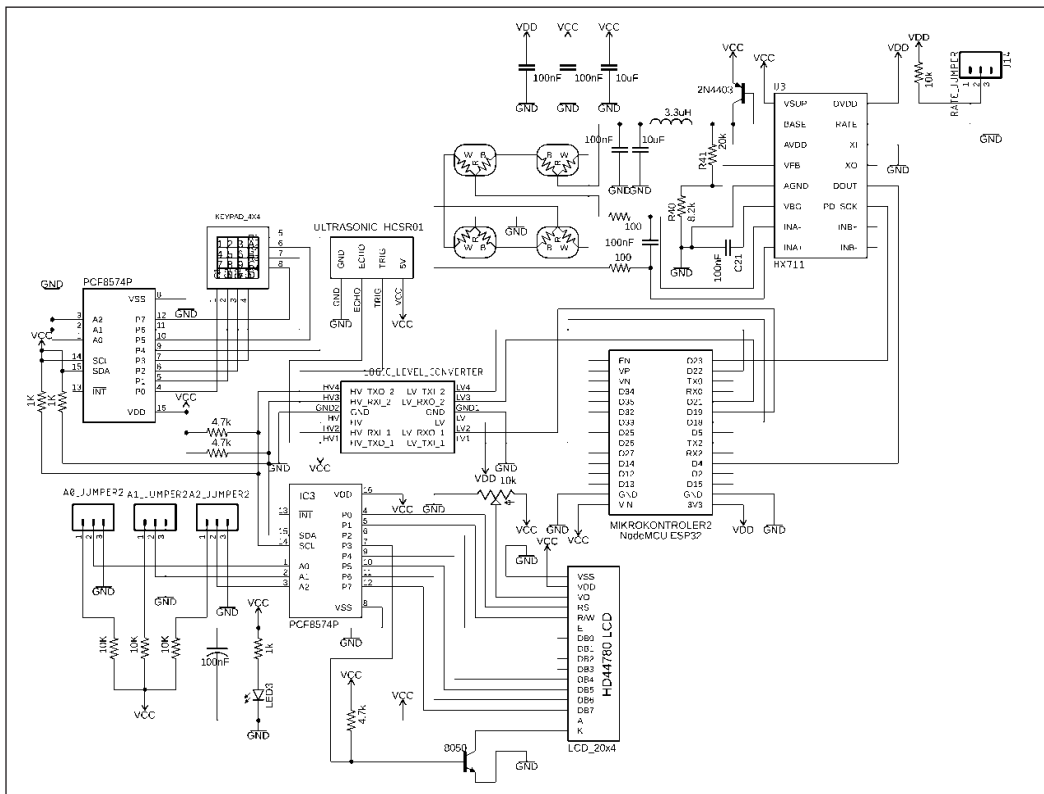


Figure 2. The circuit schematic of baby weight and length measurement system

All data that NodeMCU ESP32 has processed is sent to the database server using a WiFi connection to be displayed on the website and to assess nutritional status. Weight measurement, length measurement, and nutritional status assessment results are also displayed on a 20×4 LCD. The website also shows the measurement record based on ID to track the body weight and length changes in graphs and tables.

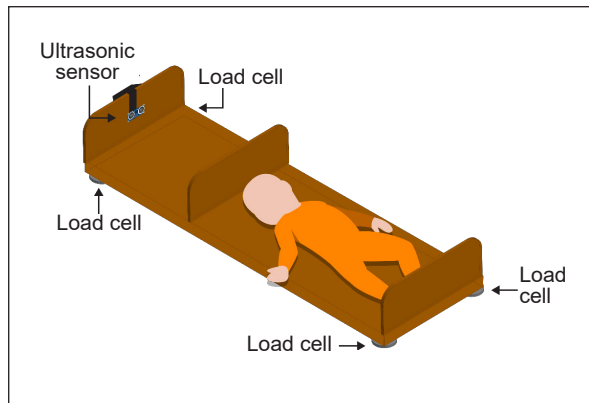


Figure 3. The hardware design of the baby weight and length measurement system

### Characterization of HC-SR04 and Load Cell Sensor

Sensor characterization is used to determine the sensitivity of a sensor by subjecting it to a series of tests. A ruler is used to characterize the HC-SR04 sensor, and the weight scale is used to characterize the load cell sensor. The characterization of the HC-SR04 sensor is done by giving the sensor several distances and recording the time for the ultrasonic wave to propagate from the transmitter and back to the receiver. The recorded time is then used to find the transfer function to calculate the distance.

The load cell sensor characterization is done by connecting the load cell sensor to HX711 ADC and then to the microcontroller. The characterization is done by giving the sensor various masses and recording each ADC decimal output from HX711. This value is then used to find the calibration factor to determine the measured mass.

### Software Design

The software is used to control how the hardware works. Figure 4 shows the flowchart of how the software works. NodeMCU ESP32 will try to connect to the WiFi network. If NodeMCU ESP32 cannot connect to the WiFi network, the NodeMCU will open the WiFi setting page, and if the NodeMCU ESP32 connects to the WiFi network, the system will wait for ID input from the keypad. The system will read the name, gender, and age in the database based on the input ID. The system will measure the weight from the load cell sensor and length from the ultrasonic sensor until the save button is pressed. After pressing the save button, the NodeMCU ESP32 will send the measured height and weight to the database. The database will send back the nutritional assessment result, and the LCD will display the length measurement result, weight measurement result, and nutritional assessment status.

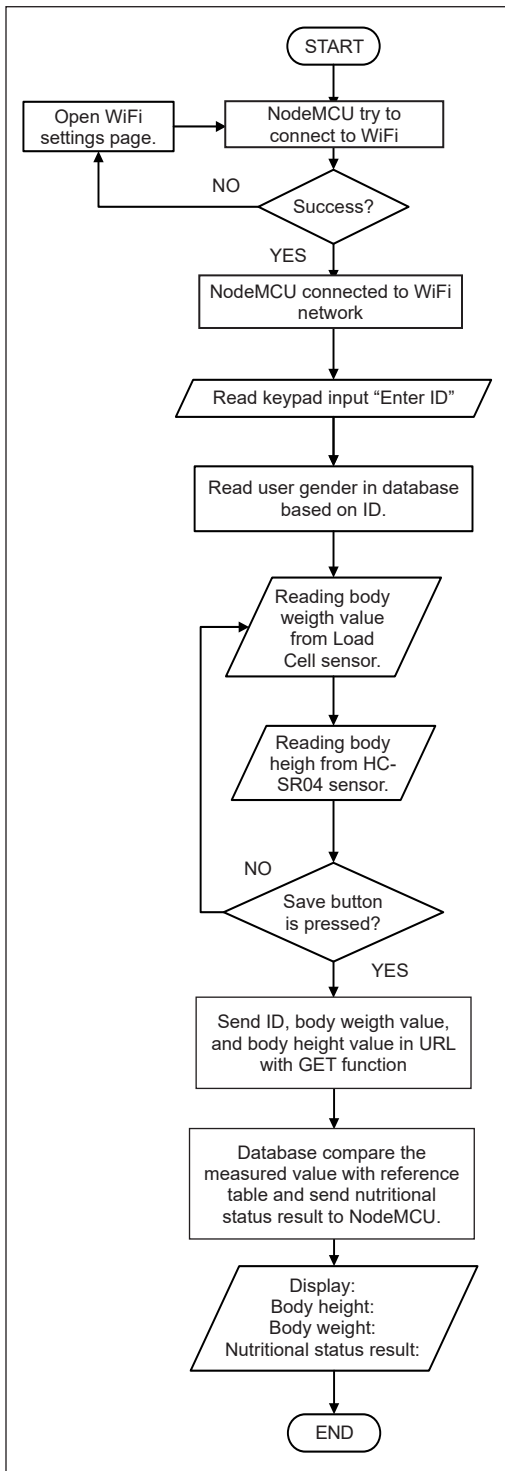


Figure 4. The software flowchart of baby weight and length measurement system

### Database Design

The database in this system is built with MySQL and uses XAMPP software. The database is used to store the required data for the system. The database consists of several tables that have their own function.

### Website Design

The website is used as an interface system for the user. The website displayed the data from the database to be easy to understand. The website can also change user data such as name, date of birth, and gender. The website consists of several pages that have their function. The pages are index, view, edit, and add users.

## RESULT AND DISCUSSION

### Characterization and Testing of the HC-SR04 Sensor as a Distance Sensor

Characterizing the HC-SR04 sensor begins with giving the sensor various distances and recording the ultrasonic sound time to propagate from transmitter to receiver. The record time is from 0 cm to 50 cm with an increase of 5 cm. The graph of change in distance with time is shown in Figure 4. According to Figure 5, the transfer function of the ultrasonic sensor is  $y = -17.7x + 115.41$ , and this equation is used to find the distance in the ultrasonic sensor.

Testing the HC-SR04 sensor begins by giving the sensor various distances and comparing the distance reading from the sensor with a ruler. The distance is set from 5 cm to 50 cm with an increase of 5 cm. Table 1 shows the result of the HC-SR04 sensor



test with an average error of 0.494%. It indicates that the sensor used in this system can operate properly.

**Characterization and Testing of the Load Cell Sensor with HX711 ADC as a Weight Sensor**

The load cell sensor characterization begins by giving the sensor several weights and recording the decimal number from the HX711 ADC output to find the calibration factor. The calibration factor value is obtained by subtracting the decimal value when there is a mass with a decimal value when no mass is given and dividing the value by a known mass value. The characterization result of the load cell sensor with HX711 ADC is shown in Table 2. The average calibration factor is then used to calculate the body weight.

The load cell sensor testing begins by giving the sensor various weights and comparing the weight reading from the sensor with the weight scale. The weight is set from 1 kg to 20 kg with an increase of 1 kg. Table 3 shows the load cell sensor test result with an average error of 0.949%, and the sensor used in this system can operate properly.

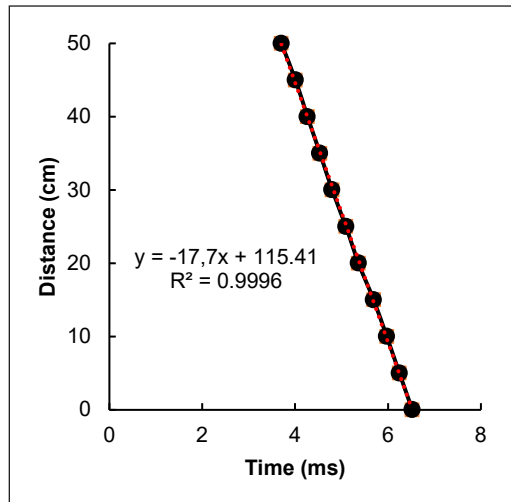


Figure 5. Graph of the distance over time

Table 1  
HC-SR04 sensor testing result

Ruler	HC-SR04 sensor					Average	Error (%)
	I	II	Attempt No-III	IV	V		
5	4.960	5.080	5.010	5.080	5.080	5.042	0.840
10	9.840	9.960	9.900	9.900	9.900	9.900	1.000
15	15.020	15.020	14.850	14.900	14.900	14.938	0.413
20	19.950	19.950	19.890	19.890	19.840	19.904	0.480
25	25.140	25.140	25.020	25.020	25.070	25.078	0.312
30	29.770	29.770	30.120	29.740	30.240	29.928	0.240
35	35.020	35.120	35.070	35.070	35.070	35.070	0.200
40	39.960	39.990	39.960	39.690	39.960	39.912	0.220
45	44.680	44.660	45.070	45.070	45.070	44.910	0.200
50	49.360	49.410	49.410	49.820	49.410	49.482	1.036
Average error (%)							0.494

Table 2  
*Characterization of load cell sensor*

Mass (g)	Decimal output					Average	Tare value	Calibration factor
	Attempt No-							
	I	II	III	IV	V			
0	1122396	1112411	1112387	1112418	1112366	1114396	-	-
1000	1132303	1132354	1132477	1132502	1132542	1132436	20070	20.07
2000	1155578	1155544	1155600	1155583	1155587	1155578	43212	21.61
3000	1176700	1176719	1176714	1176711	1176718	1176712	64346	21.45
4000	1199026	1199098	1199062	1199052	1199055	1199059	86693	21.67
5000	1221840	1221748	1221693	1221660	1221695	1221727	109361	21.87
6000	1242535	1242518	1242521	1242531	1242559	1242533	130167	21.69
7000	1262268	1262239	1262199	1262204	1262225	1262227	149861	21.41
8000	1284563	1284560	1284562	1284600	1284596	1284576	172210	21.53
9000	1305386	1305505	1305604	1305700	1305747	1305588	193222	21.47
10000	1327521	1327493	1327413	1327411	1327420	1327452	215086	21.51
11000	1350261	1350293	1350238	1350256	1350219	1350253	237887	21.63
12000	1372009	1371996	1371945	1371888	1371875	1371943	259577	21.63
13000	1393600	1393604	1393515	1393458	1393447	1393525	281159	21.63
14000	1418121	1417783	1417790	1417619	1417640	1417791	305425	21.82
15000	1437050	1436997	1437027	1436984	1436968	1437005	324639	21.64
16000	1458779	1458772	1458694	1458646	1458567	1458692	346326	21.65
17000	1480731	1480753	1480707	1480671	1480609	1480694	368328	21.67
18000	1502852	1502438	1502206	1502022	1501965	1502297	389931	21.66
19000	1524726	1524718	1524614	1524466	1524386	1524582	412216	21.70
20000	1548779	1548733	1548653	1548614	1548552	1548666	436300	21.82
Average calibration factor								21.56

Table 3  
*Result of load cell sensor testing*

Weight scale	Load cell					Average	Error (%)
	Attempt No-						
	I	II	III	IV	V		
1	1.02	1.02	0.98	0.95	0.92	0.98	2.200
2	2.01	2.00	2.01	2.04	2.05	2.02	1.100
3	2.97	2.97	2.97	2.98	2.99	2.98	0.800
4	3.95	4.07	4.06	4.07	4.06	4.04	1.050
5	4.86	5.11	5.11	5.12	5.13	5.07	1.320
6	6.08	6.09	6.12	6.09	6.10	6.10	1.600
7	7.09	7.11	7.12	7.14	7.13	7.12	1.686
8	8.10	8.11	8.10	8.11	8.09	8.10	1.275

Table 3 (continue)

Weight scale	Load cell					Average	Error (%)
	I	II	Attempt No- III	IV	V		
9	9.16	9.18	9.15	9.14	9.13	9.15	1.689
10	10.13	10.18	10.15	10.16	9.96	10.12	1.160
11	11.14	11.14	11.14	11.15	11.14	11.14	1.291
12	12.15	11.99	12.00	12.01	12.02	12.03	0.283
13	13.03	13.05	13.06	13.05	13.10	13.06	0.446
14	14.15	14.10	14.14	14.08	14.06	14.11	0.757
15	15.13	15.11	15.11	15.11	15.09	15.11	0.733
16	15.96	15.94	15.92	15.93	15.91	15.93	0.425
17	16.96	16.97	16.96	16.95	16.94	16.96	0.259
18	17.96	17.96	17.91	17.91	17.91	17.93	0.389
19	18.94	18.93	18.94	18.91	18.91	18.93	0.389
20	20.00	20.02	20.04	20.04	20.03	20.03	0.130
Average error (%)							0.949

### System Database

A database of baby weight and length measurement systems has been successfully built. This database is used to store the data for the website. The database is consisting of several table such as `bb_pb_l`, `bb_pb_w`, `bb_u_l`, `bb_u_w`, `gender`, `length_status`, `pb_u_l`, `pb_u_w`, `record`, `user`, `weight_status`, and `weight_status_by_length`.

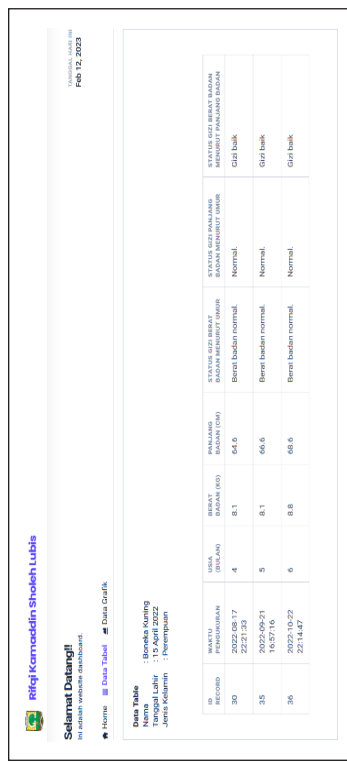
### Overall Test of Baby Weight and Length Measurement System

A comprehensive test of the system is done by giving four doll subjects with different lengths and masses with their ID. The test begins with giving ID input from the keypad. The system will display the name, gender, and age in LCD based on ID. The system then measures the weight with the load cell sensor and the length with the HC-SR04 sensor. While measuring, the user can choose to save the measurement result in the database by pressing A in the keypad, do the tare on weight scales by pressing B in the keypad, or recalibrate the load cell sensor to find the new calibration factor by pressing C in the keypad. When the A button is pressed, the system will record the weight and length measurement result and send it to the database for assessment of nutritional status. The database returns the assessment result to the system, displaying the LCD's measured weight, length, and nutritional status. The overall test result of the system can be seen in Table 4.

Measurement results and nutritional status data are also successfully stored in the database and displayed on the website. The website displayed the measurement history in two forms: the table form and the graph form (Figure 6).

Table 4  
Overall system test result

ID	Subject/Gender (M/F)	Age (Month)	Comparator		Designed system		Error (%)	
			Length (cm)	Weight (kg)	Length (cm)	Weight (kg)	Length (cm)	Weight (kg)
1	Yellow doll/F	4	65	8.1	64.6	8.1	0.662	0.124
		5	66	8.3	66.6	8.1	0.848	2.289
		6	68	9.0	68.6	8.8	0.897	2.333
2	Red doll/M	7	70	9.3	70.9	9.2	1.243	1.392
		8	72	9.5	72.7	9.4	1.000	1.677
		9	74	9.7	74.6	9.6	0.865	1.232
3	Blue doll/F	2	57	5.7	57.6	5.7	0.965	0.526
		3	60	7.0	60.8	6.7	1.333	3.885
		4	62	7.5	62.6	7.4	1.065	1.065
4	Rabbit doll/M	2	58	6.2	58.1	6.1	0.310	2.419
		3	62	6.5	62.6	6.4	1.016	1.538
		4	64	7.3	65.1	7.1	1.703	2.195
Average Error							0.988	1.723



(a) (b)

Figure 6. Website view: (a) table view; and (b) graph view

## CONCLUSION

This research has successfully developed a system for measuring body weight and length using MySQL database data storage. The load cell sensor can be utilized with a calibration factor value of 21.56 and has an error percentage of 0.949% in weight measurement. The HC-SR04 sensor produces an average error of 0.494% in length measurement with transfer function  $y = -17.7x + 115.41$ . The system also successfully sent the measurement result to the database, which can be accessed using a web browser to see measurement history and nutritional status. Thus, the system is functioning well and suitable for use.

The system can store measurement results and classify nutritional status, which is impossible with the system designed by Fajri and Wildian (2014). The system also uses a WiFi network to transfer data, which offers greater flexibility and eliminates the need for cables. In contrast, the system designed by Akbar and Rachmat (2018) still uses a cable, and the system designed by Ardianto uses Bluetooth, which can only transmit data over short distances.

## ACKNOWLEDGEMENT

The author thanks everyone who had helped and supported completing the study and publication. The author also thanks the reviewers for their dedication, timing, and fruitful comments in improving and increasing the quality of the manuscript.

## REFERENCES

- Ajibola, O. O. E., Sunday, O. O., & Eyehorua, D. O. (2018). Development of an automated intravenous blood infusion monitoring system using a load cell sensor. *African Journals of Applied Sciences and Environmental Management*, 22(10), 1557-1561. <https://dx.doi.org/10.4314/jasem.v22i10.04>
- Akbar, W. A., & Rachmat, H. H. (2018). Rancang bangun sistem pengukur massa tubuh dan panjang badan elektronik terintegrasi untuk evaluasi gizi balita [Design of an integrated electronic body mass and body length measurement system for evaluating toddler nutrition]. *ELKOMIKA*, 6(1), 125-139. <https://doi.org/10.26760/elkomika.v6i1.125>
- Adarsh, S., Kaleemuddin, S. M., Bose, D., & Ramachandran, K. I. (2016). Performance comparison of infrared and ultrasonic sensors for obstacles of different materials in vehicle/ robot navigation applications. *IOP Conference Series: Materials Science and Engineering*, 149(1), Article 012141. <https://dx.doi.org/10.1088/1757-899X/149/1/012141>
- Ardianto, E. T., Elisanti, A. D., & Husin, H. (2022). Arduino and android-based anthropometric detection tools for Indonesian children. In *2nd International Conference on Social Science, Humanity and Public Health (ICOSHIP 2021)* (pp. 254-259). Atlantis Press. <https://doi.org/10.2991/assehr.k.220207.043>
- Casini, M. (2016). *Smart Buildings: Advanced Materials and Nanotechnology to Improve Energy Efficiency and Environmental Performance*. Elsevier. <https://doi.org/10.1016/C2015-0-00182-4>

- Fajri, N., & Wildian. (2014). Rancang bangun alat ukur tinggi dan berat badan bayi berbasis mikrokontroler ATmega8535 dengan sensor fototransistor [Design of a baby height and weight measuring instrument based on an ATmega8535 microcontroller with a phototransistor sensor]. *Jurnal Fisika Unand*, 3(3), 163-169.
- Fraden, J. (2016). *Handbook of Modern Sensors*. Springer International Publishing. <https://doi.org/10.1007/978-3-319-19303-8>
- Gabriel, M. M., & Kuria, K. P. (2020). Arduino uno, ultrasonic sensor HC-SR04 motion detector with display of distance in the LCD. *International Journal of Engineering Research & Technology*, 9(5), 936-942. <http://dx.doi.org/10.17577/IJERTV9IS050677>
- Kementrian Kesehatan Republik Indonesia. (2020, January 20). *Peraturan Menteri Kesehatan Republik Indonesia no.2 tahun 2020 tentang standar antropometri anak* [Regulation of the Minister of Health of the Republic of Indonesia No.2 of 2020 concerning Child Anthropometric Standards]. <https://peraturan.bpk.go.id/Home/Download/144762/Permenkes%20Nomor%20%20Tahun%202020.pdf>
- Kho, D. (2018, May 31). *Pengertian LCD (liquid crystal display) dan prinsip kerja LCD* [Understanding LCD (liquid crystal display) and working principles of LCD]. Teknik Elektronika. <https://teknikelektronika.com/pengertian-lcd-liquid-crystal-display-prinsip-kerja-lcd/>
- Marcelino, K. B., Sunarya, U., & Nurmantis, D. A. (2018). Perancangan dan implementasi alat ukur berat dan tinggi badan untuk bayi 1–18 bulan berbasis mikrokontroler ATmega328 [Design and implementation of a weight and height measuring instrument for babies 1 – 18 months based on the ATmega328 microcontroller.]. *e-Proceeding of Applied Science, Indonesia*, 4(3), 2584-2593.
- Merita. (2019). Tumbuh kembang anak usia 0–5 tahun [Growth and development of children aged 0-5 years]. *Jurnal Abdimas Kesehatan (JAK)*, 1(2), 83-89. <http://dx.doi.org/10.36565/jak.v1i2.29>
- Sari, D. Y., Dewanto, W. K., & Surateno. (2017). Aplikasi pemantauan status gizi berdasarkan pengukuran antropometri menggunakan metode fuzzy logic [Nutritional status monitoring application based on anthropometric measurements using the fuzzy logic method]. *Jurnal Teknologi Informatika dan Terapan*, 4(1), 71-79. <https://doi.org/10.25047/jtit.v5i1.80>
- Wahyudi, B., Adella, D. J., & ABA, M. U. N. (2021). Analisis data berat badan dan panjang bayi dengan alat ukur panjang dan berat badan bayi [Analysis of baby weight and length data with baby length and weight measuring instruments]. *Elektrika*, 13(2), 42-46. <http://dx.doi.org/10.26623/elektrika.v13i2.3161>
- Wilson, J. S. (2005). *Sensor Technology Handbook*. Elsevier. <https://doi.org/10.1016/B978-0-7506-7729-5.X5040-X>
- Zhmud, V. A., Kondratiev, N. O., Kuznetsov, K. A., Trubin, V. G., & Dimitrov, L. V. (2018). Application of ultrasonic sensor for measuring distances in robotics. *Journal of Physics: Conference Series*, 1015(3), 1-9. <https://dx.doi.org/10.1088/1742-6596/1015/3/032189>

*Review Article*

## **Integration of Unmanned Aerial Vehicle and Multispectral Sensor for Paddy Growth Monitoring Application: A Review**

**Nur Adibah Mohidem<sup>1,2</sup>, Suhami Jaafar<sup>2</sup> and Nik Norasma Che'Ya<sup>2,3,4,5\*</sup>**

<sup>1</sup>Public Health Unit, Department of Primary Health Care, Faculty of Medicine and Health Sciences, Universiti Sains Islam Malaysia, Bandar Baru Nilai, 71800 Nilai, Negeri Sembilan, Malaysia

<sup>2</sup>Department of Agriculture Technology, Faculty of Agriculture, Universiti Putra Malaysia, 43400 Serdang, Selangor, Malaysia

<sup>3</sup>Centre for Advanced Lightning, Power and Energy Research (ALPER), Universiti Putra Malaysia, 43400 Serdang, Selangor, Malaysia

<sup>4</sup>Smart Farming Technology Research Centre (SFTRC), Faculty of Engineering, Universiti Putra Malaysia, 43400 Serdang, Selangor, Malaysia

<sup>5</sup>Laboratory of Plantation System Technology and Mechanization (PSTM), Institute of Plantation Studies, Universiti Putra Malaysia, 43400 Serdang, Selangor, Malaysia

### **ABSTRACT**

Using a conventional approach via visual observation on the ground, farmers encounter difficulties monitoring the entire paddy field area, and it is time-consuming to do manually. The application of unmanned aerial vehicles (UAVs) could help farmers optimise inputs such as water and fertiliser to increase yield, productivity, and quality, allowing them to manage their operations at lower costs and with minimum environmental impact. Therefore, this article aims to provide an overview of the integration of UAV and multispectral sensors in monitoring paddy growth applications based on vegetation indices and soil plant analysis development (SPAD) data. The article briefly describes current rice production in Malaysia and a general concept of precision agriculture technologies. The application of multispectral sensors integrated with UAVs in monitoring paddy growth is highlighted. Previous research on aerial imagery derived from the multispectral sensor using the normalised difference vegetation index (NDVI) is explored to provide information regarding the health condition of the paddy. Validation of the paddy growth map using SPAD data in determining the leaf's relative chlorophyll and nitrogen content is also being discussed. Implementation of precision agriculture among low-income farmers could provide

#### ARTICLE INFO

*Article history:*

Received: 04 February 2023

Accepted: 02 October 2023

Published: 23 February 2024

DOI: <https://doi.org/10.47836/pjst.32.2.04>

*E-mail addresses:*

[nuradibahmohidem@usim.edu.my](mailto:nuradibahmohidem@usim.edu.my) (Nur Adibah binti Mohidem)

[184590@student.upm.edu.my](mailto:184590@student.upm.edu.my) (Suhami Jaafar)

[niknorasma@upm.edu.my](mailto:niknorasma@upm.edu.my) (Nik Norasma Che'Ya)

\* Corresponding author

valuable insights into the practical implications of this review. With ongoing education, training and experience, farmers can eventually manage the UAV independently in the field. This article concludes with a future research direction regarding the production of growth maps for other crops using a variety of vegetation indices and map validation using the SPAD metre values.

*Keywords:* Multispectral, normalised difference vegetation index, paddy field, soil plant analysis development, unmanned aerial vehicle

---

## INTRODUCTION

Rice (*Oryza sativa* L.) is the main food source for about half of the world's population, with 90% produced by Asian countries. However, the country-of-origin exports only 7% of the global rice production (Othman et al., 2020). Therefore, rice plays a major role in sociocultural development, food security, and government strategic intervention in developing countries, including Malaysia (Seglah et al., 2020). The country's rice policy aims to accomplish three goals: to enhance balanced income to maintain price stability, increase income for farmers, and gain consumer supply security (Akhtar & Masud, 2022). Almost 40% of Malaysian farmers rely solely on paddy cultivation.

Malaysia's rice production stood at 2.9 and 1.88 million MT, respectively, in early 2019, with the country's self-sufficiency level reported at 72.85%. Fast forward, the national SSL has dropped slightly to 69% as a result of the looming COVID-19 pandemic, which has caused food supply chain disruption and increased consumption of staple foods (Omar et al., 2020). Although rice annual production grows at a 1.6% rate, this rate is insufficient to meet the population's consumption needs. The national average rice yield is around 4.2 tonnes per acre. High-yield granaries are in IADA Barat Laut Selangor, IADA Pulau Pinang, IADA Ketara, and MADA. In contrast, the low-yield granaries are in Kemasin, IADA Pekan, and Rompin (Ministry of Agriculture, 2016). Problems farmers face in rice cultivation include climate change, invasive and native pests, reduced fertility of the soil health due to excessive fertiliser, poor nutrition management, water shortages, and pesticide-related health problems.

In general, paddy monitoring depends on ground-based surveys and visual observation to determine plant health conditions in a small farm area by evaluating a plant based on the conditions of its leaf (Gée et al., 2021). However, paddy assessment requires information that is higher than the canopy level. Data collection and validation techniques such as manual inspection and perimeter scouting are inefficient because they are time-consuming and costly (Gracia-Romero et al., 2017). Precision agriculture through site-specific crop management provides an alternative to this issue (Ponnusamy & Natarajan, 2021). It can potentially increase rice production to 10 mt/ha, thus addressing issues such as land



scarcity, rising production costs, and inefficient paddy monitoring by farmers (Bujang & Bakar, 2019). Profitability for farmers may improve as agricultural operations are managed more efficiently and able to predict yield before harvest, resulting in less strain on human resources and higher productivity levels. However, weather problems and conventional remote sensing techniques via sensor installation in the field limit data collection efficiency (Nguy-Robertson et al., 2012). Using a satellite and a piloted plane poses constraints due to low spatial and temporal resolution to capture the paddy images, resulting in low pixel resolution and unclear images. Conversely, UAVs that fly at a lower altitude generate higher spatial resolution images of the crops, with each pixel being a centimetre or millimetre (Pérez-Ortiz et al., 2016).

Unmanned aerial vehicles (UAVs) have now developed from slow-flying UAVs to fixed-wing and rotary-wing UAVs, which have gliding characteristics and require less manpower. UAVs with visible bands and multispectral scanning sensors can collect data to analyse crop growth, plant health conditions, maturity, and morphology (Olson & Anderson, 2021). The use of UAV with a multispectral sensor produces a high spatial resolution image, i.e., 3.47 cm in monitoring wheat scab during the wheat filling stage, in which support vector machine (SVM) regression has 81% accuracy for the training set and 83% for the verification set (Zhu et al., 2022). In terms of paddy, applications of aerial images generated from multispectral sensor mounted on a UAV include drought damage assessment for crop fields in Indonesia, determination of crop health in Brunei and identification of the relationship between the rice lodging and available nitrogen in soil content by assessing their spatial distributions images in a crop field in Japan (Iwahashi et al., 2022; Elfri et al., 2023; Sato et al., 2023).

Numerous vegetation indices derived by UAVs were demonstrated in detecting plant diseases, crop performance, and use of consumption on the farm (Roth et al., 2022; Boursianis et al., 2022; Feng et al., 2022). It also employs the near-infrared (NIR) and visible electromagnetic spectrum regions to determine the crop quality. Vegetation indices such as the integrated, simple ratio ( $R_{515}/R_{570}$ ), i.e., band rationing and transformed chlorophyll absorption reflectance index/optimised soil-adjusted vegetation index (TCARI/OSAVI), narrow-band indices to estimate leaf chlorophyll and crop growth are measured based on a multispectral sensor integrated with UAV (Wang et al., 2019). Corti et al. (2019) demonstrated that colour-infrared film combined with a low-cost automated camera can generate an NDVI map suitable for crop monitoring.

Instruments based on optical qualities are split into the leaf scale and the canopy scale, depending on the extent of use. UAV captures images of paddy growth, which are analysed using vegetation indices and SPAD metre values. The previous study used SPAD values to construct a relationship with spectral and textural indices. In contrast, the stepwise regression model (SRM) was used to determine the best combination of spectral and

textural indices in estimating SPAD metre values. For example, support vector machine (SVM) and random forest (RF) models are used to estimate SPAD values based on optimal combinations (Guo et al., 2022).

The different approach shows that SPAD metre values were gathered as surrogates of plant nitrogen content to create relationships on various days after transplanting for converting nitrogen index maps to SPAD maps of paddy for potential variable rate fertiliser application control (Wang et al., 2022). Vegetation indices displayed on the map allow for determining the amount of chlorophyll concentration present in rice on the images taken through the UAV that correlate with SPAD metre readings. Therefore, this review aims to elaborate on the application of UAV-mounted multispectral sensors in monitoring paddy based on vegetation indices and SPAD metre values.

### OVERVIEW OF RICE PRODUCTION IN MALAYSIA

The top three rice-producing countries; Indonesia, Vietnam, and Thailand, have allocated 11.50 million hectares, 7.54 million hectares, and 10.83 million hectares for paddy plantation areas (USDA, 2020). Among the Southeast Asian rice-producing countries, the average productivity of granaries in Malaysia comes in third, after Vietnam and Indonesia (Table 1). Malaysia has the smallest total paddy rice planting areas in Southeast Asia, with 689,268 ha (Firdaus et al., 2020), with Peninsular Malaysia accounting for two-thirds of the total planting area, whereas Sabah and Sarawak account for the remaining one-third (Ramli et al., 2012).

Paddy is one of the most crucial crops in Malaysia. Around 195000 farmers work hard to improve rice cultivation and productivity (Omar et al., 2019). The varieties local farmers produce include white rice, glutinous rice, black rice, red rice, brown rice, and aromatic rice. It provides income and livelihood for the community near paddy planting areas, mostly small farmers and landless agricultural workers. Most farmers live in larger paddy fields near granary sites with smaller paddy fields across the country (Fahmi et al., 2013).

Granaries are rice farms with adequate irrigation systems and land areas of more than 4,000 ha (Rahmat et al., 2019). Malaysia has eight main granary areas representing the country’s rice bowl and serving as the food security supply. Paddy is mostly planted in the northern and eastern parts of Peninsular Malaysia, especially in Kedah and Kelantan. Such areas in Kedah

Table 1  
*Paddy productivity in the selected Southeast Asian countries in 2017*

Country	Productivity (mt/ha)
Malaysia	4.47
Vietnam	5.89
Indonesia	4.76
Myanmar	2.91
Philippines	4.02
Laos	3.24
Cambodia	2.78
Thailand	2.89
Brunei	2.00

and Kelantan are suitable for rice farming due to the flat lowland and the soil type. Besides these recognised granaries, Malaysia has 74 secondary granaries and 172 minor granaries that contribute up to 28,441 and 47,653 hectares, respectively (Rahmat et al., 2019). The average yield per hectare was 2,311 kg/ha, whereas rice production was 2,748 mt in 2020 (Table 2).

Under the National Agricultural Policy (1984–1991), the development of main granary areas was initially reserved as the gazetted wetland paddy areas (Ministry of Agriculture, 1984). It is deemed a strategic intervention to support the paddy growth and rice industry, as well as to protect the national food security. Granary areas in Malaysia are managed by agencies such as (1) Muda Agricultural Development Authority (MADA), (2) Kemubu Agricultural Development Authority (KADA), (3) North Terengganu Integrated Agriculture Development (KETARA), (4) Project Barat Laut Selangor (PBLs), (5) Krian, (6) Seberang Perak, (7) Seberang Perai, (8) Kemasin, (9) Rompin, (10) Kota Belud, and (11) Batang Lupar. To date, granaries under KETARA, IADA Pulau Pinang, MADA, and Barat Laut Selangor have exceeded the average granary productivity per hectare. However, the average yield per hectare varies between granary areas due to geographical factors that are influenced by environmental conditions, cultivated areas, and field-based agricultural strategies (Omar et al., 2019).

Malaysians require around 110 kg of paddy per capita per year to meet the individual rice consumption (Dorairaj & Govender, 2023). Malaysians consume approximately 82.3 kg of rice annually, and the paddy field produces 3.7 metric tonnes of rice each hectare (Rusli et al., 2024). Adults consume about 2.5 plates of white rice per day (Kasim et al., 2018). This trend is expected to increase yearly since the country's population is growing. The government has set a target of increasing local rice production by up to 75% in 2022–2023 (The Star, 2019). From 2016 to 2020, the government focused on food security via sustainable measures to address the food availability and accessibility issues, especially in terms of the nation's rice consumption and production (Adnan et al., 2021).

The self-sufficiency level of the national rice production and consumption fluctuates between 67% and 70%. Rice security reflects the nation's food security; hence, accomplishing self-sufficiency through sustainable paddy farming is crucial. The Ministry of Agriculture and Food Industries (MAFI) is in charge of sustainable paddy farming via its agency, namely the Integrated Agricultural Development Authority (IADA). This agency monitors rice production to fulfil 72% of the country's demand, yet Malaysian rice productivity is still low. Malaysia imported about 740,000 tonnes of rice in 2018 for RM1.18 billion (The Star, 2019). Consequently, the government stepped up with an action plan by establishing the National Agricultural Policy (Dardak, 2015; Osman & Shahiri, 2017).

However, rice production in Malaysia has faced several challenges, including extreme weather, poor soil fertility and nutrient management, avoidance of genetically modified

Table 2  
Total paddy production and productivity of the main granary areas in Malaysia from 2016 to 2020

Granary	2016			2017			2018			2019			2020		
	Average Yield (kg/ha)	Paddy Production (mt)	Average Yield (kg/ha)	Paddy Production (mt)	Average Yield (kg/ha)	Paddy Production (mt)	Average Yield (kg/ha)	Paddy Production (mt)	Average Yield (kg/ha)	Paddy Production (mt)	Average Yield (kg/ha)	Paddy Production (mt)	Average Yield (kg/ha)	Paddy Production (mt)	
MADA	5284	1063247	4841	974387	5111	1028867	4933	993206	5611	1129218					
KADA	4610	248172	4448	240490	4695	252149	4032	203011	5082	272975					
KERIAN	3949	165027	4087	171237	3957	165790	3584	150162	4403	185039					
IADA BLS	5825	222033	4510	165571	4731	174432	4756	174088	5600	206456					
IADA	5801	148297	5737	146660	5228	133636	4660	119116	6178	157929					
PULAU PINANG	3729	103388	3180	88198	3417	94784	2923	79884	3788	105466					
SEBERANG PERAK	5623	54836	5172	50438	5349	52164	5162	50335	5828	58022					
KEMASIN SEMERAK	3771	27456	3779	26938	4079	28154	3733	28233	4294	30418					
PEKAN	2052	13425	1506	10286	2673	17183	2642	17562	2323	14943					
ROMPIN	2793	14436	3338	17028	2910	14756	23773	12120	3454	17227					
KOTA BELUD	2511	22805	3112	30096	2908	25598	3086	2907	2908	2907					
BATANG LUPAR	2009	2252	2492	2794	2754	3087	2748	2748	2748	2748					

Source: <https://www.doa.gov.my/index.php/pages/view/1053>

planting materials, and application of remote sensing constraints by farmers to monitor paddy growth conditions. Food security or the livelihood of farmers is vulnerable to functional fluctuations in global supply chains to maintain international rice trading ties. During the unprecedented COVID-19 pandemic, the movement control order (MCO) period has caused significant disruption in the food supply chain. Malaysia encountered a volatile rice import trend during the early stage of the pandemic, making it difficult to secure a committed rice trading partner. Therefore, improved paddy monitoring methods for precision agriculture in Malaysia can offer better crop health and resilience in the rice production system.

## PRECISION AGRICULTURE

According to the International Society for Precision Agriculture, precision agriculture is “a management strategy which collects, processes, and analyses temporal, spatial, and single data and merges it with other information to support management decisions to improve resource use efficiency, productivity, profitability, quality, and sustainability of crop yields based on estimated variability” (Onyango et al., 2021). Precision agriculture is associated with an increase in the number of actions made per unit area of land for each unit of time to increase the amount and/or quality of productivity and/or the environment and enhance more proactive input consumption (Monteiro et al., 2021). For example, the amount of fertiliser, herbicides, and pesticides will be calculated based on the spatial variability across the field, which is used to calculate the amount needed for a particular crop (Norasma et al., 2019).

Precision agriculture has shifted the emphasis from spatial resolution to superior decision-making, space or time. It is widely used in (1) plant protection and disease control, (2) monitoring crop canopy status, (3) crop water management, (4) map cropping systems, (5) mapping soil fertility and soil types, and (6) predict or map crop yield (Table 3). A variety of technologies, such as soil and crop sensors and global navigation satellite systems (GNSS), which are global positioning systems (GPS), geographic information

Table 3  
*Different types of applications for precision agriculture technologies*

Purpose	Precision agriculture technology	Application	References
Plant protection and disease control	Geostatistical techniques, chlorophyll fluorescence, violet diode laser-induced integrated decision support system for intercropping, a wireless sensor network, continuous time Markov process, UAV, spectral crop sensors, and site-specific application for pesticides	Crop pest and disease detection and monitoring, as well as disease-resistance breeding	Dhau et al. (2018), Nestel et al. (2019), Sui et al. (2016), Low et al. (2020), and Pretorius et al. (2017)

Table 3 (continue)

Purpose	Precision agriculture technology	Application	References
Crop growth monitoring	NDVI	Differentiate crops that grow in different environments.	Bazezew et al. (2021)
	Remote sensing	Canopy replication and plant age	Mapfumo et al. (2017)
	Multi-temporal Landsat 8 NDVI anomalies	Detecting and mapping inconsistencies in crop changes in vegetation cover	Chemura et al. (2017) Meroni et al. (2021)
Crop water management	Thermal time, wireless sensor technology indices of water stress, and simulation models	Water stress detection technology	Gohain et al. (2021), Alou et al. (2018), and Jamroen et al. (2020)
	Use of UAV	Planning and development of irrigation infrastructure	Gauram et al. (2021)
	Precision irrigation	Sufficiency of sprinkler irrigation efficiency	
	Geographical information system (GIS)	Assess the temporal and spatial distribution of irrigation water using the drip irrigation system	Chen et al. (2019)
Mapping cropping system	Recognition of machine vision schemes in satellite pictures	Differentiate the crop field from nearby green vegetation zones	Tsai et al. (2017)
	Simulation models	Estimate the proportion of tree cover inside crops	Della Chiesa et al. (2022)
	Wall-to-wall sub-metre, moderate resolution Landsat 8 imagery and WorldView	Mapping cropland for small-scale farmers	McCarty et al. (2017)
	Wireless sensor nodes	Evaluate the wireless signal for precision agriculture in terms of connection reliability and signal strength.	Karunanithy and Velusamy (2021)
	RapidEye	Mapping maize cropping systems	Richard et al. (2017)
	RapidEye combined with spatial logistic regression modelling	Differentiate land management strategies in rangelands	Ali et al. (2016)
Soil Fertility Mapping	Transect, density regression, and indigenous knowledge are integrated with gamma ray spectrometry and satellite images using non-parametric kernel geostatistical techniques	Spatial variations in soil fertility	Munnaf et al. (2020)
	RapidEye remote sensing	Building estimation models to map out the soil organic carbon	Costa et al. (2018)

Table 3 (continue)

Purpose	Precision agriculture technology	Application	References
Yield Prediction/ Mapping	Kriged maps	Determining the soil functional qualities	Takoutsing et al. (2017)
	Soil diagnostic and GIS	Establishing fertilizer recommendations based on specific site conditions	Grzebisz et al. (2021)
	Near-infrared reflectance (NIR)	For soil sampling, as well as chemical and physical analyses	Winowiecki et al. (2017)
	Remote sensing	Discovering agricultural productivity and soil fertility constraints at several spatial scales	Irmulatov et al. (2021)
	UAV		
	Vegetation and thermal indices	Estimation of cereal production	
	Random forest classifier	Yield variations in smallholder farming systems	Ibrahim et al. (2021)

systems (GIS), and variable rate applications (VRA), can be used in making decisions. It includes three data collection methods: remote sensing, field sampling, and proximal sensing. Each type of data collection is determined by the parameters monitored in the field.

## UNMANNED AERIAL VEHICLE FOR PADDY GROWTH MONITORING

Remote sensing is a data collection tool that observes the characteristics of an object without direct contact over large areas in real time (Janga et al., 2023). For precision agriculture, remote sensing platforms capture the aerial view of the entire farm, consisting of ground-based remote sensing, aerial-based remote sensing, and satellite-based remote sensing (Table 4). These platforms have been applied in paddy mapping because they provide large temporal and spatial information to monitor crop growth. Aerial plane outfitted with cameras is used to capture images of paddy to estimate the irrigated yield, a flexible and effective yield prediction tool. However, the cost of fuel and a professional pilot is expensive.

Aerial-based remote sensing platforms include high-altitude aerial vehicles and low-altitude UAVs. UAVs have been used widely in agriculture applications and have emerged as a remote sensing tool for yield prediction due to their high resolution, high throughput, and low cost (Zhang & Zhu, 2023). UAVs collect data to measure parameters such as leaf area index (LAI) and height, allowing growth control for paddy. UAVs can be used to measure common vegetation index to determine diseased plant tissues and map the defect size. On the other hand, water management is an important aspect of UAV application, as precision irrigation techniques in paddy fields improve crop management efficiency by reducing wastage in the usage of fertiliser, water, and pesticides (Mallareddy et al., 2023).

Table 4

*Comparison of quality of services between different types of remote sensing platforms in precision agriculture*

Quality of services	Types of remote sensing platforms			
	UAV	Satellite	Manned Aircraft	Ground Based
Flexibility	High	Low	Low	Low
Adaptability	High	Low	Low	Low
Cost	Low	High	High	Low
Time Consumption	Low	Low	Low	High
Risk	Low	Average	High	Low
Accuracy	High	Low	High	Moderate
Deployment	Easy	Difficult	Complex	Moderate
Feasibility	Yes	No	No	Yes
Availability	Yes	No	Yes	No
Operability	Easy	Complex	Complex	Easy

UAVs are equipped with high-resolution sensors that acquire more detailed vegetation phenotypic information to predict yield than manned aircraft and satellites. This technology is now used to gather high-quality images by mounting specified bands, including NIR (near-infrared) and IR (infrared), and as sensors, including RGB (red-green-blue), multispectral, hyperspectral, and thermal. Sensors are selected to monitor various parameters such as resolution, weight, captured images, optical quality, and price. One RGB would be sufficient for mapping paddy planting areas and extracting pure crop canopy information (Kazemi & Parmehr, 2023). Images generated from RGB can extract information such as vegetation structure and reflectance for growth monitoring and biomass estimation. RGB requires low cost and is useful for UAV applications such as orthomosaic creation because it can capture high-resolution images. In addition, they function well in different weather conditions, be it sunny or cloudy. However, due to the limited spectral range, they cannot analyse many vegetation indices.

Unlike digital RGB cameras that only capture images in the visible range, multispectral sensor can capture images in multiple spectral bands, including NIR, which provides additional spectral information to estimate yield by calculating vegetation indexes. Multispectral and hyperspectral can collect data using various spectral channels to obtain high-quality images to assess a variety of physical and biological characteristics of paddy. Unlike satellites, which have a fixed number and type of sensors, UAVs can be modified to be equipped with specific sensors to meet specific needs. Multispectral and hyperspectral are suitable for disease detection because they have many bands that are sensitive in detecting disease symptoms. In contrast, thermal is used to collect temperature data, and its usage in irrigation activities is more effective (Tsouros et al., 2019).

Because RGB and multispectral sensor are less expensive, researchers often use small or medium-sized UAVs for field trials. Most multispectral can only acquire a small



amount of spectral information in the visible and NIR bands at low spectral resolution. Hyperspectral sensor, on the other hand, provide higher spectral resolution and more continuous spectral information than multispectral. Besides, multispectral and hyperspectral have specific weather requirements to perform their tasks, which must acquire images in clear and cloud-free conditions.

Multicopter UAVs, fixed-wing UAVs, and unmanned helicopters are the types of UAVs used in agriculture. Most UAVs for field phenotyping fly at an altitude of less than 150 m, and the image resolution can reach centimetres (Stöcker et al., 2017). Multicopter UAVs can hover and turn in the air (Fu et al., 2020), but they consume much power, resulting in short battery life, usually less than 30 minutes. Furthermore, due to their small payload, multicopter UAVs can only carry a limited number and type of sensors. Fixed-wing UAVs can fly at high speed for longer periods, allowing them to cover a large area of farmland in a short amount of time. Moreover, fixed-wing UAVs with large wings have larger payloads, which can provide a wider sensor array. Fixed-wing UAVs, however, cannot collect data in small-scale farms due to the long runways required for take-off and landing, besides being unable to hover and turn flexibly in the air.

## **PADDY GROWTH MONITORING BASED ON AERIAL IMAGERY GENERATED FROM MULTISPECTRAL SENSOR**

Some locations in the paddy field may not be easily recognised or easily accessible for ground visual observation on the ground (Rosle et al., 2022). In addition, some of the farmers are elderly, so they are sometimes unable to check the entire area due to a lack of energy. Thus, it could cause inefficient paddy field management. The farm manager can now view the entire paddy field using aerial imagery without missing any locations. Therefore, aerial imagery using multispectral sensors can assist farm management in constantly monitoring paddy with ground surveying for validation (Lu et al., 2021; Sari et al., 2021).

Multispectral is often lightweight, compact, and particularly straightforward to operate on the UAV. In addition, the cost of multispectral is reasonable and will get cheaper in the future. An interference filter installed at the front of the camera lens to filter or transmit specific lights is used to create a multi-band filter and multispectral sensor. Compared to RGB, a multispectral provides more wavebands in visible and NIR spectral ranges (Figure 1) and can predict yield, biomass, nitrogen content, and other parameters. Multispectral sensor employ a variety of common spectral bands such as red, green, blue, red-edge, and NIR. They are classified into bandwidth categories: narrow-band and broadband (Deng et al., 2018). The multispectral sensor consists of at least four bands. The difference in the number of wavebands depends on the manufacturing (Figure 2) (Xie & Yang, 2020).

It is important to understand how monochrome and colour work. A photo-sensing element in monochrome cameras comprises a two-dimensional array of sensitive pixels.

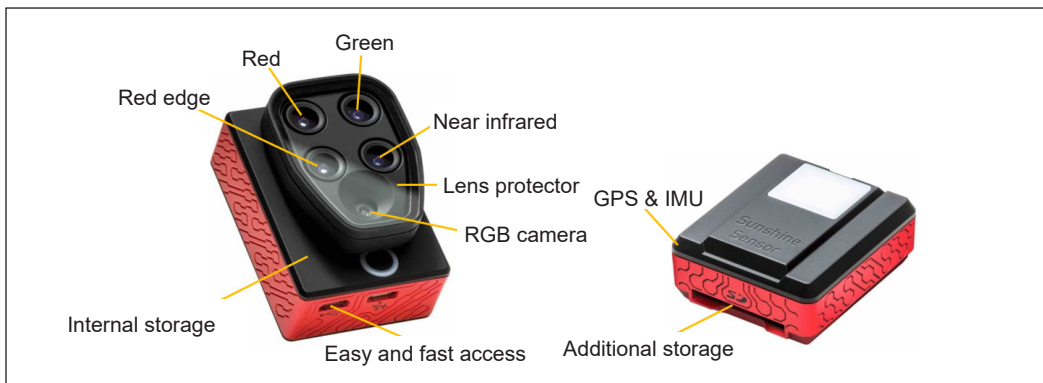


Figure 1. Multispectral sensor

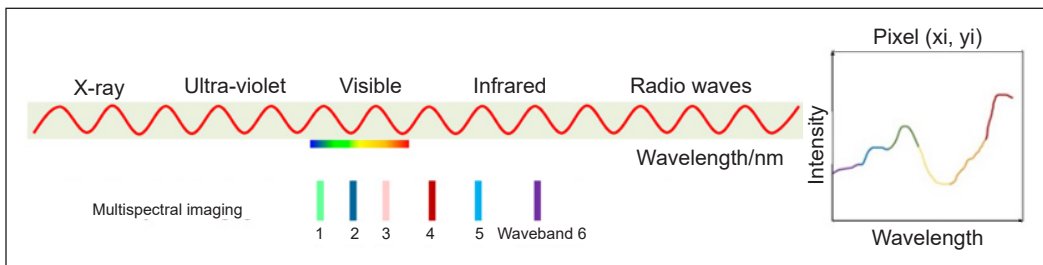


Figure 2. Multispectral imaging with six wavebands (Adapted from Abijo et al., 2023)

In monochrome CMOS image sensing, these pixels are sensitive to light emitted across a broad spectral range. A colour camera has an image that detects elements with a two-dimensional array of pixels. The remote-sensing multispectral sensor is coated with a mosaic colour pattern that transmits red, green, or blue lights. The colour pigments create the colour filter array (CFA), known as the RGB cameras (Hassan et al., 2021). Examples of multispectral sensors are Green Seeker (ground sensor) and Landsat 8 (Satellite sensor). Multispectral sensor such as RedEdge (MicaSense, Inc., Seattle, WA, USA) (Figure 3), MCA 6 (Tetramcam Inc., USA), and DJI Mavic 3 Multispectral (DJI, China) can capture images from the visible and NIR bands.

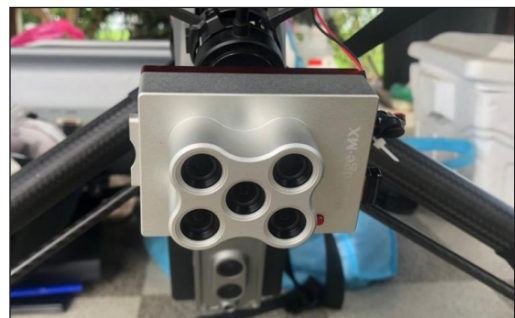


Figure 3. MicaSense-RedEdge-MX multispectral sensor

Multispectral imagery consists of 3–10 distinguished “wider” bands. The images produced can be further analysed with GIS or RS software. Norasma et al. (2019) used a MicaSense sensor to create the rice growth map. This sensor is also used by Jiang et al.

(2020) to monitor the operation parameters of low-altitude UAVs in acquiring the NDVI values across paddy fields. Therefore, the sensor can help farmers overcome the issues in the field within a shorter period. Figure 4a shows the RedEdge-MX multispectral sensor’s spectral resolution, and Figure 4b illustrates the spectral reflectance graph of healthy and stressed plants through five bands. The MicaSense RedEdge-MX can capture five types of wavebands, including red, green, blue, red edge, and NIR. Red band and NIR are utilised in the NDVI algorithm.

The principle underlying high accuracy is the use of various electromagnetic spectrum bands. They not only contribute to the data from the images obtained, but they also generate vegetation indices. Luo et al. (2022) applied multispectral sensor to map paddy fields at different growth durations (booting and heading stages) using normalised difference vegetation index (NDVI), red-edge chlorophyll index (CIred edge), green-edge chlorophyll index (CIgreen edge), two-band enhanced vegetation index (EVI2), normalised difference red edge (NDRE), wide dynamic range vegetation index (WDRVI), MERIS

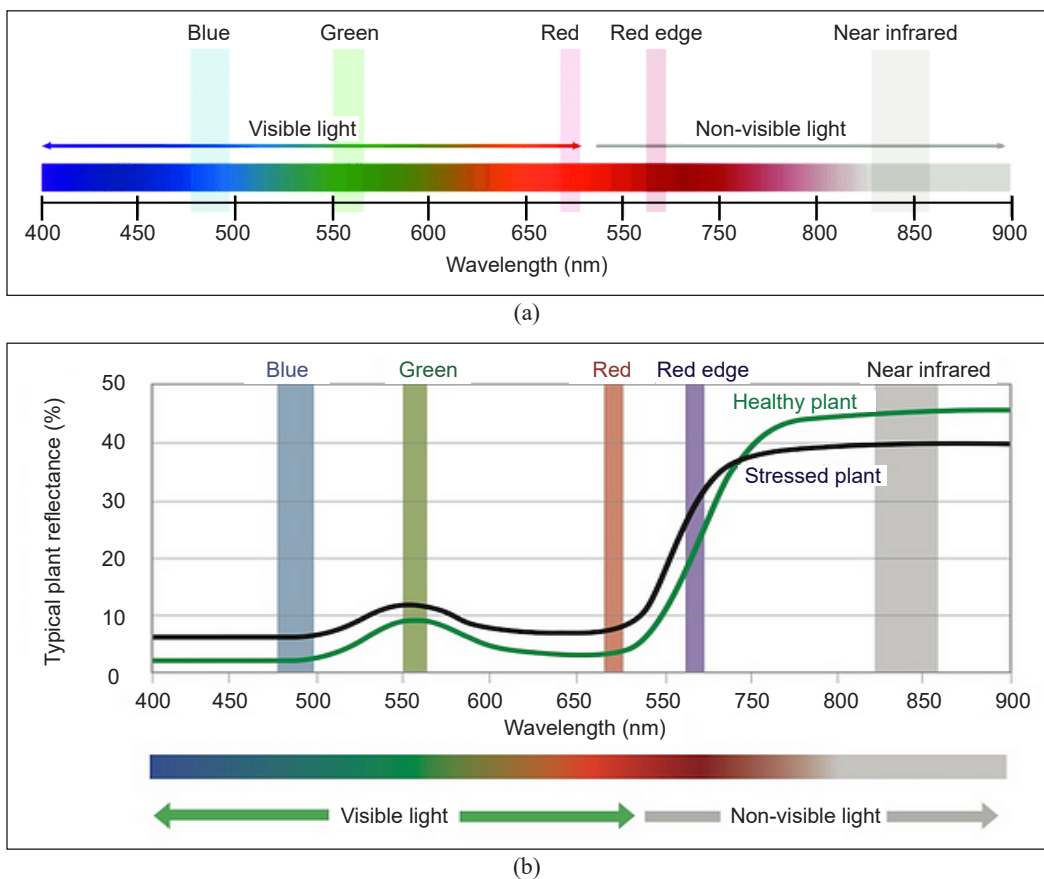


Figure 4. (a) The spectral resolution of the MicaSense-RedEdge-MX multispectral sensor; (b) Reflectance curve of the healthy and stressed plant (Roman & Ursu, 2016)

terrestrial chlorophyll index (MTCI), Normalised Difference Red Edge (Ndre) and soil-adjusted vegetation index (SAVI). Most aerial images for crop health monitoring employ multispectral sensor (Hassler et al., 2019) that generate vegetation indices such as NDVI, NDRE, and GNDRE (Kalischuk et al., 2019; Barbedo, 2019).

Vegetation indices are the most essential criteria in crop disease identification. However, the multispectral sensor requires high cost and additional work to calibrate the specific functions of the indices, including disease identification and image processing. Furthermore, multispectral sensors make it difficult to detect small changes in terms of the biophysical and biochemical characteristics of crops (Neupane & Baysal-Gurel, 2021). However, the price will be reduced in the future, and the image processing will be easier to work on.

## VEGETATION INDICES FOR PADDY GROWTH MONITORING

Data captured from UAVs is expressed using indices, including the vegetation index. Souza et al. (2020) used active and passive sensors to obtain vegetation index maps to assess crop growth. The electromagnetic spectrum is a range of all types of electromagnetic radiation based on frequency and wavelength. Each electromagnetic wave is classified according to the specific frequency, photon energies, and wavelengths. In a remote sensing context, the electromagnetic spectrum provides valuable information on the crops' condition. For example, necrosis of the leaves can be visualised under the visible light wavelength. The changes on the leaves can be detected in the visible spectrum, as well as in other electromagnetic spectra, such as the vegetation index light band (Hogan et al., 2017).

Consecutive crop monitoring enables farmers to identify small changes that are difficult to detect with the naked eye. Multispectral imaging, for instance, is useful to analyse paddy health using NDVI indices. In addition, it allows an evaluation of the absorption degree of solar radiation in certain bands; thus, the crop's health can be monitored (Ishihara et al., 2015). NDVI can be derived from satellite imagery such as Pour l'Observation de la Terre (SPOT), moderate resolution imaging spectroradiometer (MODIS), and Landsat. Nevertheless, the low temporal and spatial resolutions enhance reliable crop monitoring at the field level, particularly to obtain information for smallholder farmers. UAVs can provide high spatial resolution at 0.05 to 1-metre resolution, and the data is useful to identify the condition of certain plants. Based on aerial images, farmers can monitor the field using NDVI values.

The NDVI value can be the indicator to determine the crop conditions. However, soil colour, cloud shadow, soil brightness, leaf canopy shadow, and atmosphere have an impact on NDVI value, which needs remote sensing calibration. The NDVI equation is shown as Equation 1:

$$\text{NDVI} = (\text{NIR} - \text{RED}) / (\text{NIR} + \text{RED}) \quad (1)$$

where NIR represents the reflectance value of the NIR band; RED represents the reflectance value of the red band.

The plant greenness density is referred to detect phenological changes during the planting period. NDVI is one of the most practical vegetation indices to quantify greenness on the vegetation land cover (Roy et al., 2016). NDVI is constructed according to the red and NIR bands to identify crop health conditions, as well as monitor crop growth. The NDVI values normalise the reflectance captured from images from -1 to 1. Positive values indicate higher vegetation (vigour), while negative values indicate unvegetated surfaces such as cities, water, barren soil/land, and ice (Sishodia et al., 2020). The NDVI values of 0–0.33 indicate unhealthy or stressed conditions, 0.33–0.66 indicate moderately healthy conditions, whereas 0.66–1 signifies very healthy conditions, as illustrated in Figure 5 (Rosle et al., 2019). However, the range can be different for other crops, which requires further analysis.

NDVI is commonly evaluated in rice-related research as an important indicator of rice growth (Fenghua et al., 2016). The enhanced vegetation index (EVI), like NDVI, has received much attention in monitoring vegetation quality, where it also has multispectral capabilities. It is shown as an optimised vegetation index developed by Liu and Huete to improve the vegetation signal's sensitivity in high biomass areas. The primary application of EVI is to rectify NDVI results for atmospheric changes and serve as soil background signals, primarily in dense canopy zones. The EVI equation is shown as Equation 2:

$$EVI = 2.5 (NIR - RED) / (NIR + 6R - 7.5B + 1) \quad (2)$$

In contrast, the Landsat soil-adjusted vegetation index (SAVI) is used to rectify NDVI for the influence of soil brightness in areas with low vegetation cover. It is useful for soil and vegetation monitoring, and it has high-resolution and high-density data equipped with remotely sensed data to provide excellent spatial coverage. However, the calculation is complex since the data obtained are for operational use. The EVI equation is shown as Equation 3:

$$((NIR - R) / (NIR + R + L)) * (1 + L) \quad (3)$$

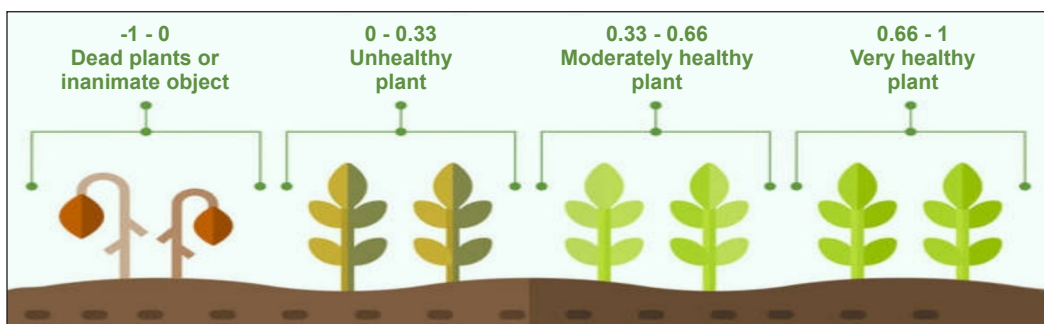


Figure 5. NDVI values of plant health classification (Cherlinka, 2023)

## SOIL PLANT ANALYSIS DEVELOPMENT ANALYSIS FOR PADDY GROWTH MONITORING

Chlorophyll is an important pigment for plant photosynthesis because it demonstrates a plant's ability to exchange material energy with its surroundings, as well as carbon sequestration ability, primary productivity, and nitrogen utilisation efficiency. Besides being an important indicator of crop condition, chlorophyll indicates the stage of plant development and growth. It also reflects plant stress. For example, when a disease spreads among plants, the leaves change from green to yellow and, subsequently, brown and white. The spectral characteristics of chlorophyll are essential in determining its content. The green and red bands were found to be the most effective in chlorophyll detection (Chusnah et al., 2023), but some studies have identified the NIR band as a fitting choice (Sharabiani et al., 2023; Raddi et al., 2022).

Previous research has also demonstrated that reflectance spectra in the visible region (400- 979 nm) are capable of estimating chlorophyll (Yang et al., 2021). Often, a steep red edge is formed between 680 and 760 nm because of the chlorophyll's substantial absorption of red light and strong reflection of NIR light. Hence, the red edge has a strong spectral response to chlorophyll. The red-edge parameter is one of the most important indicators for crop growth and chlorophyll content estimation (Naguib & Daliman, 2022). The optimum red-edge parameters are then identified by identifying spectral values and chlorophyll content, and a model signifying the relationship between them was developed (Pokhrel et al., 2023).

There are many current techniques to measure chlorophyll content in leaves, which are classified as destructive or non-destructive. The destructive methods, i.e., traditional methods, consist of ultraviolet and visible spectrophotometry, as well as fluorescence analysis, which is used to conduct quantitative chemical analysis of chlorophyll content using the spectral characteristics of the substance (Farag et al., 2022). These methods produce precise results but are time-consuming and labour-intensive, as well as destroying leaves. The soil and plant analysis development (SPAD) method serves as an alternative for ease of use, is low-cost, non-destructive, and enables quick SPAD measurement using light and electricity transmitted through leaves (Zhang et al., 2022). As chlorophyll content corresponds to plant nitrogen status, the SPAD value is used in nitrogen diagnosis to optimise nitrogen application as well as to control diseases, pests, and yield (Wan et al., 2022). A previous study on rice found that SPAD-based nitrogen management can improve grain yield and nitrogen use efficiency, where an increase in grain yield per unit of nitrogen was applied (Hou et al., 2020).

Therefore, the relative leaf chlorophyll content can be detected based on SPAD values, and the results almost resemble chemical experiments, which may replace the traditional chemical approach. The relative chlorophyll content can be detected using a non-damaging and portable chlorophyll metre, namely SPAD-502 chlorophyll metre (SPAD-502, Spectrum

Technologies, Inc., Plainfield, IL, USA) (Kamarianakis & Panagiotakis, 2023). It is one of the fastest and least invasive methods in estimating the relative chlorophyll content of a leaf per square metre, nitrogen content, and NDVI of a paddy crop (Zhang et al., 2021). It utilises the green, red, and NIR wavebands to determine a leaf's chlorophyll content. Hence, the SPAD value is determined by looking at the reflection and absorption of the spectral bands of the crop.

The SPAD readings using the SPAD-502 chlorophyll metre may indicate the growth condition of paddy, with high values indicating healthy plant growth (Guo et al., 2020). The first, second, and third readings can be obtained by fully expanded leaves from the samples (Zhao et al., 2023). Yuan et al. (2016) suggested that the fourth leaf from the top with a 2/3 position distance from the leaf base is suitable for the reading due to low measurement variance in that area. The small samples of SPAD values combined with near-surface UAV remote sensing can be employed on large-scale with high accuracy (Zhang et al., 2019). This approach, however, has limited measuring points and is not suitable for large area measurement, which can be solved by integrating remote sensing and UAV approach (Wang et al., 2022).

There are limitations to using SPAD data to monitor paddy growth because SPAD measurements only provide information on the chlorophyll content of leaves and do not take into account other factors that can affect crop health, such as water stress or disease. Sentinel series satellites' red-edge bands are used to monitor crop chlorophyll content, while sentinel-2 imagery is used to monitor canopy chlorophyll content with high accuracy (Kganyago et al., 2023). Since satellite remote sensing offers large-scale, frequent, low-cost, and massive amounts of information, it has replaced inefficient and costly traditional SPAD monitoring methods.

In other perspectives, the associations between plot-level spectral indices gathered from UAV images and data measured on the ground, such as leaf area index and SPAD values, were calculated and compared. The differences were discussed and analysed at two different paddy growth stages (Duan et al., 2019). By eliminating the backgrounds from the UAV spectral images, Shu et al. (2021) improved the estimation accuracy of SPAD values. The SPAD values were calculated using the cluster-regression method and UAV hyperspectral data (Yang et al., 2021). SPAD measurement offers effective and stable techniques for determining crop phenotyping. SPAD values can be converted to physiological parameters, including leaf chlorophyll content (Wan et al., 2020).

SPAD data has potential with other types of data, such as vegetation indices measurements or weather data of paddy growth. Aerial imagery and object-based image analysis techniques can validate vegetative indices in rice field maps using SPAD data. Normalized Difference Vegetation Index ( $R=0.957$ ), Normalized Difference Red Edge (NDRE) ( $R=0.974$ ), Soil Adjusted Vegetation Index ( $R=0.964$ ), and Optimized Soil

Adjusted Vegetation Index ( $R=0.966$ ) have proved positive linear correlations with SPAD readings. Vegetation indices showed a higher correlation compared with other vegetation indices, exhibiting a better measure for farmers to make decisions.

Therefore, the optimal combination of feature selection methods (recursive feature elimination, Pearson, and correlation-based feature selection) and machine learning regression models (random forest), elastic net, extreme gradient boosting (XGBoost), and backpropagation neural network with machine learning algorithms can predict SPAD values at individual growth stages and across growth stages of the crop from the images obtained by UAV (Yin et al., 2023). In other words, machine learning regression models (random forest), partial least squares (PLS) regression, deep neural network, and extreme gradient boosting (XGBoost) were used to establish SPAD estimation models. The algorithms such as Findpeaks, successive projections algorithm (SPA), competitive adaptive reweighted sampling, and CARS\_SPA were used to extract sensitive characteristic bands that are related to SPAD values (Sudu et al., 2022).

SPAD data are able to develop variable rate application (VRA) maps, which can help farmers apply fertilizers and other inputs more efficiently based on the specific needs of different areas of the field. The NDVI was measured with a GreenSeeker sensor, and SPAD readings were made with a SpadMeter. Geographic coordinates of the NDVI and SPAD measurements were also determined by a global navigation satellite system (GNSS). After applying these fertilization methods, NDVI and SPAD measurements were recorded. Soil and leaf samples were analysed in the laboratory to determine the content of plant nutrients for nitrogen (N), phosphorous (P) and potassium (K). Based on the images generated, NDVI and ground data, including SPAD chlorophyll readings, could have a stronger relationship (Yuhao et al., 2020). The spatial trend that integrates the SPAD chlorophyll map is presented in Figure 6.

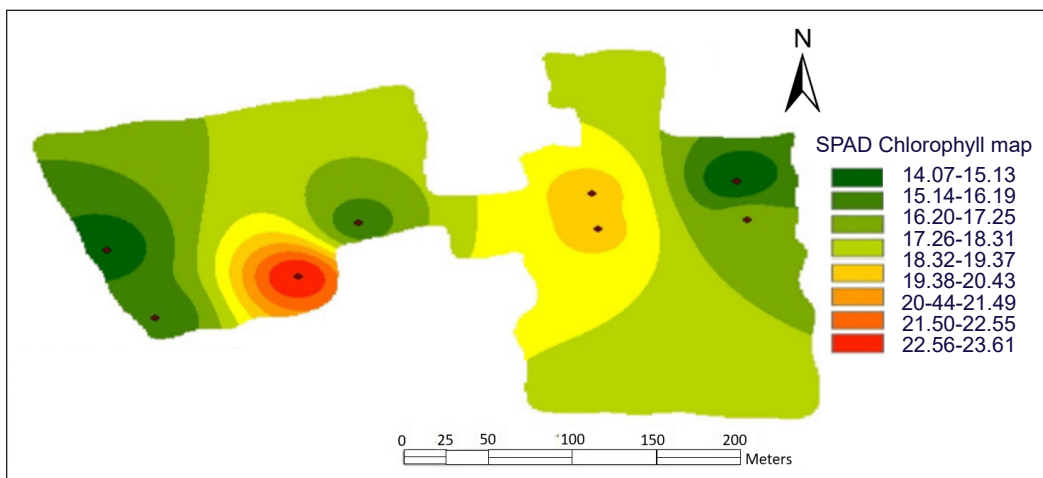


Figure 6. SPAD chlorophyll map for validation of vegetation indices (Yuhao et al., 2020)



## **IMPLEMENTATION OF PRECISION AGRICULTURE AMONG LOW-INCOME FARMERS**

Agriculture digitisation, including precision farming, has changed the way in which food is produced and land is managed. It helps to increase productivity and crop yield, lower expenses incurred for raw materials, and lower the environmental impact of on-farm operations. As the adoption cost of digital farming technology has decreased, remote sensing technologies such as UAVs are now more affordable and accessible, providing an opportunity for low-income farmers in small-scale plantations to improve their livelihood (FAO, 2022). Even if precision farming has significant potential benefits, the adoption of technologies by small-scale farmers and low-resource farming operations needs to be explored further.

One of the potential benefits of UAV usage is the ability to generate high-definition maps from UAV imagery. UAV provides a more accurate and timely representation of small-scale farms than satellite imagery, which often has lower resolution and is subject to cloud presence. It is important because farming operations often have diverse landscapes with a mix of crops, trees, and livestock that the conventional satellite images are unable to accurately represent. Maps and orthomosaics are beneficial for precision agriculture because they allow for a more comprehensive understanding of crop health and distribution (Montilla et al., 2021). Moreover, orthomosaic images can be utilised to monitor changes in the landscape over a specific period, providing useful data to make decisions for farm management. The farmers can evaluate the overall efficacy of their farming practices and identify real-time improvement by utilising orthomosaic images captured from their farms.

The orthomosaic images help them to make a better-informed decision on crop management. They can use this information to adjust their irrigation schedules, fertilisation, and pest control, resulting in increased agricultural productivity and cost savings. Farmers can obtain information on plant health and elevation data, which are generated from UAV images using various software. Also, they can obtain other information such as crop performance, soil moisture, and potential crop yield. It was found that the data helped farmers identify areas in their farms with low yields, thus allowing them to address potential problems in the future.

However, McCarthy et al. (2023) found challenges due to the widespread adoption of UAVs in the agricultural sector. Some farmers have expressed their concern in terms of cost, as well as the data accuracy and analysis. Some farmers remain sceptical about the usefulness of data provided by UAVs, as well as the privacy and security of their personal data. One of the reasons for such scepticism is the farmers' lack of education and literacy, which leads to confusion and mistrust towards technology and regulations (Dhanaraju et al., 2022). Many farmers expressed scepticism about the technology, and most of them were struggling to understand UAV applications and data. The majority of farmers are also

reluctant to share their data with government agencies or private companies, and only a small percentage are knowledgeable about UAV regulations and data-sharing laws.

To assist farmers who are less literate with technology, educational materials, training programmes, and community outreach initiatives must be accessible and clear about information on UAV technology, open data, and data privacy regulations. Radio and television, which are used for the dissemination of knowledge, could be an efficient way to reach out to such farmers. Only a small number of farmers have learnt about UAVs from traditional media sources such as print media, radio, or television. Farmers who are aware of UAVs often learn about them from friends and family. So, it is crucial to educate farmers about the benefits of UAV technology and data sharing to increase transparency in data collection and usage through collaboration with local organisations such as non-profit groups and agriculture extension agents.

When information comes from reputable sources such as government agents, educational institutions, and friends/family, it is easier to establish trust (Dhanaraju et al., 2018). Local organisations can help farmers understand the benefits and risks of UAV technology, open data, and data privacy by providing awareness, hands-on training, and dedicated support teams. Both subsistence and commercial farmers are interested in incorporating UAV technology into their farming practices, each with varying interests and concerns in specific applications. Such difference has a significant effect on agricultural policymakers and stakeholders. To encourage the use of UAV technology in agriculture, policies and programmes should take note of the differences and devise strategies to address the needs and concerns of the farmers. Policies that focus on lowering UAV costs or the provision of subsidies, for example, are more effective in persuading commercial farmers to adopt the technology. Programmes that focus on UAV training and education may be better suited for subsistence farmers. Policymakers and stakeholders must tailor their policies and programmes, taking into account their levels of interest, confidence, and perception of UAV technology.

## CONCLUSION

UAV technology has the potential to be a powerful tool to capture accurate and high-resolution images for remote sensing data in the future. Farmers may monitor crop development and paddy conditions in real-time using the NDVI map and SPAD data values. Meanwhile, advanced computer vision and machine learning algorithms can be used for image processing. Due to the large amount of data, several machine learning algorithms can be applied to UAV-based multispectral imaging using programming applications such as Python and other related web-based programmed cloud processing should be used in the near future. The analysis output can then be transferred in real-time to automation and robotics for decision-making and quick responses.

## ACKNOWLEDGEMENT

The Ministry of Higher Education Malaysia has provided financial support to conduct this review through the Long-term Research Grant Scheme (LRGS) for the research programme titled “Pest and Disease Monitoring Using Artificial Intelligent for Risk Management of Rice Under Climate Change”- LRGS/1/2019/UPM/2 (Vote No: 5545002).

## REFERENCES

- Abijo, A., Lee, C.-Y., Huang, C.-Y., Ho, P.-C., & Tsai, K.-J. (2023). The beneficial role of photobiomodulation in neurodegenerative diseases. *Biomedicines*, *11*(7), 1828-1850. <https://doi.org/10.3390/biomedicines11071828>
- Adnan, N., & Nordin, S. M. (2021). How COVID 19 effect Malaysian paddy industry? Adoption of green fertilizer a potential resolution. *Environment, Development and Sustainability*, *23*, 8089-8129. <https://doi.org/10.1007/s10668-020-00978-6>
- Akhtar, R., & Masud, M. M. (2022). Dynamic linkages between climatic variables and agriculture production in Malaysia: a generalized method of moments approach. *Environmental Science and Pollution Research*, *29*, 41557-41566. <https://doi.org/10.1007/s11356-021-18210-x>
- Ali, I., Cawkwell, F., Dwyer, E., Barrett, B., & Green, S. (2016). Satellite remote sensing of grasslands: From observation to management. *Journal of Plant Ecology*, *9*(6), 649-671. <https://doi.org/10.1093/jpe/rtw005>
- Alou, I. N., Steyn, J. M., Annandale, J. G., & Van der Laan, M. (2018). Growth, phenological, and yield response of upland rice (*Oryza sativa* L. cv. Nerica 4®) to water stress during different growth stages. *Agricultural Water Management*, *198*, 39-52. <https://doi.org/10.1016/j.agwat.2017.12.005>
- Barbedo, J. G. A. (2019). Detection of nutrition deficiencies in plants using proximal images and machine learning: A review. *Computers and Electronics in Agriculture*, *162*, 482-492. <https://doi.org/10.1016/j.compag.2019.04.035>
- Bazezew, M. N., Belay, A. T., Guda, S. T., & Kleinn, C. (2021). Developing maize yield predictive models from sentinel-2 msi derived vegetation indices: an approach to an early warning system on yield fluctuation and food security. *PFG–Journal of Photogrammetry, Remote Sensing and Geoinformation Science*, *89*, 535-548. <https://doi.org/10.1007/s41064-021-00178-5>
- Boursianis, A. D., Papadopoulou, M. S., Diamantoulakis, P., Liopa-Tsakalidi, A., Barouchas, P., Salahas, G., Karagiannidis, G., Wan, S., & Goudos, S. K. (2020). Internet of things (IoT) and agricultural unmanned aerial vehicles (UAVs) in smart farming: A comprehensive review. *Internet of Things*, *18*, Article 100187. <https://doi.org/10.1016/j.iot.2020.100187>
- Bujang, A. S., & Bakar, B. H. A. (2019, August). Precision agriculture in Malaysia. In *Proceedings of International Workshop on ICTs for Precision Agriculture* (pp. 6-8). ResearchGate.
- Chemura, A., Mutanga, O., & Dube, T. (2017). Integrating age in the detection and mapping of incongruous patches in coffee (*Coffea arabica*) plantations using multi-temporal Landsat 8 NDVI anomalies. *International Journal of Applied Earth Observation and Geoinformation*, *57*, 1-13. <https://doi.org/10.1016/j.jag.2016.12.007>

- Chen, X., Thorp, K. R., Ouyang, Z., Hou, Y., Zhou, B., & Li, Y. (2019). Energy consumption due to groundwater pumping for irrigation in the North China Plain. *Science of The Total Environment*, 669, 1033-1042. <https://doi.org/10.1016/j.scitotenv.2019.03.179>
- Cherlinka, V. (2023). *NDVI FAQ: All you need to know about index*. EOS Data Analytics. <https://eos.com/blog/ndvi-faq-all-you-need-to-know-about-ndvi/>
- Chusnah, W. N., Chu, H. J., Tatas, & Jaelani, L. M. (2023). Machine-learning estimation of high spatiotemporal resolution chlorophyll-a concentration using multi-satellite imagery. *Sustainable Environment Research*, 33(1), Article 11. <https://doi.org/10.1186/s42834-023-00170-1>
- Corti, M., Cavalli, D., Cabassi, G., Vigoni, A., Degano, L., & Gallina, P. M. (2019). Application of a low-cost camera on a UAV to estimate maize nitrogen-related variables. *Precision Agriculture*, 20, 675-696. <https://doi.org/10.1007/s11119-018-9609-y>
- Costa, E. M., Tassinari, W. D. S., Pinheiro, H. S. K., Beutler, S. J., & Dos Anjos, L. H. C. (2018). Mapping soil organic carbon and organic matter fractions by geographically weighted regression. *Journal of Environmental Quality*, 47(4), 718-725. <https://doi.org/10.2134/jeq2017.04.0178>
- Dardak, R. A. (2015). *Transformation of Agricultural Sector in Malaysia through Agricultural Policy*. Malaysian Agricultural Research and Development Institute (MARDI).
- Della Chiesa, T., Del Grosso, S. J., Hartman, M. D., Parton, W. J., Echarte, L., Yahdjian, L., & Piñeiro, G. (2022). A novel mechanism to simulate intercropping and relay cropping using the DayCent model. *Ecological Modelling*, 465, Article 109869. <https://doi.org/10.1016/j.ecolmodel.2021.109869>
- Deng, L., Mao, Z., Li, X., Hu, Z., Duan, F., & Yan, Y. (2018). UAV-based multispectral remote sensing for precision agriculture: A comparison between different cameras. *ISPRS Journal of Photogrammetry and Remote Sensing*, 146, 124-136. <https://doi.org/10.1016/j.isprsjprs.2018.09.008>
- Dhanaraju, M., Chenniappan, P., Ramalingam, K., Pazhanivelan, S., & Kaliaperumal, R. (2022). Smart farming: Internet of Things (IoT)-based sustainable agriculture. *Agriculture*, 12(10), Article 1745. <https://doi.org/10.3390/agriculture12101745>
- Dhau, I., Adam, E., Mutanga, O., & Ayisi, K. K. (2018). Detecting the severity of maize streak virus infestations in maize crop using in situ hyperspectral data. *Transactions of the Royal Society of South Africa*, 73(1), 8-15. <https://doi.org/10.1080/0035919X.2017.1370034>
- Dorairaj, D., & Govender, N. T. (2023). Rice and paddy industry in Malaysia: governance and policies, research trends, technology adoption and resilience. *Frontiers in Sustainable Food Systems*, 7, Article 1093605. <https://doi.org/10.3389/fsufs.2023.1093605>
- Duan, B., Fang, S., Zhu, R., Wu, X., Wang, S., Gong, Y., & Peng, Y. (2019) Remote estimation of rice yield with unmanned aerial vehicle (UAV) data and spectral mixture analysis. *Frontiers Plant Science*, 10, Article 204. <https://doi.org/10.3389/fpls.2019.00204>
- Elfri, M. A. A., Rahman, F. H., Newaz, S. H., Suhaili, W. S., & Au, T. W. (2023). Determining paddy crop health from aerial image using machine learning approach: A Brunei Darussalam based study. In *AIP Conference Proceedings* (Vol. 2643, No. 1). AIP Publishing. <https://doi.org/10.1063/5.0113668>

- Fahmi, Z., Samah, B. A., & Abdullah, H. (2013). Paddy industry and paddy farmers well-being: A success recipe for agriculture industry in Malaysia. *Asian Social Science*, 9(3), Article 177. <https://doi.org/10.5539/ass.v9n3p177>
- FAO. (2022). *Status of Digital Agriculture in 47 Sub-Saharan African Countries*. Food and Agriculture Organization of the United Nations. <https://www.fao.org/3/cb7943en/cb7943en.pdf>
- Farag, M. A., Sheashea, M., Zhao, C., & Maamoun, A. A. (2022). UV fingerprinting approaches for quality control analyses of food and functional food coupled to chemometrics: A comprehensive analysis of novel trends and applications. *Foods*, 11(18), Article 2867. <https://doi.org/10.3390/foods11182867>
- Feng, Z., Song, L., Duan, J., He, L., Zhang, Y., Wei, Y., & Feng, W. (2022). Monitoring wheat powdery mildew based on hyperspectral, thermal infrared, and RGB image data fusion. *Sensors*, 22(1), Article 31. <https://doi.org/10.3390/s22010031>
- Fenghua, Y., Tongyu, X., Yingli, C., Guijun, Y., Wen, D., & Shu, W. (2016). Models for estimating the leaf NDVI of japonica rice on a canopy scale by combining canopy NDVI and multisource environmental data in Northeast China. *International Journal of Agricultural and Biological Engineering*, 9(5), 132-142. <https://doi.org/10.3965/j.ijabe.20160905.2266>
- Firdaus, R. R., Leong Tan, M., Rahmat, S. R., & Senevi Gunaratne, M. (2020). Paddy, rice and food security in Malaysia: A review of climate change impacts. *Cogent Social Sciences*, 6(1), Article 1818373. <https://doi.org/10.1080/23311886.2020.1818373>
- Gée, C., Denimal, E., Merienne, J., & Larmure, A. (2021). Evaluation of weed impact on wheat biomass by combining visible imagery with a plant growth model: Towards new non-destructive indicators for weed competition. *Precision Agriculture*, 22, 550-568. <https://doi.org/10.1007/s11119-020-09776-6>
- Gohain, G. B., Singh, K. K., Singh, R. S., Dakhore, K. K., & Ghosh, K. (2022). Application of CERES-sorghum crop simulation model DSSAT v4. 7 for determining crop water stress in crop phenological stages. *Modeling Earth Systems and Environment*, 8, 1963-1975. <https://doi.org/10.1007/s40808-021-01194-5>
- Gracia-Romero, A., Kefauver, S. C., Vergara-Diaz, O., Zaman-Allah, M. A., Prasanna, B. M., Cairns, J. E., & Araus, J. L. (2017). Comparative performance of ground vs. aerially assessed RGB and multispectral indices for early-growth evaluation of maize performance under phosphorus fertilization. *Frontiers in Plant Science*, 8, Article 2004. <https://doi.org/10.3389/fpls.2017.02004>
- Grzebisz, W., & Lukowiak, R. (2021). Nitrogen gap amelioration is a core for sustainable intensification of agriculture - A concept. *Agronomy*, 11(3), Article 419. <https://doi.org/10.3390/agronomy11030419>
- Guo, Y., Chen, S., Li, X., Cunha, M., Jayavelu, S., Cammarano, D., & Fu, Y. (2022). Machine learning-based approaches for predicting SPAD values of maize using multi-spectral images. *Remote Sensing*, 14(6), Article 1337. <https://doi.org/10.3390/rs14061337>
- Guo, Y., Yin, G., Sun, H., Wang, H., Chen, S., Senthilnath, J., Wang, J., & Fu, Y. (2020). Scaling effects on chlorophyll content estimations with RGB camera mounted on a UAV platform using machine-learning methods. *Sensors*, 20(18), Article 5130. <http://doi.org/10.3390/s20185130>
- Hassan, S. I., Alam, M. M., Illahi, U., Al Ghamdi, M. A., Almotiri, S. H., & Su'ud, M. M. (2021). A systematic review on monitoring and advanced control strategies in smart agriculture. *IEEE Access*, 9, 32517-32548. <https://doi.org/10.1109/ACCESS.2021.3057865>

- Hassler, S. C., & Baysal-Gurel, F. (2019). Unmanned aircraft system (UAS) technology and applications in agriculture. *Agronomy*, 9(10), Article 618. <https://doi.org/10.3390/agronomy9100618>
- Hogan, S., Kelly, N., Stark, B., & Chen, Y. (2017). Unmanned aerial systems for agriculture and natural resources. *California Agriculture*, 71(1), 5-14. <https://doi.org/10.3733/ca.2017a0002>
- Hou, W., Tränkner, M., Lu, J., Yan, J., Huang, S., Ren, T., Cong, R., & Li, X. (2020). Diagnosis of nitrogen nutrition in rice leaves influenced by potassium levels. *Frontiers in Plant Science*, 11, Article 165. <https://doi.org/10.3389/fpls.2020.00165>
- Ibrahim, E. S., Rufin, P., Nill, L., Kamali, B., Nendel, C., & Hostert, P. (2021). Mapping crop types and cropping systems in Nigeria with sentinel-2 imagery. *Remote Sensing*, 13(17), Article 3523. <https://doi.org/10.3390/rs13173523>
- Irmulatov, B. R., Abdullaev, K. K., Komarov, A. A., & Yakushev, V. V. (2021). Prospects for precision management of wheat productivity in the conditions of Northern Kazakhstan. *Agricultural Biology*, 56(1), 92-102. <https://doi.org/10.15389/agrobiol.2021.1.92eng>
- Ishihara, M., Inoue, Y., Ono, K., Shimizu, M., & Matsuura, S. (2015). The impact of sunlight conditions on the consistency of vegetation indices in croplands - Effective usage of vegetation indices from continuous ground-based spectral measurements. *Remote Sensing*, 7(10), 14079-14098. <https://doi.org/10.3390/rs71014079>
- Iwahashi, Y., Sigit, G., Utoyo, B., Lubis, I., Junaedi, A., Trisasongko, B. H., Wijaya, I. M. A. S., Maki, M., Hongo, C., & Homma, K. (2022). Drought damage assessment for crop insurance based on vegetation index by unmanned aerial vehicle (UAV) multispectral images of paddy fields in Indonesia. *Agriculture*, 13(1), Article 113. <https://doi.org/10.3390/agriculture13010113>
- Jamroen, C., Komkum, P., Fongkerd, C., & Krongpha, W. (2020). An intelligent irrigation scheduling system using low-cost wireless sensor network toward sustainable and precision agriculture. *IEEE Access*, 8, 172756-172769. <https://doi.org/10.1109/ACCESS.2020.3025590>
- Janga, B., Asamani, G. P., Sun, Z., & Cristea, N. (2023). A review of practical ai for remote sensing in earth sciences. *Remote Sensing*, 15(16), Article 4112. <https://doi.org/10.3390/rs15164112>
- Kalischuk, M., Paret, M. L., Freeman, J. H., Raj, D., Da Silva, S., Eubanks, S., Wiggins, D. J., Lollar, M., Marois, J. J., Mellinger, H. C., & Das, J. (2019). An improved crop scouting technique incorporating unmanned aerial vehicle-assisted multispectral crop imaging into conventional scouting practice for gummy stem blight in watermelon. *Plant Disease*, 103(7), 1642-1650. <https://doi.org/10.1094/PDIS-08-18-1373-RE>
- Kamarianakis, Z., & Panagiotakis, S. (2023). Design and implementation of a low-cost chlorophyll content meter. *Sensors*, 23(5), Article 2699. <https://doi.org/10.3390/s23052699>
- Karunanithy, K., & Velusamy, B. (2021). Directional antenna based node localization and reliable data collection mechanism using local sink for wireless sensor networks. *Journal of Industrial Information Integration*, 24, Article 100222. <https://doi.org/10.1016/j.jii.2021.100222>
- Kasim, N. M., Ahmad, M. H., Shaharudin, A. B., Naidu, B. M., Chan, Y. Y., & Aris, T. (2018). Food choices among Malaysian adults: Findings from Malaysian adults nutrition survey (MANS) 2003 and MANS 2014. *Malaysian Journal of Nutrition*, 24(1), 63-75.

- Kazemi, F., & Parmehr, E. G. (2023). Evaluation of RGB vegetation indices derived from UAV images for rice crop growth monitoring. *ISPRS Annals of the Photogrammetry, Remote Sensing and Spatial Information Sciences*, 10, 385-390. <https://doi.org/10.5194/isprs-annals-X-4-W1-2022-385-2023>
- Kganyago, M., Ovakoglou, G., Mhangara, P., Adjorlolo, C., Alexandridis, T., Laneve, G., & Beltran, J. S. (2023). Evaluating the contribution of Sentinel-2 view and illumination geometry to the accuracy of retrieving essential crop parameters. *GIScience & Remote Sensing*, 60(1), Article 2163046. <https://doi.org/10.1080/15481603.2022.2163046>
- Low, J. W., Ortiz, R., Vandamme, E., Andrade, M., Biazin, B., & Grüneberg, W. J. (2020). Nutrient-dense orange-fleshed sweetpotato: Advances in drought-tolerance breeding and understanding of management practices for sustainable next-generation cropping systems in sub-Saharan Africa. *Frontiers in Sustainable Food Systems*, 4, Article 50. <https://doi.org/https://doi.org/10.3389/fsufs.2020.00050>
- Lu, W., Okayama, T., & Komatsuzaki, M. (2021). Rice height monitoring between different estimation models using UAV photogrammetry and multispectral technology. *Remote Sensing*, 14(1), Article 78. <https://doi.org/10.3390/rs14010078>
- Luo, S., Jiang, X., Jiao, W., Yang, K., Li, Y., & Fang, S. (2022). Remotely sensed prediction of rice yield at different growth durations using UAV multispectral imagery. *Agriculture*, 12(9), Article 1447. <https://doi.org/10.3390/agriculture12091447>
- Mallareddy, M., Thirumalaikumar, R., Balasubramanian, P., Naseeruddin, R., Nithya, N., Mariadoss, A., Eazhilkrishna, N., Choudhary, A. K., Deiveegan, M., Subrramanian, E., Padmaja, B., & Vijayakumar, S. (2023). Maximizing water use efficiency in rice farming: A comprehensive review of innovative irrigation management technologies. *Water*, 15(10), Article 1802. <https://doi.org/10.3390/w15101802>
- Mapfumo, R. B., Murwira, A., Masocha, M., & Andriani, R. (2017). Detection of subtle deforestation due to logging using satellite remote sensing in wet and dry savanna woodlands of Southern Africa. *Geocarto International*, 32(5), 514-530. <https://doi.org/10.1080/10106049.2016.1161074>
- McCarthy, C., Nyoni, Y., Kachamba, D. J., Banda, L. B., Moyo, B., Chisambi, C., Banfill, J., & Hoshino, B. (2023). Can drones help smallholder farmers improve agriculture efficiencies and reduce food insecurity in Sub-Saharan Africa? Local perceptions from Malawi. *Agriculture*, 13(5), Article 1075. <https://doi.org/10.3390/agriculture13051075>
- McCarty, J. L., Neigh, C. S. R., Carroll, M. L., & Wooten, M. R. (2017). Extracting smallholder cropped area in Tigray, Ethiopia with wall-to-wall sub-meter WorldView and moderate resolution Landsat 8 imagery. *Remote Sensing of Environment*, 202, 142-151. <https://doi.org/10.1016/j.rse.2017.06.040>
- Meroni, M., d'Andrimont, R., Vrieling, A., Fasbender, D., Lemoine, G., Rembold, F., Seguini, L., & Verhegghen, A. (2021). Comparing land surface phenology of major European crops as derived from SAR and multispectral data of Sentinel-1 and-2. *Remote Sensing of Environment*, 253, Article 112232. <https://doi.org/10.1016/j.rse.2020.112232>
- Ministry of Agriculture. (1984). *Third National Agricultural Policy (1998 - 2010) - Executive Summary*. [https://www.pmo.gov.my/dokumenattached/Dasar/29THIRD\\_NATIONAL\\_AGRICULTURAL\\_POLICY\\_\(1998\\_-\\_2010\)\\_-\\_EXECUTIVE\\_SUMMARY.pdf](https://www.pmo.gov.my/dokumenattached/Dasar/29THIRD_NATIONAL_AGRICULTURAL_POLICY_(1998_-_2010)_-_EXECUTIVE_SUMMARY.pdf)

- Ministry of Agriculture (2016). *Dasar Sekuriti Makanan Negara* [National Food Security Policy]. Ministry of Agriculture and Agro-based Industry. <https://www.kpk.gov.my/>
- Monteiro, A., Santos, S., & Gonçalves, P. (2021). Precision agriculture for crop and livestock farming - Brief review. *Animals*, 11(8), Article 2345. <https://doi.org/10.3390/ani11082345>
- Montilla, R., Montilla, G., Perez, E., Frassato, L., & Seijas, C. (2021). Precision agriculture for rice crops with an emphasis in low health index areas. *Revista Facultad Nacional de Agronomía Medellín*, 74(1), 9383-9393. <https://doi.org/10.15446/rfnam.v74n1.85310>
- Munnaf, M. A., Haesaert, G., Van Meirvenne, M., & Mouazen, A. M. (2020). Site-specific seeding using multi-sensor and data fusion techniques: A review. *Advances in Agronomy*, 161, 241-323. <https://doi.org/10.1016/bs.agron.2019.08.001>
- Naguib, N. S., & Daliman, S. (2022, November). Analysis of NDVI and NDRE indices using satellite images for crop identification at Kelantan. In *IOP Conference Series: Earth and Environmental Science* (Vol. 1102, No. 1, p. 012054). IOP Publishing. <https://doi.org/10.1088/1755-1315/1102/1/012054>
- Nestel, D., Cohen, Y., Shaked, B., Alchanatis, V., Nemny-Lavy, E., Miranda, M. A., Sciarretta, A., & Papadopoulos, N. T. (2019). An integrated decision support system for environmentally-friendly management of the Ethiopian fruit fly in greenhouse crops. *Agronomy*, 9(8), Article 459. <https://doi.org/10.3390/agronomy9080459>
- Neupane, K., & Baysal-Gurel, F. (2021). Automatic identification and monitoring of plant diseases using unmanned aerial vehicles: A review. *Remote Sensing*, 13(19), Article 3841. <https://doi.org/10.3390/rs13193841>
- Nguy-Robertson, A., Gitelson, A., Peng, Y., Viña, A., Arkebauer, T., & Rundquist, D. (2012). Green leaf area index estimation in maize and soybean: Combining vegetation indices to achieve maximal sensitivity. *Agronomy Journal Abstract – Biometry, Modeling and Statistics*, 104(5), 1336-1347. <https://doi.org/10.2134/agronj2012.0065>
- Norasma, C. Y. N., Fadzilah, M. A., Roslin, N. A., Zanariah, Z. W. N., Tarmidi, Z., & Candra, F. S. (2019, April). Unmanned aerial vehicle applications in agriculture. In *IOP Conference Series: Materials Science and Engineering* (Vol. 506, p. 012063). IOP Publishing. <https://doi.org/10.1088/1757-899X/506/1/012063>
- Olson, D., & Anderson, J. (2021). Review on unmanned aerial vehicles, remote sensors, imagery processing, and their applications in agriculture. *Agronomy Journal*, 113(2), 971-992. <https://doi.org/10.1002/agj2.20595>
- Omar, S. C., Shaharudin, A., & Tumin, S. A. (2019). *The Status of the Paddy and Rice Industry in Malaysia*. Khazanah Research Institute. [https://www.krinstitute.org/assets/contentMS/img/template/editor/Rice%20Report\\_Ppt%20Slide\\_Sarena.pdf](https://www.krinstitute.org/assets/contentMS/img/template/editor/Rice%20Report_Ppt%20Slide_Sarena.pdf)
- Onyango, C. M., Nyaga, J. M., Wetterlind, J., Söderström, M., & Piikki, K. (2021). Precision agriculture for resource use efficiency in smallholder farming systems in Sub-Saharan Africa: A systematic review. *Sustainability*, 13(3), Article 1158. <https://doi.org/10.3390/su13031158>
- Osman, Z., & Shahiri, H. (2017). Ethnic and gender inequality in employment during the new economic policy. *Institutions and Economies*, 6(1), 57-72.



- Othman, K., Omar, H., Fuad, H. A., Laidin, J., & Ramli, I. M. (2020). The causal impact of government support on the small strategic crop industry: Malaysia's experience. *Asian Journal of Agriculture and Rural Development*, 10(1), 298-310. <https://doi.org/10.18488/journal.1005/2020.10.1/1005.1.298.310>
- Pérez-Ortiz, M., Gutiérrez, P. A., Peña, J. M., Torres-Sánchez, J., López-Granados, F., & Hervás-Martínez, C. (2016). Machine learning paradigms for weed mapping via unmanned aerial vehicles. In *2016 IEEE symposium series on computational intelligence (SSCI)* (pp. 1-8). IEEE Publication. <https://doi.org/10.1109/SSCI.2016.7849987>
- Pokhrel, A., Virk, S., Snider, J. L., Vellidis, G., Hand, L. C., Sintim, H. Y., Parkash, V., Chalise, D. P., Lee, J. M., & Byers, C. (2023). Estimating yield-contributing physiological parameters of cotton using UAV-based imagery. *Frontiers in Plant Science*, 14. <https://doi.org/10.3389/fpls.2023.1248152>
- Ponnusamy, V., & Natarajan, S. (2021). Precision agriculture using advanced technology of IoT, unmanned aerial vehicle, augmented reality, and machine learning. In D. Gupta, C. Hugo, de Albuquerque, A. Khanna & P. L. Mehta, (Eds.), *Smart Sensors for Industrial Internet of Things* (pp. 207-229). Springer. [https://doi.org/10.1007/978-3-030-52624-5\\_14](https://doi.org/10.1007/978-3-030-52624-5_14)
- Pretorius, Z. A., Lan, C. X., Prins, R., Knight, V., McLaren, N. W., Singh, R. P., Bender, C. M., & Kloppers, F. J. (2017). Application of remote sensing to identify adult plant resistance loci to stripe rust in two bread wheat mapping populations. *Precision Agriculture*, 18, 411-428. <https://doi.org/10.1007/s11119-016-9461-x>
- Raddi, S., Giannetti, F., Martini, S., Farinella, F., Chirici, G., Tani, A., Maltoni, A., & Mariotti, B. (2022). Monitoring drought response and chlorophyll content in Quercus by consumer-grade, near-infrared (NIR) camera: A comparison with reflectance spectroscopy. *New Forests*, 53(2), 241-265. <https://doi.org/10.1007/s11056-021-09848-z>
- Rahmat, S. R., Firdaus, R. R., Mohamad Shaharudin, S., & Yee Ling, L. (2019). Leading key players and support system in Malaysian paddy production chain. *Cogent Food & Agriculture*, 5(1), Article 1708682. <https://doi.org/10.1080/23311932.2019.1708682>
- Ramli, N. N., Shamsudin, M. N., Mohamed, Z., & Radam, A. (2012). The impact of fertilizer subsidy on Malaysia paddy/rice industry using a system dynamics approach. *International Journal of Social Science and Humanity*, 2(3), Article 213.
- Richard, K., Abdel-Rahman, E. M., Subramanian, S., Nyasani, J. O., Thiel, M., Jozani, H., Borgemeister, C., & Landmann, T. (2017). Maize cropping systems mapping using rapideye observations in agro-ecological landscapes in Kenya. *Sensors*, 17(11), Article 2537. <https://doi.org/10.3390/s17112537>
- Roman, A., & Ursu, T. (2016). Multispectral satellite imagery and airborne laser scanning techniques for the detection of archaeological vegetation marks. In C. H. Opreanu & V. A. Lazarecu (Eds.), *Landscape Archaeology on the Northern Frontier of the Roman Empire at Porolissum: An Interdisciplinary Research Project* (pp. 141-152). Mega Publishing House.
- Rosle, R., Che'Ya, N. N., Roslin, N. A., Halip, R. M., & Ismail, M. R. (2019). Monitoring early stage of rice crops growth using normalized difference vegetation index generated from UAV. In *IOP Conference Series: Earth and Environmental Science* (Vol. 355, No. 1, p. 012066). IOP Publishing. <https://doi.org/10.1088/1755-1315/355/1/012066>

- Rosle, R., Sulaiman, N., Che` Ya, N. N., Radzi, M. F. M., Omar, M. H., Berahim, Z., Ilahi, W. F. F., Shah, J. A., & Ismail, M. R. (2022). Weed detection in rice fields using UAV and multispectral aerial imagery. *Chemistry Proceedings*, 10(1), Article 44. <https://doi.org/10.3390/IOCAG2022-12519>
- Roth, L., Barendregt, C., Bétrix, C. A., Hund, A., & Walter, A. (2022). High-throughput field phenotyping of soybean: Spotting an ideotype. *Remote Sensing of Environment*, 269, Article 112797. <https://doi.org/10.1016/j.rse.2021.112797>
- Rusli, N. M., Noor, Z. Z., & Taib, S. M. (2024). Life cycle assessment of rice production in Muda Granary Area, Kedah, Malaysia. *Journal of Advanced Research in Applied Sciences and Engineering Technology*, 35(2), 69-83. <https://doi.org/10.37934/araset.35.2.6983>
- Sari, M. Y. A., Hassim, Y. M. M., Hidayat, R., & Ahmad, A. (2021). Monitoring rice crop and paddy field condition using UAV RGB imagery. *International Journal on Informatics Visualization*, 5(4), 469-474. <https://dx.doi.org/10.30630/joiv.5.4.742>
- Sato, N. K., Tsuji, T., Iijima, Y., Sekiya, N., & Watanabe, K. (2023). Predicting rice lodging risk from the distribution of available nitrogen in soil using uas images in a paddy field. *Sensors*, 23(14), Article 6466. <https://doi.org/10.3390/s23146466>
- Seglah, P. A., Wang, Y., Wang, H., Bi, Y., Zhou, K., Wang, Y., Wang, Y., Wang, H., & Feng, X. (2020). Crop straw utilization and field burning in Northern region of Ghana. *Journal of Cleaner Production*, 261, Article 121191. <https://doi.org/10.1016/j.jclepro.2020.121191>
- Sharabiani, V. R., Nazarloo, A. S., Taghinezhad, E., Veza, I., Szummy, A., & Figiel, A. (2023). Prediction of winter wheat leaf chlorophyll content based on VIS/NIR spectroscopy using ANN and PLSR. *Food Science & Nutrition*, 11(5), 2166-2175. <https://doi.org/10.1002/fsn3.3071>
- Shu, M., Zuo, J., Shen, M., Yin, P., Wang, M., Yang, X., Tang, J., Li, B., & Ma, Y. (2021). Improving the estimation accuracy of SPAD values for maize leaves by removing UAV hyperspectral image backgrounds. *International Journal of Remote Sensing*, 42, 5862-5881. <https://doi.org/10.1080/01431161.2021.1931539>
- Sishodia, R. P., Ray, R. L., & Singh, S. K. (2020). Applications of remote sensing in precision agriculture: A review. *Remote Sensing*, 12(19), Article 3136. <https://doi.org/10.3390/rs12193136>
- Souza, F. H. Q., Martins, P. H. A., Martins, T. H. D., Teodoro, P. E., & Baio, F. H. R. (2020). The use of vegetation index via remote sensing allows estimation of soybean application rate. *Remote Sensing Applications: Society and Environment*, 17, Article 100279. <https://doi.org/10.1016/j.rsase.2019.100279>
- Stöcker, C., Bennett, R., Nex, F., Gerke, M., & Zevenbergen, J. (2017). Review of the current state of UAV regulations. *Remote Sensing*, 9(5), Article 459. <https://doi.org/10.3390/rs9050459>
- Sudu, B., Rong, G., Guga, S., Li, K., Zhi, F., Guo, Y., Zhang, J., & Bao, Y. (2022). Retrieving SPAD values of summer maize using UAV hyperspectral data based on multiple machine learning algorithm. *Remote Sensing*, 14(21), Article 5407. <https://doi.org/10.3390/rs14215407>
- Sui, Y. Y., Wang, Q. Y., & Yu, H. Y. (2016). Prediction of greenhouse cucumber disease based on chlorophyll fluorescence spectrum index. *Guang pu xue yu Guang pu fen xi= Guang pu*, 36(6), 1779-1782.

- Takoutsing, B., Martín, J. A. R., Weber, J. C., Shepherd, K., Sila, A., & Tondoh, J. (2017). Landscape approach to assess key soil functional properties in the highlands of Cameroon: Repercussions of spatial relationships for land management interventions. *Journal of Geochemical Exploration*, 178, 35-44. <https://doi.org/10.1016/j.gexplo.2017.03.014>
- The Star. (2019, April 13). Where does Malaysia's paddy and rice industry stand? *The Star*. <https://www.thestar.com.my/business/business-news/2019/04/13/where-does-malaysias-paddy-and-rice-industry-stand/>
- Tsai, D. M., & Chen, W. L. (2017). Coffee plantation area recognition in satellite images using Fourier transform. *Computers and Electronics in Agriculture*, 135, 115-127. <https://doi.org/10.1016/j.compag.2016.12.020>
- Tsouros, D. C., Bibi, S., & Sarigiannidis, P. G. (2019). A review on UAV-based applications for precision agriculture. *Information*, 10(11), Article 349. <https://doi.org/10.3390/info10110349>
- USDA. (2020). *World Agricultural Production*. USDA Foreign Agricultural Service, USA. <https://www.fas.usda.gov/data/world-agricultural-production>
- Wan, L., Cen, H., Zhu, J., Zhang, J., Zhu, Y., Sun, D., Du, X., Zhai, L., Weng, H., Li, Y., Li, X., Bao, Y., Shou, J., & He, Y. (2020). Grain yield prediction of rice using multi-temporal UAV-based RGB and multispectral images and model transfer - A case study of small farmlands in the South of China. *Agricultural and Forest Meteorology*, 291, Article 108096. <https://doi.org/10.1016/j.agrformet.2020.108096>
- Wan, W., Zhao, Y., Xu, J., Liu, K., Guan, S., Chai, Y., Cui, H., Wu, P., & Diao, M. (2022). Reducing and delaying nitrogen recommended by leaf critical SPAD value was more suitable for nitrogen utilization of spring wheat under a new type of drip-irrigated system. *Agronomy*, 12(10), Article 2331. <https://doi.org/10.3390/agronomy12102331>
- Wang, K., Huggins, D. R., & Tao, H. (2019). Rapid mapping of winter wheat yield, protein, and nitrogen uptake using remote and proximal sensing. *International Journal of Applied Earth Observation and Geoinformation*, 82, Article 101921. <https://doi.org/10.1016/j.jag.2019.101921>
- Wang, Y. P., Chang, Y. C., & Shen, Y. (2022). Estimation of nitrogen status of paddy rice at vegetative phase using unmanned aerial vehicle based multispectral imagery. *Precision Agriculture*, 23(1), 1-17. <https://doi.org/10.1007/s11119-021-09823-w>
- Winowiecki, L. A., Vågen, T. G., Boeckx, P., & Dungait, J. A. (2017). Landscape-scale assessments of stable carbon isotopes in soil under diverse vegetation classes in East Africa: Application of near-infrared spectroscopy. *Plant and Soil*, 421, 259-272. <https://doi.org/10.1007/s11104-017-3418-3>
- Xie, C., & Yang, C. (2020). A review on plant high-throughput phenotyping traits using UAV-based sensors. *Computers and Electronics in Agriculture*, 178, Article 105731. <https://doi.org/10.1016/j.compag.2020.105731>
- Yang, X., Yang, R., Ye, Y., Yuan, Z., Wang, D., & Hua, K. (2021). Winter wheat SPAD estimation from UAV hyperspectral data using cluster-regression methods. *International Journal of Applied Earth Observation and Geoinformation*, 105, Article 102618. <https://doi.org/10.1016/j.jag.2021.102618>
- Yin, Q., Zhang, Y., Li, W., Wang, J., Wang, W., Ahmad, I., Zhou, G., & Huo, Z. (2023). Estimation of winter wheat SPAD values based on UAV multispectral remote sensing. *Remote Sensing*, 15(14), Article 3595. <https://doi.org/10.3390/rs15143595>

- Yuan, Z., Cao, Q., Zhang, K., Ata-Ul-Karim, S. T., Tian, Y., Zhu, Y., Cao, W., & Liu, X. (2016). Optimal leaf positions for SPAD meter measurement in rice. *Frontiers in plant science*, 7, Article 719. <https://doi.org/10.3389/fpls.2016.00719>
- Yuhao, A., Che'Ya, N. N., Roslin, N. A., & Ismail, M. R. (2020). Rice chlorophyll content monitoring using vegetation indices from multispectral aerial imagery. *Pertanika Journal of Science & Technology*, 28(3), 779-795.
- Zhang, K., Liu, X., Ma, Y., Wang, Y., Cao, Q., Zhu, Y., Cao, W., & Tian, Y. (2021). A new canopy chlorophyll index-based paddy rice critical nitrogen dilution curve in eastern China. *Field Crops Research*, 266, Article 108139. <https://doi.org/10.1016/j.fcr.2021.108139>
- Zhang, R., Yang, P., Liu, S., Wang, C., & Liu, J. (2022). Evaluation of the methods for estimating leaf chlorophyll content with SPAD chlorophyll meters. *Remote Sensing*, 14(20), Article 5144. <https://doi.org/10.3390/rs14205144>
- Zhang, S., Zhao, G., Lang, K., Su, B., Chen, X., Xi, X., & Zhang, H. (2019) Integrated satellite, unmanned aerial vehicle (UAV) and ground inversion of the SPAD of winter wheat in the reviving stage. *Sensors*, 19(17), Article 1485. <http://doi.org/10.3390/s19071485>
- Zhang, Z., & Zhu, L. (2023). A review on unmanned aerial vehicle remote sensing: platforms, sensors, data processing methods, and applications. *Drones*, 7(6), Article 398. <https://doi.org/10.3390/drones7060398>
- Zhao, Y., Yang, P., Cheng, Y., Liu, Y., Yang, Y., & Liu, Z. (2023). Insights into the physiological, molecular, and genetic regulators of albinism in *Camellia sinensis* leaves. *Frontiers in Genetics*, 14. <https://doi.org/10.3389/fgene.2023.1219335>
- Zhu, W., Feng, Z., Dai, S., Zhang, P., & Wei, X. (2022). Using UAV multispectral remote sensing with appropriate spatial resolution and machine learning to monitor wheat scab. *Agriculture*, 12(11), Article 1785. <https://doi.org/10.3390/agriculture12111785>

## A Comparison of Results from Two Multi-Criteria Decision-Making Methods for Solar Photovoltaic Plant Site Location: Case Study Rio De Janeiro

**Marco Pereira de Souza\*, Luis Claudio Bernardo Moura, Carlos Alberto Nunes Cosenza, Silvio de Macedo Amaral, Rodrigo Pestana Cunha Telles, Manuel Oliveira Lemos Alexandre, Silvio Barbosa, Bruno de Sousa Elia, Maria Fernanda Zelaya Correia, Antonio Carlos de Lemos Oliveira, Rodrigo Ventura da Silva and Thais Rodrigues Pinheiro**

*Industrial Engineering Department, Alberto Luiz Coimbra Institute for Graduate Studies and Research in Engineering (COPPE-UFRJ), Rio de Janeiro, Brazil*

### ABSTRACT

Photovoltaic (PV) energy has become a low-cost, renewable, and environmentally friendly alternative to meet increasing energy demand. Nevertheless, there is still a lack of projects in this field in Brazil. Therefore, this study compares the results of two studies on the optimal site selection of PV in the Brazilian state of Rio de Janeiro. These studies used different methodologies to reach the conclusions and the resulting map. First, the final map of both studies was divided into a grid, and then the results of each cell were weighted for PV site selection. To compare the results using the maps, an intersection

of the 10% of the grid cells with the best results from each study was formed. The results showed an 83% similarity between the different Multi-Criteria Decision-Making (MCDM) methods. The other part of the comparison focused on the following rank similarity coefficients: Spearman Correlation Coefficient, WS Coefficient, Spearman Weighted Correlation Coefficient, and Blest Correlation Coefficient. All these coefficients had values greater than 0.9, indicating a high degree of correlation between the results of the studies. Therefore, the two studies have a high degree of

### ARTICLE INFO

#### Article history:

Received: 08 February 2023

Accepted: 02 October 2023

Published: 23 February 2024

DOI: <https://doi.org/10.47836/pjst.32.2.05>

#### E-mail addresses:

[marcopsh@hotmail.com](mailto:marcopsh@hotmail.com); [marcopg@gmail.com](mailto:marcopg@gmail.com) (Marco Pereira de Souza)

[luismoura.coppe@outlook.com](mailto:luismoura.coppe@outlook.com) (Luis Claudio Bernardo Moura)

[cosenzacoppe@gmail.com](mailto:cosenzacoppe@gmail.com) (Carlos Alberto Nunes Cosenza)

[silvioamaral@uol.com.br](mailto:silvioamaral@uol.com.br) (Silvio de Macedo Amaral)

[rpctelles@ufrj.br](mailto:rpctelles@ufrj.br) (Rodrigo Pestana Cunha Telles)

[manuel.alexandre@pep.ufrj.br](mailto:manuel.alexandre@pep.ufrj.br) (Manuel Oliveira Lemos Alexandre)

[silvio.barbosa@coppe.ufrj.br](mailto:silvio.barbosa@coppe.ufrj.br) (Silvio Barbosa)

[prof.brunoelia@gmail.com](mailto:prof.brunoelia@gmail.com) (Bruno de Sousa Elia)

[mfernandazelaya@hotmail.com](mailto:mfernandazelaya@hotmail.com) (Maria Fernanda Zelaya Correia)

[prof.lemos@gmail.com](mailto:prof.lemos@gmail.com) (Antonio Carlos de Lemos Oliveira)

[ventrod@yahoo.com.br](mailto:ventrod@yahoo.com.br) (Rodrigo Ventura da Silva)

[thais\\_ufrj.pep@hotmail.com](mailto:thais_ufrj.pep@hotmail.com) (Thais Rodrigues Pinheiro)

\* Corresponding author

similarity and a high potential for installing photovoltaic solar power plants in Rio de Janeiro, especially in its intersection zones.

*Keywords:* GIS, multi-criteria decision making (MCDM), Rio de Janeiro, site selection, solar photovoltaic (PV)

---

## INTRODUCTION

One of the main issues of sustainable development lies in the innovations and technological advances for transforming and using natural resources (Pereira et al., 2017). According to the Intergovernmental Panel on Climate Change (IPCC), the temperature increase has reached about 1°C. It is important to keep it below 1.5°C, considering the values from before the Industrial Revolution, to mitigate the consequences of global warming. Therefore, it is necessary to reduce the use of fossil fuels, including in energy production (Allen et al., 2018).

Several studies show that solar energy has numerous advantages compared to other renewable energy sources. Moreover, photovoltaics is one of the best options to meet the increasing energy demand in the future (Razykov et al., 2011; Uyan, 2013). For example, solar energy is everywhere on Earth, accounting for 99.8% of the total energy reaching Earth's surface. It also comes from the sun, making it an accessible and inexhaustible source of energy (Al-Shamisi et al., 2013; Jain et al., 2011; Ramedani et al., 2013), and if only 0.1% of this energy were converted into electricity at an efficiency rate of 10%, this amount would be sufficient to meet the planet's needs several times over (Thirugnanasambandam et al., 2010). In addition, the cost of solar photovoltaics is decreasing; for example, between 2010 and 2019, it decreased by 82%, making PV competitive with traditional energy sources (IRENA, 2020). In 2020, the estimated cost of new PV projects is 0.057 USD/kWh, while fossil fuel costs range from 0.055 to 0.236 USD/kWh, and the 2030 target is 0.02 USD/kWh, according to the Office of Energy Efficiency & Renewable Energy (<https://www.energy.gov/eere/solar/articles/2030-solar-cost-targets>; La Camera, 2020).

On the demand side, electricity consumption in Brazil is expected to increase by about 30% by 2030 and about 95% by 2050. In addition, Brazil recently experienced an unprecedented drought, a serious problem since most of its electricity generation comes from hydropower (<http://www.ons.org.br/paginas/energia-agora/reservatorios>; EPE, 2020a, 2020b, 2016). Therefore, clean, reliable renewable energy sources are needed to meet the increasing demand projected for the coming years.

Rio de Janeiro, one of the 27 federative units of Brazil, is a state with an area of 43,752 km<sup>2</sup> (CEPERJ, 2022a), a GDP of BRL 758 billion, which is about 10.8% of the total GDP of the country, and the second largest economy (CEPERJ, 2019), with a population of 17.4 million people, the third largest in Brazil (IBGE, 2022). The state is divided into seven regions, which are very different from each other. The metropolitan area of Rio de

Janeiro, the capital, concentrates 70% of the population and most of the economic and industrial resources (CEPERJ, 2022b). The state's geography is very heterogeneous, with high cliffs, hills, and valleys, as well as an extensive plateau that covers the entire western part of the territory and several areas of the Atlantic Forest (Ribeiro & Nunes, 2019). Regarding solar irradiation, the state has excellent levels, averaging between 4 and 5.5 kWh/m<sup>2</sup> across different regions (EGPEnergia & PUC-Rio, 2016). Despite the potential, Rio de Janeiro generated only 65 GWh of energy from solar PV in 2019, less than 1% of its total electricity generation (EPE, 2020a).

Various factors must be considered when determining the best locations for solar photovoltaic plants, including solar irradiation, existing infrastructure, and surrounding terrain characteristics (San Cristóbal, 2011; Zoghi et al., 2017). These factors range from the proximity of the grid and the road to the azimuth and slope of the terrain, apart from many restriction zones, i.e., locations where PV plant projects cannot be implemented. For this reason, searching for the most suitable sites for Rio de Janeiro requires the right tools and methods.

Multi-Criteria Decision-Making (MCDM) methods find extensive application across diverse fields, aiding decision-makers in navigating complex and often conflicting criteria (Figueira et al., 2005; Roy, 2016; Sařabun & Piegat, 2017). To this end, the result of the MCDM methods usually ranks the available alternatives, with the best ones in first place (Bandyopadhyay, 2016). These methods are commonly used for various problems, including renewable energy (Kolios et al., 2016; Sařabun & Piegat, 2017). Due to the complexity of this issue, renewable energy site selection often involves multiple alternatives based on a variety of criteria (Shao et al., 2020).

Mapping is an important method of analysis in the arts, humanities, and sciences that uses geospatial technologies to collect data about people and places (Manson et al., 2017). A Geographic Information System (GIS) is a computerized system based on cartography, geography, and remote sensing that can perform multiple functions, such as collecting, storing, analyzing, and presenting large data sets as maps (Das & Bhuyan, 2017; Wang et al., 2019). There are several examples where GIS is combined with MCDM. One of the main advantages of this tool is its excellent ability to perform an analysis of optimal locations for renewable energy plants through the possibility of using multiple layers (e.g., slope and solar irradiation) that provide maps and numerical information in one database (Janke, 2010; Sánchez-Lozano et al., 2016a; Van Haaren & Fthenakis, 2011). For example, according to Shao et al., of the 85 papers on renewable energy siting that their study reviewed, 52 used GIS (Shao et al., 2020).

Multi-criteria Decision-Making methods have become progressively popular in renewable energy power plant site selection (Shao et al., 2020). Recently, many studies have been conducted in different countries to evaluate the suitability of solar PV plants

by combining GIS with MCDM: Yushchenko et al. (2018) in West Africa (ECOWAS region), Aly et al. (2017) in Tanzania, Uyan (2013) for the Konya Region in Turkey, Al Garni and Awasthi (2017) for Saudi Arabia, Kwak et al. (2021) for the state of Illinois in the United States, Sánchez-Lozano et al. (2016b) for Murcia region in Spain, Zoghi et al. (2017) for Isfahan region in Iran, Qiu et al. (2022) in China, Sindhu et al. (2017) for the Haryana region in India, Janke (2010), Doorga et al. (2019) for Mauritius, Palmer et al. (2019) for the United Kingdom and several others. There is no single MCDM method in these studies, although AHP (Analytical Hierarchical Process) is the most commonly used (Shao et al., 2020).

Many MCDM methods exist, but none is perfect and suitable for every decision-making situation. Moreover, different approaches may lead to different results (Guitouni & Martel, 1998; Zanakis et al., 1998), and several factors may explain this divergence, such as the adoption of different weights for the selected criteria or the differences between the methods and algorithms themselves (Zanakis et al., 1998). Researchers and decision-makers should consider the trade-offs between various MCDM models (Shao et al., 2020). Therefore, by comparing the results of a variety of MCDM models, the merits and weaknesses of these different models for a given problem can be determined (Shao et al., 2020). For that reason, comparing the results of these methods for the same topic is important to obtain consistent results.

There are several ways to validate the results of the renewable energy site selection problem, including comparison with existing sites, sensitivity analysis—varying the criteria weights, comparison with other MCDM methods, and other less-used methods (Shao et al., 2020).

Numerous studies compare the results of different MCDM methods. However, only a fraction of them compare renewable energy projects, and even fewer compare the results of different studies applied to the same issue. A large proportion of these studies perform sensitivity analysis, essentially scenarios in which the weighting of the criteria is changed, and the results are compared through maps or tables (Aly et al., 2017).

Abdel-Basset et al. (2021) applied a Multi-Criteria Decision-Making approach to determine the best locations for PV solar plants in Egypt. First, the Delphi method was applied by various specialists to determine the criteria used. These criteria were described in the study as core dimensions and sub-indicators. In the next step, the importance of the selected criteria was determined using the DEMATEL (Decision-Making Trial and Evaluation Laboratory) method. Then, the VIKOR (Višekriterijumsko Kompromisno Rangiranje) method was applied to rank seven sites for photovoltaic plants. The final step compared the results with the AHP-TOPSIS and the SWARA-WASPAS methodology. The methods were compared in two ways: with the direct rank comparison and with the Spearman Rank Correlation. In both cases, the greatest agreement was found with the method AHP-TOPSIS.



Ohunakin and Sacaracoglu (2018) compared five MCDM methods to determine the most suitable location for installing Concentrated Solar Power Plants (CSP) in Nigeria. The selected methods were the Analytic Hierarchy Process (AHP), Consistency-Driven Pairwise Comparisons (CDPC), Decision Expert for Education (DEXi), Elimination, and Choice Translating Reality (ELECTRE III and IV). The study compared the ranks of nine factors on the selected MCDM without using a rank similarity coefficient. Instead, a direct comparison was made using a summary table. The study concluded that the ranks generated by the MCDM methods showed significant differences, with the highest degree of similarity observed between AHP and CDPC.

Sánchez-Lozano et al. (2016a) aimed to find the most suitable site for a PV plant in the Murcia region, Spain. The study used GIS to generate the maps and AHP to determine the weights of the selected criteria. Then, the TOPSIS and ELECTRE methods were selected to analyze the most suitable sites. Finally, comparing the best alternatives from both methods revealed the similarity. No rank similarity coefficient was used, but the analysis was based on maps and tables.

Kizielewicz et al. (2020) analyzed the criteria for determining the best locations for a wind farm using several decision support models (TOPSIS, VIKOR and COMET). They compared the results for each model using Spearman's rank correlation and the WS similarity coefficient. In addition, three scenarios were elaborated by eliminating one, two, and three of the selected criteria for comparison purposes.

Giamalaki and Tsoutsos (2019) searched for suitable sites for solar PV and CSP plants in the Mediterranean region of Rethymno using AHP and GIS. In order to verify the results, a sensitivity analysis was performed in three of the following scenarios: all criteria with equal weighting; equal weighting of techno-economic criteria and no weighting of socio-environmental criteria; equal weighting of socio-environmental criteria and no weighting of techno-economic criteria. Finally, a comparison of these scenarios was made using maps.

Villacreses et al. (2017) studied suitable sites for wind farms in Ecuador. The study used four Multi-Criteria Decision-Making methods combined with GIS. For this, they developed a standardization process. The MCDMs that were compared were AHP, OCRA (Occupational Repetitive Actions), VIKOR, and TOPSIS. Finally, the Pearson correlation coefficient was used to analyze the mutual agreement between these methods through the raster map values for the processing of each pixel for all sites and the best sites only, showing a greater correlation for all methods for the best sites.

Sánchez-Lozano et al. (2016a) compared the TOPSIS and ELECTRE methods to find the best locations for PV plants in the Murcia region, Spain. The study used the AHP to determine the weights of the selected criteria and ranked the results using the TOPSIS and ELECTRE methods. A remarkable similarity of the results was found in the comparative analysis of the maps. In addition, a detailed comparison was made between the results

of the top 10 alternatives from TOPSIS and ELECTRE, which was presented in a table without applying a correlation coefficient.

Shorabeh et al. (2019) studied the most suitable sites for a PV plant in the Iranian provinces of Mazandaran, Kermanshah, Razavi Khorasan and Yazd. The study combined the Ordered Weighted Averaging (OWA) model with GIS for different levels of decision risks. The last step was to perform a sensitivity analysis on the results, changing the weights of the selected criteria to check the impact on the results. This analysis showed that the slope and road network criteria had the greatest impact on the area ranked as highly desirable.

Rios and Duarte (2021) searched for ideal sites for developing large-scale solar PV projects in Peru. The analysis in the study involved the integration of AHP with GIS, and a sensitivity analysis was performed at the end. Three scenarios were analyzed: equal weighting, weighting of the literature review, and weighting associated only with the technical factors. In these different scenarios, the percentage of adequacy of the area was compared, and the resulting maps were drawn.

Through this overview of the applications of different MCDM methods in the renewable energy field and their comparability, it is clear that they are very useful tools for solving problems related to the search for suitable sites for PV plants. Therefore, this study will compare two studies in which the best locations for PV plants in Rio de Janeiro were analyzed using different MCDM methods. It is relevant because the intersection of the two studies reaffirmed excellent potential sites for installing PV plants, making it a solid result for both studies and validating them.

These two papers (De Souza et al., 2019; De Souza et al., 2021a) were selected to elaborate on the studies presented and relate complementary research. In addition, there are few researches on the location of solar photovoltaic plants in Rio de Janeiro. It makes this relationship even more relevant.

## LITERATURE REVIEW

### Similarity Coefficients

In a simple way, correlation is a measure of association between variables and is one of the most used and reported statistical methods for summarizing scientific research data (Schober et al., 2018; Schober & Schwarte, 2018). A correlation coefficient with the value of zero indicates that no association exists between the variables, and as it gets closer to  $\pm 1$ , the stronger the association. A positive correlation means that an increase in one variable will lead to an increase in the other criteria. In contrast, a negative correlation means that an increase in one variable will lead to a decrease in the other. Hypothesis tests and confidence intervals should be used to analyze the statistical significance of the results (Rodgers & Nicewander, 1988).

The concept of measuring rank correlation has been applied in several studies, and its utility is to compare results from different sources and determine how similar they are. In the MCDM, they prove to be very useful, as the alternatives are ranked at the end according to the selected criteria (Fagin et al., 2003; Figueira et al., 2016; Sałabun et al., 2020; Shekhovtsov & Kolodziejczyk, 2020; Shieh, 1998). This study will compare the ranking obtained by two studies using the following correlation coefficients: Spearman Correlation Coefficient, Spearman Weighted Correlation Coefficient, WS Coefficient, and Blest Correlation Coefficient.

Kendall and Goodman-Kruskal correlation coefficients are not used because they directly compare the number of matched pairs, i.e., equal pairs (Sałabun & Urbaniak, 2020). Since the number of cells generated by the grid is very large, more than 27 thousand cells were analyzed, so only a few pairs are equal.

**Spearman Correlation Coefficient.** The Spearman rank correlation coefficient ( $r_s$ ) is one of the most popular tools to evaluate and analyze the similarity of rankings (Ceballos et al., 2016; Ishizaka & Siraj, 2018; Ivlev et al., 2016; Mulliner et al., 2016; Sałabun et al., 2020; Sałabun & Urbaniak, 2020) and can be used as a measure of monotonic association between ranks instead of raw data. The data is ordered and converted into ranks (Asuero et al., 2006; Schober et al., 2018; Zar, 2005). The rank correlation coefficient ( $r_s$ ) is expressed as Equation 1 (Zar, 1972).

$$\text{Spearman Rank Correlation Coefficient, } r_s = 1 - 6 \sum \frac{d_i^2}{(N^3 - N)} \quad [1]$$

The number of measurements of the two variables is  $N$ , and  $d_i$  is the difference between the ranks of these variables ( $d_i = R_{xi} - R_{yi}$ ). When two or more data have the same value, i.e., are of equal rank, each can be set as the mean of the ranks of the positions (Zar, 2005). This rank is the percentage of the rank variance of one variable explained by the other (Sałabun & Urbaniak, 2020).

**Spearman Weighted Correlation Coefficient.** Da Costa and Soares (2005) developed and proposed this rank. According to their study, the Spearman rank is unsuitable for some applications because it treats all ranks equally. Therefore, they developed the Spearman Weighted Correlation Coefficient ( $r_w$ ), where the higher ranks (best positions) have more weight than the lower ranks (worst positions). Equation 2 shows the formula for the  $r_w$  Coefficient.

$$\begin{aligned} & \text{Spearman Weighted Correlation Coefficient, } r_w \\ & = 1 - 6 \sum \frac{(R_{xi} - R_{yi})^2 ((N - R_{xi} + 1) + (N - R_{yi} + 1))}{N \cdot (N^3 + N^2 - N - 1)} \quad [2] \end{aligned}$$

The coefficient is  $r_w$ , the length of ranking is  $N$  and  $R_{xi}$  and  $R_{yi}$  are the positions in the rank order for each element in rank order  $x$  and rank order  $y$ , respectively.

**WS Coefficient.** The development of this coefficient has shown that the ranks are used to find the best solutions; therefore, the differences between the higher positions should be more significant; thus, the higher ranks are more relevant than the lower ranks (Sałabun & Urbaniak, 2020). Equation 3 shows the formula for the WS Coefficient.

$$WS \text{ Coefficient}, WS = 1 - \sum (2^{-R_{xi}} \cdot \frac{|R_{xi} - R_{yi}|}{\max\{|1 - R_{xi}|, |N - R_{xi}|\}}) \quad [3]$$

The similarity coefficient value is  $WS$ , the length of ranking is  $N$ , and  $R_{xi}$  and  $R_{yi}$  are the positions in the rank order for each element in rank order  $x$  and rank order  $y$ , respectively.

**Blest Correlation Coefficient.** Blest Correlation Coefficient ( $V_n$ ) was published by Blest (2000). As the other rank similarities presented in this study, the Blest Correlation Coefficient shows that higher ranks are more important than lower ones. Equation 4 shows the formula for the  $V_n$  Coefficient.

$$\begin{aligned} \text{Blest Correlation Coefficient}, V_n \\ = 1 - \frac{12 \sum (N + 1 - R_{xi})^2 R_{yi} - N(N + 1)^2 (N + 2)}{N(N + 1)^2 (N - 1)} \end{aligned} \quad [4]$$

The similarity coefficient value is  $V_n$ , the length of ranking is  $N$ , and  $R_{xi}$  and  $R_{yi}$  are the positions in the rank order for each element in rank order  $x$  and  $y$ , respectively.

## METHODOLOGY

### Conceptual Framework

This study aims to analyze and compare the results of two different studies (De Souza et al., 2019) in which the best locations for solar PV plants in Rio de Janeiro were determined using different MCDM methods. De Souza et al. (2019) applied the AHP to find the optimal locations, while De Souza et al. (2021a) used the COPPE-COSENZA method to pursue the same objective. To this end, the study developed the following framework (Figure 1).

The first step is to compare and analyze the two studies to rank the alternatives for the most suitable sites, i.e., the result of each

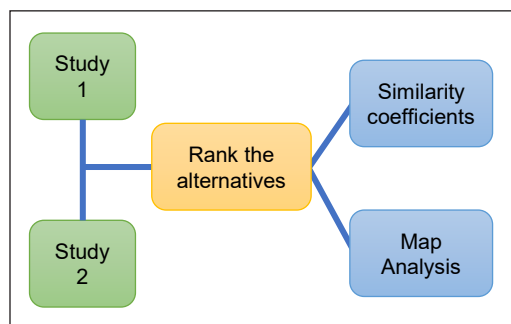


Figure 1. Framework for the research

study. When combined through GIS, the different criteria selected to determine the best locations for PV plants resulted in a georeferenced layer for each study showing these optimal locations within Rio de Janeiro. This layer was called the “resulting map.”

For each of these resulting maps, the data were converted to a raster format, which means that a grid was generated, and each grid cell contains a numeric attribute corresponding to the georeferenced location of the resulting map. For this article, each grid cell is 1 km × 1 km and has a unique ID.

It is possible to rank each location and compare studies using the grid cells. These ranks, therefore, form the basis for comparing results, i.e., for calculating the results of the map analysis and the similarity coefficients.

In the map analysis, the GIS was used to compare and superimpose each study’s top 10% ranks, making it possible to examine the intersections, the suitable regions in both studies and the regions indicated as suitable by only one of the MCDM methods. The rank of the alternatives in each grid cell was also used to apply the following similarity coefficients: Spearman Correlation Coefficient, Spearman Weighted Correlation Coefficient, WS Coefficient, and Blest Correlation Coefficient.

## Map Analysis

According to Visser and de Nijs (2006), there are several reasons to compare maps, such as to compare different models, methodologies, or scenarios and to validate land use models. Map analysis provides ways to deal with data and understand spatial patterns. There are four main methods to analyze data presented in maps: Point Pattern, Autocorrelation, Proximity, and Correlation. These types of analysis differ by the focus of investigation (location and/or attribute), the geometric feature (point and/or area), and a number of topics (Manson et al., 2017).

Spatial analysis can be performed using a variety of techniques using statistics or even visual examination, although a more formal approach is often required (Paramasivam & Venkatramanan, 2019; Scott, 2015). For example, statistical spatial analysis is the most common type of spatial analysis performed with georeferenced data (Bishop & Giardino, 2021).

For this study, correlation analysis was used, i.e., determining the spatial relationship between the attributes of studies 01 and 02, in other words, how they are spatially related (Manson et al., 2017).

There are few examples in the literature of systematic methodologies for analyzing the similarity of maps that fit the proposed problem of this study; in this sense, the most common application of map comparison is land use. Usually, studies select the best sites for each MCDM method and only compare the maps visually. The objective of this study is to go further.

A selection process was conducted to identify the most promising sites for PV plants using the resulting map and the overlaid grid cells. Specifically, the top 10% of grid cells that showed the most favorable results were selected. As shown in Figure 2, a  $10 \times 10$  grid with a total of 100 cells, only the 10 highest scores were selected. It is important to emphasize that this selection procedure was applied to the resulting maps from both studies analyzed.

The maps were then superimposed, and the intersection of results was achieved using a unique identifier for each cell. An example of this procedure can be found in Figure 3, where a total of 7 grid cells represent the overlap of results.

The reason for comparing only the best sites is that the studies are looking for locations for a PV plant, so matching these is essential.

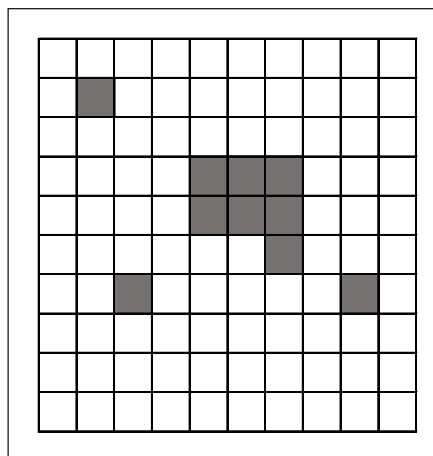


Figure 2. Example of the 10% best results on the grid cells

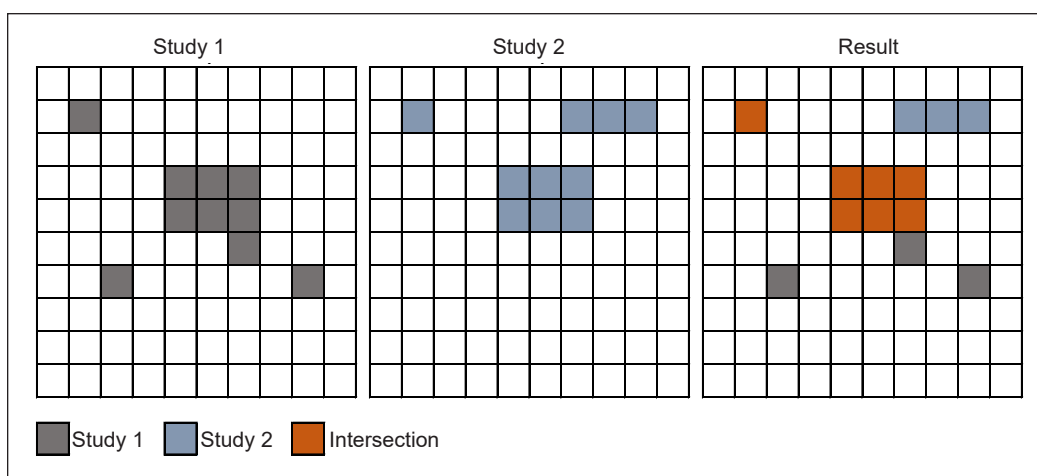


Figure 3. Intersection of the 10% best cells example

## Study Analysis

It is worth mentioning that both papers used the same restriction zones, the same criteria, the same grid base, and the same sources or databases for the GIS layers. The main differences are the MCDM methods, the year the study was conducted, and the interviewing of specialists. In addition, the result of the studies, a suitability map, was merged into a grid base with 1 km of range, which means that they became cells in the form of squares with a length of 1 km.

## Study 1

Study 01 (De Souza et al., 2019; De Souza et al., 2021b) was published in 2019 and then presented at a congress in 2021. The study took the following steps to identify the best sites for the PV plant in the state of Rio de Janeiro:

1. Several academic papers were reviewed to define the criteria for the plant's location.
2. The papers in which the AHP method was used were selected to determine the weight of these criteria (the degree of importance).
3. The average weight of the selected criteria was calculated and then normalized so that the sum of all weights was one.
4. The restriction zones, i.e., the sites where the plant cannot be established, were determined.
5. The final GIS layer that weighted all factors were generated, thus showing the best sites for the PV plant.

The selected criteria and the respective degree of importance are the following: Solar irradiation (42.42%), average temperature (11.34%), distance to transmission lines (9.12%), distance to transport links (5.33%), distance to urban centers (5.68%), slope (13.69%), azimuth (8.50%) and land use (3.92%).

The coverage level in each grid cell weighted the degree of importance of the criteria. Then, the fuzzy membership functions determined the degree of suitability to produce the map of the most suitable sites for PV plants (Figure 4).

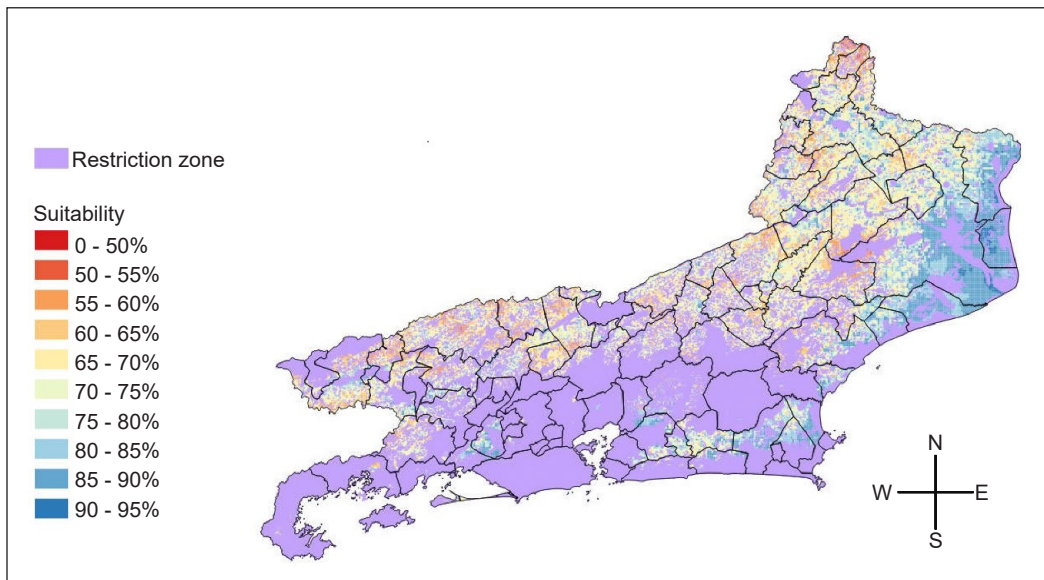


Figure 4. Suitability map—Study 01

## Study 2

The Study 02 (De Souza et al., 2019; De Souza et al., 2021a; De Souza et al., 2021c) was published and presented at a congress in 2021. The study used the method COPPE-COSENZA and took the following steps to identify the best sites for the PV plant in the state of Rio de Janeiro:

1. Twenty academic papers were reviewed to determine the criteria for the plant's location.
2. The degree of importance of the selected criteria was determined through questionnaires completed by 14 specialists using the Google Forms tool. They were asked to rank the importance of the criteria as “critical,” “conditional,” “non-restrictive,” or “irrelevant.”
3. The restriction zones, i.e., locations where the plant cannot be established, were determined.
4. The COPPE-COSENZA method was applied by combining the specialists' responses with the coverage level of selected criteria for each grid cell.
5. The final GIS layer, which weights all factors, was created, indicating the best sites for the PV plant.

The final GIS layer, which weights all factors, was created, indicating the best sites for the PV plant. Table 1 shows the ranking of the criteria according to the questionnaires used. Most specialists ranked solar irradiation as the most decisive criterion, but the others are also important, such as distance to transmission lines and slope. In contrast, the specialists ranked land use and distance from urban centers less important.

The weighting of the selected criteria that resulted from the interviews was compared with the degree of coverage in each grid cell. Then, the degree of suitability was determined using fuzzy membership functions to map the most suitable locations for the PV plant (Figure 5). In the COPPE-COSENZA method, when the proposed index is equal to or greater than one, all factors are offered at the level required for the project, which means that the region is suitable for the proposed project, in this case, a solar PV plant (Cosenza et al., 2015).

Table 1  
*Importance criteria*

	Solar Irradiation	Average Temperature	Distance to Transmission Lines	Distance to Transport Links	Distance to Urban Centers	Slope	Azimuth	Land Use
Critical	10	2	6	3	1	5	2	0
Conditioning	3	3	7	4	1	3	5	5
Not Restrictive	1	8	0	5	7	4	5	5
Irrelevant	0	1	1	2	5	2	2	4



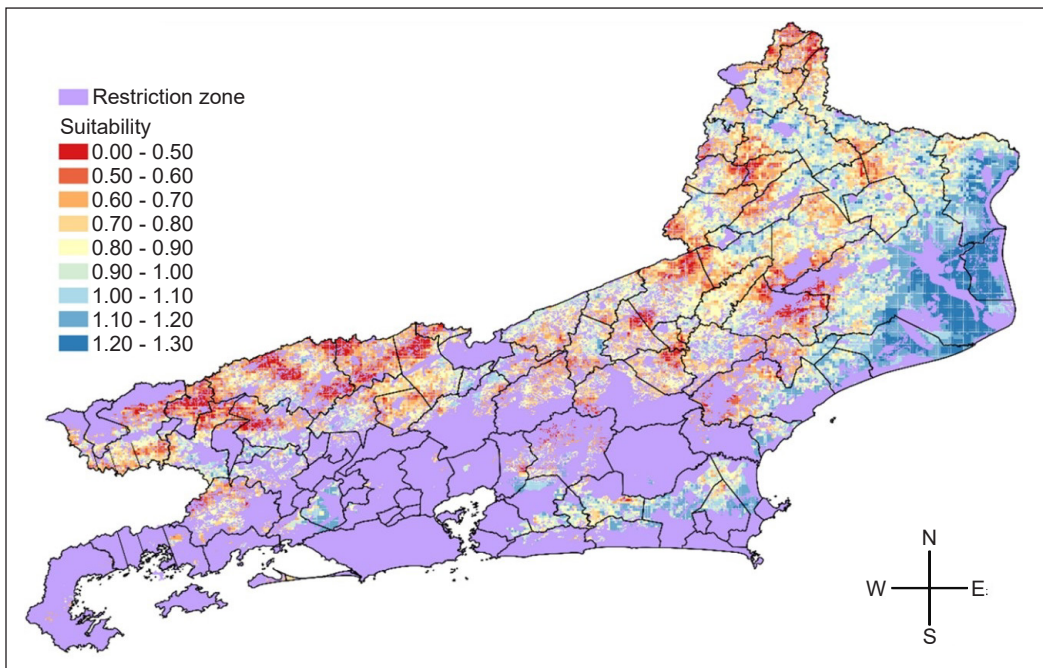


Figure 5. Suitability map—Study 02

## RESULTS AND DISCUSSION

The results of the proposed approach are explained to compare two studies that identified the best sites for PV plants in Rio de Janeiro using different MCDA techniques (AHP and COPPE-COSENZA). The results were organized into two parts: the map analysis, in which the results of both studies were presented and compared through a map overlapping the results, and the second part is the calculation of the four similarity coefficients, namely Spearman, Weighted Spearman, WS, and Blest.

As previously mentioned, the maps resulting from both studies were first divided into 27,159 grid cells of 1 km<sup>2</sup> (1 km × 1 km), and each of these georeferenced cells was the basis for comparing the maps and applying the similarity coefficients.

### Map Analysis

The first step was mapping analysis. Of the 27,159 base grid cells generated, 2,716 (10%) of the cells that presented the best results for suitable sites for PV plants were selected for comparison for each study. It means that 2,716 cells that presented the best results from Study 1 (De Souza et al., 2019) were selected, and the same was done for Study 2 (De Souza et al., 2021a), as shown in Figure 6.

Visually, both maps have a high degree of similarity, but it is important to know how similar they are. Analysis of the maps shows that of these 2,716 cells, there is an intersection

of 2,242 cells, i.e., an 83% similarity between the results of the AHP (de Souza et al., 2019) and COPPE-COSENZA (De Souza et al., 2021a) methods. This result shows a high level of agreement between the studies in terms of the most suitable sites alone. Analysis of the results presented in Figure 7, which is an overlap map of the two results, shows that most of the intersections of the data are located near the state's northern coast.

The region where the best results were obtained has excellent solar irradiation—the best in Rio de Janeiro—is flat and has good infrastructure for electricity transmission and roads. Based on the studies evaluated, solar irradiation is probably the most important factor in determining the best locations for PV plants. On the other hand, the central region has a mountainous landscape and low solar irradiation, so there were no suitable sites in this area.

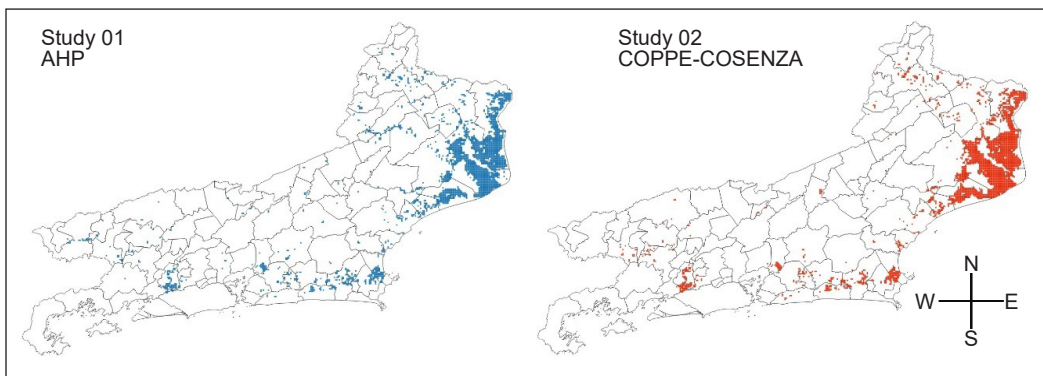


Figure 6. 10% of the best sites of both studies

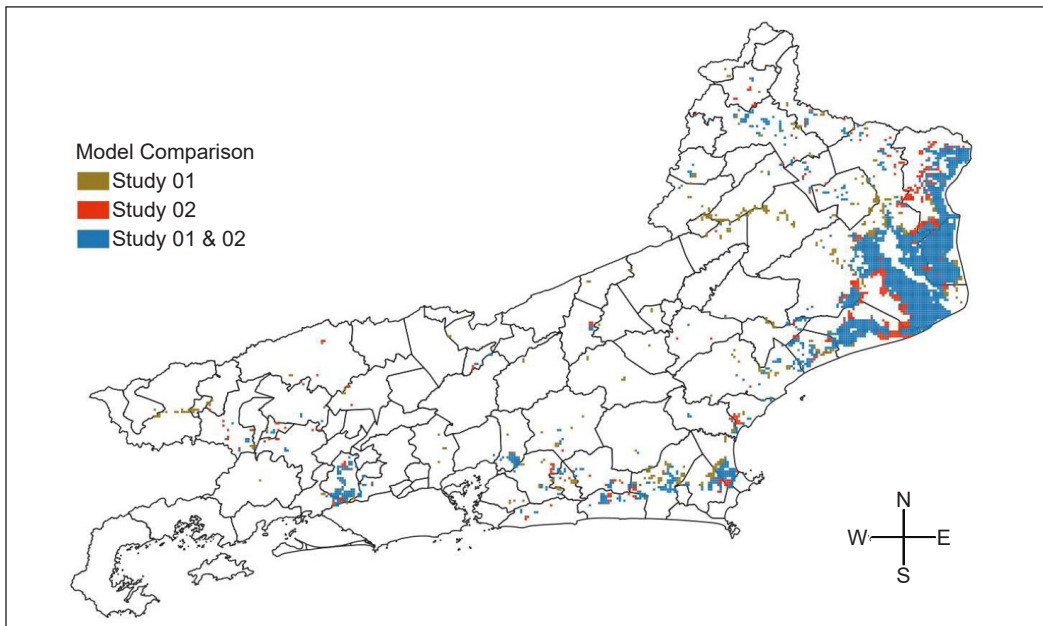


Figure 7. Comparison of the maps for Rio de Janeiro

## Similarity Coefficients

In this step, several correlation coefficients were applied using the 27,159 grid cells, that is, all cells. The Spearman Correlation Coefficient ( $r_s$ ) is 0.9036, indicating a very strong correlation between the results of the studies (Asuero et al., 2006; Schober et al., 2018). Due to the large number of samples, the resulting p-value was zero. The WS Coefficient is 0.9577, indicating a very strong correlation, especially for the best sites for the PV plant (Salabun & Urbaniak, 2020). The Spearman Weighted Correlation Coefficient ( $r_w$ ) value is 0.9118, indicating a very strong correlation. The Blest Correlation Coefficient ( $V_n$ ) is also 0.9264, a very strong correlation. Thus, all the similarity coefficients showed a very high degree of correlation above 0.9. Table 2 shows the value for each of the coefficients.

By comparing the maps and applying the similarity coefficients, the results of the two studies, each using different analytical approaches, show a consistent result. While the Multi-Criteria Decision-Making technique requires the expertise of specialists to determine the results, the similarity coefficients, as nonparametric indices, do not require prior assumptions. It led to a comprehensive evaluation of the results and allowed for a solid and unbiased evaluation.

Table 2  
*The similarity coefficients results*

Coefficient	Value
Spearman Correlation Coefficient	0.9036
WS Coefficient	0.9577
Spearman Weighted Correlation Coefficient	0.9118
Blest Correlation Coefficient	0.9264

## CONCLUSION

Environmental issues are becoming increasingly important worldwide, and global warming is central to these concerns. In this scenario, solar energy emerges as an environmentally friendly alternative that has become financially competitive with traditional generation sources (fossil fuels, hydropower, and nuclear).

The generation of photovoltaic energy in Brazil, including the state of Rio de Janeiro, still occupies a small percentage of the energy matrix. However, all the basic requirements for operation on a larger scale have been met. Several studies use different MCDM methods to search for the optimal siting of PV plants in a variety of countries using different MCDM methods, and each of these methods has its peculiarities that can affect the result.

Although there are many studies on finding better sites, few compare the site selection results for renewable energy projects. Therefore, the objective of this study was to compare the results of two studies that identified the most suitable sites for a PV plant in Rio de Janeiro. This comparison was carried out in two ways: by map analysis and by applying different correlation coefficients. It is worth noting that in the reviewed papers, the MCDM results are usually compared using only one of the following options: Tables, one or two correlation coefficients, and graphs.

The map comparison showed a high similarity of results; 83% of the best sites were identical in studies 01 and 02. It is relevant because the intersections of this study show great potential for PV plants as different methods validated them. The four coefficients used had a very high degree of correlation, with all of them above 0.9. Thus, the consistency of all the ranks also validates the results of both studies since they gave similar results, although they were tested in different ways. Therefore, the consistency of the results of the analyzed studies indicates the potential for installing photovoltaic solar power plants in Rio de Janeiro and validates the methods used and the results themselves.

## ACKNOWLEDGEMENT

The authors thank all the colleagues and teachers who helped to complete this project successfully at COPPE-UFRJ, Rio de Janeiro, Brazil. The authors also extend their appreciation to the reviewers for their valuable comments and suggestions aimed at enhancing the paper's clarity and overall quality.

## REFERENCES

- Abdel-Basset, M., Gamal, A., & ELkomy, O. M. (2021). Hybrid multi-criteria decision making approach for the evaluation of sustainable photovoltaic farms locations. *Journal of Cleaner Production*, 328(July), Article 129526. <https://doi.org/10.1016/j.jclepro.2021.129526>
- Al-Shamisi, M. H., Assi, A. H., & Hejase, H. A. N. (2013). Artificial neural networks for predicting global solar radiation in Al Ain City - UAE. *International Journal of Green Energy*, 10(5), 443-456. <https://doi.org/10.1080/15435075.2011.641187>
- Al Garni, H. Z., & Awasthi, A. (2017). Solar PV power plant site selection using a GIS-AHP based approach with application in Saudi Arabia. *Applied Energy*, 206, 1225-1240. <https://doi.org/10.1016/j.apenergy.2017.10.024>
- Allen, M. R., Pauline Dube, O., Solecki, W., Aragón-Durand, F., Cramer France, W., Humphreys, S., Dasgupta, P., Millar, R., Dube, O., Solecki, W., Aragón-Durand, F., Cramer, W., Humphreys, S., Kainuma, M., Kala, J., Mahowald, N., Mulugetta, Y., Perez, R., Wairiu, M., ... & Waterfield, T. (2018). *Special Report: Global warming of 1.5 °C*. The Intergovernmental Panel on Climate Change. <https://www.ipcc.ch/sr15/>
- Aly, A., Jensen, S. S., & Pedersen, A. B. (2017). Solar power potential of Tanzania: Identifying CSP and PV hot spots through a GIS multicriteria decision making analysis. *Renewable Energy*, 113, 159-175. <https://doi.org/10.1016/J.RENENE.2017.05.077>
- Asuero, A. G., Sayago, A., & González, A. G. (2006). The correlation coefficient: An overview. *Critical Reviews in Analytical Chemistry*, 36(1), 41-59. <https://doi.org/10.1080/10408340500526766>
- Bandyopadhyay, S. (2016). Ranking of suppliers with MCDA technique and probabilistic criteria. In *2016 International Conference on Data Science and Engineering (ICDSE)* (pp. 1-5). IEEE Publication. <https://doi.org/10.1109/ICDSE.2016.7823948>

- Bishop, M. P., & Giardino, J. R. (2021). Technology-driven geomorphology: introduction and overview. *Treatise on Geomorphology*, 1, 1-17. <https://doi.org/10.1016/B978-0-12-818234-5.00171-1>
- Blest, D. C. (2000). Theory & methods: Rank correlation - An alternative measure. *Australian and New Zealand Journal of Statistics*, 42(1), 101-111. <https://doi.org/10.1111/1467-842X.00110>
- Ceballos, B., Lamata, M. T., & Pelta, D. A. (2016). A comparative analysis of multi-criteria decision-making methods. *Progress in Artificial Intelligence*, 5, 315-322. <https://doi.org/10.1007/s13748-016-0093-1>
- CEPERJ. (2019). *Fundação Estadual de Estatísticas, Pesquisas e Formação de Servidores do Estado do Rio de Janeiro*. [Foundation for Statistics, Research, and Training of Civil Servants of the State of Rio de Janeiro]. <https://www.ceperj.rj.gov.br/wp-content/uploads/2021/07/PIB-ESTADUAL2018.pdf>
- CEPERJ. (2022a). *Histórico e Características* | CEPERJ. Fundação Estadual de Estatísticas, Pesquisas e Formação de Servidores Do Estado Do Rio de Janeiro [Foundation for Statistics, Research, and Training of Civil Servants of the State of Rio de Janeiro]. [https://www.ceperj.rj.gov.br/?page\\_id=260](https://www.ceperj.rj.gov.br/?page_id=260)
- CEPERJ. (2022b). *Regiões* | CEPERJ. Fundação Estadual de Estatísticas, Pesquisas e Formação de Servidores Do Estado Do Rio de Janeiro [Foundation for Statistics, Research, and Training of Civil Servants of the State of Rio de Janeiro]. [https://www.ceperj.rj.gov.br/?page\\_id=262](https://www.ceperj.rj.gov.br/?page_id=262)
- Cosenza, C. A. N., Doria, F. A., & Pessôa, L. A. M. (2015). Hierarchy models for the organization of economic spaces. *Procedia Computer Science*, 55, 82-91. <https://doi.org/10.1016/j.procs.2015.07.010>
- Da Costa, J. P., & Soares, C. (2005). A weighted rank measure of correlation. *Australian and New Zealand Journal of Statistics*, 47(4), 515-529. <https://doi.org/10.1111/j.1467-842X.2005.00413.x>
- Das, A. K., & Bhuyan, P. K. (2017). Hardel method for defining LOS criteria of urban streets. *International Journal of Civil Engineering*, 15, 1077-1086. <https://doi.org/10.1007/S40999-017-0207-6>
- de Souza, M. P., Moura, L. C. B., & Cosenza, C. A. N. (2019). Analysis to determine the most suitable location for a photovoltaic solar plant in the state of Rio De Janeiro, Brazil. *International Journal of Development Research*, 09(11), Article 17462.
- de Souza, M. P., Moura, L. C. B., Cosenza, C. A. N., Brasil, C. N. F., Cosenza, H. J. S. R., Amaral, S. de M., & Dias, S. M. P. (2021a). Analysis to determine the most suitable location for a photovoltaic solar plant using coppe-cosenza method: Case study Rio De Janeiro. *International Journal of Development Research*, 11(04), 46378-46382.
- de Souza, M. P., Moura, L. C. B., & Cosenza, C. A. N. (2021b). Análise para a localização ótima de uma usina solar fotovoltaica no estado do Rio de Janeiro [Analysis for the optimal location of a photovoltaic solar plant in the state of Rio de Janeiro]. *Revista Brasileira de Energia*, 27(4), 8-37. <https://doi.org/10.47168/rbe.v27i4.491>
- de Souza, M. P., Moura, L. C. B., Cosenza, C. A. N., Dias, S. M. P., & Barata, P. R. (2021c, October 18-21). Determinação da Localização de uma Usina Solar Fotovoltaica com o Auxílio de Método de Decisão Multicritério [Determination of the location of a solar photovoltaic plant with the aid of a multicriteria decision method]. In *Proceedings of the National Production Engineering Meeting - Enegep* (pp. 1-12). Paraná, Brazil. [https://doi.org/10.14488/enegep2021\\_tn\\_sto\\_362\\_1872\\_41849](https://doi.org/10.14488/enegep2021_tn_sto_362_1872_41849)

- Doorga, J. R. S., Rughooputh, S. D. D. V., & Boojhawon, R. (2019). Multi-criteria GIS-based modelling technique for identifying potential solar farm sites: A case study in Mauritius. *Renewable Energy*, *133*, 1201-1219. <https://doi.org/10.1016/j.renene.2018.08.105>
- EGPEnergia, & PUC-Rio. (2016). *Atlas Rio Solar - Atlas Solarimétrico do Estado do Rio de Janeiro* [Rio Solar Atlas - Solimeric Atlas of the State of Rio de Janeiro].
- EPE. (2020a). *Balço energético nacional 2020* [National energy balance 2020]. Empresa de Pesquisa Energética. <https://www.epe.gov.br/pt/publicacoes-dados-abertos/publicacoes/balanco-energetico-nacional-2020>
- EPE. (2020b). Plano decenal de expansão de energia 2029 [Ten-year energy expansion plan 2029]. Empresa de Pesquisa Energética. <https://www.epe.gov.br/pt/publicacoes-dados-abertos/publicacoes/plano-decenal-de-expansao-de-energia-2029>
- EPE. (2016). *Estudos da demanda de energia: Demanda de energia 2050* [Energy Demand Studies: Energy Demand 2050]. [https://www.epe.gov.br/sites-pt/publicacoes-dados-abertos/publicacoes/PublicacoesArquivos/publicacao-227/topico-458/DEA\\_13-15\\_Demanda\\_de\\_Energia\\_2050.pdf](https://www.epe.gov.br/sites-pt/publicacoes-dados-abertos/publicacoes/PublicacoesArquivos/publicacao-227/topico-458/DEA_13-15_Demanda_de_Energia_2050.pdf)
- Fagin, R., Kumar, R., & Sivakumar, D. (2003). Comparing top k lists. *Journal on Discrete Mathematics*, *17*(1), 134-160. <https://doi.org/10.1137/S0895480102412856>
- Figueira, J., Greco, S., & Ehrgott, M. (2005). *Multiple Criteria Decision Analysis: State of the Art Surveys*. Springer. <https://doi.org/10.1007/b100605>
- Figueira, J. R., Mousseau, V., & Roy, B. (2016). ELECTRE methods. In S. Greco, M. Ehrgott & J. Figueira (Eds.), *Multiple Criteria Decision Analysis. International Series in Operations Research & Management Science* (Vol. 233; pp. 155-185). Springer. [https://doi.org/10.1007/978-1-4939-3094-4\\_5](https://doi.org/10.1007/978-1-4939-3094-4_5)
- Giamalaki, M., & Tsoutsos, T. (2019). Sustainable siting of solar power installations in the Mediterranean using a GIS/AHP approach. *Renewable Energy*, *141*, 64-75. <https://doi.org/10.1016/j.renene.2019.03.100>
- Guitouni, A., & Martel, J. M. (1998). Tentative guidelines to help choosing an appropriate MCDA method. *European Journal of Operational Research*, *109*(2), 501-521. [https://doi.org/10.1016/S0377-2217\(98\)00073-3](https://doi.org/10.1016/S0377-2217(98)00073-3)
- IBGE. (2022). *Cidades e Estados* [Cities and States]. IBGE. <https://www.ibge.gov.br/cidades-e-estados/rj.html>
- IRENA. (2020). *Renewable Power Generation Costs in 2019 - Key Findings*. International Renewable Energy Agency. <https://www.irena.org/publications/2020/Jun/Renewable-Power-Costs-in-2019>
- Ishizaka, A., & Siraj, S. (2018). Are multi-criteria decision-making tools useful? An experimental comparative study of three methods. *European Journal of Operational Research*, *264*(2), 462-471. <https://doi.org/10.1016/j.ejor.2017.05.041>
- Ivlev, I., Jablonsky, J., & Kneppo, P. (2016). Multiple-criteria comparative analysis of magnetic resonance imaging systems. *International Journal of Medical Engineering and Informatics*, *8*(2), 124-141. <https://doi.org/10.1504/IJMEI.2016.075757>
- Jain, A., Mehta, R., & Mittal, S. K. (2011). Modeling impact of solar radiation on site selection for solar pv power plants in India. *International Journal of Green Energy*, *8*(4), 486-498. <https://doi.org/10.1080/15435075.2011.576293>

- Janke, J. R. (2010). Multi-criteria GIS modeling of wind and solar farms in Colorado. *Renewable Energy*, 35(10), 2228-2234. <https://doi.org/10.1016/j.renene.2010.03.014>
- Kizielewicz, B., Wątróbski, J., & Sałabun, W. (2020). Identification of relevant criteria set in the MCDA process - Wind farm location case study. *Energies*, 13(24), Article 6548. <https://doi.org/10.3390/en13246548>
- Kolios, A., Mytilinou, V., Lozano-Minguez, E., & Salonitis, K. (2016). A comparative study of multiple-criteria decision-making methods under stochastic inputs. *Energies*, 9(7), 1-21. <https://doi.org/10.3390/en9070566>
- Kwak, Y., Deal, B., & Heavisides, T. (2021). A large scale multi-criteria suitability analysis for identifying solar development potential: A decision support approach for the state of Illinois, USA. *Renewable Energy*, 177, 554-567. <https://doi.org/10.1016/j.renene.2021.05.165>
- La Camera, F. (2020). *Renewable Power Generation Costs in 2019*. International Renewable Energy Agency. [https://www.irena.org/-/media/Files/IRENA/Agency/Publication/2018/Jan/IRENA\\_2017\\_Power\\_Costs\\_2018.pdf](https://www.irena.org/-/media/Files/IRENA/Agency/Publication/2018/Jan/IRENA_2017_Power_Costs_2018.pdf)
- Manson, S., Matson, L., Kernik, M., DeLuca, E., Bonsal, D., & Nelson, S. (2017). *Mapping, Society, and Technology*. Libraries Publishing.
- Mulliner, E., Malys, N., & Maliene, V. (2016). Comparative analysis of MCDM methods for the assessment of sustainable housing affordability. *Omega*, 59(Part B), 146-156. <https://doi.org/10.1016/j.omega.2015.05.013>
- Ohunakin, O. S., & Saracoglu, B. O. (2018). A comparative study of selected multi-criteria decision-making methodologies for location selection of very large concentrated solar power plants in Nigeria. *African Journal of Science, Technology, Innovation and Development*, 10(5), 551-567. <https://doi.org/10.1080/20421338.2018.1495305>
- Palmer, D., Gottschalg, R., & Betts, T. (2019). The future scope of large-scale solar in the UK: Site suitability and target analysis. *Renewable Energy*, 133, 1136-1146. <https://doi.org/10.1016/j.renene.2018.08.109>
- Paramasivam, C. R., & Venkatramanan, S. (2019). Chapter 3 - An introduction to various spatial analysis techniques. In *GIS and Geostatistical Techniques for Groundwater Science* (pp. 23-30). Elsevier. <https://doi.org/10.1016/B978-0-12-815413-7.00003-1>
- Pereira, E. B., Martins, F. R., Gonçalves, A. R., Costa, R. S., Lima, F. J. L. de, Rütther, R., Abreu, S. L. de, Tiepolo, G. M., Pereira, S. V., & Souza, J. G. de. (2017). *Atlas Brasileiro Energia Solar 2ª Edição* [Brazilian Solar Energy Atlas 2nd Edition]. Instituto Nacional de Pesquisas Espaciais.
- Qiu, T., Wang, L., Lu, Y., Zhang, M., Qin, W., Wang, S., & Wang, L. (2022). Potential assessment of photovoltaic power generation in China. *Renewable and Sustainable Energy Reviews*, 154, Article 111900. <https://doi.org/10.1016/j.rser.2021.111900>
- Ramedani, Z., Omid, M., & Keyhani, A. (2013). Modeling solar energy potential in a Tehran province using artificial neural networks. *International Journal of Green Energy*, 10(4), 427-441. <https://doi.org/10.1080/15435075.2011.647172>
- Razykov, T. M., Ferekides, C. S., Morel, D., Stefanakos, E., Ullal, H. S., & Upadhyaya, H. M. (2011). Solar photovoltaic electricity: Current status and future prospects. *Solar Energy*, 85(8), 1580-1608. <https://doi.org/10.1016/j.solener.2010.12.002>

- Ribeiro, M. A., & Nunes, N. da S. (2019). *Geografia do Estado do Rio de Janeiro* [Geography of the State of Rio de Janeiro]. CECIERJ. <https://canal.cecierj.edu.br/022020/6a6bfdba31d1653c8e1cb37b757a531a.pdf>
- Rios, R., & Duarte, S. (2021). Selection of ideal sites for the development of large-scale solar photovoltaic projects through analytical hierarchical process – Geographic information systems (AHP-GIS) in Peru. *Renewable and Sustainable Energy Reviews*, 149, Article 111310. <https://doi.org/10.1016/j.rser.2021.111310>
- Rodgers, J. L., & Nicewander, W. A. (1988). Thirteen ways to look at the correlation coefficient. *American Statistician*, 42(1), 59-66. <https://doi.org/10.1080/00031305.1988.10475524>
- Roy, B. (2016). Paradigms and challenges. In S. Greco, M. Ehrgott & J. Figueira (Eds.), *Multiple Criteria Decision Analysis* (pp 19-39). Springer. [https://doi.org/10.1007/978-1-4939-3094-4\\_2](https://doi.org/10.1007/978-1-4939-3094-4_2)
- Saġabun, W., & Piegat, A. (2017). Comparative analysis of MCDM methods for the assessment of mortality in patients with acute coronary syndrome. *Artificial Intelligence Review*, 48, 557-571. <https://doi.org/10.1007/s10462-016-9511-9>
- Saġabun, W., & Urbaniak, K. (2020). A new coefficient of rankings similarity in decision-making problems. In V. Krzhizhanovskaya, G. Závodszy, M. H. Lees, J. J. Dongarra, P. M. A. Sloot, S. Brissos & J. Teixeira (Eds.), *Computational Science - ICCS 2020. ICCS 2020. Lecture Notes in Computer Science* (pp. 632-645). Springer. [https://doi.org/10.1007/978-3-030-50417-5\\_47](https://doi.org/10.1007/978-3-030-50417-5_47)
- Saġabun, W., Watróbski, J., & Shekhovtsov, A. (2020). Are MCDA methods benchmarkable? A comparative study of TOPSIS, VIKOR, COPRAS, and PROMETHEE II methods. *Symmetry*, 12(9), Article 1549. <https://doi.org/10.3390/SYM12091549>
- San Cristóbal, J. R. (2011). Multi-criteria decision-making in the selection of a renewable energy project in Spain: The Vikor method. *Renewable Energy*, 36(2), 498-502. <https://doi.org/10.1016/j.renene.2010.07.031>
- Sánchez-Lozano, J. M., García-Cascales, M. S., & Lamata, M. T. (2016a). Comparative TOPSIS-ELECTRE TRI methods for optimal sites for photovoltaic solar farms. Case study in Spain. *Journal of Cleaner Production*, 127, 387-398. <https://doi.org/10.1016/j.jclepro.2016.04.005>
- Sánchez-Lozano, J. M., García-Cascales, M. S., & Lamata, M. T. (2016b). Comparative TOPSIS-ELECTRE TRI methods for optimal sites for photovoltaic solar farms. Case study in Spain. *Journal of Cleaner Production*, 127, 387-398. <https://doi.org/10.1016/j.jclepro.2016.04.005>
- Schober, P., & Schwarte, L. A. (2018). Correlation coefficients: Appropriate use and interpretation. *Anesthesia and Analgesia*, 126(5), 1763-1768. <https://doi.org/10.1213/ANE.0000000000002864>
- Scott, L. M. (2015). Spatial pattern, analysis of. In J. D. Wright (Ed), *International Encyclopedia of the Social & Behavioral Sciences: Second Edition* (Vol. 22). Elsevier. <https://doi.org/10.1016/B978-0-08-097086-8.72064-2>
- Shao, M., Han, Z., Sun, J., Xiao, C., Zhang, S., & Zhao, Y. (2020). A review of multi-criteria decision-making applications for renewable energy site selection. *Renewable Energy*, 157, 377-403. <https://doi.org/10.1016/j.renene.2020.04.137>



- Shekhovtsov, A., & Kolodziejczyk, J. (2020). Do distance-based multi-criteria decision analysis methods create similar rankings? *Procedia Computer Science*, 176, 3718-3729. <https://doi.org/10.1016/j.procs.2020.09.015>
- Shieh, G. S. (1998). A weighted Kendall's tau statistic. *Statistics and Probability Letters*, 39(1), 17-24. [https://doi.org/10.1016/s0167-7152\(98\)00006-6](https://doi.org/10.1016/s0167-7152(98)00006-6)
- Shorabeh, S. N., Firozjaei, M. K., Nematollahi, O., Firozjaei, H. K., & Jelokhani-Niaraki, M. (2019). A risk-based multi-criteria spatial decision analysis for solar power plant site selection in different climates: A case study in Iran. *Renewable Energy*, 143, 958-973. <https://doi.org/10.1016/j.renene.2019.05.063>
- Sindhu, S., Nehra, V., & Luthra, S. (2017). Investigation of feasibility study of solar farms deployment using hybrid AHP-TOPSIS analysis: Case study of India. *Renewable and Sustainable Energy Reviews*, 73, 496-511. <https://doi.org/10.1016/j.rser.2017.01.135>
- Taylor, R. (1990). Interpretation of the correlation coefficient: A basic review. *Journal of Diagnostic Medical Sonography*, 6(1), 35-39. <https://doi.org/10.1177/875647939000600106>
- Thirugnanasambandam, M., Iniyan, S., & Goic, R. (2010). A review of solar thermal technologies. *Renewable and Sustainable Energy Reviews*, 14(1), 312-322. <https://doi.org/10.1016/J.RSER.2009.07.014>
- Uyan, M. (2013). GIS-based solar farms site selection using analytic hierarchy process (AHP) in Karapinar region Konya/Turkey. *Renewable and Sustainable Energy Reviews*, 28, 11-17. <https://doi.org/10.1016/j.rser.2013.07.042>
- Van Haaren, R., & Fthenakis, V. (2011). GIS-based wind farm site selection using spatial multi-criteria analysis (SMCA): Evaluating the case for New York State. *Renewable and Sustainable Energy Reviews*, 15(7), 3332-3340. <https://doi.org/10.1016/J.RSER.2011.04.010>
- Villacreses, G., Gaona, G., Martínez-Gómez, J., & Jijón, D. J. (2017). Wind farms suitability location using geographical information system (GIS), based on multi-criteria decision making (MCDM) methods: The case of continental Ecuador. *Renewable Energy*, 109, 275-286. <https://doi.org/10.1016/j.renene.2017.03.041>
- Visser, H., & De Nijs, T. (2006). The map comparison kit. *Environmental Modelling and Software*, 21(3), 346-358. <https://doi.org/10.1016/j.envsoft.2004.11.013>
- Wang, H., Pan, Y., & Luo, X. (2019). Integration of BIM and GIS in sustainable built environment: A review and bibliometric analysis. *Automation in Construction*, 103, 41-52. <https://doi.org/10.1016/J.AUTCON.2019.03.005>
- Yushchenko, A., de Bono, A., Chatenoux, B., Patel, M. K., & Ray, N. (2018). GIS-based assessment of photovoltaic (PV) and concentrated solar power (CSP) generation potential in West Africa. *Renewable and Sustainable Energy Reviews*, 81(Part 2), 2088-2103. <https://doi.org/10.1016/j.rser.2017.06.021>
- Zanakis, S. H., Solomon, A., Wishart, N., & Dublisch, S. (1998). Multi-attribute decision making: A simulation comparison of select methods. *European Journal of Operational Research*, 107(3), 507-529. [https://doi.org/10.1016/S0377-2217\(97\)00147-1](https://doi.org/10.1016/S0377-2217(97)00147-1)
- Zar, J. H. (1972). Significance testing of the Spearman rank correlation coefficient. *Journal of the American Statistical Association*, 67(339), 578-580. <https://doi.org/10.1080/01621459.1972.10481251>

Marco Pereira de Souza, Luis Claudio Bernardo Moura, Carlos Alberto Nunes Cosenza, Silvio de Macedo Amaral, Rodrigo Pestana Cunha Telles, Manuel Oliveira Lemos Alexandre, Silvio Barbosa, Bruno de Sousa Elia, Maria Fernanda Zelaya Correia, Antonio Carlos de Lemos Oliveira, Rodrigo Ventura da Silva, Thais Rodrigues Pinheiro

Zar, J. H. (2005). Spearman rank correlation. In *Encyclopedia of Biostatistics*. Wiley. <https://doi.org/10.1002/0470011815.B2A15150>

Zoghi, M., Ehsani, A. H., Sadat, M., Amiri, M. J., & Karimi, S. (2017). Optimization solar site selection by fuzzy logic model and weighted linear combination method in arid and semi-arid region: A case study Isfahan-IRAN. *Renewable and Sustainable Energy Reviews*, 68(Part 2), 986-996. <https://doi.org/10.1016/j.rser.2015.07.014>

## Modelling and Optimisation of Cooling-Slope Parameters of Magnesium AZ91D using Improvement Multi-Objective Jaya Approach for Predicted Feedstock Performance

Rahaini Mohd Said<sup>1,2\*</sup>, Roselina Salleh@Sallehuddin<sup>2</sup>, Norhaizan Mohamed Radzi<sup>2</sup>, Wan Fahmin Faiz Wan Ali<sup>3</sup> and Mohamad Ridzuan Mohamad Kamal<sup>3,4</sup>

<sup>1</sup>Department of Electronic and Computer Engineering Technology, Faculty of Electrical and Electronic Engineering Technology, Universiti Teknikal Malaysia Melaka, 76100, Durian Tunggal, Melaka, Malaysia

<sup>2</sup>Department of Computer Science, Faculty of Computing, Universiti Teknologi Malaysia, 81300 Skudai, Johor, Malaysia

<sup>3</sup>Department of Materials, Manufacturing and Industrial Engineering, Faculty of Mechanical, Universiti Teknologi Malaysia, 81300 Skudai, Johor, Malaysia

<sup>4</sup>Department of Manufacturing Engineering Technology, Faculty of Mechanical and Manufacturing Engineering Technology, Universiti Teknikal Malaysia Melaka, 76100, Durian Tunggal, Melaka, Malaysia

### ABSTRACT

The cooling-slope (CS) casting technique is one of the simple semi-solid processing (SSP) processes a foundryman uses to produce the feedstock. This study attempts to develop mathematical regression models and optimise the CS parameters process for predicting optimal feedstock performance, which utilises tensile strength and impact strength to reduce the number of experimental runs and material wastage. This study considers several parameters, including pouring temperature, pouring distance, and slanting angles for producing quality feedstock. Hence, multi-objective optimisation (MOO) techniques using computational approaches utilised alongside the caster while deciding to design are applied to help produce faster and more accurate output. The experiment was performed

based on the full factorial design (FFD). Then, mathematical regression models were developed from the data obtained and implemented as an objective function equation in the MOO optimisation process. In this study, MOO named multi-objective Jaya (MOJaya) was improved in terms of hybrid MOJaya and inertia weight with archive K-Nearest Neighbor (MOiJaya-aKNN) algorithm. The proposed algorithm

### ARTICLE INFO

#### Article history:

Received: 12 February 2023

Accepted: 24 August 2023

Published: 14 March 2024

DOI: <https://doi.org/10.47836/pjst.32.2.06>

#### E-mail addresses:

rahaini@utem.edu.my (Rahaini Mohd Said)  
roselinasallehuddin@gmail.com (Roselina Sallehuddin)  
haizan@utm.my (Norhaizan Mohamed Radzi)  
wan\_fahmin@utm.my (Wan Fahmin Faiz Wan Ali)  
mohamadridzuan@utem.edu.my (Mohamad Ridzuan Mohamad Kamal)

\* Corresponding author

was improved in terms of the search process and archive selection to achieve a better feedstock performance through the CS. The study's findings showed that the values of tensile and impact strengths from MOiJaya\_aKNN are close to the experiment values. The results show that the hybrid MOJaya has improved the prediction of feedstock using optimal CS parameters.

*Keywords:* Chaotic inertia weight, cooling-slope casting process, feedstock, impact strength, k-nearest neighbour, MOJaya, tensile strength

---

## INTRODUCTION

The cooling-slope (CS) casting technique is a simple semi-solid processing (SSP) method utilised by foundrymen or casters to procure feedstock. The SSP is a near-net-shaped approach for processing metal and alloys in a semi-solid state and has been employed extensively in manufacturing processes (Nafisi & Ghomashchi, 2019). Among the advantages of SSP-fabricated components processed conventionally are reduced porosity, macro-segregation, and better mechanical properties (Son et al., 2021). Consequently, SSP has been commercially applied for producing feedstock in several approaches, such as cooling-slope casting (CSC), continuous casting with magneto-hydrodynamic (MHD), and semi-solid and gas-induced semi-solid rheocasting (GISS).

This study uses magnesium (Mg) AZ91D as a metal in producing feedstock using the CS process. AZ91D is one of the earliest and lightest metal steels with potential applications across various industries, including electronics, aerospace, and automotive (Annamalai et al., 2019). The metal has also gained attention among researchers, thus resulting in several investigations on magnesium and its alloys, including alloy design and optimisation, microstructure characterisation and observation, and functional materials (Wu et al., 2021). Furthermore, the metal is considered the best green material in the 21st century due to its excellent physical and chemical properties, including low density, high specific strength and stiffness and good damping performance biocompatibility (Guo et al., 2018). Consequently, the advantages of AZ91D necessitate evaluations to produce feedstock via the CS casting approach.

The CS is one of the methods employed by industries to produce feedstock. The technique is one of the steps applied at the precursor level to ensure the quality of the processed feedstock. These feedstocks, known as treatment feedstock, are utilised as raw materials in manufacturing to produce quality products. Accordingly, the primary challenge of procuring excellent feedstock is providing high-quality precursor resources, especially controlling process parameters during casting (Balachandran, 2018).

Grain refinement strengthening is the primary issue casters encounter during designing and producing quality feedstock, which, alongside numerous other parameters, would affect the feedstock performance (tensile and impact strengths) obtained. Commonly, experts

select CS casting process parameters based on experience, established processing plant guide, or casting handbook (Kumar et al., 2014). Nevertheless, determining the optimum multi-parameters for producing feedstock with excellent performance is complicated and costly because the best parameter combination has arguable results, as the results do not guarantee the CS process's optimal performance.

The primary objective of the designing stage is to produce high-quality feedstock and products at optimal conditions. Consequently, choosing ideal process parameters is crucial (Rao, 2011). Nonetheless, the selection process is currently conducted on a trial-and-error basis due to a lack of fixed theoretical procedures (Kor et al., 2011). The present study proposed utilising computational techniques to acquire the optimal conditions during the decision-making step. The application of the approach during design process selection could aid in faster and more accurate output procurement.

Rao (2018) highlighted the modelling and optimisation stages to obtain ideal parameters. The report also specified that representing the manufacturing process as a model for optimisation is necessary. Accordingly, developing the mathematical model is the first step of process parameter enhancement. The process is critical as the model is developed as an objective function for optimisation.

Researchers considered several approaches to model a casting process, such as regression (Brezocnik & Župerl, 2021), response surface methodology (RSM) (Patel et al., 2015), numerical simulation (Zheng et al., 2020), and artificial neural network (ANN) (Zhou et al., 2022). The regression model is one of the most practical and well-known modelling techniques applicable to soft computing (Esonye et al., 2021; Fadaee et al., 2022; Onifade et al., 2022; Singh et al., 2021). For example, Khosravi et al. (2014) adopted the regression approach to model the CS parameters: the pouring temperature (Pt), pouring distance (Pd), and slanting slope angle (Sa).

Most studies on casting optimisation that applied the multi-objective approach employed regression as a modelling technique. Binesh and Aghaie-Khafri (2017) generated a polynomial regression model to represent the relationship between casting performance and the process parameters. In another report, the non-linear regression model was utilised to procure the model denoting the relationship between the squeeze cast process parameters and its performance before optimising it via a genetic algorithm (Patel et al., 2015). Moreover, multiple regression is a flexible method to examine the relationship between a variable and multiple outcome variables. This model was used as the objective function in the optimisation process.

In optimisation, algorithms are designed and developed to solve the problems using computers. It can be classified into two categories: deterministic and stochastic. The deterministic approach finds the same solution in each run but becomes trapped in locally optimal solutions due to local optimisation. However, stochastic approaches find different

solutions in each run due to stochastic mechanisms. It assists them in avoiding sub-optimal solutions better. Most stochastic approaches are applied in most heuristic and metaheuristic approaches that can be classified into single and multi-objective optimisation (Premkumar et al., 2021).

Optimisation could be classified into single- and multi-objective (MOO) optimisations. Nevertheless, the single-objective approach provides insufficient information for casters to analyse decisions holistically. Consequently, MOO provides a practical technique for selecting ideal casting process conditions (Rao, 2018). The MOO approach is employed in casting optimisation to solve design issues, including multiple design variables, conflicting objectives, and numerous constraints. Furthermore, MOO computing methods are easy to implement and require lower energy, time, and cost than the trial-and-error practice.

Recently, the metaheuristic algorithm (MA), which is more flexible and convenient, has been widely utilised to procure near-optimum solutions in manufacturing processes (Li et al., 2020; Mishra & Sahu, 2018; Agarwal et al., 2018; Mohd Said et al., 2021; Tavakolpour-Saleh, 2017). A variety of MA has been investigated for application in manufacturing processes, such as multi-objective genetic algorithm (MOGA) (Feng & Zhou, 2019), non-dominate sorting genetic algorithm II (NSGA II) (Asadollahi-Yazdi et al., 2018), multi-objective partial swarm optimisation (MOPSO) (Patel et al., 2016; Wu et al., 2021) multi-objective whale optimisation algorithm (MOWOA) (Tanvir et al., 2020), and multi-objective artificial bee colony (MOABC) (Feng et al., 2018; García-Alcaraz & Pérez-Domínguez, 2014), multi-objective ant colony optimisation (MOOACO) (Ji & Xie, 2008), and multi-objective Jaya (MOJaya) (Rao et al., 2016).

The MOJaya technique that Rao introduced has been successfully applied in several real-world settings (Raed et al., 2020). The method is a simple, flexible, and efficient population-based search algorithm to solve constrained and unconstrained optimisation issues. The MOJaya algorithm is a parameters-less approach that iterates towards the best solution search space. Furthermore, the MOJaya algorithm has the advantage of avoiding the difficulty of adjusting parameters as well as reducing the amount of time required for optimisation. Recently, the Jaya or MOJaya technique gained attention due to the simplicity of its framework and the fact that it only requires a single operator. The approach has also reportedly solved optimisation issues in various fields (El-Ashmawi et al., 2020; Jian & Weng, 2020; Rao et al., 2019; Vinh & Nguyen, 2020; Zamli et al., 2018). However, as a metaheuristic algorithm, MOJaya suffers from a few limitations and inescapable drawbacks during the search process. The search process in MOJaya focuses more on exploitation than exploration. It causes the solution to be easily trapped in local minima and get less diversified solutions.

Several improvements in the exploitation abilities of the search process in MOJaya were proposed to ensure the optimal solution is not easily trapped in local minimal. Wu

and He (2020) combined the basic Jaya algorithm with the mutation and crossover operator to enhance the diversity of the population and exploration ability. The results showed that both improvement algorithms from their studies obtained superior results in terms of solution quality, such as diversity and convergence. Goudos et al. (2019) proposed hybrid Jaya algorithms and self-adaptive differential evolution algorithms. The simulation results showed the efficiency of the purpose algorithms, such as the Jaya-JDE algorithm, by achieving good trade-off solutions.

Zhenghao et al. (2020) enhanced the Jaya algorithm using a combination of the Tree Seeds algorithm and K-means clustering, namely C-Jaya-TSA. The clustering strategy is used to replace solutions with low-quality objective values. The results show the effectiveness of the C-Jaya-TSA algorithm to enhance the exploitation ability. Premkumar et al. (2021) enhanced the Jaya algorithm with a chaotic mechanism to classify the parameters of various photovoltaic models, including single-diode and double-diode models. Adaptive weight chaos is added to the proposed algorithm to regulate the trend and avoid the worst solution. The proposed technique utilises self-adaptive weights to reach the best solution during the first phase, followed by a second phase that includes a local search, which increases exploration capacity. Based on comprehensive analysis and experimental results, the suggested algorithm is highly competitive in accuracy and reliability compared to other algorithms in the literature.

Based on Narayanan et al. (2023), early MOO algorithms evaluated two solutions simultaneously based on Pareto dominance throughout the iterative process to find the optimal solution to achieve ultimate outcomes. An effective approach for multi-objective optimisation problems is the Pareto optimal front method, which can elicit sets of optimum solutions widely known as Pareto-optimal front solutions (Zitzler et al., 1999). Recently, many researchers used Pareto optimal front approach to solve MOO problems such as Multi-objective Moth Flame Optimization (MaOMFO), Decomposition-based multi-objective symbiotic organism search (MOSOS/D), Multi-Objective Marine-Predator Algorithm (MOMPA), Multi-Objective Generalized Normal Distribution Optimization (MOGNDO), and Multi-Objective Plasma Generation Optimization (MOPGO) (Abdin et al., 2022; Ganesh et al., 2023; Jangir et al., 2023; Kumar et al., 2021; Pandya et al., 2022). However, another limitation reported in the literature is the selection criteria of solutions for solving MOJaya problems using the Pareto approach. Warid et al. (2018) proposed fuzzy decision-making and incorporated it into the Jaya algorithm as selection criteria for best and worst solutions using the Pareto approach.

Moreover, some recent work used an archive mechanism of non-dominated solutions to approximately the Pareto front to solve MOO problems. Britto et al. (2012) explored several archiving methods from the literature used by MOPSO to store the selected leaders into MOO problems. The main goal was to observe how each method influences the MOPSO

algorithm in terms of convergence and diversity over the Pareto front. This method guided the MOPSO search to a region near the knee of the Pareto front.

Li et al. (2019) proposed two archives evolutionary algorithms for constrained to solve MOO problems. The author highlighted an important issue in MOO: balancing convergence, diversity, and feasibility. This paper proposes a parameter-free constraint handling technique, a two-archive evolutionary algorithm, for constrained multi-objective optimisation to address this issue. The first archive, denoted as the convergence archive, is the driving force that pushes the population toward the Pareto front. The second archive, denoted as the diversity archive, mainly tends to maintain population diversity.

Premkumar et al. (2022) have developed a bio-inspired multi-objective grey wolf optimisation algorithm (MOGWO) that includes Pareto optimality, dominance, and external archiving. Archives are storage units that store or retrieve the non-dominated Pareto optimal solution. Archives are managed by archive controllers when solutions enter the archive, or the archive is completely occupied. According to the performance comparison of the MOGWO algorithm with other algorithms selected, the MOGWO algorithm provides the best solution. Thus, it is motivated to propose MOiJaya\_aKNN to enhance MOJaya performance and get the optimal CS casting parameters to produce optimal feedstock performances.

Although researchers have proposed various MOO approaches to solving the issues involved during the casting process, most are based on different metals employed in other casting processes. Moreover, limited studies have considered MOO to improve manufacturing processes. Accordingly, the present study developed a mathematical regression model and enhanced the MOJaya algorithm for estimating optimised CS casting process parameters to predict two feedstock performance mechanical properties: tensile and impact strength.

## MATERIALS AND METHODS

The current study focused on the material used, modelling and optimising feedstock performances to assess the optimal machining conditions in CS casting. Overall, this study comprised three major stages as follows (Figure 1):

1. Experiment and casting data: Experimental data of feedstock performances, parameters, and boundaries were collected. Two mechanical properties, tensile and impact strengths, were considered feedstock performance. The parameters involved were Pt, Pd, and Sa.
2. Modelling: Polynomial regression models for

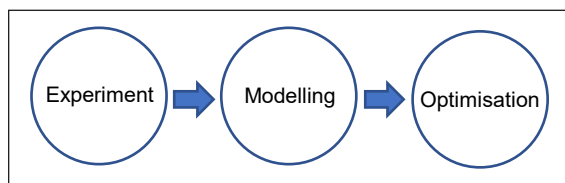


Figure 1. The basic flow of the study



feedstock performance were developed and utilised as an objective function for optimisation. Statistical analyses were performed to evaluate the validity of the models before conducting optimisation.

3. Optimisation: The final step comprised CS-produced feedstock performance optimisation with the improved MOJaya. The results were compared with actual experiment results, which were considered benchmarks.

## Material

A commercially available Mg AZ91D composite was employed in the present study. The detailed chemical composition and mechanical properties of the metal are listed in Table 1.

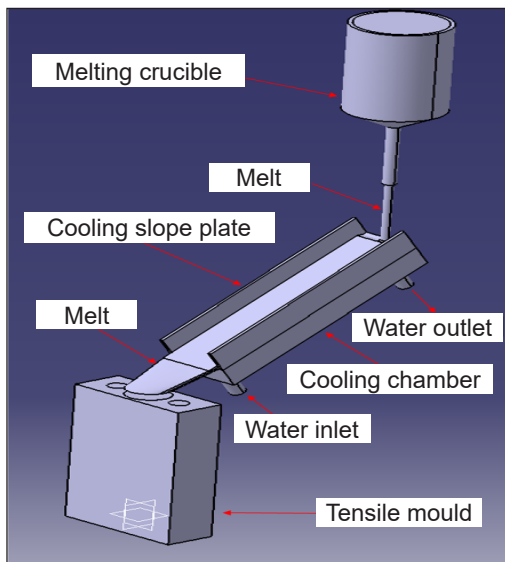
## The CS Casting Process

The present study utilises the CS casting process, a gravity-based casting technique. 800g of AZ91D magnesium ingot was fed inside the stainless-steel melting crucible in the heating furnace and melted at 680°C, 700°C and 720°C. Then, the melt was poured onto the cooling plate and flowed into a metal mould according to the parameter's setup. K-type thermocouples were placed

Table 1

*The chemical composition of AZ91D*

Element	Mass (%)
Aluminium (Al)	8.50
Manganese (Mn)	0.20
Zinc (Zn)	0.55
Silicon (Si)	0.10
Copper (Cu)	0.03
Nickel (Ni)	0.002
Iron (Fe)	0.005
Mg	Balance



(a)



(b)

Figure 2. (a) Computer Aided Diagram (CAD) diagram of C and (b) CS experiment setup

on the cooling slope to measure the temperature. The cooling slope experimental process was performed by varying the pouring temperature, slanting angle, and pouring distance (Table 2). Finally, the molten metal flow was full of the mould and defined as as-cast. Figure 2(a) shows the Computer Aided Diagram (CAD) diagram of CS, while Figure 2(b) details the CS experiment setup.

Figure 3 demonstrates an as-cast specimen post the CS procedure. After machining them into specific shapes, the specimens obtained were subjected to tensile and impact strength evaluations. Figures 4(a) and (b) and Figures 5(a) and (b) display the respective measurements and shapes of the as-cast samples for the tensile and impact strength evaluations. The as-cast subjected to impact strength assessment was prismatic bar-shaped, while the sample evaluated for its tensile strength had a transverse notch cut in the middle of a side.

Tensile strength assesses the ability of a metal to resist breaking or pulling apart into two pieces. On the other hand, the value of impact energy absorbed by a material during fracturing under impact denotes the strength of the material. The tensile strengths of the specimens in this study were evaluated with a Universal Tensile Machine, Instron 5982, while an Instron Ceast 9050 Test Machine was utilised to determine their impact strengths. The estimation models in the present study were then developed with a design of experimental (DOE) software by employing the CS casting process parameters data.



Figure 3. An as-cast specimen

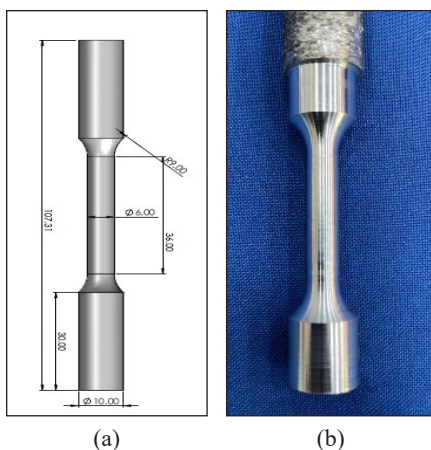


Figure 4. The (a) measurement and (b) shape of the tensile strength test specimen (unit dimension = mm)

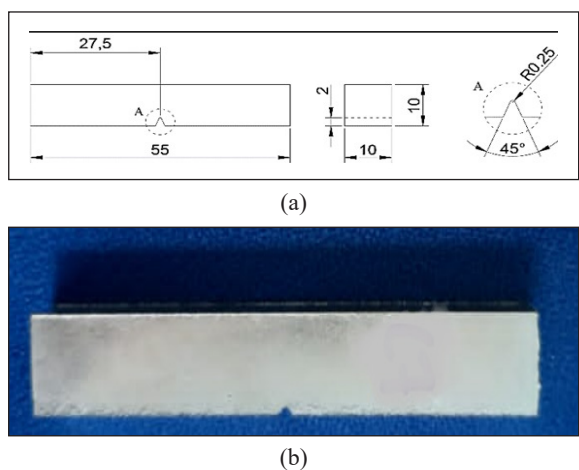


Figure 5. The (a) measurement and (b) shape of the impact strength test specimen (unit dimension = mm)

## Design of Experimental (DOE)

The DOE is a systematic and efficient method of examining the relationship between multiple input (factors) and key output (responses) variables. This study performed experiments based on a full factorial design (FFD) that involved three levels and three parameters as input variables. The three selected CS parameters, namely the Pd, Pt, and Sa, were considered the most significant factors affecting the related response based on previous reports. The selection of the range for CS parameters is based on the type of metal used, which is AZ91D magnesium that has a characteristic and chemical composition that needs to be considered and also based on previous researcher recommendations (Abdelgneia et al., 2019; Khosravi et al., 2014; Kumar et al., 2014; Kumar et al., 2013; Tugiman et al., 2019). The fractional combinations of the conditions were obtained by employing the Design Expert 11.0 software. Table 2 summarises the range values of the parameters.

Table 2  
*The range value of CS parameters*

Casting parameters	Unit	Level		
		1	2	3
Pouring temperature	Celsius	680	700	720
Pouring Distance	mm	300	400	500
Slanting angle	Degree	30	45	60

In this study, the Pt employed ranged between 680–720°C, Pd was from 300 to 500 cm, and Sa was between 30–60°. Based on the values, 27 runs with four centre points resulted in a 3<sup>3</sup> FFD. A full factorial denotes a design setting that includes all possible input parameters. Table 3 shows the full factorial design experimental layout of the CS.

The regression estimation models in the current study were developed from the CS casting parameters with the Design expert software. The adequacy and significance of the models, indicated by coefficient (R<sup>2</sup>) values, were determined with variance analysis (ANOVA). Each model was validated with mean square error (MSE) and root means square error (RMSE). Equation 1 expresses the Stepwise regression model of the CS process, and the modelling process flow of the CS casting is illustrated in Figure 6.

$$y = b_0 + b_1(Pt) + b_2(Pd) + b_3(Sa) + b_4(Pt)(Pd) + b_5(Pt)(Sa) + b_6(Pd)(Sa) + b_7(Pt)^2 + b_8(Pd)^2 + b_9(Sa)^2 + x\varepsilon \quad [1]$$

Where is  $b_0$  constant,  $b$  is the coefficient of regression mode. The input process parameters are slanting angle (Sa), pouring distance (Pd) and pouring temperature (Pt). The flow process of modelling for the CS casting process is illustrated in Figure 6. The tensile and impact strength equations were expressed as Equations 2 and 3.

Table 3  
The full factorial design experimental layout of the CS

Standard order	CS parameters			Feedstock performance	
	Pouring Temperature	Slanting angle	Pouring distance	Tensile strength	Impact strength
1	680	30	300	90.6208	4.013
2	680	45	300	104.06	3.276
3	680	60	300	100.527	4.521
4	680	30	400	97.6055	4.225
5	680	45	400	111.444	3.644
24	720	60	400	138.033	4.334
25	720	30	500	126.499	4.112
26	720	45	500	131.116	4.581
27	720	60	500	129.1	4.578

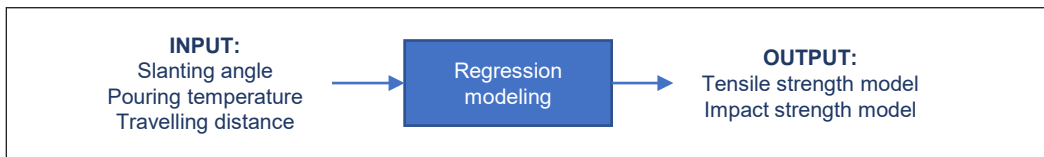


Figure 6. The process of modelling for the CS casting process

$$\begin{aligned} \text{Maximize tensile strength} = & a + \text{slanting angle} + \text{Pouring temperature} + \\ & \text{Travelling distance} + \text{slanting angle}^2 + \text{Pouring} \\ & \text{temperature}^2 + \dots + e \end{aligned} \quad [2]$$

$$\begin{aligned} \text{Maximize impact strength} = & a + \text{slanting angle} + \text{Pouring temperature} + \\ & \text{Travelling distance} + \text{slanting angle}^2 + \text{Pouring} \\ & \text{temperature}^2 + \dots + e \end{aligned} \quad [3]$$

### Multi-Objective Optimisation (MOO) Problems

Optimisation problems are among the most common problems in engineering practical and scientific research. The MOO problem is an area of multiple criteria decision-making that concerns mathematical optimisation problems involving more than one objective function being optimised simultaneously. The primary study objective for conducting MOO optimisation and using the Pareto front approach to solve MOO optimisation problems is to find the optimal solution. The standard equation for the MOO optimisation process is given in Equations 4 to 6.

Therefore, the MOO will take the following mathematical formulation:

Maximise or minimise:

$$F(x,u) = [f_1(x,u), f_2(x,u)]^T, \dots, f_k(x,u)]^T \quad [4]$$

Subject to:

$$g(x,u) = 0 \quad [5]$$

and

$$h(x,u) \leq 0 \quad [6]$$

where  $F(x,u)$  and  $k$  represents the vector and a total number of objective functions,  $g(x,u)$  is a set of equality constraints,  $h(x,u)$  is the set of inequality constraints,  $x$  is the vector of dependent variables or state variables, and  $u$  is the vector of independent or control variables.

### Hybrid Chaotic Inertia and Archive K Nearest Neighbour in MOJaya

There is a two-phase improvement for MOJaya in this study. The first phase, the movement update equation operator, is improved by adding a chaotic random inertia weight called MOiJaya.

In the first phase of improvement, adding the chaotic inertia weight in the MOJaya solution update equation possesses specific attributes, including ergodicity and randomness, which enabled the algorithm to overcome the optimal local solution. During the early iteration of the algorithm, the current study selected the best and random solution to explore more search space processes. The optimal solution was chosen to guide the population to a better region, while the random solution was selected to expand the search space. Nevertheless, the best solution at each generation might be trapped in local minima when solving conflicting objectives, affecting the succeeding solution update equation. Hence, the modified solution update equation in the present study was conducted according to the following steps:

Step 1: Select a random number,  $Z$ , in the interval of  $[0,1]$  then, select a random number,  $rand()$ , in the interval  $[0,1]$ .

Step 2: Produce logistic mapping:  $z = 4 \times z \times (1 - z)$  ;

Step 3:  $\varpi = 0.5 \times rand() + 0.5z$

Step 4: Modify the solution update Equation 7 by incorporating the chaotic inertia weight mechanism.

$$x_{(i+1,j,k)} = x_{(i,j,k)} + \varpi * r_{(i,j,1)} \left[ x_{(i,j)} - \left| x_{(i,j,k)} \right| \right] - \varpi * r_{(i,j,2)} \left[ x_{(i,j,w)} - \left| x_{(i,j,k)} \right| \right] [7]$$

Where  $X'_{i,j,k}$  denotes the modified value of the  $i$ -th design variable, the second term represents the approach of the modified solution to proceed nearer to the optimum solution, and the third expression is attributed to the proclivity of the solution to avoid the worst solution.

The next improvement is made in the selection criteria process where archive K-nearest neighbour (aKNN) is employed and known as MOiJaya\_aKNN. In this phase, improvements are made to the selection criteria, which are the best and worst solutions. The selection of the first P is based on the non-dominated ranking and crowding distance. The selection is important during the selection process because this solution is a guide and search towards the Pareto-optimal set. Potential solutions might be rejected and not selected due to the crowded region during the selection search space. Consequently, the process is crucial to choose a set of solutions that could lead to convergence toward true Pareto-optimal. Furthermore, the step is essential to avoid Pareto breakouts when it is stuck in local optima, which would occur. An improper selection might also delay the convergence as it is required to break the local optima. Hence, the rejected or not selected solutions in the crowded region were considered for the next iteration during the step and applied to the archive KNN.

This study employed an external archive mechanism as a repository to store potential solutions among the rejected and not selected solutions. Consequently, the archive could potentially possess solutions closer to the Pareto front as it possesses higher chances of comprising the best potential solution. The KNN was employed to obtain the possible solution close to the Pareto front. The method is a simple classification algorithm that utilises the Euclidean metric as the distance metric, where the K parameter controls the classification. The KNN was also employed to reduce the archive size by manipulating the K values and selecting archive members close to the most optimum solution in the Pareto front.

The second strategy adopted in the present study was improving the selection process to reduce the complexity of multi-objective problems based on Pareto dominance. Figure 7 demonstrates the improvements implemented on the hybrid MOJaya. The hybrid MOJaya with chaotic inertia weight and archive KNN (MOiJaya\_aKNN) was then utilised to optimise the CS casting parameters process to predict optimal feedstock performance.

### Algorithm Performance

These proposed improvement algorithms were evaluated using ZDT bio-objective test problems. These test problems are chosen because ZDT is a set of test problems that focuses on multi-objective optimisation and consists of two objective functions (Table 4). These

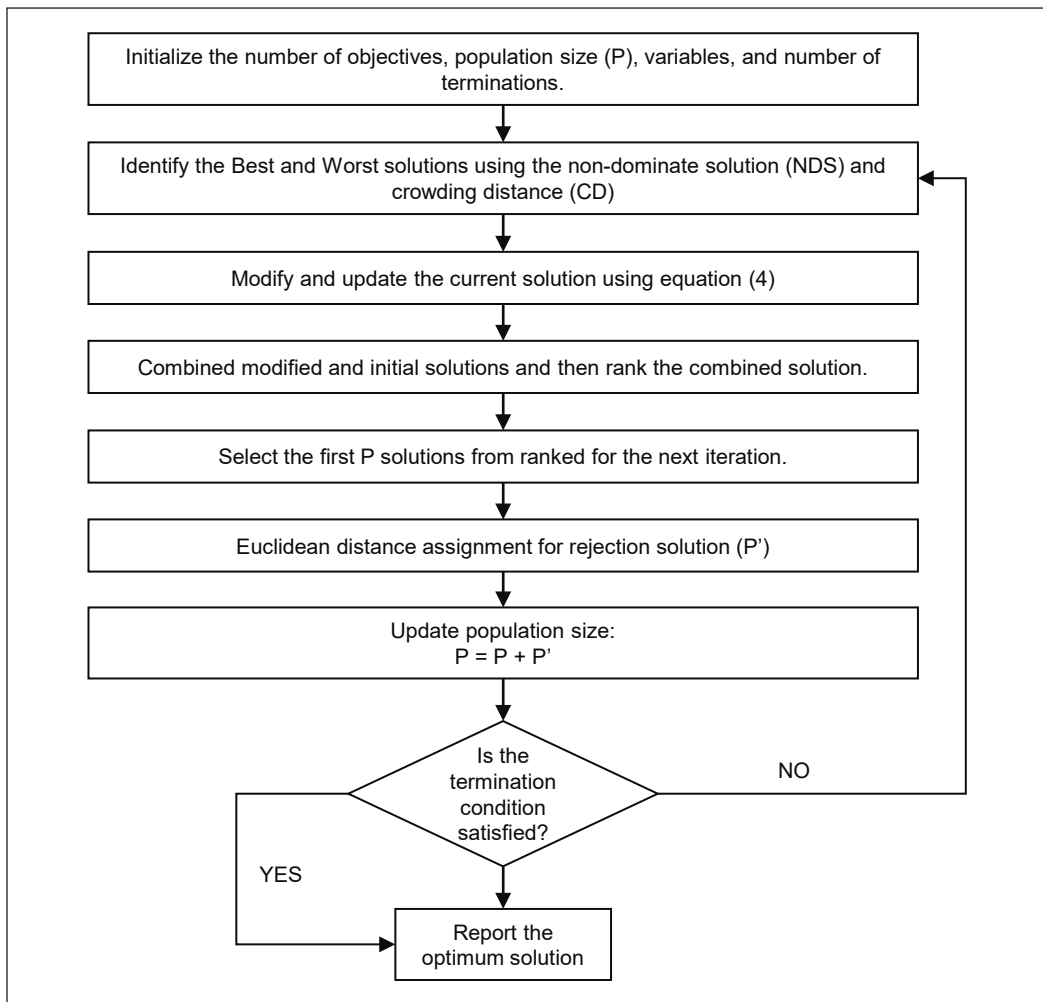


Figure 7. Flowchart of MOiJaya\_aKNN algorithm

types of problems are suitable for CS casting process optimisation, which consists of two objective functions: tensile strength and impact strength. Then, the proposed algorithm performance using the ZDT test problem was evaluated using the convergence metric (Generational distance) and diversity metric (spread). ZDT is also easy to implement and has several test cases with different difficulties. For each ZDT test problem, 30 times experiments were conducted. Then, the results of MOiJaya and MOiJaya\_aKNN algorithms were compared with previously published results. All analyses regarding the algorithm's performance are discussed.

The main evaluation of algorithm performance used in this study is convergence and diversity metrics. Convergence metrics were developed and introduced by Deb et al. (2002). These metrics measure the distance between the reference set and the obtained Pareto front.

Table 4  
ZDT bio-objective test problems (Deb et al., 2002)

Problem	N	Variable bounds	Objective Functions	Optimal Solutions	Comments
ZDT 1	30	[0,1]	$f_1(x) = x_1$ $f_2(x) = g(x) \left[ 1 - \sqrt{x_1 / g(x)} \right]$ $h(f_1) = 1 + 9 \left( \sum_{i=2}^n x_i \right) (n-1)$	$x_1 \in [0, 1]$ $x_1 = 0$ $i = 2, \dots, n$	Convex
ZDT 2	30	[0,1]	$f_1(x) = x_1$ $f_2(x) = g(x) \left[ 1 - (x_1 / g(x))^2 \right]$ $h(f_1) = 1 + 9 \left( \sum_{i=2}^n x_i \right) (n-1)$	$x_1 \in [0, 1]$ $x_1 = 0$ $i = 2, \dots, n$	Nonconvex
ZDT 3	30	[0,1]	$f_1(x) = x_1$ $f_2(x) = g(x) \left[ 1 - \sqrt{x_1 / g(x)} - \frac{x_1}{g(x)} \sin(10\pi x_1) \right]$ $h(f_1) = 1 + 9 \left( \sum_{i=2}^n x_i \right) (n-1)$	$x_1 \in [0, 1]$ $x_1 = 0$ $i = 2, \dots, n$	Convex Disconnected
ZDT 4	30	[0,1]	$f_1(x) = x_1$ $f_2(x) = g(x) \left[ 1 - \sqrt{x_1 / g(x)} \right]$ $h(f_1) = 1 + 10(n-1) + \sum_{i=2}^n x_i^2 - 10 \cos(4\pi x_i)$	$x_1 \in [0, 1]$ $x_1 = 0$ $i = 2, \dots, n$	Convex
ZDT 6	30	[0,1]	$f_1(x) = 1 - \exp(-4x_1) \sin^6(6\pi x_1)$ $f_2(x) = g(x) \left[ 1 - (x_1 / g(x))^2 \right]$ $h(f_1) = 1 + 9 \left[ \left( \sum_{i=2}^n x_i \right) (n-1) \right]^{-0.25}$	$x_1 \in [0, 1]$ $x_1 = 0$ $i = 2, \dots, n$	Nonconvex Nonuniformly spaced



A reference set (Pareto-optimal front) can be defined as a set of optimal true Pareto Front solutions or a non-dominated set of solutions. The convergence measurement produces a better algorithm when the solution obtained is closer to the reference point. Then, a lower convergence metric value can produce a better MOO algorithm.

### Convergence Metric

The following steps can compute the convergence metric:

- Step 1: Find the non-dominated  $F(t)$  population set.
- Step 2: For each solution,  $i$  in  $F(t)$ , calculate the smallest normalised Euclidian Distance,  $d_i$  to the reference set as Equation 8:

$$d_i = \min_{j=1}^N \sqrt{\sum_{k=1}^M \left( \frac{f_k(i) - f_k(j)}{f_k \max - f_k \min} \right)^2} \tag{8}$$

Here,  $M$  is the number objective,  $f_k \max$  and  $f_k \min$  are the maximum and minimum function values of the  $k^{\text{th}}$  objective function in the reference set, respectively, and  $N$  is the size of the reference set.

- Step 3: Find the convergence metric value  $C(P(t))$  by finding the normalised distance average for all points in  $F(t)$  as Equation 9.

$$C(P(t)) = \frac{\sum_{i=1}^{|F(t)|} d_i}{|F(t)|} \tag{9}$$

Diversity metric can be calculated using Equation 10:

$$DIV = \frac{d_f + d_l + \sum_{i=1}^{N-1} |d_i - \bar{d}|}{d_f + d_l + (N - 1)\bar{d}} \tag{10}$$

Here  $\bar{d}$  is the average of all distances  $d_i$  ( $i = 1, \dots, N$ ), assuming  $N$  solutions are in the obtained non-dominated set.  $d_i$  is the Euclidean distance between the consecutive solutions in the obtained non-dominated set of solutions.  $(N - 1)$  is total  $d_i$  produced.  $d_f$  and  $d_l$  represent the Euclidean Distance between the boundary solutions and extreme value.

### Comparison Results with Benchmark MOO Algorithm

The results were compared with three well-known multi-objective algorithms (MOEA/D, PESA-II and MOALO) to investigate the efficiency of the proposed MOiJaya\_aKNN. The parameter settings were adopted for all the algorithms: population size  $P = 100$  and Number of iterations = 500. Table 5 shows the performance metric’s comparison of MOEA/D, PESA-II, MOALO, MOMSA, MOJaya, MOiJaya, and the MOiJaya\_aKNN. As

Table 5

*Performance metric comparison for convergence and diversity metric evaluation metrics on ZDT bi-objective between MOiJaya\_aKNN and other algorithms*

Case	Algorithm	Convergence (mean±sd)	Diversity (mean±sd)
ZDT1	MOMSA	0.028±0.014	0.581±0.696
	MOEA	0.159±0.102	1.044±0.133
	MOALA	0.044±0.026	1.345±0.081
	PESA-II	0.079±0.026	0.763±0.052
	MOJAYA	0.233±0.055	0.020±0.042
	MOiJAYA_aKNN	<b>0.009±0.001</b>	<b>0.015±0.00065</b>
ZDT2	MOMSA	0.029±0.024	1.011±0.153
	MOEA	<b>0.033±0.043</b>	1.045±0.048
	MOALA	<b>0.033±0.015</b>	1.126±0.091
	PESA-II	0.095±0.015	0.721±0.065
	MOJAYA	0.265±0.225	0.044±0.027
	MOiJAYA_aKNN	<b>0.033±0.055</b>	<b>0.023±0.015</b>
ZDT3	MOMSA	0.017±0.005	0.910±0.033
	MOEA	0.220±0.150	1.330±0.044
	MOALA	0.028±0.022	1.552±0.082
	PESA-II	0.0875±0.056	0.958±0.082
	MOJAYA	0.046±0.005	0.066±0.122
	MOiJAYA_aKNN	<b>0.0071±0.007</b>	<b>0.026±0.004</b>
ZDT4	MOMSA	0.391±0.294	1.102±0.160
	MOEA	7.901±1.504	1.161±0.031
	MOALA	21.070±16.94	1.008±0.008
	PESA-II	17.466±10.931	0.973±0.029
	MOJAYA	<b>0.217±0.0516</b>	0.255±0.0644
	MOiJAYA_aKNN	0.29512±0.03720	<b>0.01017±0.00180</b>
ZDT6	MOMSA	0.063±0.024	1.476±0.195
	MOEA	0.1311±0.207	1.137±0.052
	MOALA	0.325±0.198	1.425±0.053
	PESA-II	0.325±0.464	1.211±0.190
	MOJAYA	0.560±0.470	0.076±0.084
	MOiJAYA_aKNN	<b>0.022±0.010</b>	<b>0.01329±0.00197</b>

can be seen, the developed MOiJaya algorithm was superior in most standard bi-objectives compared to others.

Regarding the convergence metric, while MOiJaya\_aKNN with the lowest mean convergence metric outperformed other algorithms in optimising were 0.009 for ZDT 1, 0.0071 for ZDT3, and 0.022 for ZDT6 benchmark functions, the MOEA and MOALA algorithms demonstrate same results of 0.0033 for ZDT2. Moreover, MOJaya algorithms

obtained better results were 0.217 for ZDT4. Therefore, it can be said that the MOiJaya\_aKNN could find the non-dominant solutions with minimum distance from the Pareto front and had a better distribution than the five other algorithms.

In terms of the diversity metric, the MOiJaya\_aKNN with the lowest diversity metric outperformed all the ZDT bi-objective benchmark functions. For example, the average value of the diversity metric for the ZDT1 benchmark function obtained by the MOiJaya\_aKNN algorithm was 0.015, while the corresponding values for MOMSA, MOEA/D, MOALA, PESA-II, MOJaya and MOiJaya algorithms were 0.581, 1.044, 1.345, 0.763, 0.020 and 0.016, respectively, indicating the higher performance of the MOiJaya\_aKNN compared to the other algorithms. The results for other diversity metrics (dm) demonstrated that the MOiJaya was 0.02354 for ZDT2, 0.02687 for ZDT3, 0.01017 for ZDT4, and 0.01329 for ZDT6. As seen in Table 6, the proposed MOiJaya\_aKNN was the only model with impressive diversity results. It could produce a better distribution and spread for the non-dominated solutions on the Pareto front compared to the original MOJaya. Meanwhile, integration with aKNN provides a possible solution for obtaining the best solution value for optimisation.

These results indicate that the probability of premature convergence and the unbalancing of exploration and exploitation of MOJaya has been improved by introducing chaotic random inertia weight and archiving K-nearest neighbour, which improves both convergence and diversity.

### Optimisation of Cooling Slope Casting Process using Hybrid MOJaya

The proposed MOiJaya\_aKNN hybrid algorithm developed in this study was utilised to improve the basic MOJaya algorithm. Subsequently, the enhanced algorithm was employed to optimise the CS parameters for predicting optimal feedstock performance in terms of mechanical properties (tensile and impact strengths) via the MOO approach.

The first step in developing the MOiJaya\_aKNN algorithm was parameter initialisation, which was required before optimisation. During the initialisation step, a population-sized solution space was generated randomly between the high and low values of the variables (Pt, Sa, and Pd) range limits. Table 6 lists the details of the parameters executed in MATLAB software employed in this study. Steps 1–11 describe the MOiJaya\_aKNN algorithm development.

The following steps describe the MOiJaya\_aKNN algorithm to solve the multi-objective optimisation in the CS process:

Table 6  
*MOiJaya\_aKNN initialisation*

Parameters	Command
Population size	100
Maximum iteration (MI)	500
Number of variables (NVAR)	3
Lower Boundary (LB)	[680, 30, 300]
Upper Boundary (UB)	[720, 60, 500]

- Step 1: Define the input process parameters (Pt, Pd, and Sa) and objective functions (tensile and impact strengths).
- Step 2: Identify the population size, number of variables, and stopping criteria.
- Step 3: Generate the Initial population size (P) randomly.
- Step 4: Evaluate the objective function, which is the mathematical model for Tensile strength and Impact strength expressed in Equations 5 and 6, respectively, as a function for the MOJaya algorithm. The process parameters bounds are expressed by Equations 11 to 15. Maximise:

$$\begin{aligned} \text{Tensile Strength} = & 6790.30937 - 19.12184 * Pt - 1.63463 * Sa \\ & - 0.21772 * Pd + 0.013738 * Pt * Pt \\ & + 0.022938 * Sa * Sa + 0.000508 * Pd * Pd \end{aligned} \quad [11]$$

Maximise

$$\begin{aligned} \text{Impact strength} = & 147.34224 - 0.412945 * Pt - 0.003288 * Sa - 0.003761 * Pd \\ & - 0.00050 * Sa * Pd + 0.000297 * Pt * Pt \\ & + 0.000372 * Sa * Sa + 0.00012 * Pd * Pd \end{aligned} \quad [12]$$

Parameter

$$680 \leq A \leq 720 \quad [13]$$

$$300 \leq B \leq 500 \quad [14]$$

$$30 \leq C \leq 60 \quad [15]$$

- Step 5: Identify the best and worst candidates among the population in terms of identified objective functions generated from the equation and parameter boundaries from Equations 5 to 9.
- Step 6: Based on the best and worst solutions from Step 5, substitute the value to modify all candidate solutions using expressed as Equation 4.
- Step 7: Combine the modified solution with the initial solutions. Calculate the crowding distance and ranking using non-dominated sorting, considering both functions. Then, select the first P for the next iteration.
- Step 8: Sort P' (rejection solution) by ascending ranking and descending crowding distance. Trim P' into its original size of P
- Step 9: Update using KNN,  $P=P' + K$  size archive
- Step 10: If the termination criterion is satisfied, exit and proceed with Step 11; if not, go back to Step 5.
- Step 11: The stopping criteria are applied in the algorithm; if the solutions satisfy the condition, the algorithm will stop and, otherwise, return to Step 4.

## RESULTS AND DISCUSSION

The current study employed a mathematical regression model to validate the impact strength in Equation 11 and tensile strength in Equation 12 (feedstock performance) as objective functions in MOJaya algorithms. Their significance needs to be validated before the models are used in the optimisation process. The significance and coefficient determination values for the models are summarised in Tables 7 and 8. The models were then utilised to optimise the CS process parameters.

Tables 7 and 8 indicate that the SR model for tensile strength and impact strength with a 95% confidence interval is statistically significant with a  $p$ -value less than 0.0001. A  $p$ -value equal to or less than 0.5 is considered significant, while a  $p$ -value higher than 0.5 is considered insignificant. The result of each CS casting process parameter for both SR models shows that all parameters are significant to the model with  $p$  a  $p$ -value less than 0.05.

Both models proposed in the present study were significant since their  $p$ -values were under 0.05. The models also recorded  $R^2$  values over 80%, as tabulated in Table 9, indicating

Table 7  
*ANOVA of tensile strength*

Source	Sum of Squares	df	Mean Square	F-value	p-value
<b>Model</b>	6281.41		1046.90	10.00	< 0.0001
A-Pouring Temperature	384.20	1	384.20	3.67	0.00673
B-Slanting Angle	1941.01	1	1941.01	18.55	0.0002
C-Pouring distance	1961.32	1	1961.32	18.74	0.0002
AC	415.53	1	415.53	3.97	0.0578
A <sup>2</sup>	808.82	1	808.82	7.73	0.0104
B <sup>2</sup>	455.15	1	455.15	4.35	0.0478
<b>Residual</b>	2511.31	24	104.64		
<b>Total</b>	8792.72	30			

Table 8  
*ANOVA of impact strength*

Source	Sum of Squares	df	Mean Square	F-value	p-value
<b>Model</b>	3.21		0.4583	14.11	< 0.0001
A-Pouring Temperature	0.0578	1	0.0578	1.78	0.01952
B-Slanting Angle	0.4128	1	0.4128	12.71	0.0016
C-Pouring distance	2.29	1	2.29	70.68	< 0.0001
BC	0.0684	1	0.0684	2.11	0.01602
A <sup>2</sup>	0.0991	1	0.0991	3.05	0.00940
B <sup>2</sup>	0.0493	1	0.0493	1.52	0.02303
C <sup>2</sup>	0.1010	1	0.1010	3.11	0.0910
<b>Residual</b>	0.7468	23	0.0325		
<b>Total</b>	3.95	30			

Table 9  
*Model summary statistics for tensile strength and impact strength*

Model	R <sup>2</sup>	Adj-R <sup>2</sup>	Pred-R <sup>2</sup>
Tensile Strength	0.8959	0.8698	0.8849
Impact strength	0.8112	0.7537	0.6315

a perfect fit and the models explained over 80% of the performance feedstock variance, which arose from the CS process parameters. Furthermore, the accuracy of both models was validated with actual data and mathematical models.

The pred-R<sup>2</sup> value in the current study defines the ability of a model to predict feedstock performance for new observations, where a higher value indicates a significant prediction ability. Both models obtained in this study were documented under a 0.2 difference between the adj-R<sup>2</sup> and pred-R<sup>2</sup> values. Then, the models were acceptable. The results demonstrated that the regression model equations for mechanical properties (tensile and impact strengths) could be utilised to predict feedstock performance effectively.

Next, the optimal CS parameters values generated from MOiJaya\_aKNN; Pouring Temperature= 701.5456°C, Slanting angle =44.0902° and Pouring distance = 411.82938cm. Next, the algorithm performances were determined by comparing the generated output from MOiJaya\_aKNN and the initial experiment. Table 10 shows that the difference between experiment results and MOiJaya\_aKNN results is only 2.17% per cent different for Tensile strength, and Impact strength is 5.52% per cent different. MOiJaya\_aKNN results are considered accepted since there is a slight percentage improvement. Hence, MOiJaya\_aKNN can help the caster solve real problems in the CS casting process for predicted optimum feedstock performance without using repeated experiments that are costly and time-consuming.

Table 10  
*Optimisation result of the CS casting process*

Feedstock Performance	Method	Value	Percentage improvement (%)
Tensile strength	MOiJAYA_aKNN	146.8586	2.17%
	Initial Experiment	143.732	
Impact strength	MOiJAYA_aKNN	4.8751	5.52%
	Initial Experiment	4.606	

## CONCLUSION

Based on the AZ91D magnesium alloy CS casting optimisation with MOiJaya\_aKNN algorithm performed in the current study, the following conclusions were derived:

1. The results indicate that the probability of premature convergence occurring and the unbalance of exploration and exploitation have been improved by introducing

- chaotic, random inertia weight and archiving K-nearest neighbour while improving both convergence and diversity of the original MOJaya algorithm.
2. The regression analysis successfully developed a prediction model for feedstock performance (tensile and impact strengths). Furthermore, the predicted values were in good agreement with measured output responses, where the  $R^2$  adjusted values were high ( $> 70\%$ ), indicating the models' superior ability to predict.
  3. The optimum CS casting parameters were  $701.5456^\circ\text{C}$  of Pt,  $44.0902^\circ$  of Sa, and  $411.82938\text{cm}$  of Pd.
  4. Compared to initial experimental data, the values tensile and impact strengths from MOiJaya\_aKNN are close to the initial experiment values as the difference is  $2.17\%$  and  $5.52\%$ , respectively.

## ACKNOWLEDGEMENT

Thanks to the reviewers for their useful advice and comments. The authors want to acknowledge the University Teknikal Malaysia Melaka, Universiti Teknologi Malaysia and those who supported this research. The author also thanks Universiti Teknikal Malaysia Melaka for sponsoring this work under the Grant Tabung Penerbitan Fakulti dan Tabung Penerbitan CRIM Universiti Teknikal Malaysia Melaka.

## REFERENCES

- Abdelgneia, M. A. H., Omar, M. Z., Ghazalib, M. J., Gebrillb, M. A., & Mohammed, M. N. (2019). The effect of the rheocast process on the microstructure and mechanical properties of Al-5.7Si-2Cu-0.3Mg alloy. *Jurnal Kejuruteraan*, *31*(2), 317-326. [https://doi.org/10.17576/jkukm-2019-31\(2\)-17](https://doi.org/10.17576/jkukm-2019-31(2)-17)
- Abdin, Z., Prabantariksob, R. M., Fahmy, E., & Farhan, A. (2022). Analysis of the efficiency of insurance companies in Indonesia. *Decision Science Letters*, *11*(2022), 105-112. <https://doi.org/10.5267/j.dsl.2022.1.002>
- Agarwal, N., Pradhan, M. K., & Shrivastava, N. (2018). A new respond Jaya algorithm for optimization of EDM process parameters. *Materials Today's Proceedings*, *5*(11, Part 3), 23759-23768. <https://doi.org/10.1016/j.matpr.2018.10.167>
- Annamalai, S., Periyakoundar, S., & Gunasekaran, S. (2019). Magnesium alloys: A review of applications. *Materials and Technology*, *53*(6), 881-890. <https://doi.org/10.17222/mit.2019.065>
- Asadollahi-Yazdi, E., Gardan, J., & Lafon, P. (2018). Multi-objective optimization of additive manufacturing process. *IFAC-PapersOnLine*, *51*(11), 152-157. <https://doi.org/10.1016/j.ifacol.2018.08.250>
- Balachandran, G. (2018). Challenges in special steel making. *IOP Conference Series: Materials Science and Engineering*, *314*, Article 012016. <https://doi.org/10.1088/1757-899X/314/1/012016>
- Binesh, B., & Aghaie-Khafri, M. (2017). Modelling and optimization of semi-solid processing of 7075 Al alloy. *Materials Research Express*, *4*, Article 096502. <https://doi.org/10.1088/2053-1591/aa8272>

- Brezocnik, M., & Župerl, U. (2021). Optimization of the continuous casting process of hypoeutectoid steel grades using multiple linear regression and genetic programming - An industrial study. *Metals*, 11(6), Article 972. <https://doi.org/10.3390/met11060972>
- Britto, A., & Pozo, A. (2012). Using archiving methods to control convergence and diversity for many-objective problems in particle swarm optimization. In *2012 IEEE Congress on Evolutionary Computation* (pp. 1-8). IEEE Publishing. <https://doi.org/10.1109/CEC.2012.6256149>
- Deb, K., Pratap, A., Agarwal, S., & Meyarivan, T. A. M. T. (2002). A fast and elitist multiobjective genetic algorithm: NSGA-II. *IEEE transactions on evolutionary computation*, 6(2), 182-197.
- El-Ashmawi, W. H., Ali, A. F., & Slowik, A. (2020). An improved Jaya algorithm with a modified swap operator for solving team formation problem. *Soft Computing*, 24, 16627-16641. <https://doi.org/10.1007/s00500-020-04965-x>
- Esonye, C., Onukwuli, O. D., Anadebe, V. C., Ezeugo, J. N. O., & Ogbodo, N. J. (2021). Application of soft-computing techniques for statistical modeling and optimization of *Dyacrodus edulis* seed oil extraction using polar and non-polar solvents. *Heliyon*, 7(3), Article e06342. <https://doi.org/10.1016/j.heliyon.2021.e06342>
- Fadaee, M., Mahdavi-Meymand, A., & Zounemat-Kermani, M. (2022). Suspended sediment prediction using integrative soft computing models: On the analogy between the butterfly optimization and genetic algorithms. *Geocarto International*, 37(4), 961-977. <https://doi.org/10.1080/10106049.2020.1753821>
- Feng, Q., & Zhou, X. (2019). Automated and robust multi-objective optimal design of thin-walled product injection process based on hybrid RBF-MOGA. *The International Journal of Advanced Manufacturing Technology*, 101, 2217-2231. <https://doi.org/10.1007/s00170-018-3084-5>
- Feng, Y., Lu, R., Gao, Y., Zheng, H., Wang, Y., & Mo, W. (2018). Multi-objective optimization of VBHF in sheet metal deep-drawing using Kriging, MOABC, and set pair analysis. *The International Journal of Advanced Manufacturing Technology*, 96, 3127-3138. <https://doi.org/10.1007/s00170-017-1506-4>
- Ganesh, N., Shankar, R., Kalita, K., Jangir, P., Oliva, D., & Pérez-Cisneros, M. (2023). A novel decomposition-based multi-objective symbiotic organism search optimization algorithm. *Mathematics*, 11(8), Article 1898. <https://doi.org/10.3390/math11081898>
- Goudos, S. K., Deruyck, M., Plets, D., Martens, L., Psannis, K. E., Sarigiannidis, P., & Joseph, W. (2019). A novel design approach for 5G massive MIMO and NB-IoT green networks using a hybrid jaya-differential evolution algorithm. *IEEE Access*, 7, 105687-105700. <https://doi.org/10.1109/ACCESS.2019.2932042>
- Guo, Y., Liu, W., Sun, M., Xu, B., & Li, D. (2018). A method based on semi-solid forming for eliminating coarse dendrites and shrinkage porosity of H13 tool steel. *Metals*, 8(4), Article 277. <https://doi.org/10.3390/met8040277>
- Jangir, P., Buch, H., Mirjalili, S., & Manoharan, P. (2023). MOMPA: Multi-objective marine predator algorithm for solving multi-objective optimization problems. *Evolutionary Intelligence*, 16, 169-195. <https://doi.org/10.1007/s12065-021-00649-z>
- Ji, Z., & Xie, Z. (2008). Multi-objective optimization of continuous casting billet based on ant colony system algorithm. In *2008 IEEE Pacific-Asia Workshop on Computational Intelligence and Industrial Application* (Vol. 1, pp. 262-266). IEEE Publishing. <https://doi.org/10.1109/PACIIA.2008.28>



- Jian, X., & Weng, Z. (2020). A logistic chaotic JAYA algorithm for parameters identification of photovoltaic cell and module models. *Optik*, 203, Article 164041. <https://doi.org/10.1016/j.ijleo.2019.164041>
- Khosravi, H., Eslami-Farsani, R., & Askari-Paykani, M. (2014). Modeling and optimization of cooling slope process parameters for semi-solid casting of A356 Al alloy. *Transactions of Nonferrous Metals Society of China (English Edition)*, 24(4), 961-968. [https://doi.org/10.1016/S1003-6326\(14\)63149-6](https://doi.org/10.1016/S1003-6326(14)63149-6)
- Kor, J., Chen, X., Sun, Z., & Hu, H. (2011). Casting design through multi-objective optimization. *IFAC Proceedings*, 44(1), 11642-11647. <https://doi.org/10.3182/20110828-6-IT-1002.01726>
- Kumar, S., Jangir, P., Tejani, G. G., Premkumar, M., & Alhelou, H. H. (2021). MOPGO: A new physics-based multi-objective plasma generation optimizer for solving structural optimization problems. *IEEE Access*, 9, 84982-85016. <https://doi.org/10.1109/ACCESS.2021.3087739>
- Kumar, S. D., Mandal, A., & Chakraborty, M. (2014). Cooling slope casting process of semi-solid aluminum alloys: A review. *International Journal of Engineering Research & Technology (IJERT)*, 3(7), 269-283.
- Kumar, S. B., Idris, M. H., Farah, N. F. N., & Kamal, R. (2013). Investigation of mechanical properties of AZ91D magnesium alloy by gravity die casting process. *Jurnal Mekanikal*, 36, 1-9.
- Li, K., Chen, R., Fu, G., & Yao, X. (2019). Two-archive evolutionary algorithm for constrained multiobjective optimization. *IEEE Transactions on Evolutionary Computation*, 23(2), 303-315. <https://doi.org/10.1109/TEVC.2018.2855411>
- Li, S., Fan, X., Huang, H., & Cao, Y. (2020). Multi-objective optimization of injection molding parameters, based on the Gkriging-NSGA-vague method. *Journal of Applied Polymer Science*, 137(19), Article 48659. <https://doi.org/10.1002/app.48659>
- Mishra, P., & Sahu, A. (2018). Manufacturing process optimization using pso by optimal machine combination on cluster level. *Materials Today: Proceedings*, 5(9), 19200-19208. <https://doi.org/10.1016/j.matpr.2018.06.275>
- Nafisi, S., & Ghomashchi, R. (2019). Semi-solid processing of alloys and composites. *Metals*, 9(5), Article 526. <https://doi.org/10.3390/met9050526>
- Narayanan, R. C., Ganesh, N., Čep, R., Jangir, P., Chohan, J. S., & Kalita, K. (2023). A novel many-objective sine-cosine algorithm (MaOSCA) for engineering applications. *Mathematics*, 11(10), Article 2301. <https://doi.org/10.3390/math11102301>
- Onifade, M., Lawal, A. I., Aladejare, A. E., Bada, S., & Idris, M. A. (2022). Prediction of gross calorific value of solid fuels from their proximate analysis using soft computing and regression analysis. *International Journal of Coal Preparation and Utilization*, 42(4), 1170-1184. <https://doi.org/10.1080/19392699.2019.1695605>
- Pandya, S. B., Visumathi, J., Mahdal, M., Mahanta, T. K., & Jangir, P. (2022). A novel MOGNDO algorithm for security-constrained optimal power flow problems. *Electronics*, 11(22), Article 3825. <https://doi.org/10.3390/electronics11223825>
- Patel, G. C. M., Krishna, P., Vundavilli, P. R., & Parappagoudar, M. B. (2016a). Multi-objective optimization of squeeze casting process using genetic algorithm and particle swarm optimization. *Archives of Foundry Engineering*, 16(3), 172-186. <https://doi.org/10.1515/afe-2016-0073>

- Patel, G. C. M., Krishna, P., & Parappagoudar, M. B. (2016b). Modelling and multi-objective optimisation of squeeze casting process using regression analysis and genetic algorithm. *Australian Journal of Mechanical Engineering*, 14(3), 182-198. <https://doi.org/10.1080/14484846.2015.1093231>
- Patel, G. C. M., Krishna, P., & Parappagoudar, M. B. (2015). Modelling of squeeze casting process using design of experiments and response surface methodology. *International Journal of Cast Metals Research*, 28(3), 167-180. <https://doi.org/10.1179/1743133614Y.0000000144>
- Premkumar, M., Jangir, P., Sowmya, R., Elavarasan, R. M., & Kumar, B. S. (2021). Enhanced chaotic JAYA algorithm for parameter estimation of photovoltaic cell/modules. *ISA Transactions*, 116, 139-166. <https://doi.org/10.1016/j.isatra.2021.01.045>
- Premkumar, M., Jangir, P., Kumar, B. S., Alqudah, M. A., & Nisar, K. S. (2022). Multi-objective grey wolf optimization algorithm for solving real-world BLDC motor design problem. *Computers, Materials & Continua*, 70(2), 2435-2452. <https://doi.org/10.32604/cmc.2022.016488>
- Raed, A. Z., Mohammed, Z., Al, A., Awadallah, M. A., Doush, I. A., & Assaleh, K. (2022). An intensive and comprehensive overview of JAYA Algorithm, its versions and applications. *Archives of Computational Methods in Engineering*, 29(2), 763-792. <https://doi.org/10.1007/s11831-021-09585-8>
- Rao, R. V. (2011). *Advanced modeling and optimization of manufacturing processes*. Springer. <https://doi.org/10.1007/978-0-85729-015-1>
- Rao, R. V., Rai, D. P., Ramkumar, J., & Balic, J. (2016). A new multi-objective Jaya algorithm for optimization of modern machining processes. *Advances in Production Engineering & Management*, 11(4), 271-286. <http://dx.doi.org/10.14743/apem2016.4.226>
- Rao, R. Venkata, Keesari, H. S., Oclon, P., & Taler, J. (2019). Improved multi-objective Jaya optimization algorithm for a solar dish Stirling engine. *Journal of Renewable and Sustainable Energy*, 11(2), Article 025903. <https://doi.org/10.1063/1.5083142>
- Rao, R. V. (2018). *Jaya: An advanced optimization algorithm and its engineering applications*. Springer. <https://doi.org/10.1007/978-3-319-78922-4>
- Said, R. M., Sallehuddin, R., Mohd Radzi, N. H., & Mohd Kamal, M. R. (2021). Jaya algorithm for optimization of cooling slope casting process parameters. *Journal of Physics: Conference Series*, 2129(1), Article 012042. <https://doi.org/10.1088/1742-6596/2129/1/012042>
- Singh, A., Singh, R. M., Kumar, A. R. S., Kumar, A., Hanwat, S., & Tripathi, V. K. (2021). Evaluation of soft computing and regression-based techniques for the estimation of evaporation. *Journal of Water and Climate Change*, 12(1), 32-43. <https://doi.org/10.2166/wcc.2019.101>
- Son, Y. G., Jung, S. S., Park, Y. H., & Lee, Y. C. (2021). Effect of semi-solid processing on the microstructure and mechanical properties of aluminum alloy chips with eutectic Mg<sub>2</sub>Si intermetallics. *Metals*, 11(9), Article 1414. <https://doi.org/10.3390/met11091414>
- Tanvir, M. H., Hussain, A., Rahman, M. M. T., & Ishraq, S., Zishan, K., Rahul, S. T., & Habib, M. A. (2020). Multi-objective optimization of turning operation of stainless steel using a hybrid whale optimization algorithm. *Journal of Manufacturing and Materials Processing*, 4(3), Article 64. <https://doi.org/10.3390/jmmp4030064>

- Tavakolpour-Saleh, A. R., Zare, S. H., & Badjian, H. (2017). Multi-objective optimization of stirling heat engine using gray wolf optimization algorithm. *International Journal of Engineering*, 30(6), 150-160.
- Tugiman, T., Thayab, A., Ariani, F., Sitorus, T., Suhandi, S., & Rizki, R. (2019). The effect of cooling slope on mechanical properties of aluminum-8.5wt.% Si alloy produced by gravity casting. In *Proceedings of the 2nd Annual Conference of Engineering and Implementation on Vocational Education (ACEIVE 2018)* (pp. 1-7). EAI Publishing. <https://doi.org/10.4108/eai.3-11-2018.2285718>
- Vinh, L., & Nguyen, N. S. (2020). Parameters extraction of solar cells using modified JAYA algorithm. *Optik*, 203, Article 164034. <https://doi.org/10.1016/j.ijleo.2019.164034>
- Warid, W., Hizam, H., Mariun, N., & Wahab, N. I. A. (2018). A novel quasi-oppositional modified Jaya algorithm for multi-objective optimal power flow solution. *Applied Soft Computing*, 65, 360-373. <https://doi.org/10.1016/j.asoc.2018.01.039>
- Wu, C., & He, Y. (2020). Solving the set-union knapsack problem by a novel hybrid Jaya algorithm. *Soft Computing*, 24, 1883-1902. <https://doi.org/10.1007/s00500-019-04021-3>
- Wu, H., Yang, X., Cao, G., Zhao, L., & Yang, L. (2021). Design and optimisation of die casting process for heavy-duty automatic transmission oil circuit board. *International Journal of Cast Metals Research*, 31(2), 88-96. <https://doi.org/10.1080/13640461.2021.1904673>
- Zamli, K., Alsewari, A., & S. Ahmed, B. (2018). Multi-start jaya algorithm for software module clustering problem. *Azerbaijan Journal of High Performance Computing*, 1(1), 87-112.
- Zheng, K., Lin, Y., Chen, W., & Liu, L. (2020). Numerical simulation and optimization of casting process of copper alloy water-meter shell. *Advances in Mechanical Engineering*, 12(5), 1-12. <https://doi.org/10.1177/1687814020923450>
- Zhenghao, Li, J., & Hao, H. (2020). Non-probabilistic method to consider uncertainties in structural damage identification based on hybrid Jaya and tree seeds algorithm. *Engineering Structures*, 220, Article 110925. <https://doi.org/10.1016/j.engstruct.2020.110925>
- Zhou, D., Kang, Z., Yang, C., Su, X., & Chen, C. C. (2022). A novel approach to model and optimize qualities of castings produced by differential pressure casting process. *International Journal of Metalcasting*, 16, 259-277. <https://doi.org/10.1007/s40962-021-00596-6>
- Zitzler, E., Deb, K., & Thiele, L. (1999). Comparison of multiobjective evolutionary algorithms: empirical results. *Evolutionary Computation*, 8(2), 173-195. <https://doi.org/10.1162/106365600568202>



## Microencapsulation of *Citrus Hystrix* Essential Oil by Gelatin B/Chitosan Complex Coacervation Technique

Siti Afiqah 'Aisyah Murtadza<sup>1</sup>, Nurul Asyikin Md Zaki<sup>1\*</sup>, Junaidah Jai<sup>1</sup>, Fazlena Hamzah<sup>1</sup>, Nur Suhanawati Ashaari<sup>2</sup>, Dewi Selvia Fardhyanti<sup>3</sup>, Megawati<sup>3</sup> and Nadya Alfa Cahaya Imani<sup>3</sup>

<sup>1</sup>*School of Chemical Engineering, College of Engineering, Universiti Teknologi MARA, 40450 Shah Alam, Selangor, Malaysia*

<sup>2</sup>*Malaysia Genome and Vaccine Institute, National Institutes of Biotechnology Malaysia, Jalan Bangi, 43000 Kajang, Selangor, Malaysia*

<sup>3</sup>*Department of Chemical Engineering, Faculty of Engineering, Universitas Negeri Semarang, Gunungpati, 50229, Semarang, Indonesia*

### ABSTRACT

Complex coacervation is an encapsulation technique used to preserve the bio functionality of essential oils as well as provide controlled release. In this present work, encapsulation of *Citrus Hystrix* essential oil (CHEO) was formed by a complex coacervation technique with Gelatin-B (Gel B) and Chitosan (Chi) as the capping materials. The suitable encapsulation formulation was investigated as a function of pH and wall ratio using Zeta Potential analysis. Turbidity measurement and coacervate yield were carried out to confirm the suitable condition. Total Phenolic Content (TPC) was used to obtain the encapsulation efficiency (EE%) of the process. Results show that the suitable condition for coacervate

formation between Gel B and Chi ratio of 5:1 was at pH 5.8, which produced a high encapsulation efficiency of  $94.81\% \pm 2.60$ . FTIR analysis validates the formation of coacervate as well as the encapsulated CHEO. The encapsulates obtained were spherical and dominated by 194.557  $\mu\text{m}$  particles. The CHEO was successfully encapsulated by a complex coacervation method.

**Keywords:** Chitosan, coacervation, encapsulation efficiency, essential oils, gelatin, microencapsulation

### ARTICLE INFO

#### Article history:

Received: 18 February 2023

Accepted: 12 October 2023

Published: 14 March 2024

DOI: <https://doi.org/10.47836/pjst.32.2.07>

#### E-mail addresses:

[aisyahmurtadza@gmail.com](mailto:aisyahmurtadza@gmail.com) (Siti Afiqah 'Aisyah Murtadza)

[asyikin6760@uitm.edu.my](mailto:asyikin6760@uitm.edu.my) (Nurul Asyikin Md Zaki)

[junejai@uitm.edu.my](mailto:junejai@uitm.edu.my) (Junaidah Jai)

[fazlena@uitm.edu.my](mailto:fazlena@uitm.edu.my) (Fazlena Hamzah)

[suhana\\_bio@yahoo.com](mailto:suhana_bio@yahoo.com) (Nur Suhanawati Ashaari)

[dewiselvia@mail.unnes.ac.id](mailto:dewiselvia@mail.unnes.ac.id) (Dewi Selvia Fardhyanti)

[megawati@mail.unnes.ac.id](mailto:megawati@mail.unnes.ac.id) (Megawati)

[nadya.alfa@mail.unnes.ac.id](mailto:nadya.alfa@mail.unnes.ac.id) (Nadya Alfa Cahaya Imani)

\* Corresponding author

## INTRODUCTION

*Citrus Hystrix* essential oil (CHEO) has been extensively studied for its beneficial attributes as an antimicrobial (e.g., Sreepian et al., 2019; Srifuengfung et al., 2020) and antioxidant (Venkatachalam, 2019; Wijaya et al., 2017). However, like many other essential oils, its potential application is often limited by its high susceptibility to harsh and extreme environmental conditions (Adamiec et al., 2012). Therefore, encapsulation is a promising technique introduced to improve the stability of essential oils as well as provide controlled release. Encapsulation is a process where essential oils are polymeric coated within a capsule. Adamiec et al. (2012) previously encapsulated CHEO using konjac glucomannan and gum Arabic and reported the efficacy of the encapsulated CHEO in acting as an antibacterial comparable to the standard antibiotics.

Though many techniques could be employed to encapsulate, complex coacervation has been amongst the oldest and most widely used techniques to encapsulate as it offers advantages such as cost saving, simple processes and allows for industrial scalability with very high payloads up to 99% (Bakry et al., 2016; Timilsena et al., 2019). The complex coacervation technique makes use of the principle of separating a colloidal system into two phases: (1) the polymer-rich dense phase (coacervate) and (2) the poor polymer continuous phase (coacervation medium) (Yan & Zhang, 2014). Coacervation formation is induced by the interaction of two oppositely charged polymers, usually using a combination of protein and polysaccharides (Lakkis, 2016). This results in the deposition of wall materials around the core material. The gelatin-gum acacia system is a widely studied and understood coating system (Poshadri & Aparna, 2010). However, there is a need to explore other potential gelatin/polymer systems to further enhance the potential use of encapsulation systems using gelatin. The Latin-chitosan system has been considered a potential combination of polymeric systems encapsulating bioactive compounds. Their combinations have been well-studied for many applications. For example, in a recent study by Wang et al. (2023), their combination was used to stabilize lutein as printable edible inks for food application.

Gelatin is a protein containing many glycine, proline and 4-hydroxyproline residues (Fang & Bhandari, 2010). It can form complex coacervates with large amounts of anionic polymers for its excellent solubility, emulsifying activity, and gelling capability, making it the most commonly used protein for complex coacervation (Wang et al., 2018). Besides that, gelatin is cheap, readily available and possesses relatively low antigenicity compared to collagen. There are two types of commercialized gelatin: Type A gelatin and Type B gelatin, differentiated from its origin (Elzoghby, 2013).

Chitosan is a deacetylated chitin derivative and the second most widely used polysaccharide after cellulose (Vishwakarma et al., 2016). Polysaccharides have been of interest as encapsulating wall material since they can easily be abundant from many sources

(such as algal, microorganisms, plants, and animals) and are low-cost in processing (Yang et al., 2015). It is made up of  $\beta$ - (1 $\rightarrow$ 4) linked monosaccharide units of  $\beta$ -(1,4)-2- amino-2-deoxy-D-glucose. The positive charge of Chi is attributed to the free amino groups that allow for reaction with negatively charged surfaces and anionic polymers (Pedro et al., 2009). Parameters such as the degree of deacetylation (DD) and the molecular weight (MW) of Chi are very important as they could affect the functionality of the polymer (Pedro et al., 2009).

In order to design an optimized coacervation process, an understanding of the physicochemical factors involved in the coacervate formation is crucial. Although many kinds of literature have reported on the optimization of many polymeric systems to achieve a stable coacervate formation (e.g., Ghadermazi et al., 2019; Otálora et al., 2019; Timilsena et al., 2016), the different polymeric system exhibits distinct characteristics, thus, require different optimal parameters to induce coacervate formation. Though previous studies (e.g., Singh & Sheikh, 2022; Fan et al., 2023) have succeeded in encapsulating essential oils using gelatin and chitosan complexes, to our knowledge, no study has been reported on its application to encapsulate CHEO. Therefore, this study used gelatine type B (Gel-B) and chitosan (Chi) as wall materials to encapsulate CHEO through a complex coacervation technique. Since critical factors such as pH and mixing ratio have a great influence on the coacervate formation, the suitable condition was investigated through zeta potential, coacervate yield, and turbidity study. The combination of Gel-B and Chi as wall material should be able to improve the stability of CHEO as well as provide a controlled release to enhance its applications.

## METHODOLOGY

### Materials

*Citrus Hystrix* essential oil (CHEO) (pure essential oil) was purchased from BF1 (Malaysia). Gelatin-B (Gel-B) (type B, from bovine) was supplied from Halagel Sdn. Bhd. (Malaysia). Chitosan (Chi) (>80% deacetylation degree) was obtained from Nacalai Tesque (Japan). Oligomeric proanthocyanidins (OPCs), as a naturally occurring source of cross-linker, were derived from the outer shells of red grape seeds; also known as grape seed extracts (GSE-OPCs), contain approximately 98% of proanthocyanidin and was purchased from VitaHealth. Other chemicals used in this experiment were of analytical research grade. Sodium hydroxide (NaOH), Folin & Ciocalteu's Phenol Reagent (FC), and phosphate buffer pH 7 were purchased from R&M Chemicals. As for glacial acetic acid (CH<sub>3</sub>COOH), sodium carbonate and ethanol (95%, denatured) were obtained from Friendemann Schmidt, Bendosen, and System Chemicals, respectively. Deionized water (DI) was used throughout the experiment.

## Preparation of Stock Solutions

The preparation method of stock biopolymers was adapted from Aziz et al. (2016) with slight modifications. Both biopolymers were prepared at a concentration of 1% (w/v). An adequate amount of powdered Gel-B was first soaked in DI water for 30 minutes. The bloomed Gel-B solution was sealed and left stirring at 300 rpm with a temperature of 50°C for 1 hour. Chi flakes were weighted and dissolved in 1% (v/v) CH<sub>3</sub>COOH to prepare Chi solution. The Chi mixture was left stirring (500 rpm) at room temperature for at least 6 hours. Both biopolymer solutions were sonicated for 6 minutes to eliminate the gas bubbles (Dima et al., 2016).

## Zeta Potential of Individual Solution

Zeta potential values of the biopolymer solutions were determined using Zetasizer Nano Series (Malvern Instruments Ltd., Worcestershire, UK). Measurements were performed at pH values of 4, 4.4, 4.8, 5.0, 5.2, 5.4, 5.6, 5.8, and 6, as suggested by previous studies (Aziz et al., 2016; Prata & Grosso, 2015). The pH values were adjusted using an aqueous solution of NaOH (0.1 M) and CH<sub>3</sub>COOH (0.1 M). Dilution effects from pH adjustment were considered negligible. All measurements were performed in triplicate samples. Results were presented in millivolts (mV) units. A summary of the preparation process is illustrated in Figure 1.

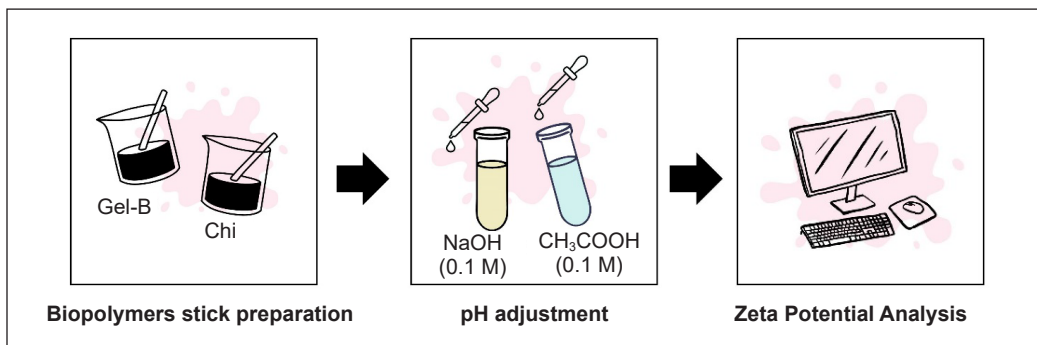


Figure 1. Illustration of the zeta potential measurement process flow

## Fourier Transform Infra-Red (FTIR)

In liquid form, FTIR spectra of Gel-B, Chi, and Gel-B/Chi coacervate (pH of 5.8) were obtained using a spectrophotometer FT-IR (Perkin Elmer Inc., Waltham, MA). FTIR spectra were recorded in transmittance (T) mode between 4000–515 cm<sup>-1</sup> in the wavelength range.

## Preparation of Biopolymers Mixture

Based on the zeta potential result, a mixture of biopolymers was prepared according to the determined ratio of 5:1 between Gel-B and Chi. The total biopolymer volume and concentration were fixed at 60 ml and 1% (w/v) to achieve optimum biopolymer ratios



(Gharanjig et al., 2020). The mixture was stirred for 20 mins at 300 rpm and a temperature of 50°C. Once a homogenized solution was obtained, 10 ml of the mixture was transferred into separate beakers. Then, the pH of the mixture was adjusted using an aqueous solution of NaOH (0.1 M) and CH<sub>3</sub>COOH (0.1 M) to obtain desired pH of 5.0, 5.2, 5.4, 5.6, 5.8 and 6. To ensure the biopolymers ratio was maintained, a different sample of the mixture was used for each pH value.

Dilution effects from pH adjustment were considered negligible. When the desired pH was obtained, the sample mixture was left stirring at 300 rpm and 50°C for 15 minutes to ensure the homogeneity of the solution. The best operating pH was selected for maximum coacervate formation using coacervate yield and turbidity analysis. For turbidity analysis, turbidity measurement was taken on each sample using UV-Vis (Agilent Technologies Cary 60 UV-Vis) at 600 nm (Kang et al., 2012). Distilled water was used as blank. Results were presented in absorbance value. The sample was centrifuged at 3000 rpm for 30 minutes to determine coacervate yield. The supernatant was decanted, and the sediment was left dried in an oven from 50°C to 60°C until the constant weight of the dry coacervate was achieved. A summary of the preparation process is illustrated in Figure 2. Coacervate yield (CY%) refers to the percentage of coacervate weight versus the total weight of biopolymers used to prepare the coacervate and was calculated as Equation 1:

$$CY\% = \frac{W_c}{W_{all}} \times 100\% \quad (1)$$

where  $W_c$  is the weight (g) of dry coacervate, and  $W_{all}$  is the weight (g) of the total biopolymers used to prepare the coacervate.

All measurements were performed in triplicate samples. FTIR, zeta potential analysis and visual evaluation were performed on each sample as described previously to better understand the coacervate formation.

## Encapsulation of CHEO

The overall process of encapsulating CHEO was carried out using the adapted method from Aziz et al. (2016) and Rungwasantisuk and Raibhu (2020). Before encapsulation, a stock of biopolymers was prepared as previously described. The encapsulation procedure was divided into eight steps. All necessary information, including sample preparation, equipment settings, and operating parameters, were summarized in Figure 3.

## Morphology Analysis of Encapsulates

The morphology of encapsulates in the suspension was revealed using an optical microscope (RZ-5, Meiji Techno, Japan) alongside a digital camera and registered under Image Pro Plus 4.0 software. The microscopic images were taken at 40× magnification.

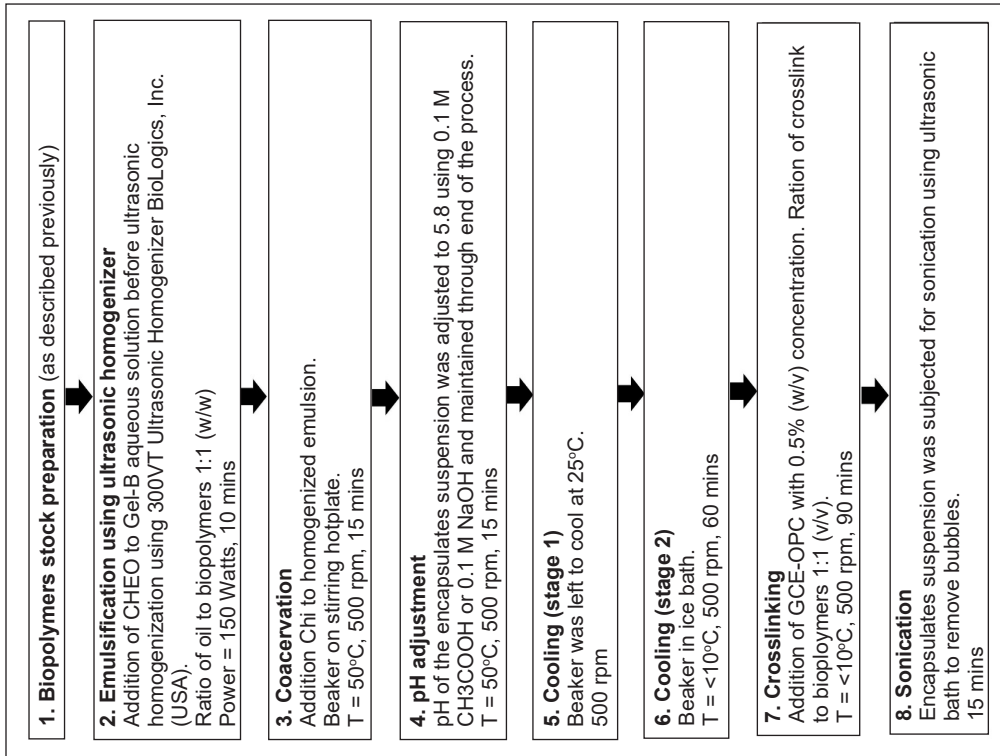


Figure 3. Procedure to encapsulate CHEO using Gel-B and Chi

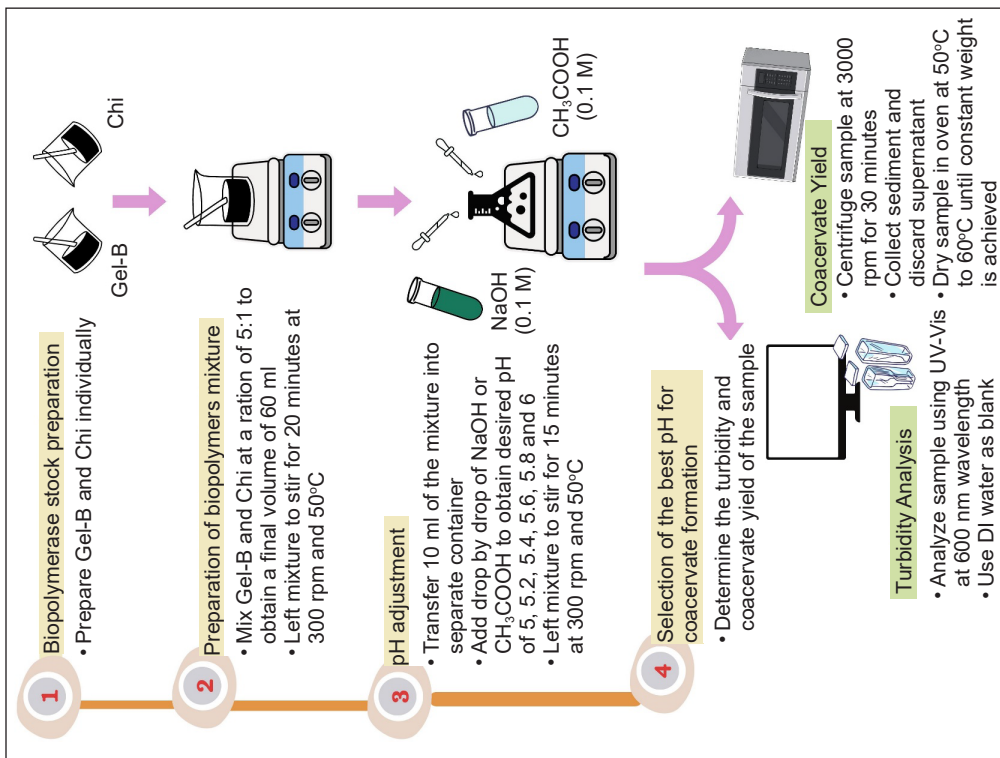


Figure 2. Illustration of the preparation of biopolymers mixture

## Particle Size Analysis

Determination of the encapsulate size in the suspension and particle size distribution were conducted using laser light scattering (Mastersizer 2000, Malvern Instruments Ltd., Worcestershire, UK) at 1 min, 2500 rpm. An appropriate portion of the wet encapsulates was added dropwise to the instrument's wet dispersing accessory. Triplicate samples were analyzed, and the mean volumetric diameter (D<sub>4,3</sub>) was reported.

## GCMS

Gas Chromatography–Mass Spectrometry (GCMS) analysis was conducted to identify the phenolic compounds and terpenoids present in the CHEO. The analysis was performed using an Agilent 7890 gas chromatograph model coupled to an Agilent 5975 quadrupole mass detector (Agilent Technologies, Santa Clara, CA, USA). The operating method was adopted by Ashaari et al. (2021). One microliter of CHEO was injected into the GC injection port with a 1:50 split mode and separated on an HP-5MS capillary column (30 m × 250 µm inner diameter × 0.25 µm film thickness). Helium was used as carrier gas with a flow rate set at 1 mL/min. The operation temperature was programmed at a rate of 10°C/min to increase the temperature gradually from 50°C to 280°C in 3 minutes. The electron-impact (EI) mode was used while operating the spectrometer with 70 eV ionization energy. The inlet/transfer line and ionization source temperatures were set at 280°C and 220°C, respectively. The volatile components of CHEO were identified through mass spectra comparison using MSD Chemstation Enhanced Data Analysis Software (E.02.02.1431 version, Agilent Technologies) and the National Institute of Standards and Technology library database (NIST 20).

## TPC Quantification

Total Phenolic Content (TPC) quantification of CHEO was carried out using the Folin-Ciocalteu method as described by Shetta et al. (2019) and Do et al. (2014) with slight modifications. 1 ml of CHEO (0.9203 g/ml) was added into 9 mL of ethanol and diluted 10x with DI water. Then, 1 mL of previously diluted CHEO mixture was mixed with 2.5 ml of freshly prepared FC reagent diluted in water (10% v/v). The solution was left for 3 minutes incubation at room temperature and in dark conditions. Then, 2.0 ml of Na<sub>2</sub>CO<sub>3</sub> (7.5% w/v) was added to the solution and mixed again. After 30 minutes of reaction time at ambient temperature (25°C) and in dark conditions, the absorbance of the sample was measured at 765 nm wavelength against blank using UV-Vis (Agilent Technologies Cary 60 UV-Vis). TPC of CHEO was determined as Gallic Acid Equivalents (GAE) by entering the absorbance value of CHEO extracted to the equation of the Gallic Acid standard curve that was initially prepared ( $y=0.12523x + 0.03961$ ;  $R^2=0.99870$ ). The result was used as a control to calculate the amount of CHEO for encapsulation efficiency. All measurements were performed in triplicate samples.

## Determination of Encapsulation Efficiency

This study determined the amount of unencapsulated CHEO by analyzing the excess CHEO available in the suspension after the encapsulation process. 5 ml of accurately measured homogenized encapsulated suspension was placed in a 15 ml tube. Then, 30 mL of ethanol was added into the tube to extract unencapsulated oil. The solution was then mixed up using a vortex mixture for 5 minutes at 1500 rpm (Fraj et al., 2021; Yu et al., 2017) to enhance the extraction of unencapsulated oil. After extraction, the dispersion was filtered using a Whatman #41 paper filter (Shi et al., 2018). The free (unencapsulated) oil filtrate was collected and evaluated for spectrophotometric quantification of total phenolic compounds using UV-Vis (Agilent Technologies Cary 60 UV-Vis) at 765 nm wavelength. All measurements were performed in triplicate samples. The encapsulation process efficiency (EE%) was calculated as Equation 2 (Girardi et al., 2017):

$$EE\% = \frac{W_0 - W_s}{W_0} \times 100\% \quad (2)$$

where EE% is the weight percentage of encapsulated CHEO in a certain amount of encapsulated suspension,  $W_s$  is the weight (g) of unencapsulated CHEO in a certain amount of encapsulated suspension, and  $W_0$  is the weight (g) of the CHEO used to prepare the same amount of encapsulates suspension.

## Statistical Analysis

All experiments were carried out at least three times under the same conditions. Results were presented as average with standard deviation values. Statistical analysis was performed using Microsoft Excel and IBM SPSS software. Determination of the statistical difference between groups and probability value of  $p < 0.05$  was specified with a one-way analysis of variance (ANOVA) using Post hoc Tukey's test.

## RESULTS AND DISCUSSION

### Analysis of Individual Biopolymer

Recently, determining the zeta potential of individual polymers has become an interest since it could help to reduce the number of assays needed to determine the pH range where interaction between polyelectrolytes possible to occur (e.g., Espinosa-Andrews et al., 2013; Gharanjig et al., 2020). Protein and polysaccharides usually carry a functional group that gives them either a positive or negative charge depending on the introduced pH.

Figure 4 presents the zeta potential of individual Gel-B and Chi at different pHs from 4.0 to 6.0. As can be observed from the Figure 4, all zeta potential values over the pH range tested for Chi are positive. It indicates that Chi is positively charged and could

function as a polycation in the pH range between 4.0 and 6.0. Chi naturally exhibits cationic properties in an acidic environment due to the protonation of amino groups, thus making it soluble in water (Aziz et al., 2016; Cheung et al., 2015). However, the zeta potential values are decreasing as the pH approaches 6.0. According to Espinosa-Andrews et al. (2013), this decreasing behavior occurred due to the loss of charge of the glucosamine segments and the reduction of any electrostatic screening effects. For Chi to become soluble in an aqueous form, the pH of the solution must

be less than its pKa (6.5) (Prata & Grosso, 2015), or otherwise, it will become insoluble, precipitates (Sogias et al., 2010) and manifests in the formation of a cloudy solution. Preliminary studies in this experiment have shown that at pH 6, the solution turns cloudy, and therefore, considering the solubility of Chi, the pH selected is limited to only 6 (Gonçalves et al., 2018).

On the other hand, the zeta potential values for Gel-B show positive values between pH 4 and 5 and negative values from pH 5.2 up to 6.0. Similar to the findings by Lv et al. (2012), in which Gel-B exhibits amphoteric characteristics. Typically, Gel-B is an anionic protein with an isoelectric point (pI) between pH 4.8–5 (Elzoghby, 2013). From the analysis of the result, we found that the pI of Gel-B was approximately at pH 5.1. At this pH, Gel-B exhibits a zero-charge density from shielding the carboxylic moieties by excess H<sup>+</sup> counterions (Espinosa-Andrews et al., 2013). In designing operating conditions for complex coacervation, it is important for protein and polysaccharide to have opposite charges to induce coacervate formation from the electrostatic interactions through carboxylate groups located on Gel-B and protonated amine/amide of Chi. Above the pI value, Gel-B will behave as an anionic protein through dissociation of the carboxylic groups ( $-\text{COOH} \rightarrow -\text{COO}^- + \text{H}^+$ ) and, hence, able to neutralize the protonated amine groups of cationic polysaccharides (Chi). Thus, in this study, pH 5.0, 5.2, 5.4, 5.6 and 6.0 were selected for further study.

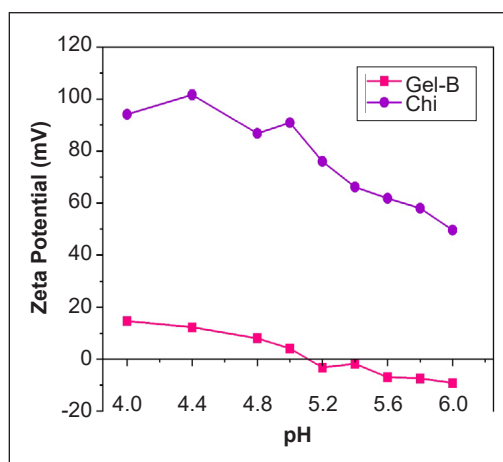


Figure 4. Zeta potential value for Gel (B) and Chitosan

### Determination of the Best pH and Wall Ratio for Complex Coacervates Formation

Optimizing a coacervate formation is a complex process as critical parameters such as pH and mixing ratio need to be individually optimized as they are interdependent (Yan & Zhang, 2014). The mixing ratio is an important factor for optimum coacervate formation as

it indicates the charge balance between the protein and polysaccharide involved (Kaushik et al., 2015) and determines the intensity of interaction and complexation (Eghbal & Choudhary, 2018). Timilsena et al. (2016) reported that an optimum coacervation was achieved at a mixing ratio of chia seed protein isolate (CPI) to chia seed gum (CSG) of 6:1 at an identified optimum pH of 2.7. Further increase of CPI in the mixing ratio at the same pH results in decreased coacervate yield. Increasing the ratio from its optimum proportion will cause one component to become deficient and another in excess (Timilsena et al., 2019). The excess polymer will not be able to react with soluble form in the equilibrium phase. Meanwhile, in a study by Gharanjig et al. (2020), the authors found that a decreasing pattern of pH optimum was observed as they increased the ratio of gum to gelatin. It indicates that pH influences coacervate formation, and a specific optimized mixing ratio at different pH exists. An optimum mixing ratio occurs when both polyelectrolytes are in equivalent amounts in which none of the polyelectrolytes are in excess. Therefore, zeta's potential evaluation should exhibit a charge of zero or almost near zero (Emamverdian et al., 2020).

The data from zeta potential values of individual polymers can be used to develop a mixing ratio between Gel-B and Chi (Prata & Grosso, 2015). Theoretically, if an anionic protein has a -5mV charge and a cationic polysaccharide carries a 25mV charge at pH titration of 5. Thus, it would be necessary to increase the use of protein 5 times to neutralize the positive charge of polysaccharides, whereas the mixing ratio for protein to polysaccharides would be 5:1.

Table 1 presents five possible mixing ratios of Gel-B:Chi; 24:1, 7:1, 36:1, 9:1, 8:1 and 5:1 that were developed by taking into account charge on both biopolymers. However, considering economic interest, only a mixing ratio of 5:1 was used for further analysis since this combination ratio used the least amount of biopolymers as the raw materials.

Table 1  
*Developing wall ratio from Gel (B) and Chi charge*

pH	Gel	Chi	Multiplier	Round off	Gel:Chi	
4	14.67 <sup>i</sup> ± 0.06	94.15 <sup>g</sup> ± 0.49	-	-	-	-
4.4	12.27 <sup>h</sup> ± 0.23	101.67 <sup>h</sup> ± 2.08	-	-	-	-
4.8	8.03 <sup>e</sup> ± 0.10	86.80 <sup>f</sup> ± 1.06	-	-	-	-
5	4.10 <sup>f</sup> ± 0.04	90.87 <sup>g</sup> ± 1.10	-	-	-	-
5.2	-3.23 <sup>d</sup> ± 0.03	76.03 <sup>e</sup> ± 0.78	-23.56	~24	24	1
5.4	-1.83 <sup>e</sup> ± 0.01	66.17 <sup>d</sup> ± 1.33	-36.16	~36	36	1
5.6	-6.94 <sup>c</sup> ± 0.07	61.83 <sup>c</sup> ± 0.86	-8.91	~9	9	1
5.8	-7.45 <sup>b</sup> ± 0.27	58.00 <sup>b</sup> ± 0.56	-7.78	~8	8	1
6	-9.18 <sup>a</sup> ± 0.11	49.60 <sup>a</sup> ± 1.08	-5.41	~5	5	1

*Note.* The superscript alphabet denotes the statistically significant difference between groups ( $p < 0.05$ ) for each column. The level of significance is determined by alphabetical order. Groups with the same alphabet indicate no statistical difference between groups.

The interaction between two biopolymers can become evident in several ways: (1) small soluble complexes (SC) are formed by manifesting themselves in murky solutions, and (2) depending on interaction; if the interaction is weak, a homogeneous weak gel is formed, but if the interaction is strong, precipitation of both biopolymers will occur (Espinosa-Andrews et al., 2013). Many literatures (e.g., Kaushik et al., 2015; Lv et al., 2013; Shinde & Nagarsenker, 2009) have reported on different evaluation methods used to validate the formation of this precipitate or coacervate. Common methods include turbidity/visual appearance, coacervate yield, and zeta potential analysis. Turbidity is related to the concentration of the polyelectrolyte solutions and their molecular weight (Meka et al., 2017). The coacervate formation will reduce the transparency of the biopolymer mixture, causing a higher absorbance value (Kang et al., 2012). Meanwhile, the use of zeta potential or electrophoretic mobility to predict the extent of coacervate formation has been explained by Burgess and Carless (1984).

Sometimes, observing more than one method to validate each parameter is compulsory. For instance, one should consider the relationship between the absorbance increase and insolubility in justifying turbidity measurement alone. In some cases, like a study by Prata and Grosso (2015), they found that the turbidity of a system with a pH greater than 6.5 represents the insolubility of the Chi rather than the formation of complexes owing to a large number of reactive groups in Chi. Though significant electrostatic interaction that initiates complex coacervation is induced from the large charges on the polyelectrolytes, charges that are too large will cause precipitation (Aziz et al., 2016).

The coacervate yield and absorbance value of coacervate formation over a range of pH tests are presented in Figure 5. As can be seen from the Figure 5, both dependent variables showed a similar pattern, validating each other responses towards pH variables that were being tested in the experiment. As demonstrated by one-way ANOVA, a statistically significant difference was observed in both dependent variables: coacervate yield ( $F(5,12)=61.229, p=0.001$ ) and absorbance ( $F(5,12)=91.865, p=0.001$ ) illustrating legitimate pH effects towards both dependent variables tested. However, in both dependent variables, a statistically significant difference was more prominent at lower pH ranges as compared to higher pH ranges. This statistical evidence also implied the need to observe at least two validating parameters, as mentioned before, since the coacervate yield and absorbance value were unlikely to be statistically significant toward pH values at higher pH tests.

In particular, the coacervate yield and absorbance values were highest at pH 5.8 compared to other pH ranges, indicating the highest coacervate formation occurred at this pH. Therefore, this pH should be maintained to achieve an optimum coacervate formation for a mixing ratio 5:1 between Gel-B/Chi. A quite similar finding was also reported by Kang et al. (2012) when encapsulating using a combination of Gel-B and Chi. Though the study indicated that the best mixing ratio and pH for Gel-B and Chi are 15:1 (w:w)

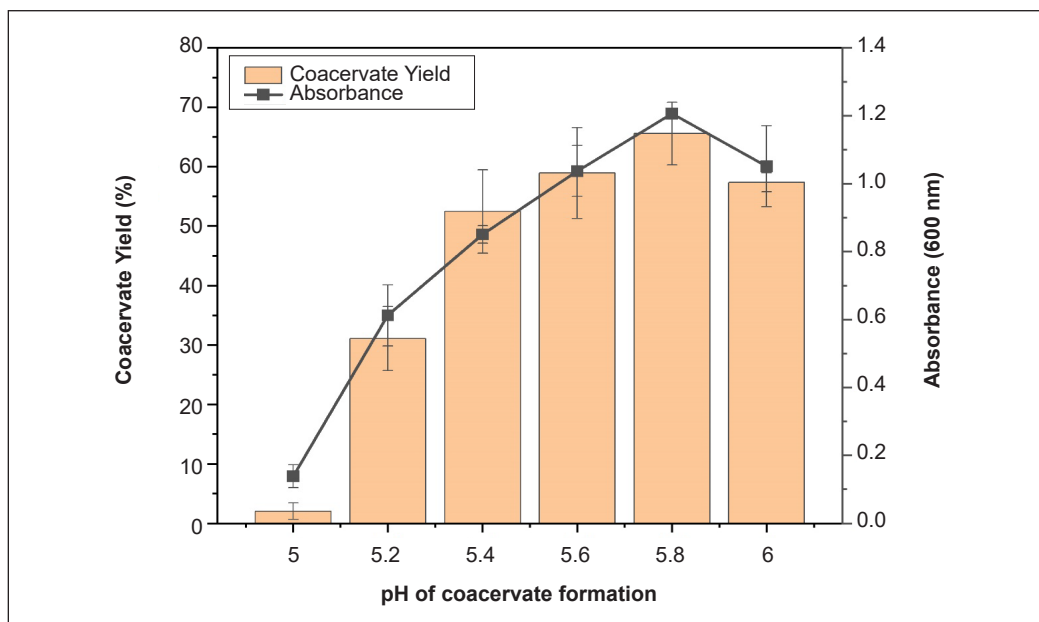


Figure 5. Absorbance value for Gel (B)-Chi (5:1) mixture (Alphabet is used to denote the statistically significant difference between groups ( $p < 0.05$ ). Given coacervate yield: pH 5.0<sup>a</sup>, 5.2<sup>b</sup>, 5.4<sup>c</sup>, 5.6<sup>c</sup>, 5.8<sup>c</sup>, 6.0<sup>c</sup>; absorbance: pH 5.0<sup>a</sup>, 5.2<sup>b</sup>, 5.4<sup>c</sup>, 5.6<sup>cd</sup>, 5.8<sup>d</sup>, 6.0<sup>d</sup>. Level of significant is determined by alphabetical order. Groups with the same alphabet indicates no statistical difference between groups)

and 6.0, respectively, the actual ratio between glucosamine residue of Chi and acidic amino acid residue of Gel-B was calculated to be roughly 1:5. Another study reported by Espinosa-Andrews et al., (2013) has shown that a shift towards a higher optimum pH ( $> 5$ ) was observed when a smaller ratio between Gum Arabic and Chi was used; [5.5:1], [3:1], [1:1], meaning when Chi as polycation was in excess, optimum pH is more likely to be achieved at higher pH value.

It also explained the unlikely statistically significant difference of coacervate formation observed in our study at higher pH values tested. A good justification for this observation is that when the basicity of the system increases, the absolute charge density of Chi decreases but remains in the positive region. At the same time, the zeta potential of Gel-B achieves a maximum degree of ionization, as seen in Figure 4. Therefore, the zeta potentials of Chi and Gel-B become almost equivalent, rendering a complex with almost no/near to zero residue charge. A zero or near-to-zero residue charge of the complex would reduce electrostatic repulsions between particles and colloidal stability of the system, causing precipitates and, hence, resulting in maximum turbidity and coacervate yield.

Meanwhile, Figure 6 shows the behavior of charge density and the visual appearance of the coacervate. Two significant pieces of information should be observed. First, all coacervates exhibit a positive charge density value regardless of pH. The inference derived was an excess of Chi (Prata & Grosso, 2015) as polycations in the system. As observed



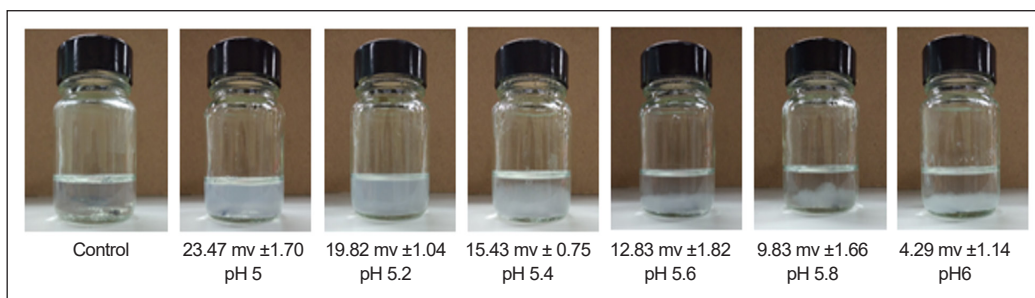


Figure 6. Visual evaluation and zeta potential of Gel (B)-Chi mixture

in Figure 4, Chi exhibits a larger absolute charge density than Gel-B; thus, more Gel-B is needed to neutralize the positive charge of Chi. However, this mixing ratio might not be the ideal for Gel-B and Chi used in this study. Second, the charge density of coacervate showed a decreasing pattern when the pH was increased. As discussed previously, this observation agrees with the absorbance and coacervate yield result. More coacervate was formed when the pH was increased, but at pH 6.0, the reduction observed was contributed by the influence of the alkali addition, which tends to neutralize the negatively charged group of the Chi (Prata & Grosso, 2015). In a study by Silva and Andrade (2009), the author also found a significant reduction in turbidity for all combinations of Gel-B and Chi systems studied at pH 6.0.

As evidence, analysis of individual polymers showed the carboxylate groups located on proteins and protonated amine/amide of the polysaccharides (Gharanjig et al., 2020). The negative charge of proteins is associated with the presence of carboxylate groups. Figure 7 shows the FTIR spectrums related to Gel-B, Chi, and their complex coacervate analyzed at pH 5.8. As shown in Figure 7, the three spectrums showed an overall similar pattern with two significant peaks. A wide, strong peak was observed at wavelength  $3308.61\text{ cm}^{-1}$  and  $3337.03\text{ cm}^{-1}$  for Gel-B and Chi, respectively. These peaks correspond to normal polymeric O-H stretching vibrations and N-H stretching of amines and amides. Characteristic peaks of Chi were due to the stretching and bending from O-H groups of the pyranose ring and the stretching vibration of N-H functional groups of the primary amine in Chi's backbone (Roy et al., 2018). Meanwhile, short, weak peaks at  $1635.24\text{ cm}^{-1}$  for Gel-B and  $1636.13\text{ cm}^{-1}$  for Chi result from the N-H bending of amines and the C-O stretching of amides.

The formation of coacervates between Gel-B and Chi was evidenced by a slight change in the coacervate spectrum, suggesting that the functional groups of coacervate underwent substantial alteration. A shift towards a lower wavelength range was due to the formation of hydrogen bonds between Chi and Gel-B molecules. Notably, the resultant coacervate spectrum exhibits slightly lower absorption strength at around  $3207.91\text{ cm}^{-1}$  compared to native biopolymers alone due to interaction between the C=O group of Gel-B and the N-H groups of Chi. As stated before, the formation of complex coacervate between Gel-B

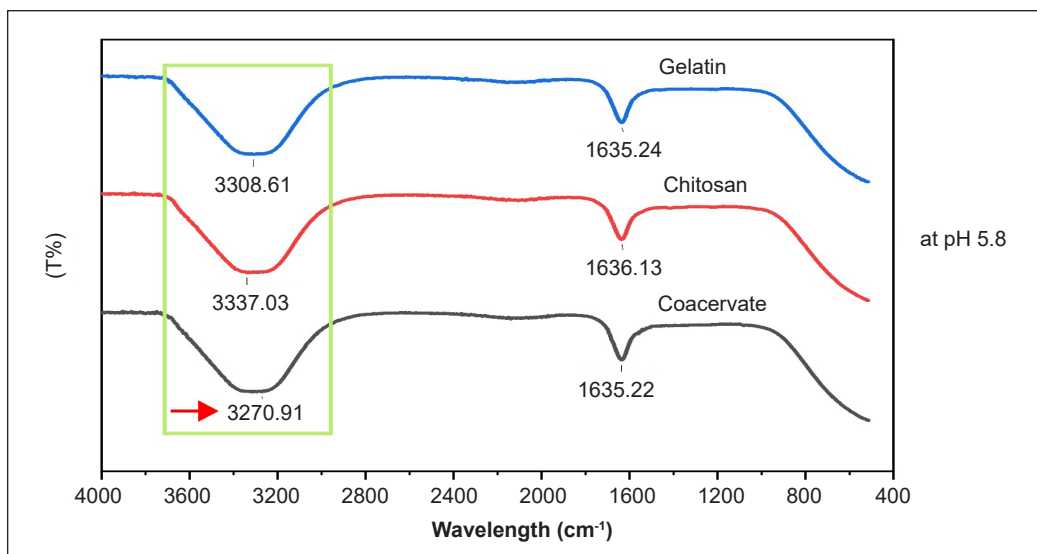


Figure 7. FTIR spectrums related to Gel-B, Chi and their complex coacervate at pH 5.8

and Chi was driven by the electrostatic interactions through carboxylate groups located on Gel-B and protonated amine/amide of Chi.

### Characterization of CHEO

Analysis of the TPC in the CHEO used in this study confirmed the presence of CHEO contains almost  $2.01 \pm 0.02$  mg of GAE/g of oil. The TPC value obtained was expected to be lowered compared to findings from Wijaya et al. (2017) and Houg et al. (2023) since CHEO used in this study was simply purchased from available commercialized CHEO. Some susceptible phenolic compounds might have been lost throughout the extraction and manufacturing processes. Deterioration of the compounds or volatile loss is likely to occur owing to the high temperature and long duration of the extraction procedures (Phong et al., 2022). Besides, different amounts and variation types of active constituents found in CHEO are due to various factors such as the method of extraction (Wijaya et al., 2017) and agroclimatic influences such as seasonal, geographical, or climatical of the location where CHEO was obtained (Ahmed et al., 2019).

From the analysis of GCMS data, 102 chemical compounds were identified in CHEO and used in this experiment. Such compounds would include Isopropyl myristate (41.3399%), Isopropyl palmitate (26.5571%), D-Limonene (4.6678%), Polypropylene glycol (4.2105%), Solvanol (3.4694%), Hexylcinnamaldehyde (2.6428%), d-Camphor (2.5863%), Palmitic acid (2.3143%), Myristic acid (1.8121%), Dipropylene glycol (1.4956%) and other compounds that make up less than 1% of the total composition of CHEO (Table 2).

Based on the result, it can be concluded that some of the major compounds typically presented in CHEO (Lubinska-Szczygeł et al., 2018; Othman et al., 2016) that belong to the terpenes were detected such as D-Limonene, linalool,  $\alpha$ -Terpinol, L- $\beta$ -Pinene, L-4-terpineol, d- $\alpha$ -Pinene, Terpinolene, Citronellol,  $\beta$ -mircene, Camphene, Citronellyl palmitoleate,  $\alpha$ -Sabinene,  $\beta$ -Copaene and citronellal. The bio functionalities of CHEO as an antimicrobial and antioxidant are mainly contributed by the synergistic effects between these active constituents present in CHEO (Qin et al., 2018). Ensuring these active constituents are successfully entrapped should be a primary concern when encapsulating CHEO.

Table 2  
*List of chemical constituents present in CHEO*

RT	Compound	%
15.9973	Isopropyl myristate	41.3399
17.9849	Isopropyl palmitate	26.5571
5.7856	D-Limonene	4.6678
6.6560	Polypropylene glycol	4.2105
13.6688	Solvanol	3.4694
15.3067	Hexylcinnamaldehyde	2.6428
7.5516	d-Camphor	2.5863
18.0257	Palmitic acid	2.3143
16.1052	Myristic acid	1.8121
5.9371	Dipropylene glycol	1.4956

### Encapsulation Efficiency

One of the important parameters to evaluate the performance of an encapsulation process is calculating the encapsulation efficiency (EE) value. Encapsulation efficiency (EE) is the percentage of essential oil successfully entrapped within the wall material over the essential oil introduced at the beginning of the process (De Matos et al., 2018). Previous studies (e.g., Hussein et al., 2016; Rosli et al., 2018) have shown that Total Phenolic Content (TPC) can be used to calculate EE for essential oil encapsulation. This experiment achieved a high EE value at almost  $94.81\% \pm 2.60$ . This result is expected as, according to Timilsena et al. (2019), complex coacervation provides a high EE value of up to almost 99%. Other studies by Manaf et al. (2018) and Mousavi et al. (2021) also reported high EE values at around 94% and 87% when using Gel-B and Chi as their capping material. A high percentage of encapsulation efficiency indicates that less CHEO is present on the surface of encapsulates or not encapsulated in the process. It also implies that the encapsulation process was conducted successfully, and that Gel-B and Chi can be used as the perfect combination of wall materials to encapsulate CHEO.

### Physical Properties of Encapsulates

Generally, the types and structure of encapsulates produced are influenced by the wall materials used and the encapsulation condition and method (Bakry et al., 2016). Different characteristics in terms of morphology and size of encapsulates can be obtained by manipulating chemical, physical, and condition parameters throughout the

encapsulation process (Aziz et al., 2015; Aziz et al., 2014). Figure 8 shows the image of encapsulates under observation using an optical microscope at 40× magnification. It can be seen from the Figure 8 that the encapsulates produced were spherical, mononucleated, and a single core with a definite wall (Fang & Bhandari, 2010), as indicated in the red circles. This finding was also in line with encapsulates produced in a study by Oliveira et al. (2019), who observed encapsulates with mononuclear structures when encapsulating pequin oil with gelatin and gum Arabic using complex coacervation. However, this result was in contrast with the findings from Raksa et al. (2017).

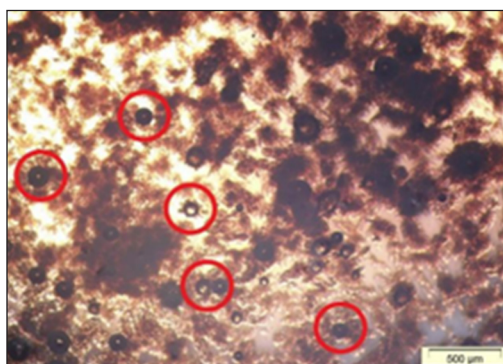


Figure 8. Optical microscopic image of wet encapsulates prior encapsulation process taken at 40× magnification (Red circles indicate individual wet encapsulates produced in the suspension)

In the study, the authors observed encapsulates with spherical and matrix-type structures in which loading of CHEO presented as small spherical particles inside the encapsulate. The formation of a matrix type or multicore encapsulates is caused by the aggregation of many single-core encapsulates and could be seen in encapsulation using the coacervation process (Dong et al., 2007; Wang et al., 2014). Meanwhile, in the encapsulation process, which involves thermal treatment such as spray drying, the formation of a multicore structure might be caused by the outward movement of a small amount of volatilized EOs that are later embedded inside the crust wall (Adamiciec et al., 2012) or stays on the surface (Ngamekaue & Chitprasert, 2019). As found in our study, the formation of mononucleated structure encapsulates could be due to the homogenization step involved during the emulsification process.

Lemetter et al. (2009) investigated the effect of shear rate on the formation of encapsulates and discovered that as the rotation speed increased, more mononucleated encapsulates were detected. It is also interesting to note that most encapsulates in this study were well dispersed as individuals in the suspension with less agglomeration as compared to encapsulates produced by Aziz et al. (2016). The author obtained the final products of encapsulates clustered together, forming agglomerates, and justified that excess Gel-B or the wall materials that underwent phase changes from liquid to solid were likely to go through a sticky stage, making it difficult to avoid agglomeration. Meanwhile, Prata and Grosso (2015) inferred that unencapsulated oil on the encapsulated surface would, over time, promote encapsulates to attach and form agglomerates.

However, less agglomeration observed in our study could be due to less polymer concentration used in the coacervation process than Aziz et al. (2016). While Burgess and

Carless (1985) justified the reduction in coacervate formation was due to the increment in the polymer concentration, Oliveira et al. (2019) used this justification to explain the formation of agglomeration when investigating the effect of concentration on the morphology of encapsulates produced. It is inferred that as the concentration of polymers increases, the neighboring molecules are induced to neutralize each other through coulombic attraction, forming a large, stable gel-type network fortified by hydrogen bonding.

The size distribution of encapsulates is shown in Figure 9. As can be seen, a monomodal distribution was observed in which the largest particle size,  $d(0.9)$  of 194.557  $\mu\text{m}$ , was dominating. The encapsulates were also characterized by a mean size diameter  $d(4,3)$  of 108.395  $\mu\text{m}$ . The size range is within an acceptable range of microparticles produced from the complex coacervation process, which is between 0.1–500  $\mu\text{m}$  (Comunian & Favaro-Trindade, 2016), suggesting that the encapsulation technique employed in this study successfully produced microencapsulates. The width of distribution (span) was considered small (2.398) owing to the mononucleated structure and homogenization process preventing multicore encapsulation formation through aggregation.

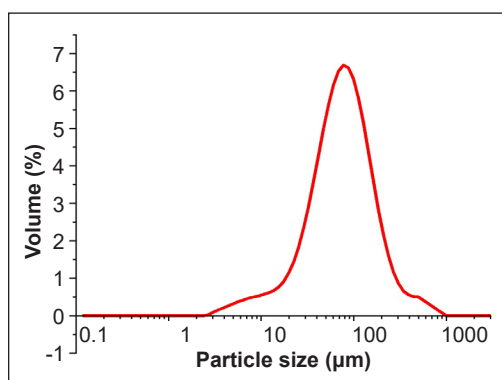


Figure 9. Size distribution of wet encapsulates

## CONCLUSION

In the present study, CHEO encapsulates were successfully produced and characterized through complex coacervation. Gel-B and Chi were excellent wall materials to encapsulate CHEO at 5:1 and pH 5.8 mixing ratios. FTIR analysis confirmed the formation of coacervates between Gel-B and Chi. These operating conditions obtained a high EE value at almost  $94.81\% \pm 2.60$ . Characterization of CHEO used in this study revealed the presence of phenolic compounds at  $2.01 \pm 0.02$  mg of GAE/g of oil. From GCMS data analysis, major compounds presented in the CHEO belong to the terpenes group. The encapsulates produced were spherical with a mononucleated structure and had a particle size within the microcapsule range between 23.270  $\mu\text{m}$  and 194.557  $\mu\text{m}$ .

## ACKNOWLEDGEMENTS

This work was funded by Malaysia's Ministry of Education (MOE) Fundamental Research Grant Scheme (FRGS) through a 600-RMI/FRGS/5/3 (186/2019) grant. We are very grateful for the assistance provided by all parties in assisting the research activities.

## REFERENCES

- Adamiec, J., Borompichaichartkul, C., Srzednicki, G., Panket, W., Piriyaunsakul, S., & Zhao, J. (2012). Microencapsulation of kaffir lime oil and its functional properties. *Drying Technology*, 30(9), 914-920. <https://doi.org/10.1080/07373937.2012.666777>
- Ahmed, A. F., Attia, F. A. K., Liu, Z., Li, C., Wei, J., & Kang, W. (2019). Antioxidant activity and total phenolic content of essential oils and extracts of sweet basil (*Ocimum basilicum* L.) plants. *Food Science and Human Wellness*, 8(3), 299-305. <https://doi.org/10.1016/j.fshw.2019.07.004>
- Ashaari, N. S., Mohamad, N. E., Afzinizam, A. H., Rahim, M. H. A., Lai, K. S., & Abdullah, J. O. (2021). Chemical composition of hexane-extracted plectranthus amboinicus leaf essential oil: Maximizing contents on harvested plant materials. *Applied Sciences*, 11(22), Article 10838. <https://doi.org/10.3390/app112210838>
- Aziz, F. R. A., Jai, J., Raslan, R., & Subuki, I. (2015). Microencapsulation of essential oils application in textile: A review. *Advanced Materials Research*, 1113, 346-351. <https://doi.org/10.4028/www.scientific.net/amr.1113.346>
- Aziz, F. R. A., Jai, J., Raslan, R., & Subuki, I. (2016). Microencapsulation of citronella oil by complex coacervation using chitosan-gelatin (b) system: Operating design, preparation and characterization. *MATEC Web of Conferences*, 69, Article 04002. <https://doi.org/10.1051/mateconf/20166904002>
- Aziz, S., Gill, J., Dutilleul, P., Neufeld, R., & Kermasha, S. (2014). Microencapsulation of krill oil using complex coacervation. *Journal of Microencapsulation*, 31(8), 774-784. <https://doi.org/10.3109/02652048.2014.932028>
- Bakry, A. M., Abbas, S., Ali, B., Majeed, H., Abouelwafa, M. Y., Mousa, A., & Liang, L. (2016). Microencapsulation of oils: A comprehensive review of benefits, techniques, and applications. *Comprehensive Reviews in Food Science and Food Safety*, 15(1), 143-182. <https://doi.org/10.1111/1541-4337.12179>
- Burgess, D. J., & Carless, J. E. (1984). Microelectrophoretic studies of gelatin and acacia for the prediction of complex coacervation. *Journal of Colloid and Interface Science*, 98(1), 1-8. [https://doi.org/10.1016/0021-9797\(84\)90472-7](https://doi.org/10.1016/0021-9797(84)90472-7)
- Burgess, D. J., & Carless, J. E. (1985). Manufacture of gelatin/gelatin coacervate microcapsules. *International Journal of Pharmaceutics*, 27(1), 61-70. [https://doi.org/10.1016/0378-5173\(85\)90185-1](https://doi.org/10.1016/0378-5173(85)90185-1)
- Cheung, R. C. F., Ng, T. B., Wong, J. H., & Chan, W. Y. (2015). Chitosan: An update on potential biomedical and pharmaceutical applications. *Marine Drugs*, 13(8), 5156-5186. <https://doi.org/10.3390/md13085156>
- Comunian, T. A., & Favaro-Trindade, C. S. (2016). Microencapsulation using biopolymers as an alternative to produce food enhanced with phytosterols and omega-3 fatty acids: A review. *Food Hydrocolloids*, 61, 442-457. <https://doi.org/10.1016/j.foodhyd.2016.06.003>
- De Matos, E. F., Scopel, B. S., & Dettmer, A. (2018). Citronella essential oil microencapsulation by complex coacervation with leather waste gelatin and sodium alginate. *Journal of Environmental Chemical Engineering*, 6(2), 1989-1994. <https://doi.org/10.1016/j.jece.2018.03.002>

- Dima, C., Pătrașcu, L., Cantaragiu, A., Alexe, P., & Dima, Ș. (2016). The kinetics of the swelling process and the release mechanisms of *Coriandrum sativum* L. essential oil from chitosan/alginate/inulin microcapsules. *Food Chemistry*, *195*, 39-48. <https://doi.org/10.1016/j.foodchem.2015.05.044>
- Do, Q. D., Angkawijaya, A. E., Tran-Nguyen, P. L., Huynh, L. H., Soetaredjo, F. E., Ismadji, S., & Ju, Y. H. (2014). Effect of extraction solvent on total phenol content, total flavonoid content, and antioxidant activity of *Limnophila aromatica*. *Journal of Food and Drug Analysis*, *22*(3), 296-302. <https://doi.org/10.1016/j.jfda.2013.11.001>
- Dong, Z. J., Touré, A., Jia, C. S., Zhang, X. M., & Xu, S. Y. (2007). Effect of processing parameters on the formation of spherical multinuclear microcapsules encapsulating peppermint oil by coacervation. *Journal of Microencapsulation*, *24*(7), 634-646. <https://doi.org/10.1080/02652040701500632>
- Eghbal, N., & Choudhary, R. (2018). Complex coacervation: Encapsulation and controlled release of active agents in food systems. *LWT*, *90*, 254-264. <https://doi.org/10.1016/j.lwt.2017.12.036>
- Elzoghby, A. O. (2013). Gelatin-based nanoparticles as drug and gene delivery systems: Reviewing three decades of research. *Journal of Controlled Release*, *172*(3), 1075-1091. <https://doi.org/10.1016/j.jconrel.2013.09.019>
- Emamverdian, P., Moghaddas Kia, E., Ghanbarzadeh, B., & Ghasempour, Z. (2020). Characterization and optimization of complex coacervation between soluble fraction of Persian gum and gelatin. *Colloids and Surfaces A: Physicochemical and Engineering Aspects*, *607*, Article 125436. <https://doi.org/10.1016/j.colsurfa.2020.125436>
- Espinosa-Andrews, H., Enríquez-Ramírez, K. E., García-Márquez, E., Ramírez-Santiago, C., Lobato-calleros, C., & Vernon-Carter, J. (2013). Interrelationship between the zeta potential and viscoelastic properties in coacervates complexes. *Carbohydrate Polymers*, *95*(1), 161-166. <https://doi.org/10.1016/j.carbpol.2013.02.053>
- Fan, S., Wang, D., Wen, X., Li, X., Fang, F., Richel, A., Xiao, N., Fauconnier, M., Hou, C., & Zhang, D. (2023). Incorporation of cinnamon essential oil-loaded pickering emulsion for improving antimicrobial properties and control release of chitosan/gelatin films. *Food Hydrocolloids*, *138*, Article 108438. <https://doi.org/10.1016/j.foodhyd.2022.108438>
- Fang, Z., & Bhandari, B. (2010). Encapsulation of polyphenols - A review. *Trends in Food Science and Technology*, *21*(10), 510-523. <https://doi.org/10.1016/j.tifs.2010.08.003>
- Fraj, J., Petrović, L., Đekić, L., Budinčić, J. M., Bučko, S., & Katona, J. (2021). Encapsulation and release of vitamin C in double W/O/W emulsions followed by complex coacervation in gelatin-sodium caseinate system. *Journal of Food Engineering*, *292*, Article 110353. <https://doi.org/10.1016/j.jfoodeng.2020.110353>
- Ghadermazi, R., Asl, A. K., & Tamjidi, F. (2019). Optimization of whey protein isolate-quince seed mucilage complex coacervation. *International Journal of Biological Macromolecules*, *131*, 368-377. <https://doi.org/10.1016/j.ijbiomac.2019.03.026>
- Gharanjig, H., Gharanjig, K., Hosseinezhad, M., & Jafari, S. M. (2020). Development and optimization of complex coacervates based on zedo gum, cress seed gum and gelatin. *International Journal of Biological Macromolecules*, *148*, 31-40. <https://doi.org/10.1016/j.ijbiomac.2020.01.115>

- Girardi, N. S., García, D., Passone, M. A., Nesci, A., & Etcheverry, M. (2017). Microencapsulation of *Lippia turbinata* essential oil and its impact on peanut seed quality preservation. *International Biodeterioration and Biodegradation*, *116*, 227-233. <https://doi.org/10.1016/j.ibiod.2016.11.003>
- Gonçalves, N. D., Grosso, C. R. F., Rabelo, R. S., Hubinger, M. D., & Prata, A. S. (2018). Comparison of microparticles produced with combinations of gelatin, chitosan and gum Arabic. *Carbohydrate Polymers*, *196*, 427-432. <https://doi.org/10.1016/j.carbpol.2018.05.027>
- Houng, P., Ly, K., & Lay, S. (2023). Valorization of kaffir lime peel through extraction of essential oil and process optimization for phenolic compounds. *Journal of Chemical Technology & Biotechnology*, *98*(11), 2745-2753. <https://doi.org/10.1002/jctb.7354>
- Hussein, A. M. S., Lotfy, S. N., Kamil, M. M., & Hassan, M. E. (2016). Effect of microencapsulation on chemical composition and antioxidant activity of cumin and fennel essential oils. *Research Journal of Pharmaceutical, Biological and Chemical Sciences*, *7*(3), 1565-1574.
- Kang, M. K., Dai, J., & Kim, J. C. (2012). Ethylcellulose microparticles containing chitosan and gelatin: pH-dependent release caused by complex coacervation. *Journal of Industrial and Engineering Chemistry*, *18*(1), 355-359. <https://doi.org/10.1016/j.jiec.2011.11.099>
- Kaushik, P., Dowling, K., Barrow, C. J., & Adhikari, B. (2015). Complex coacervation between flaxseed protein isolate and flaxseed gum. *Food Research International*, *72*, 91-97. <https://doi.org/10.1016/j.foodres.2015.03.046>
- Lakkis, J. M. (2016). *Encapsulation and controlled release technologies in food systems*. John Wiley & Sons. <https://doi.org/10.1002/9781118946893>
- Lemetter, C. Y. G., Meeuse, F. M., & Zuidam, N. J. (2009). Control of the morphology and the size of complex coacervate microcapsules during scale-up. *AIChE Journal*, *55*(6), 1487-1496. <https://doi.org/10.1002/aic.11816>
- Lubinska-Szczygeł, M., Różańska, A., Dymerski, T., Namieśnik, J., Katrich, E., & Gorinstein, S. (2018). A novel analytical approach in the assessment of unprocessed kaffir lime peel and pulp as potential raw materials for cosmetic applications. *Industrial Crops and Products*, *120*, 313-321. <https://doi.org/10.1016/j.indcrop.2018.04.036>
- Lv, Y., Zhang, X., Abbas, S., & Karangwa, E. (2012). Simplified optimization for microcapsule preparation by complex coacervation based on the correlation between coacervates and the corresponding microcapsule. *Journal of Food Engineering*, *111*(2), 225-233. <https://doi.org/10.1016/j.jfoodeng.2012.02.030>
- Lv, Y., Zhang, X., Zhang, H., Abbas, S., & Karangwa, E. (2013). The study of pH-dependent complexation between gelatin and gum arabic by morphology evolution and conformational transition. *Food Hydrocolloids*, *30*(1), 323-332. <https://doi.org/10.1016/j.foodhyd.2012.06.007>
- Manaf, M. A., Subuki, I., Jai, J., Raslan, R., & Mustapa, A. N. (2018, May). Encapsulation of volatile citronella essential oil by coacervation: Efficiency and release study. In *IOP Conference Series: Materials Science and Engineering* (Vol. 358, p. 012072). IOP Publishing. <https://doi.org/10.1088/1757-899X/358/1/012072>



- Meka, V. S., Sing, M. K. G., Pichika, M. R., Nali, S. R., Kolapalli, V. R. M., & Kesharwani, P. (2017). A comprehensive review on polyelectrolyte complexes. *Drug Discovery Today*, 22(11), 1697-1706. <https://doi.org/10.1016/j.drudis.2017.06.008>
- Mousavi, M. M., Torbati, M., Farshi, P., Hosseini, H., Mohammadi, M. A., Hosseini, S. M., & Hosseinzadeh, S. (2021). Evaluation of design and fabrication of food-grade nanofibers from chitosan-gelatin for nanoencapsulation of stigmasterol using the electrospinning method. *Advanced Pharmaceutical Bulletin*, 11(3), 514-521. <https://doi.org/10.34172/apb.2021.059>
- Ngamekaue, N., & Chitprasert, P. (2019). Effects of beeswax-carboxymethyl cellulose composite coating on shelf-life stability and intestinal delivery of holy basil essential oil-loaded gelatin microcapsules. *International Journal of Biological Macromolecules*, 135, 1088-1097. <https://doi.org/10.1016/j.ijbiomac.2019.06.002>
- Oliveira, W. Q., Araújo, A. W. O., Wurlitzer, N. J., & Maria, S. R. (2019). Effect of the reaction volume on the formation of microparticles of the pequi (*Caryocar coriaceum* Wittm.) oil by complex coacervation. *Chemical Engineering Transactions*, 74, 445-450. <https://doi.org/10.3303/CET1974075>
- Otálora, M. C., Castaño, J. A. G., & Wilches-Torres, A. (2019). Preparation, study and characterization of complex coacervates formed between gelatin and cactus mucilage extracted from cladodes of *Opuntia ficus-indica*. *LWT*, 112, Article 108234. <https://doi.org/10.1016/j.lwt.2019.06.001>
- Othman, S. N. A. M., Hassan, M. A., Nahar, L., Basar, N., Jamil, S., Sarker, S., Othman, S. M., Hassan, M. A., Nahar, L., Basar, N., Jamil, S., & Sarker, S. (2016). Essential oils from the Malaysian citrus (Rutaceae) medicinal plants. *Medicines*, 3(2), Article 13. <https://doi.org/10.3390/medicines3020013>
- Pedro, A. S., Cabral-Albuquerque, E., Ferreira, D., & Sarmiento, B. (2009). Chitosan: An option for development of essential oil delivery systems for oral cavity care? *Carbohydrate Polymers*, 76(4), 501-508. <https://doi.org/10.1016/j.carbpol.2008.12.016>
- Phong, W. N., Gibberd, M. R., Payne, A. D., Dykes, G. A., & Coorey, R. (2022). Methods used for extraction of plant volatiles have potential to preserve truffle aroma: A review. *Comprehensive Reviews in Food Science and Food Safety*, 21(2), 1677-1701. <https://doi.org/10.1111/1541-4337.12927>
- Poshadri, A., & Aparna, K. (2010). Microencapsulation technology: A review. *Journal of Research ANGRAU*, 38(1), 86-102.
- Prata, A. S., & Grosso, C. R. F. (2015). Production of microparticles with gelatin and chitosan. *Carbohydrate Polymers*, 116, 292-299. <https://doi.org/10.1016/j.carbpol.2014.03.056>
- Qin, X., Lu, Y., Peng, Z., Fan, S., & Yao, Y. (2018). Systematic chemical analysis approach reveals superior antioxidant capacity via the synergistic effect of flavonoid compounds in red vegetative tissues. *Frontiers in Chemistry*, 6, Article 314274. <https://doi.org/10.3389/fchem.2018.00009>
- Raksa, A., Sawaddee, P., Raksa, P., & Aldred, A. K. (2017). Microencapsulation, chemical characterization, and antibacterial activity of Citrus hystrix DC (kaffir lime) peel essential oil. *Monatshefte Fur Chemie*, 148, 1229-1234. <https://doi.org/10.1007/s00706-017-2015-8>

- Rosli, N. A., Hasham, R., & Aziz, A. A. (2018). Design and physicochemical evaluation of nanostructured lipid carrier encapsulated zingiber zerumbet oil by d-optimal mixture design. *Jurnal Teknologi*, 80(3), 105-113. <https://doi.org/10.11113/jt.v80.11268>
- Roy, J. C., Giraud, S., Ferri, A., Mossotti, R., Guan, J., & Salaün, F. (2018). Influence of process parameters on microcapsule formation from chitosan - Type B gelatin complex coacervates. *Carbohydrate Polymers*, 198, 281-293. <https://doi.org/10.1016/j.carbpol.2018.06.087>
- Rungwasantisuk, A., & Raibhu, S. (2020). Application of encapsulating lavender essential oil in gelatin/gum-Arabic complex coacervate and varnish screen-printing in making fragrant gift-wrapping paper. *Progress in Organic Coatings*, 149, Article 105924. <https://doi.org/10.1016/j.porgcoat.2020.105924>
- Shetta, A., Kegere, J., & Mamdouh, W. (2019). Comparative study of encapsulated peppermint and green tea essential oils in chitosan nanoparticles: Encapsulation, thermal stability, in-vitro release, antioxidant and antibacterial activities. *International Journal of Biological Macromolecules*, 126, 731-742. <https://doi.org/10.1016/j.ijbiomac.2018.12.161>
- Shi, L., Beamer, S. K., Yang, H., & Jaczynski, J. (2018). Micro-emulsification/encapsulation of krill oil by complex coacervation with krill protein isolated using isoelectric solubilization/precipitation. *Food Chemistry*, 244, 284-291. <https://doi.org/10.1016/j.foodchem.2017.10.050>
- Shinde, U. A., & Nagarsenker, M. S. (2009). Characterization of gelatin-sodium alginate complex coacervation system. *Indian Journal of Pharmaceutical Sciences*, 71(3), 313-317. <https://doi.org/10.4103/0250-474X.56033>
- Silva, M. C., & Andrade, C. T. (2009). Evaluating conditions for the formation of chitosan/gelatin microparticles. *Polimeros*, 19(2), 133-137. <https://doi.org/10.1590/S0104-14282009000200010>
- Singh, N., & Sheikh, J. (2022). Novel Chitosan-Gelatin microcapsules containing rosemary essential oil for the preparation of bioactive and protective linen. *Industrial Crops and Products*, 178, Article 114549. <https://doi.org/10.1016/j.indcrop.2022.114549>
- Sogias, I. A., Khutoryanskiy, V. V., & Williams, A. C. (2010). Exploring the factors affecting the solubility of chitosan in water. *Macromolecular Chemistry and Physics*, 211(4), 426-433. <https://doi.org/10.1002/macp.200900385>
- Sreepian, A., Sreepian, P. M., Chanthong, C., Mingkhwancheep, T., & Prathit, P. (2019). Antibacterial activity of essential oil extracted from *Citrus hystrix* (kaffir lime) peels: An in vitro study. *Tropical Biomedicine*, 36(2), 531-541.
- Srifuengfung, S., Bunyaphatsara, N., Satitpatipan, V., Tribuddharat, C., Junyaprasert, V. B., Tungrugsasut, W., & Srisukh, V. (2020). Antibacterial oral sprays from kaffir lime (*Citrus hystrix* DC.) fruit peel oil and leaf oil and their activities against respiratory tract pathogens. *Journal of Traditional and Complementary Medicine*, 10(6), 594-598. <https://doi.org/10.1016/j.jtcme.2019.09.003>
- Timilsena, Y. P., Akanbi, T. O., Khalid, N., Adhikari, B., & Barrow, C. J. (2019). Complex coacervation: Principles, mechanisms and applications in microencapsulation. *International Journal of Biological Macromolecules*, 121, 1276-1286. <https://doi.org/10.1016/j.ijbiomac.2018.10.144>

- Timilsena, Y. P., Wang, B., Adhikari, R., & Adhikari, B. (2016). Preparation and characterization of chia seed protein isolate-chia seed gum complex coacervates. *Food Hydrocolloids*, *52*, 554-563. <https://doi.org/10.1016/j.foodhyd.2015.07.033>
- Venkatachalam, K. (2019). Changes in phytochemicals and antioxidant properties of kaffir lime leaves under chilling storage. *Kaen Kaset= Khon Kaen Agriculture Journal*, *47*(Suppl. 1), 531-536.
- Vishwakarma, G. S., Gautam, N., Babu, J. N., Mittal, S., & Jaitak, V. (2016). Polymeric encapsulates of essential oils and their constituents: A review of preparation techniques, characterization, and sustainable release mechanisms. *Polymer Reviews*, *56*(4), 668-701. <https://doi.org/10.1080/15583724.2015.1123725>
- Wang, B., Adhikari, B., & Barrow, C. J. (2014). Optimisation of the microencapsulation of tuna oil in gelatin-sodium hexametaphosphate using complex coacervation. *Food Chemistry*, *158*, 358-365. <https://doi.org/10.1016/j.foodchem.2014.02.135>
- Wang, B., Akanbi, T. O., Agyei, D., Holland, B. J., & Barrow, C. J. (2018). Coacervation technique as an encapsulation and delivery tool for hydrophobic biofunctional compounds. In A. M. Grumezescu & A. M. Holban (Eds.), *Role of Materials Science in Food Bioengineering* (pp. 235-261). Academic Press. <https://doi.org/10.1016/C2016-0-00658-7>
- Wang, H., Lin, X., Zhu, J., Yang, Y., Qiao, S., Jiao, B., Ma, L., & Zhang, Y. (2023). Encapsulation of lutein in gelatin type A/B-chitosan systems via tunable chains and bonds from tweens: Thermal stability, rheologic property and food 2D/3D printability. *Food Research International*, *173*, Article 113392. <https://doi.org/10.1016/j.foodres.2023.113392>
- Wijaya, Y. A., Widyadinata, D., Irawaty, W., & Ayucitra, A. (2017). Fractionation of phenolic and flavonoid compounds from kaffir lime (*Citrus hystrix*) peel extract and evaluation of antioxidant activity. *Reaktor*, *17*(3), 111-117. <https://doi.org/10.14710/reaktor.17.3.111-117>
- Yan, C., & Zhang, W. (2014). Coacervation processes. In R. Sobel (Ed.), *Microencapsulation in the Food Industry: A Practical Implementation Guide* (pp. 125-137). Academic Press. United States. <https://doi.org/10.1016/C2012-0-00852-6>
- Yang, J., Han, S., Zheng, H., Dong, H., & Liu, J. (2015). Preparation and application of micro/nanoparticles based on natural polysaccharides. *Carbohydrate Polymers*, *123*, 53-66. <https://doi.org/10.1016/j.carbpol.2015.01.029>
- Yu, F., Li, Z., Zhang, T., Wei, Y., Xue, Y., & Xue, C. (2017). Influence of encapsulation techniques on the structure, physical properties, and thermal stability of fish oil microcapsules by spray drying. *Journal of Food Process Engineering*, *40*(6), Article e12576. <https://doi.org/10.1111/jfpe.12576>



Review Article

## Current Insight on *Siraitia grosvenorii* Flavonoids Extraction Process and its Bioactivity Characteristic: A Review

Zhao Jing<sup>1</sup>, Douglas Law<sup>2</sup>, Ahmed Najm<sup>1</sup>, Cheah Yew Hoong<sup>3</sup> and Shazrul Fazry<sup>1\*</sup>

<sup>1</sup>Department of Food Science, Faculty of Science and Technology, Universiti Kebangsaan Malaysia, 43600, Bangi, Selangor, Malaysia

<sup>2</sup>Faculty of Health and Life Sciences, Inti International University, 71800 Nilai, Negeri Sembilan, Malaysia

<sup>3</sup>ZACH Biotech Depot Sdn. Bhd., No. 19-2, Jalan SC 5/A, Kawasan Perindustrian Sg. Chua, 43000, Kajang, Selangor, Malaysia

### ABSTRACT

The *Siraitia grosvenorii* is a Chinese herb with various bioactive properties that has been widely used as a culinary ingredient and in traditional medicine. Flavonoids are among the important bioactive compounds in *S. grosvenorii*, which contribute significantly to the biological activity of *S. grosvenorii*. *S. grosvenorii*-flavonoids have been reported to possess various biological and pharmacological activities, including antioxidant, antibacterial, anti-inflammatory, hypolipidemic, and anti-diabetic, which are important for human health. Based on previous reports, the structure, extraction technology, biological activity and further development regarding *S. grosvenorii*-flavonoids are reviewed in this paper, providing appropriate insights and references for future development of *S. grosvenorii*-flavonoids.

**Keywords:** Bioactivity, extraction process, flavonoids, pharmacological activity, *Siraitia grosvenorii*

### ARTICLE INFO

*Article history:*

Received: 25 February 2023

Accepted: 24 August 2023

Published: 14 March 2024

DOI: <https://doi.org/10.47836/pjst.32.2.08>

*E-mail addresses:*

p114682@siswa.ukm.edu.my (Zhao Jing)

douglas.law@gmail.com (Douglas Law)

ahmadaljemeely@gmail.com (Ahmed Najm)

yhcheah@zachbiotech.com (Cheah Yew Hoong)

shazrul@ukm.edu.my (Shazrul Fazry)

\* Corresponding author

### INTRODUCTION

The continuous development and improvement of science and technology provide people with production and life conveniences but are also fraught with innumerable risks and challenges. The potential risks of chemical food additives and drug resistance are among today's scientific challenges (Irfan et al., 2022;

Moudaka et al., 2023; Najm et al., 2022). To solve these problems, researchers are searching for new, safer, and more appropriate natural bioactive compounds as substitutes (Zang et al., 2022). *Siraitia grosvenorii* (*Luo Han Guo*) is a Cucurbitaceae herb mainly distributed in China's tropical and subtropical regions (Figure 1). The Chinese explored, applied, and recorded its medicinal potential more than 300 years ago (Gong et al., 2019). Presently, *S. grosvenorii* fruit is widely used as a food sweetener (Li, Li et al., 2022) and supplement ingredients (Abdel-Hamid et al., 2020) due to its natural sweet, low-calorie glycosides, which are regarded as an ideal new sugar source for patients with diabetes and obesity (Thakur et al., 2022). Numerous substances, including a wide variety of triterpenoids and flavonoids, as well as amino acids and two types of polysaccharides, have been isolated from *S. grosvenorii* to date (Duan et al., 2023; Gong et al., 2022), adding to its value for future development and use. Table 1 displays some common compounds and their activities in *S. grosvenorii* extracts.

Flavonoids are a class of bioactive molecules with various phenolic structures in plants' fruits, roots, stems, leaves, and flowers, among other parts of *S. grosvenorii*. Due to their antioxidant, anti-inflammatory, and anticancer properties, as well as their ability to regulate the functions of important cellular enzymes, they are regarded as essential components in numerous contemporary food, pharmaceutical, and cosmetic applications (Shen et al., 2022; Čižmarová et al., 2023). Additionally, with the rise of numerous cardiovascular, cerebrovascular, and immune diseases in recent years, flavonoid research and application in the management of numerous cerebrovascular diseases and immune deficiency diseases has garnered particular interest (Barreca et al., 2023; Keyhani et al., 2023). It was discovered that flavonoids, mainly flavonoids and flavonols, are one of the primary active components



Figure 1. The distribution of *Siraitia grosvenorii* in China

Table 1  
Some common compounds and their activities in *S. grosvenorii* extracts

Classification	Compounds	Plant Part	Bioactivities	<i>In vivo</i> / <i>In vitro</i>	References
Polysaccharide	SGP-I	Fruit	Anti-oxidant	<i>In vitro</i>	Zhu et al., 2020
	SGP-I-1	Fruit	Anti-oxidant; Hypoglycemic	<i>In vitro</i>	Gong et al., 2022
Triterpenes	Mogrol	Fruit	Anti-inflammatory; Anti-colitis; Anti-cancer; Anti-osteoporosis; Anti-proliferative	<i>In vivo</i> ; <i>In vitro</i>	Li, Liu et al., 2022; Chen et al., 2022; Song et al., 2022
	11-oxo-mogrol	Fruit	Induced neuronal damages	<i>In vitro</i>	Ju et al., 2020
	Siemenoside I	Fruit	Anti-diabetic; Anti-alzheimer	<i>In vivo</i> ; <i>In vitro</i>	Liu et al., 2019; Cai et al., 2023
	Mogroside III	Fruit	Anti-diabetic; Anti-alzheimer	<i>In vivo</i> ; <i>In vitro</i>	Liu et al., 2019; Cai et al., 2023
	Mogroside IV	Fruit	Anti-diabetic; Anti-alzheimer	<i>In vivo</i> ; <i>In vitro</i>	Liu et al., 2023; Cai et al., 2023
	Mogroside V	Fruit	Anti-oxidant; Anti-inflammatory; Against neuronal damages; Anti-diabetic	<i>In vivo</i> ; <i>In vitro</i>	Luo et al., 2022; Shen et al., 2022; Liu et al., 2023
	Mogroside IIE	Fruit	Anti-lung injury; Anti-inflammatory	<i>In vivo</i>	Lü et al., 2024
	Mogroside IIIE	Fruit	Anti-inflammatory; Anti-fibrosis	<i>In vivo</i> ; <i>In vitro</i>	Yanan et al., 2023
Flavonoids	$\beta$ -amyryn	Fruit	Therapeutic intervention in tuberculosis	<i>In vitro</i> ; <i>In vitro</i>	Beg et al., 2022
	Afzelin	Fruit	Anti-bacterial; Anti-oxidant; Anti-tumor; Anti-oxidant	<i>In vivo</i> ; <i>In vitro</i>	Wang et al., 2015; Akter et al., 2022
	Kaempferol	Flower; Leaves	Anti-bacterial; Anti-oxidant; Hypoglycemic; Anti-obesity;	<i>In vitro</i>	Li et al., 2018; Bian et al., 2022
	Kaempferol-7-O- $\alpha$ -L-rhamnopyranoside	Fruit; Flower; Leaves	Anti-oxidant	<i>In vivo</i> ; <i>In vitro</i>	Fang et al., 2017; Mo and Li, 2009
	Kaempferitrin	Leaves; Fruit	Anti-bacterial; Anti-oxidant; Anti-tumor	<i>In vivo</i> ; <i>In vitro</i>	Wang et al., 2015; Su et al., 2023)

Table 1 (continue)

Classification	Compounds	Plant Part	Bioactivities	<i>In vivo</i> / <i>In vitro</i>	References
Others	Grosvenerine	Flower; Leaves; Fruit	Anti-hyperglycemic; Anti-inflammatory	<i>In vivo</i> ; <i>In vitro</i>	Sung et al., 2020; Zhang et al., 2020
	7-methoxyl-kaempferol-3-O- $\alpha$ -L-rhamnopyranoside	Flower	Anti-oxidant	<i>In vivo</i>	Mo and Li, 2009
	7-methoxy-kaempferol-3-O- $\beta$ -D-glucopyranoside	Flower	Anti-oxidant; Anti-hyperglycaemic	<i>In vivo</i>	Janibekov et al., 2018; Mo and Li, 2009
	Aloe-emodin	Leaves	Anti-bacterial; Cerebroprotective	<i>In vitro</i> ; <i>In silico</i> ; <i>In vivo</i>	Yang et al., 2016; Pasala et al., 2022
	Aloe-emodin acetate	Leaves	Anti-bacterial; Cerebroprotective	<i>In vitro</i> ; <i>In silico</i> ; <i>In vivo</i>	Yang et al., 2016; Pasala et al., 2022
	p-Hydroxybenzoic Acid	Leaves			Yang et al., 2016
	Rutin	Fruit			Fang et al., 2017
	Gemistein	Fruit			Fang et al., 2017
	Siraitic acid II	Root	Anti-diabetic	<i>In vitro</i>	Lu et al., 2023
	Cucurbitacin B	Root	Anti-diabetic	<i>In vitro</i>	Lu et al., 2023
	(-)-Iariciresinol	Root	Anti-diabetic	<i>In vitro</i>	Lu et al., 2023
	Siraitic Acid F	Root			Lu et al., 2023
	Cucurbitacin B	Root			Lu et al., 2023
	23,24-Dihydrocucurbitacin B	Root			Lu et al., 2023



of *S. grosvenorii*. The *S. grosvenorii*-flavonoids, in contrast to mogrosides, are present not only in the fruit but also in the leaves, roots, and flowers.

These flavonoids exhibit potent antioxidant, antibacterial, anticancer, and hypoglycemic properties (Lu et al., 2023; Wang et al., 2015; Wu et al., 2022). Prior research on the flavonoids from *S. grosvenorii* focused primarily on extraction methods, structural characterization, and in vitro activity detection, while in vivo activity, mechanism of action, and clinical applications were the subject of relatively few studies. It is necessary to conduct exhaustive research on these compounds to broaden and extend the applicability field and direction of the *S. grosvenorii* extract. In this review, the extraction processing, chemical structure, pharmacological activity, and future development of *S. grosvenorii*-flavonoids are discussed to provide a reference as well as the future direction for the in-depth research and application of active compounds in *S. grosvenorii*.

## THE EXTRACTION PROCESSING

### Extraction Method

Extraction of components is frequently the initial step in compound research. Since various extraction techniques and extraction procedures have a significant impact on the extraction efficiency of compounds and the subsequent investigation of chemicals, choosing the best extraction methods and conditions is crucial. *S. grosvenorii*-flavonoids are primarily extracted using organic solvent extraction, ultrasound-assisted extraction (UAE), microwave-assisted extraction (MAE), and enzyme-assisted extraction (EAE). Table 2 displays the procedures utilized to extract *S. grosvenorii*-flavonoids.

Solvent extraction transfers a target substance from one solvent to another by utilizing various substances' different partition coefficients and solubilities. There are numerous examples of solvent extraction of flavonoids. For example, In the latest study, Lu et al. (2023) extracted several active flavonoids from the roots of *S. grosvenorii* with 75% ethanol. Wuttisin and Boonsook (2019) extracted total flavonoids from *S. grosvenorii* using distilled water, n-hexane, ethyl acetate, 95% ethanol, and propylene glycol and compared the effect of different solvents on the extraction rate. The results revealed that using distilled water as the extractant agent yielded the highest extraction rate.

Some organic components in solid or semi-solid substances can be extracted with the help of a microwave by using the electromagnetic field to pull them away from the matrix. This method has several advantages over conventional extraction techniques, including high efficiency, energy efficiency, safety, and environmental protection. Zhang et al. (2013) used microwave extraction techniques to extract flavonoids from *S. grosvenorii* flowers. They found that the following process parameters worked best: solvent: 60% ethanol solution; solid-liquid ratio: 1: 30 (g/mL); microwave power: 350 W; radiation time: 20 min. Under this condition, the yield of flavonoids in *S. grosvenorii* flowers can reach 7.6%. In addition,

Table 2  
*The methods to extract S. grosvenorii-flavonoids*

Method	Solvent	Temperature (°C)	Time (min)	Solid-liquid Ratio (g/ml)	Other	References
Soxhlet Extraction	70% Ethanol	25°C		1:10		Lu et al., 2023
Organic Solvent extraction	Distilled water	80°C	60			Wuttisin & Boonsook, 2019
	n-hexane	25°C	1440			
	Ethyl Acetate	25°C	1440			
	95% Ethanol	25°C	1440			
	Propylene Glycol	25°C	1440			
Microwave-assisted Extraction (MAE)	60% Ethanol		20	1:30	Microwave Power:350 W	Zhang et al., 2013
Ultrasonic-assisted Extraction (UAE)	67% Ethanol		43	1:15	Ultrasonic Power: 208 W	Zhang et al., 2016
Subcritical Fluid Extraction	Sub-critical water; 15% Ethanol	140°C	20	1:30	Pressure: 4 MPa	Xu et al., 2017
Enzyme Assisted Extraction (EAE)	Ethanol; Petroleum benzine; ethyl acetate	65°C	80	1:8; 3:1; 2:1	Cellulase (50 U/ml); pH 5.2	Wang et al., 2006

Zhang et al. (2016) used ultrasonic-assisted extraction technology to extract total flavonoids in the flowers of *S. grosvenorii*, optimized the extraction process through orthogonal experiments, and finally determined the optimal process conditions: the concentration of ethanol was 67%, the extraction time was 43 min, the ultrasonic power was 208 W, and the ratio of solvent-to-solid was 1:15 (g/mL). Under these conditions, the extraction rate of total flavonoids could reach 6.5%.

Subcritical water extraction (SWE) technology is a process in which the raw materials are put into subcritical fluids for extraction according to the principle of similar compatibility, and the effective components in the materials are extracted under different conditions. Xu et al. (2017) used subcritical extraction technology to extract the active substances in *S. grosvenorii* and determined the optimal process conditions of the method: the extraction temperature was 140°C, the ethanol addition was 15%, and the extraction time was 20 min. Under the extraction conditions, the content of flavonoids was up to 11.90 mg/g, and the antioxidant activity of the extracts was found to be optimal. Enzyme-assisted extraction is a method that uses active enzymes to hydrolyze certain substances with specific structures to obtain target substances. Currently, this method is mostly used

in the auxiliary production and extraction of mogrosides, while flavonoid extraction in *S. grosvenorii* is rarely mentioned. However, as early as 2006, Wang et al. used the enzyme (cellulase)-solvent method to extract flavonoids from *S. grosvenorii* and found that the optimal extraction conditions: cellulase concentration 50 U/ml, pH 5.2, temperature 65°C, time 80 min.

In conclusion, different extraction conditions have different effects on the extraction rate of *S. grosvenorii*-flavonoids, with the most influential parameters being extraction temperature, solid-liquid ratio, extraction duration, and extraction concentration.

### Isolation and Purification Method

The process of isolating a substance from a mixture is isolation and purification. Typically, flavonoids are purified and separated using column chromatography, solution extraction, and supercritical fluid extraction. Table 3 lists the techniques for isolating and purifying *S. grosvenorii*-flavonoids.

Table 3  
The methods for the isolation and purification of *S. grosvenorii*-flavonoids

Method	Isolated flavonoid compounds	References
HPLC	Kaempferitrin; Afzelin; a-Rhamnoisorobin; Kaempferol	Wang et al., 2015
UF-HPLC; MCI CHP-20P Column Chromatography; HSCCC	3,4'-dimethoxy-4,9,9'-trihydroxy-benzofuranolignan-7'-ene; 23,24-dihydrocucurbitacin F; 23,24-dihydrocucurbitacin F-25-acetate	Lu et al., 2023
UHPLC	Kaempferol-3-O- $\alpha$ -L-[4-O-(4-carboxy-3-hydroxy-3-methylbutanoyl)]-rhamnopyranoside-7-O- $\alpha$ -L-rhamnopyranoside; Grosvenorine; Kaempferitrin; Afzelin	Lu et al., 2020
Unitary-C18 column	Quercetin; Rutin; Neohesperidin; Naringin; kaempferol O-glycoside-rhamcoside; quercetin O-arabinoside-O'-glycoside-rhamnoside; 4'-methoxyl-kaempferol	Qing et al., 2017

Column chromatography is one of the most traditional and widespread separation techniques. This method is a separation procedure in which the components in the mixture are separated from each other by repeated distribution in the stationary phase and mobile phase with varying partition coefficients. Based on the different adsorbents, the method is mostly made up of polyamide column chromatography, silica gel column chromatography, dextran gel column chromatography, the macroporous resin adsorption method, and high-performance liquid chromatography (HPLC). The HPLC was used to separate the flavonoids from the biologically active kaempferitrin, afzelin, -a-rhamnoisorobin, and kaempferol in *S. grosvenorii* (Wang et al., 2015). In a recent study, Lu et al. (2023) used ultrafiltration (UF) combined with high-performance liquid chromatography (HPLC) to target  $\alpha$ -glucosidase inhibitors from *S. grosvenorii* roots.

Also, researchers used ultra-high performance liquid chromatography (UHPLC) with electrospray ionization quadrupole time-of-flight mass to separate and identify 34 flavonoids from the leaves of *S. grosvenorii*. It included 19 kaempferol O-glycosides, 4 quercetin O-glycosides, 6 flavanone derivatives, and 5 polymethoxy-flavones (Lu et al., 2020). Qing et al. (2017) isolated 53 flavonols and flavonols glycosides from *S. grosvenorii* by using a unitary C18 column (HPLC). At the same time, two isoflavones (4',7-dihydroxyisoflavone (Daidzein) and 4',5,7-trihydroxyisoflavone (Genistein) were isolated and purified from the *S. grosvenorii* extracts using C-18 column chromatography (Chaturvedula & Prakash, 2013).

## THE COMPONENTS DISTRIBUTION AND STRUCTURE

### The Components Distribution

It has been discovered that the fruit, leaves, stems, and flowers of *S. grosvenorii* contain a significant quantity of flavonoids, with the stems, leaves, and flowers containing more. Some parts of *S. grosvenorii* used in the industries are shown in Figure 2.

Wuttisin and Boonsook (2019) extracted the flavonoids from *S. grosvenorii* using various solvents (distillate water, propylene glycol, 95% ethanol, ethyl acetate, and hexane). The results showed that compared with other solvent extracts, the total flavonoid content of the distilled water extract was up to  $25.229 \pm 0.904$   $\mu\text{g}$  QE/mg solid crude extract. However, the 95% ethanol extract had the highest polyphenol content. At the same time, DPPH and ABTS methods were used to evaluate the antioxidant activity of *S. grosvenorii* extracts, and it was found that the distilled water extract had the most significant antioxidant activity, suggesting that the antioxidant activity of *S. grosvenorii* extracts may be associated with the presence of flavonoids.

In addition, Metabolic profiling analysis was used to analyze and identify the compositional characteristics of green and yellow fruits of *S. grosvenorii* (Fang et al., 2017). The results revealed that yellow fruits contained fewer flavonoids than green fruits and that the peel contained more flavonoids than the fruit. Zhang et al. (2013) used HPLC-TOF-MS combined with the PCA pattern recognition method to compare and analyze the chemical

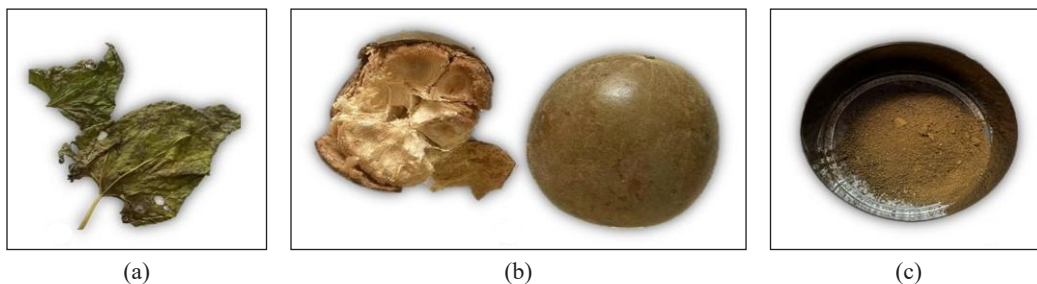


Figure 2. Parts of *S. grosvenorii*. (a) leaf, (b) ripe fruit, (c) dried fruit powder of *S. grosvenorii*

components of different parts of *S. grosvenorii*. The analysis showed that the chemical components of the fruit and pericarp were similar but significantly different from those of the leaf and stem. Mogrosides are markers of *S. grosvenorii* fruit, and five flavonoid glycosides are selected as leaf and stem markers. In addition, Rao et al. (2012) used the spectrophotometer method and kaempferin as a control to measure the flavonoid content in the fruit, stem, and leaf extracts of *S. grosvenorii*. The results showed that the content of flavonoid in the stem and leaf (345.11 mg/g) was much higher than that in the fruit (13.89 mg/g), which provides an experimental basis for the development and utilization of *S. grosvenorii* branches and leaves.

### The Structure and Composition

The *S. grosvenorii*-flavonoids are mostly found as flavones and flavonols, most of which are compounds with kaempferol or quercetin aglycones (Wu et al., 2022), and the composition and structure of flavones are also related to the plant portions in which they are found. The types and structures of flavonoids isolated from different parts of *S. grosvenorii* also vary. A variety of flavonoids have been isolated from the flowers of *S. grosvenorii*, including kaempferol, 7-methoxy-kaempferol-3-O- $\beta$ -D-glucopyranoside, kaempferol-3-O-L-rhamnoside-7-O-[ $\beta$ -D-glucosyl-(1-2)- $\alpha$ -L-rhamnoside]-3-O-L-rhamnoside and 7-methoxyl-kaempferol-3-O- $\alpha$ -L-rhamnopyranoside (Mo & Li, 2009). In addition, kaempferitrin, kaempferol-7-O- $\alpha$ -L-rhamnopyranoside, kaempferol-3,7-O-L-dirhamnopyranoside, aloe emodin acetate, aloe emodin, afzelin, and quercetin were also isolated from fruits and leaves (Yang et al., 2016; Lu et al., 2020). The composition of different parts of *S. grosvenorii* and the structure of *S. grosvenorii*-flavonoids are shown in Table 1 and Figure 3, respectively.

### BIOLOGICAL ACTIVITIES OF FLAVONES FROM *S. GROSVVENOORII*

Traditional Chinese medicine believes that *S. grosvenorii* has various physiological functions, including lung clearing, phlegm clearing, and diarrhea stopping, which can treat and relieve cough, sore throat, constipation, and other symptoms (Wu et al., 2022). Modern scientific research shows that different extracts from *S. grosvenorii* have different biological and pharmacological activities (Li, Li et al., 2022; Zhu et al., 2020).

Flavonoids have sparked interest as a natural active substance due to their high activity value. With a better understanding of this substance activity, its many biological activities, such as anticancer, anti-inflammation, anti-mutation, and antioxidant activity, have been developed and applied in a variety of fields (Mitra et al., 2022; Shen et al., 2022). Due to their antibacterial and antioxidant properties, flavonoids are commonly used in food safety and health disciplines as antioxidants and bacteriostats. Due to their unique bacteriostatic or insecticidal properties, flavonoids are also used in agriculture as insecticides. At the

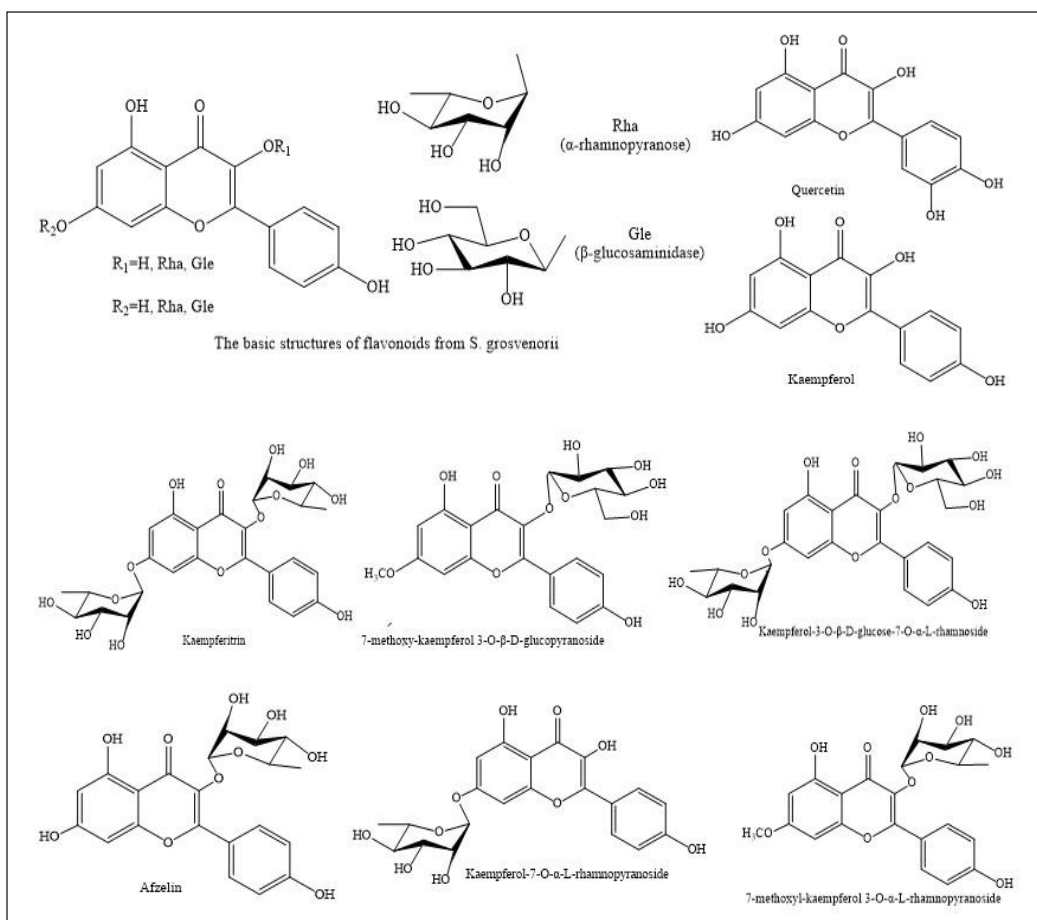


Figure 3. The structures of flavonoids extracted from *S. grosvenorii*

same time, flavonoids have been developed and used as various drugs in human medicine due to their unique medical activity, such as those for diabetes, cancer, anti-tumor therapy, and other drugs. The *S. grosvenorii*-flavonoids are a key component of the plant, and their diverse activities have been studied and reported. The biological activities of *S. grosvenorii*-flavonoids are listed in Table 1.

### Antioxidant Activity

Free radicals and reactive oxygen species are well known for causing oxidation and damage to cell membranes, DNA, and/or proteins, which can have serious consequences for human health and cause a variety of diseases such as cancer, neurodegenerative diseases, cardiovascular disease, diabetes, and aging (Ooi et al., 2021). Researchers in the food and pharmaceutical fields are often looking for active compounds that can clear and slow this damage as antioxidant molecules (Azfaralariff et al., 2022). Experiments have confirmed

that the *S. grosvenorii*-flavonoids contain a large number of phenolic hydroxyl groups, which have a significant scavenging effect on  $\alpha$ -diphenyl- $\beta$ -picrylhydrazyl (DPPH) free radicals and 2,2'-azino-bis(3-ethylbenzothiazoline-6-sulfonate) (ABTS) free radicals, and this effect is positively correlated with the concentration and action time of flavonoids. These studies have confirmed that the flavonoids extracted from *S. grosvenorii* are natural and effective free radical scavengers, which can be widely used in the food and pharmaceutical industries (Pan et al., 2012; Pandey & Chauhan, 2019).

Studies have found that compared with the propylene glycol and ethanol extracts of *S. grosvenorii*, the distilled water extract (polyphenols and flavonoids) of the substance had stronger antioxidant activity, and its  $\alpha$ -diphenyl- $\beta$ -picrylhydrazyl (DPPH) scavenging activity and 2,2'-azino-bis(3-ethylbenzothiazoline-6-sulfonate) (ABTS) scavenging activity increased with the increase of its solvent polarity (Wuttisin & Boonsook, 2019). Moreover, some studies have detected the antioxidant activity of 5 flavonoid glycosides with different structures in the *S. grosvenorii* flower (kaempferol, kaempferol-7- $\alpha$ -L-rhamnopyranoside, 7-methoxyl-kaempferol-3-O- $\alpha$ -L-rhamnopyranoside, 7-methoxyl-kaempferol-3-O- $\beta$ -D-glucopyranoside and 3-O- $\alpha$ -L-rhamnopyranosyl-kaempferol-7-O- $[\beta$ -D-glucopyranosyl-(1-2)- $\alpha$ -L-rhamnopyranoside]), and found that kaempferol and kaempferol-7- $\alpha$ -L-rhamnoside showed well anti-diabetic activities and the 7, 3-hydroxyl group in the flavonoid structure was an important factor affecting its antioxidant activity (Mo & Li, 2009). Pan et al. (2012) studied the antioxidant activity of the alcoholic extract of *S. grosvenorii* leaves, and the results showed that the ethanol crude extract (SEE) of *S. grosvenorii* had similar antioxidant activity to butylated hydroxytoluene (BHT), and found that kaempferol-3-O- $\alpha$ -L-rhamnopyranosyl-7-O- $[\beta$ -D-glucopyranosyl-(1-2)-O-L-rhamnoside], kaempferol-3-O- $\beta$ -D-glucose-7-O- $\alpha$ -L-rhamnoside and quercetin were isolated from crude ethanol extract (SEE) showed significant scavenging free energy, which can provide corresponding scientific basis and guidance for the development and utilization of *S. grosvenorii* leaves. Similarly, a strong linear correlation was found between polyphenolic compounds (including flavonoids) and their antioxidant activity in the antioxidant activity of *S. grosvenorii* cultured cells, among which kaempferol-3-O-Glc-7-O-Rha played the most important antioxidant role (Liu et al., 2022).

### Hypoglycemic Activity

Diabetes mellitus (DM) is a chronic disease characterized by metabolic disorders of the endocrine system (Yedjou et al., 2023). There are two types of diabetes mellitus: type 1 diabetes mellitus (T1DM) and type 2 diabetes mellitus (T2DM) (Sethupathi et al., 2023). The disease causes long-term damage to the living body's organs, resulting in dysfunction and failure, eventually leading to disability and premature death (Ibrahim et al., 2023; Kropp et al., 2023). This disease and its complications have caused serious distress to people and posed major economic challenges to society in both developing and developed countries.

Insulin and related reagents, biguanides, sulfonylureas,  $\alpha$ -glucosidase inhibitors, thiazolidinediones, and dipeptidyl peptidase-IV inhibitors are some of the most commonly used diabetic drugs in clinical trials (Dahlén et al., 2022). However, these chemical drugs have several negative side effects, including adverse patient reactions and high costs. As a result, researchers are looking for low-cost natural active ingredients to develop and use as new anti-diabetic drugs. Natural active ingredients, such as flavonoids, terpenoids, and saponins, have been recognized as important sources of potent anti-diabetic drugs (Khuntia et al., 2022). These active ingredients often achieve anti-diabetic effects by increasing insulin secretion or reducing intestinal glucose absorption.

Increased precursors of advanced glycation end products (AGEs), elevated levels of diacylglycerol, and increased hexosamine pathway activity are some intracellular metabolic changes that typically lead to hyperglycemia and hyperlipidemia symptoms. These changes frequently result in tissue cell damage and diabetic complications. (Singh et al., 2022). Advanced glycation end products (AGEs) are crucial in developing diabetes and its side effects. Reducing the level of glycosylation and the production of advanced glycation end products is a feasible strategy for postponing or preventing diabetic complications because the formation of these compounds is generally increased in diabetic patients.

It has become an important testing point for many natural and pharmacological compounds being investigated for their potential therapeutic potential (Cheun-Arom & Sritularak, 2023). In addition, excessive ROS/RNS in the organism is also one of the main signs of hyperglycemia and hyperlipidemia, which are usually caused by the oxidation of glucose and free fatty acids in the cells suffering from the symptoms. Therefore, it is also one of the important factors to explore in the mechanism of diabetes (Singh et al., 2022). Part of the mechanism of flavonoids in diabetes is shown in Figure 4.

Previous studies on the hypoglycemic/anti-diabetic activities of *S. grosvenorii* extracts mainly focused on mogroside, while studies on the effects of flavonoids in *S. grosvenorii* extracts were rare. However, some studies have also found that the flavonoids in *S. grosvenorii* have hypoglycemic effects. Studies have found that the high dose of flavonoids from *S. grosvenorii* (80 mg/kg) could effectively reduce the blood glucose level of STZ-induced diabetic rats (from  $22.68 \pm 2.55$  mmol/L to  $10.63 \pm 2.88$  mmol/L). The medium dose of total flavonoids (40 mg/kg) could effectively reduce blood lipids (from  $3.51 \pm 0.53$  mmol/L to  $1.26 \pm 0.37$  mmol/L) in STZ-induced diabetic rats. Moreover, it was also found that the high dosage of total flavonoids (80 mg/kg) could significantly increase the activities of SOD and GSH-Px ( $P < 0.01$ ) and the level of insulin ( $P < 0.01$ ) and reduce the content of MDA ( $P < 0.05$ ) in STZ-induced diabetic rats (Zheng et al., 2011).

Even though there have only been a small number of studies on the hypoglycemic effects of *S. grosvenorii*-flavonoids, earlier research has shown that these compounds significantly reduce sugar, inhibit  $\alpha$ -glucosidase, and safeguard the pancreas. Additionally,



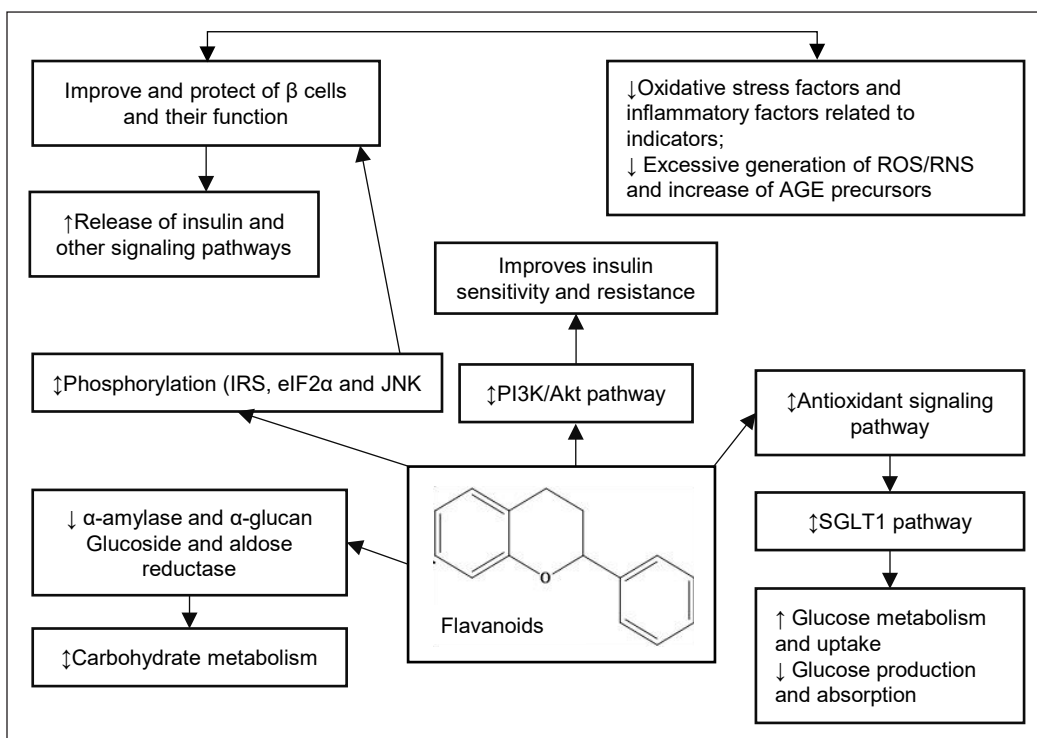


Figure 4. Part of the mechanism of flavonoids in diabetes (↑: increase, ↓: decrease and ⇆: modulatory effect)

consuming more flavonoids can lower the risk of developing diabetes. Kaempferol, which is extracted from tea, cruciferous vegetables, grapefruit, and some edible berries, can achieve anti-diabetic effects by inhibiting hepatic gluconeogenesis, reducing Caspase-3 activity in  $\beta$  cells, and enhancing  $\beta$  cell survival, improving cAMP signaling (Alkhalidy et al., 2015; Alkhalidy et al., 2018; Sharma et al., 2020). The quercetin extracted from chokeberry, black currant, apple, and cherry can also achieve anti-diabetic effects by improving the AMPK pathway, inhibiting the expression of NF- $\kappa$ B and caspase-3, and protecting the function of pancreatic beta cells (PBC) (Dhanya et al., 2017; Li et al., 2020; Eid & Haddad, 2017). These studies may provide a useful foundation for future research and development into the anti-diabetic activity of flavonoids found in *S. grosvenorii*.

### Antibacterial Activity

The widespread use of antibiotics has led to an increasing number of drug-resistant bacteria, so developing new and natural antibacterial drugs has become a hotspot in the research field (Huang et al., 2022; Shahid et al., 2022). The antibacterial properties of flavonoids have been demonstrated in several studies, and they have also been used to create new antibacterial agents and antibacterial medications. Flavonoids inhibit bacteria mainly by affecting biofilm formation, porin, permeability, and interaction with some key enzymes

(Shamsudin et al., 2022). At the same time, studies have also found that some flavonoids can combine with DNA helicase, thereby inhibiting its ATPase activity and achieving the antibacterial effect. Through structure-activity relationship studies, the antibacterial effect of flavonoids is shown to have a close relationship to the position of the hydroxyl group in the structure of the flavonoid (Adamczak et al., 2019).

Previous studies conducted via a simulated human gastrointestinal tract environment showed that grosvenorine and other metabolites (such as kaempferol, afzelin, a-rhamnoisorobin, and kaempferitrin) extracted from *S. grosvenorii* showed good antibacterial activity. In addition, these substances have higher antibacterial activity against Gram-positive bacteria than against Gram-negative bacteria. The MIC values against Gram-positive bacteria were all less than 70 mg/ml (Wang et al., 2015). Studies have shown that the active components of *S. grosvenorii*, which include kaempferol, had a clear bacteriostatic impact on spoilage bacteria isolated from sauced pork head meat, with *Proteus vulgaris* being the most significantly inhibited of the bacteria studied. (Li et al., 2018). Several investigations have indicated that total phenols and total flavonoids isolated from the roots of *S. grosvenorii* have a specific inhibitory effect on *Aspergillus* sp., *Bacillus subtilis*, *Escherichia coli*, *Pseudomonas aeruginosa*, *Staphylococcus aureus* and *Rhizopus* sp (Yang et al., 2022).

### Anti-inflammatory Activity

Inflammation is a complex protective response produced by the body to eliminate harmful stimuli such as pathogens, irritants, or damaged cells, and it is implicated in many diseases such as diabetes, asthma, cardiovascular disease, and cancer (Kaur & Singh, 2022; Razak et al., 2023). Although anti-inflammatory drugs can effectively treat diseases, their damage and side effects on the body cannot be ignored (Bibbins-Domingo, 2016). As a result, using natural compounds derived from medicinal plants to treat inflammation has become popular, with polyphenols and flavonoids receiving particular attention due to their anti-inflammatory properties (Zhang et al., 2022). The anti-inflammatory effects of flavonoids are mainly exerted by inhibiting the activities of a variety of enzymes and the production of inflammatory mediators (Suriyaprom et al., 2023; Liu et al., 2023). The anti-inflammatory effects of flavonoids are shown in Figure 5.

Studies have found that kaempferol and quercetin can achieve anti-inflammatory effects by regulating the inducible nitric oxide synthase (iNOS), inhibiting the expression of lipoxygenase (LOX), and cyclooxygenase-2 (COX-2) as well as regulating the gene expression of inflammatory molecules (Septembre-Malaterre et al., 2022; Pal et al., 2023). In addition, it has also been found that kaempferin extracted from the residual extract of *S. grosvenorii* can exert anti-inflammatory activity by inhibiting the expression of TNF- $\alpha$ /IFN- $\gamma$ -induced filaggrin and blocking MAPK activation (Sung et al., 2020).

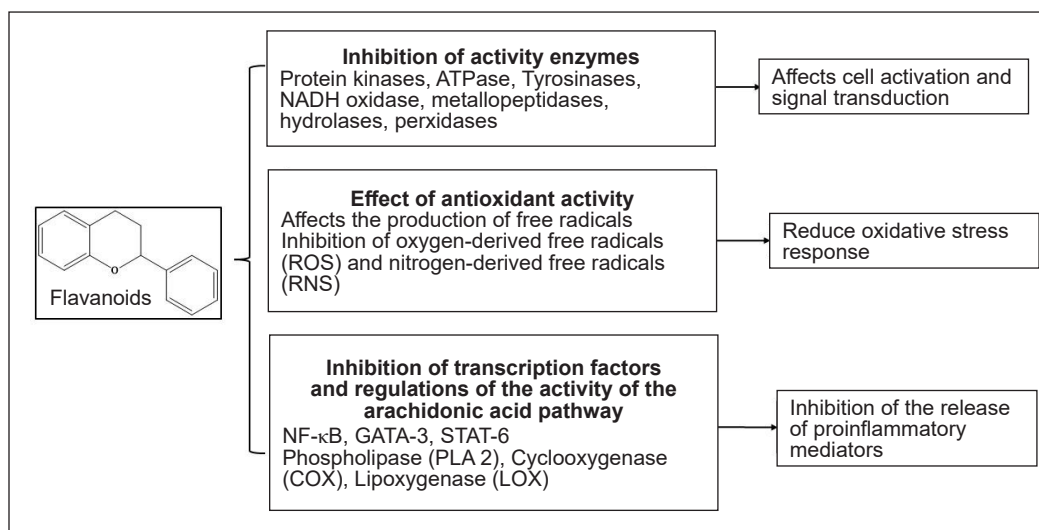


Figure 5. The anti-inflammatory effects of flavonoids

### Other Activities

*S. grosvenorii*-flavonoids have antioxidant, antibacterial and hypoglycemic biological activities that protect the cardiovascular system and relieve fatigue (Zhou, 2022). In addition, some studies have shown that flavonoids in *S. grosvenorii* promote blood circulation and remove blood stasis. It has a protective effect on thrombosis, reduces TC and TG contents in hypercholesterolemic mice, increases HDL-C levels, and prolongs coagulation time in mice.

In summary, there have been many studies on the activity of flavonoids in the past decade, but most of their themes have focused on the antioxidant activity of flavonoids. The ability of flavonoids to act as active agents in vitro has been a hot research topic, and many structure-activity relationships for activity have been established. However, few studies have been conducted on the efficacy of flavonoids in vivo and the mechanisms underlying the distinct types of activity. In order to further develop and utilize the active value of flavonoids, a large number of additional research initiatives are necessary.

### CONCLUSION AND FUTURE PERSPECTIVES

This review provides pertinent opinions and ideas for its future development by summarizing the extraction procedure, major constituents, related structures, and biological activities of *S. grosvenorii*-flavonoids. Previous studies have demonstrated that *S. grosvenorii* has tremendous potential as a food additive and medication. Due to their wide variety of biological activities, its various extracts have also been shown to have tremendous application potential. Although mogrosides are believed to be the primary active ingredients in *S. grosvenorii*, other active ingredients contribute to the organism's

functionality. *S. grosvenorii*-flavonoids are an essential component of the plant for which research, development, and utilization are indispensable.

Presently, there are few studies on *S. grosvenorii*-flavonoids, with the majority of these studies focusing on the extraction procedure and a small quantity of activity research. Given the current problems and deficiencies in *S. grosvenorii*-flavonoids research, we have proposed a new direction for future research: (1) in order to further understand the characteristics of *S. grosvenorii* and its extracts, it is necessary to explore and discover more biological activities, (2) in order to better develop and apply the biological activity of *S. grosvenorii*, the mechanisms of its activity should be further explored, (3) based on in vitro activity studies, different levels of activity studies were comprehensively carried out, including *in vivo*, *in ovo*, and (4) make full use of its activity and apply it in related fields.

In conclusion, if fully developed and utilized, *S. grosvenorii*'s active compounds will be of immeasurable value for future research. The active components from *S. grosvenorii* still need to be developed further, and more research needs to be done on the individual components' active properties so that new applications can be developed.

## ACKNOWLEDGEMENTS

This work was supported by the Department of Food Sciences, Faculty of Science and Technology, Universiti Kebangsaan Malaysia (Funding No.:ST-2019-013, UKM-TR-018, and ST-2021-010) and supported by INTI International University, Malaysia (INTI-FHLS-11-03-2022 and INTI-FHLS-01-03-2022).

## REFERENCES

- Abdel-Hamid, M., Romeih, E., Huang, Z., Enomoto, T., Huang, L., & Li, L. (2020). Bioactive properties of probiotic set-yogurt supplemented with *Siraitia grosvenorii* fruit extract. *Food Chemistry*, 303, Article 125400. <https://doi.org/10.1016/j.foodchem.2019.125400>
- Adamczak, A., Ożarowski, M., & Karpiński, T. M. (2019). Antibacterial activity of some flavonoids and organic acids widely distributed in plants. *Journal of Clinical Medicine*, 9(1), Article 109. <https://doi.org/10.3390/jcm9010109>
- Akter, M., Parvin, M. S., Hasan, M. M., Rahman, M. A. A., & Islam, M. E. (2022). Anti-tumor and antioxidant activity of kaempferol-3-O-alpha-L-rhamnoside (Afzelin) isolated from *Pithecellobium dulce* leaves. *BMC Complementary Medicine and Therapies*, 22(1), Article 169. <https://doi.org/10.1186/s12906-022-03633-x>
- Alkhalidy, H., Moore, W., Wang, A., Luo, J., McMillan, R. P., Wang, Y., Zhen, W., Hulver, M. W., & Liu, D. (2018). Kaempferol ameliorates hyperglycemia through suppressing hepatic gluconeogenesis and enhancing hepatic insulin sensitivity in diet-induced obese mice. *The Journal of Nutritional Biochemistry*, 58, 90-101. <https://doi.org/10.1016/j.jnutbio.2018.04.014>
- Alkhalidy, H., Moore, W., Zhang, Y., McMillan, R., Wang, A., Ali, M., Suh, K.S., Zhen, W., Cheng, Z., Jia, Z., & Hulver, M. (2015). Small molecule kaempferol promotes insulin sensitivity and preserved pancreatic

- $\beta$ -cell mass in middle-aged obese diabetic mice. *Journal of Diabetes Research*, 2015, 1-14. <https://doi.org/10.1155/2015/532984>
- Azfaralariff, A., Farahfaiqah, F., Shahid, M., Sanusi, S. A., Law, D., Isa, A. R.M., Muhamad, M., Tsui, T. T., & Fazry, S. (2022). *Marantodes pumilum*: Systematic computational approach to identify their therapeutic potential and effectiveness. *Journal of Ethnopharmacology*, 283, Article 114751. <https://doi.org/10.1016/j.jep.2021.114751>
- Barreca, M. M., Alessandro, R., & Corrado, C. (2023). Effects of flavonoids on cancer, cardiovascular and neurodegenerative diseases: Role of NF- $\kappa$ B signaling pathway. *International Journal of Molecular Sciences*, 24(11), Article 9236. <https://doi.org/10.3390/ijms24119236>
- Beg, M. A., Shivangi, Afzal, O., Akhtar, M. S., Altamimi, A. S., Hussain, A., Imam, M. A., Ahmad, M. N., Chopra, S., & Athar, F. (2022). Potential efficacy of  $\beta$ -Amyrin targeting mycobacterial universal stress protein by *in vitro* and *in silico* approach. *Molecules*, 27(14), Article 4581. <https://doi.org/10.3390/molecules27144581>
- Bian, Y., Lei, J., Zhong, J., Wang, B., Wan, Y., Li, J., Liao, C., He, Y., Liu, Z., Ito, K., & Zhang, B. (2022). Kaempferol reduces obesity, prevents intestinal inflammation, and modulates gut microbiota in high-fat diet mice. *The Journal of Nutritional Biochemistry*, 99, Article 108840. <https://doi.org/10.1016/j.jnutbio.2021.108840>
- Bibbins-Domingo, K. (2016). Aspirin use for the primary prevention of cardiovascular disease and colorectal cancer: US preventive services task force recommendation statement. *Annals of Internal Medicine*, 164(12), 836-845. <https://doi.org/10.7326/M16-0577>
- Cai Shi, D., Long, C., Vardeman, E., Kennelly, E. J., Lawton, M. A., & Di, R. (2023). Potential anti-alzheimer properties of mogrosides in vitamin B12-deficient caenorhabditis elegans. *Molecules*, 28(4), Article 1826. <https://doi.org/10.3390/molecules28041826>
- Chaturvedula, V. S. P., & Prakash, I. (2013). Isolation and structure elucidation of daidzein and genistein from *Siraitia grosvenorii*. *Asian Journal of Pharmaceutical Research and Development*, 1(1), 67-72.
- Chen, Y., Zhang, L., Li, Z., Wu, Z., Lin, X., Li, N., Shen, R., Wei, G., Yu, N., Gong, F., & Ji, G. (2022). Mogrol attenuates osteoclast formation and bone resorption by inhibiting the TRAF6/MAPK/NF- $\kappa$ B signaling pathway *in vitro* and protects against osteoporosis in postmenopausal mice. *Frontiers in Pharmacology*, 13, Article 803880. <https://doi.org/10.3389/fphar.2022.803880>
- Cheun-Arom, T., & Sritularak, B. (2023). *In vitro* antidiabetic and advanced glycation end products inhibitory activity of methanol extracts of various dendrobium species. *Journal of Applied Pharmaceutical Science*, 13(6), 100-107. <https://doi.org/10.7324/JAPS.2023.75102>
- Čižmarová, B., Hubková, B., Tomečková, V., & Birková, A. (2023). Flavonoids as promising natural compounds in the prevention and treatment of selected skin diseases. *International Journal of Molecular Sciences*, 24(7), Article 6324. <https://doi.org/10.3390/ijms24076324>
- Dahlén, A. D., Dashi, G., Maslov, I., Attwood, M. M., Jonsson, J., Trukhan, V., & Schiöth, H. B. (2022). Trends in antidiabetic drug discovery: FDA approved drugs, new drugs in clinical trials and global sales. *Frontiers in Pharmacology*, 12, Article 807548. <https://doi.org/10.3389/fphar.2021.807548>

- Dhanya, R., Arya, A. D., Nisha, P., & Jayamurthy, P. (2017). Quercetin, a lead compound against type 2 diabetes ameliorates glucose uptake via AMPK pathway in skeletal muscle cell line. *Frontiers in Pharmacology*, 8, Article 336. <https://doi.org/10.3389/fphar.2017.00336>
- Duan, J., Zhu, D., Zheng, X., Ju, Y., Wang, F., Sun, Y., & Fan, B. (2023). *Siraitia grosvenorii* (Swingle) C. Jeffrey: Research progress of its active components, pharmacological effects, and extraction methods. *Foods*, 12(7), Article 1373. <https://doi.org/10.3390/foods12071373>
- Eid, H. M., & Haddad, P. S. (2017). The antidiabetic potential of quercetin: underlying mechanisms. *Current Medicinal Chemistry*, 24(4), 355-364. <https://doi.org/10.2174/0929867323666160909153707>
- Fang, C., Wang, Q., Liu, X., & Xu, G. (2017). Metabolic profiling analysis of *Siraitia grosvenorii* revealed different characteristics of green fruit and saccharified yellow fruit. *Journal of Pharmaceutical and Biomedical Analysis*, 145, 158-168. <https://doi.org/10.1016/j.jpba.2017.06.046>
- Gong, P., Guo, Y., Chen, X., Cui, D., Wang, M., Yang, W., & Chen, F. (2022). Structural characteristics, antioxidant and hypoglycemic activities of polysaccharide from *Siraitia grosvenorii*. *Molecules*, 27(13), Article 4192. <https://doi.org/10.3390/molecules27134192>
- Gong, X., Chen, N., Ren, K., Jia, J., Wei, K., Zhang, L., Lv, Y., Wang, J. and Li, M. (2019). The fruits of *Siraitia grosvenorii*: A review of a Chinese food-medicine. *Frontiers in Pharmacology*, 10, Article 1400. <https://doi.org/10.3389/fphar.2019.01400>
- Huang, W., Wang, Y., Tian, W., Cui, X., Tu, P., Li, J., Shi, S., & Liu, X. (2022). Biosynthesis investigations of terpenoid, alkaloid, and flavonoid antimicrobial agents derived from medicinal plants. *Antibiotics*, 11(10), Article 1380. <https://doi.org/10.3390/antibiotics11101380>
- Ibrahim, N. N. A., Wan Mustapha, W. A., Sofian-Seng, N. S., Lim, S. J., Razali, N. S. M., Teh, A. H., & Mediani, A. (2023). A comprehensive review with future prospects on the medicinal properties and biological activities of *Curcuma caesia* Roxb. *Evidence-Based Complementary and Alternative Medicine*, 2023, Article 7006565. <https://doi.org/10.1155/2023/7006565>
- Irfan, M., Almotiri, A., & AlZeyadi, Z. A. (2022). Antimicrobial resistance and its drivers - A review. *Antibiotics*, 11(10), Article 1362. <https://doi.org/10.3390/antibiotics11101362>
- Janibekov, A. A., Youssef, F. S., Ashour, M. L., & Mamadalieva, N. Z. (2018). New flavonoid glycosides from two *Astragalus* species (*Fabaceae*) and validation of their antihyperglycaemic activity using molecular modelling and *in vitro* studies. *Industrial Crops and Products*, 118, 142-148. <https://doi.org/10.1016/j.indcrop.2018.03.034>
- Ju, P., Ding, W., Chen, J., Cheng, Y., Yang, B., Huang, L., Zhou, Q., Zhu, C., Li, X., Wang, M., & Chen, J. (2020). The protective effects of Mogroside V and its metabolite 11-oxo-mogrol of intestinal microbiota against MK801-induced neuronal damages. *Psychopharmacology*, 237, 1011-1026. <https://doi.org/10.1007/s00213-019-05431-9>
- Kaur, B., & Singh, P. (2022). Inflammation: Biochemistry, cellular targets, anti-inflammatory agents and challenges with special emphasis on cyclooxygenase-2. *Bioorganic Chemistry*, 121, 105663. <https://doi.org/10.1016/j.bioorg.2022.105663>
- Keylani, K., Mojeni, F. A., Khalaji, A., Rasouli, A., Aminzade, D., Karimi, M. A., Sanaye, P. M., Khajevand, N., Nemayandeh, N., Poudineh, M., & Deravi, N. (2023). Endoplasmic reticulum as a target in cardiovascular

- diseases: Is there a role for flavonoids? *Frontiers in Pharmacology*, 13, Article 1027633. <https://doi.org/10.3389/fphar.2022.1027633>
- Khuntia, A., Martorell, M., Ilango, K., Bungau, S. G., Radu, A. F., Behl, T., & Sharifi-Rad, J. (2022). Theoretical evaluation of Cleome species' bioactive compounds and therapeutic potential: A literature review. *Biomedicine & Pharmacotherapy*, 151, Article 113161. <https://doi.org/10.1016/j.biopha.2022.113161>
- Kropp, M., Golubnitschaja, O., Mazurakova, A., Koklesova, L., Sargheini, N., Vo, T. T. K. S., De Clerck, E., Polivka J. J., Potuznik, P., Polivka, J., Stetkarova, I., Kubatka, P., & Thumann, G. (2023). Diabetic retinopathy as the leading cause of blindness and early predictor of cascading complications - Risks and mitigation. *EPMA Journal*, 14, 21-42. <https://doi.org/10.1007/s13167-023-00314-8>
- Li, D., Jiang, C., Mei, G., Zhao, Y., Chen, L., Liu, J., Tang, Y., Gao, C., & Yao, P. (2020). Quercetin alleviates ferroptosis of pancreatic  $\beta$  cells in type 2 diabetes. *Nutrients*, 12(10), Article 2954. <https://doi.org/10.3390/nu12102954>
- Li, H., Li, R., Jiang, W., & Zhou, L. (2022). Research progress of pharmacological effects of *Siraitia grosvenorii* extract. *Journal of Pharmacy and Pharmacology*, 74(7), 953-960. <https://doi.org/10.1093/jpp/rgab150>
- Li, H., Liu, L., Chen, H. Y., Yan, X., Li, R. L., Lan, J., Xue, K.Y., Li, X., Zhuo, C.L., Lin, L., & Zhou, L. (2022). Mogrol suppresses lung cancer cell growth by activating AMPK-dependent autophagic death and inducing *p53-dependent* cell cycle arrest and apoptosis. *Toxicology and Applied Pharmacology*, 444, Article 116037. <https://doi.org/10.1016/j.taap.2022.116037>
- Li, X., Xu, L. Y., Cui, Y. Q., Pang, M. X., Wang, F., & Qi, J. H. (2018). Anti-bacteria effect of active ingredients of *Siraitia grosvenorii* on the spoilage bacteria isolated from sauced pork head meat. *Conference Series: Materials Science and Engineering*, 292, Article 012012. <https://doi.org/10.1088/1757-899X/292/1/012012>
- Liu, H., Du, Y., Liu, L. L., Liu, Q. S., Mao, H., & Cheng, Y. (2023). Anti-depression-like effect of Mogroside V is related to the inhibition of inflammatory and oxidative stress pathways. *European Journal of Pharmacology*, 955, Article 175828. <https://doi.org/10.1016/j.ejphar.2023.175828>
- Liu, W., Cui, X., Zhong, Y., Ma, R., Liu, B., & Xia, Y. (2023). Phenolic metabolites as therapeutic in inflammation and neoplasms: molecular pathways explaining their efficacy. *Pharmacological Research*, 193, Article 106812. <https://doi.org/10.1016/j.phrs.2023.106812>
- Liu, X., Zhang, J., Li, Y., Sun, L., Xiao, Y., Gao, W., & Zhang, Z. (2019). Mogroside derivatives exert hypoglycemics effects by decreasing blood glucose level in HepG2 cells and alleviates insulin resistance in T2DM rats. *Journal of Functional Foods*, 63, Article 103566. <https://doi.org/10.1016/j.jff.2019.103566>
- Liu, Z., Zhu, X., Mohsin, A., Yin, Z., Zhuang, Y., Zhou, B., Du, L., Yin, X., Liu, N., Wang, Z., & Guo, M. (2022). Embryogenic callus induction, cell suspension culture, and spectrum-effect relationship between antioxidant activity and polyphenols composition of *Siraitia grosvenorii* cultured cells. *Industrial Crops and Products*, 176, Article 114380. <https://doi.org/10.1016/j.indcrop.2021.114380>
- Lu, F., Sun, J., Jiang, X., Song, J., Yan, X., Teng, Q., & Li, D. (2023). Identification and isolation of  $\alpha$ -glucosidase inhibitors from *Siraitia grosvenorii* roots using bio-affinity ultrafiltration and comprehensive chromatography. *International Journal of Molecular Sciences*, 24(12), Article 10178. <https://doi.org/10.3390/ijms241210178>

- Lü, W., Ren, G., Shimizu, K., Li, R., & Zhang, C. (2024). Mogroside IIE, an *in vivo* metabolite of sweet agent, alleviates acute lung injury via Pla2g2a-EGFR inhibition. *Food Science and Human Wellness*, 13(1), 299-312. <https://doi.org/10.26599/FSHW.2022.9250025>
- Lu, Y., Zhu, S., He, Y., Mo, C., Wu, C., Zhang, R., Zheng, X., & Tang, Q. (2020). Systematic characterization of flavonoids from *Siraitia grosvenorii* leaf extract using an integrated strategy of high-speed counter-current chromatography combined with ultra-highperformance liquid chromatography and electrospray ionization quadrupole time-of-flight mass spectrometry. *Journal of Separation Science*, 43(5), 852-864. <https://doi.org/10.1002/jssc.201900789>
- Luo, H., Peng, C., Xu, X., Peng, Y., Shi, F., Li, Q., Dong, J., & Chen, M. (2022). The protective effects of mogroside V against neuronal damages by attenuating mitochondrial dysfunction via upregulating Sirtuin3. *Molecular Neurobiology*, 59(4), 2068-2084. <https://doi.org/10.1007/s12035-021-02689-z>
- Mitra, S., Lami, M. S., Uddin, T. M., Das, R., Islam, F., Anjum, J., Hossain, M.J., & Emran, T. B. (2022). Prospective multifunctional roles and pharmacological potential of dietary flavonoid narirutin. *Biomedicine & Pharmacotherapy*, 150, Article 112932. <https://doi.org/10.1016/j.biopha.2022.112932>
- Mo, L., & Li, D. (2009). Antioxidant activity of flavonol glycosides of *Siraitia grosvenorii* flower. *Modern Food Science and Technology*, 25(5), 484-486.
- Moudaka, T. E., Murugan, P., Abdul Rahman, M. B., & Tejo, B. A. (2023). Discovery of mycobacterium tuberculosis CYP121 new inhibitor via structure-based drug repurposing. *Pertanika Journal of Science & Technology*, 31(3), 1503-1521. <https://doi.org/10.47836/pjst.31.3.21>
- Najm, A. A., Azfaralarriff, A., Dyari, H. R. E., Alwi, S. S. S., Khalili, N., Othman, B. A., Law, D., Shahid, M., & Fazry, S. (2022). A systematic review of antimicrobial peptides from fish with anticancer properties. *Pertanika Journal of Science & Technology*, 30(2), 1171-1196. <https://doi.org/10.47836/pjst.30.2.18>
- Ooi, T. C., Ibrahim, F. W., Ahmad, S., Chan, K. M., Leong, L. M., Mohammad, N., & Rajab, N. F. (2021). Antimutagenic, cytoprotective and antioxidant properties of ficus deltoidea aqueous extract *in vitro*. *Molecules*, 26(11), Article 3287. <https://doi.org/10.3390/molecules26113287>
- Pal, R., Kumar, L., Anand, S., & Bharadvaja, N. (2023). Role of natural flavonoid products in managing osteoarthritis. *Revista Brasileira de Farmacognosia*, 33, 663-675. <https://doi.org/10.1007/s43450-023-00387-6>
- Pan, Y., Wei, L., Zhu, Z., Liang, Y., Huang, C., Wang, H., & Wang, K. (2012). Processing of *Siraitia grosvenorii* leaves: Extraction of antioxidant substances. *Biomass and Bioenergy*, 36, 419-426. <https://doi.org/10.1016/j.biombioe.2011.11.011>
- Pandey, A. K., & Chauhan, O. P. (2019). Monk fruit (*Siraitia grosvenorii*) - Health aspects and food applications. *Pantnagar Journal of Research*, 17(3), 191-198.
- Pasala, P. K., Shaik, R. A., Rudrapal, M., Khan, J., Alaidarous, M. A., Khairnar, S. J., Bendale, A. R., Naphade, V. D., Sahoo, R. K., Zothantluanga, J. H., & Walode, S. G. (2022). Cerebroprotective effect of Aloe Emodin: In silico and *in vivo* studies. *Saudi Journal of Biological Sciences*, 29(2), 998-1005. <https://doi.org/10.1016/j.sjbs.2021.09.077>
- Qing, Z. X., Zhao, H., Tang, Q., Mo, C. M., Huang, P., Cheng, P., Yang, P., Yang, X. Y., Liu, X. B., Zheng, Y. J., & Zeng, J. G. (2017). Systematic identification of flavonols, flavonol glycosides, triterpene and siraitic



- acid glycosides from *Siraitia grosvenorii* using high-performance liquid chromatography/quadrupole-time-of-flight mass spectrometry combined with a screening strategy. *Journal of Pharmaceutical and Biomedical Analysis*, 138, 240-248. <https://doi.org/10.1016/j.jpba.2017.01.059>
- Rao, R., Yang, R. J., Deng, Y. Y., He, X. Y., Ye, X. C., & Liu, Y. W. (2012). Determination of total flavonoids in *Siraitia grosvenorii* swingle fruit extract and vine leaf extract. *China Pharmacist*, 15, 7-9.
- Razak, A. M., Zakaria, S. N. A., Sani, N. F. A., Rani, N. A., Hakimi, N. H., Said, M. M., Jen, K. T., Han, K. G., & Makpol, S. (2023). A subcritical water extract of soil grown *Zingiber officinale* Roscoe: Comparative analysis of antioxidant and anti-inflammatory effects and evaluation of bioactive metabolites. *Frontiers in Pharmacology*, 14, Article 1006265. <https://doi.org/10.3389/fphar.2023.1006265>
- Septembre-Malaterre, A., Boumendjel, A., Seteyen, A. L. S., Boina, C., Gasque, P., Guiraud, P., & Sélambarom, J. (2022). Focus on the high therapeutic potentials of quercetin and its derivatives. *Phytomedicine Plus*, 2(1), Article 100220. <https://doi.org/10.1016/j.phyplu.2022.100220>
- Sethupathi, P., Matetić, A., Bang, V., Myint, P. K., Rendon, I., Bagur, R., Diaz-Arocutipa, C., Ricalde, A., & Mamas, M. A. (2023). Association of diabetes mellitus and its types with in-hospital management and outcomes of patients with acute myocardial infarction. *Cardiovascular Revascularization Medicine*, 52, 16-22 <https://doi.org/10.1016/j.carrev.2023.02.008>
- Shahid, M., Law, D., Azfaralariff, A., Mackeen, M. M., Chong, T. F., & Fazry, S. (2022). Phytochemicals and biological activities of *Garcinia atroviridis*: A critical review. *Toxics*, 10(11), Article 656. <https://doi.org/10.3390/toxics10110656>
- Shamsudin, N. F., Ahmed, Q. U., Mahmood, S., Shah, S. A. A., Khatib, A., Mukhtar, S., Alsharif, M.A., Parveen, H., & Zakaria, Z. A. (2022). Antibacterial effects of flavonoids and their structure-activity relationship study: A comparative interpretation. *Molecules*, 27(4), Article 1149. <https://doi.org/10.3390/molecules27041149>
- Sharma, D., Tekade, R. K., & Kalia, K. (2020). Kaempferol in ameliorating diabetes-induced fibrosis and renal damage: An *in vitro* and *in vivo* study in diabetic nephropathy mice model. *Phytomedicine*, 76, Article 153235. <https://doi.org/10.1016/j.phymed.2020.153235>
- Shen, J., Shen, D., Tang, Q., Li, Z., Jin, X., & Li, C. (2022). Mogroside V exerts anti-inflammatory effects on fine particulate matter-induced inflammation in porcine alveolar macrophages. *Toxicology in Vitro*, 80, Article 105326. <https://doi.org/10.1016/j.tiv.2022.105326>
- Shen, N., Wang, T., Gan, Q., Liu, S., Wang, L., & Jin, B. (2022). Plant flavonoids: Classification, distribution, biosynthesis, and antioxidant activity. *Food Chemistry*, 383, Article 132531. <https://doi.org/10.1016/j.foodchem.2022.132531>
- Singh, A., Kukreti, R., Saso, L., & Kukreti, S. (2022). Mechanistic insight into oxidative stress-triggered signaling pathways and type 2 diabetes. *Molecules*, 27(3), Article 950. <https://doi.org/10.3390/molecules27030950>
- Song, J. R., Li, N., Wei, Y. L., Lu, F. L., & Li, D. P. (2022). Design and synthesis of mogrol derivatives modified on a ring with anti-inflammatory and anti-proliferative activities. *Bioorganic & Medicinal Chemistry Letters*, 74, Article 128924. <https://doi.org/10.1016/j.bmcl.2022.128924>

- Su, M., Li, Z., Zhou, S., Zhang, H., Xiao, Y., Li, W., Shang, H., & Li, J. (2023). Kaempferitrin, a major compound from ethanol extract of *Chenopodium ambrosioides*, exerts antitumour and hepatoprotective effects in the mice model of human liver cancer xenografts. *Journal of Pharmacy and Pharmacology*, 75(8), 1066-1075. <https://doi.org/10.1093/jpp/rgad046>
- Sung, Y. Y., Yuk, H. J., Yang, W. K., Kim, S. H., & Kim, D. S. (2020). *Siraitia grosvenorii* residual extract attenuates atopic dermatitis by regulating immune dysfunction and skin barrier abnormality. *Nutrients*, 12(12), Article 3638. <https://doi.org/10.3390/nu12123638>
- Suriyaprom, S., Srisai, P., Intachaisri, V., Kaewkod, T., Pekkoh, J., Desvaux, M., & Tragoolpua, Y. (2023). Antioxidant and anti-inflammatory activity on LPS-stimulated RAW 264.7 macrophage cells of white mulberry (*Morus alba* L.) leaf extracts. *Molecules*, 28(11), Article 4395. <https://doi.org/10.3390/molecules28114395>
- Thakur, K., Partap, M., Kumar, P., Sharma, R., & Warghat, A. R. (2022). Understandings of bioactive composition, molecular regulation, and biotechnological interventions in the development and usage of specialized metabolites as health-promoting substances in *Siraitia grosvenorii* (Swingle) C. Jeffrey. *Journal of Food Composition and Analysis*, 116, Article 105070. <https://doi.org/10.1016/j.jfca.2022.105070>
- Wang, M., Xing, S., Luu, T., Fan, M., & Li, X. (2015). The gastrointestinal tract metabolism and pharmacological activities of *grosvenorine*, a major and characteristic flavonoid in the fruits of *Siraitia grosvenorii*. *Chemistry & Biodiversity*, 12(11), 1652-1664. <https://doi.org/10.1002/cbdv.201400397>
- Wang, Y., Li, H. B., Bai, X. F., Zhang, M., Li, X. M. (2006). Study on enzyme-solvent extraction process for flavonoid from *Momordica grosvenorii*. *Food Science and Technology*, 31, 125-127.
- Wu, J., Jian, Y., Wang, H., Huang, H., Gong, L., Liu, G., Yang, Y., & Wang, W. (2022). A review of the phytochemistry and pharmacology of the fruit of *Siraitia grosvenorii* (Swingle): A traditional Chinese medicinal food. *Molecules*, 27(19), Article 6618. <https://doi.org/10.3390/molecules27196618>
- Wuttisin, N., & Boonsook, W. (2019). Total phenolic, flavonoid contents and antioxidant activity of *Siraitia grosvenorii* fruits extracts. *Food and Applied Bioscience Journal*, 7(3), 131-141.
- Xu, H., Xu, M., Yuan, F., & Gao, Y. (2017). Chemical and antioxidant properties of functional compounds extracted from *Siraitia grosvenorii* by subcritical water. *Acta Alimentaria*, 46(2), 162-171. <https://doi.org/10.1556/066.2016.0006>
- Yanan, S., Bohan, L., Shuaifeng, S., Wendan, T., Ma, Z., & Wei, L. (2023). Inhibition of Mogroside III E on isoproterenol-induced myocardial fibrosis through the TLR4/MyD88/NF- $\kappa$ B signaling pathway. *Iranian Journal of Basic Medical Sciences*, 26(1), 114-120.
- Yang, L., Zeng, S., Li, Z. H., & Pan, Y. M. (2016). Chemical components of the leaves of *Siraitia grosvenorii*. *Chemistry of Natural Compounds*, 52, 891-892. <https://doi.org/10.1007/s10600-016-1805-2>
- Yang, Z., Wang, H., Qi, G., Chen, G., Cao, C., & Wang, S. (2022). Antimicrobial effects of a compound solution of three medicine food homology plants. *Food Bioscience*, 49, Article 101845. <https://doi.org/10.1016/j.fbio.2022.101845>
- Yedjou, C. G., Grigsby, J., Mbemi, A., Nelson, D., Mildort, B., Latinwo, L., & Tchounwou, P. B. (2023). The management of diabetes mellitus using medicinal plants and vitamins. *International Journal of Molecular Sciences*, 24(10), Article 9085. <https://doi.org/10.3390/ijms24109085>

- Zang, E., Jiang, L., Cui, H., Li, X., Yan, Y., Liu, Q., Chen, Z., & Li, M. (2022). Only plant-based food additives: An overview on application, safety, and key challenges in the food industry. *Food Reviews International*, 39(8), 5132-5163. <https://doi.org/10.1080/87559129.2022.2062764>
- Zhang, C., Rong, D., & Zhang, Z. (2013). 罗汉果花中黄酮的提取及结构表征 (Extraction and structural characterization of flavonoids from monk fruit flowers). *Spectroscopy Laboratory*, 30(3), 1389-1394. <https://doi.org/10.3969/j.issn.1004-8138.2013.03.080>
- Zhang, H. Y., Yang, H. H., Zhang, M., Wang, Y. R., Wang, J. R., Jiang, Z. H., & Hu, P. (2013). Comparative analysis of chemical constituents in different parts of *Siraitia grosvenorii* using UPLC-MS combined with pattern recognition. *Chinese Traditional and Herbal Drugs*, 44(1), 19-23.
- Zhang, Y., Zhou, G., Peng, Y., Wang, M., & Li, X. (2020). Anti-hyperglycemic and anti-hyperlipidemic effects of a special fraction of luohan guo extract on obese T2DM rats. *Journal of Ethnopharmacology*, 247, Article 112273. <https://doi.org/10.1016/j.jep.2019.112273>
- Zhang, Z., Li, X., Sang, S., McClements, D. J., Chen, L., Long, J., Jiao, A., Jin, Z., & Qiu, C. (2022). Polyphenols as plant-based nutraceuticals: Health effects, encapsulation, nano-delivery, and application. *Foods*, 11(15), Article 2189. <https://doi.org/10.3390/foods11152189>
- Zhang, Z. R., Sun, G. R., Duan, X. Y., & Jiang, G. Q. (2016) Optimization of ultrasonic-assisted extraction process for total flavonoids from *Siraitia grosvenorii* flower by response surface methodology. *Hubei Agricultural Science*, 55, 1518-1522.
- Zhou, H. (2022). Study on the role of nutrients in food to improve the motion state of athletes. *Italian Journal of Food Science*, 34(2), 28-33. <https://doi.org/10.15586/ijfs.v34i2.2126>
- Zhu, Y. M., Pan, L. C., Zhang, L. J., Yin, Y., Zhu, Z. Y., Sun, H. Q., & Liu, C. Y. (2020). Chemical structure and antioxidant activity of a polysaccharide from *Siraitia grosvenorii*. *International Journal of Biological Macromolecules*, 165, 1900-1910. <https://doi.org/10.1016/j.ijbiomac.2020.10.127>



# Loss-of-Life Analyses Based on Modified Arrhenius and Relative Aging Rate for Non-Thermally Upgraded Paper in Oil-Immersed Transformer

Najiyah Saleh<sup>1,2</sup>, Norhafiz Azis<sup>1,3\*</sup>, Jasronita Jasni<sup>1</sup>, Mohd Zainal Abidin Ab Kadir<sup>1</sup> and Mohd Aizam Talib<sup>4</sup>

<sup>1</sup>Advanced Lightning, Power and Energy Research Centre (ALPER), Faculty of Engineering, Universiti Putra Malaysia, 43400 UPM, Serdang, Selangor, Malaysia

<sup>2</sup>Electrical Technology Section, Universiti Kuala Lumpur British Malaysian Institute, 53100 Gombak, Selangor, Malaysia

<sup>3</sup>Institute of Nanoscience and Nanotechnology (ION2), Faculty of Engineering, Universiti Putra Malaysia, 43400 UPM, Serdang, Selangor, Malaysia

<sup>4</sup>TNB Research Sdn Bhd, No. 1, Lorong Ayer Itam, Kawasan Institut Penyelidikan, 43000 Kajang, Selangor, Malaysia

## ABSTRACT

This study evaluates the Loss-of-Life (LOL) based on the modified relative aging rate of an Oil Natural Air Natural (ONAN) transformer with voltage and power ratings of 132/33 kV and 60 MVA. The study's methodology included the determination of the Hotspot Temperature (HST) based on the differential equation in IEC 60076-7. The loading and ambient temperature profiles for HST determination are forecasted based on the Seasonal Autoregressive Integrated Moving Average (SARIMA). Next, a new relative aging rate was developed based on the Arrhenius equation, considering the pre-exponential factors governed by oxygen, moisture in paper, and acids at different content levels. The LOL was computed based on the new relative aging rate. The study's main aim is to examine

the impact of pre-exponential factors on the LOL based on modified Arrhenius and relative aging rate. The results indicate that the LOLs for different conditions increase as the oxygen, moisture, low molecular weight acid (LMA), and high molecular weight acid (HMA) increase. The LOLs are 46 days, 1,354 days, and 2,662 days in the presence of 12,000 ppm, 21,000 ppm, and 30,000 ppm of oxygen. In 1%, 3%, and 5%

## ARTICLE INFO

### Article history:

Received: 28 February 2023

Accepted: 24 August 2023

Published: 14 March 2024

DOI: <https://doi.org/10.47836/pjst.32.2.09>

### E-mail addresses:

[najiyahsaleh87@gmail.com](mailto:najiyahsaleh87@gmail.com) (Najiyah Saleh)

[norhafiz@upm.edu.my](mailto:norhafiz@upm.edu.my) (Norhafiz Azis)

[jas@upm.edu.my](mailto:jas@upm.edu.my) (Jasronita Jasni)

[mzk@upm.edu.my](mailto:mzk@upm.edu.my) (Mohd Zainal Abidin Ab Kadir)

[aizam.talib@tmb.com.my](mailto:aizam.talib@tmb.com.my) (Mohd Aizam Talib)

\* Corresponding author

moisture, the LOLs are 477 days, 2,799 days, and 7,315 days. At 1% moisture, the LOL is 1,418 days for LMA, while for HMA, it is 122 days. The LMA has the highest impact on the LOL compared to other aging acceleration factors.

*Keywords:* Arrhenius equation, cellulose aging, loss-of-life, pre-exponential factor, relative aging rate

---

## INTRODUCTION

It is known that the life of power transformers predominantly relies on cellulose-based insulation. Among the approaches to analyzing the life of cellulose paper insulation is thermal life modeling. This approach determines the hot-spot temperature (HST), insulation paper aging rate, and loss-of-life (LOL) of transformers. The input data of ambient temperature and time-varying load control these parameters. The HST, aging rate, and LOL can be computed through models in international standards.

A sufficient input parameter such as loading and ambient temperature profile is essential to increase the accuracy of HST for assessment of the paper aging rate and LOL. However, in most cases, these parameters are not always available, especially for long intervals. Therefore, forecasting these input data would help with long-term analyses. Several methods to forecast the loading were established by Agrawal et al. (2018), Chen et al. (2017), Hou et al. (2021), Khalid et al. (2020), Khorsheed (2021), Mohammed and Al-Bazi (2022), and Sinha et al. (2021). In addition, the ambient temperature profiles were found in Afzali et al. (2011), Hou et al. (2022), Ma et al. (2020), Radhika and Shashi (2009), Tripathy and Prusty (2021), and Van den Berg et al. (2022). Seasonal Autoregressive Integrated Moving Average (SARIMA) is one of the established methods that can be utilized to forecast any short, medium, or long-term data with the characteristic of strong seasonal patterns and univariate time series (Al-Shaikh et al., 2019). The method is promising for forecasting the future loading and ambient temperature profiles for the transformer's application.

Among the primary contributors to the degradation of insulation paper are temperature and aging acceleration factors, i.e., oxygen, moisture in paper, and acids. Due to non-uniform temperature distribution within a transformer, the region that experiences the highest temperature, referred to as the hot spot, undergoes the most substantial degradation and affects the aging rate of the paper. The modeling of the relative aging rate as per IEC 60076-7 (Feng, 2013; Novkovic et al., 2022) relies mainly on the HST as the important parameter without considering other aging acceleration factors. The model is also applied widely in various studies conducted by Biçen et al. (2011, 2012), Najdenkoski et al. (2007), BL and Mathew (2016) and Piatniczka et al. (2022).

A relative aging rate model that considers several aging acceleration factors was previously examined (Hosseinkhanloo et al., 2022). The relative aging rate is obtained

through the ratio of the paper aging rate for any temperatures and conditions over the paper aging rate at the rated condition. The previous study considers two aging factors, i.e., oxygen and moisture, to determine the relative aging rate (Hosseinkhanloo et al., 2022). Recently, the importance of low molecular acid (LMA) and high molecular acid (HMA) to govern paper aging is highlighted, which prompts further modeling study on this aspect. Since the aging in a transformer is a dynamic process, it is anticipated that the pre-exponential factors and activation energies for oxygen and moisture that are directly applied to the CIGRE Brochure 393 (2009) could vary based on the specific aging mechanism to evaluate the relative aging rate.

Modeling paper aging is one of the key aspects of evaluating the integrity of the transformers (Feng, 2013). Currently, there are various methods based on either laboratory accelerated aging experimental data or in-service data that are introduced to evaluate paper aging (Arshad et al., 2004; Liao et al., 2011; Li et al., 2018; Liu et al., 2015; Zhang et al., 2021). The Arrhenius model is one of the common approaches to determining the paper aging rate by considering the aging factors and mechanisms (Feng, 2013). The paper aging rate depends on the HST, pre-exponential factor, and activation energy. Recently, a modified relative aging rate model has been proposed based on the Arrhenius model (Novkovic et al., 2022), which considers the variation of pre-exponential factors according to the paper aging acceleration factors and activation energies, which are based on the aging mechanism (Saleh et al., 2022).

Utilizing the information on pre-exponential factors from the previous work (Saleh et al., 2022), the long-term life assessment based on the modified relative aging rate model is examined. First, the HST is calculated using the differential equation according to IEC 60076-7 (Feng, 2013; Novkovic et al., 2022). The HST computation's loading and ambient temperature profiles are forecasted based on SARIMA. Next, the new relative aging rate is determined based on the pre-exponential factors, the Arrhenius model, and the relative aging rate as per IEC 60076-7 (Feng, 2013; Novkovic et al., 2022). Finally, the LOL is computed based on the pre-determined new relative aging rate. The computation of the new relative aging rate and LOL based on a single aging factor of either oxygen, moisture in paper, or acids in the paper is also examined.

## METHODOLOGY

### Seasonal Autoregressive Integrated Moving Average (SARIMA)

The forecasting of loading input parameters and ambient temperature profiles was modeled using SARIMA since it supported univariate data with seasonal change. The recorded actual loading profile, taken at 15-minute intervals over 15 days, was utilized to forecast the data for one year. Similar to the loading profile, the ambient temperature profile, recorded at 1-hour intervals for seven months, was used to forecast data for one year.

SARIMA is an enhancement based on the ARIMA model that incorporates the parameters of  $(p,d,q) \times (P,D,Q)m$  whereby  $p$  and  $P$  represent the autoregressive and seasonal autoregressive orders, while  $d$  and  $D$  denote the difference and seasonal difference orders, respectively. Additionally,  $q$  and  $Q$  indicate the moving averages and seasonal moving average orders, respectively, and  $m$  stands for the seasonal period. The SARIMA is expressed by Equation 1 (Cabrera et al., 2013), where each term is mathematically defined as in Equations 2, 3, 4, and 5, respectively.

$$\phi_p(B)\Phi_P(B^S)\nabla^d\nabla_S^D Z_t = \theta_q(B)\Theta_Q(B^S)a_t \tag{1}$$

where:

$$\phi_p(B) = 1 - \phi_1 B - \phi_2 B^2 - \dots - \phi_p B^p \tag{2}$$

$$\Phi_P(B^S) = 1 - \Phi_S B^S - \Phi_{2S} B^{2S} - \dots - \Phi_{PS} B^S \tag{3}$$

$$\theta_q(B) = 1 - \theta_1 B - \theta_2 B^2 - \dots - \theta_q B^q \tag{4}$$

$$\Theta_Q(B^S) = 1 - \Theta_S B^S - \Theta_{2S} B^{2S} - \dots - \Theta_{QS} B^S \tag{5}$$

Where  $p$  represents the order of non-seasonal auto-regression,  $d$  is the number of regular differencing,  $q$  denotes the order of non-seasonal MA,  $P$  signifies the order of seasonal auto-regression,  $D$  is the number of seasonal differencing,  $Q$  indicates the order of seasonal MA,  $S$  denotes the length of seasonality,  $\phi$  is the AR operator of order  $p$ ,  $\Phi$  is the seasonal AR parameter of order  $P$ ,  $\nabla$  is the differencing operator,  $D$  is the seasonal differencing operator,  $Z_t$  is the observed value at time point  $t$ ,  $\theta$  is the MA operator of order  $q$ ,  $\Theta$  is the seasonal MA parameter of order  $Q$  and  $a_t$  is the white noise component of the stochastic model (Cabrera et al., 2013).

### Accuracy Measurement

The accuracy measurement of the forecasted loading profile and ambient temperature profile was conducted based on three metrics known as Mean Absolute Percentage Error (MAPE), Mean Absolute Error (MAE), and Root Mean Square Error (RMSE). Low MAPE, MAE, and RMSE indicate a well-fitted model, defined by Equations 6, 7, and 8, respectively.

$$MAPE = \frac{1}{N} \left( \sum_{t=1}^N \left| \frac{Y_t - \hat{Y}_t}{Y_t} \right| \right) \times 100 \tag{6}$$

$$MAE = \frac{1}{N} \left( \sum_{t=1}^N |Y_t - \hat{Y}_t| \right) \tag{7}$$

$$RMSE = \sqrt{\frac{\sum_{t=1}^N (Y_t - \hat{Y}_t)^2}{N}} \tag{8}$$



Where  $N$  is the number of actual data,  $Y_t$  is the actual data at time,  $t$  and  $\hat{Y}_t$  is the forecasted data at time,  $t$ .

### Thermal Modelling Parameters

The thermal modeling parameters are essential as the input data to determine a transformer's Top-oil Temperature (TOT) and HST based on the differential equation method. The thermal modeling parameters can typically be obtained from the transformer-specific thermal constants (Susa et al., 2005a; Susa et al., 2005b). The standard thermal modeling parameters can be acquired from IEC 60076-7 without specific thermal constants.

Table 1 shows the thermal modelling parameters for the transformer. The thermal modelling parameters were selected based on the ONAN medium and large power transformers as per IEC 60076-7 (Feng, 2013). The oil time constant,  $\tau_o$ ; winding time constant,  $\tau_w$ ; oil exponent,  $x$ ; winding exponent,  $y$ ; the constants,  $k_{11}$ ,  $k_{21}$ , and  $k_{22}$ , were acquired as per IEC 60076-7. The ratio of load losses (copper loss) to no-load losses (iron loss),  $R$  and top-oil temperature rise at rated current,  $\Delta\Theta_{or}$  were obtained per the temperature rise report. The hot-spot to top-oil temperature at rated current,  $\Delta\Theta_{hr}$ , was calculated based on Equation 9 as per IEC 60076-7 (Feng, 2013; Novkovic et al., 2022; Susa et al., 2005a).

$$\Delta\theta_{hr} = H \times g_r \quad [9]$$

Where  $\Delta\theta_{hr}$  is the hot-spot to top-oil temperature at rated current,  $H$  is the hot-spot factor while  $g_r$  is the average winding to average oil gradient. The value of hot-spot factor,  $H$  was directly obtained from (Feng, 2013) and the average winding to average oil gradient,  $g_r$  was acquired based on the temperature rise report. The time step value,  $D_3$ , was set at three minutes since it should be less than half the shortest winding time constant,  $\tau_w$  as per IEC 60076-7 (Feng, 2013; Novkovic et al., 2022).

### Top-Oil Temperature (TOT) and Hot-Spot Temperature (HST) based on IEC60076-7

The TOT and HST were determined based on differential method as per IEC 60076-7 (Feng, 2013; Novkovic et al., 2022). The differential method was selected for its adaptability to the time-varying load and ambient temperature (Feng, 2013). The

Table 1  
*The thermal modelling parameters*

Characteristic	Parameter
Oil exponent, $x$	0.8
Winding exponent, $y$	1.3
Constant, $k_{11}$	0.5
Constant, $k_{21}$	2.0
Constant, $k_{22}$	2.0
Oil time constant, $\tau_o$	210
Winding time constant, $\tau_w$	10
Ratio of load losses to no-load losses, $R$	4.66
Top-oil temperature rise at rated current, $\Delta\Theta_{or}$	44.07
Hot-spot to top-oil temperature at rated current, $\Delta\Theta_{hr}$	33.624
Time step, $D_3$	3 minutes

input parameters of thermal modeling forecasted loading and ambient temperature profiles were utilized to compute the TOT. Subsequently, the HST was computed based on the forecasted loading profile, ambient temperature profile and pre-determined TOT. The evaluation of TOT and HST was considered for a paper’s modified relative aging rate.

### Relative Aging Rate

According to IEC 60076-7, the HST of 98 °C refers to the aging rate of the transformer’s inter-turn insulation under the time and temperature effects for the NTUP (Feng, 2013; Novkovic et al., 2022). Furthermore, the relative aging rate,  $V$  was defined based on Equation 10.

$$V = 2^{(\theta_{hst} - 98)/6} \tag{10}$$

Where  $V$  is the relative aging rate for NTUP while  $\theta_{hst}$  is the HST in °C. It is based on Montsigner’s life expectancy (Feng, 2013) and Dankin’s aging rate formulas (IEEE Standards, 2012), simplified from the Arrhenius equation as shown in Equation 11.

$$\frac{1}{DP_{end}} - \frac{1}{DP_{start}} = A e^{-\frac{E_a}{R(\theta_{hst} + 273)}} \times t \tag{11}$$

Where  $DP_{end}$  and  $DP_{start}$  are the paper DP at any time,  $t$ , or the end-of-life criterion, while  $DP_{start}$  is the initial paper DP. On the other hand,  $A$  is the pre-exponential factor in 1/h;  $E_a$  is the activation energy in kJ/mol,  $R$  is the gas constant in 8.314 J/mol/K,  $\theta_{hst}$  is the HST in °C and  $t$  is the lifetime of the insulation in an hour.

Equation 10 implies that the aging rate does not consider different aging factors, i.e., oxygen, moisture, and acids, and it is simply dependent on HST only. The aging rate,  $k$  of the insulation paper is given based on Equation 12 (Feng, 2013). The Arrhenius equation assumes that the degradation process of an insulation paper is controlled by the aging rate,  $k$  proportional to  $\exp(-E_a/RT)$ .

$$k = A e^{-\frac{E_a}{RT}} \tag{12}$$

If an aging rate at a certain temperature, as well as the paper aging acceleration factors, are rated as 1.0, then the new relative aging rate,  $V_{ntup,modified}$  can be written as Equation 13.

$$V_{ntup,modified} = \frac{\frac{A}{A_r} e^{\frac{1}{R} \left( \frac{E_{a_r}}{\theta_{hst,r} + 273} - \frac{E_a}{\theta_{hst} + 273} \right)}}{2^{(\theta_{hst} - 98)/6}} \tag{13}$$

where  $V_{ntup,modified}$  is the new relative aging rate for NTUP, and the subscript  $r$  represents the rated condition. The rated relative aging rate  $V = 1.0$ , at this condition, was set according to the IEC 60076-7 approach (Feng, 2013; Novkovic et al., 2022), which corresponds to a temperature of 98 °C for NTUP (CIGRE Brochure 738, 2018).

The flow chart of the modified relative aging rate based on aging factors is shown in Figure 1. The first step was to obtain the data of HST,  $\theta_{hst}$  based on the differential equation method in IEC 60076-7. Next, the rated condition of activation energy,  $E_{ar}$  was determined based on the maximum activation energy variation (Ese et al., 2010; Teymouri & Vahidi, 2019; Lundgaard et al., 2008). The rated pre-exponential factor,  $A_r$  was obtained from Saleh et al. (2022) based on the maximum aging factors condition. The activation energy,  $E_a$  for each of the aging mechanisms was set based on Ese et al. (2010) for oxidation, while the values for hydrolysis and acid-catalyzed hydrolysis were set based on the average activation energies from Teymouri and Vahidi (2019) and Lundgaard et al. (2008), respectively.

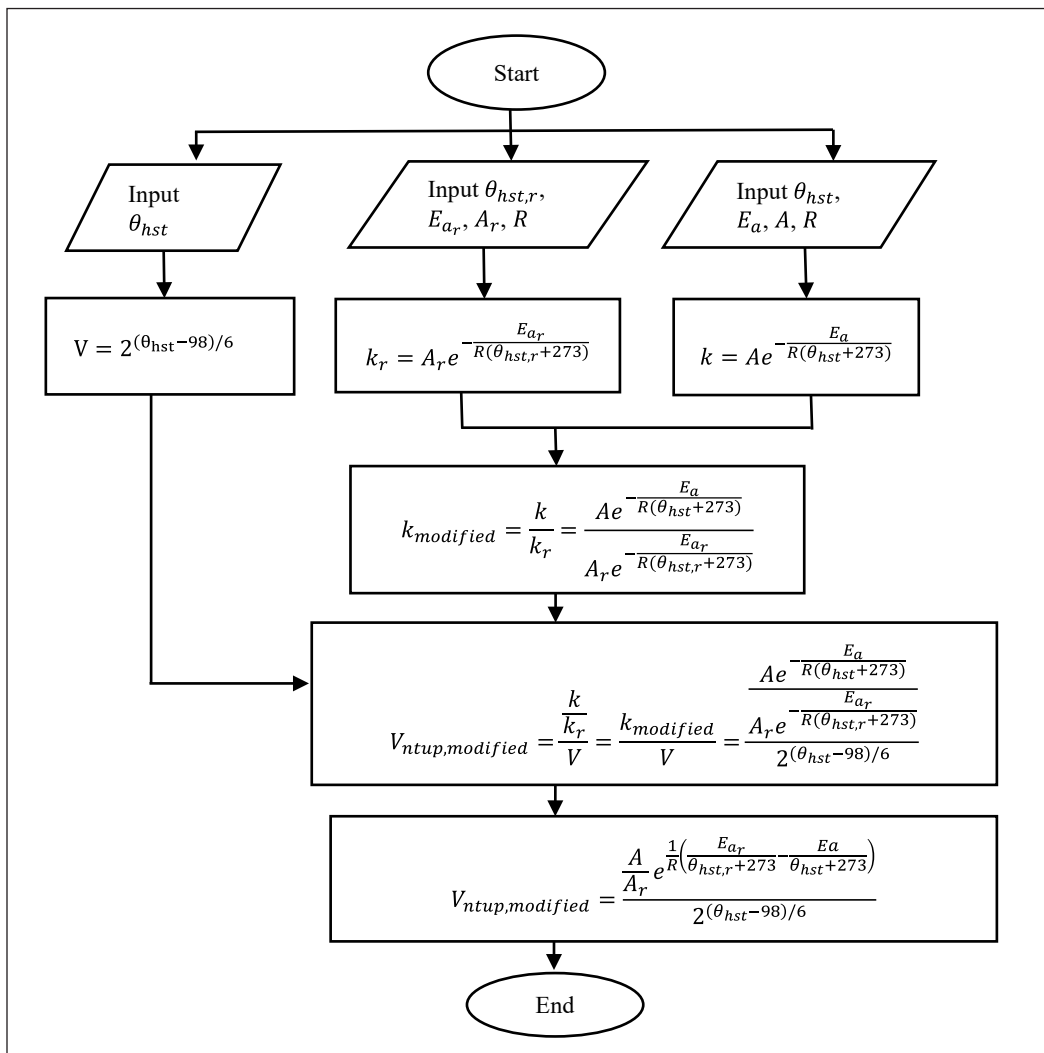


Figure 1. The flow chart of modified relative aging rate based on the aging factors

Similarly, the pre-exponential factor,  $A$  was obtained from Saleh et al. (2022) and relied on the types and concentrations of aging factors. All inputs were applied to the formula of the relative aging rate as per IEC 60076-7 (Feng, 2013; Novkovic et al., 2022), the aging rate under the effects of aging factors,  $k$  and the rated condition of the aging rate,  $k_r$ . The aging rate according to the oxygen, moisture and acids,  $k_{modified}$  was determined based on the ratio of  $k$  and  $k_r$  (Hosseinkhanloo et al., 2022; Novkovic et al., 2022). The modified relative aging rate with temperature, oxygen, moisture and acids content as a controlling parameter,  $V_{ntup,modified}$  is the ratio between  $k_{modified}$  and  $V$ .

**Loss-of-Life (LOL)**

The loss-of-life,  $L$  over a certain period is given by Equation 14.

$$L = \int_{t_1}^{t_2} V_{ntup,modified} dt \text{ or } L \approx \sum_{n=1}^N V_{ntup,modified} t_n \tag{14}$$

where  $V_{ntup,modified}$  is the relative aging rate during interval according to Equation 13,  $t_n$  is the  $n$ th time interval,  $n$  is the number of each time interval, and  $N$  is the total number of intervals during the period.

**RESULTS AND ANALYSIS**

**Forecasting of Transformer Loading and Ambient Temperature Profile**

The loading profile of an ONAN transformer with voltage and power ratings of 132/33 kV and 60 MVA is shown in Figure 2. The actual loading profile was obtained based on the interval of 15 minutes for a duration of up to 15 days. Next, the loading profile was forecasted up to 24 steps to obtain one year of data. The accuracy measurement based on MAPE, MAE, and RMSE was utilized to determine the best SARIMA model for each

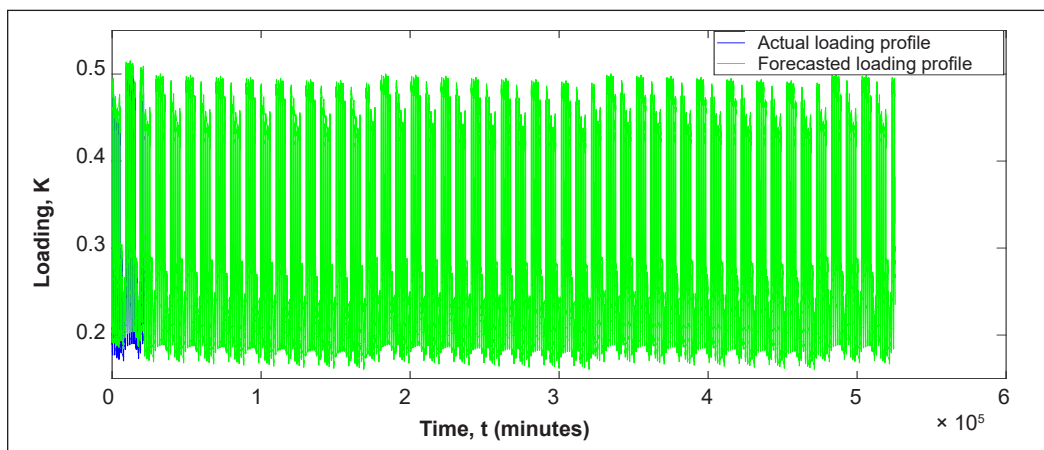


Figure 2. The loading profile of the ONAN transformer for one year

predicted loading profile, as seen in Table 2 (Saleh et al., 2021). MAPE, MAE and RMSE indicate the errors between the actual and forecasted data. The forecasted loading profile, validated by comparison with the actual loading profile, shows that the MAPE, MAE, and RMSE are less than 10% (Saleh et al., 2021).

Table 2  
*The best mode of the SARIMA model for forecasted loading profile*

Forecasting	Model (p,d,q)x(P,D,Q) <sub>672</sub>	MAPE	MAE	RMSE
1-step ahead	010×110	0.1376	0.0375	0.0788
2-steps ahead	112×110	0.2206	0.0643	0.1089
3-steps ahead	112×110	0.2219	0.0657	0.1090
4-steps ahead	112×110	0.2368	0.0725	0.1145
5-steps ahead	112×110	0.2405	0.0746	0.1172
6-steps ahead	112×110	0.1421	0.0445	0.0809
7-steps ahead	112×110	0.0611	0.0183	0.0254
8-steps ahead	010×110	0.1376	0.0375	0.0788
9-steps ahead	112×110	0.2206	0.0643	0.1089
10-steps ahead	112×110	0.2219	0.0657	0.1090
11-steps ahead	112×110	0.2368	0.0725	0.1145
12-steps ahead	112×110	0.2405	0.0746	0.1172
13-steps ahead	112×110	0.1421	0.0445	0.0809
14-steps ahead	112×110	0.0611	0.0183	0.0254
15-steps ahead	010×110	0.1376	0.0375	0.0788
16-steps ahead	112×110	0.2206	0.0643	0.1089
17-steps ahead	112×110	0.2219	0.0657	0.1090
18-steps ahead	112×110	0.2368	0.0725	0.1145
19-steps ahead	112×110	0.2405	0.0746	0.1172
20-steps ahead	112×110	0.1421	0.0445	0.0809
21-steps ahead	112×110	0.0611	0.0183	0.0254
22-steps ahead	010×110	0.1376	0.0375	0.0788
23-steps ahead	112×110	0.2206	0.0643	0.1089
24-steps ahead	112×110	0.2033	0.0669	0.1058

Figure 3 shows the ambient temperature profile recorded at one-hour intervals for seven months. The best modes of the SARIMA model for each forecasted ambient temperature profile are shown in Table 3. The comparison between the forecasted and the actual ambient temperature profiles based on the MAPE, MAE, and RMSE are below 10%, signifying a high level of accuracy.

### **Top-Oil Temperature (TOT) and Hot-Spot Temperature (HST)**

The TOT profile based on the predicted ambient temperature profile and loading profile is depicted in Figure 4. The highest value of TOT is 54.6°C, while the lowest TOT is 36°C.

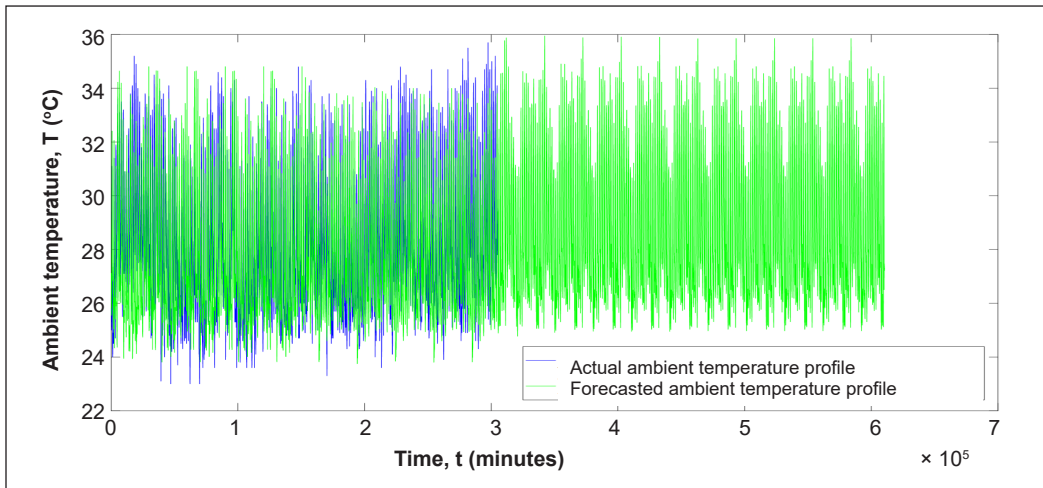


Figure 3. The ambient temperature profile of ONAN transformer for one year

Table 3

The best mode of the SARIMA model for forecasted ambient temperature profile

Forecasting	Model (p,d,q)x(P,D,Q) <sub>168</sub>	MAPE	MAE	RMSE
1-step ahead	000×231	0.0607	1.6778	2.3417
2-steps ahead	000×132	0.0512	1.4447	2.0065

Note. For each 1-step ahead of forecasting, it is equal to 3.5 months or 14 weeks

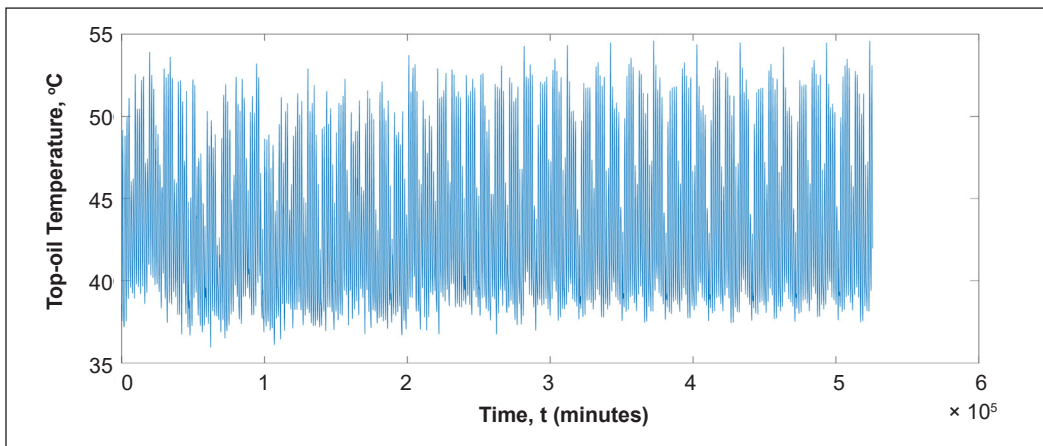


Figure 4. The TOT profile of ONAN transformer for one year

The average TOT is 43.2°C. The HST was computed based on the forecasted loading profile, ambient temperature profile and TOT shown in Figure 5. The highest predicted HST is 68.1°C, whereas the lowest HST is 39.5°C. The average HST is 50.2°C for one year.

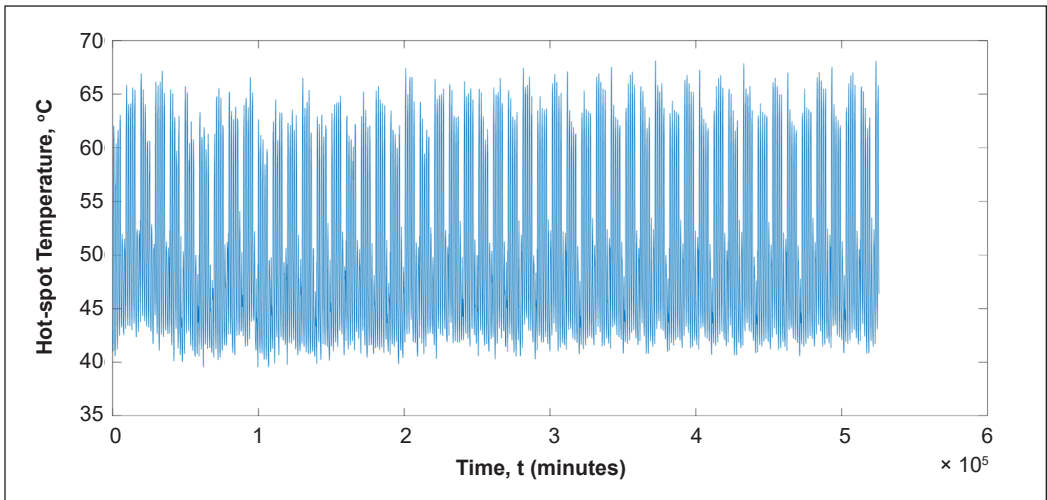
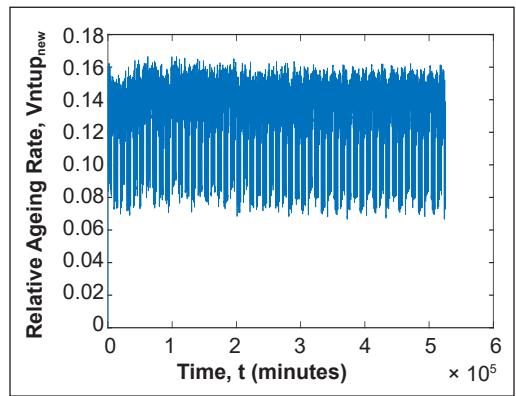


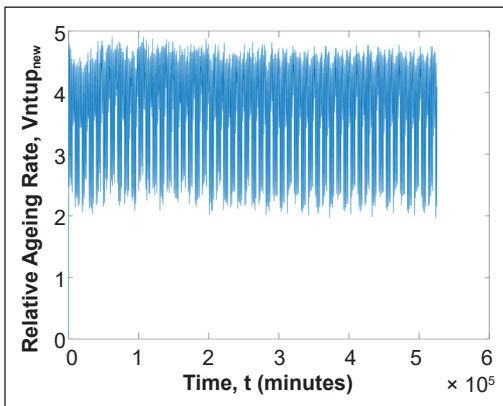
Figure 5. The HST profile of the ONAN transformer for one year

### Loss-of-Life (LOL) with Different Oxygen Concentrations

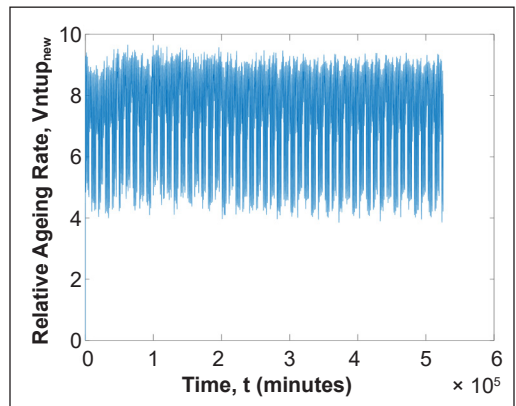
The relative aging rate of a transformer at different oxygen concentrations and moisture in paper less than 0.5% is shown in Figures 6(a) to 6(c). The corresponding pre-exponential factor was obtained for each oxygen concentration (Saleh et al., 2022). The activation energy was 74 kJ/mol, while the oxygen concentration was varied. The rated pre-exponential factor was set once



(a)



(b)



(c)

Figure 6. The relative aging rate of a transformer at moisture less than 0.5% under oxygen concentration of (a) 12,000 ppm, (b) 21,000 ppm, and (c) 30,000 ppm

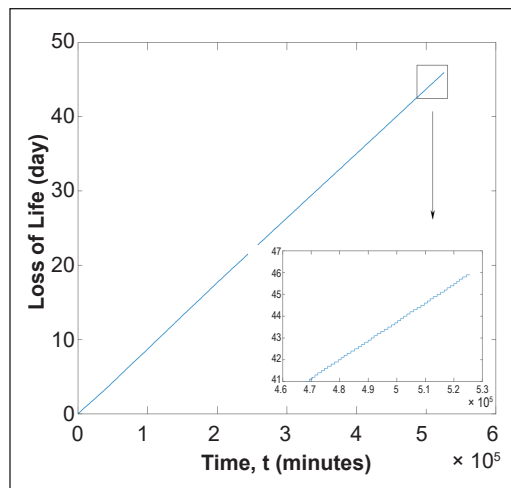
the oxygen concentration of 30,000 ppm was reached (CIGRE Brochure 738, 2018). The increment of oxygen concentration causes the average and highest relative aging rate to increase linearly (Table 4).

Table 4

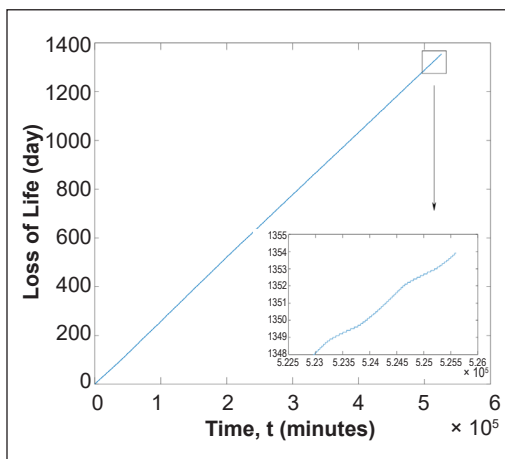
The average and highest relative aging rate of a transformer at different oxygen concentrations and moisture less than 0.5%

Oxygen concentration, P (ppm)	Average relative ageing rate	Highest relative ageing rate
12,000	0.1259	0.1665
21,000	3.7094	4.9082
30,000	7.2929	9.6500

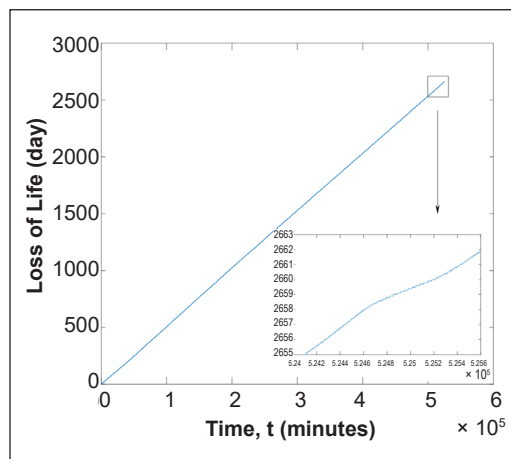
For each of the increasing steps, The LOL at different oxygen concentrations and moisture in paper less than 0.5% exponentially increases with time, as shown in Figures 7(a) to 7(c). The increment of oxygen concentration from 12,000 ppm to 21,000 ppm causes the LOL to increase by 29.5 (Table 5). The LOL factor increases to two when the oxygen concentration increases from 21,000 ppm to 30,000 ppm. Overall, the oxygen concentration increments from 12,000 ppm to 30,000 ppm, incrementing the LOL factor by 57.9.



(a)



(b)



(c)

Figure 7. The LOL of a transformer at moisture less than 0.5% under oxygen concentration of (a) 12,000 ppm, (b) 21,000 ppm, and (c) 30,000 ppm



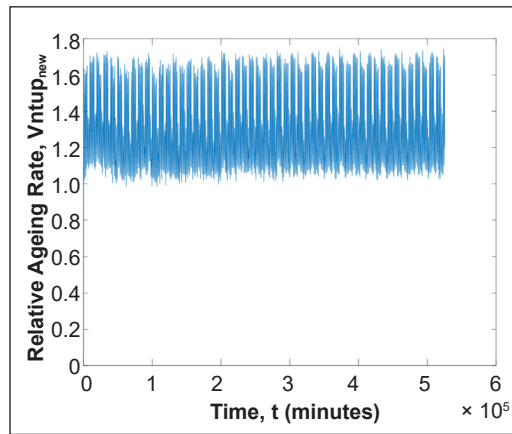
Table 5

The accumulated LOL value for a transformer at different oxygen concentrations and moisture less than 0.5%

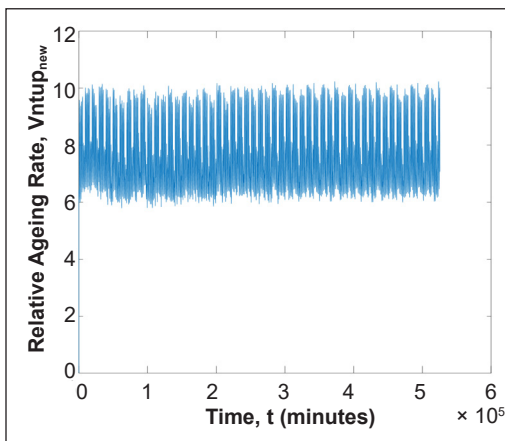
Oxygen concentration, P (ppm)	Loss-of-Life (minutes)	Loss-of-Life (days)	Loss-of-Life (years)
12,000	$6.6152 \times 10^4$	45.9392	$\approx 0.1$
21,000	$1.9496 \times 10^6$	$1.3539 \times 10^3$	$\approx 4$
30,000	$3.8331 \times 10^6$	$2.6619 \times 10^3$	$\approx 7$

**Loss-of-Life (LOL) with Different Moisture Contents**

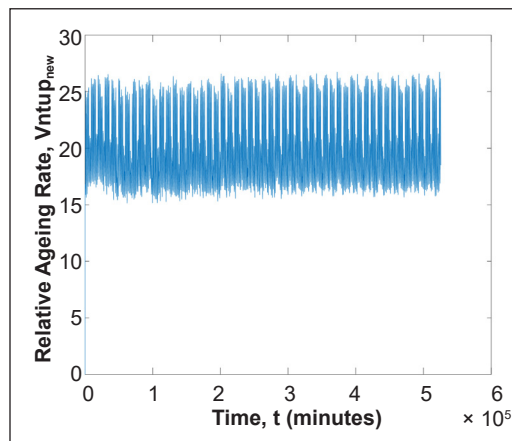
The pre-exponential factors for the moisture in the paper of 1%, 3%, and 5% were utilized based on Saleh et al. (2022) to determine the relative aging rate of a transformer. The factor was determined based on the low oxygen concentration, i.e., less than 7,000 ppm. The transformer’s relative aging rate at various moisture contents under low oxygen concentration is depicted in Figures 8(a) to 8(c). The activation energy for different moisture content was set to 120 kJ/mol, while the rated activation energy was set to 130 kJ/mol since it represents a hydrolysis aging mechanism (Teymouri & Vahidi, 2019). The moisture content of the rated pre-exponential factor was 5.0%, indicating wet conditions (Arshad & Islam, 2011). The average and highest relative aging rate increases approximately linear once there is an increment of moisture content in the paper (Table 6).



(a)



(b)



(c)

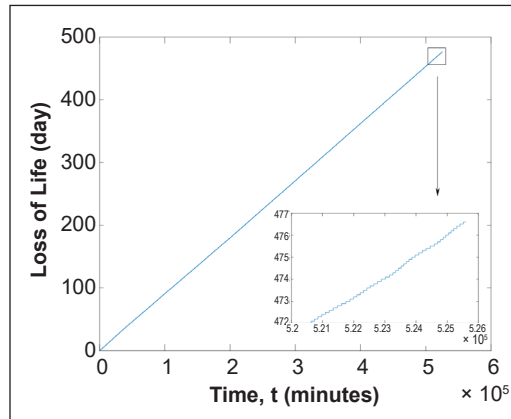
Figure 8. The relative aging rate of a transformer at low oxygen concentration under moisture content of (a) 1.0%, (b) 3.0%, and (c) 5.0%

Table 6

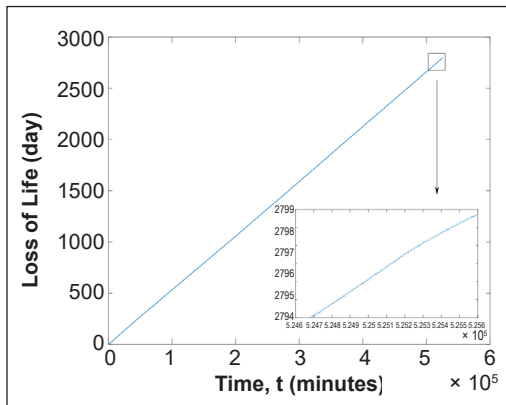
The average and highest relative aging rate of a transformer at various moisture content under a low oxygen concentration

Moisture content, w (%)	Average relative aging rate	Highest relative aging rate
1.0	1.3058	1.7423
3.0	7.6677	10.2307
5.0	20.0407	26.7394

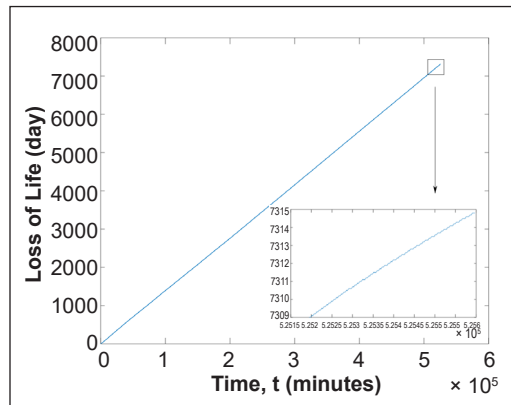
The LOL of a transformer at various moisture content in the paper under low oxygen concentrations is shown in Figure 9(a) to (c). The LOL of a transformer increases over one year once the moisture content increases from 1.0% to 5.0%. The LOL increases exponentially with time for each of the increasing step intervals. The increment of moisture content from 1% to 3% causes the LOL to increase by 5.9 (Table 7). The LOL factor increases further by 2.6 once



(a)



(b)



(c)

Figure 9. The LOL of a transformer at low oxygen concentration under moisture content of (a) 1.0%, (b) 3.0%, and (c) 5.0%

Table 7

The accumulated LOL value for a transformer at various moisture content under low oxygen concentration

Moisture content, w (%)	Loss-of-Life (minutes)	Loss-of-Life (days)	Loss-of-Life (years)
1.0	$6.8633 \times 10^5$	476.6153	$\approx 1$
3.0	$4.0302 \times 10^6$	$2.7987 \times 10^3$	$\approx 8$
5.0	$1.0533 \times 10^7$	$7.3148 \times 10^3$	$\approx 20$

the moisture content increases from 3% to 5%. The LOL factor increases by 15.3 once the moisture content increases from 1% to 5%.

### Loss-of-Life (LOL) with Acids

The pre-exponential factors for LMA and HMA were obtained based on Saleh et al. (2022). These factors were chosen at a moisture content of 1% for both acids while the activation energy was 95 kJ/mol. The pre-exponential factor of LMA at 5% of moisture content was used for the rated condition. The rated activation energy was set to 105 kJ/mol. The relative aging rate for a transformer under LMA and HMA with 1% moisture content can be observed in Figures 10 and 11, respectively. The recorded average and highest relative aging rate for a transformer under LMA and HMA at 1% of moisture content is shown in Table 8. The HMA has a lower average and highest relative aging rates as compared to the LMA.

The LOL of a transformer under LMA and HMA at 1% of moisture content are shown in Figures 12 and 13. The LOL of a transformer under LMA is high, and it can cause a higher impact on paper degradation as compared to the HMA. The LOL rises exponentially with increasing step intervals over one year. The LOL increases by a factor of 11.6 for LMA relative to the HMA at a moisture content of 1% (Table 9).

Table 8  
The average and highest relative aging rate for a transformer under LMA and HMA at 1% of moisture content

Moisture content, w (%)	Type of acids	Average relative aging rate	Highest relative aging rate
1.0	LMA	3.8858	4.0635
	HMA	0.3352	0.3505

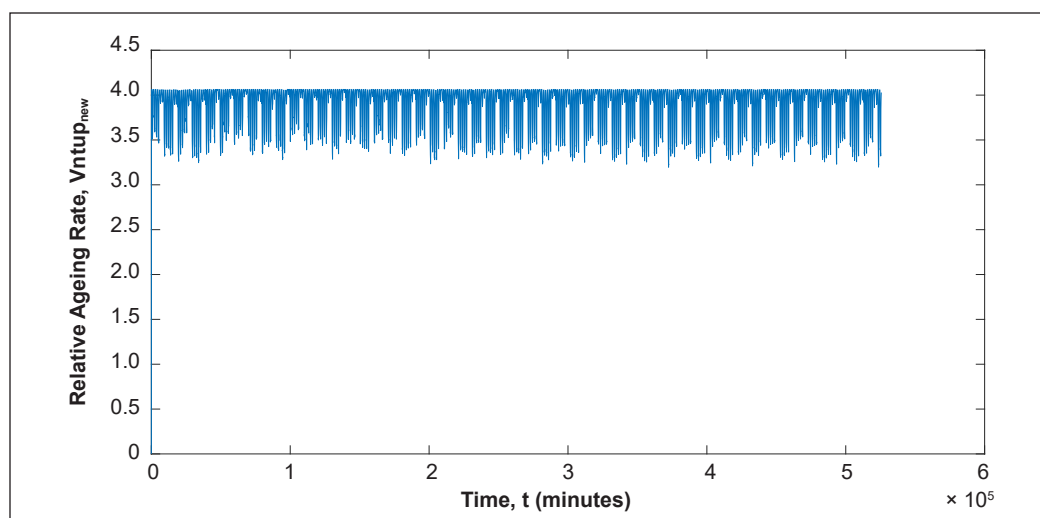


Figure 10. The relative aging rate of a transformer under LMA at the moisture content of 1%

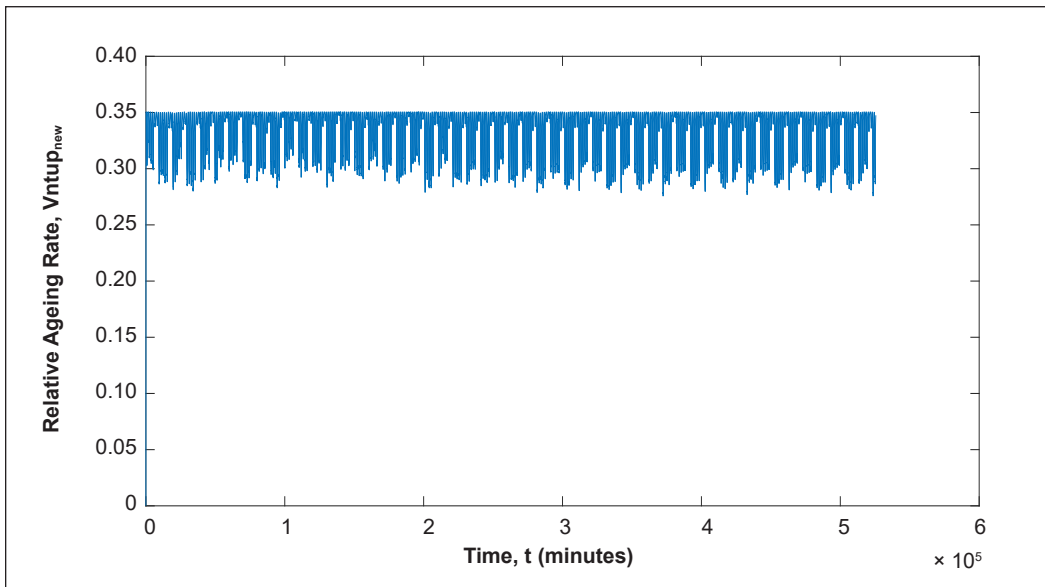


Figure 11. The relative aging rate of a transformer under HMA at the moisture content of 1%

Table 9

The accumulated LOL of a transformer under LMA and HMA at the moisture of 1%

Moisture content, w (%)	Type of acids	Loss-of-Life (minutes)	Loss-of-Life (days)	Loss-of-Life (years)
1.0	LMA	$2.0424 \times 10^6$	1418.3241	$\approx 4$
	HMA	$1.7616 \times 10^5$	122.3365	$\approx 0.3$

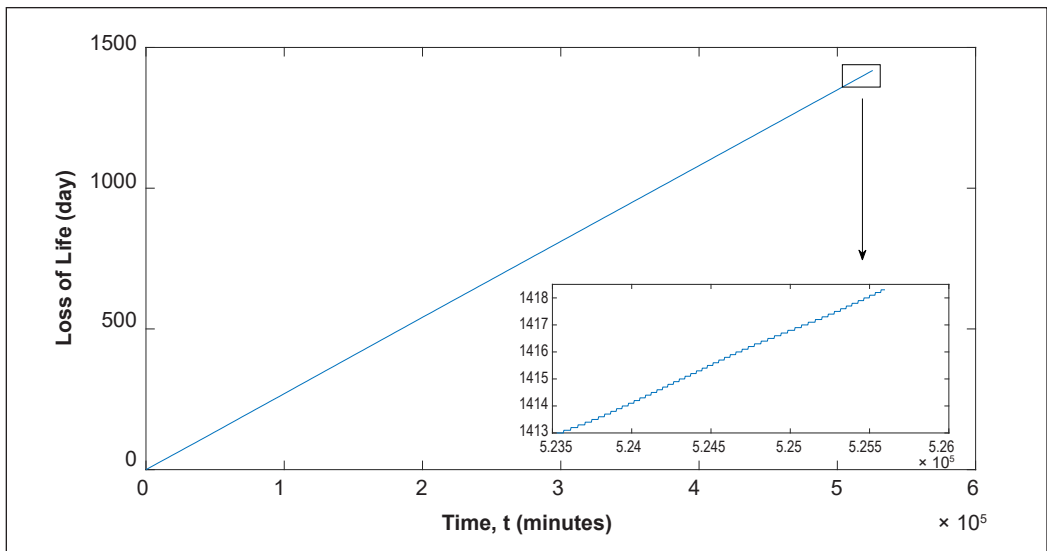


Figure 12. The LOL of a transformer under LMA at the moisture content of 1%

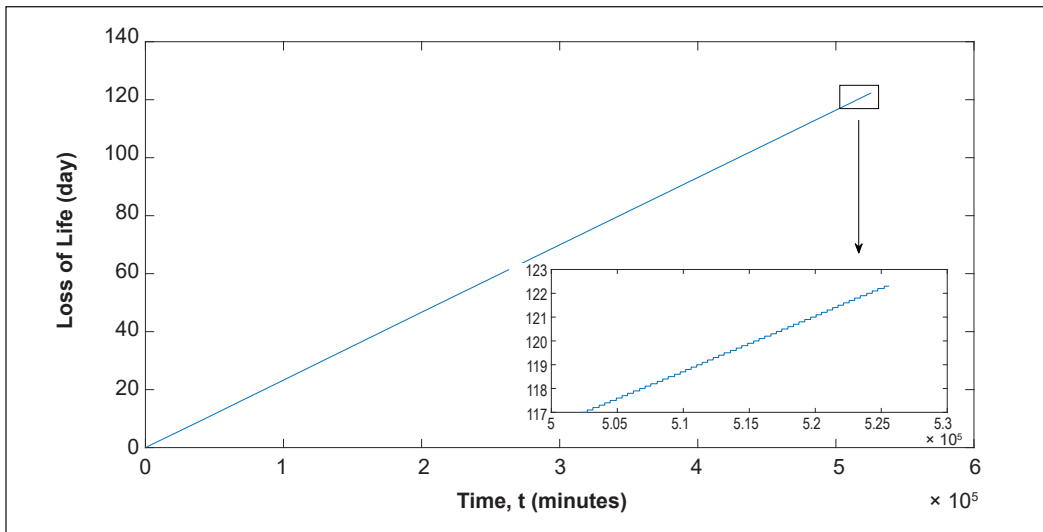


Figure 13. The LOL of a transformer under HMA at the moisture content of 1%

## DISCUSSION

Based on the current study, the LOL under the effects of oxygen, moisture, LMA and HMA increases exponentially throughout one year of duration. The LOL increases linearly due to the small range between each time step and the large range between the initial and final computations. The LOL under LMA gives the most impact compared to another factor since it is known to react together with moisture to enhance the hydrolysis mechanism (CIGRE Brochure 323, 2007; Lundgaard et al., 2008). The increment of oxygen concentration up to 1,000 ppm can cause the LOL of a transformer to increase by factors between one and four.

The increment of moisture content in paper to 0.5% can cause an increment of LOL by factors between one and two. As the oxygen concentration and moisture content increase, the factor decreases. The decreasing factor means that the transformer's life will continue to gradually decline until it reaches zero, which means the transformer is at the very end of its life and can no longer be used. For an NTUP, it is obvious that the moisture can cause a higher impact on the transformer's LOL as compared to the oxygen (CIGRE Brochure 323, 2007; Hosseinkhanloo et al., 2022). It is apparent that the assessment of transformer LOL depends not only on the loading, ambient temperature, and HST but also on the aging factor and mechanism reaction of a transformer.

The comparison of LOL based on different effects of the aging factor for a transformer can be seen in Figure 14. The LOL, for one year of duration based on temperature is the lowest, at only two days. In contrast, the LOL under moisture content of 5% at low oxygen concentration gives the highest LOL for one year. The factor of LOL is 20.5 for 12,000 ppm of oxygen concentration relative to the function of temperature at moisture less than

0.5%. The oxygen concentration of 21,000 ppm and 30,000 ppm relative to the function of temperature yields the factor of 602.8 and 1185.2. The factors of LOL at 1%, 3%, and 5% of moisture content relative to the function of temperature under low oxygen concentration are 212.2, 1246.1, and 3256.8. The factor of LOL for LMA with regard to the temperature at 1% of moisture content is 631.5. On the other hand, the LOL factor for HMA relative to the function of temperature at 1% of moisture content is 54.5. Based on Figure 14, LMA at 1% moisture content results in higher LOL for the one-year duration compared to LOL under 1% moisture content at low oxygen concentration.

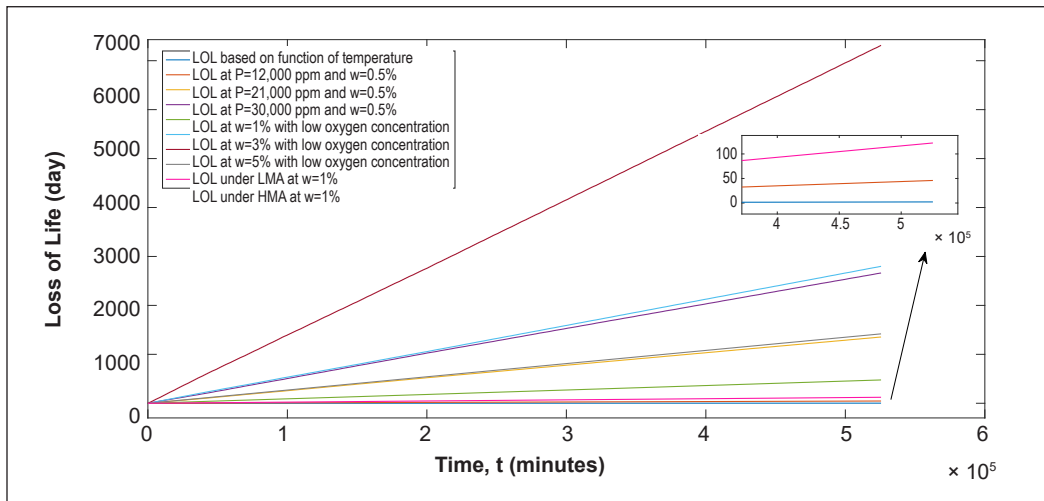


Figure 14. The comparison of LOL based on different effects of the aging factor

## CONCLUSION

It is apparent that with the newly developed relative aging rate, the LMA has the most significant impact on the transformer’s LOL, followed by moisture, oxygen, and HMA. Based on the current study, the LOL increases with increasing oxygen concentration from 12,000 ppm to 30,000 ppm. The increment of moisture content from 0.5% to 5% also increases the LOL of a transformer. The LOL of a transformer increases exponentially with time for each increasing step interval regardless of the presence of any aging factors. LMA has a higher impact than HMA, leading to 1,418 days of LOL compared to 122 days of LOL. The transformer’s LOL in days increases proportionally in the presence of oxygen concentration and moisture content. The impact of oxygen on a transformer’s LOL is low compared to moisture and LMA for the NTUP.

## ACKNOWLEDGEMENTS

The authors would like to thank the Ministry of Higher Education Malaysia, for funding the study under the FRGS scheme of FRGS/1/2019/TK07/UPM/02/3 (03-01-19-2071FR).

## REFERENCES

- Afzali, M., Afzali, A., & Zahedi, G. (2011). Ambient air temperature forecasting using artificial neural network approach. In *2011 International Conference on Environmental and Computer Science IPCBEE* (Vol. 19, pp. 176-180). IACSIT Press.
- Agrawal, R. K., Muchahary, F., & Tripathi, M. M. (2018). Long term load forecasting with hourly predictions based on long-short-term-memory networks. In *2018 IEEE Texas Power and Energy Conference (TPEC)* (pp. 1-6). IEEE Publishing. <https://doi.org/10.1109/TPEC.2018.8312088>
- Al-Shaikh, H., Rahman, M. A., & Zubair, A. (2019). Short-term electric demand forecasting for power systems using similar months approach based SARIMA. In *2019 IEEE International Conference on Power, Electrical, and Electronics and Industrial Applications (PEEIACON)* (pp. 122-126). IEEE Publishing. <https://doi.org/10.1109/PEEIACON48840.2019.9071939>
- Arshad, M., & Islam, S. M. (2011). Significance of cellulose power transformer condition assessment. *IEEE Transactions on Dielectrics and Electrical Insulation*, 18(5), 1591-1598. <https://doi.org/10.1109/TDEI.2011.6032829>
- Arshad, M., Islam, S. M., & Khaliq, A. (2004). Power transformer aging and life extension. In *8th International Conference on Probabilistic Methods Applied to Power Systems* (pp. 498-501). IEEE Publishing.
- Biçen, Y., Çilliyüz Y., Aras, F. & Aydugan, G. (2012). Aging of paper insulation in natural ester & mineral oil. *Electrical and Electronic Engineering*, 2(3), 141-146. <https://doi.org/10.5923/j.eee.20120203.06>
- Biçen, Y., Çilliyüz, Y., Aras, F., & Aydugan, G. (2011). An assessment on aging model of IEEE/IEC standards for natural and mineral oil-immersed transformer. In *2011 IEEE International Conference on Dielectric Liquids* (pp 1-4). IEEE Publishing. <https://doi.org/10.1109/ICDL.2011.6015442>
- Kumar, B. L. P., & Mathew, R. (2016). Asset management of transformer based on loss of life calculation. In *2016 IEEE 6th International Conference on Power Systems (ICPS)* (pp. 1-5). IEEE Publishing. <https://doi.org/10.1109/ICPES.2016.7584000>
- Cabrera, N. G., Gutiérrez-Alcaraz, G., & Gil, E. (2013). Load forecasting assessment using SARIMA model and fuzzy inductive reasoning. In *2013 IEEE International Conference on Industrial Engineering and Engineering Management* (pp. 561-565). IEEE Publishing. <https://doi.org/10.1109/IEEM.2013.6962474>
- Chen, Y., Xu, P., Chu, Y., Li, W., Wu, Y., Ni, L., Bao, Y., & Wang, K. (2017). Short-term electrical load forecasting using the support vector regression (SVR) model to calculate the demand response baseline for office buildings. *Applied Energy*, 195, 659-670. <https://doi.org/10.1016/j.apenergy.2017.03.034>
- CIGRE Brochure 323. (2007). Ageing of cellulose in mineral-oil insulated transformers. In *D1 Materials and Emerging Test Techniques*. CIGRE. <https://www.e-cigre.org/publications/detail/323-ageing-of-cellulose-in-mineral-oil-insulated-transformers.html>,
- CIGRE Brochure 393. (2009). Thermal performance of transformers. In *A2 Power Transformers and Reactors*. CIGRE. <https://www.e-cigre.org/publications/detail/393-thermal-performance-of-transformers.html>
- CIGRE Brochure 738. (2018). Ageing of liquid impregnated cellulose for power transformers. In *D1 Materials and Emerging Test Techniques*. CIGRE. <https://www.e-cigre.org/publications/detail/738-ageing-of-liquid-impregnated-cellulose-for-power-transformers.html>

- Ese, M. H. G., Liland, K. B., & Lundgaard, L. E. (2010). Oxidation of paper insulation in transformers. *IEEE Transactions on Dielectrics and Electrical Insulation*, 17(3), 939-946. <https://doi.org/10.1109/TDEI.2010.5492270>
- Feng, D. (2013). *Life Expectancy Investigation of Transmission Power Transformers* (Doctoral dissertation). The University of Manchester, England. <https://www.escholar.manchester.ac.uk/api/datastream?publicationPid=uk-ac-man-scw:187566&datastreamId=FULL-TEXT.PDF>
- Hosseinkhanloo, M., Kalantari, N. T., Behjat, V., & Ravadanegh, S. N. (2022). Optimal exploitation of power transformer fleet considering loss of life and economic evaluation based on failure probability. *Electric Power Systems Research*, 213, Article 108801. <https://doi.org/10.1016/j.epsr.2022.108801>
- Hou, J., Wang, Y., Zhou, J., & Tian, Q. (2022). Prediction of hourly air temperature based on CNN-LSTM. *Geomatics, Natural Hazards and Risk*, 13(1), 1962-1986. <https://doi.org/10.1080/19475705.2022.2102942>
- Hou, T., Fang, R., Tang, J., Ge, G., Yang, D., Liu, J., & Zhang, W. (2021). A novel short-term residential electric load forecasting method based on adaptive load aggregation and deep learning algorithms. *Energies*, 14(22), Article 7820. <https://doi.org/10.3390/en14227820>
- Khalid, R., Javaid, N., Al-zahrani, F. A., Aurangzeb, K., Qazi, E. U. H., & Ashfaq, T. (2020). Electricity load and price forecasting using Jaya-Long Short Term Memory (JLSTM) in smart grids. *Entropy*, 22, Article 10. <https://doi.org/10.3390/e22010010>
- Khorsheed, E. (2021). Energy load forecasting: Bayesian and exponential smoothing hybrid methodology. *International Journal of Energy Sector Management*, 15(2), 294-308. <https://doi.org/10.1108/IJESM-06-2019-0005>
- Li, J., Zhang, J., Wang, F., Huang, Z., & Zhou, Q. (2018). A novel aging indicator of transformer paper insulation based on dispersion staining colors of cellulose fibers in oil. *IEEE Electrical Insulation Magazine*, 34(4), 8-16. <https://doi.org/10.1109/MEI.2018.8430039>
- Liao, R. J., Yang, L. J., Li, J., & Grzybowski, S. (2011). Aging condition assessment of transformer oil-paper insulation model based on partial discharge analysis. *IEEE Transactions on Dielectrics and Electrical Insulation*, 18(1), 303-311. <https://doi.org/10.1109/TDEI.2011.5704522>
- Liu, J., Liao, R., Zhang, Y., Gong, C., Wang, C., & Gao, J. (2015). Condition evaluation for aging state of transformer oil-paper insulation based on time-frequency domain dielectric characteristics. *Electric Power Components and Systems*, 43(7), 759-769. <https://doi.org/10.1080/15325008.2014.991462>
- Lundgaard, L. E., Hansen, W., & Ingebrigtsen, S. (2008). Ageing of mineral oil impregnated cellulose by acid catalysis. *IEEE Transactions on Dielectrics and Electrical Insulation*, 15(2), 540-546. <https://doi.org/10.1109/TDEI.2008.4483475>
- Ma, X., Fang, C., & Ji, J. (2020). Prediction of outdoor air temperature and humidity using Xgboost. *IOP Conference Series: Earth and Environmental Science*, 427, Article 012013. <https://doi.org/10.1088/1755-1315/427/1/012013>
- Mohammed, N. A., & Al-Bazi, A. (2022). An adaptive backpropagation algorithm for long-term electricity load forecasting. *Neural Computing and Applications*, 34, 477-491. <https://doi.org/10.1007/s00521-021-06384-x>



- Najdenkoski, K., Rafajlovski, G., & Dimcevic, V. (2007). Thermal aging of distribution transformers according to IEEE and IEC standards. In *2007 IEEE Power Engineering Society General Meeting* (pp. 1-5). IEEE Publishing. <https://doi.org/10.1109/PES.2007.385642>
- Novkovic, M., Popovic, A., Briosso, E., Iglesias, R. M., & Radakovic, Z. (2022). Dynamic thermal model of liquid-immersed shell-type transformers. *International Journal of Electrical Power & Energy Systems*, *142*, Article 108347. <https://doi.org/10.1016/j.ijepes.2022.108347>
- Piatniczka, A., Kockott, M., Bistaffa, G., & Paduraru, S. (2022). Transformer loss of life monitoring: A review of in-service highlighting achieved benefits. In *2022 75th Annual Conference for Protective Relay Engineers (CPRE)* (pp. 1-7). IEEE Publishing. <https://doi.org/10.1109/CPRE55809.2022.9776562>
- Radhika, Y., & Shashi, M. (2009). Atmospheric temperature prediction using support vector machines. *International Journal of Computer Theory and Engineering*, *1*(1), 55-58. <https://doi.org/10.7763/ijcte.2009.v1.9>
- Saleh, N., Azis, N., Jasni, J., Kadir, M. Z. A. A., & Talib, M. A. (2021). Prediction of a transformer's loading and ambient temperature based on SARIMA approach for hot-spot temperature and loss-of-life analyses. In *IEEE International Conference on the Properties and Applications of Dielectric Materials (ICPADM)* (pp. 123-126). IEEE Publishing. <https://doi.org/10.1109/ICPADM49635.2021.9493865>
- Saleh, N., Azis, N., Jasni, J., Kadir, M. Z. A. A., & Talib, M. A. (2022). Paper lifetime mathematical modelling based on multi pre-exponential factors for oil-immersed transformer. *Pertanika Journal of Science and Technology*, *30*(2), 1115-1133. <https://doi.org/10.47836/pjst.30.2.15>
- Sinha, A., Tayal, R., Vyas, A., Pandey, P., & Vyas, O. P. (2021). Forecasting electricity load with hybrid scalable model based on stacked non linear residual approach. *Frontiers in Energy Research*, *9*, 1-17. <https://doi.org/10.3389/fenrg.2021.720406>
- Susa, D., Lehtonen, M., & Nordman, H. (2005a). Dynamic thermal modeling of distribution transformers. *IEEE Transactions on Power Delivery*, *20*(3), 1919-1929. <https://doi.org/10.1109/TPWRD.2005.848675>
- Susa, D., Lehtonen, M., & Nordman, H. (2005b). Dynamic thermal modelling of power transformers. *IEEE Transactions on Power Delivery*, *20*(1), 197-204. <https://doi.org/10.1109/TPWRD.2004.835255>
- Teymouri, A., & Vahidi, B. (2019). Estimation of power transformer remaining life from activation energy and pre-exponential factor in the Arrhenius equation. *Cellulose*, *26*, 9709-9720. <https://doi.org/10.1007/s10570-019-02746-w>
- Tripathy, D. S., & Prusty, B. R. (2021). Quantile regression averaging-based probabilistic forecasting of daily ambient temperature. *International Journal of Numerical Modelling: Electronic Networks, Devices and Fields*, *34*(3), 1-19. <https://doi.org/10.1002/jnm.2846>
- Van den Berg, A. P. B., Bootsma, L. R., Bovenber, T. F. A., Moerbeek, A. R., De Jong, E., Khalil, S., Koch, T., & Dugundji, E. R. (2022). Year-ahead ambient temperature forecasting in pharmaceutical transport lanes thermal conditions. *Procedia Computer Science*, *201*, 255-264. <https://doi.org/10.1016/j.procs.2022.03.035>
- Zhang, E., Zheng, H., Zhang, C., Wang, J., Shi, K., Guo, J., Schwarz, H., & Zhang, C. (2021). Aging state assessment of transformer cellulosic paper insulation using multivariate chemical indicators. *Cellulose*, *28*. <https://doi.org/10.1007/s10570-021-03683-3>



## Performance of Waste Cooking Oil Esterification for Biodiesel Production Using Various Catalysts

Indah Thuraya Herman<sup>1</sup>, Khairuddin Md Isa<sup>2\*</sup>, Naimah Ibrahim<sup>1</sup>, Saiful Azhar Saad<sup>2</sup>, Tuan Amran Tuan Abdullah<sup>3</sup>, Mohd Aizudin Abd Aziz<sup>4</sup> and Muhammad Auni Hairunnaja<sup>4</sup>

<sup>1</sup>Faculty of Civil Engineering Technology, Universiti Malaysia Perlis (UniMAP), 02600, Arau, Perlis, Malaysia

<sup>2</sup>Faculty of Chemical Engineering Technology, Universiti Malaysia Perlis (UniMAP), 02600, Arau, Perlis, Malaysia

<sup>3</sup>Faculty of Chemical and Energy Engineering, Universiti Teknologi Malaysia, UTM, Johor Bahru, 81310 Skudai, Johor, Malaysia

<sup>4</sup>Faculty of Chemical and Process Engineering Technology, University Malaysia Pahang (UMP), Lebuhraya Tun Razak, 26300 Gambang, Pahang, Malaysia

### ABSTRACT

In this study, waste cooking oil (WCO) with high free fatty acid (FFA) content was esterified to produce biodiesel, and the catalysts' performance was investigated. Two deep eutectic solvents (DESs) were employed as the liquid catalysts (K<sub>2</sub>CO<sub>3</sub>-Gly and KOH-Gly), while the solid heterogeneous catalysts used were spent bleaching earth (SBE), KCC-1, and Na/KCC-1. DESs were prepared by mixing at reaction temperature and time of 80°C and 120 min, respectively. The American Standard Testing Method (ASTM) D974 determined the acid value. The catalysts were first screened for their catalytic activity in WCO esterification. The parameters investigated in this study were oil-to-methanol

molar ratio, catalyst loading, reaction time, and temperature. The highest conversion (94.7%) was obtained using Na/KCC-1. The performance of solid and liquid catalysts was evaluated using KOH-Gly and SBE for the reduction of FFA in WCO under different conditions of oil-to-methanol molar ratio (1:6–1:10), catalysts loading (0.2–2.0 g), reaction time (30–60 min), and temperature (40–100°C). The highest reduction of FFA in the esterification process for KOH-Gly and SBE as catalysts was 97.74% and 84.2%, respectively. Transesterification of the

### ARTICLE INFO

#### Article history:

Received: 16 March 2023

Accepted: 12 September 2023

Published: 14 March 2024

DOI: <https://doi.org/10.47836/pjst.32.2.10>

#### E-mail addresses:

indahherman10@gmail.com (Indah Thuraya Herman)

khairudin@unimap.edu.my (Khairuddin Md Isa)

Naimah@unimap.edu.my (Naimah Ibrahim)

Saifulazhar@unimap.edu.my (Saiful Azhar Saad)

Tamran@utm.my (Tuan Amran Tuan Abdullah)

maizudin@ump.edu.my (Mohd Aizudin Abd Aziz)

mauliduni97@gmail.com (Muhammad Auni Hairunnaja)

\* Corresponding author

esterified oil shows a promising result (97%), and the process can potentially be scaled up. The GC-MS result shows that the produced oil has the highest percentage of hexadecanoic acid and methyl ester.

*Keywords:* Biodiesel, deep eutectic solvents, heterogeneous catalysts, waste cooking oil

---

## INTRODUCTION

The requirement and demand for energy have been driven by fossil resource consumption, which negatively affects the environment and causes global warming issues (Aziz et al., 2017). Fossil fuels are known as limited energy sources due to the impact of climate change. Thus, renewable fuels are preferred to overcome the issue of increasing energy (Bobadilla et al., 2017; Japar et al., 2019; Rahman & Aziz, 2022). Biodiesel, produced from renewable feedstock, has received much attention worldwide in the energy sector (Nguyen et al., 2020; Aziz et al., 2019). Among the feedstock for biodiesel production includes animal fats, both edible and non-edible oils, as well as waste vegetable oils (Yusuff & Popoola, 2019; Rahman et al., 2019). High unsaturated fatty acid content is one of the main issues for most non-edible feedstock because two consecutive processes, namely esterification and transesterification, are required to deal with non-edible feedstock with high free fatty acid (FFA) content to produce biodiesel (Chuah et al., 2016., Azhar et al., 2021). Nowadays, waste cooking oil (WCO) has the economic advantage and potential to become the oil feedstock for biodiesel production. Reusing WCO is a good practice to prevent homes and restaurants from dumping WCO into wastewater (Razali et al., 2018; Razali et al., 2020).

Deep eutectic solvents (DESs) are mixtures of hydrogen bond donors with hydrogen bond acceptor materials. These mixtures have lower melting points than their constituting compounds (Shahbaz et al., 2013; Fatt et al., 2021). The development of DESs as low-cost and environmentally friendly solvents has several major advantages over conventional ionic liquids and organic solvents, such as sample preparation, low cost, low toxicity, and high biodegradability (Taslim et al., 2017; Ismail et al., 2019), and DESs have been used as biodiesel catalysts. Previous research revealed that various types of DESs were used in biodiesel production. Hayyan et al. (2014) utilized choline chloride (ChCl)-based DES as the catalyst to pretreat acidic crude palm oil in biodiesel synthesis. ChCl-based DESs were used to convert *Pongamia pinnata* into biodiesel (Kadapure et al., 2017; Isa et al., 2017; Dahawi et al., 2019).

The use of potassium carbonate ( $K_2CO_3$ )-based DESs have been applied for biodiesel synthesis, for example, in the biodiesel purification step (Manurung, Arief et al., 2018) and the extraction of minor components in palm methyl ester (Manurung & Liang, 2018).  $K_2CO_3$ -based DES was utilized to purify palm biodiesel, where the purity of biodiesel of 98.6453% was achieved using a biodiesel-to-DES ratio of 1:3.5 (Manurung, Hutauruk et al.,

2018). Other than that, Sander et al. used  $K_2CO_3$ -based DES to catalyze the deacidification of waste coffee grounds oil. A potassium-based DES was successfully used to extract FFA from waste coffee grounds oil (WCGO) and fresh coffee grounds oil (FCGO). The total acid number of WCGO and FCGO was lower than 1 mg KOH/g for 30 min reaction time using extractive deacidification with  $K_2CO_3$ -based DES. The extraction efficiency ranged from 86.18% to 94.15% (Sander et al., 2020; Azahar et al., 2023). Recently,  $K_2CO_3$ -based DES was used to purify waste cooking oil to avoid saponification during biodiesel synthesis. The total acid value decreased from 2.362 to 0.574 mg KOH/g in 30 min (Petračić et al., 2020).

Solid catalysts are a general type of heterogeneous catalyst, and their activity and selectivity determine their performance in catalyzing a reaction. Currently, many industries use heterogeneous catalysts that offer many advantages and are environmentally friendly, including non-corrosive, easily separated from the product through filtration, and can be used repeatedly over a long period (Sumarlan & Mentari, 2020; Mahmud et al., 2019). In a study of esterification of rapeseed oil fatty acids (RFA) using a carbon-based heterogeneous acid catalyst, biodiesel with an ester content of  $\geq 96.5\%$  was successfully obtained from pure RFA under optimal esterification conditions (Malins et al., 2016). Spent bleaching earth (SBE) was previously used in biodiesel production (Petračić et al., 2020; Sumarlan & Mentari, 2020), but fewer studies of biodiesel production use SBE and KCC-1 as catalysts. Thus, using SBE and mesoporous silica KCC-1 as biodiesel catalysts provides an opportunity to explore biodiesel synthesis.

Therefore, this study investigates the performance of various catalysts in the esterification of waste cooking oil (WCO) for biodiesel production. This work reduced the FFA content in WCO via the esterification process using various DES and solid catalysts. The DESs used in this study were potassium carbonate-glycerol ( $K_2CO_3$ -Gly) and potassium hydroxide-glycerol (KOH-Gly). Meanwhile, the solid catalysts used were KCC-1, modified KCC-1 (Na/KCC-1), and SBE. Free fatty acid conversion will be determined using titration in compliance with American Standard Testing Method (ASTM) D974. The transesterification process for the highest conversion from treated waste cooking oil will be performed with potassium hydroxide as a catalyst.

## MATERIALS AND METHODS

### Catalyst Preparation

**Deep Eutectic Solvents.** Potassium carbonate ( $K_2CO_3$ ) and potassium hydroxide (KOH) were used to synthesize DESs using glycerol as a hydrogen bond donor. The DESs used in this work were synthesized following previous work (Herman, Isa et al., 2021; Chandraseagar et al., 2019). Glycerol was added to  $K_2CO_3$  with a mass ratio of 20:1 and homogeneously mixed for 120 min at 80 °C until a clear colorless mixture formed. Similar procedures were repeated using KOH for DES synthesis. A vacuum desiccator was used to

store the resultant  $K_2CO_3$ -Gly and KOH-Gly to preserve the physicochemical properties of the catalysts.

**Solid Catalysts.** The microwave-assisted hydrothermal method was used to synthesize parent KCC-1, as Hamid et al. (2018) reported, whereas Na/KCC-1 was prepared by our research collaborators (Hanif et al., 2021). KCC-1 and SBE were supplied by Universiti Teknologi Malaysia and used as received.

**Characterization of Catalyst Samples.** The following procedures explain the characterization of SBE. An X-ray diffractometer (Shimadzu 6000 XRD) was utilized to evaluate the crystalline phase of the samples. The measurements were performed using  $Cu-K\alpha$  radiation ( $\lambda = 1.5418 \text{ \AA}$ ) in the range of  $20\text{--}80^\circ$  in  $2\theta$  at an accelerating voltage of 40 kV and an intensity of 30 mA. The data was collected at  $0.02^\circ$  intervals and a speed of  $2^\circ \text{ min}^{-1}$ . A Perkin-Elmer Spectrum 65 spectrometer was used to analyze Fourier transform infrared (FTIR) spectroscopy and identify the functional groups introduced onto the catalysts. Hanif et al. (2021) reported the characterization of Na/KCC-1 in the previous study.

**Esterification of Waste Cooking Oil.** The WCO utilized in this process was collected from restaurants in Perlis, Malaysia. The conditions used for the esterification process are presented in Table 1. The sample size of WCO was kept constant at 40 g for every reaction of the experiment. The esterification reaction was performed in a 250 ml reaction flask equipped with a magnetic stirrer and thermometer. DESs as catalysts were dissolved in methanol and mixed with oil in the reaction flask. Meanwhile, the selected catalysts were added to the preheated oil for solid catalysts, and the mixture was stirred continuously at 600 rpm. Temperature was monitored using a thermometer. After the reaction, the liquid mixture was separated from the catalyst using a simple centrifuge.

Table 1  
*Conditions of solid and liquid catalysts in the esterification process*

Parameter	Conditions
Oil-to-methanol molar ratio, OMMR	1:6, 1:8, and 1:10
Catalyst loading, CL (g)	0.8, 1.2, 1.6, and 2.0
Reaction time, RT (min)	30, 45, and 60
Temperature, T ( $^\circ\text{C}$ )	40, 60, 80, and 100

Titration was applied to determine the FFA content of the tested samples. The samples were titrated with 0.1 N KOH after they were dissolved in a mixture of isopropyl alcohol and phenolphthalein. The equation reported by Thoai et al. (2019) was employed to determine the FFA conversion and acid value. Experimental works were replicated three times.

**Transesterification of Treated WCO.** The SBE and KOH-Gly treated oils were used in the transesterification process catalyzed by KOH. The transesterification conditions

employed were oil-to-methanol molar ratio (1:6), catalyst loading (0.55 wt.%), reaction time (60 min), and temperature (65 °C). The KOH-based catalyst was first dissolved in methanol and stirred at room temperature for three minutes while treated oil was heated in a round bottom flask. When the treated oil reached the temperature of 65 °C, potassium methoxide was mixed into the oil for one hour of reaction time. After that, the mixture was poured into a separating funnel. The ester layer was separated by gravity and located at the upper layer. The glycerol, extra methanol and undesired products were removed in the lower layer. The ester layer was washed several times with a small amount of hot water until it met the requirements.

The ester layer was analyzed using gas chromatography-mass spectrometry to identify the ester component produced in the sample. The stoichiometry of the transesterification reaction requires 3 mol of alcohol per mol of triglyceride to yield 3 mol of alkyl ester biodiesel and 1 mol of glycerol. The biodiesel and reaction for FAME conversions were calculated using Equation 1 (Changmai et al., 2020).

$$\text{Yield of FAME (\%)} = \frac{\text{Weight of methyl ester (g)}}{\text{Weight of oil used in reaction (g)}} \times 100\% \quad (1)$$

## RESULTS AND DISCUSSION

### Characteristics of Catalysts

Parent KCC-1 and Na/KCC-1 were characterized in the previous work of our research group and reported by Hanif et al. (2021). Figure 1 presents the results of the X-ray diffraction (XRD) analysis of SBE.

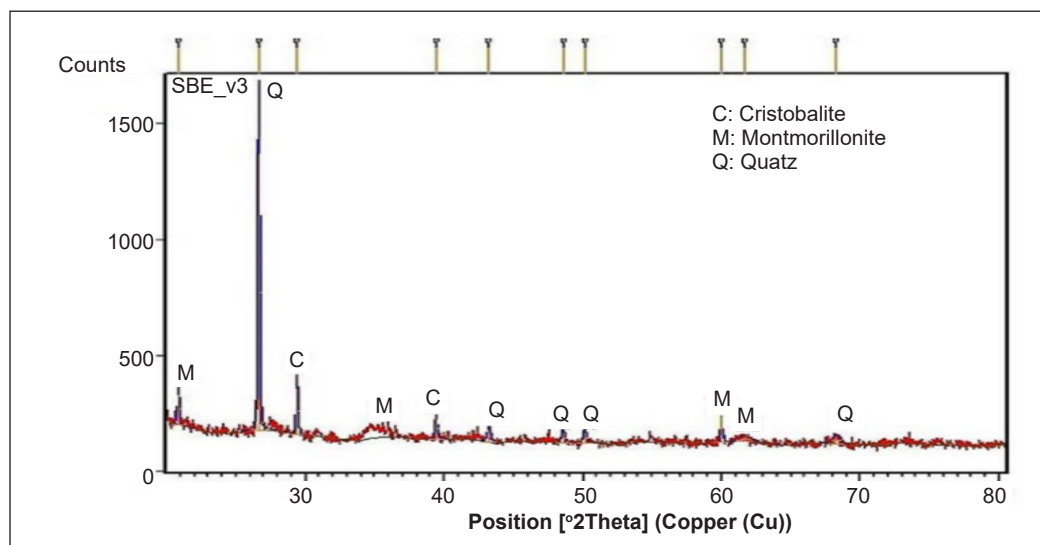


Figure 1. XRD pattern of SBE

A partially amorphous phase with ten obvious peaks of montmorillonite, cristobalite, and quartz can be seen in the SBE sample. Raw SBE mainly contains quartz that is obtained at the peak of the crystalline quartz impurities ( $\text{SiO}_2$ ). The presence of montmorillonite in SBE proved that it could act as a relative catalyst to lower the FFA content in WCO esterification (Kanda et al., 2017; Ismail et al., 2021). The presence of montmorillonite in SBE patterns also aligns with the result of FTIR obtained (Figure 2).

Figure 2 shows the FTIR result consisting of various vibration and absorption bands. The vibration bands observed in SBE at  $3214 \text{ cm}^{-1}$  correspond to the O-H stretching of structural hydroxyl groups and hydration water molecules, respectively, indicating the possibility of the hydroxyl linkage. Also, a strong stretching vibration band of  $\text{CH}_2\text{-CH}_3$  was observed at  $2923 \text{ cm}^{-1}$  in SBE, indicating saturated carbonaceous oil chains and FFAs in SBE. The broad band at  $1464 \text{ cm}^{-1}$  in the FTIR spectrum of SBE represents C-H bending, showing high oil content in SBE. A strong adsorption bank in the region of  $1649 \text{ cm}^{-1}$  in SBE indicates O-H bending vibrations of physisorbed water molecules, proving the presence of Brønsted acid sites in SBE due to hydration. Absorption bands Si-O and Si-O-Al at  $969 \text{ cm}^{-1}$  confirm the montmorillonite structure in SBE. The band at  $643 \text{ cm}^{-1}$  of SBE probably indicates the presence of Al-O impurities and out-of-the-plane Si-O coupling, also known as cristobalite (Kanda et al., 2017).

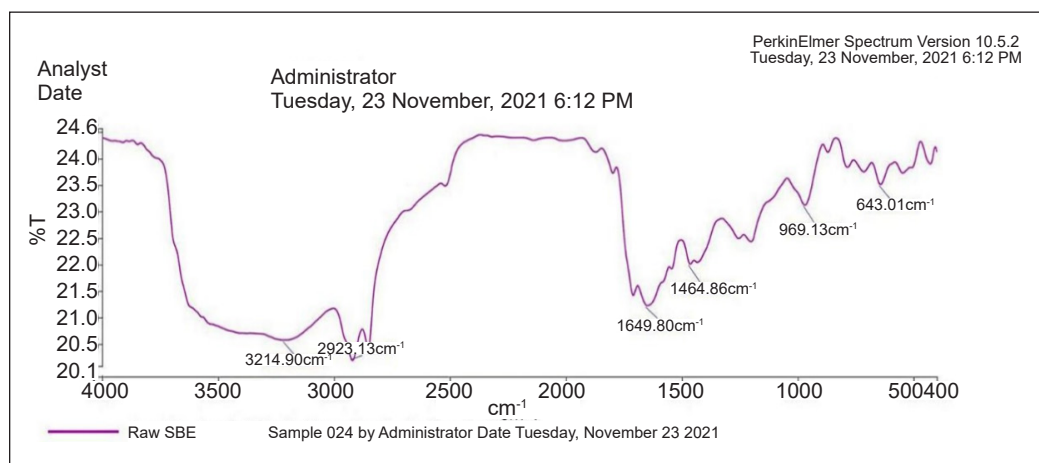


Figure 2. FTIR analysis of SBE

## Effect of Solid and Liquid Catalysts on Waste Cooking Oil Esterification

**Screening The Effect of Solid Catalysts in Waste Cooking Oil Esterification.** Figure 3 shows the effect of the type catalyst used on the FFA conversion of WCO, where the oil-to-methanol molar ratio, reaction time, catalyst loading, and temperature were fixed at 1:10, 60 min, 2 g, and  $60^\circ\text{C}$ , respectively. The parameters were set according to the preliminary study in the laboratory and were found suitable for screening purposes. The FFA conversion was



obtained in the 76%–94% range. The lowest and highest conversions were obtained using KCC-1 (76.7%) and Na/KCC-1 (94.66%).

Although WCO esterification using solid catalysts has been reported in many studies (Sumarlan & Mentari, 2020; Malins et al., 2016; Aziz et al., 2017), the use of KCC-1 and Na/KCC-1 as catalysts for esterification is still new, and they offer interesting prospects to explore for the next study. The use of Na/KCC-1 in this study demonstrated the efficiency of the catalyst as the FFA conversion exceeded 90%. Although the combination of Na/KCC-1 showed a promising result, due to the limited sample of KCC-1, the comparison of solid and liquid catalysts with SBE as a catalyst was pursued. The combination of Na/KCC-1 will be investigated in the next study.

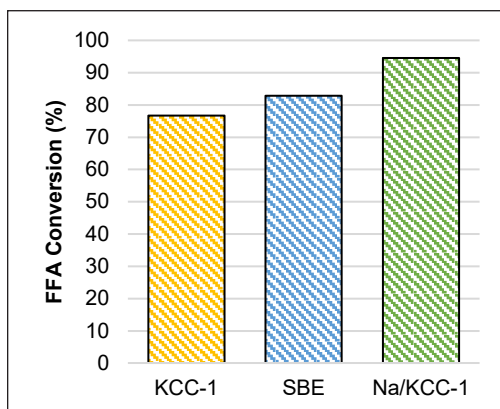


Figure 3. FFA conversion of WCO for screening of solid catalysts at 60 min, 60 °C, and 1:10 oil-to-methanol molar ratio (Replicated three times with standard deviation of 0.20–0.25)

**Screening the Effect of DESs and Comparing the Performance of DESs and Solid Catalysts in WCO Esterification.** The FFA conversion in WCO using DESs as catalysts with a constant loading of 2 g is shown in Figure 4. High FFA conversion was obtained using KOH-Gly (90.26%) compared to 87.65% using  $K_2CO_3$ -Gly. The two layers of the final product were obtained from the esterification of WCO and DES. The separation of the product was easier compared to solid catalysts. It was reported that biodiesel yield increased in the presence of DESs (Kadapuri et al., 2017).  $K_2CO_3$ -based DESs (Pourvusughi, 2012; Malins et al., 2016) and KOH-based DESs (Herman, Mukhrofut et al., 2021) were previously used in several studies for biodiesel production.

The performance of DESs and solid catalysts is shown in Table 2. Similar works from previous studies have proven the efficiency of reducing acid values using solid catalysts and DESs. A sulfonated carbon-based catalyst prepared using bamboo and palm kernel shell was used to

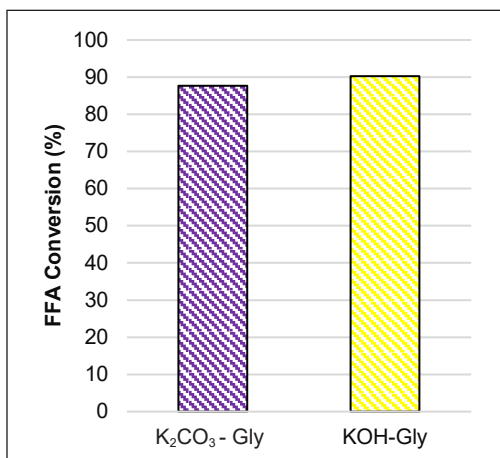


Figure 4. FFA conversion of WCO for screening of DESs at 60 min, 60°C, and 1:10 oil-to-methanol molar ratio (Replicated three times with standard deviation of 0.20–0.25)

esterify palm fatty acid distillate (PFAD), and the acid value obtained was lower than the maximum threshold (0.45 mg KOH/g) (Farabi et al., 2019). This study obtained the highest reduction using KOH-Gly and Na/KCC-1 with 0.81 and 0.45 mg KOH/g, respectively. KCC-1 recorded the lowest FFA reduction for this work.

Table 2  
*Acid value after WCO esterification*

Sample	Catalyst	Acid Value (mg KOH/g)
WCO	Blank	8.42
	KCC-1	1.96
	SBE	1.43
	K <sub>2</sub> CO <sub>3</sub> -Gly	1.04
	KOH-Gly	0.81
	Na/KCC-1	0.45

### Comparison of the Effect of SBE and DES as Catalysts

**Effect of Catalyst Loading.** Figure 5 shows the relationship between FFA conversion and catalyst loading, while the oil-to-methanol molar ratio, reaction time, and temperature were fixed at 1:10, 60 min, and 60°C, respectively. The FFA conversion using KOH-Gly and SBE increased from 34.32% to 83.49% and 78.62% to 79.57%, respectively, as the catalysts loading increased from 0.8 g to 2.0 g. The significant increase in the conversion shows that the amount of catalyst dosage influences the FFA conversion in this reaction process (Alhassan et al., 2015). The increase in fatty acid methyl ester (FAME) yield can be attributed to higher viscosity with higher CL, which reduces the diffusion of a three-phase system (methanol-oil-catalyst) (Ali et al., 2020). A similar trend in the esterification of PFAD was reported by Chongkhong et al. (2007).

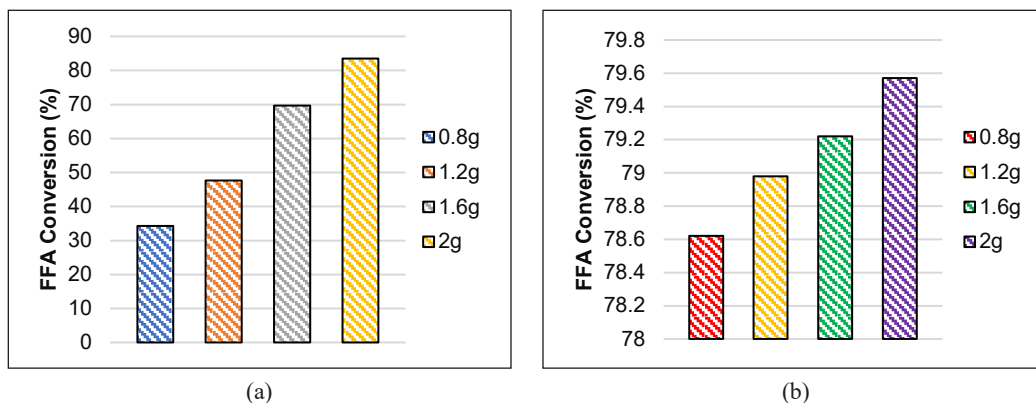


Figure 5. Effect of catalyst loading on FFA conversion at 60 min, 60°C, and 1:10 oil-to-methanol molar ratio using (a) KOH-Gly and (b) SBE catalysts (Replicated three times with standard deviation of 0.20–0.25)

**Effect of Oil-to-Methanol Molar Ratio.** Figure 6 illustrates the effect of the oil-to-methanol molar ratio on FFA conversion at 60 min and 60°C. Figure 6 shows high conversion is possible with a high oil-to-methanol molar ratio. The FFA conversion using

KOH-Gly increased at the ratio of 1:6 and continued to increase at the ratios of 1:8 and 1:10. The highest conversion for KOH-Gly was 97.74% at the ratio of 1:10. Meanwhile, the FFA conversion using SBE ranged between 78% and 83%. The Le Chatelier principle can be used to explain the upward trend in conversion. Increased methanol concentration resulted in a higher final conversion of FFA to methyl ester (Al-Sakkari et al., 2017). A previous study demonstrated that increasing the molar ratio to 1:18 increased the FFA conversion (Gan et al., 2009). Furthermore, increasing the oil-to-methanol molar ratio reduces the viscosity of the reaction mixture from a mass transfer standpoint. It improves the mixing of reactants and catalysts, resulting in a higher conversion in a given period due to the increasing mass transfer rate (Gan et al., 2010).

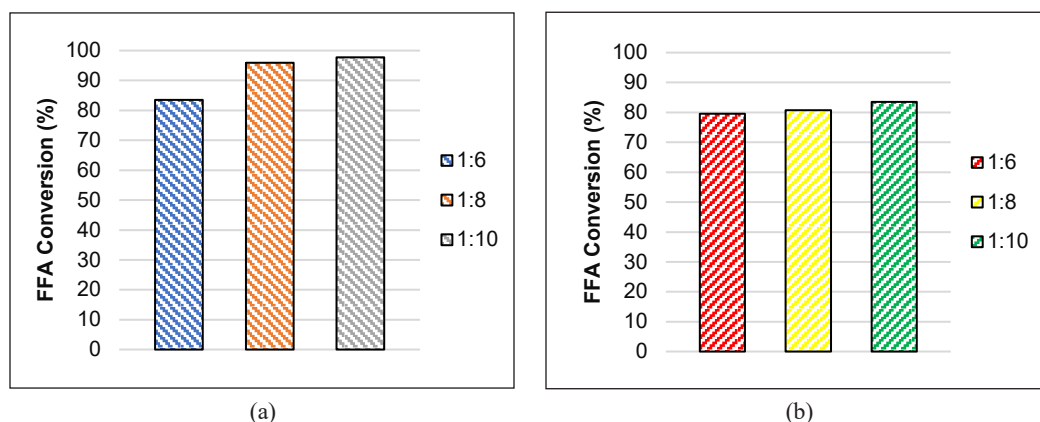


Figure 6. Effect of oil-to-methanol molar ratio on FFA conversion at 60 min, 60°C, and 2 g of catalyst loading using (a) KOH-Gly and (b) SBE catalysts (Replicated three times with standard deviation of 0.20–0.25)

**Effect of Temperature.** Figure 7 presents the study's results on the effect of temperature at 40, 60, 80, and 100°C for the oil-to-methanol molar ratio of 1:10 and reaction time of 60 min. From the Figure 7, higher FFA conversion rates are achieved at higher reaction times because esterification is endothermic (Bhatia et al., 2020). Furthermore, due to the agitation effect, a pseudo-homogeneous reaction mixture is produced after methanol droplets are broken.

Esterification should be conducted at a temperature lower than 65°C to avoid excessive methanol evaporation, which can induce the backward reaction and lower the conversion reaction (Al-Sakkari et al., 2020). A previous study did not observe a significant change in FFA conversion when the temperature was increased from 65°C to 85°C. The FFA conversion exceeded 90% at the optimized temperature of 65°C (Farabi et al., 2019). However, some studies have shown a similar trend to the current study, in which a higher conversion of FFA was obtained at a temperature of more than 65 °C. The dissolution follows the diffusion of FFA toward the catalyst in methanol. Subsequently, the penetration

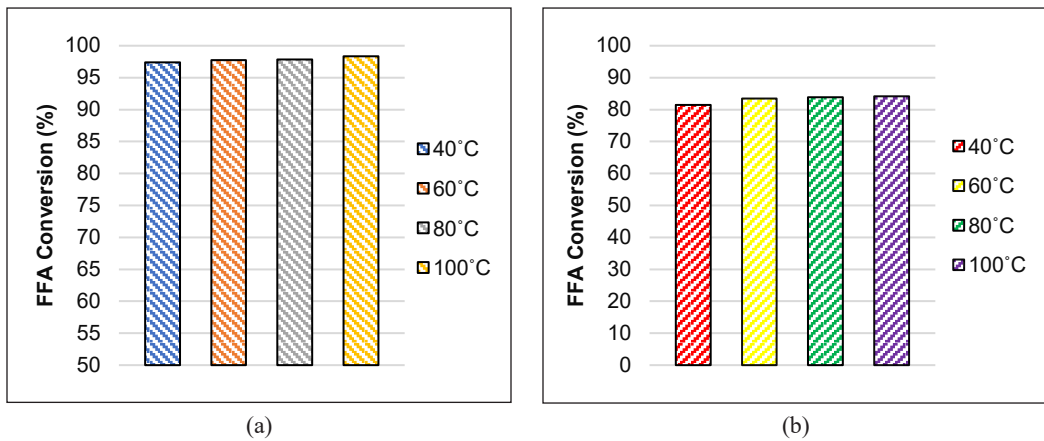


Figure 7. Effect of temperature on FFA conversion at 60 min, 1:10 oil-to-methanol molar ratio, and 2 g of catalyst loading using (a) KOH-Gly and (b) SBE catalysts (Replicated three times with standard deviation of 0.20–0.25)

of FFA inside the pores of the catalyst enables the FFA to undergo catalysis on the inner and outer surfaces (Boffito et al., 2013). As the viscosity of WCO drops, better mixing can be achieved between reactants and catalysts (Gan et al., 2010).

**Effect of Reaction Time.** The effect of reaction time on FFA conversion was studied by varying the reaction time from 30 to 60 min while other parameters were fixed. Figure 8 shows the FFA conversion of WCO. From the results, the FFA conversion increases with reaction time.

The oil-methanol immiscibility at the beginning of esterification influences the increase in FFA conversion with time (Rabie et al., 2019; Sofi et al., 2019). Hence, in this work, the maximum yields of 97.74% and 83.49% were obtained in 60 min at 100°C for the reaction

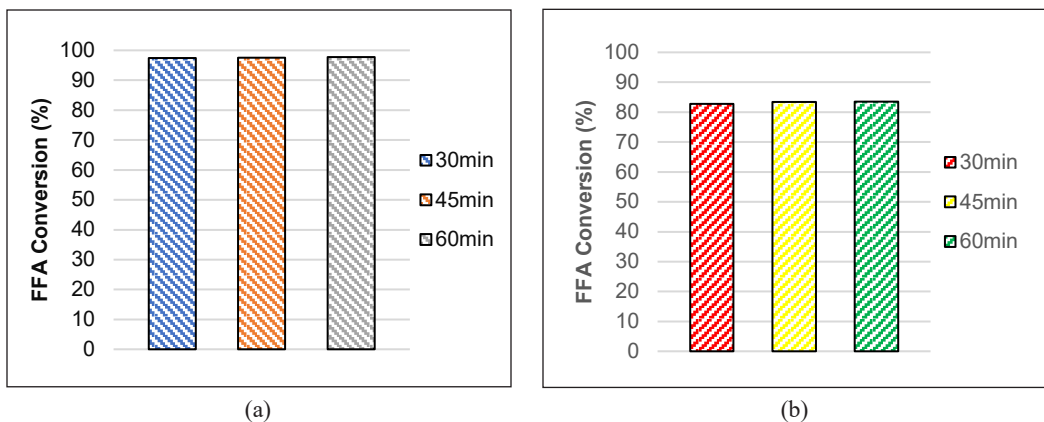


Figure 8. Effect of reaction time on FFA conversion at 60°C, 1:10 oil-to-methanol molar ratio, and 2 g of catalyst loading using (a) KOH-Gly and (b) SBE catalysts (Replicated three times with standard deviation of 0.20–0.25)

catalyzed by KOH-Gly and SBE, respectively. However, based on the results, 30 min is a suitable time for the esterification process because no significant increment was observed for FFA conversion of WCO at prolonged reaction times.

**Transesterification of Treated WCO.** The oil treated with KOH-Gly and SBE was used as the feedstock for biodiesel production via transesterification. The process was performed under similar conditions (1:6 oil-to-methanol molar ratio, 0.55 wt.% KOH, 1 h, and 65°C). High conversion of FAME was obtained in the 90%–97% range for KOH-Gly-treated oil and 80%–85% for SBE-treated oil.

Gas chromatography-mass spectrometry was utilized to identify the chemical composition of the biodiesel produced from the treated oil. Five main chemical compositions were analyzed: ester, acid, alcohol, ketone, and phenol. The analysis determined that the chemical composition of biodiesel from the treated oil using KOH-Gly was 98.54% ester, 0.22% acid, 0.03% alcohol, 0.02% phenol, 0.1% ketone, and 1.09% other compounds. Meanwhile, the biodiesel produced from the treated oil using SBE indicated 98.41% ester, 0.23% acid, 0.37% alcohol, 0.04% phenol, 0.11% ketone, and 0.84% other compounds. The composition of FAME produced from the treated oil using KOH-Gly and SBE is given in Table 3. Each biodiesel's highest fatty acid composition is hexadecanoic acid methyl ester, which is naturally present in crude palm oil and is the feedstock's source.

Table 3  
Composition of FAME

Fatty Acid	Formula	Composition of Methyl Ester (%)	
		KOH-Gly Biodiesel	SBE Biodiesel
Dodecanoic acid, methyl ester	C <sub>13</sub> H <sub>26</sub> O <sub>2</sub>	0.56	0.64
Methyl tetradecanoate	C <sub>15</sub> H <sub>30</sub> O <sub>2</sub>	2.07	2.44
9-Hexadecenoic acid, methyl ester, (Z)-	C <sub>17</sub> H <sub>32</sub> O <sub>2</sub>	0.95	1.04
Hexadecanoic acid, methyl ester	C <sub>17</sub> H <sub>34</sub> O <sub>2</sub>	60.24	58.78
Tetradecanoic acid, 2,3-dihydroxy propyl ester	C <sub>17</sub> H <sub>34</sub> O <sub>4</sub>	0.49	0.14
9,12-Octadecadienoic acid (Z,Z)-, methyl ester	C <sub>19</sub> H <sub>34</sub> O <sub>2</sub>	7.76	9.3
9-Octadecenoic acid, methyl ester	C <sub>19</sub> H <sub>36</sub> O <sub>2</sub>	18.16	17.47
Octadecanoic acid, methyl ester	C <sub>19</sub> H <sub>38</sub> O <sub>2</sub>	7.99	8.02
Eicosanoic acid, methyl ester	C <sub>21</sub> H <sub>42</sub> O <sub>2</sub>	0.29	0.27

## CONCLUSION

This research is a forerunner for a novel process in which DESs and solid catalysts (KCC-1, Na/KCC-1, and SBE) were used as the pretreatment catalysts prior to biodiesel production. The results revealed that FFA conversion reached the highest at 94.66% and 90.38% using Na/KCC-1 and KOH-Gly, respectively. FFA reduction in WCO shows that

the samples can be potentially used as a feedstock to produce biodiesel. A further study of WCO esterification using KOH-Gly and SBE as catalysts was conducted. The highest conversion was achieved using KOH-Gly at 98.34%. Meanwhile, the conversion using SBE as a catalyst was lower than KOH-Gly with 84.2%. The transesterification process found that the conversion was 80%–97% using KOH-Gly and SBE-treated oil. The highest FAME for each biodiesel is hexadecanoic acid, a methyl ester that can improve the properties of biodiesel due to its higher cetane number. From a practical viewpoint, modified KCC-1 can be widely explored as a catalyst for WCO esterification and transesterification for biodiesel production.

## ACKNOWLEDGEMENTS

The authors acknowledge the support of the Fundamental Research Grant Scheme (FRGS) under the grant number FRGS/1/12019/STG05/UNIMAP/02/4 from the Ministry of Higher Education Malaysia. In addition, the authors thank Tuan Amran Tuan Abdullah (UTM) and Muhammad Adli Hanif (UniMAP), who provided solid catalysts for completing the project.

## REFERENCES

- Al-Sakkari, E. G., Abdeldayem, O. M., El-Sheltawy, S. T., Abadir, M. F., Soliman, A., Rene, E. R., & Ismail, I. (2020). Esterification of high FFA content waste cooking oil through different techniques including the utilization of cement kiln dust as a heterogeneous catalyst: A comparative study. *Fuel*, 279, Article 118519. <https://doi.org/10.1016/j.fuel.2020.118519>
- Al-Sakkari, E. G., El-Sheltawy, S. T., Abadir, M. F., Attia, N. K., & El Diwani, G. (2017). Investigation of cement kiln dust utilization for catalyzing biodiesel production via response surface methodology. *International Journal of Energy Research*, 41(4), 593-603. <https://doi.org/10.1002/er.3635>
- Alhassan, F. H., Rashid, U., & Taufiq-Yap, Y. H. (2015). Synthesis of waste cooking oil-based biodiesel via effectual recyclable bi-functional  $\text{Fe}_2\text{O}_3\text{MnOSO}_4^{2-}/\text{ZrO}_2$  nanoparticle solid catalyst. *Fuel*, 142, 38-45. <https://doi.org/10.1016/j.fuel.2014.10.038>
- Ali, R. M., Elkatory, M. R., & Hamad, H. A. (2020). Highly active and stable magnetically recyclable  $\text{CuFe}_2\text{O}_4$  as a heterogenous catalyst for efficient conversion of waste frying oil to biodiesel. *Fuel*, 268, Article 117297. <https://doi.org/10.1016/j.fuel.2020.117297>
- Azhar, N. I., Mokhtar, N. M., Mahmood, S., Aziz, M. A. A., & Arifin, M. A. (2023). Evaluation of *Piper betle* L. extracts and its antivirulence activity towards *P. Aeruginosa*. *Jurnal Teknologi*, 85(1), 133-140. <https://doi.org/10.11113/jurnalteknologi.v85.18892>
- Azhar, M. A., Rahman, N. W. A., Aziz, M. A. A., & Isa, K. M. (2021). Identification of chemical compounds from agarwood hydrosol (*Aquilaria malaccensis*) fruits via LC-QTOF-MS/MS analysis. *IOP Conference Series: Earth and Environmental Science*, 765, Article 012010. <https://doi.org/10.1088/1755-1315/765/1/012010>

- Aziz, M. A. A., Isa, K. M., & Rashid, R. A. (2017). Pneumatic jiggling: Influence of operating parameters on separation efficiency of solid waste materials. *Waste Management and Research*, 35(6), 647-655. <https://doi.org/10.1177/0734242X17697815>
- Aziz, M. A., Yusop, A. F., Yasin, M. H. M., Hamidi, M. A., Alias, A., Hussin, H., & Hamri, S. (2017). Study of alcohol fuel of butanol and ethanol effect on the compression ignition (CI) engine performance, combustion and emission characteristic. *IOP Conference Series: Materials Science and Engineering*, 257, Article 012079. <https://doi.org/10.1088/1757-899X/257/1/012079>
- Bhatia, S. K., Gurav, R., Choi, T., Kim, H. J., Yang, S., Song, H., Park, J. Y., Park, Y., Han, Y., Choi, Y., Kim, S., Yoon, J., & Yang, Y. (2020). Conversion of waste cooking oil into biodiesel using heterogenous catalyst derived from cork biochar. *Bioresource Technology*, 302, Article 122872. <https://doi.org/10.1016/j.biortech.2020.122872>
- Bobadilla, M. C., Lorza, R. L., García, R. E., Gómez, F. S., & González, E. P. V. (2017). An improvement in biodiesel production from waste cooking oil by applying thought multi-response surface methodology using desirability functions. *Energies*, 10(1), Article 130. <https://doi.org/10.3390/en10010130>
- Boffito, D. C., Pirola, C., Galli, F., Di Michele, A., & Bianchi, C. (2013). Free fatty acids esterification of waste cooking oil and its mixtures with rapeseed oil and diesel. *Fuel*, 108, 612-619. <https://doi.org/10.1016/j.fuel.2012.10.069>
- Chandraseagar, S., Abdulrazik, A. H., Abdulrahman, S. N., & Abdaziz, M. A. (2019). Aspen Plus simulation and optimization of industrial spent caustic wastewater treatment by wet oxidation method. *IOP Conference Series: Materials Science and Engineering*, 702, Article 012011. <https://doi.org/10.1088/1757-899X/702/1/012011>
- Changmai, B., Vanlalveni, C., Ingle, A. P., Bhagat, R., & Rokhum, S. L. (2020). Widely used catalysts in biodiesel production: A review. *RSC Advances*, 10, 41625-41679. <https://doi.org/10.1039/D0RA07931F>
- Chongkhong, S., Tongurai, C., Chetpattananondh, P., & Bunyakan, C. (2007). Biodiesel production by esterification of palm fatty acid distillate. *Biomass and Bioenergy*, 31, 563- 568. <https://doi.org/10.1016/j.biombioe.2007.03.001>
- Chuah, L. F., Yusup, S., Aziz, A. R. A., Klemeš, J. J., Bokhari, A., & Abdullah, M. Z. (2016). Influence of fatty acids content in non-edible oil for biodiesel properties. *Clean Technologies and Environmental Policy*, 18, 473-482. <https://doi.org/10.1007/s10098-015-1022-x>
- Dahawi, Y. A., Abdulrazik, A., Seman, M. N. A., Aziz, M. A. A., & Yunus, M. Y. M. (2019). Aspen plus simulation of bio-char production from a biomass-based slow pyrolysis process. *Key Engineering Materials*, 797, 336-341. <https://doi.org/10.4028/www.scientific.net/KEM.797.336>
- Farabi, M. S. A., Ibrahim, M. L., Rashid, U., & Taufiq-Yap, Y. H. (2019). Esterification of palm fatty acid distillate using sulfonated carbon-based catalyst derived from palm kernel shell and bamboo. *Energy Conversion and Management*, 181, 562-570. <https://doi.org/10.1016/j.enconman.2018.12.033>
- Fatt, L. C., Rahman, N. W. A., Aziz, M. A. A., & Isa, K. M. (2021). Identification of the chemical constituents of curcuma caesia (Black Turmeric) hydrosol extracted by hydro-distillation method. *IOP Conference Series: Earth and Environmental Science*, 765, Article 012025. <https://doi.org/10.1088/1755-1315/765/1/012025>

- Gan, M., Pan, D., Ma, L., Yue, E., & Hong, J. (2009). The kinetics of the esterification of free fatty acids in waste cooking oil using  $\text{Fe}_2(\text{SO}_4)_3/\text{C}$  Catalyst. *Chinese Journal of Chemical Engineering*, 17(1), 83-87. [https://doi.org/10.1016/S1004-9541\(09\)60037-9](https://doi.org/10.1016/S1004-9541(09)60037-9)
- Gan, S., Ng, H. K., Ooi, C. W., Motala, N. O., & Ismail, M. A. F. (2010). Ferric sulphate catalysed esterification of free fatty acids in waste cooking oil. *Bioresource Technology*, 101(19), 7338-7343. <https://doi.org/10.1016/j.biortech.2010.04.028>
- Hamid, M. Y. S., Triwahyono, S., Jalil, A. A., Jusoh, N. W. C., Izan, S. M., & Abdullah, T. A. T. (2018). Tailoring the properties of metal oxide loaded/KCC-1 toward a different mechanism of  $\text{CO}_2$  methanation by in situ IR and ESR. *Inorganic Chemistry*, 57(1), 5859-5869. <https://doi.org/10.1021/acs.inorgchem.8b00241>
- Hanif, M. A., Ibrahim, N., Isa, K. M., Abdullah, T. A. T., & Jalil, A. A. (2021). Sulfur dioxide removal by mesoporous silica KCC-1 modified with low-coverage metal nitrates. *Materials Today: Proceedings*, 47(Part 6), 1323-1328. <https://doi.org/10.1016/j.matpr.2021.02.807>
- Hayyan, A., Hashim, M. A., Hayyan, M., Mjalli, F. S., & Alnashef, I. M. (2014). A new processing route for cleaner production of biodiesel fuel using a choline chloride based deep eutectic solvent. *Journal Clean Production*, 65, 246-251. <https://doi.org/10.1016/j.jclepro.2013.08.031>
- Herman, I. T., Isa, K. M., Ibrahim, N., Kasim, F. H., & Aziz, M. A. A. (2021). A single step transesterification process to produce biodiesel from the spent cooking oil. *IOP Conference Series: Earth and Environmental Science*, 765, Article 012077. <https://doi.org/10.1088/1755-1315/765/1/012077>
- Herman, I. T., Mukhrofum, F., Md Isa, K., Ibrahim, N., & Aziz, M. A. A. (2021). Methanolysis of Ceiba Petandra (Kapok) seed for high yield fatty acid methyl ester (FAME): A parametric study. *IOP Conference Series: Earth and Environmental Science* 765, Article 012075. <https://doi.org/10.1088/1755-1315/765/1/012075>
- Isa, K. M., Kasim, F. H., Saad, S. A., Rahim, M. A. A., Aziz, M. A. A., & Ali, U. F. M. (2017). Influence of operating parameters on biomass conversion under sub- and supercritical water conditions. *Chemical Engineering and Technology*, 40(3), 537-545. <https://doi.org/10.1002/ceat.201600343>
- Ismail, N. A., Aziz, M. A. A., Hisyam, A., & Abidin, M. A. (2021). Separation of samarium from medium rare earth mixture using multi-stage counter-current extraction. *Chemical Engineering Communications*, 208(5), 764-774. <https://doi.org/10.1080/00986445.2020.1746654>
- Ismail, N. A., Yunus, M. M., Aziz, M. A. A., & Abidin, M. A. (2019). Comparison of optimal solvent extraction stages between P204 and [A336][P204] for the separation of europium and gadolinium. *IOP Conference Series: Materials Science and Engineering*, 702, Article 012044. <https://doi.org/10.1088/1757-899X/702/1/012044>
- Japar, N. S., A. Aziz, M. A., & Razali, M. N. (2019). Formulation of fumed silica grease from waste transformer oil as base oil. *Egyptian Journal of Petroleum*, 28(1), 91-96. <https://doi.org/10.1016/j.ejpe.2018.12.001>
- Kadapure, S. A., Kiran, A., Anant, J., Dayanand, N., Rahul, P., & Poonam, K. (2017). Optimization of conversion of Pongamia pinnata oil with high FFA to biodiesel using novel deep eutectic solvent. *Journal of Environmental Chemical Engineering*, 5(6), 5331-5336. <https://doi.org/10.1016/j.jece.2017.10.018>
- Kanda, L. R. S., Corazza, M. L., Zatta, L., & Wypych, F. (2017). Kinetics evaluation of the ethyl esterification of long chain fatty acids using commercial montmorillonite K10 as catalyst. *Fuel*, 193, 265-274. <https://doi.org/10.1016/j.fuel.2016.12.055>



- Mahmud, M. S., Ishak, S., Razali, M. N., Aziz, M. A. A., & Musa, M. (2019). Grease quality issues on middle voltage switchgear: Corrosivity, resistivity, safety and ageing. *IJUM Engineering Journal*, 20, 216-228. <https://doi.org/10.31436/iiumej.v20i1.995>
- Malins, K., Brinks, J., Kampars, V., & Malina, I. (2016). Esterification of rapeseed oil fatty acids using a carbon-based heterogeneous acid catalyst derived from cellulose. *Applied Catalysis A: General*, 519, 99-106. <https://doi.org/10.1016/j.apcata.2016.03.020>
- Manurung, R., Arief, A., & Hutauruk, G. R. (2018). Purification of red palm biodiesel by using  $K_2CO_3$  based deep eutectic solvent (DES) with glycerol as hydrogen bond donor (HBD). In *AIP Conference Proceedings* (Vol. 1977, No. 1). AIP Publishing. <https://doi.org/10.1063/1.5042866>
- Manurung, R., Hutauruk, G. R., & Arief, A. (2018). Vitamin E extraction from redpalm biodiesel by using  $K_2CO_3$  based deep eutectic solvent with glycerol as hydrogen bond donor. In *AIP Conference Proceedings* (Vol. 1977, No. 1). AIP Publishing. <https://doi.org/10.1063/1.5042867>
- Manurung, R., & Liang, A. (2018). Minor component extraction from palm methyl ester using potassium carbonate glycerol based deep eutectic solvent (DES). *Rasayan Journal of Chemistry*, 11(4), 1519-1524. <http://dx.doi.org/10.31788/RJC.2018.1143079>
- Nguyen, H. C., Nguyen, M. L., Wang, F., Juan, H., & Su, C. (2020). Biodiesel production by direct transesterification of wet spent coffee grounds using switchable solvent as a catalyst and solvent. *Bioresource Technology*, 296, Article 122334. <https://doi.org/10.1016/j.biortech.2019.122334>
- Petračić, A., Gavran, M., Skunca, L., Stajduhar, L., & Sander, A. (2020). Deep eutectic solvents for purification of waste cooking oil and crude biodiesel. *Technologica Acta*, 13(1), 21-26. <http://dx.doi.org/10.5281/zenodo.4059934>
- Pourvusughi, N. (2012). An optimized process for biodiesel production from high FFA spent bleaching earth. *International Journal of Engineering*, 26(12), 1546-1550.
- Rabie, A. M., Shaban, M., Abukhadra, M. R., Hosny, R., Ahmed, S. A., & Negm, N. A. (2019). Diatomite supported by CaO/MgO nanocomposite as heterogeneous catalyst for biodiesel production from waste cooking oil. *Journal of Molecular Liquids*, 279, 224-231. <https://doi.org/10.1016/j.molliq.2019.01.096>
- Rahman, N. W. B. A., & Aziz, M. A. B. A. (2022). The effects of additives on anti-wear properties of lubricating grease formulated from waste engine oil. *Egyptian Journal of Petroleum*, 31(3), 71-76. <https://doi.org/10.1016/j.ejpe.2022.07.002>
- Rahman, N. W. A., Japar, N. S. A., Aziz, M. A. A., Razik, A. H. A., & Yunus, M. Y. M. (2019). Sodium grease formulation from waste engine oil. *IOP Conference Series: Earth and Environmental Science*, 257, Article 012018. <https://doi.org/10.1088/1755-1315/257/1/012018>
- Razali, M. N., Aziz, M. A. A., Jamin, N. F. M., & Salehan, N. A. M. (2018). Modification of bitumen using polyacrylic wig waste. In *AIP Conference Proceedings* (Vol. 1930, No. 1). AIP Publishing. <https://doi.org/10.1063/1.5022945>
- Razali, M. N., Isa, S. N. E. M., Salehan, N. A. M., Musa, M., Aziz, M. A. A., Nour, A. H., & Yunus, R. M. (2020). Formulation of emulsified modification bitumen from industrial wastes. *Indonesian Journal of Chemistry*, 20(1), 96-104. <https://doi.org/10.22146/ijc.40888>

- Sander, A., Petračić, A., Parlov Vuković, J., & Husinec, L. (2020). From coffee to biodiesel - Deep eutectic solvents for feedstock and biodiesel purification. *Separations*, 7(2), Article 22. <https://doi.org/10.3390/separations7020022>
- Shahbaz, K., Bagh, F. S. G., Mjalli, F. S., Alnashef, I. M., & Hashim, M. A. (2013). Prediction of refractive index and density of deep eutectic solvents using atomic contributions. *Fluid Phase Equilibria*, 354, 304-311. <https://doi.org/10.1016/j.fluid.2013.06.050>
- Sofi, S. N. A. M., Aziz, M. A. A., Japar, N. S. A., Rahman, N. W. A., Abdulhalim, A. R., & Yunus, M. M. M. (2019). Preparation and characterization of grease formulated from waste transformer oil. *IOP Conference Series: Materials Science and Engineering*, 702, Article 012034. <http://dx.doi.org/10.1088/1757-899X/702/1/012034>
- Sumarlan, I., & Mentari, R. B. (2020). Esterification of waste cooking oil using heterogeneous catalyst from pearl shell. *Jurnal Akademika Kimia*, 9(3), 183-190.
- Taslim, Indra, L., Manurung, R., Winarta, A., & Ramadhani, D. A. (2017). Biodiesel production from ethanolysis of DPO using deep eutectic solvent (DES) based choline chloride - ethylene glycol as co-solvent. In *AIP Conference Proceedings* (Vol. 1823, No. 1). AIP Publishing. <https://doi.org/10.1063/1.4978079>
- Thoai, D. N., Le Hang, P. T., & Lan, D. T. (2019). Pre-treatment of waste cooking oil with high free fatty acids content for biodiesel production: An optimization study via response surface methodology. *Vietnam Journal of Chemistry*, 57(5), 568-573. <https://doi.org/10.1002/vjch.201900072>
- Yusuff, A. S., & Popoola, L. T. (2019). Optimization of biodiesel production from waste frying oil over alumina supported chicken eggshell catalyst using experimental design tool. *Acta Polytechnica*, 59(1), 88-97. <https://doi.org/10.14311/AP.2019.59.0088>

# Smart Hydroponic Farming System Integrated with LED Grow Lights

Primadiyanti Nirbita, Kah-Yoong Chan\*, Gregory Soon How Thien and Chu-Liang Lee

*Centre for Advanced Devices and Systems, Faculty of Engineering, Multimedia University, Persiaran Multimedia, 63100 Cyberjaya, Selangor, Malaysia*

## ABSTRACT

Vertical farming, including hydroponics, is a growing trend in the agricultural sector due to the increasing demand for food and urbanisation. Thus, hydroponics can save space and achieve faster plant growth compared to traditional farming methods. The concept of smart farming has been applied in this study to improve the ease of control and monitoring of hydroponic systems. The effects of light-emitting diodes (LEDs), light distance, and colour (purple and white) on water spinach growth in a hydroponic system were investigated. Additionally, an Internet of Things (IoT) controller was developed and implemented to facilitate the use of the system in an indoor hydroponic-based environment system. Based on the results, the distance between the LED light of 15 cm and the plants and the colour of the LED light (white) can positively impact plant growth in a hydroponic system. Using an IoT controller also allows for continuous monitoring and control of factors that influence plant growth. Hence, this research would catalyse the local smart hydroponic farming system for improved deliverables.

*Keywords:* Grow light, hydroponic, IoT controller, light emitting diodes, smart farming

## ARTICLE INFO

### *Article history:*

Received: 03 January 2023

Accepted: 20 July 2023

Published: 14 March 2024

DOI: <https://doi.org/10.47836/pjst.32.2.11>

### *E-mail addresses:*

[prndyt@gmail.com](mailto:prndyt@gmail.com) (Primadiyanti Nirbita)

[kychan@mmu.edu.my](mailto:kychan@mmu.edu.my) (Kah-Yoong Chan)

[gregorytsh88@gmail.com](mailto:gregorytsh88@gmail.com) (Gregory Soon How Thien)

[cllee@mmu.edu.my](mailto:cllee@mmu.edu.my) (Chu-Liang Lee)

\* Corresponding author

## INTRODUCTION

Soilless agriculture can be traced back to ancient Egyptian civilisation, as depicted in a painting in the Temple of Deir el Bahari (Torabi et al., 2012). Irish scientist Robert Boyle subsequently conducted the first known experiment on growing plants with submerged roots. John Woodward's experiments in 1699 demonstrated that soil

and water could provide essential nutrients for plant growth. This observation led to the development of mineral nutrient solutions by Julius von Sachs, now widely used in soilless agriculture worldwide (De Rijck & Schrevels, 1998; Suryaningprang et al., 2021). Before 1929, the study of hydroponics was primarily focused on biological research. Nonetheless, William Frederick Gericke's efforts in the late 1920s began exploring hydroponics's commercial potential and the hydroponic system's development as it is known today (Torabi et al., 2012).

Hydroponics has emerged as a potential solution to meet the increasing demand for food due to rapid population growth and the limited availability of land for agriculture due to urbanisation (Lem et al., 2014; Satterthwaite et al., 2010). The term "hydroponics" comes from the Greek words "*hydro*," which is water, and "*ponos*," which is labour. It is a method of growing plants by immersing their roots in a nutrient solution. Hydroponics offers several advantages, such as the ability to grow plants in a smaller space by placing them closer together, the ability to control the climate through temperature, humidity, and light exposure, and improved nutrient efficiency and overall growth rates (Balashova et al., 2019; Magwaza et al., 2020). Nevertheless, hydroponics requires specialised knowledge and time to maintain the appropriate pH levels, nutrient concentrations, and water levels for optimal plant growth. In hydroponics systems, the roots of the plants are directly immersed in a nutrient solution, which must be carefully monitored. The nutrient solution must contain 13 essential macro- and micronutrients necessary for plant growth, including Ca, N, Mg, K, P, S, B, Cl, Cu, Fe, Mn, Mo, and Zn (Bugbee, 2004). Two factors that must be regularly checked in hydroponic systems are the pH level of the nutrient solution and the electrical conductivity (EC). The pH level is not essential for plant growth but determines the availability of nutrients in the solution. The EC of the nutrient solution indicates the number of ions in the root zone (Al Meselmani, 2022).

In hydroponic systems, there were approximately six system types which could generally be classified, such as Deep Water Culture (DWC) (Hamza et al., 2022; Janeczko & Timmons, 2019), Nutrient Film Technique (NFT) (Suryaningprang et al., 2021), drip irrigation (Taofik et al., 2019), ebb and flow (flood and drain) (Setiawan et al., 2022), aeroponics (Wang et al., 2019; Wimmerova et al., 2022), and wick system (Hartanti & Sulistyowati, 2022). In the DWC technique, plant roots were submerged in nutrient-rich water while plants floated in the solution. Although DWC was simple to install and maintain, the oxygen levels in the water were challenging to control. Meanwhile, NFT plants were inserted in a narrow channel, where a thin layer of the nutritional solution ran over their roots. NFT was water-efficient and suitable for the cultivation of small plants. Nonetheless, it was challenging to maintain consistent nutrient levels. For drip irrigation, a network of tubes with miniature drippers allowed a nutrient solution to drip onto the roots of the plants.

Drip irrigation was versatile and simple to install but required proper and advanced planning to avoid wastage. Alternatively, plants in ebb and flow were cultivated in a growing medium-filled tray. Periodically, the tray was saturated with a nutritious solution and then emptied. Despite the ebb and flow method being advantageous for growing huge plants and mechanised, it was prone to clogging. Plant roots were suspended in air and sprayed with nourishing in aeroponics. Aeroponics could generate rapid growth rates and great yields, but its setup was more difficult and costly. Lastly, the wick system involved plants in a growing medium and a wick transported nutrient solution from a reservoir to the plants' roots. This simple method required low maintenance, but wick systems were unsuitable for larger plants. Therefore, the choice of the hydroponic system relied on several criteria, including the type of plants being produced, the available space and resources, and the grower's experience level (Namgyel et al., 2018).

Light-emitting diodes (LEDs) are semiconductor devices that emit light through electroluminescence. The first LED was discovered by James Biard et al. in 1961, but it was not until 1944 that Shuji Nakamura developed an LED with a high-brightness blue colour suitable for plant growth (Gupta & Agarwal, 2017). LED lights are more efficient than other types of artificial lighting because they use less power but have a longer lifespan. Additionally, LEDs emit specific wavelengths, while the placement of LEDs plays a significant role in plant growth. The optimal placement of LEDs depends on the type of plant, the LED itself, the coverage area, the environmental conditions, and manufacturer recommendations (Dunn & Mills-Ibibofori, 2016). If the LED is placed too close to the plants, it can burn them, but if placed too far, the plants will grow weak due to insufficient light. Previous studies have shown that the absorption peaks of chlorophylls are in the red and blue regions (625–675 nm and 425–475 nm) (Gupta & Agarwal, 2017). On the contrary, the blue region produced a higher peak than the red region. Additionally, the peaks of phytochrome are in the red and far-red regions (660 and 730 nm, respectively) (Gupta & Agarwal, 2017). Another study found that wavelengths between 400–520 nm reported the highest absorption rate of chlorophyll and carotenoids, pigments found in plants (Xu et al., 2016). In contrast, the 610–720 nm wavelength produced a low absorption rate of chlorophyll but a high absorption rate of phytochrome (Runkle, 2016). Therefore, plants grown under red LED lights (600–700 nm) tend to be tall but have smaller leaves.

Smart farming utilises the Internet of Things (IoT) and big data analytics to monitor crops and their environment to improve sustainability in the agriculture sector (Din et al., 2018; Madushanki et al., 2019; Paul & Jeyaraj, 2019). IoT can help farmers address traditional farming challenges such as drought response, irrigation, yield, and pest control (Ayaz et al., 2019). Smart farming technologies differ from conventional farming methods. They are being increasingly adopted, as the global smart farming market is predicted to grow 19.3% annually from 2017 to 2022. Some applications of smart farming in hydroponic

systems include crop disease and pest management. The Food and Agriculture Organisation of the United Nations (FAO) estimates that 20 to 40% of global crop yields are lost due to damage caused by plant pests and diseases (Gráda, 1992). Pesticides and agrochemicals are essential for increasing crop yield, but their use can also harm the environment. Thus, IoT-based devices can monitor crop disease and pest management, providing real-time monitoring and disease forecasting that is more effective than traditional methods. Devices such as field sensors and remote sensing satellites can provide real-time monitoring.

Several IoT-based devices were employed to monitor crop disease and pest control in hydroponic farming (Mamatha & Kavitha, 2023). These devices collected and transmitted data on environmental elements that affected crop health to a central monitoring system. Smart pest monitoring systems utilise cameras and sensors to identify and monitor the movement of pests in a field of crops (Ullo & Sinha, 2020). Additionally, they could detect individual species of problems and inform farmers to take the necessary measures. For automated weather stations, the sensors capture data on temperature, humidity, precipitation, wind speed, and other meteorological characteristics (Dunaieva et al., 2021). In addition, they provided forecasts for the coming days, which assisted farmers with irrigation and pest control planning. Meanwhile, soil moisture sensors measured the soil's moisture content and provided information on the ideal irrigation period (Yu et al., 2021). This data aided farmers in avoiding excessive irrigation, which resulted in waterlogging and pest infestations. In drone-based imaging systems, drones with cameras and sensors supply crop fields with high-resolution photographs (Chan et al., 2021). This information identified regions of an area infested with pests or illnesses, allowing for specific measures to eradicate the infestation. Thus, IoT-based devices for monitoring crop disease and pest control provide real-time data, limit toxic pesticides and agrochemicals use, and help farmers optimise irrigation and pest control (Khan et al., 2021). By embracing these technologies, farmers could increase their yields and contribute to the agriculture industry's sustainable growth.

Another use of smart farming is in fertiliser (nutrient solution). Fertilisers provide essential nutrients for plant growth, but excessive use can harm the environment. Smart farming technologies, such as the Normalised Difference Vegetation Index (NDVI), can help estimate the amount of fertiliser plants need without causing harm (Zhou et al., 2021). Yield monitoring, forecasting, and harvesting are efficient examples of smart farming. Yield monitoring involves analysing various aspects of agricultural yield, while yield forecasting predicts yield before the harvest. A yield monitoring, forecasting, and harvesting system provides real-time data that can be used to estimate production and yield quality. Sensors and technologies such as auto-pumps and auto-LEDs can be applied to optimise hydroponic systems, especially in small-scale hydroponic farms. These features allow the user to control the pump and LED from their smartphone. Some sensors that can be used in hydroponic systems include pH, electrical conductivity (EC), temperature and humidity,

and water level sensors. These sensors can provide real-time data to help monitor and maintain optimal conditions for plant growth in hydroponic systems.

This study aimed to examine the effects of LED light distance and colour on the growth of water spinach in a hydroponic system. Furthermore, an IoT controller was installed to facilitate the usage of the system in an indoor hydroponic-based environment system. The distance and colour of LED light were expected to influence the growth of water spinach in a hydroponic system. An IoT controller would allow for continuous monitoring and adjustment of growth-influencing parameters. The optimal distance for LED lighting was determined to be 15 cm, and white LED lighting was more conducive to plant growth than purple LED lighting. In addition, the IoT-controlled smart farming system accurately monitored the environment, pH level of the nutrient solution, and amount of nutrients, enabling continuous monitoring and optimisation of these elements for plant growth. Hence, this study contributes to developing an efficient hydroponic system and introducing new paths for local smart farming.

## MATERIALS AND METHODS

### The Distance Between White LED and Plant for Plant Growth

The distance between White LED lights and plants was investigated to determine the optimal distance for plant growth in this study. A hydroponic system with four trays was used, three equipped with LED lights and one without LED lights (Figure 1). The LED lights were white and were turned on for 14 hours daily, from 7 am to 9 pm. The plant was water spinach, grown in rockwool as the growing medium. The plants underwent a 10-day germination process without LED lights and a 20-day germination process with LED lights. On day 30, the water spinach was harvested, and the experiment was completed. The width and height of the plants were measured every five days starting from day 11.

### The LED Colour for Plant Growth

Following the completion of the first part of the study, the effect of LED colour on plant growth was investigated using the recommended distance between LED lights

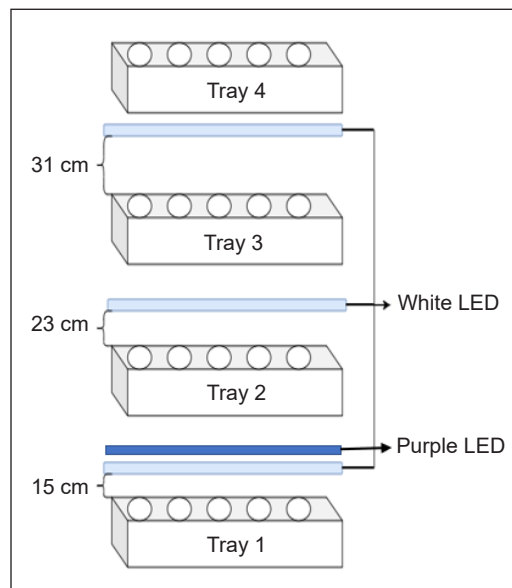


Figure 1. Schematic diagram of the hydroponic system used for LED testing

and plants from the first part. For this part of the study, only one tray was used and equipped with purple LED lights, as revealed in Figure 1. Like the last part, the LED lights were turned on every day from 7 am to 9 pm. The plant was water spinach, grown in rockwool as the growing medium. The plants underwent a 10-day germination process without LED lights and a 20-day germination process with LED lights. The width and height of the plants were measured every five days starting from day 11.

### IoT Controller for Hydroponic System

The IoT controller used in this study was based on the NodeMCU platform, which features an ESP8266 Wi-Fi-enabled chip, has simple, Arduino-like hardware input/output capabilities, and is cost-effective. The Blynk application interfered with the IoT controller, providing device management, private clouds, machine learning, and data analytics capabilities. The system employed three sensors: a DHT22 sensor, a pH sensor, and a water float sensor. The flow chart of the IoT controller is illustrated in Figure 2.

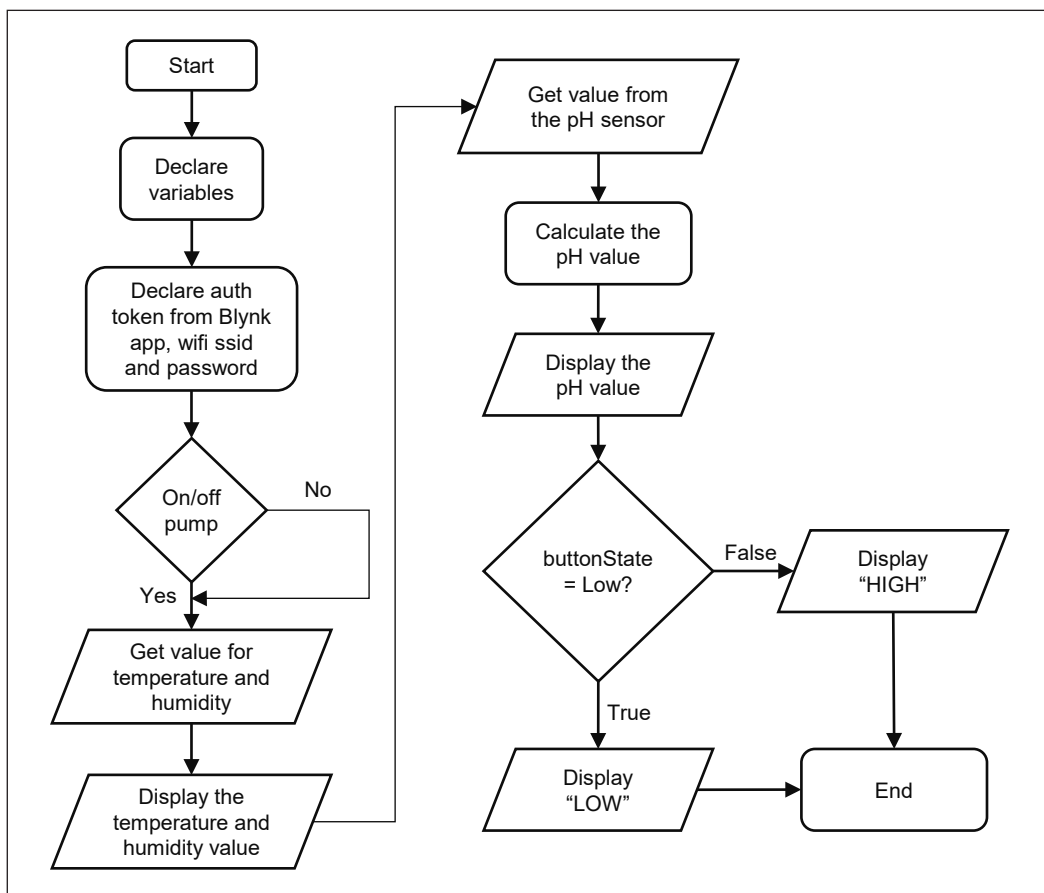


Figure 2. Schematic flow chart of the overall system in this study



## RESULTS AND DISCUSSION

### Optimised Distance Between White LED and Plant for Plant Growth

The height and width of the plants for the different distances between the white LED and the plants are tabulated in Table 1. The “LED-15 cm” condition represents 15 cm between the LED lights and plants, the “LED-23 cm” condition represents 23 cm, and the “LED-31 cm” condition represents 31 cm. The “No-LED” condition represents the absence of LED lights.

Table 1

Summary of the height and width of the plants for the varying distances between the white LED source and the plants within 20 days

Number of Germination Days	Parameters	Sample Name			
		LED-15 cm	LED-23 cm	LED-31 cm	No-LED
Day 1	Height (cm)	07.55	07.65	08.40	08.45
	Width (mm)	01.00	01.00	01.00	01.00
Day 5	Height (cm)	12.55	12.65	12.94	10.25
	Width (mm)	02.05	02.35	01.90	01.20
Day 10	Height (cm)	24.05	22.90	22.35	11.45
	Width (mm)	03.45	02.95	03.10	01.20
Day 15	Height (cm)	38.25	46.00	35.65	11.10
	Width (mm)	04.25	03.33	03.25	01.20
Day 20	Height (cm)	50.75	57.90	54.05	11.4
	Width (mm)	05.35	04.05	03.45	01.20

Figure 3 presents the investigation results of the optimal distance between LED lights and plants for plant growth. As demonstrated in Figure 3, the height of the plants under the LED-15 cm condition increased steadily while the width increased sharply. These plants

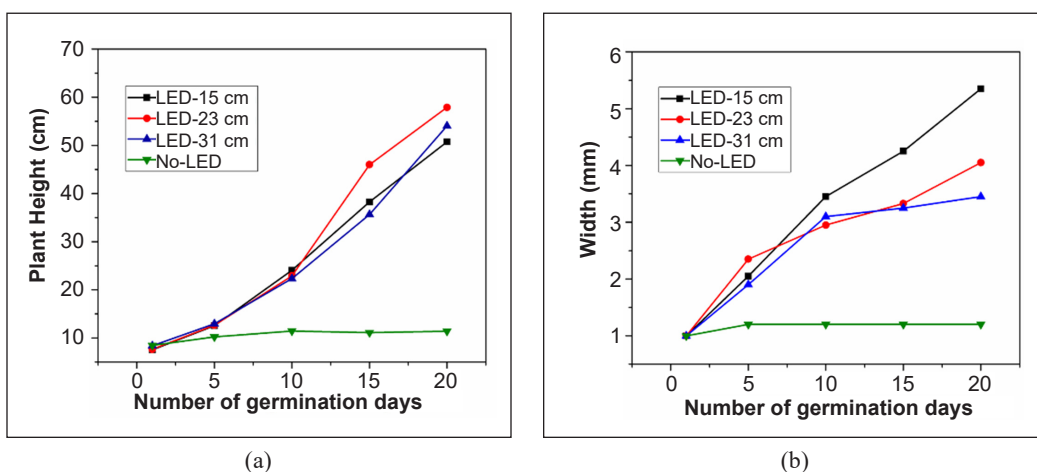


Figure 3. Graphs indicating the optimal distance between LED lights and plants for plant growth, which includes (a) height (cm) versus days and (b) width (mm) versus days

had the widest and strongest stems compared to the other conditions. The height and width of the plants under the LED-23 cm and LED-31 cm conditions also increased steadily. In contrast, these plants were taller with thin stems, causing them to bend. Alternatively, the height and width of the plant under No-LED increased for the first five days and remained constant until the end of the experiment (Day 20).

Based on the results, it was concluded that the LED 15 cm distance was optimal for water spinach growth. Although not tall, it produced solid stems and large leaves, essential for water spinach (Figure 4) (Khwankaew et al., 2018). It is important to note that the optimal LED distance may vary for other plant species and LED types, depending on the plant type, LED type, coverage area, environmental conditions, and manufacturer recommendations (Runkle, 2016).

Table 2  
Summary of the intensity of light for each distance between LED and plants

Distance between LED and water spinach	Intensity (lx)
No-LED	154.05
LED-15 cm	$2.129 \times 10^3$
LED-23 cm	$1.764 \times 10^3$
LED-31 cm	$1.545 \times 10^3$

Table 2 summarises the light intensity at each distance, measured using a lux meter positioned at the pot level facing the LED source at noon. Since No-LED

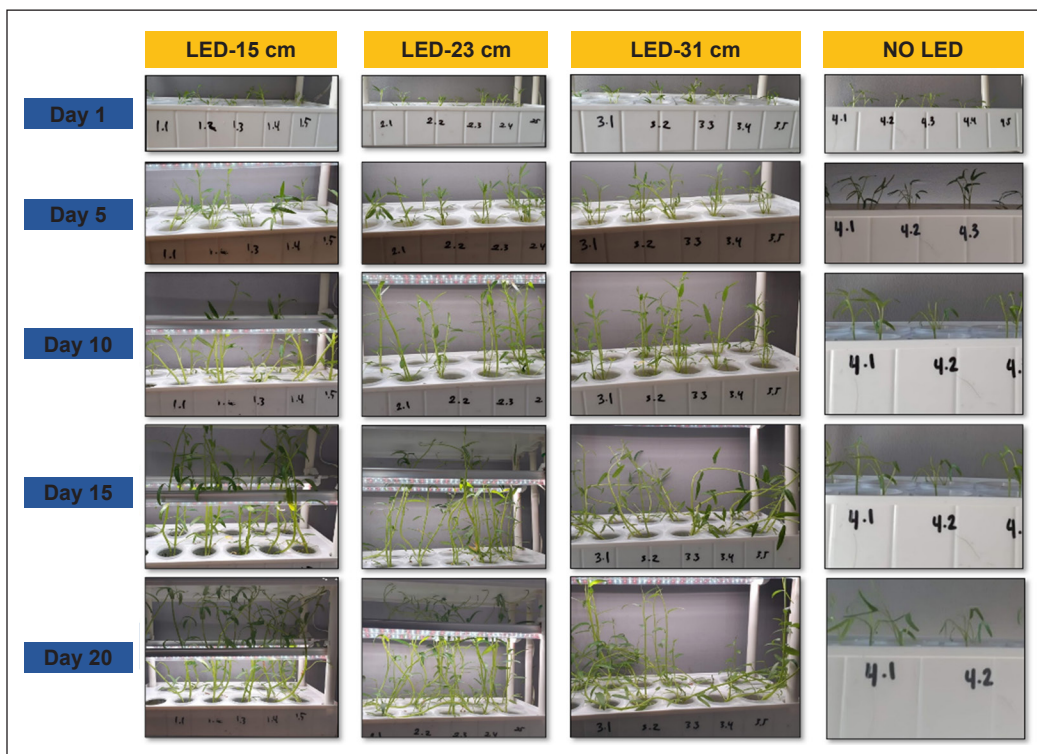


Figure 4. Photographs of water spinach plant growth under the influence of the white LED source and without LED

conditions produced very low light intensity, it is obvious the water spinach plant could not significantly grow within the germination period. The highest intensity was recorded for the LED-15 cm condition, which confirmed the most optimised condition for the water spinach growth compared to LED-23 cm and LED-31 cm conditions.

### Influence of Purple and White LED Colours for Plant Growth

This part studied two LED colours: white LED and purple LED. The LED-15 cm distance was selected throughout this experiment based on the results. Thus, the results are tabulated in Table 3.

Even though the height and width of plants grown under white LED were slightly smaller than those grown under purple LED (Figure 5), the plants grown under white LED produced bigger leaves than those grown under purple LED. For water spinach, the number and size of the leaves are more important than the size of the stem, as most people eat the leaves. Therefore, it can be concluded that white LED is better compared to purple LED for plant growth for water spinach.

Based on the information given by the manufacturer, the purple LED consists of 4 blue and 11 red LED lights. The wavelengths for blue and red LED are 450 and 660 nm, respectively. Since the white LED came together with the hydroponic system, the wavelength of the white LED was unknown. Based on the literature, the wavelength of white LED varied between 365–445 nm depending on the amount of phosphor used and 465 nm for GaN-based LED (Al Shafouri et al., 2018; Singh, 2009). Bian et al. (2018) stated that the photosynthesis rate of plants grown under the white LED was higher than those produced under the purple LED. Another study also found the highest absorption peak in the blue region (425–475 nm). Other than that, it was also found that the peaks of phytochrome absorption are in the red and far-red regions (660 and 730 nm, respectively) (Gupta & Agarwal, 2017).

Table 3  
*Summary of the height and width of the plants under purple and white LED sources within 20 days*

Number of Germination Days	Parameters	LED source	
		White	Purple
Day 1	Height (cm)	07.55	09.77
	Width (mm)	01.00	02.00
Day 5	Height (cm)	12.55	16.33
	Width (mm)	02.05	03.20
Day 10	Height (cm)	24.05	22.53
	Width (mm)	03.45	04.00
Day 15	Height (cm)	38.25	36.13
	Width (mm)	04.25	04.60
Day 20	Height (cm)	50.75	58.87
	Width (mm)	05.35	04.60

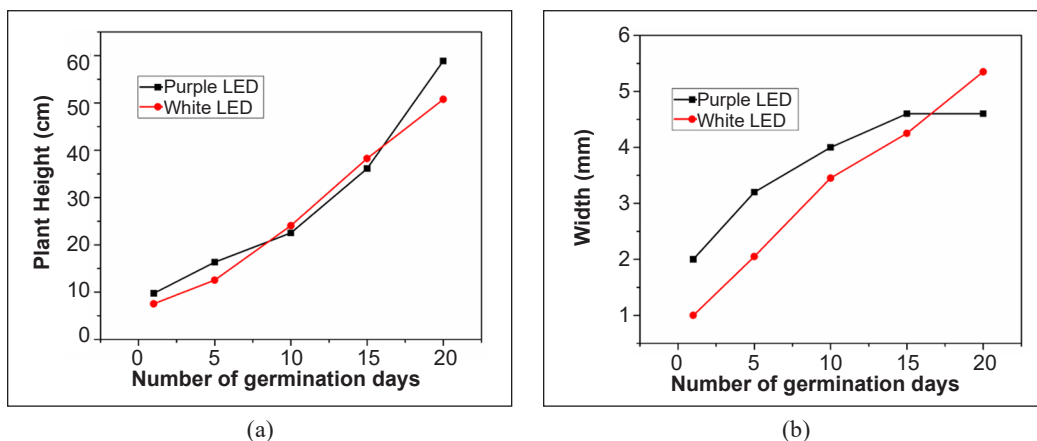


Figure 5. Graphs indicating the (a) height and (b) width variations under white and purple LED sources for plant growth

Another researchers also found that the wavelength between 400–520 nm produced the largest absorption of chlorophyll and carotenoids, a pigment found in plants (Ayaz et al., 2019). In contrast, a wavelength of 610–720 nm produced a low chlorophyll absorption rate but a high phytochrome absorption rate (Gráda, 1992). Therefore, the plants grown under red LED (600–700 nm) are tall but produce smaller leaves. White LEDs' wavelength falls under the wavelength range with large chlorophyll absorption. One of the lights, purple LED, also falls under the wavelength with high chlorophyll absorption, which is blue. However, there were only four blue LEDs out of 11 LEDs. The remaining LEDs were red, which falls under the wavelength range with a low chlorophyll absorption rate. Since the percentage of the blue LED is much smaller than the red LED, purple LED plants were taller but produced smaller leaves (Figure 6).

Although water spinach plants were demonstrated to grow effectively under white LED, it was known that different plants might have specific light requirements. The ideal wavelengths for photosynthesis varied among plant species, as did the maximum absorption rates of chlorophyll and carotenoids. It was reported that the best LED wavelengths for leafy greens, such as lettuce and spinach, were in the blue and red spectra, with a chlorophyll absorption peak around 450–460 nm and 660–680 nm (Gao et al., 2020). Some research suggested that green light (500–550 nm) could boost some plants' development and nutritional value. Herbs, such as basil and mint, were discovered to require ideal LED wavelengths comparable to those for leafy greens, with chlorophyll absorption peaking between 450–460 nm and 660–680 nm (Kondratieva et al., 2022). Conversely, herbs could benefit from increased blue light, as it might stimulate the formation of essential oils.

Fruit-bearing plants, such as tomatoes and peppers, demonstrated a greater need for red light, with chlorophyll absorption peaking between 660 and 680 nm (Ngcobo et al.,

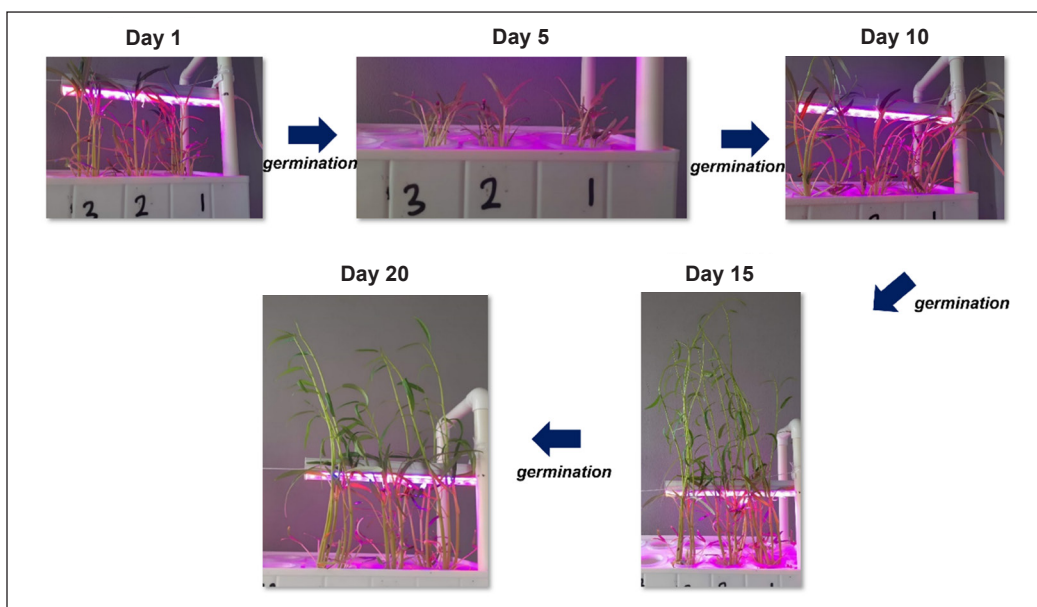


Figure 6. Photographs of water spinach plant growth under the purple LED source in this study

2022). However, they also required blue light with a peak absorption rate of 450–460 nm for vegetative growth. Root vegetables, such as carrots and potatoes, produced a lower demand for blue light but still required some development (Kim & Son, 2022). Important red light had a peak absorption rate for chlorophyll between 660 and 680 nm. Far-red light (about 730–740 nm) could boost root development in some plants (Bantis et al., 2020). For producers to optimise plant growth and output under artificial lighting conditions, it was essential to comprehend different crops' individual light spectrum needs. Hence, assessing light intensity and spectrum could assist producers in ensuring that their plants receive the optimal quantity and quality of light for optimal growth and development.

### Integrating IoT Controller for Hydroponic System

The IoT is a network of interconnected objects, devices, vehicles, equipment, and buildings that exchange information through sensors and software. Five key technologies that enable the IoT, particularly in agricultural engineering, are as follows:

1. Wireless Sensor Networks (WSN) are infrastructure-less networks that use a variety of sensors to monitor factors such as temperature, humidity, and pH with water levels to transmit data for observation or analysis (Patel & Kumar, 2018; Rathinam et al., 2019).
2. Cloud Computing (CC) delivers computing services over the internet. In this project, the user used Blynk to monitor crops and their environment (Darwish et al., 2019; Namani & Gonen, 2020).

3. Embedded systems combine hardware and software to monitor hydroponic systems (Susanto et al., 2021). A NodeMCU in this system, which can be programmed using the Arduino language, was used.
4. Big data analytics examines large and varied data sets to uncover new insights (Coble et al., 2018; Huang et al., 2018). It can increase crop efficiency by collecting data from sensors and using the data to prevent events that could negatively impact crop cultivation.
5. Communication protocols are rules for transmitting data between nodes in a network (Thakur et al., 2019). They define data exchange formats, encoding, and addressing.

This study used a relay and three sensors (DHT22, pH sensor, and water float sensor). The relay can be connected to a pump or LED light to automate these systems. The schematic diagram is observed in Figure 7a. After the IoT controller was developed, it was implemented in the hydroponic system, as depicted in Figure 7b. Hence, real-time data was successfully integrated into the smart hydroponic system. When the application display was switched on, data was recorded, such as the temperature of 32.2°C, 75.3% humidity, high float sensor, the pH level of 7.53, and the relay was switched off. Based on the integration, this system can assist the development of future smart farming, particularly for local farmers and industries.

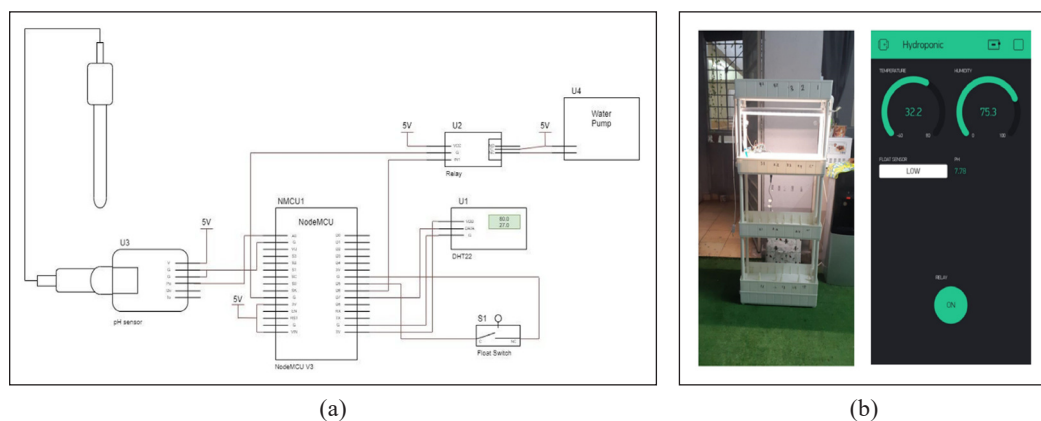


Figure 7. (a) Schematic diagram of the IoT system used in this study. (b) Photographs of the smart hydroponic system and the Blynk application

## CONCLUSION

In conclusion, the distance and colour of the LED light source toward the growth of water spinach in a hydroponic system were successfully demonstrated in this study. Based on the results, the distance of 15 cm between the LED light source and the plants was indicated to be the most optimal value. Furthermore, the white LED light was more suitable for plant

growth than the purple LED light owing to the increased number and size of the water spinach leaves. A successful IoT controller was also effectively integrated into this study, which included several sensors for temperature, humidity, pH, and water level. These parameters are important factors for the growth of water spinach plants in the hydroponic system. The smart farming system efficiently measured the environment, the pH level of the nutrient solution, and the number of nutrients. Thus, the embedment of the IoT controller allowed for continuous monitoring and optimisation of these factors to necessitate plant growth. This research would allow for future developments of a local smart hydroponic farming technology for the agricultural sector.

## ACKNOWLEDGEMENTS

This research was funded by the Fundamental Research Grant Scheme (FRGS 2020-1) under the Ministry of Higher Education (MOHE), Malaysia (Project Ref: FRGS/1/2020/TK0/MMU/03/4). The authors thank MOHE for the financial sponsorship of this research project through the FRGS Fund.

## REFERENCES

- Al Meselmani, M. A. (2022). Nutrient solution for hydroponics. In P. M. Turan, A. P. S. Argin, P. E. Yildirim & D. A. Güneş (Eds.), *Soilless Culture [Working Title]* (p. Ch. 3). IntechOpen. <https://doi.org/10.5772/intechopen.101604>
- Al Shafouri, M., Ahmed, N. M., Hassan, Z., & Almessiere, M. A. (2018). The effect of the wavelength of the LED used to pump phosphor produced from curcuminoids dye extracted from turmeric (*Curcuma Longa* L.) to Produce white light. In *IOP Conference Series: Materials Science and Engineering* (Vol. 454, No. 1, p. 012048). IOP Publishing. <https://doi.org/10.1088/1757-899X/454/1/012048>
- Ayaz, M., Ammad-Uddin, M., Sharif, Z., Mansour, A., & Aggoune, E. H. M. (2019). Internet-of-Things (IoT)-based smart agriculture: Toward making the fields talk. *IEEE Access*, 7, 129551-129583. <https://doi.org/10.1109/ACCESS.2019.2932609>
- Balashova, I., Sirota, S., & Pinchuk, Y. (2019). Vertical vegetable growing: Creating tomato varieties for multi-tiered hydroponic installations. *IOP Conference Series: Earth and Environmental Science*, 395(1), Article 012079. <https://doi.org/10.1088/1755-1315/395/1/012079>
- Bantis, F., Fotelli, M., Ilić, Z. S., & Koukounaras, A. (2020). Physiological and phytochemical responses of spinach baby leaves grown in a PFAL system with leds and saline nutrient solution. *Agriculture*, 10(11), Article 574. <https://doi.org/10.3390/agriculture10110574>
- Bian, Z., Jiang, N., Grundy, S., & Lu, C. (2018). Uncovering LED light effects on plant growth: New angles and perspectives - LED light for improving plant growth, nutrition and energy-use efficiency. *Acta Horticulturae*, 1227(1227), 491-498. <https://doi.org/10.17660/ActaHortic.2018.1227.62>
- Bugbee, B. (2004). Nutrient management in recirculating hydroponic culture. *Acta Horticulturae*, 648(648), 99-112. <https://doi.org/10.17660/ActaHortic.2004.648.12>

- Chan, Y. K., Koo, V. C., Choong, E. H. K., & Lim, C. S. (2021). The Drone Based Hyperspectral Imaging System for Precision Agriculture. *Natural Volatiles & Essential Oils Journal*, 8(5), 5561-5573.
- Coble, K. H., Mishra, A. K., Ferrell, S., & Griffin, T. (2018). Big data in agriculture: A challenge for the future. *Applied Economic Perspectives and Policy*, 40(1), 79-96. <https://doi.org/10.1093/aep/ppx056>
- Darwish, A., Hassanien, A. E., Elhoseny, M., Sangaiah, A. K., & Muhammad, K. (2019). The impact of the hybrid platform of internet of things and cloud computing on healthcare systems: opportunities, challenges, and open problems. *Journal of Ambient Intelligence and Humanized Computing*, 10(10), 4151-4166. <https://doi.org/10.1007/s12652-017-0659-1>
- De Rijck, G., & Schrevels, E. (1998). Comparison of the mineral composition of twelve standard nutrient solutions. *Journal of Plant Nutrition*, 21(10), 2115-2125. <https://doi.org/10.1080/01904169809365548>
- Din, S., Paul, A., Ahmad, A., Gupta, B. B., & Rho, S. (2018). Service orchestration of optimizing continuous features in industrial surveillance using big data based fog-enabled Internet of Things. *IEEE Access*, 6, 21582-21591. <https://doi.org/10.1109/ACCESS.2018.2800758>
- Dunaieva, I., Vecherkov, V., Filina, Y., Popovych, V., Barbotkina, E., Pashtetsky, V., Terleev, V., Mirschel, W., & Akimov, L. (2021). Review of automatized meteorological stations use for agricultural purposes. In *IOP Conference Series: Earth and Environmental Science* (Vol. 937, No. 3, p. 032097). IOP Publishing. <https://doi.org/10.1088/1755-1315/937/3/032097>
- Dunn, B., & Mills-Ibibofori, T. (2016). *LED Lighting for Plant Production*. Division of Agricultural Sciences and Natural Resources. <https://doi.org/10.13140/RG.2.2.28851.84000>
- Gao, W., He, D., Ji, F., Zhang, S., & Zheng, J. (2020). Effects of daily light integral and LED spectrum on growth and nutritional quality of hydroponic spinach. *Agronomy*, 10(8), Article 1082. <https://doi.org/10.3390/agronomy10081082>
- Gráda, C. Ó. (1992). *Ireland's Great Famine*. Department of Economics University College Dublin.
- Gupta, S. D., & Agarwal, A. (2017). Artificial lighting system for plant growth and development: Chronological advancement, working principles, and comparative assessment. In S. D. Gupta (Ed.), *Light Emitting Diodes for Agriculture* (pp. 1-25). Springer. [https://doi.org/10.1007/978-981-10-5807-3\\_1](https://doi.org/10.1007/978-981-10-5807-3_1)
- Hamza, A., Abdelraouf, R. E., Helmy, Y. I., & El-Sawy, S. M. M. (2022). Using deep water culture as one of the important hydroponic systems for saving water, mineral fertilizers and improving the productivity of lettuce crop. *International Journal of Health Sciences*, 6, 2311-2331. <https://doi.org/10.53730/ijhs.v6nS9.12932>
- Hartanti, A., & Sulistyowati, R. (2022). The effectiveness of using types of containers and concentration AB mix on the growth and production of white packcoy (*Brassica rapa* L.) Var. dakota uses wick system hydroponics. *Nabatia*, 10(2), 101-109. <https://doi.org/10.21070/nabatia.v10i2.1613>
- Huang, Y., Chen, Z., Yu, T., Huang, X., & Gu, X. (2018). Agricultural remote sensing big data: Management and applications. *Journal of Integrative Agriculture*, 17(9), 1915-1931. [https://doi.org/10.1016/S2095-3119\(17\)61859-8](https://doi.org/10.1016/S2095-3119(17)61859-8)
- Janezko, D. B., & Timmons, M. B. (2019). Effects of seeding pattern and cultivar on productivity of baby spinach (*Spinacia oleracea*) grown hydroponically in deep-water culture. *Horticulturae*, 5(1), Article 20. <https://doi.org/10.3390/horticulturae5010020>



- Khan, N., Ray, R. L., Sargani, G. R., Ihtisham, M., Khayyam, M., & Ismail, S. (2021). Current progress and future prospects of agriculture technology: Gateway to sustainable agriculture. *Sustainability*, *13*(9), Article 4883. <https://doi.org/10.3390/su13094883>
- Khwankaew, J., Nguyen, D. T., Kagawa, N., Takagaki, M., Maharjan, G., & Lu, N. (2018). Growth and nutrient level of water spinach (*Ipomoea aquatica* Forssk.) in response to LED light quality in a plant factory. *Acta Horticulturae*, *1227*, 653-660. <https://doi.org/10.17660/ActaHortic.2018.1227.83>
- Kim, D., & Son, J. E. (2022). Adding far-red to red, blue supplemental light-emitting diode interlighting improved sweet pepper yield but attenuated carotenoid content. *Frontiers in Plant Science*, *13*, Article 938199. <https://doi.org/10.3389/fpls.2022.938199>
- Kondratieva, V. V., Voronkova, T. V., Semenova, M. V., Olekhovich, L. S., & Shelepova, O. V. (2022). Effect of LEDs on the growth and physiological responses of sweet basil (*Ocimum basilicum* L.). *IOP Conference Series: Earth and Environmental Science*, *1045*(1), Article 12090. <https://doi.org/10.1088/1755-1315/1045/1/012090>
- Lem, A., Bjørndal, A., & Lappo, T. (2014). Economic analysis of supply and demand for food up to 2030. In *FAO Fisheries and Aquaculture Circular (FAO) eng no. 1089* (Vol. 1089, Issue 1089). Food and Agriculture Organization.
- Madushanki, A. A. R., Halgamuge, M. N., Wirasagoda, W. A. H. S., & Syed, A. (2019). Adoption of the Internet of Things (IoT) in agriculture and smart farming towards urban greening: A review. *International Journal of Advanced Computer Science and Applications*, *10*(4), 11-28. <https://doi.org/10.14569/IJACSA.2019.0100402>
- Magwaza, S. T., Magwaza, L. S., Odindo, A. O., & Mditshwa, A. (2020). Hydroponic technology as decentralised system for domestic wastewater treatment and vegetable production in urban agriculture: A review. *Science of The Total Environment*, *698*, Article 134154. <https://doi.org/10.1016/j.scitotenv.2019.134154>
- Mamatha, V., & Kavitha, J. C. (2023). Machine learning based crop growth management in greenhouse environment using hydroponics farming techniques. *Measurement: Sensors*, *25*, Article 100665. <https://doi.org/https://doi.org/10.1016/j.measen.2023.100665>
- Namani, S., & Gonen, B. (2020). Smart agriculture based on IoT and cloud computing. In *2020 3rd International Conference on Information and Computer Technologies (ICICT)* (pp. 553-556). IEEE Publishing. <https://doi.org/10.1109/ICICT50521.2020.00094>
- Namgyel, T., Siyang, S., Khunarak, C., Pobkrut, T., Norbu, J., Chaiyasit, T., & Kerdcharoen, T. (2018). IoT based hydroponic system with supplementary LED light for smart home farming of lettuce. In *2018 15th International Conference on Electrical Engineering/Electronics, Computer, Telecommunications and Information Technology (ECTI-CON)* (pp. 221-224). IEEE Publishing. <https://doi.org/10.1109/ECTICon.2018.8619983>
- Ngcobo, B. L., Bertling, I., & Clulow, A. D. (2022). Artificial daylength enhancement (pre-sunrise and post-sunset) with blue and red led lights affects tomato plant development, yield, and fruit nutritional quality. *Horticulture, Environment, and Biotechnology*, *63*(6), 847-856. <https://doi.org/10.1007/s13580-022-00447-1>

- Patel, N. R., & Kumar, S. (2018). Wireless sensor networks' challenges and future prospects. 2018 In *International Conference on System Modeling & Advancement in Research Trends (SMART)* (pp. 60-65). IEEE Publishing. <https://doi.org/10.1109/SYSMART.2018.8746937>
- Paul, A., & Jeyaraj, R. (2019). Internet of Things: A primer. *Human Behavior and Emerging Technologies*, 1(1), 37-47. <https://doi.org/https://doi.org/10.1002/hbe2.133>
- Rathinam, D. D. K., Surendran, D., Shilpa, A., Grace, A. S., & Sherin, J. (2019). Modern agriculture using wireless sensor network (WSN). In *2019 5th International Conference on Advanced Computing & Communication Systems (ICACCS)* (pp. 515-519). IEEE Publishing. <https://doi.org/10.1109/ICACCS.2019.8728284>
- Runkle, E. (2016). *Red Light and Plant Growth*. GPN Magazine. [https://gpnmag.com/wp-content/uploads/2016/08/GPNAugust\\_TechSpeak.pdf](https://gpnmag.com/wp-content/uploads/2016/08/GPNAugust_TechSpeak.pdf)
- Satterthwaite, D., McGranahan, G., & Tacoli, C. (2010). Urbanization and its implications for food and farming. *Philosophical Transactions of the Royal Society B: Biological Sciences*, 365(1554), 2809-2820. <https://doi.org/10.1098/rstb.2010.0136>
- Setiawan, D., Siswati, L., & Ariyanto, A. (2022). Water pump control system in hydroponic plants using the ebb and flow method. In *IOP Conference Series: Earth and Environmental Science* (Vol. 1041, No. 1, p. 012020). IOP Publishing. <https://doi.org/10.1088/1755-1315/1041/1/012020>
- Singh, S. (2009). Basics of light emitting diodes, characterizations and applications. In *Handbook of Light Emitting and Schottky Diode Research* (pp. 1-36). Nova Science Publishers
- Suryaningprang, A., Suteja, J., Mulyaningrum, M., & Herlinawati, E. (2021). Hydroponic: Empowering local farmer knowhow to gain value added on agriculture commodity. *Budapest International Research and Critics Institute (BIRCI-Journal): Humanities and Social Sciences*, 4(1), 787-796. <https://doi.org/10.33258/birci.v4i1.1676>
- Susanto, F., Nurtantio, P., Soeleman, M. A., Sunarya, P. A., Pujino, & Nursasongko, E. (2021). P2P for prototype embedded system information on agriculture result using IoT. In *2021 International Seminar on Application for Technology of Information and Communication (ISemantic)* (pp. 348-352). IEEE Publishing. <https://doi.org/10.1109/iSemantic52711.2021.9573206>
- Taofik, A., Frasetya, B., Nugraha, R., & Sudrajat, A. (2019). The effects of subtrat composition on the growth of *Brassica oleraceae* Var. Achepala with drip hydroponic. In *Journal of Physics: Conference Series* (Vol. 1402, No. 3, p. 033031). IOP Publishing. <https://doi.org/10.1088/1742-6596/1402/3/033031>
- Thakur, D., Kumar, Y., Kumar, A., & Singh, P. K. (2019). Applicability of wireless sensor networks in precision agriculture: A review. *Wireless Personal Communications*, 107(1), 471-512. <https://doi.org/10.1007/s11277-019-06285-2>
- Torabi, M., Mokhtarzadeh, A., & Mahlooji, M. (2012). The role of hydroponics technique as a standard methodology in various aspects of plant biology researches. In T. Asao (Ed.), *Hydroponics - A Standard Methodology for Plant Biological Researches* (pp. 113-134). InTech. <https://doi.org/10.5772/36612>
- Ullo, S. L., & Sinha, G. R. (2020). Advances in smart environment monitoring systems using IoT and sensors. *Sensors*, 20(11), Article 3113. <https://doi.org/10.3390/s20113113>

- Wang, M., Dong, C., & Gao, W. (2019). Evaluation of the growth, photosynthetic characteristics, antioxidant capacity, biomass yield and quality of tomato using aeroponics, hydroponics and porous tube-vermiculite systems in bio-regenerative life support systems. *Life Sciences in Space Research*, 22, 68-75. <https://doi.org/10.1016/j.lssr.2019.07.008>
- Wimmerova, L., Keken, Z., Solcova, O., Bartos, L., & Spacilova, M. (2022). A comparative LCA of aeroponic, hydroponic, and soil cultivations of bioactive substance producing plants. *Sustainability*, 14(4), Article 2421. <https://doi.org/10.3390/su14042421>
- Xu, Y., Chang, Y., Chen, G., & Lin, H. (2016). The research on LED supplementary lighting system for plants. *Optik*, 127(18), 7193-7201. <https://doi.org/10.1016/j.ijleo.2016.05.056>
- Yu, L., Gao, W., R Shamshiri, R., Tao, S., Ren, Y., Zhang, Y., & Su, G. (2021). *Review of Research Progress on Soil Moisture Sensor Technology*. Verlag nicht ermittelbar. <http://dx.doi.org/10.34657/10037>
- Zhou, J., Chen, J., Chen, X., Zhu, X., Qiu, Y., Song, H., Rao, Y., Zhang, C., Cao, X., & Cui, X. (2021). Sensitivity of six typical spatiotemporal fusion methods to different influential factors: A comparative study for a normalized difference vegetation index time series reconstruction. *Remote Sensing of Environment*, 252, Article 112130. <https://doi.org/10.1016/j.rse.2020.112130>



## Biochemical and Agronomic Responses of Soybean (*Glycine max* L. Merrill) to Spent and Deoiled Bleaching Earth of NPK Fertilization on Filler Basis

Muhammad Parikesit Wisnubroto<sup>1,2</sup>, Eka Tarwaca Susila Putra<sup>2\*</sup> and Budiastuti Kurniasih<sup>2</sup>

<sup>1</sup>Department of Agroecotechnology, Faculty of Agriculture, Universitas Andalas, Pulau Punjung, Dharmasraya 27573, West Sumatra, Indonesia

<sup>2</sup>Department of Agronomy, Faculty of Agriculture, Universitas Gadjah Mada, Bulaksumur, Sleman 55281, Yogyakarta, Indonesia

### ABSTRACT

Spent bleaching earth (SBE) is the largest waste produced by the palm oil industry. However, according to several studies, SBE and its recovery product DBE have the potential as filler materials in NPK fertilizers. This study examines the influence of NPK fertilizer with SBE and DBE as filler materials on soybean plants' biochemical and agronomic properties. The field-based experiment was done in a single-factor randomized complete block design with 4 replicates. We tested fertilizers of 10% bentonite clay mineral using NPK on a filler basis (control), 5% bentonite clay mineral with 5% SBE of NPK on a filler basis, and 5% bentonite clay mineral with 5% DBE using NPK on a filler basis. The variables observed include soil chemical properties after applying fertilizer, which involves the concentrations of several heavy metals. Biochemical characteristics, including the content of hydrogen peroxide (H<sub>2</sub>O<sub>2</sub>) and peroxidase (POD), superoxide dismutase (SOD) activity, malondialdehyde (MDA), relative electrolyte leakage (REL), total phenolic content, and proline content. The agronomic characteristics of soybean plants, including root and shoot dry weight. The data were analyzed using ANOVA and tested using the least significant difference test at a 95% confidence interval. The results indicated that materials of SBE and DBE could partially substitute the filler elements in bentonite clay mineral of NPK fertilizer on a filler basis, and they had the same

### ARTICLE INFO

#### Article history:

Received: 15 January 2023

Accepted: 07 September 2023

Published: 14 March 2024

DOI: <https://doi.org/10.47836/pjst.32.2.12>

#### E-mail addresses:

[muhhammadparikesit@agr.unand.ac.id](mailto:muhhammadparikesit@agr.unand.ac.id) (Muhammad Parikesit Wisnubroto)

[eka.tarwaca.s@ugm.ac.id](mailto:eka.tarwaca.s@ugm.ac.id) (Eka Tarwaca Susila Putra)

[tuti\\_b@ugm.ac.id](mailto:tuti_b@ugm.ac.id) (Budiastuti Kurniasih)

\* Corresponding author

influence in SOD activity, H<sub>2</sub>O<sub>2</sub> content, POD, MDA, REL, total phenolic, proline and root dry weight and shoot of soybean plants.

*Keywords:* Agronomic, biochemical, NPK, soybean, spent bleaching earth

---

## INTRODUCTION

Spent bleaching earth (SBE) is the largest waste produced by the palm oil industry. The increase in palm oil production has resulted in increased waste from bleaching, contributing to the production of SBE. According to the Government Regulation of the Republic of Indonesia No. 101/2014 concerning the Management of Hazardous and Toxic Wastage, SBE is classified as category 2 hazardous and toxic (B3) waste (Pasaribu & Sukandar, 2017).

SBE, along with the recovery, could produce deoiled SBE (DBE), and it contains some heavy metals, such as Cu, Zn, Cd, Ag, and Ni, when re-purified by removing the oil content (Loh et al., 2015). These elements cause the materials of SBE and DBE to be combustible and cause environmental pollution because of the content of these heavy metals. It highlights the need to manage SBE and DBE waste and how to reuse them. Reusing them could help address B3 waste issues because the waste could be transformed into economically useful materials, including the replacement of filler elements in NPK fertilizers. Bentonite (brown) clay is frequently used as filler and has identical properties to bleaching earth (BE) (Anugrah et al., 2020; Wisnubroto et al., 2021).

However, the effects of using SBE and DBE as a partial substitution of NPK fertilizer filler on the environment and plants still require further evaluation, considering that both materials contain some essential and non-essential heavy metals (Purba et al., 2020; Wisnubroto et al., 2020). Plants can respond positively or negatively to changes in the environment, depending on the type and cultivar. This response can be seen from changes in biochemical and agronomic processes in plants (Wisnubroto et al., 2023). Pratap et al. (2012) and Zakiah et al. (2017) state that soybeans occupy a premier position among agricultural crops, being the most important source of good-quality concentrated proteins as well as vegetable oil. The soybean plant is known to be slightly sensitive to environmental conditions, especially toxic elements such as heavy metals (Taufiq & Sundari, 2012). This study used soybean plant as a model plant to determine whether SBE and DBE materials can be used to replace some of the filler components in NPK fertilizer based on biochemical and agronomic processes in plants.

## MATERIALS AND METHODS

### Study Area

The study was carried out between October 2018 and January 2019 at the Agro-Technology Innovation Center (PIAT), Universitas Gadjah Mada, Yogyakarta, Indonesia (Figure 1). The

study was located 124 m above sea level in terms of altitude. According to the classification by Oldeman, Berbah is classified into a C3 climate, consisting of 5 to 6 rainy months and 5 to 6 dry months, respectively (Harmoni, 2014). The materials used in the experiment were cultivar. Grobogan soybean plants were cultivated extensively around the area. The other materials were NPK fertilizer (15:15:15) with 10% bentonite clay mineral, 5% bentonite clay mineral with 5% DBE, and 5% mineral clay with 5% SBE as filler elements.

The experiment was done in one-factor field within randomized complete block design (RCBD) with 4 replicates. 10% of bentonite clay using NPK fertilization on filler basis (control), 5% of bentonite clay with 5% of SBE using NPK fertilization on filler basis, and 5% of bentonite clay with 5% of DBE using NPK fertilization on filler basis were the treatments tested. The SBE and DBE were obtained from PT. Sentana Adidaya Pratama (SADP), a part of the Wilmar Group Indonesia. For all treatments, NPK fertilizers were administered two times: on the 14<sup>th</sup> and 35<sup>th</sup> day after planting with the amount of 150 kg/ha and 225 kg/ha, consecutively. A deep placement scheme with ±5 cm in distance from the plant roots was used, and then the fertilizer was spread to avoid disturbing the roots.

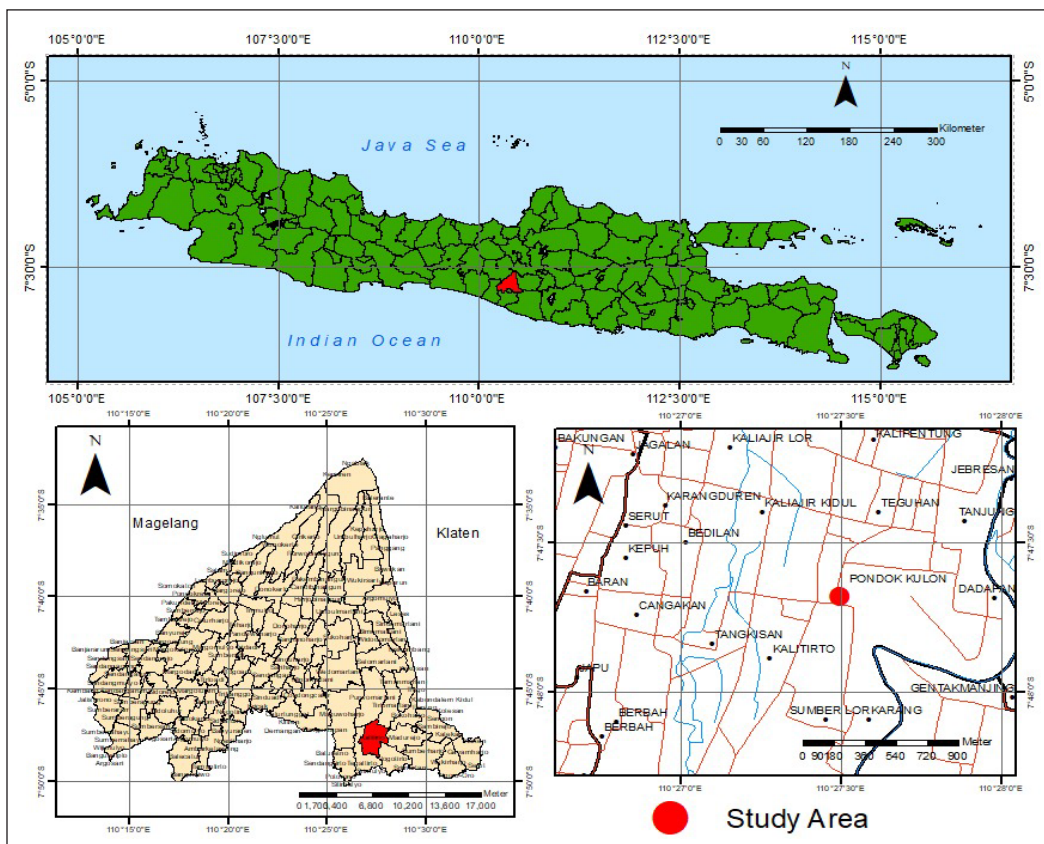


Figure 1. Research location at the Agro-Technology Innovation Center (PIAT) at Universitas Gadjah Mada, Yogyakarta, Indonesia

## Procedures

The variables observed were soil chemical properties after being fertilized. These included the concentrations of Cu, Zn, Cd, Ag, and Ni. The observation was conducted 21 days after planting. Biochemical characteristics, including the content of hydrogen peroxide (H<sub>2</sub>O<sub>2</sub>) and peroxidase (POD), activity of superoxide dismutase (SOD), malondialdehyde (MDA), relative electrolyte leakage (REL), total phenolic content and proline content, were observed 70 days post planting. The agronomic characteristics of soybean plants, including root and shoot dry weight, were observed 70 days post-planting.

**Soil Chemical Properties.** Soil chemical properties observed in this study were the concentrations of Cu, Zn, Cd, Ag, and Ni using diethylene triamine penta acetic acid (DTPA) extract described by Eviati and Sulaeman (2009). DTPA extract can dissolve metal ions in the form of chelate compounds. DTPA solution has the strongest chelating power to extract iron and other metals at a pH of 7.3. A total of 10 g of a good sample of soil (<2 mm) was weighed and added with 20 mL of DTPA extracting solution, then shaken with a shaking machine for 2 hours. The suspension was filtered or centrifuged to obtain a clear extract. Each element was then measured with the AAS tool (Equation 1).

$$\begin{aligned}
 & \text{The concentrations of heavy metals (ppm)} \\
 & = \text{ppm of the curve} \times \text{mL of the extract} \times 1000 \text{ mL}^{-1} \times 1000 \text{ g (g sample)}^{-1} \times \text{fp} \times \text{fk} \\
 & = \text{ppm of the curve} \times 20 \times 1000^{-1} \times 1000 \times 10^{-1} \times \text{fp} \times \text{fk} \\
 & = \text{ppm of the curve} \times 2 \times \text{fp} \times \text{fk} \qquad \qquad \qquad [1]
 \end{aligned}$$

Remarks:

ppm = the sample concentration received out of the relationship curve of the standard range and the reading after blank correction

fp = dilution factor (if any)

fk = correction factor of moisture content = 100 / (100 - % moisture content)

**The Concentrations of Heavy Metals in Plant Tissues.** Concentrations of Cu, Zn, Cd, Ag, and Ni in the tissue were measured on leaves 70 days after planting. These heavy metals can be extracted by wet ashing by mixing the concentration of HNO<sub>3</sub> and HClO<sub>4</sub> acids. Heavy metal concentrations in the extract were measured with AAS (Eviati & Sulaeman, 2009).

The concentration of heavy metals was measured by carefully weighing 2.5 g of good samples of plant <0.5 mm. The samples were placed in a digest tube, added with 5 mL of nitric acid concentration, and left overnight. The following day, the samples were heated at 100°C for 1 hour and 30 minutes and cooled. Then, 5 mL of nitric acid concentration and 1 mL of perchloric acid concentration were added. The samples were then heated to 130°C for 1 hour and 150°C within 2 and a half hours until yellow steam disappeared. The heating time was prolonged when yellow steam continued to form after 2.5 hours. Once



the yellow steam disappeared, the temperature rose to 170°C for 1 hour and then to 200°C for 1 hour until white vapor was formed. Destruction was finished when a white precipitate or the remainder of a clear solution of about 1 mL was formed. The extract was cooled and diluted with 25 mL of ion-free water. Then, it was shaken until homogeneous and left overnight. The clear extract measured the concentration (ppm) of Cu, Zn, Cd, Ag, and Ni using the SSA method on the flame method (Equation 2).

The level of heavy metals (ppm)

$$\begin{aligned}
 &= \text{ppm of the curve} \times \text{mL of the extract} \times 1000 \text{ mL}^{-1} \times 1000 \text{ g (g sample)}^{-1} \times \text{fp} \times \text{fk} \\
 &= \text{ppm of the curve} \times 25 \text{ mL} \times 1000 \text{ mL}^{-1} \times 1000 \text{ g} \times 2.5^{-1} \text{ g sample} \times \text{fp} \times \text{fk} \\
 &= \text{ppm of the curve} \times 10 \times \text{fp} \times \text{fk}
 \end{aligned}
 \tag{2}$$

Remarks:

ppm = the sample concentration received out of the relationship curve of the standard range and the reading after blank correction

fp = dilution factor (if any)

fk = correction factor of moisture content =  $100 / (100 - \% \text{ moisture content})$

**Biochemical Characteristics.** SOD activity testing was carried out based on the autoxidation of pyrogallol developed by Marklund and Marklund (1974). Briefly, 50 mM of Tris-HCl buffer with a pH of 8.2 and 1 mM 25 EDTA were used as a medium of reaction. They were combined with a 40-60 mg sample of protein extract and mixed with 100  $\mu$ L 0.2 mM of pyrogallol solvated in 50 mM of PPB pH 6.5 to initiate the reaction. A decrease in the absorbance of pyrogallol was monitored at 420 nm. The activity of SOD was conveyed in units per mg of protein ( $\text{U mg}^{-1} \text{ protein}$ ).

The content of  $\text{H}_2\text{O}_2$  was measured according to the spectrophotometric method developed by Alexieva et al. (2001). Fresh leaves of 0.5 g were crushed and put into a test tube, and then 5 mL of 0.1% (w / v) trichloroacetic acid (TCA) was added for homogenization. A total of 0.5 mL of supernatant was placed in the test tube, and then 0.5 mL of 100 mM potassium phosphate buffer and 2 mL of potassium iodide (KI) reagent (1 M KI w / in  $\text{H}_2\text{O}$ ) were added. The solution was then left in a dark place for an hour. Next, the sample was put into the cuvette, and the absorbance was read using Spectronic 21D at a wavelength of 390 nm. One-tenth of one percent of TCA was utilized as blank. The content of  $\text{H}_2\text{O}_2$  was calculated with the  $\text{H}_2\text{O}_2$  standard curve equation whose concentrations were known. The standard curve was determined using different concentrations of pure  $\text{H}_2\text{O}_2$ . A 1000 ppm of  $\text{H}_2\text{O}_2$  stock solution was prepared and diluted to a certain concentration, and the absorbance was then read using Spectronic 21D at a wavelength of 390 nm. The  $\text{H}_2\text{O}_2$  content is expressed in parts per million (ppm).

POD content was determined according to the spectrophotometric method developed by Zhang et al. (1995). The fresh leaves were crushed, then 1 gram of the crushed leaves

was taken and added with 1 mL phosphate buffer with a pH of 7, then placed into a 2 mL tube. The solution was centrifuged at 1500 rpm for 10 minutes at 4°C. Then reagents, consisting of 1000  $\mu\text{L}$   $\text{dH}_2\text{O}$ , 160  $\mu\text{L}$  potassium phosphate buffer with a pH of 6 at 20°C, 80  $\mu\text{L}$  peroxide solution, 180  $\mu\text{L}$  pyrogallol solution, and 100  $\mu\text{L}$  supernatant sample, were prepared. The solution mixture was then inserted into the cuvette and read using a spectrophotometer with an absorbance of 420 nm. It was then observed three times with intervals of 30 seconds. The POD content is expressed in units per mL of the enzyme ( $\text{U mL}^{-1}$  enzyme) and can be calculated using the following Equation 3:

$$\text{POD content} = \frac{(\Delta A_{420/20 \text{ sec test sample}} - \Delta A_{420/20 \text{ sec blank}}) \times 1.55 \times 1}{(12) (0.1)} \quad [3]$$

Lipid peroxidation was determined with MDA as the final product using the thiobarbituric acid (TBA) method developed by Cakmak and Horst (1991). One g of fresh leaves was crushed and homogenized with 2 mL of 0.1% (w / v) trichloroacetic acid (TCA) solution. Next, 1.5 ml of the solution was centrifuged at 15,000 g for 10 minutes. A half mL supernatant was added to 1.5 mL of 0.5% thiobarbituric acid (TBA) in 20% TCA. The mixture was shaken and incubated in a water bath at 90°C for 20 minutes. The tube for testing was placed in a beaker filled with ice, which was centrifuged at 10,000 g within five minutes after cooling down. The supernatant was loaded into the cuvette, and the absorbance was read with Spectronic 21D at 532 and 600 nm wavelengths. An absorption coefficient of  $155 \text{ mM}^{-1} \text{ cm}^{-1}$  calculated MDA. The blank used was 0.1% TCA. The MDA content is expressed in  $\mu\text{M}$  per leaf fresh weight ( $\mu\text{M fresh}^{-1}$  weight of leaves) that can be calculated using the following Equation 4:

$$\text{MDA} = \frac{((\text{difference in absorbance of 532 and 600 nm}) / 155 \text{ mM}^{-1} \text{ cm}^{-1} \times 10^6)}{\text{Fresh weight of leaves}} \quad [4]$$

The leakage of electrolytes can be measured by measuring the concentrations of electrolytes leaking from the cell using REL. REL levels were determined according to Dionisio-Sese and Tobita's method (1998). One-tenth of a g of fresh leaves were sliced with a length of 5.0 mm and put in a testing tube with 10 mL of deionized distilled water. Next, the tubes were enclosed in plastic and put in a water bath at a temperature of 32°C. After 2 hours, the first electrical conductivity of the medium ( $\text{EC}_1$ ) was measured using an electrical conductivity meter (CM-115, Kyoto Electronics, Kyoto, Japan). The sample was then autoclaved at 121°C for 20 minutes to destroy the tissue and release all electrolytes. The sample was cooled to 25°C, and the last electrical conductivity ( $\text{EC}_2$ )

was measured. REL levels are expressed in percent (%) that can be determined by the following Equation 5:

$$\text{REL} = \frac{\text{EC}_1}{\text{EC}_2} \times 100\% \quad [5]$$

Total phenolic content was measured using a visible spectrometric method following the procedure of Chun et al. (2003). The plant leaves were put in an oven for 48 hours at 40°C, then mashed (0.05 g) and put into a test tube. Four-tenths of a mL of Folin-ciocalteu was added, left for 5–8 minutes, added with 4 mL of 7% Na<sub>2</sub>CO<sub>3</sub>, and filtered with filter paper. The mixing result was placed in a 10-ml volumetric flask, and aqua bidestilata was added to the limit of 10 ml and left to stand for 2 hours. The mixture was then put into the cuvette, and the absorbance was read at a wavelength of 765 nm using Spectronic 21D. The blank used was aquabidest. The total phenolic content was calculated using the standard curve equation for total phenolics whose concentrations were recognized. The total phenolic standard curve was determined using different concentrations of pure phenol. A 1000 ppm phenol stock solution was prepared and diluted to definite concentrations, and the absorbance was read with Spectronic 21D at 765 nm of wavelength. The total phenolic is expressed in parts per million (ppm).

Proline content was determined by a method developed by Bates et al. (1973). The fresh leaves (0.5 g) were pounded with a mortar in 10 ml of 3% sulfosalicylic acid solution. The collision leads to the results being by Whatman filter paper. Next, a ninhydrin acid solution was created by dissolving 1 g of ninhydrin in 24 ml of glacial acetic acid, and the test tube was kept warm until the solution turned blue. A total of 2.5 ml of phosphoric acid plus 5.5 ml of distilled water was added to the ninhydrin solution and was heated until dissolved. Two ml of the filtrate was reacted with 2 ml of ninhydrin acid and 2 ml of glacial acetic acid in a test tube at 100°C for 1 hour. The reaction was finalized by placing the test tube into a beaker filled with ice. The mixture was extracted with 4 ml of toluene and shaken with a stirrer for 15–20 seconds. The red tolerant comprising proline at the top was sucked with a pipette. The absorbance of the solution was read with a Spectronic 21D at a wavelength of 520 nm. Proline content is expressed in μmol proline per gram (μmol proline g<sup>-1</sup>) that can be determined by the following Equation 6:

$$\text{Proline content} = 64.3649 \times \text{absorbance reading} + (-5.2987) \times 0.347 \quad [6]$$

**Agronomic Characteristics.** The agronomic characteristics are shown in the form of plant biomass, including root and shoot dry weight. Plant dry weight showed how organic compounds that were integrated from inorganic substances by plants were accumulated

and acquired after the drying plant segments at 80°C in the oven for  $\pm 48$  hours until they reached sustained weight. It could be determined by measuring the weight of the plants a few times at 24-hour intervals. Weight measurement uses analytical scales, and the weight is expressed in grams per plant ( $\text{g plant}^{-1}$ ).

### **Data Analysis**

The data gathered were tested with variance (ANOVA) analysis. Tests of data assumptions on the normal distribution and homogeneity were previously carried out. Based on the results of the ANOVA, the data showed significant differences between treatments and were tested using the least significant difference (LSD) test at a 95% confidence interval. Data analysis was done using SAS version 9.4 software.

## **RESULTS AND DISCUSSIONS**

### **Soil Chemical Properties**

Naturally, soil accommodates diverse heavy metals (Alloway, 1995). Handayanto et al. (2017) stated that they are originally from parent material weathering done at low levels and are generally not dangerous. In addition, heavy metals in the soil can also originate from human activities, usually called anthropogenic activities, producing greater concentrations of metals than natural sources. Metal pollutants from such sources include inorganic or organic fertilizers, mining, and pesticides (Erfandy & Juarsah, 2014).

NPK fertilizers used in this study: Cu, Zn, Cd, Ag, and Ni are heavy metals known to contaminate the soil indirectly when used. Some of these are among the priority metals, such as Cu, Ni, and Zn. The 5% SBE and DBE used as fillers in NPK fertilizer are thought to have higher heavy metallic content compared to the 10% clay mineral added as filler in NPK fertilizer because SBE and DBE are derived from bleaching earth materials, which are not only used as a bleaching agent but are also used to reduce other undesired elements such as heavy metals. The concentrations of heavy metals in the soil at the research site after being fertilized are shown in Table 1.

The analysis showed that the three treatments did not significantly influence the concentrations of heavy metals tested. Furthermore, Alloway (1995) reported that all kinds of heavy metals concentrations in the research site soil were still lower than the critical limit, except for Ag (Table 1). High concentrations of Ag may damage plants as they inhibit fertilization by inhibiting cell elongation in roots. They also damage vacuoles and cell walls and reduce magnesium, phosphorus, and sulfur nutrient absorption, eventually disrupting the formation of roots (Shofi, 2017).

The toxic limit of Ag varies in diverse species of plants, ranging from extremely hazardous to slightly hazardous. In soybean plants, applying Ag nanoparticles by 30 ppm

Table 1

*Concentrations of heavy metals in the soil post-NPK fertilizer treatments with diverse filler materials 21 days after planting*

Treatment	Ag	Cd	Cu	Ni	Zn
	----- ppm -----				
NPK + 10% of bentonite clay mineral	3.88 a	undetected	55.35 a	undetected	42.58 a
NPK + 5% of bentonite clay mineral + 5% of SBE	4.97 a	undetected	57.81 a	undetected	44.37 a
NPK + 5% of bentonite clay mineral + 5% of DBE	4.42 a	undetected	53.13 a	undetected	42.14 a
CV (%)	17.08	-	2.36	-	2.29
Critical limit of heavy metals in the soil (ppm)*	2	75–100	60–125	100	70–400

*Note.* The same letters that follow the means do not differ significantly in accordance with a test of least significant difference (LSD) at a 95% confidence interval; the concentrations of Cd and Ni after treatments were undetected or lower than the detection limit (detection limit of Cd = 0.01 ppm and Ni = 0.25 ppm); \*Critical limit of heavy metals in the soil by Alloway (1995)

of concentration to the soil does not present any significant influence on the root fresh weight, even though it has a tendency to decline with the increase of dosages given (Li et al., 2017). The presence of Ag in the soil at the research site, pre- and post-treatments, was still safe for the growth and development of the soybean plants.

### Concentrations of Heavy Metals in Plant Tissues

In plants, heavy metals could enter the tissue via roots and stomata (Alloway, 1995). Heavy metals, such as Cu, Ni, and Zn, are vital components that plants need in small proportions. However, when they are highly concentrated, they can disturb plant growth (Deswati et al., 2020; Rusnam et al., 2013). In contrast, Ag, Cd, Cr, and Pb are not significant elements of the soil as they disturb plant growth (Harmiwati et al., 2015; Janoušková et al., 2006; Rusnam et al., 2022). The concentrations of heavy metals in the tissues of soybean plants are shown in Table 2.

It has been shown that giving such treatments had no significant influence on the concentrations of heavy metals in plant tissues 70 days post-planting, except Cu and Zn (Table 2). The concentrations of all metals in the plant tissue were still lower than the soybean plants' critical limit. The presence of Cd was undetected, indicating that the concentration was lower than 0.01 ppm. This result is at a constant ratio to the concentration of Cd in the soil in this study (Table 1).

The concentration of Zn in DBE used as filler material in NPK treatment had a significant difference and was higher than in the control treatment. Sharma et al. (1994) stated that Zn plays a role as a cofactor for enzymes which functions as the antioxidant, superoxide dismutase (SOD). Zn, along with Cu, binds to the SOD enzyme to create

Table 2

*Concentrations of heavy metals in soybean plant tissues as a result of diverse fertilization treatments 70 days after planting*

Heavy metal element	Treatment	Concentration of heavy metal elements in plant tissues (ppm)	CV (%)	Critical limit of heavy metal element content in soybean (ppm)
Ag	BC	0.01 a	20.40	1–30 Li et al. (2017)
	SBE	0.32 a		
	DBE	0.46 a		
Cu	BC	8.88 b	7.93	100–500 Nair and Chung (2014)
	SBE	11.02 ab		
	DBE	14.13 a		
Ni	BC	0.94 a	31.51	50–100 Fitriani et al. (2019)
	SBE	0.25 a		
	DBE	2.28 a		
Zn	BC	14.17 a	9.02	150–200 Fageria et al. (1997)
	SBE	17.85 ab		
	DBE	26.70 a		

*Note.* The same letters that follow the means do not differ significantly in accordance with a test of least significant difference (LSD) at a 95% confidence interval. The concentration of Cd was undetected or lower than the detection limit (detection limit of Cd=0.01 ppm). BC = NPK + 10% of bentonite clay, SBE = NPK + 5% of bentonite clay with 5% of SBE, DBE = NPK + 5% of bentonite clay with 5% of DBE

CuZnSOD, which frequently exists in cells of plants to increase plant oxidative stress tolerance. It is possible that the concentrations of Zn increase in plant tissue treated with DBE as filler material in NPK fertilization since the nano-sized pores of materials resulting from the deoiling process are filled with minerals, allowing the plants to supply these components.

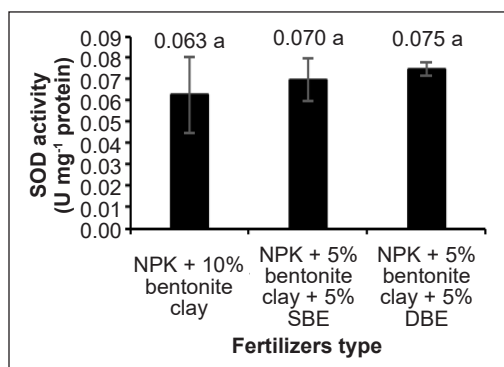
### Biochemical Characteristics

At the molecular level, high concentrations of heavy metals in plant cells can disrupt the balance of cellular redox reactions and influence oxidative stress directly or indirectly, depending on their chemical characteristics (Fargasova, 2001; Smeets et al., 2009). Metals classified as active redox, such as Cr, Cu, Mn, and Fe, can induce the production of reactive oxygen species (ROS) directly through the reaction of Fenton and Haber-Weiss (Yruela, 2005). On the contrary, inactive redox metals, for example, Cd, Ni, Hg, Zn, and Al, only induce the production of ROS via indirect methods, such as inhibiting antioxidant enzymes or stimulating ROS-producing enzymes (NADPH oxidase) (Bücker-Neto et al., 2017; Smeets et al., 2008; Stoyanova & Doncheva, 2002). During the process, reactive oxygen species (ROS) are created and thus change the balance of redox into the pro-oxidative side.

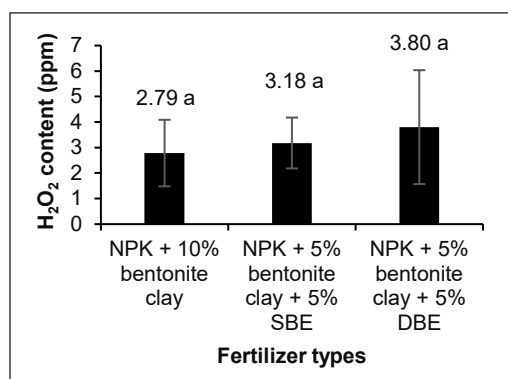
In general, plant cells continuously form free radical ions in the form of ROS as a by-product of aerobic metabolism that takes place in various cellular compartments such as cell walls, cytoplasm, peroxisomes, mitochondria and chloroplasts (Vianello et al., 2007). The formation of free radical ions such as ROS will increase when plants experience both abiotic and biotic stress. The accumulation of free radical ions in the form of ROS at high concentrations will damage cellular and macromolecular components, including the plasma membrane, nucleic acids, and proteins. The formation of ROS also has a function as an effector and regulator in the process of programmed cell death (Malecka et al., 2014).

In dealing with this oxidative stress, plants have enzymatic defense systems like superoxide dismutase (SOD), catalase (CAT), and peroxidase (POD). In addition, plants also have a non-enzymatic defense system that is antioxidant, including ascorbic acid (AsA), tocopherols, phenolic, alkaloids, proline, and carotenoid compounds (lignin, tannins, flavonoids), which act as ROS fasteners (Sharma et al., 2012). According to Kumalaningsih (2007), antioxidants are substances with molecular structures that possess the ability to supply free electrons to free radical molecules without being disrupted in their entirety and to break the free-radical chain reaction. The two defense systems work synergistically to neutralize the toxic effects of ROS compounds so that ROS is only present in small amounts needed to maintain normal cell function.

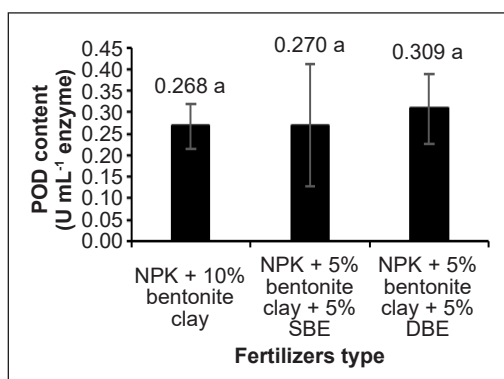
SOD activity, H<sub>2</sub>O<sub>2</sub> content, and POD content on the leaves were observed 70 days after planting (Figure 2).



(a)



(b)



(c)

Figure 2. (a) SOD activity, (b) H<sub>2</sub>O<sub>2</sub> content, and (c) POD content as influenced by NPK fertilization with various filler materials 70 days after planting. Remark: The data presented are standard deviation ± mean; the same letters that follow the means do not differ significantly in accordance with a test of least significant difference (LSD) at a 95% confidence interval

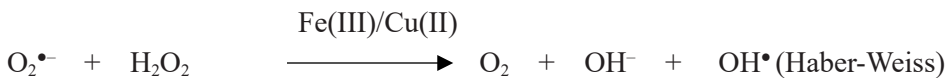
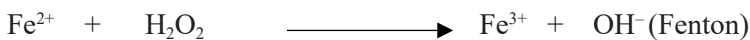
The results found that those treatments did not significantly influence the SOD activity, H<sub>2</sub>O<sub>2</sub> content, and POD content. The findings suggest that the use of SBE and DBE as filler materials did not influence the three variables observed. However, the use of 5% SBE and DBE tended to increase SOD activity, H<sub>2</sub>O<sub>2</sub> content, and POD content by 11.11% and 19.05%, 13.96%, and 36.35%, and 0.75% and 15.30%, respectively, compared to control treatment (Figure 2).

This increase was most likely due to the presence of Zn metal in the 5% SBE and DBE of NPK fertilizer on a filler basis, which was higher than in the 10% clay mineral using NPK on a filler basis (control). It could increase the metal content in the soil and plant tissue. The increase in SOD enzyme activity in the 5% NPK fertilization on the filler basis of SBE and DBE shows that soybean plants are tolerant to the presence of Zn because they respond to the excess of these elements in plants. This increase is directly proportional to the H<sub>2</sub>O<sub>2</sub> and the POD enzymes formed.

Superoxide dismutase (SOD) is an enzyme containing the essential metals of Cu and Zn to catalyze several chemical reactions in cells. Oxygen-free radicals in the form of superoxide anions (O<sub>2</sub><sup>•-</sup>), which are formed due to heavy metal stress, will be catalyzed by SOD to form hydrogen peroxide (H<sub>2</sub>O<sub>2</sub>) and oxygen (O<sub>2</sub>) (Löffler & Petrides, 1988).



H<sub>2</sub>O<sub>2</sub> is formed in the plant body as a short-term product of a biochemical process and is toxic to cells. As the next defense system, plants will produce antioxidants in the form of POD in response to the accumulation of ROS in the form of H<sub>2</sub>O<sub>2</sub> (Békésiová et al., 2008). According to Vicuna et al. (2011), POD is one of the key enzymes that plays a role in maintaining cells against oxidative stress by catalyzing the change of H<sub>2</sub>O<sub>2</sub> to water (H<sub>2</sub>O). Wang et al. (2008) state that plants that are tolerant of heavy metals will show an increase in POD content when exposed to high concentrations of heavy metals. If this were not the case, H<sub>2</sub>O<sub>2</sub> might undergo a Fenton and Haber-Weiss reaction to produce more damaging hydroxyl radicals (OH<sup>•</sup>) (Stadtman, 1992). The reaction is as follows (Cuyppers et al., 2013):



However, when exposure levels to heavy metals are too high, these defense mechanisms often fail to neutralize the effects of excess ROS, resulting in increased lipid peroxidation and electrolyte leakage (Howlett & Avery, 1997; Wang et al., 2008; Zhang et al., 2007) that can be used as a marker of the level of cell damage. The products can detect lipid peroxidation, including MDA (malondialdehyde) (Marciniak et al., 2009). MDA is formed



as a result of the reaction between free radicals (ROS) and unsaturated fatty acids (PUFA = Poly Unsaturated Fatty Acid), which is the main element of the cell membrane. The electrolyte leakage can be detected by measuring the amount of electrolyte leaking from the cell using REL (relative electrolyte leakage) as an indicator (Ehlert & Hinch, 2008; Kocheva et al., 2005).

The observations of lipid peroxidation and electrolyte leakage with MDA and REL as indicators were performed on the leaves for 70 days after planting, and the data are presented in Figure 3.

The results indicated that the MDA and REL content had no significant influence on the three treatments. It indicates that the application of SBE and DBE as filler materials in NPK fertilizer does not influence the two variables that are observed. Nevertheless, the use of 5% SBE and DBE in NPK fertilizer had a tendency to increase the MDA and REL content in soybean plants by 0.80%, 1.25%, 20.84%, and 21.66%, respectively, compared to the control treatment (Figure 3).

An increase in MDA and REL content influenced by the 5% NPK fertilization on the filler basis of SBE and DBE indicated that soybean plants experienced oxidative stress. This result is at a constant ratio to the SOD activity and the content of H<sub>2</sub>O<sub>2</sub> and POD, which also increased (Figure 1). The findings also suggest a decrease does not always follow high antioxidant status in MDA and REL levels. These results indicate that the antioxidants produced are not sufficient in neutralizing the oxidative stress caused by ROS.

In addition to mechanisms using enzymes, plants have non-enzymatic defense systems in managing oxidative stress, including phenolic and proline compounds. The data of phenolic and proline content are presented in Figure 4.

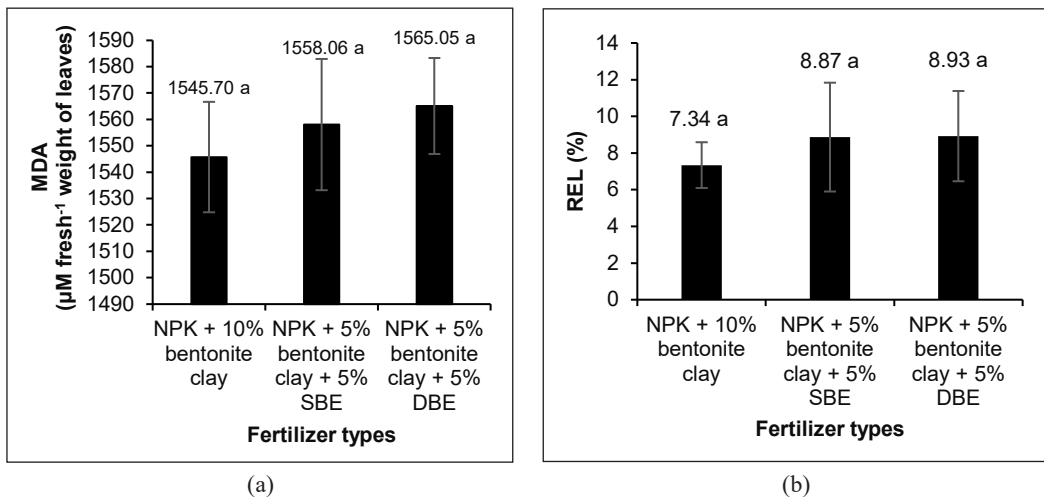


Figure 3. (a) MDA and (b) REL as influenced by NPK fertilization with various filler materials 70 days after planting. Remark: The data presented are standard deviation ± mean; the same letters that follow the means do not differ significantly in accordance with a test of least significant difference (LSD) at a 95% confidence interval

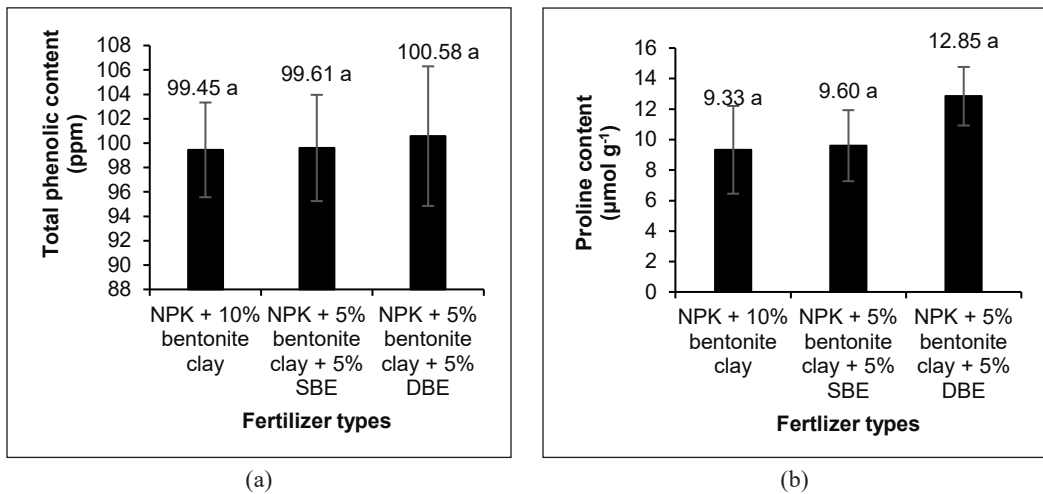


Figure 4. (a) Content of total phenolic and (b) proline as influenced by NPK fertilization with various filler materials 70 days after planting. Remark: The data presented are standard deviation  $\pm$  mean; the same letters that follow the means do not differ significantly in accordance with a test of least significant difference (LSD) at a 95% confidence interval

The results indicated that the total phenolic and proline content had no significant difference in the three treatments. It indicates that the application of SBE and DBE in NPK fertilizers does not influence the two observed variables. Nevertheless, the application of 5% SBE and DBE in NPK fertilizers tended to increase the content of total phenolic and proline in soybean plants by 0.16%, 1.14%, and proline by 2.89% and 37.73%, respectively, compared to the control treatment (Figure 4).

Phenolic substances play a role as antioxidants in plants. Phenolic compounds have one or more hydroxyl groups fixed to the aromatic ring; in other words, they are compounds that have at least one phenyl group (Dhurhanian & Novianto, 2019). Phenolic compounds can be classified into distinguished groups by the number of constitutive carbon atoms connected with the basic phenolic structure: benzoic acids, simple phenols, flavonoids and phenylpropanoids (Michalak, 2006).

According to Hanin and Pratiwi (2017), phenolics are compounds produced by plants when responding to environmental stress, for example, heavy metals. Phenolic compound biosynthesis induction was observed in wheat in its reaction to the toxicity of nickel (Díaz et al., 2001) and maize when responding to aluminum (Winkel-Shirley, 2002). The increase in phenolic levels is probably because of the compounds' protective function on heavy metal stress (Brown et al., 1998).

The antioxidant properties of phenolics have a high tendency to chelate metals. Phenolics own hydroxyl and carboxyl groups that can bind metals, especially copper and iron (Jung et al., 2003). In addition, there are other mechanisms underlying the antioxidant abilities of phenolic compounds. Milić et al. (1998) stated that metal ions could break

down lipid hydroperoxide (LOOH) through hemolytic cleavage of O-O bonds and produce alkoxy lipid radicals, initiating chain reactions of free radicals. Phenolic antioxidants disturb lipid peroxidation by putting these lipid alkoxy radicals into traps.

No definite proof for a direct role of proline in cellular detoxification against heavy metal stress is found, and many differing opinions regarding how proline reduces metal toxicity are actually found (Mishra & Dubey, 2006). Paleg et al. (1984) stated that proline maintains a favorable water balance in plant tissue by acting as an osmoprotectant. In addition, proline can also act as a stabilizer of protein (Sharma & Dubey, 2004), metal chelating (Farago & Mullen, 1979), inhibitor of lipid peroxidation (Mehta & Gaur, 1999), and neutralizer of free radicals (Alia et al., 2001). Because of its high zwitterionic and hydrophilic properties, proline can protect biomolecules and enzymes (Siripornadulsil et al., 2002). Bertrand and Guary (2002) state that the accumulation of proline in plants is most likely not a direct influence on the stress of heavy metals but the impact of water deficit stress caused by heavy metals.

Biochemically, the phytotoxicity of heavy metals in plants can occur because of these three main factors. These are oxidative stress due to heavy metal induction, a direct effect of metal ions with sulfhydryl groups on protein membranes causing them to malfunction, and inactivation of important enzymes by cation replacement activation with heavy metal ions (Vangronsveld & Clijsters, 1994). Consequently, they may cause functional disturbances in physiological processes as well as anatomical-morphological changes and damage, which can then influence the agronomic characteristics of plants in biomass, including root and shoot dry weight.

### Agronomic Characteristics

Plant dry weight shows organic compounds integrated from inorganic substances by plants. According to Shah et al. (2010), the dry weight is formed through the assimilation process of CO<sub>2</sub> during plant growth. The root and shoot dry weight of soybean plants was observed 70 days after planting, and the data are presented in Table 3.

The value of dry weight can be used as an indicator of metabolic processes in plants. The higher the dry weight of the plant, the better the plant growth. The root and shoot dry weight tends to increase as the plant ages. Dry weight is an important

Table 3  
*Dry weight of shoot and root of soybean plants as influenced by NPK fertilizer with diverse filler materials 70 days post-planting*

Treatment	Dry weight	
	Root	Shoot
	----- g plant <sup>-1</sup> -----	
NPK + 10% bentonite clay mineral	3.91 a	52.58 a
NPK + 5% bentonite clay mineral + 5% SBE	4.38 a	60.37 a
NPK + 5% bentonite clay mineral + 5% DBE	4.45 a	61.29 a
CV (%)	15.91	13.37

*Note.* The same letters that follow the means in the same column do not significantly differ in accordance with the test of least significant difference (LSD) at a 95% confidence interval

observation variable because it shows all processes that occur in the plants. The results indicated that the root and shoot dry weight was not significantly influenced by the three treatments 70 days after planting, which shows that applying SBE and DBE did not influence the two observed variables (Table 3).

## CONCLUSION

Overall, the results suggest that the materials of SBE and DBE could partially substitute the filler elements in bentonite clay of NPK fertilizer on a filler basis, which were shown to have the same effect on SOD activity, H<sub>2</sub>O<sub>2</sub> content, POD content, MDA, REL, total phenolic content, proline content, and shoot and root dry weight.

## ACKNOWLEDGEMENT

The authors want to extend their gratitude to Wilmar Group Indonesia for funding this study.

## REFERENCES

- Alexieva, V., Sergiev, I., Mapelli, S., & Karanov, E. (2001). The effect of drought and ultraviolet radiation on growth and stress markers in pea and wheat. *Plant, Cell and Environment*, 24(12), 1337-1344. <https://doi.org/10.1046/j.1365-3040.2001.00778.x>
- Alia, Mohanty, P., & Matysik, J. (2001). Effect of proline on the production of singlet oxygen. *Amino Acids*, 21(2), 195-200. <https://doi.org/10.1007/s007260170026>
- Alloway, B. J. (1995). *Heavy metals in soils* (2<sup>nd</sup> ed.). Blackie Academic & Professional.
- Anugrah, C., Indradewa, D., & Putra, E. T. S. (2020). Biochemical response of hybrid maize (*Zea mays* L.) to NPK fertilization based on spent bleaching earth in field scale. *E3S Web of Conferences*, 142, 1-9. <https://doi.org/10.1051/e3sconf/202014201004>
- Bates, L. S., Waldren, R. P., & Teare, I. D. (1973). Rapid determination of free proline for water-stress studies. *Plant and Soil*, 39, 205-207.
- Békésiová, B., Hraška, Š., Libantová, J., Moravčíková, J., & Matušíková, I. (2008). Heavy-metal stress induced accumulation of chitinase isoforms in plants. *Molecular Biology Reports*, 35(4), 579-588. <https://doi.org/10.1007/s11033-007-9127-x>
- Bertrand, M., & Guary, J. C. (2002). Handbook of plant and crop physiology. In M. Pessarakli (Ed.), *How Plants Adopt their Physiology to an Excess of Metals* (2<sup>nd</sup> ed., pp. 751-761). Marcel Dekker.
- Brown, J. E., Khodr, H., Hider, R. C., & Rice-evans, C. A. (1998). Structural dependence of flavonoid interactions with Cu<sup>2+</sup> ions: Implications for their antioxidant properties. *Biochemical Journal*, 330(3), 1173-1178. <https://doi.org/10.1042/bj3301173>
- Bücker-Neto, L., Paiva, A. L. S., Machado, R. D., Arenhart, R. A., & Margis-Pinheiro, M. (2017). Interactions between plant hormones and heavy metals responses. *Genetics and Molecular Biology*, 40(1), 373-386. <https://doi.org/10.1590/1678-4685-gmb-2016-0087>

- Cakmak, I., & Horst, W. J. (1991). Effect of aluminium on lipid peroxidation, superoxide dismutase, catalase, and peroxidase activities in root tips of soybean (*Glycine max*). *Physiologia Plantarum*, 83(3), 463-468. <https://doi.org/10.1111/j.1399-3054.1991.tb00121.x>
- Chun, O. K., Kim, D. O., & Lee, C. Y. (2003). Superoxide radical scavenging activity of the major polyphenols in fresh plums. *Journal of Agricultural and Food Chemistry*, 51(27), 8067-8072. <https://doi.org/10.1021/jf034740d>
- Cuypers, A., Remans, T., Weyens, N., Colpaert, J., Vassilev, A., & Vangronsveld, J. (2013). Soil-plant relationships of heavy metals and metalloids. In B. J. Alloway (Ed.), *Heavy Metals in Soils: Trace Metals and Metalloids in Soils and Their Bioavailability* (pp. 161-193). Springer Science+Business Media.
- Deswati, D., Khairiyah, K., Safni, S., Yusuf, Y., Refinel, R., & Pardi, H. (2020). Environmental detoxification of heavy metals in flood & drain aquaponic system based on biofloc technology. *International Journal of Environmental Analytical Chemistry*, 102(18), 7155-7164. <https://doi.org/10.1080/03067319.2020.1826463>
- Dhurhania, C. E., & Novianto, A. (2019). Uji kandungan fenolik total dan pengaruhnya terhadap aktivitas antioksidan dari berbagai bentuk sediaan sarang semut (*Myrmecodia pendens*) [Test of total phenolic content and its effect on antioxidant activity of various forms ant nest plant (*Myrmecodia pendens*)]. *Jurnal Farmasi dan Ilmu Kefarmasian Indonesia*, 5(2), 62-68. <https://doi.org/10.20473/jfiki.v5i22018.62-68>
- Diaz, J., Bernal, A., Pomar, F., & Merino, F. (2001). Induction of shikimate dehydrogenase and peroxidase in pepper (*Capsicum annuum* L.) seedlings in response to copper stress and its relation to lignification. *Plant Science*, 161(1), 179-188. [https://doi.org/10.1016/S0168-9452\(01\)00410-1](https://doi.org/10.1016/S0168-9452(01)00410-1)
- Dionisio-Sese, M. L., & Tobita, S. (1998). Antioxidant responses of rice seedlings to salinity stress. *Plant Science*, 135(1), 1-9. [https://doi.org/10.1016/S0168-9452\(98\)00025-9](https://doi.org/10.1016/S0168-9452(98)00025-9)
- Ehlert, B., & Hinch, D. K. (2008). Chlorophyll fluorescence imaging accurately quantifies freezing damage and cold acclimation responses in *Arabidopsis* leaves. *Plant Methods*, 4(1), 1-7. <https://doi.org/10.1186/1746-4811-4-12>
- Erfandy, D., & Juarsah, I. (2014). Teknologi pengendalian pencemaran logam berat [Control technology for heavy metal pollution]. In *Konservasi Tanah Menghadapi Perubahan Iklim* (pp. 159-186). Balai Penelitian Tanah.
- Eviati, & Sulaeman. (2009). Analisis Kimia Tanah, Tanaman, Air, dan Pupuk [Chemical analysis of soil, plant, water, and fertilizer]. Balai Penelitian Tanah.
- Fageria, N. K., Baligar, V. C., & Jones, C. A. (1997). *Growth and mineral nutrition of field crop*. Marcel Dekker. Inc.
- Farago, M. E., & Mullen, W. A. (1979). Plants which accumulate metals. Part IV. A possible copper-proline complex from the roots of *Armeria maritima*. *Inorganica Chimica Acta*, 32, 93-94. [https://doi.org/10.1016/S0020-1693\(00\)91627-X](https://doi.org/10.1016/S0020-1693(00)91627-X)
- Fargasova, A. (2001). Phytotoxic effects of Cd, Zn, Pb, Cu and Fe on *Sinapis alba* L. seedlings and their accumulation in roots and shoots. *Biologia Plantarum*, 44(3), 471-473. <https://doi.org/10.1023/A:1012456507827>

- Fitriani, R. N., Budiyanto, S., & Sukarjo, S. (2019). Respon tanaman kedelai (*Glycine max* L. Merrill) pada berbagai konsentrasi cemaran ion logam Ni<sup>2+</sup> dengan pemberian biokompos [Response of soybean (*Glycine max* L.) at various contamination concentrations ion of nickel metal (Ni<sup>2+</sup>) with biocompost application]. *Journal of Agro Complex*, 3(3), 184-193. <https://doi.org/10.14710/joac.3.3.184-193>
- Handayanto, E., Nuraini, Y., Muddarisna, N., Netty, S., & Fiqri, A. (2017). *Fitoremediasi dan phytomining logam berat pencemar tanah* [Phytoremediation and phytomining of heavy metal soil contaminants]. UB Press.
- Hanin, N. N. F., & Pratiwi, R. (2017). Kandungan fenolik, flavonoid dan aktivitas antioksidan ekstrak daun paku laut (*Acrostichum aureum* L.) fertil dan steril di kawasan mangrove Kulon Progo, Yogyakarta [Phenolic content, flavonoids and antioxidant activity of fertile and sterile sea fern (*Acrostichum aureum* L.) leaf extracts]. *Journal of Tropical Biodiversity and Biotechnology*, 2(2017), 51-56. <https://doi.org/10.22146/jtbb.29819>
- Harmiwati, H., Salmariza, S., Kurniawati, D., Lestari, I., Munaf, E., Desmiarti, R., & Zein, R. (2015). Biosorption of cadmium ion from aqueous solutions by low-cost soybean waste (*Glycine max*). *Journal of Chemical and Pharmaceutical Research*, 7(9), 94-100.
- Harmoni, K. (2014). *Analisis persebaran iklim Klasifikasi Oldeman di Provinsi Daerah Istimewa Yogyakarta* [Analysis of Oldeman climate clasification spreading in Daerah Istimewa Yogyakarta]. [Undergraduate Thesis]. Universitas Muhammadiyah Surakarta, Indonesia.
- Howlett, N. G., & Avery, S. V. (1997). Induction of lipid peroxidation during heavy metal stress in *Saccharomyces cerevisiae* and influence of plasma membrane fatty acid unsaturation. *Applied and Environmental Microbiology*, 63(8), 2971-2976. <https://doi.org/10.1128/aem.63.8.2971-2976.1997>
- Janoušková, M., Pavlíková, D., & Vosátka, M. (2006). Potential contribution of arbuscular mycorrhiza to cadmium immobilisation in soil. *Chemosphere*, 65(11), 1959-1965. <https://doi.org/10.1016/j.chemosphere.2006.07.007>
- Jung, C., Maeder, V., Funk, F., Frey, B., Sticher, H., & Frossard, E. (2003). Release of phenols from *Lupinus albus* L. roots exposed to Cu and their possible role in Cu detoxification. *Plant and Soil*, 252(2), 301-312. <https://doi.org/10.1023/A:1024775803759>
- Kocheva, K. V., Georgiev, G. I., & Kochev, V. K. (2005). A diffusion approach to the electrolyte leakage from plant tissues. *Physiologia Plantarum*, 125(1), 1-9. <https://doi.org/10.1111/j.1399-3054.2005.00533.x>
- Kumalaningsih, S. (2007). *Antioksidan Alami Penangkal Radikal Bebas* [Natural Free Radical Scavengers]. Trubus Agrisarana.
- Li, C., Dang, F., Li, M., Zhu, M., Zhong, H., Hintelmann, H., & Zhou, D. (2017). Effects of exposure pathways on the accumulation and phytotoxicity of silver nanoparticles in soybean and rice. *Nanotoxicology*, 11(5), 699-709. <https://doi.org/10.1080/17435390.2017.1344740>
- Löffler, G., & Petrides, P. E. (1988). *Physiologische chemie* (4<sup>th</sup> ed.). Springer.
- Loh, S. K., Cheong, K. Y., Choo, Y. M., & Salimon, J. (2015). Formulation and optimisation of spent bleaching earth-based bio organic fertiliser. *Journal of Oil Palm Research*, 27(1), 57-66.

- Malecka, A., Piechalak, A., Zielińska, B., Kutrowska, A., & Tomaszewska, B. (2014). Response of the pea roots defense systems to the two-element combinations of metals (Cu, Zn, Cd, Pb). *Acta Biochimica Polonica*, 61(1), 23-28. [https://doi.org/10.18388/abp.2014\\_1918](https://doi.org/10.18388/abp.2014_1918)
- Marciniak, A., Brzeszczyńska, J., Gwoździński, K., & Jegier, A. (2009). Antioxidant capacity and physical exercise. *Biology of Sport*, 26(3), 197-213. <https://doi.org/10.5604/20831862.894649>
- Marklund, S., & Marklund, G. (1974). Involvement of the superoxide anion radical in the autoxidation of pyrogallol and a convenient assay for superoxide dismutase. *European Journal of Biochemistry*, 47(3), 469-474. <https://doi.org/10.1111/j.1432-1033.1974.tb03714.x>
- Mehta, S. K., & Gaur, J. P. (1999). Heavy metal-induced proline accumulation and its role in ameliorating metal toxicity in *Chlorella vulgaris*. *New Phytologist*, 143(2), 253-259. <https://doi.org/10.1046/j.1469-8137.1999.00447.x>
- Michalak, A. (2006). Phenolic compounds and their antioxidant activity in plants growing under heavy metal stress. *Polish Journal of Environmental Studies*, 15(4), 523-530.
- Milić, B. L., Djilas, S. M., & Čanadanović-Brunet, J. M. (1998). Antioxidative activity of phenolic compounds on the metal-ion breakdown of lipid peroxidation system. *Food Chemistry*, 61(4), 443-447. [https://doi.org/10.1016/S0308-8146\(97\)00126-X](https://doi.org/10.1016/S0308-8146(97)00126-X)
- Mishra, S., & Dubey, R. S. (2006). Heavy metal uptake and detoxification mechanisms in plants. *International Journal of Agricultural Research*, 1(2), 122-141. <https://doi.org/10.3923/ijar.2006.122.141>
- Nair, P. M. G., & Chung, I. M. (2014). A mechanistic study on the toxic effect of copper oxide nanoparticles in soybean (*Glycine max* L.) root development and lignification of root cells. *Biological Trace Element Research*, 162(1-3), 342-352. <https://doi.org/10.1007/s12011-014-0106-5>
- Paleg, L. G., Stewart, G. R., & Bradbeer, J. W. (1984). Proline and glycine betaine influence protein solvation. *Plant Physiology*, 75(4), 974-978. <https://doi.org/10.1104/pp.75.4.974>
- Pasaribu, K. F., & Sukandar, S. (2017). Analisis manfaat biaya pengelolaan limbah spent bleaching earth melalui pemanfaatan dan penimbunan dengan memperhitungkan nilai gas rumah kaca [Benefit-cost analysis of spent bleaching earth management through recovery and landfilling by using greenhouse gases as externality]. *Jurnal Teknik Lingkungan*, 23(2), 33-42. <https://doi.org/10.5614/j.tl.2017.23.2.4>
- Pratap, A., Gupta, S. K., Kumar, J., & Solanki, R. K. (2012). Soybean. In S. K. Gupta (Ed.), *Technological Innovations in Major World Oil Crops, Volume 1: Breeding* (pp. 1-405). Springer Science+Business Media. <https://doi.org/10.1007/978-1-4614-0356-2>
- Purba, R. S., Irwan, S. N. R., & Putra, E. T. S. (2020). The effect of spent bleaching earth filler-based NPK fertilization on proline, growth and yield of maize. *Caraka Tani: Journal of Sustainable Agriculture*, 35(1), 44-53. <https://doi.org/10.20961/carakatani.v35i1.34166>
- Rusnam, R., Asmiwati, A., Efrizal, E., & Sofyani, A. (2013). The influence of water hyacinth to decrease the heavy metals mercury (Hg) concentration for irrigation. *International Journal on Advanced Science Engineering and Information Technology*, 3(6), Article 368. <https://doi.org/10.18517/ijaseit.3.6.350>

- Rusnam, R., Puari, A. T., Yanti, N. R., & Efrizal, E. (2022). Utilisation of exhausted coffee husk as low-cost bio-sorbent for adsorption of Pb<sup>2+</sup>. *Tropical Life Sciences Research*, 33(3), 229-252. <https://doi.org/10.21315/tlsr2022.33.3.12>
- Shah, F. U. R., Ahmad, N., Masood, K. R., Peralta-Videa, J. R., & Ahmad, F. D. (2010). Heavy metal toxicity in plants. In M. Ashraf (Ed.), *Plant Adaptation and Phytoremediation* (pp. 1-481). Springer Science+Business Media. <https://doi.org/10.1007/978-90-481-9370-7>
- Sharma, P., & Dubey, R. S. (2004). Ascorbate peroxidase from rice seedlings: Properties of enzyme isoforms, effects of stresses and protective roles of osmolytes. *Plant Science*, 167(3), 541-550. <https://doi.org/10.1016/j.plantsci.2004.04.028>
- Sharma, P., Jha, A. B., Dubey, R. S., & Pessaraki, M. (2012). Reactive oxygen species, oxidative damage, and antioxidative defense mechanism in plants under stressful conditions. *Journal of Botany*, 2012, 1-26. <https://doi.org/10.1155/2012/217037>
- Sharma, P. N., Kumar, N., & Bisht, S. S. (1994). Effect of zinc deficiency on chlorophyll contents, photosynthesis, and water relations of cauliflower plants. *Photosynthetica*, 30, 353-359.
- Shofi, M. (2017). Daya hambat perak nitrat (AgNO<sub>3</sub>) pada perkecambah biji kacang hijau (*Vigna radiata*) [Inhibition of silver nitrate (AgNO<sub>3</sub>) to seed germination of mung bean (*Vigna radiata*)]. *Al-Kaunyah: Jurnal Biologi*, 10(2), 98-104. <https://doi.org/10.15408/kaunyah.v10i2.4869>
- Siripornadulsil, S., Traina, S., Verma, D. P. S., & Sayre, R. T. (2002). Molecular mechanisms of proline-mediated tolerance to toxic heavy metals in transgenic microalgae. *Plant Cell*, 14(11), 2837-2847. <https://doi.org/10.1105/tpc.004853>
- Smeets, K., Opdenakker, K., Remans, T., Van Sanden, S., Van Belleghem, F., Semane, B., Horemans, N., Guisez, Y., Vangronsveld, J., & Cuypers, A. (2009). Oxidative stress-related responses at transcriptional and enzymatic levels after exposure to Cd or Cu in a multipollution context. *Journal of Plant Physiology*, 166(18), 1982-1992. <https://doi.org/10.1016/j.jplph.2009.06.014>
- Smeets, K., Ruytinx, J., Van Belleghem, F., Semane, B., Lin, D., Vangronsveld, J., & Cuypers, A. (2008). Critical evaluation and statistical validation of a hydroponic culture system for *Arabidopsis thaliana*. *Plant Physiology and Biochemistry*, 46(2), 212-218. <https://doi.org/10.1016/j.plaphy.2007.09.014>
- Stadtman, E. R. (1992). Protein oxidation and aging. *Science*, 257(5074), 1220-1224. <https://doi.org/10.1080/10715760600918142>
- Stoyanova, Z., & Doncheva, S. (2002). The effect of zinc supply and succinate treatment on plant growth and mineral uptake in pea plant. *Brazilian Journal of Plant Physiology*, 14(2), 111-116. <https://doi.org/10.1590/S1677-04202002000200005>
- Taufiq, A., & Sundari, T. (2012). Respons tanaman kedelai terhadap lingkungan tumbuh [Soybean response to grow environment]. *Buletin Palawija*, 22, 13-26.
- Vangronsveld, J., & Clijsters, H. (1994). Toxic effects of metals. In *Plants and the Chemical Elements. Biochemistry, Uptake, Tolerance and Toxicity* (pp. 150-177). VCH Publishers.



- Vianello, A., Zancani, M., Peresson, C., Petrusa, E., Casolo, V., Krajňáková, J., Patui, S., Braidot, E., & Macri, F. (2007). Plant mitochondrial pathway leading to programmed cell death. *Physiologia Plantarum*, 129(1), 242-252. <https://doi.org/10.1111/j.1399-3054.2006.00767.x>
- Vicuna, D., Malone, R. P., & Dix, P. J. (2011). Increased tolerance to abiotic stresses in tobacco plants expressing a barley cell wall peroxidase. *Journal of Plant Sciences*, 6(1), 1-13. <https://doi.org/10.3923/jps.2011.1.13>
- Wang, Z., Zhang, Y., Huang, Z., & Huang, L. (2008). Antioxidative response of metal-accumulator and non-accumulator plants under cadmium stress. *Plant and Soil*, 310(1-2), 137-149. <https://doi.org/10.1007/s11104-008-9641-1>
- Winkel-Shirley, B. (2002). Biosynthesis of flavonoids and effects of stress. *Current Opinion in Plant Biology*, 5(3), 218-223. [https://doi.org/10.1016/S1369-5266\(02\)00256-X](https://doi.org/10.1016/S1369-5266(02)00256-X)
- Wisnubroto, M. P., Putra, E. T. S., & Kurniasih, B. (2020). *Tanggapan Biokemis, Fisiologis, dan Agronomis Kedelai (Glycine max L. Merrill) terhadap Pemupukan NPK Berperekat Spent dan Deoiled Bleaching Earth* [Biochemical, physiological, and agronomic responses of soybean (*Glycine max* L. Merrill) to spent and deoiled bleaching earth filler-based NPK fertilization]. [Unpublished Master's Thesis]. Universitas Gadjah Mada, Indonesia.
- Wisnubroto, M. P., Putra, E. T. S., & Kurniasih, B. (2021). Effects of spent and deoiled bleaching earth filler-based NPK Fertilization on the soil nutrient status and growth of soybean (*Glycine max* (L.) Merrill). *Caraka Tani: Journal of Sustainable Agriculture*, 36(2), Article 213. <https://doi.org/10.20961/carakatani.v36i2.43847>
- Wisnubroto, M. P., Putra, E. T. S., & Kurniasih, B. (2023). Agronomic responses of soybean (*Glycine max* L. Merrill) to spent and deoiled bleaching earth filler-based NPK fertilization. *Jurnal Agronomi Tanaman Tropika (JUATIKA)*, 5(1), 172-184. <https://doi.org/https://doi.org/10.36378/juatika.v5i1.2685>
- Yruela, I. (2005). Copper in plants. *Brazilian Journal of Plant Physiology*, 17(1), 145-156. <https://doi.org/10.1590/s1677-04202005000100012>
- Zakiah, Z., Suliansyah, I., Bakhtiar, A., & Mansyurdin. (2017). Effect of crude extracts of six plants on vegetative growth of soybean (*Glycine max* Merr.). *International Journal of Advances in Agricultural Science and Technology*, 4(7), 1-12.
- Zhang, F. Q., Wang, Y. S., Lou, Z. P., & Dong, J. De. (2007). Effect of heavy metal stress on antioxidative enzymes and lipid peroxidation in leaves and roots of two mangrove plant seedlings (*Kandelia candel* and *Bruguiera gymnorrhiza*). *Chemosphere*, 67(1), 44-50. <https://doi.org/10.1016/j.chemosphere.2006.10.007>
- Zhang, J., Cui, S., Li, J., Wei, J., & Kirkham, M. B. (1995). Protoplasmic factors, antioxidant responses and chilling resistance in maize. *Plant Physiology Biochemistry*, 33(5), 567-575.



## Physical Properties of Full-ripe Dabai (*Canarium odontophyllum* miq. Variety Song) at Different Fractions

Nur Afiqah Hani Abdul Rashid<sup>1,2</sup>, Rosnah Shamsudin<sup>1,2\*</sup>, Siti Hajar Ariffin<sup>1</sup>, Wan Nor Zanariah Zainol@Abdullah<sup>3</sup> and Puteri Nurain Megat Ahmad Azman<sup>1</sup>

<sup>1</sup>Department of Process and Food Engineering, Faculty of Engineering, Universiti Putra Malaysia, 43400 UPM, Serdang, Selangor, Malaysia

<sup>2</sup>Laboratory of Halal Services, Halal Products Research Institute, Universiti Putra Malaysia, 43400 UPM, Serdang, Selangor, Malaysia

<sup>3</sup>Department of Basic Science and Engineering, Faculty of Agriculture and Food Sciences, Universiti Putra Malaysia, Bintulu Sarawak Campus, Nyabau Road, 97008 Bintulu, Sarawak, Malaysia

### ABSTRACT

Dabai fruit is an exotic and seasonal fruit in Sarawak. Among the varieties available, the Song variety was chosen due to better taste and high demand amongst local consumers. This study determined the physical properties of dabai (Song variety) at three different fractions: whole fruit, nut, and kernel. According to the results, whole fruit had the highest values in geometric mean diameter (27.86 mm), volume (12.70 cm<sup>3</sup>), mass (13.89 g), surface area (2442.60 mm<sup>2</sup>) and angle of repose (39.06°) when compared to nut and kernel. Bulk density of dabai nut reached the highest with the value of 0.63 gcm<sup>-3</sup>. Kernel had the highest percentage of porosity (80.50) compared to others. The correlations of physical properties between whole fruit, nut and kernel were further analysed using Principal Component Analysis (PCA). The findings can potentially be useful in the design of handling and processing equipment.

*Keywords:* *Canarium odontophyllum*, correlations, fractions, physical properties

### ARTICLE INFO

#### Article history:

Received: 28 January 2023

Accepted: 24 August 2023

Published: 14 March 2024

DOI: <https://doi.org/10.47836/pjst.32.2.13>

#### E-mail addresses:

haniabdrashid@gmail.com (Nur Afiqah Hani Abdul Rashid)

rosnahs@upm.edu.my (Rosnah Shamsudin)

hajarariffin@upm.edu.my (Siti Hajar Ariffin)

wnzz@upm.edu.my (Wan Nor Zanariah Zainol @Abdullah)

puteri.nurain@ymail.com (Puteri Nurain Megat Ahmad Azman)

\* Corresponding author

### INTRODUCTION

*Canarium odontophyllum*, known as dabai fruit, is an indigenous and seasonal crop unique to Sarawak. Dabai fruit is composed of a thin layer of skin (epidermis) surrounding the flesh (mesocarp or pulp) and a sub-triangular hard-shell seed with three chambers (endocarp or nut) containing a single kernel. Ariffin et al. (2020) reported

that the light green skin turns dark purple, and the fleshy pulp becomes creamer yellow, indicating a fully ripe fruit. The ‘Song’ variety was chosen due to its better taste, high buyer demand, and local consumers’ preferences. In recent years, dabai has been promoted by the Agriculture Department of Sarawak as a speciality fruit and a future economic crop of Sarawak (Ding & Tee, 2011; Chua et al., 2015). The dabai fruits are graded into three grades: grade A, grade B, and grade C. Grade A has the biggest size, thicker flesh and larger nuts compared to grades B and C (Hady, 2021).

Size, shape and weight and relationships of physical properties are determined as important to design and optimise a machine for sorting, grading, sizing, handling, packaging, storage and transport of fruits (Altuntaş & Yildiz, 2007; Milošević et al., 2014; Azman et al., 2020). However, detailed studies concerning the correlation of its physical and chemical attributes associated with different fractions are still scarce up to now. Thus, this research aims to (1) determine the physical properties of dabai fruit at different fractions and (2) investigate the correlations between physical properties and dabai fractions. The result of this study will contribute to the evaluation of dabai biodiversity and aid in designing the handling and processing equipment for potential commercial production.

## MATERIALS AND METHODS

### Fruit Materials

Matured grade A dabai fruit (‘Song’ variety) was purchased at a local market at Kuching, Sarawak, located in northwest Borneo Island. The fruits were transported on the same day by flight, immediately delivered to the laboratory at Universiti Putra Malaysia, and stored in a freezer (SJC318, Sharp, Malaysia) with a temperature of  $-14^{\circ}\text{C}$  upon arrival. A total of 20 random samples of grade A dabai fruit with good quality and free from defect or physical injury were selected for the testing.

### Sample Preparation

Twenty replicates of dabai fruits from the bulk sample were chosen. The whole fruit was measured after being thawed for five minutes after being taken out from the freezer. Then, the fruit fractions were manually separated into nut and kernel, as indicated in Figure 1. Firstly, the flesh of the fruit was peeled using a knife to obtain the sub-triangular nut. Notably, the remaining flesh must be

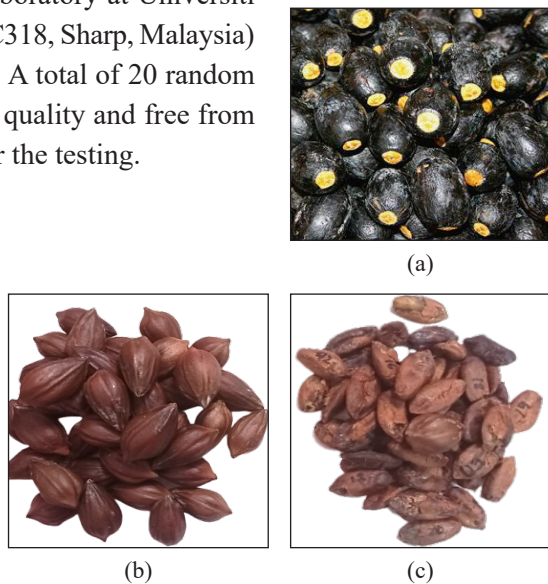


Figure 1. (a) Whole fruit, (b) nut, and (c) kernel of *Canarium odontophyllum* Miq.

removed fully, and the nut must be washed under water to ensure an accurate reading. Next, the hard shell of the same set of nut samples was cracked carefully using a c-clamp to obtain its single kernel.

### Determination of Geometric Properties

The geometric properties of each fruit fraction examined included dimensions (sizes), sphericity, aspect ratio, volume, and surface area. The size of all fruit fractions was expressed in terms of three spatial dimensions such as length (L), width (W) and thickness (T), that correspond to major, intermediate, and minor diameters, respectively, and was measured using a digital vernier calliper (Series 500, Mitutoyo, Japan) with 0.01 mm sensitivity.

Each fraction's actual volume (V) was measured using the water displacement method (Khoshnam et al., 2007; Ehiem et al., 2016; Yang et al., 2018). The fruits generally have irregular shapes and need to be expressed in standard shapes. Therefore, the whole fruit, nut, and kernel of dabai were presumed to be a standard elliptical shape. Accordingly, ellipsoid (*Vellip*) volume was calculated using Equation 1 (Azman et al., 2020):

$$V_{ellip} = \frac{4\pi}{3} \left(\frac{L}{2}\right) \left(\frac{W}{2}\right) \left(\frac{T}{2}\right) \quad [1]$$

The sphericity ( $\Phi$ ), aspect ratio (AR), geometric mean diameter ( $D_g$ ), and arithmetic mean diameter ( $D_a$ ) were calculated by using the following Equations 2 to 5 suggested by Khoshnam et al. (2007), Milošević et al. (2014), Ehiem et al. (2016) and Azman et al. (2020), respectively:

$$\Phi = \frac{(LW)^{\frac{1}{3}}}{L} \quad [2]$$

$$AR = \frac{L}{W} \quad [3]$$

$$D_g = (LWT)^{\frac{1}{3}} \quad [4]$$

$$D_a = \frac{(L+W+T)}{3} \quad [5]$$

Surface area (SA) can be defined as the total three-dimensional (3D) shape areas of all surfaces. It was calculated using Equation 6 (Burubai & Amber, 2014):

$$A_s = \pi D_g^2 \quad [6]$$

### Determination of Gravimetric Properties

Gravimetric properties like mass, true density, bulk density, and porosity of each fraction were measured. Individual 20 fruit mass (M) was weighed using an electronic balance

(ATY224, Shimadzu Corp., Japan) with a precision of  $\pm 0.0001$  mg. The water displacement method was carried out to determine the true density of the fruit fraction. The true density ( $\rho_t$ ) of the fruit is the ratio of the mass of a fruit sample to the solid volume occupied by the sample, which was calculated using Equation 7 (Altuntaş & Yildiz, 2007).

$$\rho_t = \frac{M_i}{V_i} \quad [7]$$

where  $M_i$  – mass of individual fruit (g),  $V_i$  – volume of individual fruit ( $\text{cm}^3$ )

Bulk density ( $\rho_b$ ) is defined as the ratio of the mass of a fruit sample to its total volume and was determined with a weight per hectolitre tester calibrated in kg per hectolitre (Aydin, 2003). It is the sample mass ratio to the container volume it occupies, as Ehiem et al. (2016) suggested. The bulk density of whole fruit was determined by filling the sample to the brim with a  $200 \text{ cm}^3$  measuring cylinder and levelling off the excess samples with a flat object. The whole sample was weighed, and similar steps were repeated by using a  $100 \text{ cm}^3$  measuring cylinder to determine the bulk density of the nut and kernel based on the following Equation 8:

$$\rho_b = \frac{M_b}{V_c} \quad [8]$$

where  $M_b$  – mass of bulk sample (g),  $V_c$  – volume of the container ( $\text{cm}^3$ )

The porosity ( $P$ ) of fruit fraction was computed from the values of true density and bulk density using the relationship given by Binoj et al. (2016) using Equation 9:

$$P = \frac{\rho_t - \rho_b}{\rho_t} \times 100 \quad [9]$$

### Frictional Properties

Frictional properties like the angle of repose ( $\theta$ ) were determined at whole fruit, nut, and kernel fractions using Equation 10. The angle of repose is the horizontal angle at which the material will stand when piled. It was determined as suggested by Sessiz et al. (2007), Altuntaş & Yildiz (2007) and Liu (2011) with slight modification. A topless and bottomless cylinder of 168 mm diameter and 163 mm height, 76 mm diameter and 96 mm height, 20 mm diameter and 73 mm height were used for dabai fruit, nut, and kernel, respectively. The samples were placed into hollow cylinders of respective diameters and heights atop a selected base, which is the centre of white paper on a flat surface. The cylinder was lifted slowly until a cone of fruit fractions formed on the paper base.

$$\theta = \frac{h}{r} \quad [10]$$

where  $\theta$  – angle of repose,  $h$  – height of cone of fruit fractions formed,  $r$  – radius of cone of fruit fractions formed.

## Statistical Analysis

All values are expressed as group mean  $\pm$  standard deviation and analysed using Minitab Statistic 19 Edition. A one-way analysis of variance (ANOVA) was applied to determine the difference among the means of fractions in the physical fruit properties to determine the differences in the means. Probability values at a 5% level ( $p < 0.05$ ) using Tukey's Honest Significant Difference (HSD) test were significantly different. Correlation coefficients were determined by the Pearson correlation matrix method. Principal Component Analysis (PCA) was performed to evaluate interrelationships among variables and any possible fruit fraction grouping based on similar properties by using the Minitab® 19 procedure.

## RESULTS AND DISCUSSION

### Determination of Geometric Properties of Dabai Fractions

The geometric properties of different dabai fractions of whole fruit, nut, and kernel are presented in Table 1.

Table 1  
*Some physical properties of different fractions of dabai fruit*

Properties			Whole Fruit	Nut	Kernel
Geometric Property					
Length, L	mm	Mean	37.58 $\pm$ 1.95 <sup>a</sup>	28.04 $\pm$ 1.65 <sup>b</sup>	23.65 $\pm$ 1.10 <sup>c</sup>
		Range	(34.00–42.50)	(25.40–30.80)	(21.90–25.80)
Width, W	mm	Mean	24.33 $\pm$ 1.00 <sup>a</sup>	15.33 $\pm$ 0.96 <sup>b</sup>	11.84 $\pm$ 0.62 <sup>c</sup>
		Range	(22.30–25.70)	(13.40–16.90)	(10.50–12.90)
Thickness, T	mm	Mean	23.69 $\pm$ 1.12 <sup>a</sup>	14.83 $\pm$ 0.92 <sup>b</sup>	7.20 $\pm$ 0.63 <sup>c</sup>
		Range	(21.30–25.40)	(13.20–16.50)	(5.60–8.00)
Sphericity, S		Mean	0.74 $\pm$ 0.03 <sup>a</sup>	0.66 $\pm$ 0.02 <sup>b</sup>	0.53 $\pm$ 0.02 <sup>c</sup>
		Range	(0.70–0.78)	(0.62–0.70)	(0.50–0.57)
Aspect ratio, AR		Mean	1.55 $\pm$ 0.08 <sup>a</sup>	1.83 $\pm$ 0.12 <sup>b</sup>	2.00 $\pm$ 0.02 <sup>c</sup>
		Range	(1.43–1.69)	(1.64–2.10)	(0.50–0.60)
Geometric mean diameter, $D_g$	mm	Mean	27.86 $\pm$ 1.10 <sup>a</sup>	18.53 $\pm$ 1.01 <sup>b</sup>	12.61 $\pm$ 0.61 <sup>c</sup>
		Range	(25.71–29.51)	(16.50–20.48)	(11.19–13.48)
Arithmetic mean diameter, $D_a$	mm	Mean	28.53 $\pm$ 1.13 <sup>a</sup>	19.40 $\pm$ 1.04 <sup>b</sup>	14.23 $\pm$ 0.59 <sup>c</sup>
		Range	(26.37–30.57)	(17.33–21.40)	(13.00–15.27)
Surface area, SA	mm <sup>2</sup>	Mean	2442.60 $\pm$ 190.90 <sup>a</sup>	1082.00 $\pm$ 118.20 <sup>b</sup>	501.10 $\pm$ 47.40 <sup>c</sup>
		Range	(2076.80–2736.50)	(855.40–1317.50)	(393.20–570.40)
Actual volume, V	cm <sup>3</sup>	Mean	12.70 $\pm$ 1.34 <sup>a</sup>	4.75 $\pm$ 0.79 <sup>b</sup>	0.97 $\pm$ 0.32 <sup>c</sup>
		Range	(10.00–15.00)	(4.00–6.00)	(0.20–2.00)
Ellipsoid volume, $V_{\text{ellip}}$	cm <sup>3</sup>	Mean	11.38 $\pm$ 1.33 <sup>a</sup>	3.36 $\pm$ 0.55 <sup>b</sup>	1.06 $\pm$ 0.15 <sup>c</sup>
		Range	(8.90–13.46)	(2.35–4.50)	(0.73–1.28)

Table 1 (continue)

Properties			Whole Fruit	Nut	Kernel
Gravimetric Property					
Mass, M	g	Mean	13.89 ± 1.55 <sup>a</sup>	5.10 ± 0.49 <sup>b</sup>	0.89 ± 0.16 <sup>c</sup>
		Range	(10.94–16.93)	(4.38–6.02)	(0.403–1.09)
True density,	g/cm <sup>3</sup>	Mean	1.09 ± 0.04 <sup>a</sup>	1.09 ± 0.12 <sup>a</sup>	0.99 ± 0.29 <sup>a</sup>
		Range	(1.02–1.16)	(0.91–1.35)	(0.51–2.02)
Bulk density,	g/cm <sup>3</sup>	Mean	0.49 ± 0.02 <sup>a</sup>	0.63 ± 0.01 <sup>b</sup>	0.18 ± 0 <sup>c</sup>
		Range	(0.46–0.52)	(0.62–0.67)	(0.18)
Porosity, P	%	Mean	54.97 ± 2.08 <sup>a</sup>	41.05 ± 6.53 <sup>b</sup>	80.50 ± 5.20 <sup>c</sup>
		Range	(50.03–58.33)	(29.37–54.38)	(64.29–91.03)
Frictional Property					
Angle of repose	°	Mean	39.06 ± 6.82 <sup>a</sup>	31.22 ± 2.89 <sup>a</sup>	32.09 ± 6.76 <sup>a</sup>
		Range	(28.89–47.45)	(28.39–35.59)	(20.69–37.49)

Data are expressed in mean (± standard error) with 20 replicates. Different lower-case letters indicate significant differences ( $p \leq 0.05$ ) by Tukey's HSD test within the same row.

## Dimensions

There were significant differences ( $p \leq 0.05$ ) among the dabai fractions with respect to the dimensions. The mean values of length (L), width (W), and thickness (T) for the whole fruit were  $37.58 \pm 1.95$  mm,  $24.33 \pm 1.00$  mm, and  $23.69 \pm 1.12$  mm, respectively. Table 1 indicated that the length had the highest value with 35 % and 37 % differences compared to the width and thickness of the whole fruit, respectively. In a previous study by Chua et al. (2015), the dabai variety 'Song' had the closest length measurement with dabai *Besar* (36.00 mm) and a similar width with dabai *Bujur* (24.00mm).

Meanwhile, dabai nut had the mean values of  $28.04 \pm 1.65$  mm,  $15.33 \pm 0.96$  mm, and  $14.83 \pm 0.92$  mm for length, width, and thickness, respectively. A similar trend was observed in the whole fruit, with the length obviously having the greatest value compared to the width and thickness of dabai nut, with the differences in percentage at 45% and 47%, respectively. In comparison to previous studies, the length and width of the dabai variety 'Song' were higher than those of pistachio nuts (Kashaninejad et al., 2006) but relatively lower than those of pili nut (Gallegos et al., 2013) under different moisture conditions.

Next, the kernel's mean length, thickness, and width values were  $23.65 \pm 1.10$  mm,  $11.84 \pm 0.62$  mm, and  $7.20 \pm 0.63$  mm, respectively. The kernel length had the highest reading compared to thickness and width. Compared to the width and thickness of the dabai kernel, the length is 50% and 70% higher. The length and width of the kernel were compared with other seeds, and it was observed that the length and width of the dabai variety Song's kernel were lower than the pili kernel (Gallegos et al., 2013). In contrast, they were larger than the Ohadi pistachio nut (Kashaninejad et al., 2006).



The whole fruit of dabai consists of the highest value of dimensions with significant difference ( $p \leq 0.05$ ) among all the three fractions (whole fruit > nut > kernel). Therefore, these conclude that the length of whole fruit was 35% and 37% greater than that of nut and kernel. Besides, the width and thickness of whole fruit were 37% and 51% higher than the width of nut and kernel, respectively, while 37% and 70% greater than the thickness of nut and kernel.

### Sphericity

Concerning the sphericity of dabai, there were significant differences ( $p \leq 0.05$ ) among dabai fruit, nut, and kernel, as presented in Table 1. The mean sphericity value for the whole fruit was  $0.74 \pm 0.03$ . The dabai nut had a mean value of  $0.66 \pm 0.02$  for sphericity. Meanwhile, the dabai kernel's mean value of sphericity was  $0.53 \pm 0.02$ . Earlier, Gallegos et al. (2013) reported that the sphericity value for pili nut and its kernel ranged between 0.584–0.5315 and 0.5355–0.5463, respectively. Meanwhile, *Jatropha* fruit, nut, and kernel gave sphericity values of 0.95, 0.64, and 0.68, respectively (Sirisomboon et al., 2007), which were lower than dabai nut but higher than the kernel for its sphericity. Overall, the whole dabai variety 'Song' fruit ranged between 0.70 to 0.78, tended to roll better, and its shape was an ideal sphere compared to its nut and kernel.

### Aspect Ratio

The aspect ratio relates to the width and length of the fruit, which can be calculated to determine its relationship with fruit shape (Milošević et al., 2014). According to Table 1, there were differences ( $p \leq 0.05$ ) among the dabai fractions with respect to the aspect ratio parameter.

The mean value of the aspect ratio of whole fruit was  $1.55 \pm 0.09$ . The dabai nut had a mean value of  $1.83 \pm 0.12$  for the aspect ratio. Meanwhile, the mean value of the aspect ratio of the kernel was  $2.00 \pm 0.02$ . Hence, the aspect ratio of the dabai kernel was the highest with the following sequence: kernel > nut > whole fruit. Asoiro et al. (2017) also investigated and reported a similar trend where the kernel had the highest aspect ratio for velvet tamarind with kernel > unshelled > shelled sequence.

### Geometric Mean Diameter

Table 1 presents that the  $D_g$  mean value of dabai whole fruit was  $27.86 \text{ mm} \pm 1.10$ . The dabai nut had a mean value of  $18.53 \text{ mm} \pm 1.01$ , while the dabai kernel had  $12.61 \text{ mm} \pm 0.61$ . By comparing the different fractions, dabai whole fruit had a 33 % difference from the nut, 55% higher than dabai kernel for  $D_g$ . Other than that, the  $D_g$  of dabai nut and kernel were relatively lower than pili nut (32.46–33.06 mm) and kernel (18.73–20.03 mm), while tomato fruit had the highest  $D_g$  (34.75 mm) compared to dabai variety 'Song'. Overall,

it can be concluded that for  $D_g$  of dabai variety ‘Song’, the whole fruit had the highest mean value and differed significantly ( $p \leq 0.05$ ) among all the three fractions (whole fruit > nut > kernel) with the values ranging from 25.71 mm to 29.51 mm (whole fruit), 16.50 mm–20.48 mm (nut), and 11.91 mm–13.48 mm (kernel).

### Arithmetic Mean Diameter

Arithmetic Mean Diameter ( $D_a$ ) is the diameter average of all the particles in the sample. According to Table 1, the  $D_a$  of dabai whole fruit, nut, and kernel were recorded at the mean values of  $28.53 \pm 1.13$  mm,  $19.40 \pm 1.04$  mm, and  $14.23 \pm 0.59$  mm, respectively. Meanwhile, their range was from 26.37 mm to 30.57 mm for whole fruit, 17.33 mm to 21.40 mm for nut, and 13.00 mm to 15.27 mm for kernel. A similar trend was observed with the  $D_a$ , whereby the whole fruit had the greatest value compared to the nut and kernel, with percentage differences of 32% and 50%, respectively.  $D_a$  of all three fractions was significantly different at  $p \leq 0.05$  (whole fruit > nut > kernel).

### Surface Area

Table 1 shows significant differences ( $p \leq 0.05$ ) amongst whole fruit, nut, and kernel. The mean values of surface areas of the dabai variety ‘Song’ were  $2442.60 \pm 190.90$  mm<sup>2</sup> (whole fruit),  $1082.00 \pm 118.20$  mm<sup>2</sup> (nut), and  $501.10 \pm 47.40$  mm<sup>2</sup> (kernel). Thus, the highest mean surface area value was whole fruit ( $2442.60$  mm<sup>2</sup>), 56% and 79% greater than dabai nut and kernel, respectively. In a previous study, walnut surface area from four different genotypes ranged from 908.37 to 1042.21 mm<sup>2</sup> (Ebrahimi et al., 2009), lower than in the dabai variety ‘Song’. Meanwhile, by comparing within the *Canarium* family, the whole fruit of the dabai variety ‘Song’ was relatively larger than the surface area of *Canarium schweinfurthii* Engl fruits ( $920.72$  mm<sup>2</sup>) at a particular moisture content range (Ehiem et al., 2019). The surface area is key in determining the shape of the fruits and indicates how the kernels will behave on oscillating surfaces during processing (Ghadge & Prasad, 2012).

### Actual Volume and Ellipsoid Volume

According to Table 1, other physical properties of dabai are actual and ellipsoid volume. For the whole fruit of dabai, the mean values of actual volume and ellipsoid volume were  $12.70 \pm 1.34$  cm<sup>3</sup> and  $11.38 \pm 1.33$  cm<sup>3</sup>, respectively. It was followed by nut at  $4.75 \pm 0.79$  cm<sup>3</sup> and  $3.36 \pm 0.55$  cm<sup>3</sup>, respectively. The values are  $0.97 \pm 0.32$  cm<sup>3</sup> and  $1.06 \pm 0.15$  cm<sup>3</sup> for the kernel’s average actual and ellipsoid volumes, respectively. Overall, the whole fruit of dabai had the highest range values of actual and ellipsoid volumes compared to other fractions, which ranged from 10.00 to 15.00 cm<sup>3</sup> and 8.90 to 13.46 cm<sup>3</sup>, respectively. As with other geometric attributes, both volumes differ significantly amongst each fruit

fraction. Fruit volume plays a vital role in yield traits in horticultural crop processing, and its estimation is mainly related to fruit shape.

### Determination of Gravimetric Properties of Dabai Fractions

**Mass.** There were significant differences ( $p \leq 0.05$ ) among the dabai fractions with respect to the fruit mass. The mean value of the whole dabai fruit mass was  $13.89 \text{ g} \pm 1.55$ . Meanwhile, the dabai nut had a mean weight value of  $5.10 \text{ g} \pm 0.49$ . Lastly, the mean value of kernel weight was  $0.89 \text{ g} \pm 0.16$ . Therefore, the weight of the whole fruit section was the greatest compared to the other fractions within the range of 10.94 g to 16.93 g. Comparing to a study by Chua et al. (2015), the mean of total mass and kernel for different genotypes of dabai were within 7.60 g to 15.33 g and 0.48 g to 1.33 g, respectively. In a previous study, Ding and Tee (2011) recorded the seed weights of two superior bud-grafted clones, 'Laja' and 'Lulong,' which were 7.7g and 5.0 g, respectively. Prasad et al. (2011) stated that the pulp and seed contributed to the bulk of the fruit weight, comprising 46% and 44%, respectively, while peel constituted 10%. Abdul-Hamid et al. (2020) reported that the physical features, including flesh weight, seed weight, and length and diameter of dates, differed significantly (at a 5% probability level) from one variety to another.

**True and Bulk Density.** Table 1 presents the results of the true density and bulk density of dabai fruit. The results obtained for whole fruit were  $1.09 \text{ g/cm}^3 \pm 0.04$  and  $0.49 \text{ g/cm}^3 \pm 0.02$  for both density readings. The mean value of true density for dabai nut was  $1.09 \text{ g/cm}^3 \pm 0.12$ , almost equivalent to the former reading, while  $0.63 \text{ g/cm}^3 \pm 0.01$  is the mean value of its bulk density. The dabai kernel's mean values were  $0.99 \text{ g/cm}^3 \pm 0.29$  and  $0.18 \text{ g/cm}^3$ , respectively, for true and bulk densities. Therefore, the whole dabai fruit and nut shared the same mean values of true density ( $1.09 \text{ g/cm}^3 \pm 0.12$ ), which were the highest amongst all fractions with no significant differences (whole fruit = nut > kernel). Meanwhile, the highest mean value for bulk density belonged to dabai nut and differed significantly at  $p \leq 0.05$  when compared to the other two fractions of dabai fruit (nut > whole fruit > kernel). It may be attributed to the flesh, which is bulkier than the nutshell, such that it causes a reduction in the total mass per unit volume occupied by the flesh.

**Porosity.** With regard to the porosity of dabai, there were significant differences ( $p \leq 0.05$ ) among dabai fruit, nut, and kernel. The mean porosity values for the whole fruit, nut, and kernel were  $54.97\% \pm 2.08$ ,  $41.05\% \pm 6.53$ , and  $80.50\% \pm 5.20$ , respectively. In conclusion, the porosity for the kernel had the highest mean value based on Table 1 with the following sequence: kernel > whole fruit > nut. It may be due to strong attraction amongst the particles within the nutshell, which contributes to the difficulty of fracturing the nut, limiting its

internal pores. Bulk density, true density, and porosity are relevant tools in designing the types of equipment related to the separation, sorting, and handling systems.

### Determination of Frictional Properties of Dabai Fractions

**Angle of Repose.** Frictional properties were measured based on the lifting effect of the hollow cylinders containing either 20 replicates of whole fruit, nut, or kernel. As presented in Table 1, the average values of repose angle were recorded five times. The angle of repose mean value for whole fruit was  $39.06 \pm 6.82^\circ$ . Next, dabai nut and its kernel were recorded to have an average of  $31.22 \pm 2.89^\circ$  and  $32.09 \pm 6.76^\circ$ , respectively, for the angle of repose. However, no significant difference ( $p \leq 0.05$ ) existed amongst dabai fractions in terms of the angle of repose. This phenomenon is vital in determining the minimum flow slope in a self-emptying bin or a hopper. Hence, it can be concluded that the dabai nut has the lowest flowability compared to the whole fruit and the kernel.

### Correlations Between Physical Attributes

The dependence of the variables amongst physical attributes of dabai fractions was observed by analysis of correlation and presented in Table 2. Linear correlation showed that the whole fruit length (WFL) shared a highly positive correlation with geometric mean diameter ( $r = 0.89$ ).

Meanwhile, the correlation coefficients between whole fruit width (WFW), geometric mean diameter ( $WFD_g$ ), arithmetic mean diameter ( $WFD_a$ ), volume (WV) and mass (WFM) were highly positive with values of 0.89, 0.83, 0.86, 0.86, respectively. Next, whole fruit thickness (WFT) was positively correlated with  $WFD_g$  ( $r = 0.89$ ),  $WFD_a$  ( $r = 0.83$ ), and WFM ( $r = 0.84$ ). Furthermore, the correlation coefficients between  $WFD_g$ ,  $WFD_a$ , WV and WFM were highly positive, with the values of 0.99, 0.93 and 0.92, respectively. As indicated,  $WFD_a$  positively correlated with WV ( $r = 0.92$ ) and WFM ( $r = 0.91$ ). The WV was highly positively correlated with WFM ( $r = 0.96$ ).

Linear correlation implied that the dimension (length, width, and thickness) of the nut (NL, NW, and NT) shared positive and high correlation with similar variables; for instance, geometric mean diameter ( $ND_g$ ;  $r = 0.83$ ,  $r = 0.87$ , and  $r = 0.97$ , respectively), arithmetic mean diameter ( $ND_a$ ;  $r = 0.90$ ,  $r = 0.80$ , and  $r = 0.95$ , respectively). The  $ND_g$  was strongly positively correlated with  $ND_a$  ( $r = 0.99$ ). There were highly negative and positive correlations that existed between volume (NV) with ND ( $r = -0.80$ ) and mass ( $r = 0.80$ ).

Besides, the kernel (KL) length was highly positively correlated with an arithmetic mean diameter ( $KD_a$ ,  $r = 0.85$ ). Next, there were highly positive correlations among KT,  $KD_g$  ( $r = 0.93$ ),  $KD_a$  ( $r = 0.84$ ), and KM ( $r = 0.86$ ). The correlation coefficients among  $KD_g$ ,  $KD_a$  and KM were highly positive, with values of 0.97 and 0.94, respectively. Meanwhile, the correlation coefficients between  $KD_a$  and KM and KV and KD were high, with values

Table 2  
Correlation matrix of dabai fruit physical properties

Parameter	WFL	WFW	WFT	WFS	WFD <sub>g</sub>	WFD <sub>a</sub>	WFD <sub>s</sub>	WFM	WFD	NL	NW	NT	NS	ND <sub>g</sub>	ND <sub>a</sub>	NV	NM	ND
WFL	1																	
WFW	0.42	1																
WFT	0.41	<b>0.88</b>	1															
WFS	-0.64*	0.39	0.41	1														
WFD <sub>g</sub>	<b>0.75*</b>	<b>0.89*</b>	<b>0.89*</b>	0.02	1													
WFD <sub>a</sub>	<b>0.84*</b>	<b>0.83*</b>	<b>0.83*</b>	-0.12	<b>0.99*</b>	1												
WFD <sub>s</sub>	<b>0.69</b>	<b>0.86*</b>	<b>0.79*</b>	0.03	<b>0.93*</b>	<b>0.92*</b>	1											
WFM	<b>0.65*</b>	<b>0.86*</b>	<b>0.84*</b>	0.10	<b>0.92*</b>	<b>0.91*</b>	<b>0.96*</b>	1										
WFD	-0.05	0.11	0.28	0.23	0.13	0.10*	-4×10 <sup>-3</sup>	0.29	1									
NL	0.16	-0.35	-0.15	-0.37	-0.12	-0.06	-0.17	-0.21	-0.15	1								
NW	<b>0.54*</b>	0.22	0.36	-0.30	0.46*	0.49*	0.33	0.36	0.16	0.47*	1							
NT	0.32	-0.06	0.10	-0.30	0.16	0.20	0.09	0.11	0.08	<b>0.76*</b>	<b>0.83*</b>	1						
NS	0.36	<b>0.52*</b>	0.47*	0.05	<b>0.53*</b>	0.51	0.47	0.55	0.32	-0.41	<b>0.59*</b>	0.24	1					
ND <sub>g</sub>	0.39	-0.07	0.12	-0.37	0.19	0.24	0.10	0.10	0.03	<b>0.83*</b>	<b>0.87*</b>	<b>0.97*</b>	0.17	1				
ND <sub>a</sub>	0.34	-0.14	0.06	-0.38	0.13	0.18	0.04	0.03	-0.01	<b>0.90*</b>	<b>0.80*</b>	<b>0.95*</b>	0.04	<b>0.99*</b>	1			
NV	0.13	<b>-0.48*</b>	-0.40	-0.50*	-0.28	-0.20	-0.18	-0.20	-0.09	0.29	-0.15	-0.03	-0.47*	0.04	0.10	1		
NM	0.25	-0.34	-0.30	<b>-0.51*</b>	-0.13	-0.06	-0.10	-0.14	-0.15	0.25	-0.24	-0.17	<b>-0.55*</b>	-0.07	0.01	<b>0.80*</b>	1	
ND	0.08	0.41	0.34	0.23	0.32	0.28	0.18	0.19	0.03	-0.19	0.06	-0.06	0.24	-0.07	-0.10	<b>-0.80*</b>	-0.29	1
KL	0.31	-0.06	-0.19	-0.41	0.04	0.10	0.13	0.03	-0.31	-0.32	-0.25	-0.32	0.02	-0.33	-0.34	0.25	0.29	-0.11
KW	0.28	0.15	0.29	-0.08	0.29	0.30	0.39	0.36	-0.05	0.06	0.17	0.15	0.13	0.14	0.13	0.22	-0.05	-0.44
KT	0.21	-0.28	-0.34	-0.48*	-0.14	-0.08	0.04	-0.09	-0.44	0.07	-0.13	-0.04	-0.19	-0.04	-0.02	0.36	0.41	-0.19
KS	0.05	-0.10	0.03	-0.08	-2×10 <sup>-3</sup>	0.01	0.13	0.08	-0.14	0.36	0.18	0.32	-0.11	0.32	0.34	0.18	0.06	-0.26
KDg	0.33	-0.13	-0.16	-0.46*	0.04	0.10	0.22	0.09	-0.39	-0.03	-0.10	-0.07	-0.07	-0.08	-0.07	0.38	0.33	-0.31
KDa	0.37	-0.08	-0.14	-0.46*	0.07	0.14	0.23	0.12	-0.37	-0.16	-0.15	-0.16	-0.01	-0.17	-0.18	0.36	0.31	-0.29
KV	-0.09	-0.34	-0.34	-0.20	-0.29	-0.26	-0.11	-0.23	-0.44	-0.11	-0.21	-0.11	-0.08	-0.16	-0.15	0.36	0.15	-0.45*
KM	0.28	-0.17	-0.20	-0.44	-0.02	0.05	0.16	0.05	-0.36	0.02	0.01	0.09	0.04	0.05	0.04	0.27	0.12	-0.33
KD	0.14	0.39	0.38	0.19	0.35	0.32	0.16	0.28	0.41	-0.07	-0.01	-0.01	0.12	-1×10 <sup>-3</sup>	-0.02	-0.34	0.04	0.60*

Data are expressed: WF, whole fruit; N, nut; K, kernel; L, length; W, width; T, thickness; S, sphericity; Dg, geometric mean diameter; Da, arithmetic mean diameter; V, volume; M, mass; D, density. Absolute linear correlation coefficients ≥ 0.50 are marked in bold and starred (\*).

\* Results are significant at  $p \leq 0.05$

Table 2 (continue)

Parameter	KL	KW	KT	KS	KDg	KDa	KV	KM	KD
KL	1								
KW	0.01	1							
KT	<b>0.59*</b>	0.32	1						
KS	-0.34	<b>0.71*</b>	0.47*	1					
KDg	<b>0.69*</b>	<b>0.56*</b>	<b>0.93*</b>	0.44	1				
KDa	<b>0.85*</b>	0.47*	<b>0.84*</b>	0.21	<b>0.97*</b>	1			
KV	<b>0.51*</b>	0.35	<b>0.61*</b>	0.24	<b>0.67*</b>	<b>0.66*</b>	1		
KM	<b>0.58*</b>	<b>0.61*</b>	<b>0.86*</b>	<b>0.50</b>	<b>0.94*</b>	<b>0.89*</b>	<b>0.62*</b>	1	
KD	-0.18	-0.37	-0.33	-0.29	-0.39	-0.36	<b>-0.80*</b>	-0.45*	1

Data are expressed as K, kernel; L, length; W, width; T, thickness; S, sphericity; Dg, geometric mean diameter; Da, arithmetic mean diameter; V, volume; M, mass; D, density. Absolute linear correlation coefficients  $\geq 0.50$  are marked in bold and starred (\*)

\* Results are significant at  $p \leq 0.05$

of 0.89 and -0.80, respectively. Also, it was found that the dabai kernel did not correlate with any variables of the whole fruit or nut.

Generally, when dabai fruit, nut, and kernel were compared, the highest correlation among variables was observed between  $D_g$  and  $D_a$ . These correlations illustrated that the  $D_g$  was the best dimensional parameter for weight estimation (Mohsenin, 1986) and can be used to predict each other (Milošević et al., 2014).

These findings parallel the result of Torres et al. (2012), who found that fresh mass is the most closely related variable to diameter.

## CONCLUSION

The physical attributes of dabai, variety Song, and grade A were characterised in this study. All properties varied significantly among fruit fractions except for bulk density and angle of repose. The highest significantly positive correlation was found between geometric mean diameter and arithmetic mean diameter amongst all fractions, while actual density was the least correlated to other variables. Relationships existed amongst several other physical variables within each fraction. In comparison across dabai fractions, whole fruit was observed to have several correlations with certain variables from the nut and kernel. This study enhances the knowledge about the variation of physical properties in each fruit fraction, particularly for the dabai variety ‘Song,’ and may be relevant to crop producers, food processors, or engineers.

## ACKNOWLEDGEMENTS

The authors express their appreciation to the Ministry of Higher Education of Malaysia for providing financial support under the Fundamental Research Grants Scheme (FRGS) (Project Number: FRGS/1/2019/WAB01/UPM/02/30) and the Sarawak Biodiversity Centre for approving and issuing the R&D permit—a special thanks to Universiti Putra Malaysia for the technical support given during this research work.

## REFERENCES

- Abdul-Hamid, N. A., Mustaffer, N. H., Maulidiani, M., Mediani, A., Ismail, I. S., Tham, C. L., Shadid, K., & Abas, F. (2020). Quality evaluation of the physical properties, phytochemicals, biological activities and proximate analysis of nine Saudi date palm fruit varieties. *Journal of the Saudi Society of Agricultural Sciences*, 19(2), 151-160. <https://doi.org/10.1016/j.jssas.2018.08.004>
- Altuntaş, E., & Yildiz, M. (2007). Effect of moisture content on some physical and mechanical properties of faba bean (*Vicia faba* L.) grains. *Journal of Food Engineering*, 78(1), 174-183. <https://doi.org/10.1016/j.jfoodeng.2005.09.013>
- Ariffin, S. H., Shamsudin, R., & Tawakkal, I. S. M. A. (2020). Dabai fruit: Postharvest handling and storage. *Advances in Agricultural and Food Research Journal*, 1(2), 1-12.

- Asoiro, F. U., Ezeoha, S. L., Ugwu, C. B., & Ezenne, G. I. (2017). Physical properties of unshelled, shelled and kernel of velvet tamarind (*Dialium guineense*) fruit from Nigeria. *Cogent Food & Agriculture*, 5, 1-10. <https://doi.org/10.1080/23311932.2017.1287618>
- Aydin, C. (2003). Physical properties of almond nut and kernel. *Journal of Food Engineering*, 60(3), 315-320. [https://doi.org/10.1016/S0260-8774\(03\)00053-0](https://doi.org/10.1016/S0260-8774(03)00053-0)
- Azman, A. P. N. M., Shamsudin, R., Man, H. C., & Yaacob, M. E. (2020). Some physical properties and mass modelling at different maturity of pepper berries (*Piper Nigrum* L.) variety Kuching. *Process*, 8, 1-24.
- Binoj, J. S., Raj, R. E., Sreenivasan, V. S., & Thusnavis, G. R. (2016). Morphological, physical, mechanical, chemical and thermal characterization of sustainable Indian Areca fruit husk fibers (*Areca Catechu* L.) as potential alternate for hazardous synthetic fibers. *Journal of Bionic Engineering*, 13(1), 156-165. [https://doi.org/10.1016/S1672-6529\(14\)60170-0](https://doi.org/10.1016/S1672-6529(14)60170-0)
- Burubai, W., & Amber, B. (2014). Some physical properties and proximate composition of Ipoli fruits. *Journal of Food Processing & Technology*, 5(7), 1-5. <https://doi.org/10.4172/2157-7110.1000343>
- Chua, H. P., Nicholas, D., & Yahya, M. N. A. (2015). Physical properties and nutritional values of dabai fruit (*Canarium odontophyllum*) of different genotypes. *Journal of Tropical Agriculture and Food Science*, 43(1), 1-10.
- Ding, P., & Tee, Y. K. (2011). Physicochemical characteristics of dabai (*Canarium odontophyllum* Miq.) fruit. *Fruits*, 66(1), 47-52. <https://doi.org/10.1051/fruits/2010040>
- Ebrahimi, A., Zarei, A., Fatahi, R., & Varnamkhasti, M. G. (2009). Study on some morphological and physical attributes of walnut used in mass models. *Scientia Horticulturae*, 121(4), 490-494. <https://doi.org/10.1016/j.scienta.2009.02.021>
- Ehiem, J. C., Ndirika, V. I. O., & Onwuka, U. N. (2016). Effect of moisture content on some physical properties of *Canarium schweinfurthii* Engl. fruits. *Research in Agricultural Engineering*, 62(4), 162-169. <https://doi.org/10.17221/11/2015-RAE>
- Ehiem, J. C., Ndirika, V. I. O., Onwuka, U. N., Garipey, Y., & Raghavan, V. (2019). Water absorption characteristics of *Canarium Schweinfurthii* fruits. *Information Processing in Agriculture*, 6(3), 386-395. <https://doi.org/10.1016/j.inpa.2018.12.002>
- Gallegos, R. K. B., Suministrado, D. C., Amongo, R. M. C., & Madlangbayan, M. S. (2013). Some physical and mechanical properties of pili (*Canarium ovatum* Engl. cv. Katutubo) nut as a function of nut moisture. *Philippine Agricultural Scientist*, 96(1), 66-74.
- Ghadge, N. P., & Prasad, K. (2012). Some physical properties of rice kernels: Variety PR-106. *Journal of Food Processing & Technology*, 3(8), Article 1000175. <https://doi.org/10.4172/2157-7110.1000175>
- Hady, N. S. (2021, January 31). High prices no issue for dabai lovers. *New Sarawak Tribune*. <https://www.newsarawaktribune.com.my/high-prices-no-issue-for-dabai-lovers>
- Kashaninejad, M., Mortazavi, A., Safekordi, A., & Tabil, L. G. (2006). Some physical properties of Pistachio (*Pistacia vera* L.) nut and its kernel. *Journal of Food Engineering*, 72(1), 30-38. <https://doi.org/10.1016/j.jfoodeng.2004.11.016>



- Khoshnam, F., Tabatabaeefar, A., Varnamkhasti, M. G., & Borghei, A. (2007). Mass modeling of pomegranate (*Punica granatum* L.) fruit with some physical characteristics. *Scientia Horticulturae*, *114*, 21-26. <https://doi.org/10.1016/j.scienta.2007.05.008>
- Liu, Z. M. S. (2011). *Measuring the Angle of Repose of Granular Systems using Hollow Cylinders*. (Doctoral dissertation). University of Pittsburgh, Pennsylvania. <https://d-scholarship.pitt.edu/6401/>
- Milošević, T., Milošević, N., Glišić, I., & Glišić, I. S. (2014). Determination of size and shape properties of apricots using multivariate analysis. *Acta Scientiarum Polonorum, Hortorum Cultus*, *13*(5), 77-90.
- Mohsenin, N. N. (1986). Structure, physical characteristics and mechanical properties. In *Physical Properties of Plant and Animal Materials* (pp. 66-74). Gordon and Breach Science Publishers.
- Prasad, K. N., Chew, L. Y., Khoo, H. E., Yang, B., Azlan, A., & Ismail, A. (2011). Carotenoids and antioxidant capacities from *Canarium odontophyllum* Miq. fruit. *Food Chemistry*, *124*(4), 1549-1555. <https://doi.org/10.1016/j.foodchem.2010.08.010>
- Sessiz, A., Esgici, R., & Kizil, S. (2007). Moisture-dependent physical properties of caper (*Capparis* ssp.) fruit. *Journal of Food Engineering*, *79*(4), 1426-1431. <https://doi.org/10.1016/j.jfoodeng.2006.04.033>
- Sirisomboon, P., Kitchaiya, P., Pholpho, T., & Mahuttanyavanitch, W. (2007). Physical and mechanical properties of *Jatropha curcas* L. fruits, nuts and kernels. *Biosystems Engineering*, *97*, 201-207. <https://doi.org/10.1016/j.biosystemseng.2007.02.011>
- Torres, I. D. A., Herrera, J. J. C., & Tascón, C. E. O. (2012). Physical and mechanical properties correlation of coffee fruit (*Coffea arabica*) during its ripening. *Dyna*, *79*(172), 148-155.
- Yang, X. H., Deng, L. Z., Mujumdar, A. S., Xiao, H. W., Zhang, Q., & Kan, Z. (2018). Evolution and modeling of colour changes of red pepper (*Capsicum annuum* L.) during hot air drying. *Journal of Food Engineering*, *231*, 101-108. <https://doi.org/10.1016/j.jfoodeng.2018.03.013>



## Microencapsulation of *Acalypha indica* Linn. Extracts Using Chitosan-Polycaprolactone Blends

Maizatul Akmal Johari<sup>1</sup>, Fathilah Ali<sup>1\*</sup>, Azlin Suhaida Azmi<sup>1</sup>, Hazleen Anuar<sup>2</sup>, Jamarosliza Jamaluddin<sup>3</sup> and Rosnani Hasham<sup>4</sup>

<sup>1</sup>Department of Chemical Engineering and Sustainability, Kulliyah of Engineering, International Islamic University Malaysia, 50728 Kuala Lumpur, Malaysia

<sup>2</sup>Department of Manufacturing and Materials Engineering, Kulliyah of Engineering International Islamic University Malaysia, 50728, Kuala Lumpur, Malaysia

<sup>3</sup>Department of Chemical Engineering, Faculty of Chemical and Energy Engineering, Universiti Teknologi Malaysia, 81310 Johor Bahru, Johor, Malaysia

<sup>4</sup>Department of Bioprocess and Polymer Engineering, Faculty of Chemical and Energy Engineering, Faculty of Engineering, Universiti Teknologi Malaysia, 81310 Johor Bahru, Johor, Malaysia

### ABSTRACT

Polymer encapsulation is commonly adopted in drug delivery systems to form encapsulation that can assist in delivering active compounds to the targeted area. *Acalypha indica* (AI) crude extract was obtained from AI plants through ultrasound-assisted extraction. It is naturally unstable in the external environment and, thus, needs to be encapsulated to protect against volatility. Herein, this study emphasized the development of the encapsulations of AI extracts using a chitosan-polycaprolactone (PCL) blend by emulsion-solvent evaporation and freeze-dried methods. Four parameters for AI encapsulation were studied by fixing one parameter at a time. The percentage of encapsulation efficiency (EE%) was recorded as a response for each parameter. The study proceeded with central composite design (CCD) as the response surface methodology (RSM) optimization tool to study the interactions between the

factors. Central points were taken from the preliminary data obtained in one-parameter experiments. The validation was carried out with two data of the highest and lowest EE% suggested by CCD. The highest EE% recorded was 98.70%, and the lowest EE% was 87.80%. The results showed a difference between predicted and experimental values at a percentage lower than 7.5%. Fourier Transform Infrared Spectroscopy (FTIR),

### ARTICLE INFO

#### Article history:

Received: 28 January 2023

Accepted: 17 August 2023

Published: 14 March 2024

DOI: <https://doi.org/10.47836/pjst.32.2.14>

#### E-mail addresses:

maiez.akmal93@gmail.com (Maizatul Akmal Johari)

fathilah@iium.edu.my (Fathilah Ali)

azlinsu76@iium.edu.my (Azlin Suhaida Azmi)

hazleen@iium.edu.my (Hazleen Anuar)

jamarosliza@utm.my (Jamarosliza Jamaluddin)

r-rosnani@utm.my (Rosnani Hasham)

\* Corresponding author

scanning electron microscopy (SEM), particle size analyzer, and zeta potential were used to analyze the properties of selected microencapsulated samples. Overall, the encapsulation of AI extracts was successful and has the potential to be used in drug delivery.

*Keywords:* *Acalypha indica* Linn., central composite design, chitosan, microencapsulation, polycaprolactone

---

## INTRODUCTION

Over the past decades, a lot of research and invention has been done and keeps growing to enhance the current drug delivery system (Yusuf et al., 2023). In developing a good controlled-release drug delivery system, selecting a good drug carrier is the most challenging in the sense that the side effects of the drugs and the drug carriers on humans can be minimized (Adepu & Ramakrishna, 2021). Chitosan has been proven to be an effective polymeric drug carrier. Chitosan is found naturally from aquatic shell wastes and is one of the most abundant polymers in nature, thus providing a vast potential for commercial value. Due to good mucoadhesive properties and biodegradability, chitosan is safe for consumption (Roy & Sahoo, 2016; Szymańska & Winnicka, 2015). However, chitosan needs modification to improve its stability and solubility to form an excellent polymer matrix for microencapsulation. The limitations of chitosan can be improved through several methods of modification while maintaining the parent chain. In this way, the modification preserves the good physicochemical properties. Physically blending with another polymer is one of many ways to improve the characteristics of chitosan.

Recently, encapsulation studies have focused more on synthetic pharmaceutical drugs. However, encapsulations of certain plant extracts are somehow less explored. The challenges of maintaining stable *Acalypha indica* (AI) extracts are related to the fact that the active compounds are naturally volatile, light and temperature sensitive and susceptible to degradation (Bazana et al., 2019). AI, commonly known as Indian copperleaf, is an herbaceous species plant. However, it gets less attention because its habitat is mostly in the backyards and is often treated as a weed. However, AI can be found only in certain geographical regions (El Hady et al., 2019). Interestingly, there is a fascinating fact about this plant and its high potential for commercialization.

Previously, it was reported that the leaf extracts of AI have several bioactive compounds that can treat respiratory problems such as bronchitis, asthma, and pneumonia (Martin & Ashokkumar, 2017; Taurozzi et al., 2012). Poly- $\epsilon$ -caprolactone (PCL) is a biodegradable aliphatic polyester with better viscoelastic and allows many structures such as microspheres. Due to its properties, PCL can be easily blended with other polymers, such as chitosan, for microencapsulations (Christen & Vercesi, 2020).

Modifying the chitosan with PCL via blending can benefit the immobilization of the AI extracts against any interactions with the external environment through encapsulation (Rivas

et al., 2019). Encapsulation is very vital as without encapsulation, and the uncontrolled environmental condition has a tendency to break down certain types of beneficial bioactive compounds of the AI extracts.

The emulsion-solvent evaporation method is identified as the most suitable method to encapsulate the ethanolic AI extracts. The microencapsulation of AI extracts was conducted by blending chitosan with a PCL. First, experiments were done by fixing one factor at a time (OFAT) for four parameters: homogenization duration, the ratio of chitosan: PCL, the concentration of surfactant (PVA), and polymer matrix concentrations. Subsequently, an optimization study of the three factors (ratio of chitosan: PCL concentration, PVA concentration, and Concentration of chitosan-PCL blend) was performed using the design of experiments (DOE) by central composite design (CCD), and the percentage of encapsulation efficiency (EE%) was recorded as the response. Lastly, the microcapsules were characterized with SEM, FTIR, zeta potential and particle size analysis.

## MATERIALS AND METHODS

### Materials and Instrumentations

Chitosan (medium molecular weight 190,000-310,000 Da, Catalog No. 448877, ~85% deacetylated), poly-( $\epsilon$ -caprolactone)(PCL) (molecular weight= 45,000 Da, SKU No. 704105), and poly(vinyl alcohol) (PVA) (molecular weight= 31,000–50,000 Da, SKU No. 363138, 98%–99% hydrolyzed), were purchased from Sigma Aldrich, USA. Methylene chloride (DCM) (Catalog No. 106050, 84.93 g/mol) was purchased from Merck Millipore®, Germany. Acetic acid glacial (60.05 g/mol) analytical grade was purchased from Bendosen Laboratory Chemicals, Norway. *Acalypha indica* (AI) extracts were obtained from Universiti Teknologi Malaysia (UTM) through ultrasound-assisted extraction using a water bath sonicator and ethanol as the solvent. Anhydrous ethanol, 99.8% v/v absolute denatured grade, was purchased from HmbG® Chemicals, Germany.

### Fabrication of Chitosan-PCL Encapsulation-loaded *Acalypha indica* Extract

Following the previously reported method, the physical blending of the chitosan-PCL was done according to the emulsion-solvent evaporation method (El Hady et al., 2019). The mechanism of AI extract encapsulation was simplified, as shown in Figure 1.

Firstly, a fixed parameter was conducted per the aforementioned method following the recipe in Table 1. PCL (0.5%) was dissolved in an organic phase of DCM, PVA (2%) in deionized water, and chitosan (0.5%) in 0.2%v/v aqueous acetic acid. Then, the polymer solutions were vigorously stirred for 24 hours to dissolve the polymers, and PVA was stirred at a temperature of 60 °C. The AI extract was diluted in ethanol to get a concentration of 0.2 g/mL.

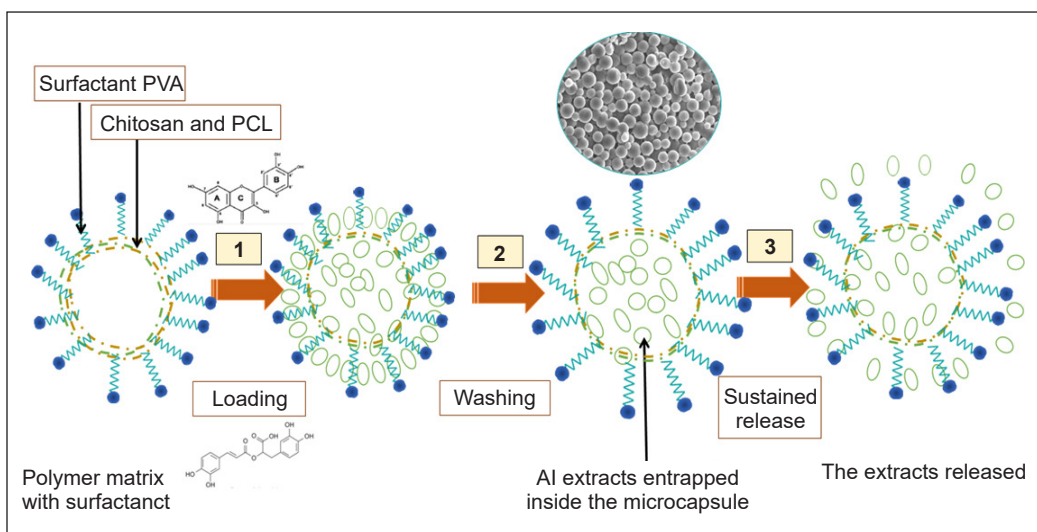


Figure 1. The overview process of encapsulation of AI extracts and the extract release

Next, the microencapsulation of *Acalypha indica* (AI) extract was fabricated. A 5 mL emulsion of PCL was transferred into a 50 mL-sized tube containing 5 mL of PVA. Then, 5 mL of each PCL, chitosan, and the AI extract were sequentially added. Immediately, solutions were homogenized under an ultrasonic homogenizer (Fisher Scientific FB705, 700 watts) with an amplitude of 90% and homogenized to form a water-in-oil (W/O) emulsion. After that, the solutions were moderately stirred with a magnetic stirrer for 24 hours at room temperature in a controlled environment. After that, the microparticles were collected by centrifuging at 13,000 rpm for 1 hour using a mini centrifuge (Eppendorf, speed x 1,000). Two layers of supernatant and precipitates were formed. The solvents were discarded and replaced by deionized water. Then, the precipitates and the deionized water were vortexed. After that, the centrifugation steps were repeated for 15 minutes every cycle until the solutions turned pH-neutral. Then, the samples were ready for freeze-drying. Following a similar procedure, the blank encapsulations were prepared without the addition of AI extracts. Next, the one parameter-at-a-time (OFAT) studies and optimization followed the same procedures. The process is illustrated in Figure 2.

### Encapsulation Efficiency of Chitosan-PCL Determination

Firstly, a series of wavelength screenings were done under ultraviolet-visible (UV-VIS) spectrophotometers from 200–1000 nm on the crude AI extract samples. The highest peak was detected at 285nm and was used as a benchmark for the highest amounts of active compounds in the crude extracts of AI.

In another experiment, the encapsulated AI extracts were released from its Chitosan-PCL microcapsules by dissolving in 1.0 mL of 99.8% ethanol to determine the percentage of

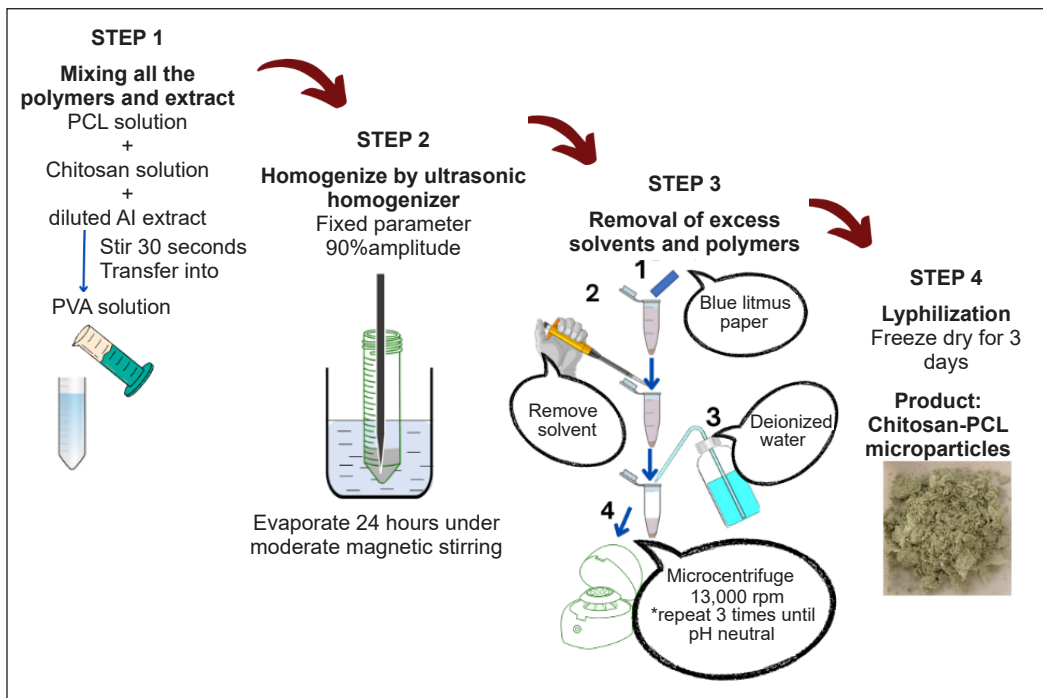


Figure 2. Schematic diagram of the emulsion-solvent evaporation method

encapsulation of AI extract entrapped in the microcapsule. The samples were centrifuged at 13,000 rpm for 1 hour. After that, the supernatant was collected and spectrophotometrically assayed at 285 nm. The amount of AI extracts entrapped was calculated using Equation 1.

$$EE\% = \frac{\text{concentration of extract in the microcapsules}}{\text{Initial concentration of AI extracts}} \times 100\% \quad [1]$$

### Optimization of Microencapsulation Process

The experiment was continued with a series of OFAT to find the preferred range for each parameter and select the desired range and levels for response surface methodology (RSM). In this experiment, only one parameter was manipulated, while the other parameters remained constant. Each run was repeated thrice.

**Homogenization Duration.** The OFAT of homogenization duration was conducted in four different durations, as shown in Table 1. Homogenization duration, which gave the highest encapsulation efficiency, was chosen for the next OFAT step based on the highest encapsulation efficiency (EE%) as the response.

**Ratio of Chitosan:PCL Concentration.** With the homogenization duration fixed at 5 minutes, the second OFAT of the Chitosan:PCL concentration ratio was conducted, where

the values were varied, as shown in Table 2. The ratio that gave the highest EE% was chosen for the next OFAT step.

**PVA Concentration.** With the ratio of Chitosan:PCL concentration fixed at 0.6:0.4, the third OFAT of PVA concentration ratio was conducted, where the values varied, as shown in Table 3—similarly, the highest EE% as the response was recorded and carried out for the next step.

**Concentration of Chitosan-PCL Blends.** With the PVA concentration fixed at 0.05%, the fourth OFAT of Chitosan-PCL blends concentration was conducted, where the values varied, as shown in Table 4, and EE% was recorded.

Table 1  
Various homogenization durations of reaction using OFAT (Factor 1)

F1: Homogenization duration	F2: Chitosan:PCL concentration ratio (%)	F3: PVA concentration as a surfactant (%)	F4: Concentration of chitosan-PCL blends (%w/v)
3	0.5:0.5	2	1
5	0.5:0.5	2	1
7	0.5:0.5	2	1
10	0.5:0.5	2	1

Table 2  
Various ratio concentrations of Chitosan:PCL using OFAT (Factor 2)

F1: Homogenization duration	F2: Chitosan:PCL concentration ratio (%)	F3: PVA concentration as a surfactant (%)	F4: Concentration of chitosan-PCL blends (%w/v)
5	0.2: 0.8	2	1
5	0.4: 0.6	2	1
5	0.5:0.5	2	1
5	0.6:0.4	2	1
5	0.8:0.2	2	1

Table 3  
Various PVA concentrations using OFAT (Factor 3)

F1: Homogenization duration	F2: Chitosan:PCL concentration ratio (%)	F3: PVA concentration as a surfactant (%)	F4: Concentration of chitosan-PCL blends (%w/v)
5	0.6:0.4	0.01	1
5	0.6:0.4	0.05	1
5	0.6:0.4	0.1	1
5	0.6:0.4	0.3	1
5	0.6:0.4	0.5	1
5	0.6:0.4	1	1
5	0.6:0.4	2	1



Table 4

*Various concentrations of Chitosan-PCL blends using OFAT (Factor 4)*

F1: Homogenization duration	F2: Chitosan:PCL concentration ratio (%)	F3: PVA concentration as a surfactant (%)	F4: Concentration of chitosan-PCL blends (%w/v)
5	0.6:0.4	0.05	0.33
5	0.6:0.4	0.05	0.67
5	0.6:0.4	0.05	1.00
5	0.6:0.4	0.05	1.33
5	0.6:0.4	0.05	1.67

### Study on Interaction Between Variables by Central Composite Design (CCD) for Surface Response Methodology (RSM)

The experiment was continued with the interaction study by response surface methodology (RSM). Central composite design (CCD) was chosen as the response surface model. The design of the experiment was aided by Design-Expert version 12 software using central composite design (CCD) to study the impact and interactions of independent variables.

Since the DOE software is unable to process the ratio values, the values used were only integer numbers. For instance, in the first factor, which is the ratio of chitosan to PCL, the value 4 means the ratio of chitosan to PCL was 0.4:0.6. Table 4 illustrates the values for the coded levels used in the DOE. For the fourth factor, the range of concentration of Chitosan-PCL blends (%w/v) in this study was limited according to the maximum concentration of chitosan that reached the gelation point for dissolution in 0.2% v/v of acetic acid. A preliminary experiment was done to find the maximum concentration reaching the gelation point. It was found that the chitosan reached the gelation point at a 1% g/mL concentration.

Thus, three factors were used to study the interactions. The independence variables of chitosan:PCL concentration ratios (X1), PVA concentration (X2), and the Concentration of chitosan-PCL blend (X3) were selected with the specific range obtained from the single experiments, OFAT. Details of the value of codified levels are tabulated in Table 5.

In CCD, three factors and one response were decided for the optimization study, and to predict the response at any point, codified units are the cube with the side [-1,1]. The design of CCD was proposed in Table 6 and simplified with the value of the coded units.

Table 5

*Codified level for independent variables used in CCD for encapsulation optimization*

Independent variables	Units	Coded levels		
		-1	0	+1
X1: Ratio of Chitosan (n) :PCL (10-n)	N chitosan	4	6	8
X2: PVA concentration	%	0.01	0.05	0.09
X3: Concentration of chitosan-PCL blend	%	0.6	1	1.4

Table 6  
*Design matrix of codified variables for central composite design*

Run	Code			Experimental		
	Factor 1: Chitosan:PCL ratio	Factor 2: PVA concentration	Factor 3: Drug:polymer ratio	Factor 1: Chitosan:PCL ratio (%)	Factor 2: PVA concentration	Factor 3: Concentration of chitosan- PCL blend
1	-1	1	-1	4	0.09	0.6
2	1	1	-1	8	0.09	0.6
3	-1	1	1	4	0.09	1.4
4	1	-1	1	8	0.01	1.4
5	1	1	1	8	0.09	1.4
6	1	-1	-1	8	0.01	0.6
7	1	0	0	8	0.05	1
8	-1	-1	1	4	0.01	1.4
9	0	-1	0	6	0.01	1
10	0	1	0	6	0.09	1
11	-1	-1	-1	4	0.01	0.6
12	0	0	-1	6	0.05	0.6
13	0	0	0	6	0.05	1
14	0	0	1	6	0.05	1.4
15	0	0	0	6	0.05	1
16	0	0	0	6	0.05	1
17	-1	0	0	4	0.05	1

## Model Validation

A validation study is an additional set of experiments carried out to validate and reproduce the output from the model. This study conducted two additional experiments referring to the new optimized parameters suggested by the DOE software. These two experiments were selected according to the highest and lowest EE% response predicted by DOE software. Subsequently, these two optimum samples were used for further characterizations.

## Characterizations

**Scanning Electron Microscope (SEM).** A scanning electron microscope (SEM) (JEOL JSM-IT 100 InTouchScope™) accelerated at 5 kV was used to examine the morphological surface of the selected microparticles. The samples were coated with sputter coating (QC7620, Quorum Ltd, London) by placing the samples on the Nisshin EM conductive carbon tape that acted as a sample holder. The prepared samples were placed in a brass holder under the vacuum holder.

**Fourier-Transform Infrared Spectroscopy (FTIR).** The Fourier-transform infrared spectroscopy (FTIR) examination of the selected AI extract microencapsulation was determined using Nicolet iS50 FT-IR spectrophotometer (Thermo Scientific, Massachusetts, US). The samples in powder form were scanned under the regions of 4000–400  $\text{cm}^{-1}$  wavenumber.

**Particle Size Analysis and Zeta Potential.** The average particle size was quantified using the dynamic light scattering (DLS) technique by Zetasizer Nano (Malvern Instruments Inc., UK). The system temperature was 25°C, the repetition was thrice, the Viscosity (cP) was 1.2, and the count rate (kcps) was 139.2. The refractive index of the material was 1.59. The microparticles were suspended in ethanol.

## RESULTS AND DISCUSSIONS

### Effects of OFAT Studies

**Homogenization Duration.** In Figure 3, encapsulation efficiency exhibited an upward trend from 3 minutes to 5 minutes of homogenization. During 3 minutes of duration homogenization, the oil/water phases did not completely break into smaller droplets. The physical observations were made from the solutions after solvent removal steps through 130 rpm/60 minutes centrifugations. Through observation in Figure 4, the solutions turned more translucent as the sonication time increased, and more precipitates were deposited. The microparticles recovered from centrifugation were similarly reported by Leong et al. (2017). From centrifugation, fewer microparticles were deposited, and the supernatant was slightly cloudy. During this time, the emulsification occurred incompletely.

After 5 minutes of homogenization, it is unlikely to result in any significant changes in encapsulation efficiency and the SEM images, but the trend of encapsulation efficiency declined. As the duration of homogenization increased, the input energy also increased, thus boosting the shear force due to acoustic cavitation. Due to this phenomenon, as time passes, more energy is dissipated to break down the larger oil/water molecules into smaller droplets (Abriata et al., 2019; Taha et al., 2020). According to Eric et al. (2017), this short homogenization duration may also result in the formation of coarse emulsion and a larger diameter of

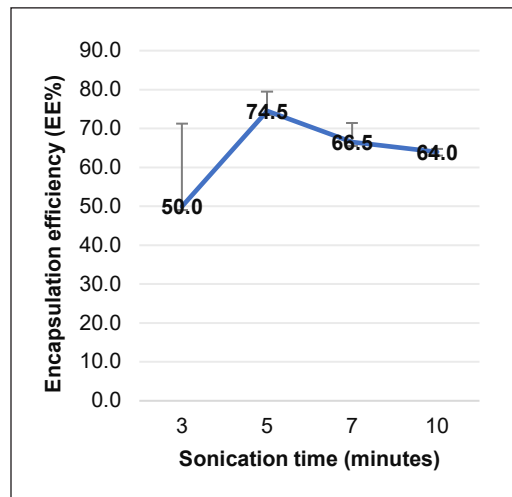


Figure 3. The effect of homogenization duration on the chitosan:PCL encapsulation efficiency

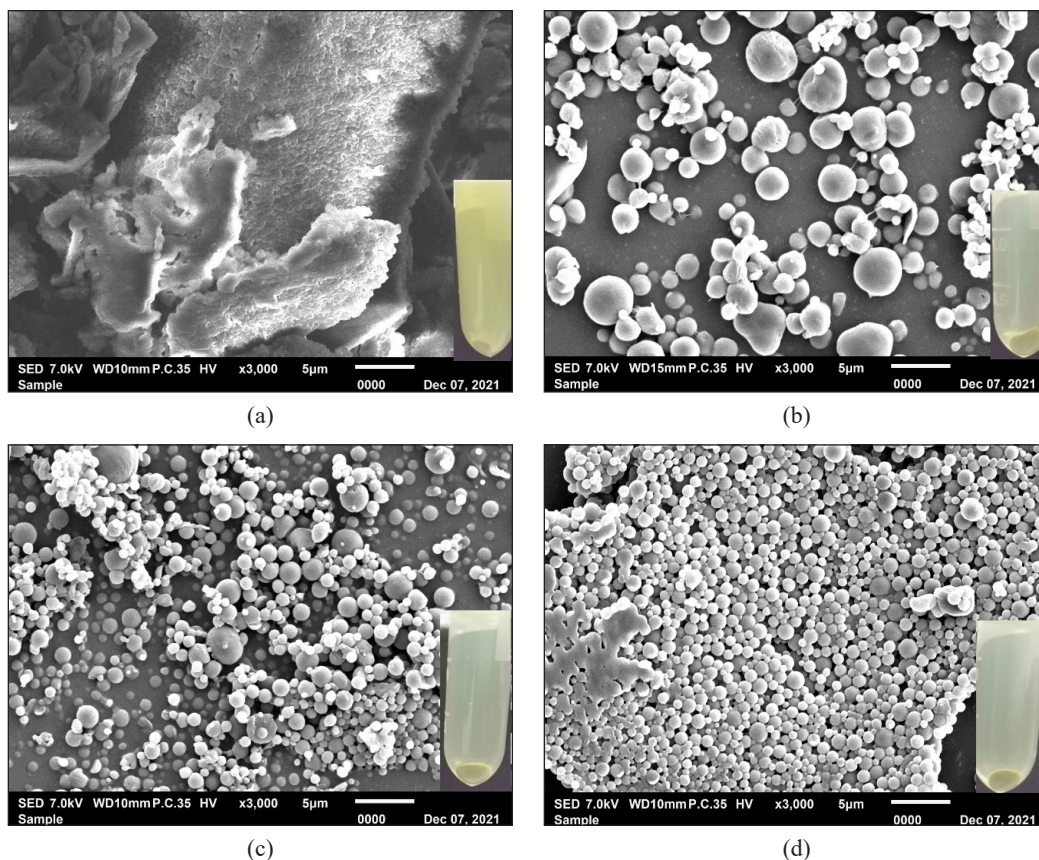


Figure 4. SEM images and visual register of the suspensions of samples at different homogenization durations: (a) 3 minutes, (b) 5 minutes, (c) 7 minutes, and (d) 10 minutes

emulsion droplets. Ten minutes duration somehow observed a good encapsulation image, but the EE% was lower than 5 and 7 minutes. The longer exposure time of the samples to homogenization may reduce the cavitation efficiency of the microtips and eroded (Taha et al., 2020). Through this experiment, 5 minutes of homogenization duration was selected and used in the next experiments.

**The Ratio of Chitosan: PCL Concentration.** The composition of chitosan and PCL is one of the most prioritized parameters that make up the concentration of chitosan-PCL blend as the carrier matrix. Figure 5 shows that the combination of a higher amount of PCL (0.2:0.8) resulted in the lowest EE% (33.80%). The EE% increased as the concentration of chitosan and PCL increased until the concentration of chitosan was more than PCL (0.6:0.4). Thus, the optimum concentration of chitosan and PCL obtained was 0.6 and 0.4 %w/v respectively with 70.10% EE%. The decrease of EE% after the 0.6 %w/v concentration of chitosan is possibly related to the viscosity of chitosan. In this case, the 0.8%w/v concentration of

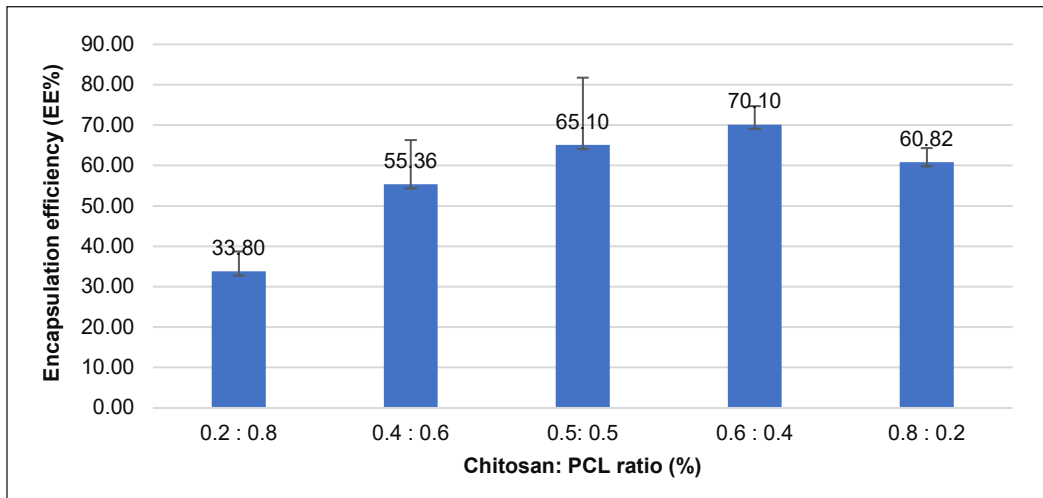


Figure 5. Chitosan-PCL copolymer encapsulation with AI extract with various ratios of chitosan:PCL

chitosan dissolved in 0.2%w/v acetic acid started to reach the gelation point. Thus, during the homogenization process, the chitosan molecules are unable to break well into smaller sizes, and the entrapment due to the chitosan not fully dissolved because the higher viscosity will reduce the intensity of the acoustic cavitation (Taurozzi et al., 2012).

Homopolymer (PCL only and Chitosan only) encapsulation does not form stable microencapsulation because, during opening or pore creation, the monomer droplets formed are very porous, unable to hold the extract, and the extract has been leaked out during the cavitation process before they start forming microemulsion (Taha et al., 2020). Unlike the heteropolymer encapsulation, while depolymerization occurs, both monomers of PCL and chitosan incorporate together, thus capping the AI extract inside. Less viscous liquid (e.g., water) undergoes cavitation more easily and becomes an emulsion phase (O/W). In summary, the ratio of 0.6:0.4 was selected for the next optimization.

**The Surfactant (PVA) Concentration.** A surface active agent commonly known as a surfactant used in this study is polyvinyl alcohol (PVA). PVA is a non-ionic surfactant, which is a nonelectrolyte. The emulsified droplets of chitosan-PCL-loaded AI extract microencapsulation need a surfactant to preserve stability as well as prevent continuous phase separation by coalescence (Leong et al., 2009).

As a stabilizer, the presence of PVA in the outer space of microparticles significantly affects the percentage of encapsulation efficiency. The maximum encapsulation efficiency was found when the concentration of PVA was 0.05%, which is 86.17% supported by the uniformly arranged morphological structure as in Figure 7. According to Figure 6, the trend of EE% started to decrease after 0.1% w/v from 74.17 to 71.11%. Thus, only 0.05% PVA is needed to reach the maximum encapsulation efficiency, 86.17%. The more PVA used, the

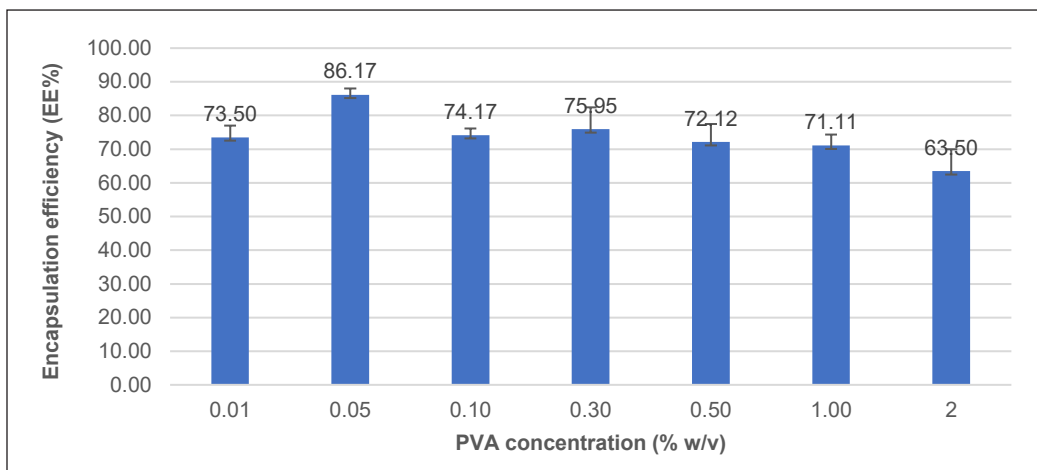


Figure 6. Effect of various PVA concentrations on encapsulation efficiency

higher the viscosity of the microemulsions, resulting in low encapsulation efficiency (Li et al., 2017).

### The Concentration of the Chitosan-PCL Blend

The concentration of the chitosan-PCL blend is an additional parameter that determines the amount of the carrier (chitosan-PCL blend) required for optimal encapsulations. The amount of AI extracts used was 0.2% concentration and kept constant for this

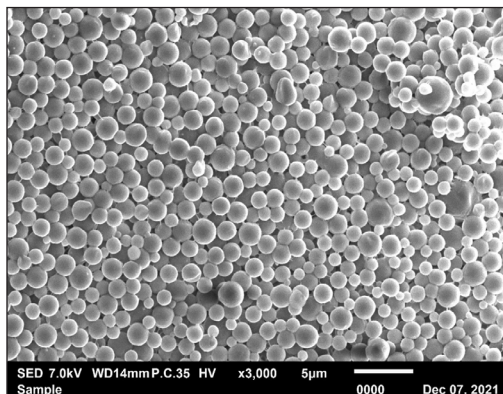


Figure 7. SEM image for 0.05% PVA

study. The polymer matrix concentration study was limited according to the maximum concentration of chitosan that reaches the gelation point when dissolved in 0.2% v/v acetic acid glacial. Figure 8 shows that the maximum Chitosan-PCL blend concentration was obtained at a concentration of 1.0%, which resulted in 92.33% of EE—beyond 1% polymer concentration, which resulted in a decrease in EE. This trend of EE% was also observed by Iqbal et al. (2015) and El Hady et al. (2019). It was due to the viscosity of the polymer that caused the AI extract entrapment to become less efficient. The increase in polymer concentration also increased the thickness of the polymer matrix.

### Response Surface Methodology

Table 7 shows ANOVA analysis for three factors, which are chitosan:PCL, PVA concentration, and polymer matrix concentration. The analysis shows that the model

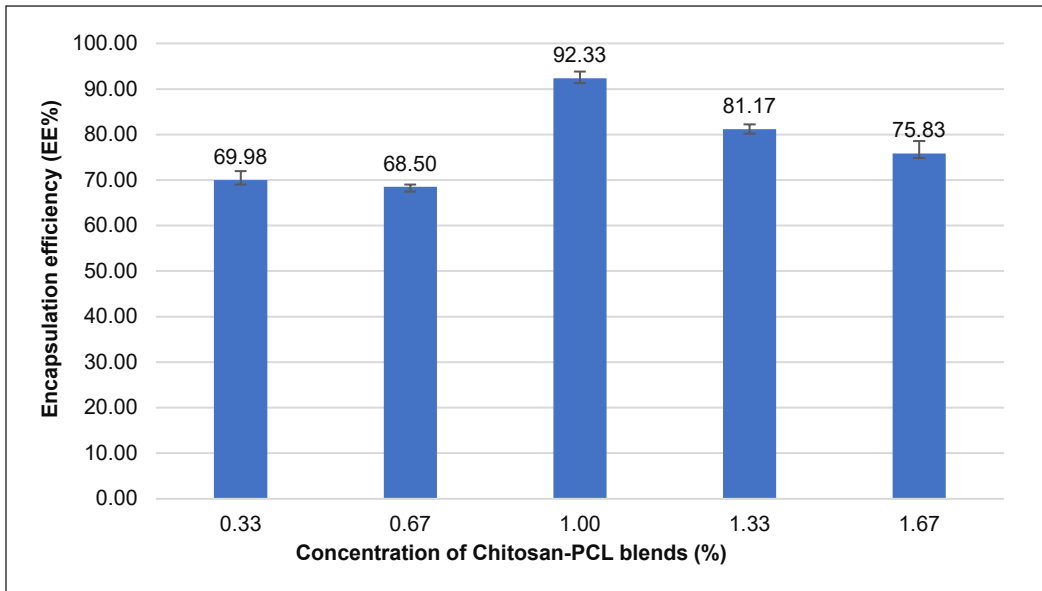


Figure 8. Concentration of Chitosan-PCL blends

Table 7  
The analysis of variance for the encapsulation efficiency

Source	Sum of Squares	df	Mean Square	F-value	p-value	Remark
Model	$5.562 \times 10^{11}$	8	$6.952 \times 10^{10}$	14.25	0.0006	significant
A-Chitosan (n) :PCL (10-n) ratio	$1.935 \times 10^{11}$	1	$1.935 \times 10^{11}$	39.66	0.0002	
B-PVA concentration	$8.209 \times 10^9$	1	$8.209 \times 10^9$	1.68	0.2308	
C- Concentration of Chitosan-PCL blends	$2.259 \times 10^{11}$	1	$2.259 \times 10^{11}$	46.31	0.0001	
AC	$2.973 \times 10^{10}$	1	$2.973 \times 10^{10}$	6.09	0.0388	
BC	$3.241 \times 10^9$	1	$3.241 \times 10^9$	0.6643	0.4386	
A <sup>2</sup>	$3.100 \times 10^9$	1	$3.100 \times 10^8$	0.0635	0.8074	
B <sup>2</sup>	$3.314 \times 10^{10}$	1	$3.314 \times 10^{10}$	6.79	0.0313	
C <sup>2</sup>	$7.568 \times 10^9$	1	$7.568 \times 10^9$	1.55	0.2482	
Residual	$3.903 \times 10^{10}$	8	$4.879 \times 10^9$			
Lack of Fit	$2.72 \times 10^{10}$	6	$4.536 \times 10^9$	0.7676	0.6611	not significant
Pure Error	$1.182 \times 10^{10}$					
Cor Total	$5.952 \times 10^{11}$					
R <sup>2</sup>	0.9344					
Adjusted R <sup>2</sup>	0.86890					
Predicted R <sup>2</sup>	0.7105					
Adeq. Precision	13.0331					
Std. Dev	69848.92					
Mean	$4.874 \times 10^5$					

*F*-value is 14.25, which implies that the model was significant, determined by a *p*-value <0.001. The regression coefficient (*R*<sup>2</sup>) recorded was higher than 0.9, which is 0.9344, indicating that the experimental data was relatively strong. The difference between the adjusted coefficient of determination (*R*<sup>2</sup>) and predicted *R*<sup>2</sup> was less than 0.2, considered reasonable agreement. The lack of fit was reported as not significant, meaning that the polynomial model fitted well and was statistically accurate (Li et al., 2017).

The 3D contour plot graphs predicted the interaction between the parameters, as shown in Figures 9 and 10. This study revealed difficulties finding the optimum conditions as the contour lines raised continuously and the shape became slightly sharp. It could be due to some limitations of the ultrasonic homogenization device contributing to external factors such as the condition of the microtips of ultrasonic homogenizer getting less efficient after many times usage. Another external factor is the temperature of the solutions during the encapsulation process. The heat dissipated during homogenization may lead to dichloromethane evaporation and decreased volume of the reacted solution (Taurozzi et al., 2012).

Figure 10 shows the linear interaction between the chitosan: PCL ratio and the polymer matrix concentration. As one increased the ratio of the chitosan:PCL, the EE% kept increasing, and while the polymer matrix concentration increased, the EE% decreased. As the concentration of the polymer matrix increased, the concentration of chitosan and PCL also increased while the ratio was maintained. This case happened due to the increasing concentration of chitosan, increasing the viscosity and hindering the ultrasonic homogenizer from breaking apart the chitosan molecules to form encapsulation (Taha et al., 2020). Figure 10 shows the relationship between PVA concentration and the concentration of the

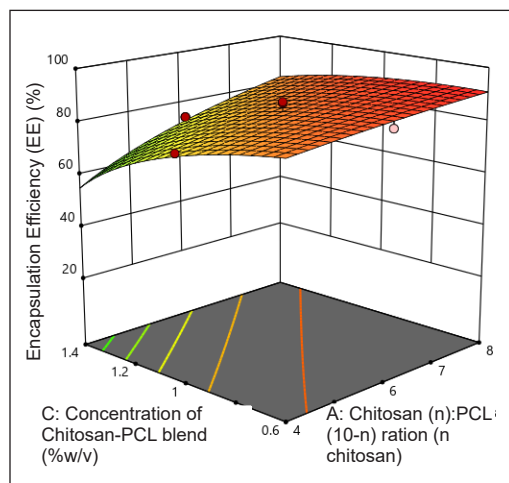


Figure 9. AC: The 3D model surface relationship between the ratio of chitosan:PCL and Polymer matrix concentration

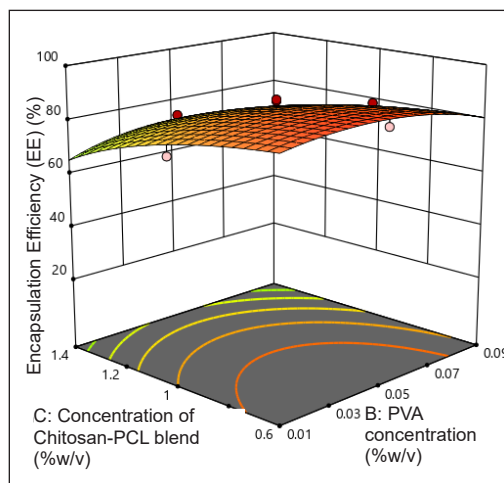


Figure 10. BC: 3D model surface relationship between PVA concentration and concentration of Chitosan-PCL blend



chitosan-PCL blend. The EE% started to increase and decrease as the polymer matrix and PVA concentration increased. In this case, only a small amount of PVA is needed to form a good encapsulation.

Next, based on this model, the second-order polynomial equation of the encapsulation efficiency was fitted into the coded Equation 2. The following equation obtained represents the quantitative effects of three factors on the encapsulation efficiency (EE%).

$$Y = 5.904 \times 10^5 + 1.391 \times 10^5 \times A - 28650.51 \times B - 1.503 \times 10^5 \times C + 60960.18 \times AC + 20128.31 \times BC - 10755.73 \times B^2 - 53148.54 \times C^2 \quad [2]$$

### Model Validation

Validation has been done to determine the validity of the hypothesized model, and the details are tabulated in Table 8. The formulations with high and low EE% were chosen as used for the next analysis. It was found that the difference between the predicted value from DOE and the experimental value was not much different and reasonable. The experimental values revealed that the prediction of DOE was acceptable. The highest EE% recorded was beyond the expectation, which is 98.7%, as compared to the predicted 91.30%, and the error was 7.5%. However, the lowest EE% prediction value was recorded. The experimental value was within the predicted range, and the error was 1.2%, which is acceptable.

Table 8  
*Validation test of the model*

Run	Factors			Encapsulation efficiency (EE %)		Error (%)
	Chitosan (n):PCL (10-n) ratio	PVA concentration	Concentration of Chitosan-PCL blends	Predicted value from DOE	Experimental value	
1	8	0.042	0.648	91.30	98.70	7.5
39	5.216	0.052	0.6	86.75	87.80	1.2

### Characterization

**Structural Properties by FTIR.** The spectra graph of the encapsulated Chitosan-PCL loaded AI extract, the encapsulated Chitosan-PCL blank, PVA, PCL, chitosan and AI extract were obtained and compared as in Figure 11.

The Chitosan parent chain is known to have an amino glucose structure linked with an amide linkage. Due to the presence of two strong functional groups, chitosan was capable of being modified to improve the limitations of chitosan. The two important functional groups are two hydroxyl groups and one primary amine group. Under the IR spectrum, the chitosan in powder form was tested, and a broad peak between 2940–2860 cm<sup>-1</sup> was exposed. The chitosan spectra can be detected due to the existence of amide I and amide II. Amide I was detected at 1650 cm<sup>-1</sup> associated with C=O stretching vibration. Amide II

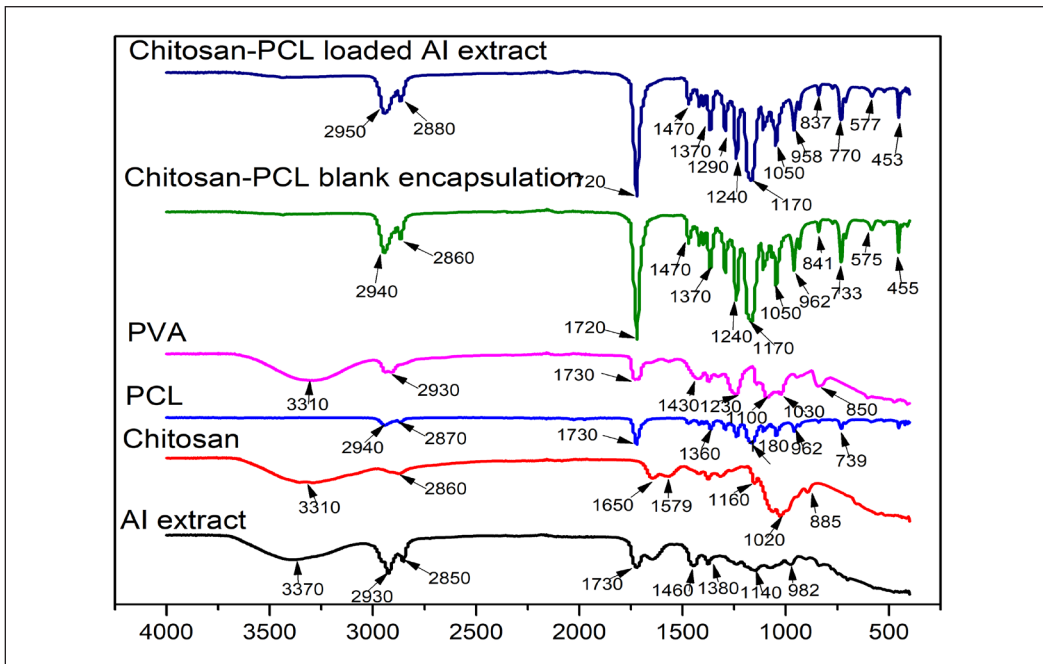


Figure 11. FTIR spectra for AI extract, chitosan, PCL, PVA, chitosan-PCL blank encapsulation and chitosan-PCL loaded AI extracts

was detected at  $1579\text{ cm}^{-1}$ , which is associated with and recognizable by N-H stretching. The C-H stretching was detected at  $2860\text{ cm}^{-1}$ . The  $\beta$ -linked glycosidic bond was detected at  $885\text{ cm}^{-1}$ .  $1020\text{ cm}^{-1}$  indicated the absorbance of O bridge stretching of glucosamine residue present. The characteristics of PCL were detected from the peak at  $2940\text{ cm}^{-1}$ , which is the asymmetric vibration stretching for the  $-\text{CH}_3$  group, and  $2870\text{ cm}^{-1}$ , which is the  $-\text{CH}_2$  (methylene) stretching. The stretching on  $1730\text{ cm}^{-1}$  indicated the  $\text{C}=\text{O}$  (ketone). The band stretching at  $1360\text{ cm}^{-1}$  indicated the presence of the C-O-C group, followed by more vibration bands by asymmetric stretching at  $1180$ ,  $962$ , and  $739\text{ cm}^{-1}$ .

The interaction of the polymer compositions showed characteristic bands at  $2950\text{--}2880\text{ cm}^{-1}$  (C-H stretching); the spectra in PCL were switched from  $1730$  to  $1720\text{ cm}^{-1}$ , which indicated ketone and several inorganic ions from  $1370\text{--}453\text{ cm}^{-1}$ , in which the similar bands existed in the single ingredients. Ultimately, similar findings were reported by Almeida et al. (2018). The encapsulation of AI extracts was successful through the presence of characteristic bands of chitosan, PCL, and the AI extracts. On the IR spectrum of chitosan-PCL loaded AI extracts, the presence of a sharp peak at  $1470\text{ cm}^{-1}$  indicates the characteristic of Amide II of chitosan. The presence of PCL was detected through the strong characteristic band of ketone at  $1720\text{ cm}^{-1}$ . The characteristic band of AI extracts were expressed at  $1470$  and  $1370\text{ cm}^{-1}$  showing the interactions of AI extracts occurred. Based on the FTIR spectra, the encapsulation of AI extract with chitosan-PCL blend occurred and can be suggested.

**Surface Morphology by Scanning Electron Microscope (SEM).** The SEM images exhibited the formation of spherical shapes with smooth surfaces for the sample with the highest EE% (98.70%) in Figure 12(a) and less polydisperse. In Figure 12(b), the surface morphology of the encapsulation with lower EE% (87.80%) also showed a spherical shape.

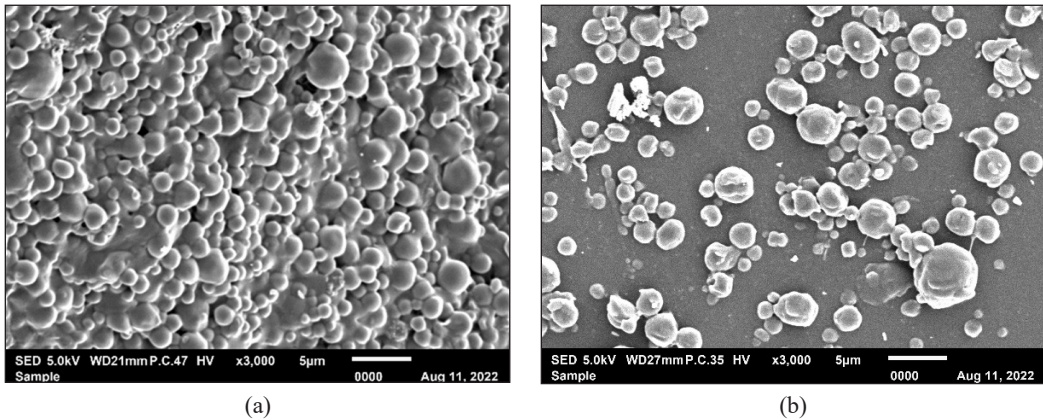


Figure 12. SEM image for chitosan-PCL loaded AI extract with (a) EE 98.70% and (b) 87.80%

**Zeta Potential and Particle Size Analysis.** Table 9 summarizes the findings on the effects of zeta potential and particle size on the EE% of the AI extract microencapsulations. In this study, the values of zeta potential were negative due to the adsorption of the surfactant on the surface of the microparticles (Abriata et al., 2019). Interestingly, most encapsulations of plant extracts studies reported found in agreement with the negative value of zeta potential obtained from this study. In 2020, the encapsulation of *Boswellia carterii* essential oil by Barre et al. (2020) found that the zeta potential was -25 to -36 mV. In 2021, the encapsulation of phenolic bioactive compounds found the zeta potential was -30 to -44 mV (Xue et al., 2021).

This result was an improvement from the previous AI extracts encapsulation study reported by Amarnath et al. (2014) and Muhaimin et al. (2020), in which the zeta potential obtained was -3.47 mV.

The high EE% was obtained from the small size of particles. The small particle size may entrap more active ingredients of AI extract, thus giving a higher EE%. The smaller

Table 9  
The zeta potential and particle size for the optimized samples

Sample validation number	Encapsulation efficiency (EE%)	Zeta potential (mV)	Particle size ( $\mu\text{m}$ )
1	98.70	-24.0	$2.631 \pm 0.14$
39	87.80	-26.2	$3.568 \pm 1.35$

size also led to the microparticles being absorbed and the active ingredients being released to the targeted parts. The particle size obtained was similar to that obtained by Amarnath et al. (2014), which encapsulated the AI extract with chitosan-casein, which was 2 $\mu$ m. Another encapsulation study of *M. gigantea* leave extracts obtained 3.6–5.9  $\mu$ m in size (Muhaimin et al., 2020).

## CONCLUSION

In conclusion, 5 minutes of the best homogenization duration has resulted in the highest encapsulation efficiency (74.5%). The other three parameters, the 0.6:0.4 ratio of Chitosan:PCL concentration was 70.10%, 0.05% concentration of PVA giving 86.17%, and the 1% concentration of Chitosan-PCL blend was 92.33% have successfully found the optimized value. The values for the parameter interaction studies were obtained by applying the central composite design (CCD) using Design-Expert v.12 software. In the validation process, the highest EE% obtained was 98.70%, and the lowest EE% was 87.80%. Surface morphology showed the spherical shape of microparticles. The zeta potential for both higher EE% and lower EE% microencapsulations resulted in a small difference. Overall, the encapsulation of *Acalypha indica* (AI) extracts has been successfully done using chitosan-PCL copolymer blends by emulsion-solvent evaporation. This research has a high potential to explore the usage of AI in pharmaceutical applications.

## ACKNOWLEDGEMENTS

This work was financially supported by a Collaborative Research grant (CRG) from Universiti Teknologi Malaysia (UTM) (Q.J130000.2451.08g10) and the University of Technology Malaysia (UTM) Fundamental Research Grant (Q.J130000.3846.22H56). The author thanks Kulliyyah of Engineering, International Islamic University Malaysia (IIUM), for providing the laboratory facilities.

## REFERENCES

- Abriata, J. P., Turatti, R. C., Luiz, M. T., Raspantini, G. L., Tofani, L. B., do Amaral, R. L. F., Swiech, K., Marcato, P. D., & Marchetti, J. M. (2019). Development, characterization and biological *in vitro* assays of paclitaxel-loaded PCL polymeric nanoparticles. *Materials Science and Engineering C*, *96*, 347-355. <https://doi.org/10.1016/j.msec.2018.11.035>
- Adepu, S., & Ramakrishna, S. (2021). Controlled drug delivery systems: Current status and future directions. *Molecules*, *26*(19), Article 5905. <https://doi.org/10.3390/molecules26195905>
- Amarnath, K., Dhanabal, J., Agarwal, I., & Seshadry, S. (2014). Cytotoxicity induction by ethanolic extract of *Acalypha indica* loaded casein-chitosan microparticles in human prostate cancer cell line *in vitro*. *Biomedicine and Preventive Nutrition*, *4*(3), 445-450. <https://doi.org/10.1016/j.bionut.2013.03.009>

- Barre, M. S., Ali, F. B., Mirghani, M. E. S., Hazri, N. F., Anuar, H., & Nasir, N. A. M. (2020). Potential food additive of *Boswellia carterii* essential oil encapsulated within gum arabic: A particle size distribution and zeta potential analysis. *Food Research*, 4, 19-23. [https://doi.org/10.26656/fr.2017.4\(S2\).339](https://doi.org/10.26656/fr.2017.4(S2).339)
- Bazana, M. T., Codevilla, C. F., & de Menezes, C. R. (2019). Nanoencapsulation of bioactive compounds: Challenges and perspectives. *Current Opinion in Food Science*, 26, 47-56. <https://doi.org/10.1016/j.cofs.2019.03.005>
- Christen, M. O., & Vercesi, F. (2020). Polycaprolactone: How a well-known and futuristic polymer has become an innovative collagen-stimulator in esthetics. *Clinical, Cosmetic and Investigational Dermatology*, 13, 31-48. <https://doi.org/10.2147/CCID.S229054>
- El Hady, W. E. A., Mohamed, E. A., El-Aazeem S. O. A., & El-Sabbagh, H. M. (2019). *In vitro-in vivo* evaluation of chitosan-PLGA nanoparticles for potentiated gastric retention and anti-ulcer activity of diosmin. *International Journal of Nanomedicine*, 14, 7191-7213. <https://doi.org/10.2147/IJN.S213836>
- Iqbal, M., Valour, J. P., Fessi, H., & Elaissari, A. (2015). Preparation of biodegradable PCL particles via double emulsion evaporation method using ultrasound technique. *Colloid and Polymer Science*, 293(3), 861-873. <https://doi.org/10.1007/s00396-014-3464-9>
- Leong, T. S. H., Martin, G. J. O., & Ashokkumar, M. (2017). Ultrasonic encapsulation - A review. *Ultrasonics Sonochemistry*, 35, 605-614. <https://doi.org/10.1016/j.ultsonch.2016.03.017>
- Leong, T. S. H., Wooster, T. J., Kentish, S. E., & Ashokkumar, M. (2009). Minimising oil droplet size using ultrasonic emulsification. *Ultrasonics Sonochemistry*, 16(6), 721-727. <https://doi.org/10.1016/J.ULTSONCH.2009.02.008>
- Li, X., Wang, L., & Wang, B. (2017). Optimization of encapsulation efficiency and average particle size of *Hohenbuehelia serotina* polysaccharides nanoemulsions using response surface methodology. *Food Chemistry*, 229, 479-486. <https://doi.org/10.1016/j.foodchem.2017.02.051>
- Muhaimin, M., Yusnaidar, Y., Syahri, W., Latief, M., & Chaerunisaa, A. Y. (2020). Microencapsulation of *Macaranga gigantea* leaf extracts: Production and characterization. *Pharmacognosy Journal*, 12(4), 716-724. <https://doi.org/10.5530/pj.2020.12.104>
- Rivas, J. C., Cabral, L. M. C., & Rocha-Leão, M. H. (2019). Stability of bioactive compounds of microencapsulated mango and passion fruit mixed pulp. *International Journal of Fruit Science*, 20(S2), S94-S110. <https://doi.org/10.1080/15538362.2019.1707746>
- Roy, S. M., & Sahoo, S. K. (2016). Controlled drug delivery: Polymeric Biomaterials for. *Encyclopedia of Biomedical Polymers and Polymeric Biomaterials*, 11, 2135-2146. <https://doi.org/10.1081/e-ebpp-120050023>
- Szymańska, E., & Winnicka, K. (2015). Stability of chitosan - A challenge for pharmaceutical and biomedical applications. *Marine Drugs*, 13(4), 1819-1846. <https://doi.org/10.3390/md13041819>
- Taha, A., Ahmed, E., Ismaiel, A., Ashokkumar, M., Xu, X., Pan, S., & Hu, H. (2020). Ultrasonic emulsification: An overview on the preparation of different emulsifiers-stabilized emulsions. *Trends in Food Science and Technology*, 105, 363-377. <https://doi.org/10.1016/j.tifs.2020.09.024>

- Taurozzi, J. S., Hackley, V. A., & Wiesner, M. R. (2012). *Preparation of Nanoparticle Dispersions from Powdered Material using Ultrasonic Disruption*. U.S. Department of Commerce. <http://dx.doi.org/10.6028/NIST.SP.1200-2>
- Xue, J., Luo, Y., Balasubramanian, B., Upadhyay, A., Li, Z., & Luo, Y. (2021). Development of novel biopolymer-based dendritic nanocomplexes for encapsulation of phenolic bioactive compounds: A proof-of-concept study. *Food Hydrocolloids*, *120*, Article 106987. <https://doi.org/10.1016/j.foodhyd.2021.106987>
- Yusuf, A., Almotairy, A. R. Z., Henidi, H., Alshehri, O. Y., & Aldughaim, M. S. (2023). Nanoparticles as drug delivery systems: A review of the implication of nanoparticles' physicochemical properties on responses in biological systems. *Polymers*, *15*(7), Article 1596. <https://doi.org/10.3390/polym15071596>

## Utilization of Aluminum Dross as a Cement Replacement Material for Sustainable Concrete Development

Nur Hidayah Mohd Zahari<sup>1</sup>, Ali Salmiaton<sup>1\*</sup>, Shafreeza Sobri<sup>1</sup>, Noor Azline Mohd Nasir<sup>2</sup> and Nor Shafizah Ishak<sup>3</sup>

<sup>1</sup>Department of Chemical and Environmental Engineering, Faculty of Engineering, Universiti Putra Malaysia, 43400 UPM, Serdang, Selangor, Malaysia

<sup>2</sup>Department of Civil Engineering, Faculty of Engineering, Universiti Putra Malaysia, 43400 UPM, Serdang, Selangor, Malaysia

<sup>3</sup>Catarim Sdn Bhd, Putra Science Park (PSP), Universiti Putra Malaysia, 43400 UPM, Serdang, Selangor, Malaysia

### ABSTRACT

The recovery of aluminum from aluminum dross waste involves intensive cost and energy. Therefore, there is a need for its utilization as an engineering material by using it as a filler material in concrete production. The cement industry is battling numerous difficulties due to the shortage of raw materials and sustainability issues related to the emission of CO<sub>2</sub> into the atmosphere. On this basis, the present study aims to utilize aluminum dross as a replacement material for cement to develop sustainable concrete. In this study, the results of control concrete samples were compared to the results of concrete samples containing aluminum dross by 5%, 10%, and 15% by weight of cement. The mechanical and chemical analysis of the M40 grade concrete employing aluminum dross as a replacement material in cement was analyzed. It was noticed that the best percentage of aluminum dross was 10%, providing better results compared with conventional concrete. It recorded the highest strength of 41.3MPa. Thermogravimetric analysis was conducted in which weight loss,

decomposition of hydration compounds, and percentage of calcium hydroxide from concrete were determined. Scanning electron microscopy analysis showed that the density of concrete increased owing to the presence of ettringite needles and calcium silicate hydrate in the matrix. Moreover, the toxicity analysis revealed that the ammonia content and the leachability of trace elements from the concrete were both low and within

### ARTICLE INFO

#### Article history:

Received: 26 February 2023

Accepted: 17 August 2023

Published: 14 March 2024

DOI: <https://doi.org/10.47836/pjst.32.2.15>

#### E-mail addresses:

gs60006@student.upm.edu.my (Nur Hidayah Mohd Zahari)

mie@upm.edu.my (Salmiaton Ali)

shafreeza@upm.edu.my (Shafreeza Sobri)

nazline@upm.edu.my (Noor Azline Mohd Nasir)

norshafizah@gmail.com (Nor Shafizah Ishak)

\* Corresponding author

acceptable ranges. The findings indicate that aluminum dross has positive results as an additional cementitious material in concrete to overcome environmental problems related to dross management and reduce cement utilization, producing more sustainable concrete.

*Keywords:* Aluminum dross, industrial waste, sustainability, toxicity analysis

---

## INTRODUCTION

Concrete is the most widely used substance on Earth that will continue to be in demand for a very long time. However, concrete is also one of the most powerful factors that contribute to global warming. Annually, the estimated amount of cement needed is around 50% to produce almost 11 billion tonnes of concrete (Imbabi et al., 2012). Cement manufacture makes concrete a heavy pollutant as it emits CO<sub>2</sub> into the atmosphere, leading to global warming (Bakhtyar et al., 2017). Naqi and Jang (2019) reported that around 90% of CO<sub>2</sub> is emitted from one ton of cement manufactured. Annually, cement production is estimated at 3.5 billion tonnes, releasing almost 3 billion tonnes of CO<sub>2</sub>. Hence, between five and seven percent of all CO<sub>2</sub> emissions are caused by the cement industry.

Subsequently, an alternative must be initiated to replace cement partially or fully with ecologically cementitious materials to control the construction costs and mitigate the environmental impact. In the last few decades, waste production and the exhaustion of natural sources have become issues in the industrial sector (Mahinroosta & Allahverdi, 2018). For the protection of the environment, the substitution of alternative building materials in concrete technology is a must. Due to the rise of worldwide awareness in the environmental sector, the utilization and recycling of industrial wastes in concrete technology have been increasing rapidly daily.

Recent studies found that various pozzolanic materials are combined with cement to produce prime concrete for its strength and durability. According to Walker and Pavía (2011), pozzolan is specifically described as a material containing a silicious or silicious and aluminous content that chemically reacts with calcium hydroxide to form hydration compounds when mixed with water. Generally, pozzolanic materials are derived from industrial waste, including rice husk ash, quarry dust, silica fume, fly ash, rice husk ash, slag cement, aluminum dross, and other materials (Elseknidy et al., 2020). Waste materials such as cement replacements have become gradually treasured in concrete production. In short, industrial waste can be replaced as a building material in concrete production.

Industrial waste, such as aluminum dross (AD), is a remarkably responsive pozzolanic material that can be added to concrete production. Remarkably, alumina and silica are the main elements of aluminum dross, which are necessary for pozzolan characteristics (Nirmale & Bhusare, 2018). Utilizing aluminum dross in concrete is a good option as it increases the workability of the concrete.



Several studies have examined the potential usage of aluminum dross in the construction industry. Panditharadhya et al. (2018) used secondary aluminum dross as a binding agent in concrete production. Initially, cement was substituted with 5%, 10%, 15%, and 20% of aluminum dross by weight of the cement, and the ideal dosage was determined to be 15%. This research observed that aluminum dross accelerated the final setting time, making it fit for hot weather conditions. The mechanical properties also improved with the optimum dosage of aluminum dross in concrete.

Soós et al. (2017) utilized aluminum dross as asphalt filler. Typically, manufacturers only used limestone as a filler in the asphalt industry. There were three trial mixes in this study: (1) Mix A (100% dross), (2) Mix B (100% limestone), and (3) Mix C (50% dross). Based on this work, Mix C, which contained 50% dross, was determined to be a potential percentage in asphalt filler as this ratio of dross produces a stiffer mix in all temperature ranges.

Dirisu et al. (2021) investigated the manufacture of silicate composites containing aluminum dross to construct ceilings. Thirty percent aluminum dross by weight of cement was found to be a suitable thermal insulator needed in building ceilings as it achieved the highest specific heat capacity with a low value of heat flux. Aluminum dross also improved its mechanical properties due to the presence of ferrous and non-ferrous metals, which developed stronger bonds in the composite.

Over the years, there was a generation of waste called dross in aluminum refining industries. Meshram and Singh (2018) stated that this kind of waste has leachable salts like KCl, so the direct disposal of such waste would be an environment issue. Most aluminum dross is disposed of in landfill sites. The disposal of aluminum dross into landfills will cause the toxic metal ions to leach into the ground, contaminating the groundwater (Zauzi et al., 2016). Sultana et al. (2013) reported that approximately 1.5% to 2.5% of dross is generated for each metric ton of molten aluminum. Consequently, recycling the aluminum dross and developing an engineered product can be practical ways to reduce sustainability problems.

## **MATERIALS AND METHOD**

### **Material Properties**

The American Society for Testing and Materials (ASTM) procedures were used throughout the study to denote the properties of materials.

For this study, cement pastes were prepared by consuming grade CEM I 52.5N ordinary Portland cement (OPC) according to BS EN 196-1 (2005). This cement grade, which contained a specific gravity of 3.20 and a bulk density of 1440 kg/m<sup>3</sup>, is equivalent to ASTM Type 1 cement.

X-Ray Fluorescence, EDX 1400, determined the quantitative measurement of chemical oxide compositions in cement and aluminum dross. The metal oxide and chemical oxide composition of the cement and aluminum dross are presented in Table 1. Portland cement

had a lower specific gravity than aluminum dross, yet the difference between the two was not significant due to the denser elements in aluminum dross, like aluminum and magnesium.

Ordinary Portland Cement (OPC) has a variety of proportions. The main constituents of cement are calcium oxide, silica, aluminum oxide, and iron oxide. Each element plays a different role in concrete development. For instance, calcium oxide (CaO), known as lime, is the major ingredient in cement manufacturing. Lime imparts strength and soundness to the cement. Kandhan and Karunakaran (2021) reported that up to 25% of lime replacement in cement can enhance the compressive strength of concrete at an early age. On the other hand, the second largest element in cement is silica (SiO<sub>2</sub>). Silica strengthens concrete by making it denser via increasing dry density and lessening porosity (Pattinaja & Tjahjani, 2015). Furthermore, aluminum oxide (Al<sub>2</sub>O<sub>3</sub>) acts as the cement’s basis, accelerating the cement’s hydration reaction. Al<sub>2</sub>O<sub>3</sub> is a nano-sized particle that serves as the filler material in the concrete matrix, influencing the microstructural properties of cement to become denser, resulting in decreased porosity and increased strength (Zhou et al., 2019; Meddah et al., 2020). Additionally, iron oxide (Fe<sub>2</sub>O<sub>3</sub>) gives color to concrete specimens. Iron oxide pigments meet the standard provided by the ASTM C 979 (American Society of Testing Materials c-979-99, 2015).

Cenviro Sdn Bhd, Port Dickson, Negeri Sembilan provided the aluminum dross used in this project. The sample was in fine powder form, blackish in color, with small aluminum pieces. The bulk density and specific gravity of aluminum dross were 774 kg/m<sup>3</sup> and 3.40, respectively. Referring to Table 1, the average particle size distribution of aluminum dross

Table 1  
Chemical oxide composition of cement and aluminum dross by XRF analysis

Metal oxide	Chemical oxide Composition (%)	
	Ordinary Portland Cement	Aluminum Dross
Aluminum oxide (Al <sub>2</sub> O <sub>3</sub> )	6	82.8
Calcium oxide (CaO)	62.5	2.8
Iron (III) oxide (Fe <sub>2</sub> O <sub>3</sub> )	3.9	2.6
Magnesium oxide (MgO)	0.9	0.5
Silicon dioxide (SiO <sub>2</sub> )	22.5	6.4
Zinc oxide (ZnO)	0	0.32
Sulfur trioxide (SO <sub>3</sub> )	1.75	0
Loss of Ignition	1.5	2.7
Others	0.95	0.88
Physical parameters		
Density (kg/m <sup>3</sup> )	1440	774
Specific gravity	3.20	3.40
Average particle size distribution d <sub>50</sub> (µm)	7.20	15.6

Note. The remaining 0.88% of aluminum dross composition is attributed to traces of TiO<sub>2</sub>, N<sub>2</sub>O, PbO, Br and P. TiO<sub>2</sub>, Na<sub>2</sub>O, K<sub>2</sub>O, and N<sub>2</sub>O existed in traces in the cement composition with 0.95%

is higher than cement due to the particle size where aluminum dross contains rougher particles. In concrete technology, the distribution of the particle size is crucial. The size of particles directly influences the hydration, setting, and hardening, strength, and heat of hydration (Udvardi et al., 2019).

### Pretreatment of Aluminum Dross

The aluminum dross was treated prior to being used in concrete production. The most effective method to remove any potential oxide generation and toxic gas formation from an aluminum dross sample is simply washing it with water (Panditharadhya et al., 2018). Before the aluminum dross was substituted in concrete, it underwent a pretreatment process by being washed in water with a solid-to-liquid ratio of 1:6. Then, it was sun-dried followed by oven-dried to eliminate water and passed through a sieve of 100  $\mu\text{m}$  before being added into concrete mixture. The sample of aluminum dross is shown in Figure 1.

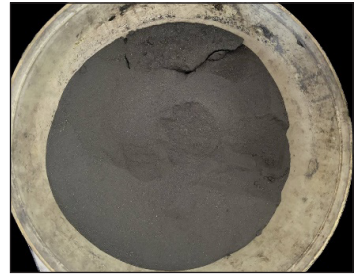


Figure 1. Aluminum dross sample

Both fine and coarse aggregates conforming to BS EN 12620 (2002) were used in this study. Easily reachable river sand, which has a fineness modulus 2.32 and a specific gravity of 2.65, was chosen as the fine aggregate. Crushed granite with a maximum size of 20 mm was used for coarse aggregate. The specific gravity and fineness modulus of coarse aggregate are 2.77 and 8.50, respectively.

Potable water that was free from any malignant substance and had a pH value between 6 and 8, as specified by MS EN 1008 (2010), was used in this research work. The water source was within the Construction Material Laboratory (MCL) of the Department of Civil Engineering, Universiti Putra Malaysia.

### Mix Proportioning of Concrete Materials

In the present work, the concrete mixtures were constructed for M40 grade concrete to achieve a minimum compressive strength of 40 MPa at the end of the curing age of 28 days. M40 is a commercial-grade concrete used in a heavy-duty application. The substructure is one of the applications included where it is constructed under the ground of a building. The building's weight is evenly distributed throughout the substructure and the ground beneath it (Khan, 2015). According to BS EN 1990 (2002), the minimum grade of structural concrete is M20. Based on the literature review, cement has been partially replaced with aluminum dross in the concrete development with a designated compressive strength of up to 35 MPa (Mailar et al., 2016; Galat et al., 2017; Elseknidy et al., 2020; Arpitha & Praveen, 2022). Therefore, this study investigated the characteristics of M40-grade concrete made with different percentages of aluminum dross.

The ratio of water-cement (w/c) at 0.4 was implemented. The slump value was assigned at 100 mm to obtain a good workable concrete. Each trial mix had a different proportion of cement and aluminum dross. All concrete mixtures were added with the same amount of aggregates. The control concrete mixture (C1) was made without substituting any aluminum dross. The experimental work was executed with the replacement values of aluminum dross at 5, 10, and 15% by weight of ordinary Portland Cement (OPC) in the C2, C3, and C4, respectively. These specimens were tested after the 7<sup>th</sup>, 21<sup>st</sup>, and 28<sup>th</sup> days of water curing age to obtain the results in three different conditions. The description of different trial mixes based on the concrete mixing of 1 m<sup>3</sup> concrete proportion is tabulated in Table 2.

Table 2  
Concrete mix proportions of 1 m<sup>3</sup> concrete

Type	Concrete mix	C1	C2	C3	C4
Cementitious materials	% of cement	100	95	90	85
	Cement (kg)	346.0	328.7	311.4	294.1
	% of Aluminum dross	0	5	10	15
	Aluminum dross (kg)	0	17.3	34.6	51.9
Fine aggregate	% of sand	100	100	100	100
	Sand (kg)	646	646	646	646
Coarse aggregate	% of gravel	100	100	100	100
	Gravel (kg)	790	790	790	790
	Water (liters)	138	138	138	138

### Fresh Concrete Properties

A slump test was performed to assess the workability of the concrete mixture, complying with the BS EN 12350-2 (2009). A slump test was done prior to casting the concrete into the molds. The slump cone, which was in the shape of a conical frustum, had a 300 mm height, 200 mm base diameter, and 100 mm upper diameter. Greater workability of concrete can be attained with slump values higher than 100 mm.

### Concrete Strength Properties

In this work, the cube samples of size 100 mm × 100 mm × 100 mm were used to test the compressive strength as per the guidelines of BS EN 12390-3 (2001). The specimen was placed at the center and loaded uniformly until the cube with a capacity of 6.0kN/s failed. The concrete samples were tested on the 7<sup>th</sup>, 21<sup>st</sup>, and 28<sup>th</sup> day of curing age.

The flexural strength test was carried out on the 28<sup>th</sup> day of curing age on concrete beams with a size of 100 mm × 100 mm × 500 mm based on BS EN 12390-5 (2019). A three-point load with a capacity of 0.1kN/s was applied to the concrete beam. The machine

for compression and flexural strength tests was provided in the Construction Material Laboratory (CML) at Universiti Putra Malaysia.

### **Concrete Durability Properties**

The water absorption rate of the concrete samples was observed by using the water absorption tests. The concrete specimens of each mix design with a size of 100 mm x 100 mm x 100 mm were tested as per the provisions of ASTM C 642-06 ( American Society for Testing and Materials, 1997). The samples curing for the 7<sup>th</sup> and 28<sup>th</sup> days were oven-dried for 24 hours before being weighed (W<sub>1</sub>). Then, the samples were immersed in water for 24 hours. The samples were removed from the water tank after 24 hours and dried with a clean, dry towel before being weighed (W<sub>2</sub>). Equation 1 was used to calculate the water absorption rate.

$$\text{Water absorption (\%)} = \frac{W_2 - W_1}{W_1} \times 100 \quad [1]$$

### **Concrete Microstructural Analysis**

This study determined the microstructure analysis through a Scanning Electron Microscope (SEM) conducted at the Material Characterization Laboratory (MCL), Universiti Putra Malaysia. The SEM images of all concrete mixes were analyzed. The morphology analysis was conducted at different magnifications from ×200 to ×40000 using SEM: JSM -5610V, JOEL. The concrete specimens were collected in a small size of 5 mm on the 28<sup>th</sup> day.

### **Concrete Thermogravimetric Analysis**

TGA analysis was carried out to categorize the decomposition of hydration compounds in the concrete. The samples were prepared by manually grounding the concrete using an agate mortar and pestle and sieving through 75 mm (Reddy & Naqash, 2019a; Vogler et al., 2022). At the end of the 28<sup>th</sup> day of curing age, approximately 1 g of sample was stored in a closed plastic bottle from each concrete mix. The analysis was performed using TGA Mettler Toledo at the Thermal Analyzer Laboratory, Faculty of Science, Universiti Putra Malaysia. The experimental setup included a platinum top-opened crucible, an active atmospheric nitrogen gas (40 ml/min), and a heating rate of 10°C/min. Then, the samples were heated at a steady rate at a temperature range of 50°C to 1000°C.

### **Concrete Toxicity Analysis**

The toxicity of ammonia level in aluminum dross was determined during the washing process and curing of concrete by using the salicylate method on the DR 900 colorimeter.

The samples were mixed with the reagent of ammonia salicylate and ammonia cyanurate for a sample that resulted in a dark green color with a reading of more than 50 mg/L of ammonia. Dilution of the sample was conducted.

The Toxicity Characteristic Leaching Procedure (TCLP) was employed to examine the toxic and heavy metals to determine whether aluminum dross concrete was ecologically suitable at 28 days of age of concrete. Initially, the coarse aggregates were removed from the concrete specimen, which was ground to obtain a finely powdered sample that could cross a 1.00 mm sieve. The concrete sample's leachate was produced in accordance with the US Environmental Protection Agency (US EPA). Then, the toxicity analysis of the leachate produced by the treated aluminum dross was performed. Perkin Elmer 2000DV spectrometer was used to conduct an Inductively coupled plasma optical emission spectroscopy (ICPOES) at Material Characterization Laboratory (MCL), Universiti Putra Malaysia, to examine the leachate elements from the finely powdered samples.

## RESULTS AND DISCUSSION

### Concrete Mix

This study incorporated aluminum dross into the concrete mixture, replacing cement. The outer layer surface of the control concrete mix, C1, was quite smooth, which offers better interaction within the matrix, as shown in Figure 2a. However, in Figures 2b, 2c, and 2d, the formation of voids was increased with the higher percentage of aluminum dross incorporation. It can be observed that 15% aluminum dross content in the concrete mix (C4) in Figure 2d showed more voids compared to the concrete mixes C2 and C3. The formation of voids could cause a decline in the concrete strength as the proportion of aluminum dross increased.

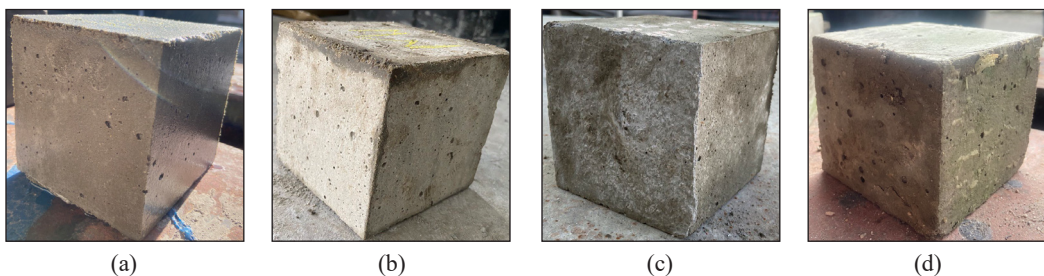


Figure 2. (a) Concrete mix C1; (b) Concrete mix C2 (5% aluminum dross); (c) Concrete mix C3 (10% aluminum dross); and (d) Concrete mix C4 (15% aluminum dross)

### Concrete Fresh Properties

From the results, the concrete mix C3 had the highest slump value with good workability because of aluminum dross at a 10% replacement value. However, the workability

decreased with the increased percentage of aluminum dross in C4. The slump values are summarized in Table 3.

Table 3  
Slump values of concrete mixes

Mix	C1	C2	C3	C4
Slump value (mm)	100	100	113	91

### Concrete Strength Properties

Figure 3 depicts the compressive strength results for all concrete mixtures on the 7<sup>th</sup>, 21<sup>st</sup>, and 28<sup>th</sup> days. Over the curing periods, the concrete mix C3 with 10% aluminum dross had higher compressive strength compared to C2 (5% aluminum dross) and C4 (15% aluminum dross). The increase in compressive strength with age is credited to the continuous formation of hydration products (Odeyemi et al., 2021). The compressive strength of mix C3 is 41.3MPa, which has shown slightly higher strength compared to the control mix C1 at 40MPa, as a basis. Hence, the ideal dosage of aluminum dross was considered at 10%. The pozzolanic action and filler effects of aluminum dross can improve compressive strength in concrete. The higher percentage replacement of aluminum dross in concrete mix C4 lowered the compressive strength. It could be because of the formation of air voids as a result of aggressive reactions and high alumina content.

The average flexural strength of the control mixture, C1, was around 9.87MPa at the end of 28 days of curing age. The flexural strengths of concrete mixes at the 28 days are presented in Figure 4. It was observed that the concrete mixtures C2 (5% aluminum dross) and C4 (15% aluminum dross) had flexural strength approximately 6.4 and 11.3% lower than the control mixture C1. The maximum flexural strength of 10.03MPa was achieved by concrete mix C3 (10% aluminum dross) at the age of 28 days due to the presence of the fined particles of aluminum dross in concrete that can compact the gap, which can strengthen the bond between the concrete component.

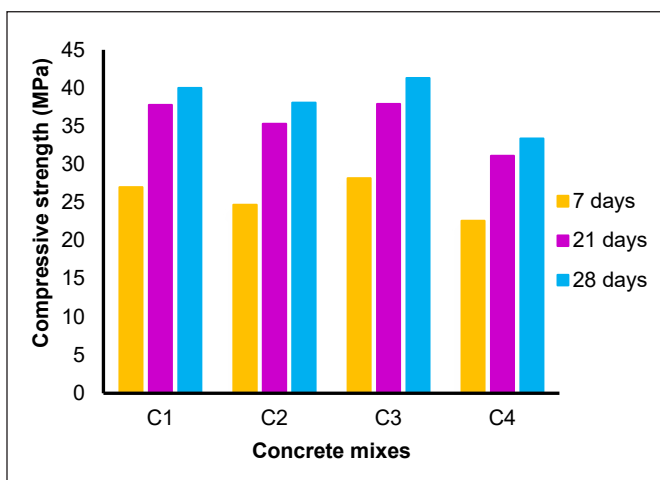


Figure 3. Compressive strength of concrete mixes at 7, 21, and 28 days

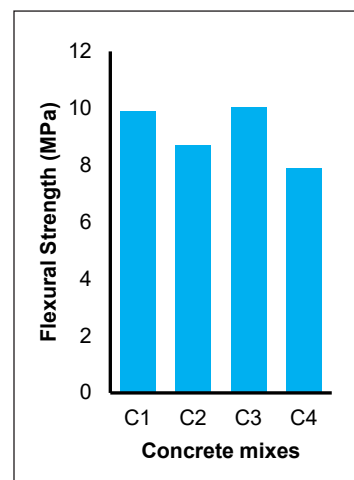


Figure 4. Flexural strength of concrete mixes at 28 days

## Concrete Durability Properties

Curing is the most vital process in concrete production. It serves to avoid premature evaporation of moisture from concrete mixtures, which could reduce the strength of the resulting concrete—specifically, lower absorption results in higher strength because there are fewer voids in the concrete specimen. Hence, the hardened concrete should be submerged in water to cure. The concrete mixes were cured for the durability test for the 7<sup>th</sup> and 28<sup>th</sup> days. Figure 5 shows water absorption rates calculated using Equation 1 on days 7 and 28 of the concrete mixes. As shown in Figure 5, out of all the aluminum dross concrete mixes, C2 (5% aluminum dross) had the lowest water absorption. On the other hand, it was discovered that concrete mix C3 (10% aluminum dross) had nearly the same water absorption as concrete mix C1. The concrete mix, C4 (15% aluminum dross), absorbed more water than the control mix, C1. Javali et al. (2017) mentioned in the report that this action is because of the behavior of aluminum dross that can result in internal micro-blisters in the concrete samples that increase the number of micropores.

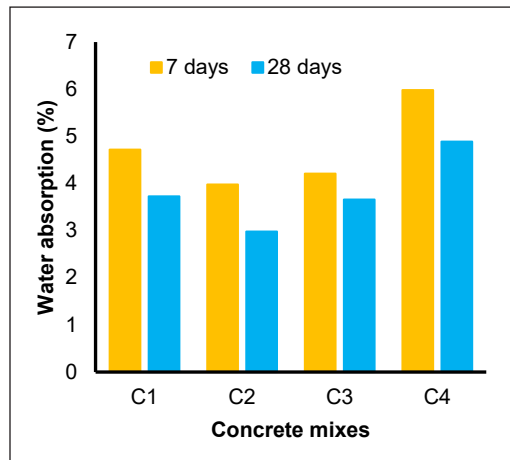


Figure 5. Water Absorption of concrete mixes at 7 and 28 days

## Concrete Microstructural Analysis

Concrete microstructure evolves over time, resulting from the concrete formulation and processes involving mixing, placement, and curing. The SEM images for all concrete mixtures are illustrated in Figure 6. The main hydration product, calcium silicate hydrate (CSH), is visible in the control concrete mix, C1 (Figure 6a). In Figure 6b, C2 is depicted as the asymmetrical shape of unreacted dross, where the SEM image of concrete mix. In Figure 6c of a concrete mix made by 10% aluminum dross (C3 mix), it can be observed that the formation of calcium hydroxide (also known as portlandite) results during the curing process when calcium reacts with water. The aluminum oxide content in aluminum dross chemically reacted with calcium hydroxide to produce hydration compounds (Mailar et al., 2016). The calcium monosulpho-aluminate (ettringite) can also be seen as smaller hexagonal hydrated crystals due to aluminum dross. It was seen that concrete containing aluminum dross has a less permeable surface due to the development of needles (ettringite) in voids compared to control concrete. The concrete with aluminum dross provided slightly higher strength compared to conventional concrete due to the filling activities of aluminum dross in voids. The image in Figure 6d (C4 mix) shows the presence of micro-pores within



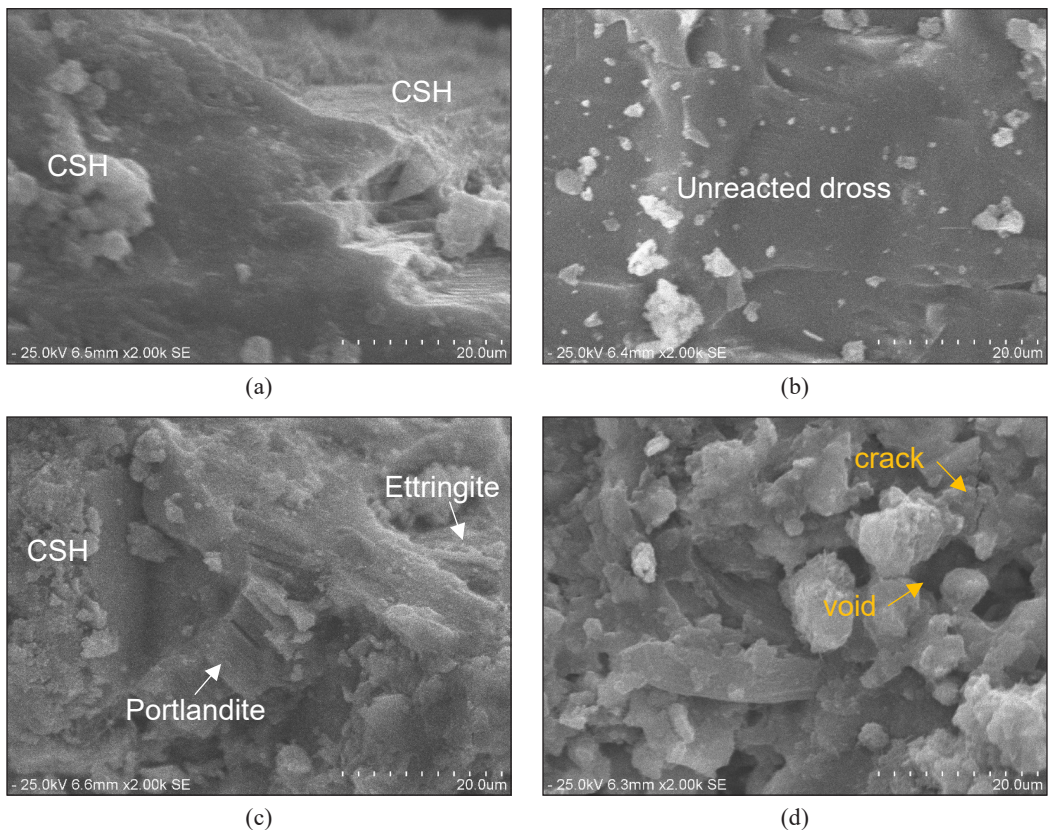


Figure 6. SEM images of concrete mixes: (a) Concrete mix C1; (b) Concrete mix C2 (5% aluminum dross); (c) Concrete mix C3 (10% aluminum dross); and (d) Concrete mix C4 (15% aluminum dross)

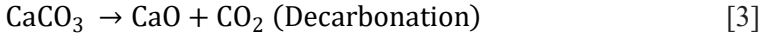
the matrix as well as the formation of micro-cracks caused by internal blisters. The matrix becomes less compact as a result of these cracks.

### Concrete Thermogravimetric Analysis

The TGA results presented in Figure 7 show the decomposition of hydration compounds in temperatures ranging from 50°C to 1000°C, and Figure 8 illustrates the weight loss of concrete mixes with respect to temperature. From Figure 7, the TG curves portray four distinct endothermic outcomes. The first effect was the evaporation of pore water from capillary pores, in the temperature range of 50°C to 100°C (Ukrainczyk et al., 2006). The second endothermic effect was subjected to the dehydration of calcium silicate hydrates and ettringite, which occurred at temperatures between 100°C and 450°C. The third effect, with peak temperature between 400°C and 500°C, was associated with the decomposition of calcium hydroxide formed during hydration, as shown in Equation 2.



In the final endothermic effect, the decarbonization of calcium carbonate in the hydrated compound was indicated at around 800°C, as shown in Equation 3.



The weight difference between the temperature at 100°C and 600°C was used to calculate the total weight loss, which included water loss from other hydrates (Vedalakshmi et al., 2003). The amount of calcium hydroxide was calculated using Equation 4 as a percentage of the weight at 580°C (Reddy & Naqash, 2019b). Calcium hydroxide has a molecular weight of 74, and water has a molecular weight of 18.

$$\text{Calcium hydroxide} = \frac{W_{400} - W_{580}}{W_{580}} \times \frac{74}{18} \times 100 \quad [4]$$

As shown in Figure 9, the percentage of calcium hydroxide was higher in the control mix, C1, compared to concrete mixes, C2, C3, and C4, which contained aluminum dross.

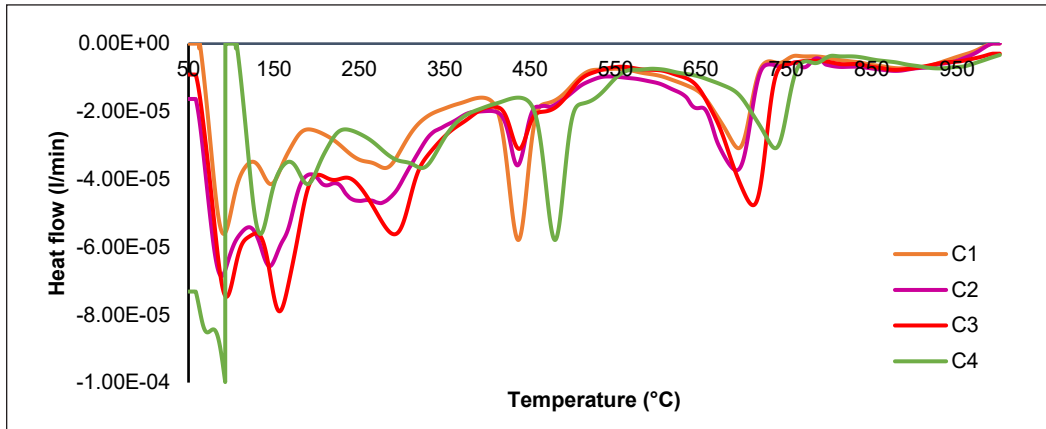


Figure 7. TG curve of concrete mixes

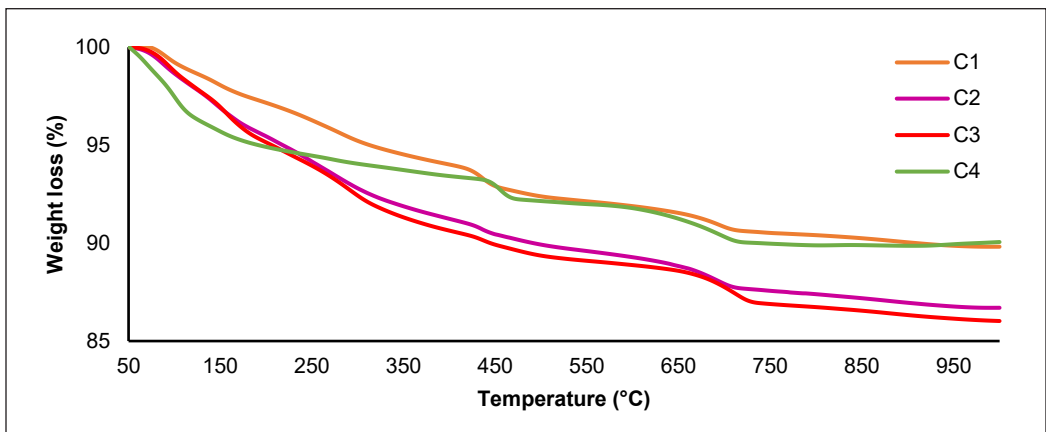


Figure 8. Percentage of weight loss of concrete mixes

In concrete mixes containing aluminum dross, calcium hydroxide was present at a lower percentage due to the pozzolanic reaction in which silicates and aluminates in aluminum dross consumed calcium hydroxide (Retgaddy & Naqash, 2019b). Reddy and Neeraja (2016) reported that aluminum dross decelerated the pozzolanic reaction with the excess calcium hydroxide produced due to the higher specific surface area of aluminum dross particles, in which high water intake is required.

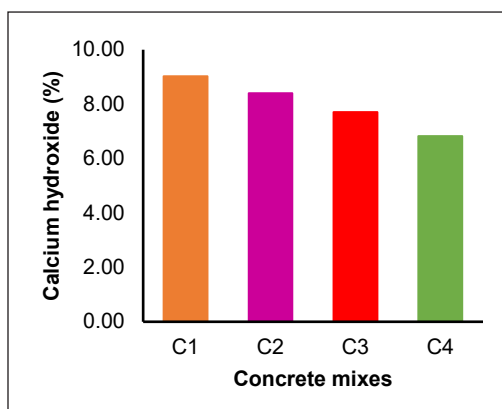


Figure 9. Percentage of calcium hydroxide of concrete mixes

### Concrete Toxicity Analysis

The ammonia level tests were conducted for aluminum dross samples and concrete mixes. Ammonia levels in the concrete mixes were tested at 7 and 28 days of curing age because of the high ammonia content in aluminum dross during the washing process. During the washing process, a pungent smell from the mixture of water and aluminum dross was present, and it turned out to be ammonia gas. A high-speed mixer at 250 rpm and two times water washing were implemented during the pretreatment process to reduce the amount of ammonia in aluminum dross. Table 4 shows the ammonia level in aluminum dross before and after the treatment (water washing) process. The results shown in Table 4 showed that the ammonia content increased up to 30 ppm. As shown in Table 5, the ammonia concentration in the control concrete mixture, C1, was absent.

Meanwhile, for concrete mixtures, C2, C3 and C4 were reduced over the curing period from 7 days to 28 days and within the limits annotated by the Occupational Safety

Table 4  
Concentration of ammonia in aluminum dross

Condition of sample collected	Concentration of ammonia (ppm)
Before treatment	0
After treatment	30

Table 5  
Concentration of ammonia in concrete mixes

Concrete mixes	Concentration of ammonia (ppm)		Regulated limit value (ppm)
	7 days	28 days	
C1	0	0	50
C2	10	3	50
C3	13	5	50
C4	19	7	50

Note. The legalized level refers to the limit stipulated by OSHA PEL

and Health Administration Permissible Exposure Limits (OSHA PEL). A higher aluminum dross incorporation value depicts higher ammonia concentration release. This correlation can be related to the morphological study of concrete. As can be observed from Figure 6d, namely the concrete mixture C4, there was a formation of microcracks and a gap between the concrete matrixes. The diffusion of ammonia gas from the concrete will render it more porous, affecting its strength (El-Aziz & Sufe, 2013).

The amount of minor to major components detected in the leachate samples of aluminum dross and concrete mixes at the end of 28 days of curing age were identified using Inductively coupled plasma optical emission spectroscopy (ICP-OES), Perkin Elmer 2000DV spectrometer. Table 6 illustrates the numerous elements found using the ICP-OES analysis at the wavelength of 90 ppm. Heavy elements in aluminum dross and concrete mixes included aluminum, arsenic, chromium, copper, nickel, and zinc. In the aluminum dross leachate sample, the concentration of the above elements (except for arsenic) was found to be within the limits prescribed by the Waste Acceptance Criteria (WAC) and the United States Environmental Protection Agency (EPA). Aluminum dross from aluminum manufacturing is recovered via a hydrometallurgical process that includes acid leaching to recover metals (Kudyba et al., 2021). Therefore, the leachate concentration in aluminum dross is higher than the leachate of concrete mixes.

It was observed that in almost all concrete mixes, including control mix C1, the heavy metal concentration was very minimal and within the limits. Concrete mix, C4, is the only concrete mix that has surpassed the WAC limit, where the concentration of arsenic and chromium is slightly higher than the regulated limit. Ordinary Portland Cement (OPC) usually has a pH of 12, which indicates high alkalinity. When OPC comes in contact with water, Concrete is highly alkaline, and when it comes into touch with water, the non-

Table 6  
Toxicity analysis of aluminum dross and concrete mixes

Element	Leachate of concrete (ppm)				Leachate of aluminum dross (ppm)	Regulated limit level (ppm)	
	C1	C2	C3	C4		US Environmental Protection Agency (US EPA)	Waste Acceptance Criteria (WAC)
Aluminum	na	0.30	0.40	0.60	0.60	0.05-0.20	
Arsenic	0.20	0.32	0.43	0.56	0.62	5.00	0.50
Cadmium	0.01	0.02	0.02	0.03	bdl	1.00	0.04
Chromium	0.09	0.13	0.49	0.67	0.19	5.00	0.50
Copper	0.33	0.44	0.45	0.39	0.87	1.30	2.00
Nickel	0.09	0.11	0.12	0.1	0.13	1.00	0.40
Zinc	0.92	2.68	3.85	2.33	1.15	1.50	4.00

Note. na: not available; bdl: below the detected level

Regulated limit level imposed by USE EPA and Waste Acceptance Criteria (WAC)

volatile metals (chromium and arsenic) are released (Sumra et al., 2020; Eckbo et al., 2022). In addition, Estokova et al. (2018) reported that substituting higher waste materials in a concrete mixture also contributes to the increase of leachate in the cement matrix. Thus, the higher concentration of chromium and arsenic in concrete samples, C4, was due to the higher percentage of aluminum dross. Table 6 shows that the concentration of elements increases as the dosage of aluminum dross increases. Based on the results of the toxicity test, the increment of the metal values was below the leaching limit value, indicating that the concrete will be safe to use as construction materials.

## CONCLUSION

The current study was performed to develop sustainable concrete by adding aluminum dross into the mixture. An easy aluminum dross treatment method that included washing, drying, and sieving was practical and efficient to acquire a material suitable for concrete. The mechanical and chemical behavior of aluminum dross concrete type were investigated. Within the scope of the project, many tests were performed to evaluate the properties of aluminum dross and concrete that contained aluminum dross.

The following conclusions are drawn as a result of this experimental investigation:

- The slump values for the concrete mix, C3 (10% aluminum dross), increased by 6.1% compared to the control mix, C1, which demonstrated that the concrete has good workability.
- The strength value of concrete decreases with increasing aluminum dross content. Compared to the control mix, C1, the compressive and flexural strength of concrete mix, C3, increased by 1.6% and 0.8%, respectively, at 28 days of curing age.
- A higher volume of aluminum dross incorporation depicts a higher water absorption rate of concrete. The results showed that at the end of 28 days of curing age, the concrete mix, C3, has an almost identical water absorption rate of approximately 0.9% lower than the control mix, C1.
- From SEM analysis, a higher amount of aluminum dross can cause the formation of micropores and micro-cracks, which will affect the strength of the concrete. Aluminum dross in concrete decreased the porous microstructure and improved the formation of hydrates. The concrete mix, C3, has the formation of calcium silicate hydrate (CSH), calcium hydroxide, and ettringite in the matrix due to the presence of aluminum dross.
- From the TGA analysis, aluminum dross concrete was found to have less calcium hydroxide due to a pozzolanic reaction with respect to the control concrete mixture. It was observed that the concrete mix, C3, has a 7.9% lower percentage of calcium hydroxide compared to the control concrete mix, C1, which makes it more stable.

- The toxicity analysis showed that the ammonia concentration in concrete decreased with curing age. In the concrete mixture, C3 has a 44.4% ammonia concentration reduction. Though the ammonia gas is still entrapped in the concrete, the strength and durability properties of the concrete would not significantly be affected. Additionally, it was observed that the concrete leachate contained no toxic materials, and the heavy metals content was within the regulated level.
- Based on the findings, it was determined that 10% was the optimum replacement value of aluminum dross in the concrete mixture. This percentage of substitution will not harm the properties of concrete, and the compressive strength will remain close to that of normal concrete.

Hence, it can be concluded that aluminum dross, as an industrial waste, can be a potential candidate to be substituted in cement for concrete production. The replacement is feasible considering enhanced properties as well as conserving environmental sustainability. For future research, various curing methods could be investigated to examine the impact on the mechanical and chemical properties of aluminum dross concrete.

## ACKNOWLEDGEMENTS

The authors acknowledge that all the experimental work described in this publication was carried out with the assistance of the Chemical and Environmental Engineering Department, Civil Engineering Department, Material Characterization Laboratory, Thermal Analyzer Laboratory, and Construction Material Laboratory, Universiti Putra Malaysia. The project is funded by FRGS/1/2020/TK0/UPM/02/15 (Evaluation of the physicochemical characteristics concerning strength and durability aspects of binary waste aluminum dross and quarry dust reinforced concrete). The authors would also like to thank the management of Cenviro Sdn Bhd for providing the raw aluminum dross used in this study.

## REFERENCES

- American Society for Testing and Materials. (1997). Standard Test Method for Density, Absorption, and Voids in Hardened Concrete C642-97. *ASTM International, March*, 1–3. <https://doi.org/10.1016/j.asej.2012.04.011>
- American Society of Testing Materials c-979-99. (2015). Standard Specification for Pigments for Integrally Colored Concrete 1. *Asm, 14(c)*, 3–7. [https://doi.org/10.1520/C0979\\_C0979M-16](https://doi.org/10.1520/C0979_C0979M-16)
- Arpitha, D. J., & Praveen, K. (2022). Experimental investigation of aluminium dross and GGBS in the production of eco-friendly concrete. In *IOP Conference Series: Materials Science and Engineering* (Vol. 1255, No. 1, p. 012003). IOP Publishing. <https://doi.org/10.1088/1757-899x/1255/1/012003>
- Bakhtyar, B., Kacemi, T., & Nawaz, M. A. (2017). A review on carbon emissions in Malaysian cement industry. *International Journal of Energy Economics and Policy*, 7(3), 282-286.
- BS EN 196-1. (2005). *Standard Cement - British Standard Methods of Testing Cement*. <https://doi.org/10.3403/30291447U>

- BS EN 12350-2. (2009). Testing fresh concrete - Part 2: Slump Test - *BSI Standards Publication*, (January). <https://doi.org/10.3403/30164882>
- BS EN 12390-3. (2001). Testing hardened concrete - Part 3: Compressive strength of test specimens. In *BSI Standards Publication* (pp. 4–10). <https://doi.org/10.3403/30360097>
- BS EN 12390-5. (2019). Testing hardened concrete - Part 5: Flexural strength of test specimens. *BSI Standards Publication*, August, 1–22. <https://doi.org/10.3403/30360073U>
- BS EN 12620. (2002). Aggregates for concrete. *BSI Standards Publication*, (August). <https://doi.org/10.3403/30192952>
- Dirisu, J. O., Oyedepo, S. O., Fayomi, O. S. I., & Akinlabi, E. T. (2021). Development of silicate aluminium dross composites for sustainable building ceilings. *Silicon*, 13(6), 1979-1991. <https://doi.org/10.1007/s12633-020-00586-z>
- Eckbo, C., Okkenhaug, G., & Hale, S. E. (2022). The effects of soil organic matter on leaching of hexavalent chromium from concrete waste: Batch and column experiments. *Journal of Environmental Management*, 309, Article 114708. <https://doi.org/10.1016/j.jenvman.2022.114708>
- Elseknidy, M. H., Salmiaton, A., Shafizah, I. N., & Saad, A. H. (2020). A study on mechanical properties of concrete incorporating aluminum dross, fly ash, and quarry dust. *Sustainability*, 12(21), 1-13. <https://doi.org/10.3390/su12219230>
- El-Aziz, M. A. A., & Sufe, W. H. (2013). Effect of sewage wastes on the physico-mechanical properties of cement and reinforced steel. *Ain Shams Engineering Journal*, 4(3), 387-391. <https://doi.org/10.1016/j.asej.2012.04.011>
- Estokova, A., Palascakova, L., & Kanuchova, M. (2018). Study on Cr(VI) leaching from cement and cement composites. *International Journal of Environmental Research and Public Health*, 15(4), 1-13. <https://doi.org/10.3390/ijerph15040824>
- Galat, N. Y., Dhawale, G. D., & Kitey, M. S. (2017). Performance of concrete using aluminium dross. *Journal of Emerging Technologies and Innovative Research*, 4(07), 5-10.
- Imbabi, M. S., Carrigan, C., & McKenna, S. (2012). Trends and developments in green cement and concrete technology. *International Journal of Sustainable Built Environment*, 1(2), 194-216. <https://doi.org/10.1016/j.ijbsbe.2013.05.001>
- Javali, S., Chandrashekar, A. R., Naganna, S. R., Manu, D. S., Hiremath, P., Preethi, H. G., & Kumar, N. V. (2017). Eco-concrete for sustainability: Utilizing aluminium dross and iron slag as partial replacement materials. *Clean Technologies and Environmental Policy*, 19(9), 2291-2304. <https://doi.org/10.1007/s10098-017-1419-9>
- Khan, M. A. (2015). Prefabrication of the substructure and construction issues. In *Accelerated Bridge Construction* (pp. 399-441). Elsevier Inc. <https://doi.org/10.1016/b978-0-12-407224-4.00009-5>
- Kandhan, K. U. M., & Karunakaran, V. (2021). Behaviour of concrete by partial replacement of lime in cement. *International Research Journal of Engineering and Technology*, 8(3), 2730- 2735.
- Kudyba, A., Akhtar, S., Johansen, I., & Safarian, J. (2021). Aluminum recovery from white aluminum dross by a mechanically activated phase separation and remelting process. *The Journal of The Minerals, Metals & Materials Society*, 73(9), 2625-2634. <https://doi.org/10.1007/s11837-021-04730-x>

- Mahinroosta, M., & Allahverdi, A. (2018). Hazardous aluminum dross characterization and recycling strategies: A critical review. *Journal of Environmental Management*, 223, 452-468. <https://doi.org/10.1016/j.jenvman.2018.06.068>
- Mailar, G., Sreedhara, B. M., Manu, D. S., Hiremath, P., & Jayakesh, K. (2016). Investigation of concrete produced using recycled aluminium dross for hot weather concreting conditions. *Resource-Efficient Technologies*, 2(2), 68-80. <https://doi.org/10.1016/j.reffit.2016.06.006>
- Meddah, M. S., Praveenkumar, T. R., Vijayalakshmi, M. M., Manigandan, S., & Arunachalam, R. (2020). Mechanical and microstructural characterization of rice husk ash and Al<sub>2</sub>O<sub>3</sub> nanoparticles modified cement concrete. *Construction and Building Materials*, 255, Article 119358. <https://doi.org/10.1016/j.conbuildmat.2020.119358>
- Meshram, A., & Singh, K. K. (2018). Recovery of valuable products from hazardous aluminum dross: A review. *Resources, Conservation and Recycling*, 130, 95-108. <https://doi.org/10.1016/j.resconrec.2017.11.026>
- Naqi, A., & Jang, J. G. (2019). Recent progress in green cement technology utilizing low-carbon emission fuels and raw materials: A review. *Sustainability*, 11(2), Article 537. <https://doi.org/10.3390/su11020537>
- Nirmale, G. B., & Bhusare, V. P. (2018). Review on studies of partially replacement concrete using aluminium dross. *Journal of Advances and Scholarly Researches in Allied Education*, 15(2), 345-348. <https://doi.org/10.29070/15/56844>
- Odeyemi, S. O., Abdulwahab, R., Anifowose, M. A., & Atoyebi, O. D. (2021). Effect of curing methods on the compressive strengths of palm kernel shell concrete. *Civil Engineering and Architecture*, 9(7), 2286-2291. <https://doi.org/10.13189/cea.2021.090716>
- Panditharadhya, B. J., Sampath, V., Mulangi, R. H., & Shankar, A. U. R. (2018). Mechanical properties of pavement quality concrete with secondary aluminium dross as partial replacement for ordinary portland cement. In *IOP conference series: materials science and engineering* (Vol. 431, No. 3, p. 032011). IOP Publishing. <https://doi.org/10.1088/1757-899X/431/3/032011>
- Pattinaja, A. M. J., & Tjahjani, A. R. I. (2015). Nano silica and silica fume for durability improvement and it ' s impact on high performance concrete. In *2nd International Conference on Green Materials and Environmental Engineering* (pp. 115-117). Atlantis Press. <https://doi.org/10.2991/gmee-15.2015.31>
- Reddy, M. S., & Neeraja, D. (2016). Mechanical and durability aspects of concrete incorporating secondary aluminium slag. *Resource-Efficient Technologies*, 2(4), 225-232. <https://doi.org/10.1016/j.reffit.2016.10.012>
- Reddy, P. N., & Naqash, J. A. (2019a). Experimental study on TGA, XRD and SEM analysis of concrete with ultra-fine slag. *International Journal of Engineering, Transactions B: Applications*, 32(5), 679-684. <https://doi.org/10.5829/ije.2019.32.05b.09>
- Reddy, P. N., & Naqash, J. A. (2019b). Properties of concrete modified with ultra-fine slag. *Karbala International Journal of Modern Science*, 5(3), 151-157. <https://doi.org/10.33640/2405-609X.1141>
- Soós, Z., Géber, R., Tóth, C., Igazvölgyi, Z., & Udvardi, B. (2017). Utilization of aluminium dross as asphalt filler. *Epitoanyag - Journal of Silicate Based and Composite Materials*, 69(3), 89-93. <https://doi.org/10.14382/epitoanyag-jsbcm.2017.15>



- Sultana, U. K., Gulshan, F., Gafur, M. A., & Kurny, A. S. W. (2013). Kinetics of recovery of alumina from aluminium casting waste through fusion with sodium hydroxide. *American Journal of Material Engineering and Technology*, 1(3), 30-34. <https://doi.org/10.12691/materials-1-3-1>
- Sumra, Y., Payam, S., & Zainah, I. (2020). The pH of cement-based materials: A review. *Journal Wuhan University of Technology, Materials Science Edition*, 35(5), 908-924. <https://doi.org/10.1007/s11595-020-2337-y>
- Udvardi, B., Géber, R., & Kocserha, I. (2019). Examination of the utilization of aluminum dross in road construction. In *IOP Conference Series: Materials Science and Engineering* (Vol. 613, No. 1, p. 012053). IOP Publishing. <https://doi.org/10.1088/1757-899X/613/1/012053>
- Ukrainczyk, N., Ukrainczyk, M., Sipusic, J., & Matusinovic, T. (2006, June 22-24). XRD and TGA investigation of hardened cement paste. In *Proceedings of the Conference on Materials, Processes, Friction and Wear* (pp. 243-249). Vela Luka, Croatia.
- Vedalakshmi, R., Raj, A. S., Srinivasan, S., & Babu, K. G. (2003). Quantification of hydrated cement products of blended cements in low and medium strength concrete using TG and DTA technique. *Thermochimica Acta*, 407(1-2), 49-60. [https://doi.org/10.1016/S0040-6031\(03\)00286-7](https://doi.org/10.1016/S0040-6031(03)00286-7)
- Vogler, N., Drabetzki, P., Lindemann, M., & Kühne, H. C. (2022). Description of the concrete carbonation process with adjusted depth-resolved thermogravimetric analysis. *Journal of Thermal Analysis and Calorimetry*, 147(11), 6167-6180. <https://doi.org/10.1007/s10973-021-10966-1>
- Walker, R., & Pavia, S. (2011). Physical properties and reactivity of pozzolans, and their influence on the properties of lime-pozzolan pastes. *Materials and Structures/Materiaux et Constructions*, 44(6), 1139-1150. <https://doi.org/10.1617/s11527-010-9689-2>
- Zauzi, N. S. A., Zakaria, M. Z. H., Bains, R., Rahman, M. R., Sutan, N. M., & Hamdan, S. (2016). Influence of alkali treatment on the surface area of aluminium dross. *Advances in Materials Science and Engineering*, 2016, Article 6306304. <https://doi.org/10.1155/2016/6306304>
- Zhou, J., Zheng, K., Liu, Z., & He, F. (2019). Chemical effect of nano-alumina on early-age hydration of Portland cement. *Cement and Concrete Research*, 116, 159-167. <https://doi.org/10.1016/j.cemconres.2018.11.007>



## Structural Deformation and Displacement of a Disc Winding due to Standard Switching Impulse Voltage via Finite Element Method

Nurul Farahwahida Md Yasid<sup>1</sup>, Norhafiz Azis<sup>1,2\*</sup>, Jasronita Jasni<sup>1</sup>, Mohd Fairouz Mohd Yousof<sup>3</sup>, Mohd Aizam Talib<sup>4</sup> and Avinash Srikanta Murthy<sup>5</sup>

<sup>1</sup>Advanced Lightning, Power and Energy Research Centre (ALPER), Faculty of Engineering, Universiti Putra Malaysia, 43400 UPM, Serdang, Selangor, Malaysia

<sup>2</sup>Institute of Nanoscience and Nanotechnology (ION2), Universiti Putra Malaysia, 43400 UPM, Serdang, Selangor, Malaysia

<sup>3</sup>Faculty of Electrical and Electronics Engineering, Universiti Tun Hussein Onn Malaysia, 86400 Parit Raja, Johor, Malaysia

<sup>4</sup>TNB Labs Sdn. Bhd, Kajang, Selangor, 43000, Malaysia

<sup>5</sup>Transformer Technology Centre, Hitachi Energy, 390013, India

### ABSTRACT

Switching operations in a power system network can lead to transient overvoltage in the high voltage (HV) winding of distribution transformers that causes high-stress build-up. This paper presents the relationship between electromagnetic force due to a standard switching impulse (SSI) and mechanical deformation/displacement behaviours for a disc-type transformer. The analysis was carried out based on a three-dimensional (3D) modelling of a continuous HV disc winding configuration whereby it is subjected to the switching transient voltage and force excitations through the finite element method (FEM). The electric transient solver analysed the static and dynamic aspects of the electromagnetic forces associated with the variation of forces versus time. The transient structural solver evaluated the structural behaviours of the disc winding related to the axial height and radial width of the winding under electromagnetic forces. It is found that the positively dominant axial force generated in the winding with a

magnitude of 8.7 N causes the top and bottom layers of disc winding to tilt and displace. In addition, the positive average radial force of 1.4 N causes the circumference of the winding to experience hoop tension and outwardly stretch.

### ARTICLE INFO

#### Article history:

Received: 12 April 2023

Accepted: 09 October 2023

Published: 14 March 2023

DOI: <https://doi.org/10.47836/pjst.32.2.16>

#### E-mail addresses:

farahwahida.yasid@gmail.com (Nurul Farahwahida Md Yasid)

norhafiz@upm.edu.my (Norhafiz Azis)

jas@upm.edu.my (Jasronita Jasni)

fairouz@uthm.edu.my (Mohd Fairouz Mohd Yousof)

aizam.talib@tnb.com.my (Mohd Aizam Talib)

avinash.murthy@hitachienergy.com (Avinash Srikanta Murthy)

\* Corresponding author

**Keywords:** Disc winding, electromagnetic forces, structural behaviours, switching transient, transformer

## INTRODUCTION

According to a global survey conducted by CIGRE WG A2.37, among the major contributors to transformer failures is the winding, including deformation cases (Tenbohlen et al., 2016; Tenbohlen et al., 2017). The winding deformations normally occur at locations between spacers and barriers (Kojima et al., 1980). These phenomena are usually caused by the high electromagnetic forces from the overvoltage/overcurrent in the power system networks (Da Costa Oliveira Rocha et al., 2014). The majority of transformer insulation failures and abnormal electromagnetic stresses on windings are caused by repetitive in-service switching operations (Agrawal, 2001b; Yasid et al., 2023; Yutthagowith, 2022).

The primary fundamental of switching transient is the interruption of the steady state of a power system network caused by the switching operations. High resonance overvoltage can occur once the oscillations of the switching operations match with the resonance of a transformer (Bjerkas, 2005). It can trigger overvoltage up to 4 or 5 times higher than the normal power frequency, resulting in a steep-fronted surge that generates large stress in a transformer (Bhuyan & Chatterjee, 2015). This condition can also occur once the transient voltage excitation wave frequencies are close to the major frequencies of the transformer (Massaro & Antunes, 2009). Surge arresters are normally installed as surge and overvoltage protection devices but are only sensitive to voltage amplitudes. Therefore, the incoming transient voltage wave might still cause resonance behaviours in the winding even when the amplitude is well below the protection level if there is a matching in the frequencies (Agrawal, 2001a; Florkowski et al., 2020).

The finite element method (FEM) is known as one of the best alternative methods to solve engineering problems, and it can provide results closer to physical phenomena (Rao et al., 2012; Rao, 2005; Yan et al., 2016). Several studies have been conducted to examine the magnetic fields, stresses and electromagnetic forces during transient conditions through the FEM. The electromagnetic forces on the transformer windings based on FEM are carried out in Arivamudhan and Santhi (2019), Dawood et al. (2019), Faiz et al. (2011) and Fonseca et al. (2016). The axial and radial forces are found to be the highest at the end and middle sections of the windings, respectively. Other studies focus on the stress concentration factors (Hodhigere et al., 2018; Muminovic et al., 2015). It is found that the irregularities in the stress distributions cause abnormal stress concentration on the winding. The previous study also examined the magnetic fields within transformers of different geometrical dimensions and magnetic parameters (Hussein & Hameed, 2022). It has been discovered that different winding configurations can affect the magnetic field and electromagnetic force distributions. In addition, the leakage flux induced by different types of faults can affect the structural deformation and displacement of the windings (Fonseca et al., 2018; Nazari, 2013; Zhang et al., 2021).

It is known that the structural displacements and deformations of windings can lead to mechanical faults. It can be divided into two main modes, which are axial displacement and radial deformation (Bagheri et al., 2012; Gutten et al., 2011; Nurmanova et al., 2019; Ou et al., 2022; Tahir & Tenbohlen, 2019). Axial displacement can cause a complete winding displacement, tilting and bending of the windings. Radial deformation causes hoop tension, forced and free buckling. When both forces are excessive, it can cause spiralling and telescoping of windings. These conditions challenge manufacturers and users to compute the changes in the structural behaviours of different winding configurations and faults since generic condition interpretation could not be applied. Furthermore, limited analysis that focuses on the disc winding configuration is available. This winding type is common in a core-type transformer but is more complex than the spiral-type winding (van Jaarsveld, 2013).

The findings of this study have significant implications for characterising the behaviours of the electromagnetic forces as well as identifying the corresponding deformation and displacement behaviours of a disc winding structure due to a switching transient. The study presents a case study of a single-phase HV winding model of a 30 MVA disc-type distribution transformer. A 3D model that considers 8-disc winding is simulated through Ansys. The electromagnetic forces and mechanical deformation/displacement due to standard switching impulse (SSI) are investigated through electric transient and transient structural analyses. The stress concentration with characteristics of deformation and displacement of the disc winding obtained from this study are anticipated to provide helpful insight for physical configurations at the design phase of the transformer winding.

## METHODS

### Design and Disc Winding Modelling

In order to evaluate the structural performance of the disc winding design, the solution strategy began with the evaluation of the numerical electric transient due to the switching transient. The geometrical winding model was constructed based on the structural parameters and material properties of a 33/11 kV, 30 MVA disc-type transformer, as shown in Tables 1 and 2. Figure 1 shows the single-phase front cross-

Table 1  
*The HV winding geometrical specifications of Dyn11, 30 MVA disc-type transformer*

Parameters	Specification
Number of discs in one phase	96
Number of turns per disc	30
Height of conductor	11.5 mm
Width of the conductor	2.4 mm
The thickness of the insulation (double-sided)	0.5 mm
Distance between each disc	3 mm
Cooling duct between layers 12 and 13	5 mm
Inner radius of the HV winding	374.5 mm
Outer radius of the HV winding	466.5 mm
Total circumference of the HV winding	79.17 mm
Height of HV winding	1437 mm
Insulation between HV – LV windings	20 mm

Table 2  
*Winding and mechanical properties used in FEM*

Part	Materials	Density (kg m <sup>-3</sup> )	ME (GPa)	PR
Conductor	Copper	7850	113	0.3
Insulation	Kraft paper	930	1.1	0.001
Fixed support	Steel	7850	200	0.3

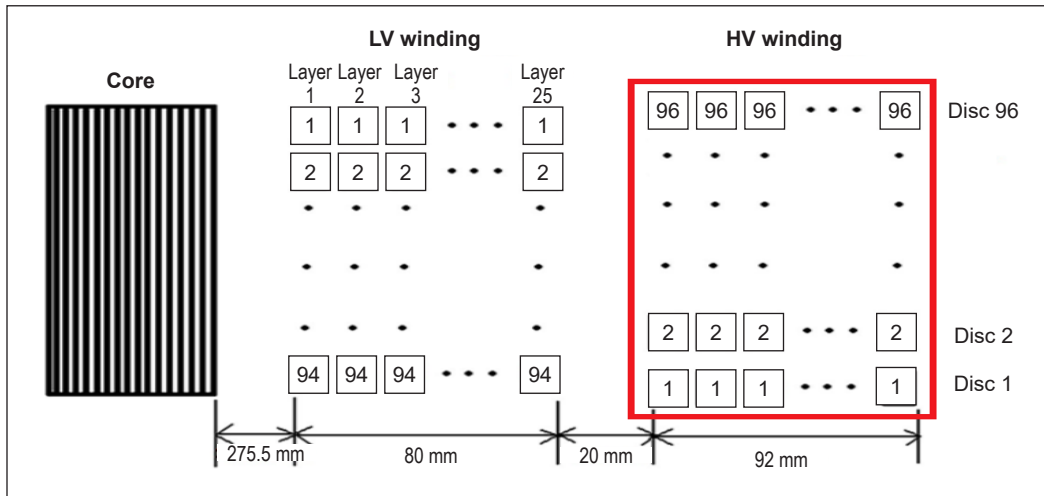
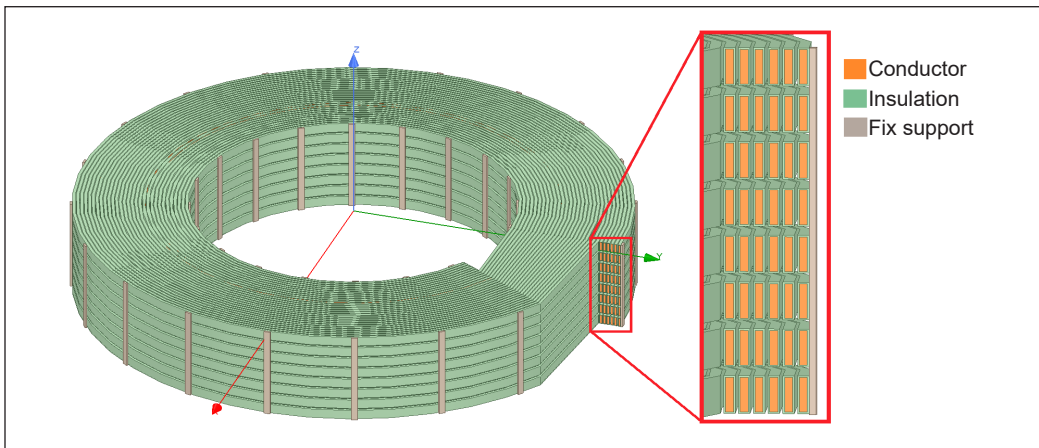


Figure 1. Single-phase 33/11 kV transformer front cross-section view

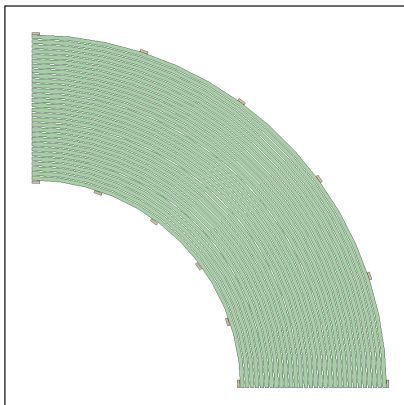
section view of the transformer winding. In this case, only HV winding was modelled and analysed since the electromagnetic forces induced by the excitation inrush mainly acted on this side (Zhang et al., 2021). It is known that the transient condition causes the transformer’s core to oversaturate, leading to reduced permeability (van Jaarsveld, 2013). Therefore, the core was not considered during transient analysis. The spacers are not considered in the electrical and mechanical analyses since it is not electrically active and is not subjected to significant mechanical loads.

The 3D geometric model of the disc winding that includes conductors, insulation materials and winding fixed supports can be seen in Figure 2. Figure 2(a) shows the perspective view, and Figure 2(b) shows the ¼ symmetrical top and trimetric views of the model. The model consists of continuous 8 discs, each comprising 6 conductors and 5 turns. Due to the nature of the transformer’s symmetrical structure, the 3D geometric model was split into 4 symmetrical parts. This symmetry boundary condition setting leads to efficient computational in terms of space and run times.

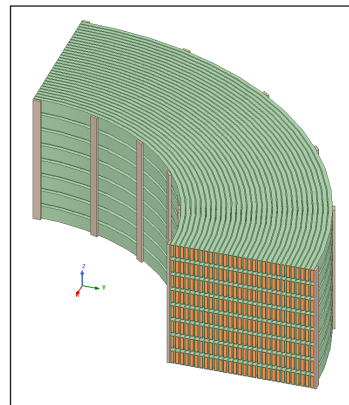
In this study, the winding modelling was simplified and considered an ideal model focused only on the 8 topmost discs. An implicit assumption was made that the winding was a rotation symmetric cylinder with a continuous arrangement of the copper conductors. The



(a)



(b)



(c)

Figure 2. Details of HV disc winding model: (a) Perspective view; and (b)  $\frac{1}{4}$  symmetrical top and trimetric view

structure presents the geometry, material properties, capacitive and inductive couplings for every element of the disc winding. The skin effect was also considered. The winding fixed supports were placed at the inner and outer layers of the winding to simulate clamping. The 3D geometric model was subjected to a mesh of free tetrahedrons network composed of 492 active bodies, 2,678,899 nodes and 1,271,896 elements.

The current simulation work was performed based on a similar approach to Murthy et al. (2020), whereby the 3D geometric model validation was conducted by comparing the results of simulated and measured frequency response analyses (FRA). The study showed good agreement between simulated and measured FRAs, which indicated that the winding model was adequate and applicable to this analysis. Another study showed that the parameters of the winding model were near the actual transformer once good agreement was found between the simulated and measured FRAs (Behjat & Mahvi, 2015).

### Standard Switching Impulse Voltage Distribution

The SSI voltage as per IEC 60071-1, 2019 and IEEE Std C37.30, 2018, defined the front and tail times as 250 and 2500  $\mu$ s. The impulse generator circuit generated the SSI voltage waveform (Ren et al., 2016). In total, 1 cycle of SSI voltage was used as the input data for the force analysis. The voltage was defined in per unit (p.u) based on the ratio of the peak overvoltage to the peak phase-to-earth voltage for the transformer winding. For this case, the analysis considered the highest magnitude of a switching surge that could be achieved, which was 5 p.u, equivalent to 165 kV. This SSI voltage was superimposed on each disc windings to determine the total electromagnetic force. Figure 3 shows the overall scheme of the SSI voltage application on the winding.

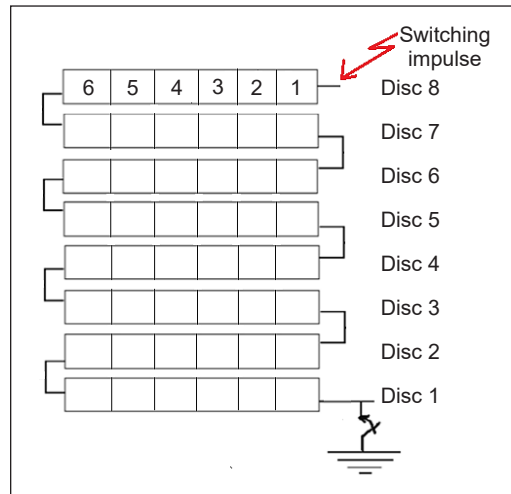


Figure 3. The overall scheme of switching impulse analysis

### Relationship of Electromagnetic Forces and Winding Displacement/Deformation

The computed electromagnetic forces from the electric transient analysis were transferred to the transient structural analysis to obtain the deformation/displacements of the winding. The winding model was remodelled using the Space Claim in the Ansys Workbench to certify its initial structure. The internal overvoltage was obtained as a result of the response within the winding due to the 1 cycle of SSI voltage. The transient current and leakage flux generated the electromagnetic forces in the winding. The forces in the winding can be obtained by the Lorentz force, as shown in Equation 1.

$$d\vec{F} = id\vec{l} \times \vec{B} \tag{1}$$

Where  $F$  is the force,  $I$  is the current density, and  $B$  is the flux density. The magnetic computation of the 3D modelling was described in  $x$ ,  $y$  and  $z$  planes since the current was normal to those planes (Feyzi & Sabahi, 2008). The component of leakage flux density can be expressed as vector potential, as seen in Equation 2 (Ahn et al., 2012).

$$B_x = -\frac{\partial A_\phi}{\partial z}, \quad B_y = 0, \quad B_z = \frac{1}{r} \frac{\partial r A_\phi}{\partial x} \tag{2}$$

Where  $B_x$ ,  $B_y$ , and  $B_z$  are directional components of leakage flux density, and  $A_\phi$  is the magnetic vector potential. The electromagnetic force on the winding was expressed using



the Lorentz force as per Equations 3 and 4 (Ahn et al., 2011).

$$F = \int_V J_y \hat{y} \times (B_x \hat{x} + B_z \hat{z}) dv = F_x \hat{x} + F_z \hat{z} \quad [3]$$

$$F_x = B_z \times J_y, \quad F_z = B_x \times J_y \quad [4]$$

Where,  $J_y$  is the y-directional current density,  $\hat{x}$ ,  $\hat{y}$  and  $\hat{z}$  are the unit vectors in the winding plane. When the winding was subjected to a high electromagnetic force, the winding deformation or displacement could be initiated. The deformation can be defined by elastic-plastic deformation, stress and strain control (Zhang et al., 2014). The relation between stress and mass force in space can be described based on Equation 5.

$$\begin{cases} \frac{\partial \sigma_r}{\partial r} + \frac{\partial \tau_{zr}}{\partial z} + \frac{\sigma_r - \sigma_\theta}{r} + f_r = 0 \\ \frac{\partial \sigma_z}{\partial z} + \frac{\partial \tau_{rz}}{\partial r} + \frac{\tau_{rz}}{r} + f_z = 0 \end{cases} \quad [5]$$

Where  $f_r$  and  $f_z$  are the radial and axial forces exerted on the winding.  $\sigma_r$ ,  $\sigma_\theta$  and  $\sigma_z$  are the radial, tangential and axial stress. The relationship between strain and displacement describes the displacement. The strain-displacement describes how the applied forces on the winding cause it to deform and result in displacement of the winding. The strain displacement can be expressed by Equation 6.

$$\begin{cases} \varepsilon_r = \frac{\partial u_r}{\partial r} & \varepsilon_\theta = \frac{u_r}{r} \\ \varepsilon_z = \frac{\partial u_z}{\partial z} & \gamma_{rz} = \frac{\partial u_r}{\partial z} + \frac{\partial u_z}{\partial r} \end{cases} \quad [6]$$

Where  $\varepsilon_r$ ,  $\varepsilon_\theta$ , and  $\varepsilon_z$  are the radial strain, tangential and axial strain,  $\gamma_{rz}$  is the shear strain,  $u_r$  and  $u_z$  are the radial and axial displacements. The relationship between stress and strain in space can be expressed by Equation 7.

$$\begin{cases} \varepsilon_r = \frac{1}{E} [\sigma_r - \mu(\sigma_\theta + \sigma_z)] & \varepsilon_\theta = \frac{1}{E} [\sigma_\theta - \mu(\sigma_z + \sigma_r)] \\ \varepsilon_z = \frac{1}{E} [\sigma_z - \mu(\sigma_r + \sigma_\theta)] & \gamma_{rz} = \frac{2(1 + \mu)}{E} \mathcal{J}_{zr} \end{cases} \quad [7]$$

Where  $\mathcal{J}_{zr}$  is the shear stress,  $\mu$  is the Poisson ratio of the winding material, and  $E$  is the elastic modulus according to the mechanical properties of the winding material.

## RESULTS AND DISCUSSIONS

The deformations were classified into two modes: which are directional and total deformations. Directional deformation refers to the deformation of the disc winding

structure in a particular defined direction known as the  $x$ -,  $y$ - and  $z$ -directions. These defined directions were correlated to the expressed electromagnetic force directions. The total deformation is the vector sum of all the directional deformations. It should be noted that the forces generated from 1 cycle of SSI would not cause the winding to deform/displace. In this case, the scale of deformations was increased to analyse the possible deformation and displacement on the disc winding.

### Electromagnetic Force Generated Due to the SSI

The electromagnetic forces generated due to 1 cycle of the SSI are displayed in the time domain, as seen in Figure 4. The forces are given into 3 directional components as the 3D model planes,  $x$ -,  $y$ - and  $z$ -directions. The  $x$ - and  $y$ -directional forces represent the radial force, while the  $z$ -directional force represents the axial force. It is found that both  $y$ - and  $z$ -directional forces increase while the  $x$ -directional force decreases after 1500  $\mu$ s. The peak amplitude of the  $x$ -,  $y$ - and  $z$ -directional forces is -0.5 N, 3.2 N, and 8.7 N, respectively. The average radially  $x$ - and  $y$ -directional force on the winding is 1.4 N, a positively directed force. This condition indicates that the width of the disc winding experiences a horizontal tensile force. The axially  $z$ -directional force is positively directed, which signifies that vertical tensile force is projected along the height of the disc winding. The axial force in the disc winding is observed to be more dominant than the radial force.

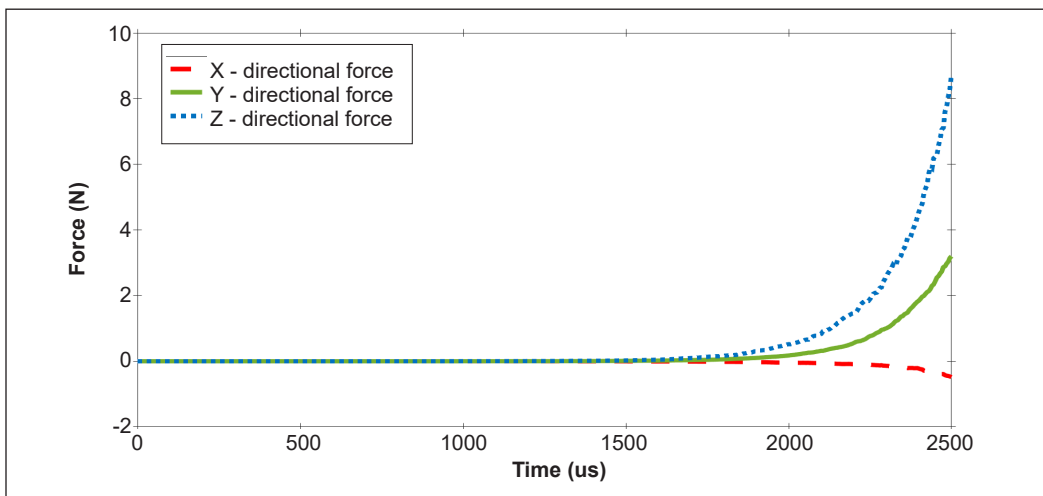


Figure 4. The electromagnetic forces generated due to 1 cycle of SSI

### Directional Deformations

The variations of winding structural behaviours along the  $x$ -,  $y$ - and  $z$ -directions over 1 cycle of SSI waveform with  $0.5\times$  deformation scale factor are shown in Tables 3 and 4. The average  $x$ -,  $y$ - and  $z$ -directional deformations are concentrated at  $x = 0$ ,  $y = 0$ , and  $z =$

Table 3

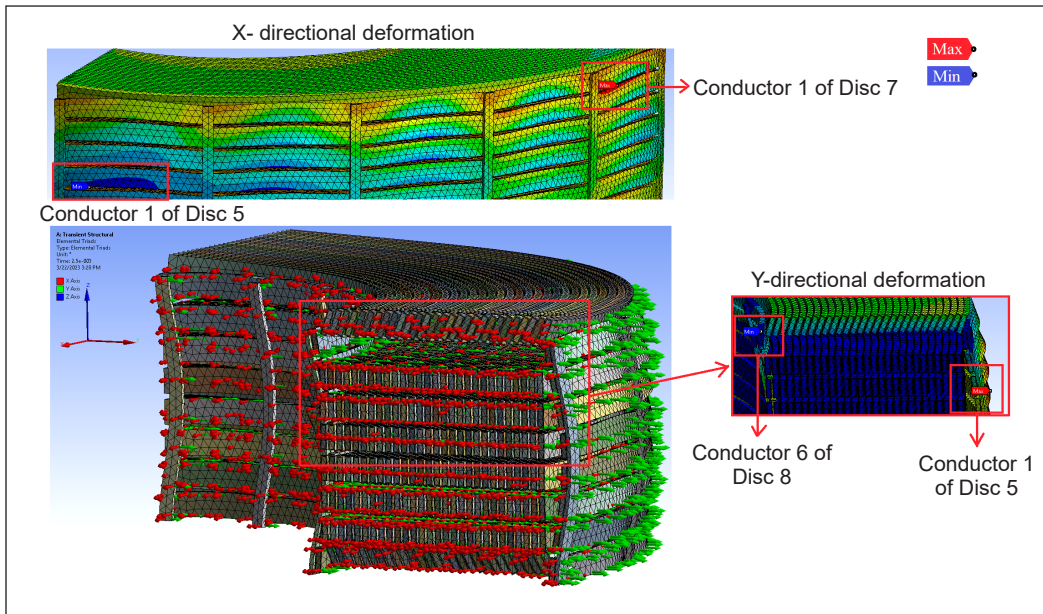
*Results of directional deformations of disc winding*

Directional deformation	Minimum (mm)	Maximum (mm)	Average (mm)	Minimum Occurs On	Maximum Occurs On
X	$-1.24 \times 10^{-5}$	$2.97 \times 10^{-6}$	$-7.22 \times 10^{-7}$	Conductor 1 (Disc 5)	Conductor 1 (Disc 7)
Y	$-1.22 \times 10^{-6}$	$3.51 \times 10^{-5}$	$3.12 \times 10^{-6}$	Conductor 6 (Disc 8)	Conductor 1 (Disc 5)
Z	$-2.56 \times 10^{-6}$	$3.81 \times 10^{-5}$	$6.11 \times 10^{-6}$	Conductor 1 (Disc 6)	Conductor 2 (Disc 8)

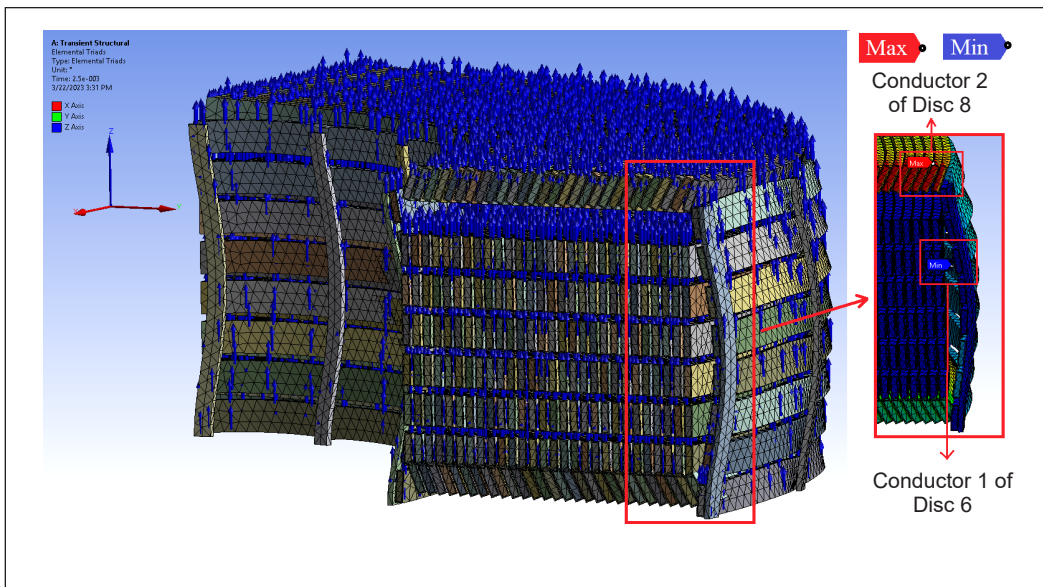
0 planes (Ahn et al., 2011). The directional deformations are presented with the element triads that show the directions of the deformation moments.

The directional deformation analysis of the disc winding shows that the maximum deformation occurs in the  $z$ -direction, which is along the axial height of the winding. The highest deformation is located on the topmost disc layer with a peak magnitude of  $3.81 \times 10^{-5}$  mm. This deformation is about 6 times higher than the average deformation of this direction. The axial displacements are obvious at the top and bottom layers of the disc winding, as seen in Figure 5. The winding experiences axial displacement and tilting of conductors. The positive  $z$ -directional deformation causes the bottom and top disc layers to displace slightly upward from their original position. In addition, it is observed that the conductors at both disc layers tilt to the right and left directions at a small angle ranging between  $5^\circ$  and  $10^\circ$ . In this case, the support structures seem to bend or not evenly align since they are experiencing deformations. It causes the axial force to be imposed unevenly on the winding, which leads to different degrees of tilting in different disc layers. These results align with the findings of Behjat et al. (2018) and Dawood et al. (2020), whereby higher axial forces are detected at the end discs and cause the tilt of conductors.

The second highest deformation occurs at the outer-most winding or circumference of the winding, which is in the  $y$ -direction with a peak magnitude of  $3.51 \times 10^{-5}$  mm. The  $y$ -directional deformation acts perpendicularly to the axis of the disc winding, causing the hoop tension. This hoop tension refers to the tensile stress that occurs perpendicularly to the winding axis. This stress leads to the stretch of the winding conductor along the circumference of the winding, which results in changes in its dimension and shape. The outer layers of the winding conductors bend outwardly between each fixed support as the fixed support structure has higher stiffness than the winding conductors, as seen in Figure 5. On the other hand, the  $x$ -directional deformation is quite small, with a peak magnitude of  $2.97 \times 10^{-6}$  mm and results in insignificant structural deformation. These results match those observed in earlier studies by Behjat et al. (2018) and Meng and Wang (2004), which found that radial forces act outward on the outer winding. Based on the overall results of the directional deformation analysis, it is observed that the deformation is higher in the axial direction as compared to the radial direction.



(a)



(b)

Figure 5. Directional deformations of disc winding at: (a) x- and y-directions; and (b) z-direction

### Total Deformation

The variation of total deformation that shows the total structural behaviours of the disc winding over 1 cycle of SSI with a  $0.5\times$  deformation scale factor is shown in Table 4 and Figure 6.

Table 4

Results of the total deformation of disc winding

Total deformation	Minimum (mm)	Maximum (mm)	Average (mm)	Minimum Occurs On	Maximum Occurs On
	0	$4.31 \times 10^{-5}$	$7.30 \times 10^{-6}$	Fixed support 1	Conductor 2 (Disc 8)

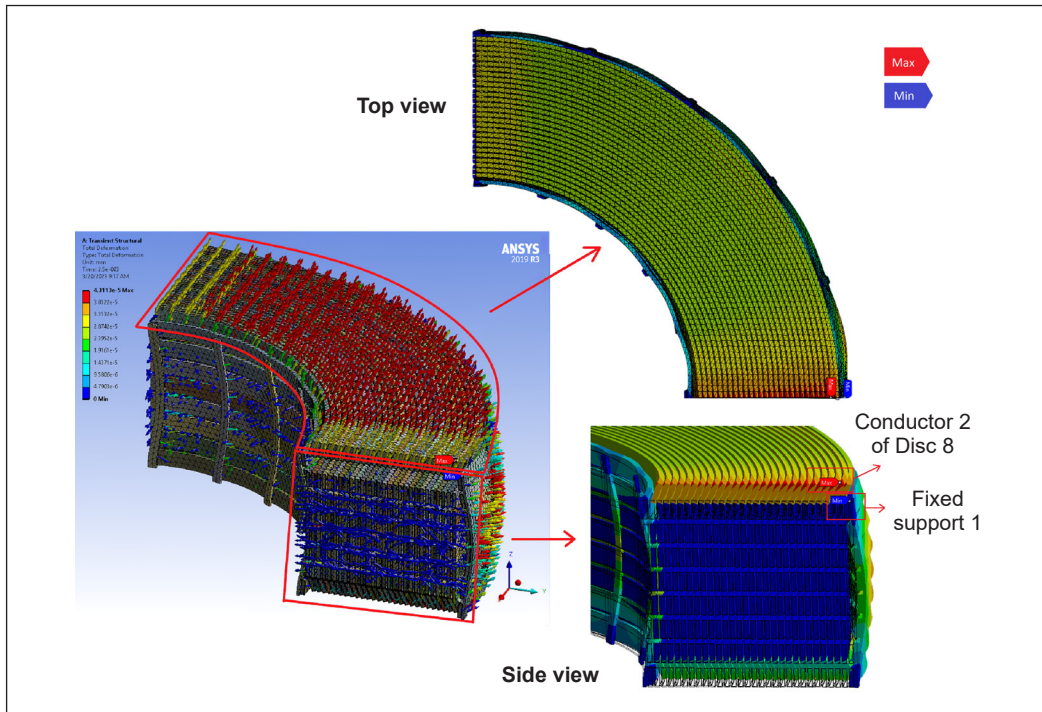


Figure 6. Total deformation of disc winding due to SSI

The total deformation analysis shows that the maximum deformation occurs on the conductor at the topmost disc layer of the winding, with a peak magnitude of  $4.31 \times 10^{-5}$  mm. The minimum deformation occurs on the fixed supports, with 0 mm. The deformations at the fixed support sections are lower than those of the winding conductors. Radial deformations are more obvious at the middle sections of the winding and uniform across the width of the winding. The deformation in the axial direction is obvious at the top and bottom disc windings. The analysis also reveals that deformation is the highest at the outer-most layer of the winding, in both radial and axial directions. It is because the sections with higher leakage flux experience higher electromagnetic forces and are prone to experience deformation and displacement (Faiz et al., 2011). The deformation and displacement computation results show that along the z-direction, the axial force gradually increases from the middle to the end of the HV windings. Along the x and y directions, the radial force linearly increases from the inner to outer sides of the HV winding.

## CONCLUSION

This work examines the electromagnetic force and structural deformation/displacement characteristics of a disc winding. The axial force generated in the winding causes the top and bottom layers of disc winding to tilt and displace with a peak magnitude of  $3.81 \times 10^{-5}$  mm. The radial force causes the circumference of the winding to experience hoop tension and outwardly stretch with an average magnitude of  $1.9 \times 10^{-5}$  mm. The deformation and displacement are more likely to occur to the outer layer of the disc winding, whether in axial or radial directions. The disc winding experiences a higher axial force; therefore, axial structural displacement is more dominant as compared to radial structural deformation. These findings generally strengthen the finding that high-stress concentration can lead to a high degree of deformation and displacement of windings. In the case of disc winding subjected to the SSI, consideration should be given to the design of the winding conductors and its axial clamping system or fixed supports to ensure the disc winding structural integrity.

## ACKNOWLEDGEMENTS

The authors thank Universiti Putra Malaysia for the funding under the Putra Grant Scheme, Inisiatif Putra Berkumpulan (GP- IPB/2022/9717000). The authors also express sincere appreciation to the TNB Labs Sdn. Bhd., Malaysia, for the technical support.

## REFERENCES

- Agrawal, K. C. (2001a). Surge arresters: Application and selection. In *Industrial Power Engineering Handbook* (Vol. 18, pp. 681-719). Butterworth-Heinemann. <https://doi.org/10.1016/b978-075067351-8/50096-9>
- Agrawal, K. C. (2001b). Voltage surges - Causes, effects and remedies. In *Industrial Power Engineering Handbook* (Vol. 17, pp. 555-585). Butterworth-Heinemann. <https://doi.org/10.1016/b978-075067351-8/50095-7>
- Ahn, H. M., Lee, J. Y., Kim, J. K., Oh, Y. H., Jung, S. Y., & Hahn, S. C. (2011). Finite-element analysis of short-circuit electromagnetic force in power transformer. *IEEE Transactions on Industry Applications*, 47(3), 1267-1272. <https://doi.org/10.1109/TIA.2011.2126031>
- Ahn, H. M., Oh, Y. H., Kim, J. K., Song, J. S., & Hahn, S. C. (2012). Experimental verification and finite element analysis of short-circuit electromagnetic force for dry-type transformer. *IEEE Transactions on Magnetics*, 48(2), 819-822. <https://doi.org/10.1109/TMAG.2011.2174212>
- Arivamudhan, M., & Santhi, S. (2019). Analysis of Mechanical integrity in power transformer using statistical techniques. In *2019 IEEE International Conference on Electrical, Computer and Communication Technologies (ICECCT)* (pp. 1-6). IEEE Publishing. <https://doi.org/10.1109/ICECCT.2019.8869152>
- Bagheri, M., Naderi, M., & Blackburn, T. (2012). Advanced transformer winding deformation diagnosis: Moving from off-line to on-line. *IEEE Transactions on Dielectrics and Electrical Insulation*, 19(6), 1860-1870. <https://doi.org/10.1109/TDEI.2012.6396941>

- Behjat, V., & Mahvi, M. (2015). Statistical approach for interpretation of power transformers frequency response analysis results. *IET Science, Measurement and Technology*, 9(3), 367-375. <https://doi.org/10.1049/iet-smt.2014.0097>
- Behjat, V., Shams, A., & Tamjidi, V. (2018). Characterization of power transformer electromagnetic forces affected by winding faults. *Journal of Operation and Automation in Power Engineering*, 6(1), 40-49. <https://doi.org/10.22098/joape.2018.2436.1210>
- Bhuyan, K., & Chatterjee, S. (2015). Electric stresses on transformer winding insulation under standard and non-standard impulse voltages. *Electric Power Systems Research*, 123, 40-47. <https://doi.org/10.1016/j.epsr.2015.01.019>
- Bjerkkan, E. (2005). High frequency modeling of power transformers - Stresses and Diagnostic (Doctoral dissertation). Norwegian University of Science and Technology, Norway. <https://ntnuopen.ntnu.no/ntnu-xmlui/handle/11250/256420>
- Da Costa Oliveira Rocha, A., Holdyk, A., Gustavsen, B., van Jaarsveld, B. J. Portillo, A., Badrazadeh, B., Roy, C., & Rahimpour, E. (2014). *Electrical Transient Interaction Between Transformer and the Power System, Part-2: Case studies*. CIGRE. <https://e-cigre.org/publication/577B-electrical-transient-interaction-between-transformers-and-the-power-system-part-2-case-studies>
- Dawood, K., Komurgoz, G., & Isik, F. (2019). Computation of the axial and radial forces in the windings of the power transformer. In *2019 4th International Conference on Power Electronics and their Applications (ICPEA)* (pp. 1-6). IEEE Publishing. <https://doi.org/10.1109/ICPEA1.2019.8911132>
- Dawood, K., Komurgoz, G., & Isik, F. (2020). Investigating the effect of axial displacement of transformer winding on the electromagnetic forces. In *2020 7th International Conference on Electrical and Electronics Engineering (ICEEE)* (pp. 360-364). IEEE Publishing. <https://doi.org/10.1109/ICEEE49618.2020.9102472>
- Faiz, J., Ebrahimi, B. M., & Abu-Elhajja, W. (2011). Computation of static and dynamic axial and radial forces on power transformer windings due to inrush and short circuit currents. In *2011 IEEE Jordan Conference on Applied Electrical Engineering and Computing Technologies (AEECT)* (pp. 1-8). IEEE Publishing. <https://doi.org/10.1109/AEECT.2011.6132487>
- Feyzi, M. R., & Sabahi, M. (2008). Finite element analyses of short circuit forces in power transformers with asymmetric conditions. In *2008 IEEE International Symposium on Industrial Electronics* (pp. 576-581). IEEE. <https://doi.org/10.1109/ISIE.2008.4677272>
- Florkowski, M., Furgał, J., & Kuniewski, M. (2020). Propagation of overvoltages in the form of impulse, chopped and oscillating waveforms in transformer windings - Time and frequency domain approach. *Energies*, 13(2), 1-17. <https://doi.org/10.3390/en13020304>
- Fonseca, W., Lima, D., Lima, A., Soeiro, N. S., & Nunes, M. V. A. (2016). Analysis of electromagnetic-mechanical stresses on the winding of a transformer under inrush currents conditions. *International Journal of Applied Electromagnetics and Mechanics*, 50(4), 511-524. <https://doi.org/10.3233/JAE-150044>
- Fonseca, W. S., Lima, D. S., Lima, A. K. F., Nunes, M. V. A., Bezerra, U. H., & Soeiro, N. S. (2018). Analysis of structural behavior of transformer's winding under inrush current conditions. *IEEE Transactions on Industry Applications*, 54(3), 2285-2294. <https://doi.org/10.1109/TIA.2018.2808273>

- Gutten, M., Ik, J. J. U. R. Č., Brandt, M., & Polansky, R. (2011). Mechanical effects of short-circuit currents analysis on autotransformer windings. *Electrical Engineering*, 87(7), 272-275. <http://pe.org.pl/articles/2011/7/62.pdf>
- Hodhigere, Y., S Jha, J., Tewari, A., & Mishra, S. (2018). Finite element analysis-based approach for stress concentration factor calculation. In *Proceedings of Fatigue, Durability and Fracture Mechanics* (pp. 1-6). Springer. <https://doi.org/10.1007/978-981-10-6002-1>
- Hussein, W. J., & Hameed, K. R. (2022). Finite-element calculation of electromagnetic forces in the deferent shapes of distribution transformers winding under short circuit condition. *Journal of Engineering and Sustainable Development*, 26(3), 44-61. <https://doi.org/10.31272/jeasd.26.3.6>
- Kojima, H., Miyata, H., Shida, S., & Okuyama, K. (1980). Buckling strength analysis of large power transformer winding subjected to electromagnetic force under short circuit. *IEEE Transactions on Power Apparatus and Systems*, PAS-99(3), 1288-1297. <https://doi.org/10.1109/TPAS.1980.319761>
- Massaro, U., & Antunes, R. (2009). Electrical transient interaction between transformers and power system - Brazilian experience. *International Conference on Power Systems Transients (IPST2009), Kyoto, Japan*, 3(6), 1-9. <http://www.ipst.org/techpapers/2009/papers/257.pdf>
- Meng, Z., & Wang, Z. (2004). The analysis of mechanical strength of HV winding using finite element method, part I calculation of electromagnetic forces. In *39th International Universities Power Engineering Conference (UPEC)* (Vol. 1, pp. 170-174). IEEE Publishing.
- Muminovic, A. J., Saric, I., & Repcic, N. (2015). Numerical analysis of stress concentration factors. *Procedia Engineering*, 100, 707-713. <https://doi.org/10.1016/j.proeng.2015.01.423>
- Murthy, A. S., Azis, N., Jasni, J., Othman, M. L., Yousof, M. F. M., & Talib, M. A. (2020). Extraction of winding parameters for 33 / 11 kV , 30 MVA transformer based on finite element method for frequency response modelling. *PLOS ONE*, 15(8), Article e0236409. <https://doi.org/10.1371/journal.pone.0236409>
- Nazari, A. (2013). Leakage fluxes and mechanical forces calculation on the single phase shell- type transformer winding under over currents by 2-D and 3-D finite element methods. *Journal of Electrical Engineering*, 13(4), 1-8.
- Nurmanova, V., Bagheri, M., Zollanvari, A., Aliakhmet, K., Akhmetov, Y., & Gharehpetian, G. B. (2019). A new transformer FRA measurement technique to reach smart interpretation for inter-disk faults. *IEEE Transactions on Power Delivery*, 34(4), 1508-1519. <https://doi.org/10.1109/TPWRD.2019.2909144>
- Ou, Q., Luo, L., Li, Y., Lin, Y., & Tian, Y. (2022). A dynamic relative displacement evaluation method for extra-high voltage transformer withstanding short-circuit impact. *IET Generation, Transmission & Distribution*, 17(6), 1310-1320. <https://doi.org/10.1049/gtd2.12736>
- Rao, M. A., Khanna, M. R., Somaiya, K. J., & Gangopadhyay, M. (2012). Applications of finite elements method (FEM) - An overview. *International Conference on Mathematical Sciences*, 28(31), 1-8. <https://doi.org/10.13140/RG.2.2.36294.42565>
- Rao, S. S. (2005). Overview of finite element method. In *The Finite Element Method in Engineering* (pp. 3-45). Elsevier. <https://doi.org/10.1016/B978-0-7506-7828-5.X5000-8>



- Ren, M., Zhang, C., Dong, M., Ye, R., & Albarracín, R. (2016). A new switching impulse generator based on transformer boosting and insulated gate bipolar transistor trigger control. *Energies*, *9*(644), 1-15. <https://doi.org/10.3390/en9080644>
- Tahir, M., & Tenbohlen, S. (2019). A comprehensive analysis of windings electrical and mechanical faults using a high-frequency model. *Energies*, *13*(1), Article 105. <https://doi.org/10.3390/en13010105>
- Tenbohlen, S., Jagers, J., & Vahidi, F. (2017). Standardized survey of transformer reliability: On behalf of CIGRE WG A2.37. In *2017 International Symposium on Electrical Insulating Materials (ISEIM)* (Vol. 2, pp. 593-596). IEEE Publishing. <https://doi.org/10.23919/ISEIM.2017.8166559>
- Tenbohlen, S., Vahidi, F., & Jagers, J. (2016). A worldwide transformer reliability survey. In *VDE High Voltage Technology 2016; ETG-Symposium* (pp. 1-6). VDE. <https://ieeexplore.ieee.org/document/7776092>
- van Jaarsveld, B. J. (2013). *Wide Band Modelling of An Air-Core Power Transformer Winding* (Master dissertation). Stellenbosch University, South Africa. <http://scholar.sun.ac.za/handle/10019.1/85823>
- Yan, X., Yu, X., Shen, M., Xie, D., Bai, B., & Wang, Y. (2016). Calculation of stray losses in power transformer structural parts using finite element method combined with analytical method. In *2015 18th International Conference on Electrical Machines and Systems (ICEMS)* (pp. 320-324). IEEE Publishing. <https://doi.org/10.1109/ICEMS.2015.7385051>
- Yasid, N. F. M., Azis, N., Yousof, M. F. M., Jasni, J., Talib, M. A., & Murthy, A. S. (2023). Electromagnetic force distribution computations due to switching surge in disc-type winding. *Indonesian Journal of Electrical Engineering and Computer Science*, *30*(2), 659-669. <https://doi.org/10.11591/ijeecs.v30.i2.pp659-669>
- Yutthagowith, P. (2022). An accurate evaluation of switching impulse voltages for high-voltage tests. *Energies*, *15*(4760), 1-10. <https://doi.org/https://doi.org/10.3390/en15134760>
- Zhang, C., Ge, W., Xie, Y. L., & Li, Y. (2021). Comprehensive Analysis of winding electromagnetic force and deformation during no-load closing and short-circuiting of power transformers. *IEEE Access*, *9*, 73335-73345. <https://doi.org/10.1109/ACCESS.2021.3068054>
- Zhang, H., Yang, B., Xu, W., Wang, S., Wang, G., Huangfu, Y., & Zhang, J. (2014). Dynamic deformation analysis of power transformer windings in short-circuit fault by FEM. *IEEE Transactions on Applied Superconductivity*, *24*(3), 5-8. <https://doi.org/10.1109/TASC.2013.2285335>



# Integrating Fuzzy Logic and Brute Force Algorithm in Optimizing Energy Management Systems for Battery Electric Vehicles

**Abdulhadi Abdulsalam Abulifa, Azura Che Soh\*, Mohd Khair Hassan, Raja Kamil and Mohd Amran Mohd Radzi**

*Department of Electrical and Electronic Engineering, Faculty of Engineering, Universiti Putra Malaysia, 43400 UPM, Serdang, Selangor, Malaysia*

## ABSTRACT

The limited driving range of BEVs is the main challenge in developing zero-emission Battery Electric Vehicles (BEVs) to replace traditional fuel-based vehicles. This limitation necessitates an increase in battery energy while balancing the power supply and consumption requirements for the vehicle's motor and auxiliaries, such as the Heating, Ventilation, and Air Conditioning (HVAC) system. This research proposes a solution to achieve more efficient control of HVAC consumption by integrating fuzzy logic techniques with brute-force algorithms to optimize the Energy Management System (EMS) in BEVs. The model was based on actual parameters, implemented using MATLAB-Simulink and ADVISOR software, and configured using a backward-facing design incorporating the technical specifications of a Malaysian electric car, the PROTON IRIZ. An optimal solution was proposed based on the Satisfaction Ratio (SR) and State of Charge (SoC) metrics to achieve the best system optimization. The results demonstrate that the optimized fuzzy EMS improved power consumption by 23.2% to 26.6% compared to a basic fuzzy EMS. The proposed solution significantly improves the driving range of BEVs.

*Keywords:* Battery electric vehicle, brute-force algorithm, energy management system, fuzzy logic, satisfaction ratio, state of charge

## ARTICLE INFO

### *Article history:*

Received: 10 May 2023

Accepted: 12 September 2023

Published: 26 March 2024

DOI: <https://doi.org/10.47836/pjst.32.2.17>

### *E-mail addresses:*

aaabulifa@gmail.com (Abdulhadi Abdulsalam Abulifa)

azuracs@upm.edu.my (Azura Che Soh)

khair@upm.edu.my (Mohd Khair Hassan)

kamil@upm.edu.my (Raja Kamil)

amranmr@upm.edu.my (Mohd Amran Mohd Radzi)

\* Corresponding author

## INTRODUCTION

An Electric Vehicle (EV) is a car that uses a minimum of one electric-powered motor rather than the traditional combustion engine. It is a second-hand innovation since this idea has existed since the mid-1800s.

Although the enthusiasm for this technology was strong during the 20<sup>th</sup> century, the demand for longer-range vehicles, the lower cost of gas, the invention of the power starter in standard cars, and the beginning of the mass development of internal burning EVs have reduced the attention on EVs until the start of the 21<sup>st</sup> century (Termiz, 2015).

The environmental issues caused by traditional transportation and increasing oil prices have revived the passion for power vehicles in recent years (Eberle & von Helmolt, 2010; Termiz, 2015). Due to pollution caused by conventional vehicles, fume emissions and the scarcity of fossil fuels, there has been much interest in the work on sustainable transportation, such as Hybrid Electric Vehicles (HEVs) (Han et al., 2018; Zhang et al., 2017) and Plug-in Hybrid Electric Vehicles (PHEVs) (Hassanzadeh & Rahmani, 2022) that can reduce the carbon impacts but are unable to remove them completely. A BEV is powered entirely on electric electricity, normally a huge electric motor and a huge battery pack, consisting of a DC-DC converter and transmission, driving cycle, and longitudinal vehicle dynamic model. Pure electric motor vehicle is a type of EV that makes use of chemical power saved in rechargeable battery packs. BEVs use electric motors and motor operators instead of internal combustion engines (ICEs) for power.

BEVs present an eco-friendly solution with exceptional drivetrain performance and energy efficiency, and the trade-off is the restricted driving range attributed to limitations in battery capacity and volume. The situation becomes more intricate with the rise in power requirements and the inclusion of multiple electrical loads due to the electrification of transportation. For BEVs that rely solely on batteries as their energy storage and need to cater to numerous loads, the challenge lies in alleviating range anxiety by devising stringent control rules and a management strategy that can effectively extend the driving range (Dou et al., 2021; Hu et al., 2020; Mohd, 2020).

An Energy Management System (EMS) is a computer-supported device utilized by drivers of electrical frameworks to manage and optimize the efficiency of transmission systems. The EMS needs to be maximized to enhance its performance and battery efficiency, as well as to increase the travel distance for Battery Electric Vehicles (BEVs) and maintain driver confidence. To improve the performance of the EMS, artificial intelligence (AI) techniques have been rapidly evolving, particularly in the field of EMS (Hussain et al., 2019; Górriz et al., 2020; Pan et al., 2021; Mohd, 2020). Their revolutionary applications provide efficient control strategies that increase the capabilities, efficiency, and accuracy of EMS, as well as reduce EVs' energy consumption. Hence comes the need for AI approaches in energy management to provide a battery power supply that fulfills power consumption for motors and auxiliaries such as heating, ventilation, and air conditioning systems (HVAC). Applying EMS is one of the AI approaches that can reallocate the electrical power flow inside the HVAC system to boost power efficiency and obtain optimum effectiveness. Therefore, this research is focused on the energy consumption of BEVs by developing

optimization algorithms based on fuzzy logic techniques to apply the best solution in EMS. Such innovative AI solutions can enhance the efficiency of smart EMS in BEVs as the future sustainable transportation.

The main aim of this study was to develop an optimal fuzzy logic control system algorithm for the energy management of an autonomous EV system. Thus, the proposed system employed an algorithm based on the optimal-fuzzy method. The structure and parameters of optimal-fuzzy were tuned using a brute-force heuristic algorithm as the optimization method. The brute force algorithm has been successfully used as an optimization technique in other applications, and it is the best learning method based on a set of small number of inputs and outputs (Pham & Månsson, 2018). However, no previous studies have used brute force with fuzzy logic techniques to find the best solution or set a strategy EMS for BEVs. Therefore, the brute-force algorithm has been chosen to integrate with the fuzzy controller because the algorithm is the best optimization for the system when involving a small number of inputs-outputs, and also, the system is not working continuously. This technique finds the best solution from a wide range of measures, where the decision is based on two or more variables. Hence, the optimized controller would be able to provide an appropriate energy supply to each auxiliary EV component, along with a significant improvement in its travel range.

## METHODS

This simulation-based study was conducted to develop improvements for the existing system using experimental simulation. Several computerized tools were used to simulate the desired system. Among the numerous vehicle modeling and analysis platforms, MATLAB/Simulink, integrating the ADVISOR library, is the most widely used platform in academic studies of mechanical engineering simulations (Tammi et al., 2018). Therefore, in this study, the simulations were based on the ADVISOR library integrated within the MATLAB/Simulink system.

The main aim of this study was to develop an optimal fuzzy logic control system for the energy management of an autonomous EV system. Thus, the proposed system employed an algorithm based on the optimal-fuzzy method. The structure and parameters of optimal-fuzzy were tuned using a brute-force heuristic algorithm as the optimization method. Hence, the optimized controller would be able to provide an appropriate energy supply to each auxiliary EV component, along with a significant improvement in its travel range.

### Design of Battery Electric Vehicle Basic System

The simulation model comprises five key components that work together to provide a comprehensive view of the electric vehicle's performance, as shown in Figure 1. These components are:

1. The driving cycle represents the pattern of acceleration and deceleration of the vehicle over time. It is an important input for the simulation as it determines the power required from the electric motor and the energy required from the battery.
2. The electric motor model models the behavior of the electric motor in response to the power demand from the driving cycle. It takes into account the motor efficiency, torque-speed characteristics, and other parameters.
3. The transmission model models the behavior of the transmission system that delivers the power from the electric motor to the wheels. It takes into account the gear ratios and the efficiency of the transmission system.
4. The battery charge controller model with the DC-DC converter models the behavior of the battery charge controller and the DC-DC converter that regulates the voltage and current flow between the battery and the electric motor.
5. The longitudinal vehicle dynamics model models the behavior of the vehicle in terms of its acceleration, speed, and distance traveled, taking into account the driving cycle, electric motor model, transmission model, and battery charge controller model.

The simulation employs a backward-facing model, which forecasts the vehicle's behavior by considering the input driving cycle and the behavior of its components. The model operates without the need for a driver, requiring the user to only input the driving pattern or velocity profile.

It is essential to have comprehensive knowledge of all relevant technical specifications to ensure the accurate utilization and optimization of the batteries. Therefore, in selecting

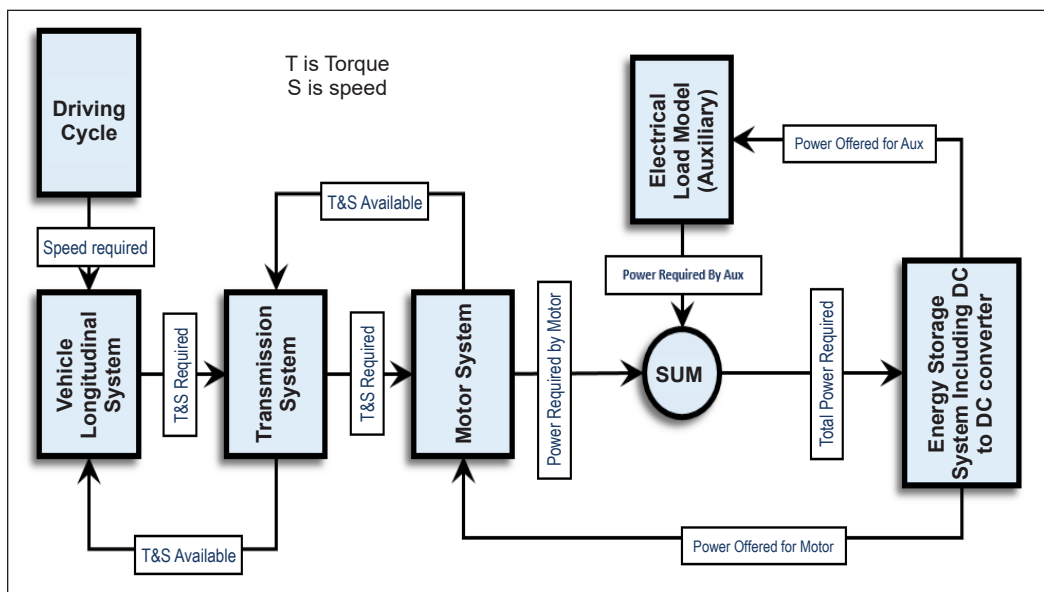


Figure 1. Block diagram of BEV system components based on a backward-facing model

the most suitable battery for the modeled EV, the technical specifications of the LG-PROTON IRIZ BEV were utilized (Table 1).

### Auxiliary Electric Load Model

Valentina et al. (2014) stated that the major challenges with EVs are the driving range and battery lifetime. The performance and efficiency of EVs need to be optimized, and consumption needs to be reduced to mitigate these problems. In order to achieve these objectives and to insert the configurable subsystems of this study, the Auxiliary Electric Load Model was added to the basic BEV model. The following Equation 1 provides an example of the typical auxiliary load:

$$AUX = HVAC + HS + SS + CS + SN \tag{1}$$

where AUX = auxiliary load; HVAC = heat, ventilation, and air conditioning; HS = heated seats; SS = sound system; CS = camera system; and SN = satellite navigation.

This study considered the Heating, Ventilation, and Air Conditioning (HVAC) system and Heated Seat (HS) because EVs have the largest auxiliary power loads. As part of the auxiliary components of cars nowadays, the HVAC and HS units may significantly deplete the energy from the battery, depending on the vehicle’s settings. If heated seats are used, as required in some European countries, energy depletion would increase even more.

The auxiliary loads in EVs, such as heating, air conditioner, sound system, and satellite navigation, use electrical energy from batteries, reducing the vehicle’s driving range. Some of these loads are considered very important. Controlling the auxiliary loads can improve the total fuel consumption without decreasing the energy consumption of the auxiliary system.

### Design of BEV with Optimal Fuzzy Logic Energy Management System

In this study, a designed fuzzy logic strategy was integrated into the EMS to improve battery power capacity utilization. The EMS system is characterized by a simple black box design and features SoC and Speed inputs. Additionally, it had three outputs, namely Heated Seats (HS), Front HVAC, and Rear HVAC, as illustrated in Figure 2.

Table 1  
*Technical specification for LG-PROTON IRIZ BEV*

Drivetrain Parameters	
Drive System	Front-wheel drive
Curb Weight	918 kg
Adds weight (Cargo)	56 kg
Gross Weight	1516 kg
Wheel/Axe	Front Wheel Drive 195/55R15 (Standard)
Accessories	Variable ACC_Small_Car
Powertrain	EV – Manual – PTC_EV
Rated Voltage	330 V
Rated Capacity	39.6 kWh, 120 Ah
Rated Lifetime	10 years \ 160,000 km
Motor Type	PMAC (YASA-400)
Max Output	116 kW
Max Torque	360 Nm
Transmission	Single Speed 3.37:1
Normal Voltage	330 V
Total Cells	360 Cells
Total Weight	540 kg

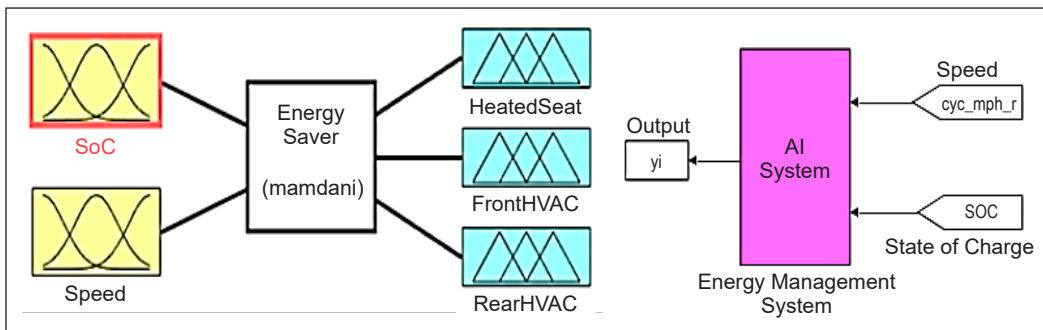


Figure 2. EMS with the fuzzy logic controller

In order to achieve optimal load consumption for the desired HVAC components, the controller was driven by the following two inputs:

- The SoC represents the remaining capacity of the power storage system, scaled as a percentage fraction ranging from 0 to 100. This input is important because it helps the controller determine how much energy is available for use by the HVAC components. By monitoring the SoC, the controller can adjust the load consumption of the HVAC components to ensure that they are not consuming more energy than is available in the power storage system.
- The speed of the vehicle is also an important input for the controller because it helps to determine the energy requirements of the HVAC components. As the speed of the vehicle increases, the energy requirements of the HVAC components also increase. Therefore, by monitoring the speed of the vehicle, the controller can adjust the load consumption of the HVAC components to ensure that they are not consuming more energy than is required for the given speed.

By combining the SoC and Speed inputs, the controller can adjust the HVAC load consumption in real-time to ensure maximum efficiency while maintaining the occupants' comfort. This approach helps to reduce energy consumption and extend the range of electric vehicles, leading to lower operating costs and a more sustainable mode of transportation. Based on the desired HVAC components provided, the output required would be three separate values, each representing the power consumption of the individual components. The three components are:

- Front HVAC: The main HVAC system facilitates the driver and is measured in watts. The power consumption of this component is assumed to be a fixed load of 1,000 watts.
- Rear HVAC: It is also the main HVAC system that facilitates the passengers instead of the driver. Similar to the front HVAC, the power consumption of this component is assumed to be a fixed load of 1,000 watts.
- Heated Seat (HS): This component represents the auxiliary seat heating in modern



vehicles and is used to facilitate the driver. The power consumption of this component is also assumed to be a fixed load of 1,000 watts.

Therefore, to provide the required output, the power consumption of each of these components needs to be calculated and expressed in watts. It is important to note that these power consumption values are based on assumptions, and actual power consumption may vary based on factors such as vehicle make and model, environmental conditions, and usage patterns. Each input and output variable has three linguistic levels, low, medium, and high, represented as membership functions. This study used a triangular shape encoded by three points (Le, He, and Re). The fuzzy logic rules were designed to depend on these values. The values calculated using the fuzzy logic for the standards of the inputs and outputs are listed in Table 2.

The rules were set based on real situations by considering different levels of real speed inside cities, highways, and mixed situations. The rules have also considered real SoCs at different levels. Moreover, the rules also considered the largest auxiliary power load in electric vehicles (EVs): the HVAC system and HS. The following rules of the fuzzy logic strategy, as produced by the software, were implemented:

1. If {(SoC is high)} and (Speed is low)} then {(HS is high) and (Front HVAC is high) and (Rear HVAC is high)}
2. If {(SoC is high)} and (Speed is medium) then {(HS is high) and (Front HVAC is high) and (Rear HVAC is high)}
3. If {(SoC is high)} and (Speed is high) then {(HS is medium) and (Front HVAC is medium) and (Rear HVAC is medium)}
4. If {(SoC is medium)} and (Speed is low) then {(HS is medium) and (Front HVAC is medium) and (Rear HVAC is medium)}
5. If {(SoC is medium)} and (Speed is medium) then {(HS is medium) and (Front HVAC is medium) and (Rear HVAC is medium)}

Table 2  
*Inputs and outputs for the membership functions*

Input		Output		
SoC Status	Speed Status	HS	Front HVAC	Rear HVAC
High	Low	High	High	High
High	Medium	High	High	High
High	High	Medium	Medium	Medium
Medium	Low	Medium	Medium	Medium
Medium	Medium	Medium	Medium	Medium
Medium	High	Low	Low	Low
Low	Low	Low	Low	Low
Low	Medium	Low	Low	Low
Low	High	Low	Low	Low

6. If {(SoC is medium)} and (Speed is high) then {(HS is low) and (Front HVAC is low) and (Rear HVAC is low)}
7. If {(SoC is low)} and (Speed is low) then {(HS is low) and (Front HVAC is low) and (Rear HVAC is low)}
8. If {(SoC is low)} and (Speed is medium) then {(HS is low) and (Front HVAC is low) and (Rear HVAC is low)}
9. If {(SoC is low)} and (Speed is high) then {(HS is low) and (Front HVAC is low) and (Rear HVAC is low)}

The goal of conducting optimization was to reduce energy consumption and extend the SoC range. Figure 3 shows the block functional design of the proposed system. This solution was based on the brute force function, which used the optimization algorithm to find the best solution from a wide range of measures. In this case, the decision can be made based on two or more conflicting measures, the SoC and the Satisfaction Ratio (SR).

The fuzzy system was built to preserve the energy level for longer. This aim was achieved by limiting the consumption of energy based on the current level of SoC and speed, which is supposed to consume more energy in an EV. However, there is an implicit relationship between the fuzzy system and the SR. More specifically, the positioning of the edges of the membership function in the fuzzy was vital in changing both SR and SoC. Therefore, the fuzzy logic was added with an optimization algorithm that simultaneously optimizes both measures. The optimization of two variables can be done by finding the Pareto front.

Figure 4 shows the flowchart of the fuzzy controller during the brute force mode. The idea was that the system would try different configurations of membership functions. The SR was memorized for every configuration, and the system continued to change the configuration with every new SoC cycle until it ended with all possible configurations. The system used the brute force algorithm from the memorized SR scores to find the optimal value sent to the controller to recalibrate the membership function. The brute-force algorithm was working offline to choose the best solutions for the membership function based on historically memorized scores of SoC and SR. Thus, this step needed to be done just once at the beginning.

Brute force is a searching algorithm for all possible solutions in the solution space. The brute force approach is to divide the solution space into small partitions. The solution space was defined by nine variables (Equation 2) because the study involves three variables, each with three membership functions. For every variable, one point needed to be changed. Table 3 shows the logic of the solution, in which every alternative solution is a function of these variables.

$$\text{Any solution } X = [x_1 \ x_2 \ x_3 \ x_4 \ x_5 \ x_6 \ x_7 \ x_8 \ x_9] \in [0 \ 1]^9 \quad (2)$$

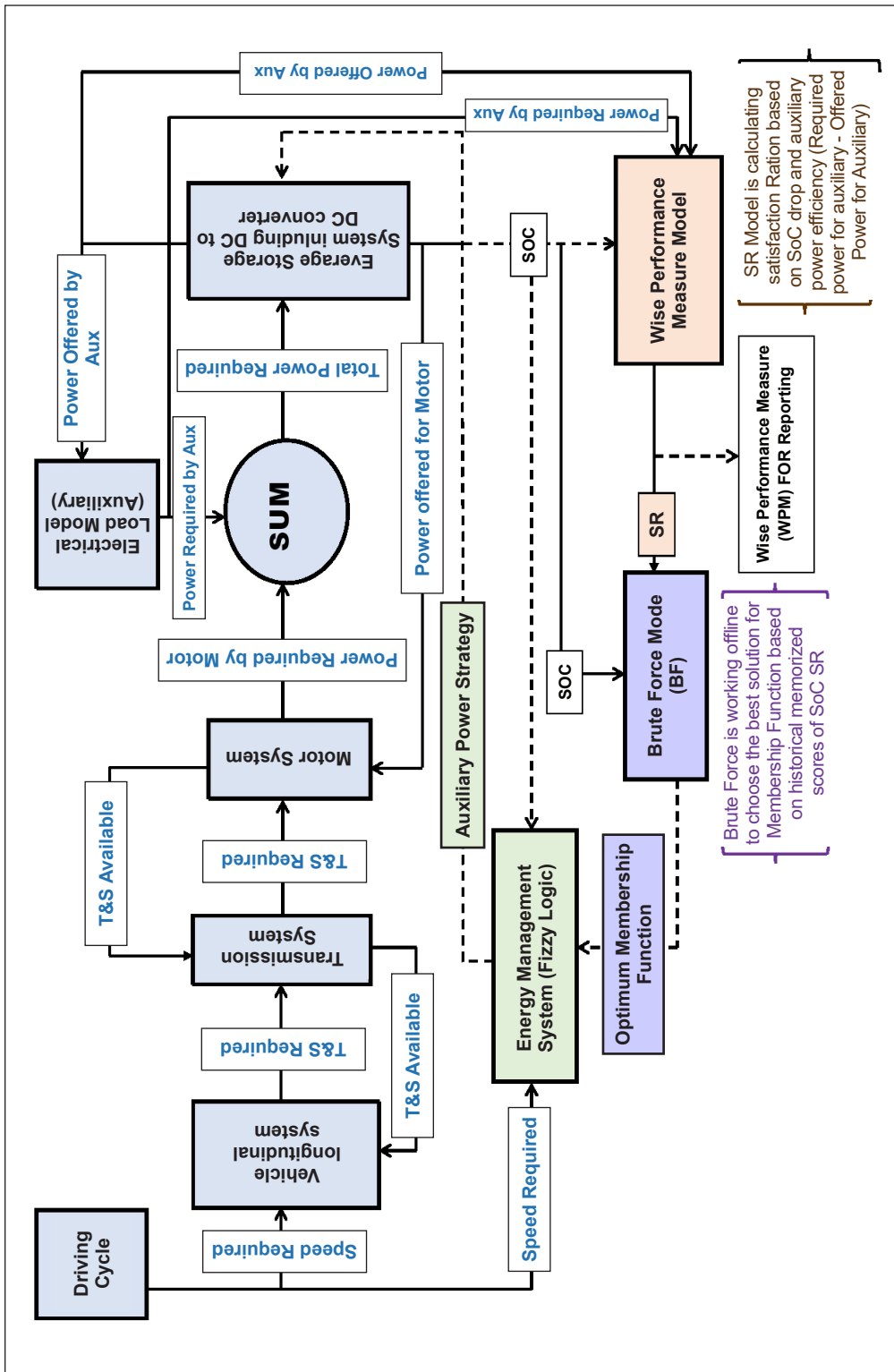


Figure 3. Design of the BEV with optimal fuzzy system

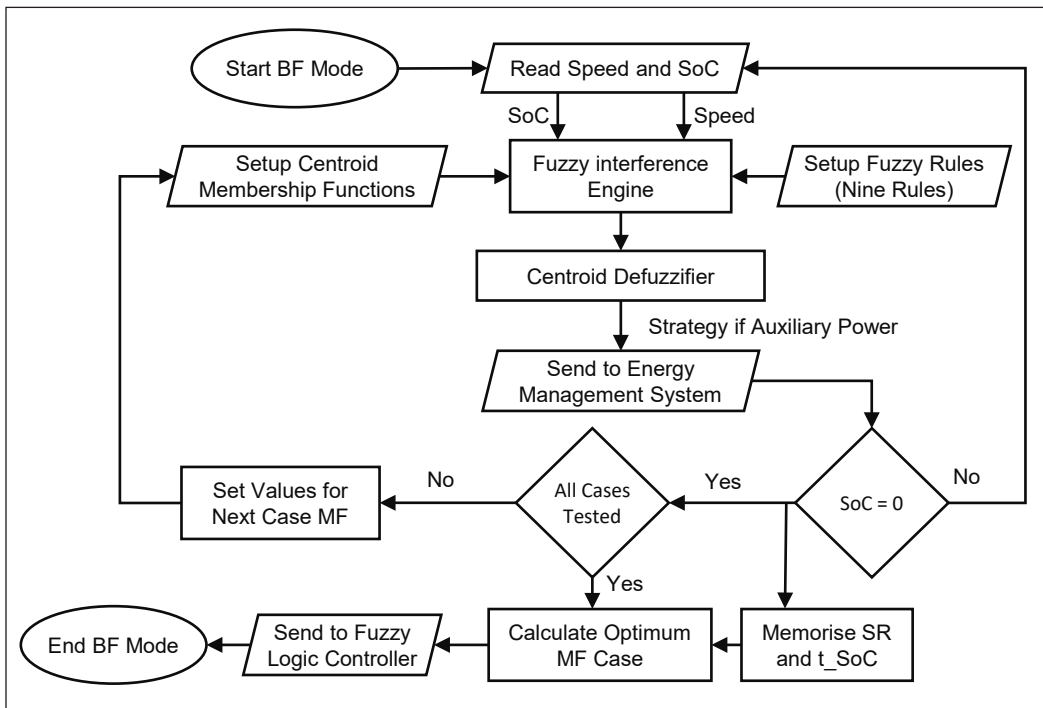


Figure 4. Optimal fuzzy logic flowchart

Table 3  
Logic for the solutions in the brute force algorithm

Solution	Dimension	Meaning
X	1 × 9	The solution defined the points as 1, 2, and 3 for every variable (two inputs and one output), which meant there were nine points in total

The process of the brute force logic solution is described as follows:

- The brute force is supposed to generate all possible X values and call the solution decoder.
- The search gave every value of  $x_i$  one of four possible values (0, 0.3, 0.6, or 0.9), which meant the size of the solution space was 262,144 (four values × nine membership functions).
- The set of all possible cases was labeled as X. Each solution consisted of two objective values: the first one was the time when SoC was zero, and the second one was SR. However, these two solutions were the opposite because the maximization of one will minimize the other when the objective was to maximize both, as shown in the example solution in Figure 5.
- The results became the final set of non-dominated solutions, known as the Pareto front.

Figure 5 shows one sample solution among the 262,144 solutions obtained. Higher satisfaction was shown to be equivalent to lower SoC and vice versa. The nature of the problem was to achieve multi-objective optimization, with conflict between the two objectives. The optimization solution that met certain required modes was extracted from the brute force results: maximum SoC was more economical, while maximum SR was more comfortable. The relationship between the SoC and the SR was conflicting. Consequently, the solutions were also conflicted because maximizing one, minimizes the other.

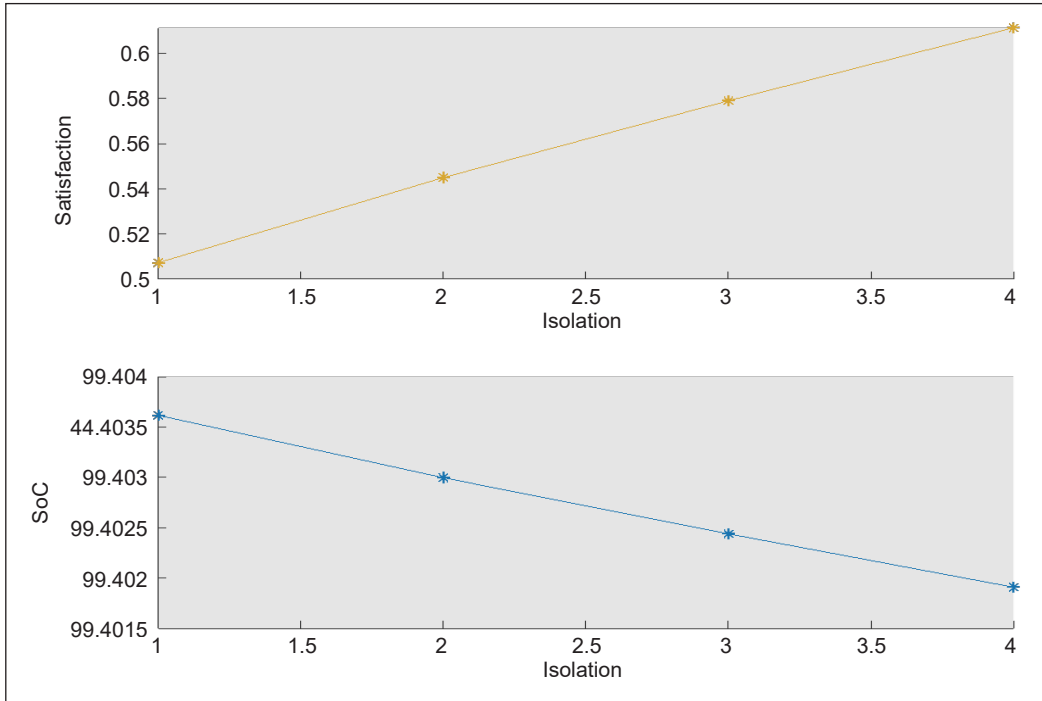


Figure 5. A subset of the solutions to show the conflicting nature between SR and SoC (one sample solution out of 262,144 solutions)

### Evaluation Performances of Energy Management System

This research aims to provide a solution to improve the driving range of EVs by keeping an acceptable level of comfort for the driving experience. The SoC refers to the energy stored in a battery or other power source at a given time. The efficiency of the SoC of the battery can be determined using the calculated current. The model used Coulombic Efficiency (CE) and optimal capability values, which are functions of temperature, to calculate the recurring battery ability in systems of ampere-hours (Ah). SoC estimation can be made using the following Equation 3:

$$SoC = \frac{(Ah_{mx\ capacity} - Ah_{used\ capacity})}{Ah_{mx\ capacity}} \tag{3}$$

where SoC is the State of Charge,  $Ah_{mx \text{ capacity}}$  is the maximum power of the battery in ampere-hours, and  $Ah_{used \text{ capacity}}$  is the used power in ampere-hours.

The drain of the State of Charge (dSoC) refers to the rate at which energy is depleted from the battery or power source. A higher drain rate in electric vehicles or other battery-powered systems can lead to reduced efficiency and shorter driving ranges, as the battery would need to be recharged more frequently. Therefore, a threshold value of 0.005 (0.5%) suggests that the researchers were concerned about the efficiency of the system and were likely investigating the power consumption and efficiency of an electric vehicle or a similar system. The fact that the study was interested in understanding the impact of different driving conditions further supports the idea that the researchers were investigating the power consumption and efficiency of an electric vehicle. Different driving conditions, such as varying speeds and terrains, can have a significant impact on the power consumption and efficiency of an electric vehicle, so studying these factors can help to optimize the design and performance of such systems.

The driving cycle(speed) is a collection of information embodying the speed of a vehicle versus time. Different nations and companies have created driving cycles to assess the functionality of cars in several ways, for instance, gas usage and pollution discharges for all auto types inside or even outside urban areas (highways). A driving cycle holds regular records offered in ADVISOR and is managed as a 2-D research table listed through Speed and Time. The driving cycles are used to test the gas economic condition and efficiency of vehicles. Moreover, the speed range of driving cycles amounted to scores from 0 to max speed in km/h based on the type of driving cycles (Giakoumis, 2017).

In this research, the thresholds for SR were set at 50%, depending on the weather in Malaysia. For example, when the weather is very hot, the driver would not use all electrical accessories, such as the heated seats. Moreover, if the driver is in a country with cold weather, the driver would not use the air conditioner. Thus, the SR is a flexible value that can be increased or decreased depending on the situation. The SR is presented in Equation 4:

$$SR = 1 - \frac{|y_{id} - y_i|}{y_{id}} \quad (4)$$

where  $y_{id}$  denotes the desired load from the user,  $y_i$  denotes the actual load from the controller, and  $|y_{id} - y_i|$  denotes the absolute value of the mean of the difference between the desired and the actual energy.

### Wise Performance Measurement (WPM)

The study also introduces a new metric called the Wise Performance Measure (WPM) to balance the energy requirements of SoC and auxiliaries. It is accomplished by setting threshold levels for SoC drop and SR and then tracking any breaches of these thresholds at regular intervals.

The new measure aims to evaluate two aspects of EV driving. The first aspect was to save the energy of the battery while driving, and the second was to satisfy the driver’s desire for energy for the usage of accessories. Thus, the new measure was developed as a combination of both SoC and SR while driving. The standard of WPM was developed based on the SoC and SR; thus, the lower the value of WPM, the better. The new measure can be calculated as follows, and as shown in Figure 6:

1. The whole-time interval of the drive is divided into sub-intervals,  $\Delta T$ , where each sub-interval expresses a part of the time that requires a lower level of SoC saving and SR
2. An accumulator of  $A = 0$  was initiated, with  $A$  denoting the WPM
3. Each  $\Delta T$  would find a two-time series of  $\frac{dSoC}{dt}$ , and the second was SR
  - Compared  $\frac{dSoC}{dt}$  with a threshold,  $T_{SoC}$ , where the value of  $\frac{dSoC}{dt}$  has to be higher than  $T_{SoC}$ 
    - $\frac{dSoC}{dt} > T_{SoC}$ , if the condition is not applied, then  $A = A + 1$ ; otherwise,  $A$  is kept without a change
  - Compared SR with a threshold,  $T_{SR}$ , where the value of SR has to be higher than  $T_{SR}$ 
    - $SR > T_{SR}$ , if the condition is not applied, then  $A = A + 1$ ; otherwise,  $A$  is kept without a change
4. At the end of the experiment, the value of  $A$  would indicate how many times the condition was not applied. Thus, the goal would be to minimize  $A$ . The improved performance would be equivalent to a lower value of  $A$ .

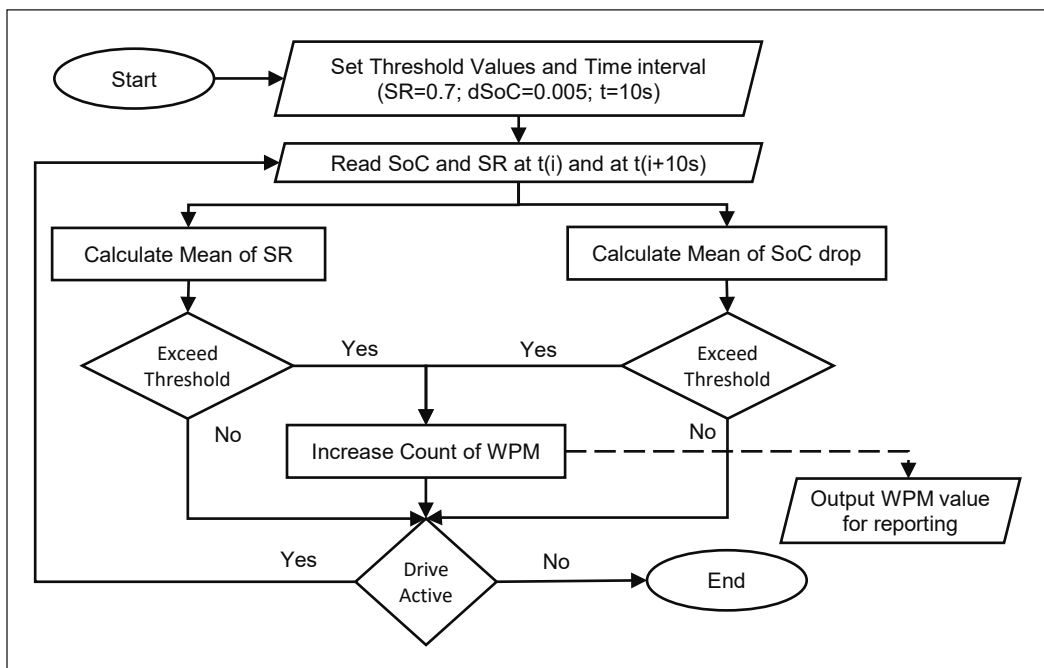


Figure 6. WPM calculator flowchart

As shown in Equation 4, this study selected  $T_{SR} = 0.5$ , which means that the SR has to be at least 50%. Two experiments were conducted to calculate  $T_{SoC}$ : (1) without a load and (2) with a full load. The entire SoC was recorded for both experiments. Subsequently, this study identified the threshold as a new time series that indicates a 50% slope between SoC1 and SoC2. Based on this observation, the drain of the SoC must remain below the threshold value of 0.005 (0.5%) at any time interval. In this research, the threshold for draining the SoC (dSoC) was set at 0.5%, depending on the changes in driving cycle time. All parameters were measured at different stages. The SoC and speed (driving cycle) were measured during the developmental stage of the Fuzzy Logic Controller (FLC), as they were inputs for the FLC. The SR and WPM were measured during the developmental stage of the Brute Force (BF) method. The SR was one of the inputs for BF and one of the outputs for WPM.

## RESULTS AND DISCUSSION

The optimal fuzzy controller of this study is an adaptive version of the traditional fuzzy logic by integrating another technique to reconfigure the fuzzy membership function based on calculating the different SRs and SoC in different conditions and then deciding the best configuration. The simulation is based on three driving cycles: The New European Driving Cycle (NEDC), the Urban Dynamometer Driving Schedule (UDDS) and the Japanese 10-15 Mode Driving Cycle (Japan 10-15).

Based on the results presented in Figure 7, it can be concluded that the model using a fuzzy logic controller and optimization by brute-force algorithm for the NEDC with a maximum accumulative load of 3000W for the HVAC system has a better range than the other models. The achieved SoC of 25605 seconds corresponds to a full trip distance of 238.9 km, which is better than the range achieved by the basic model with a load for the NEDC, which is about 193.9 km, and the basic fuzzy logic model, which is about 216.6 km as shown in Table 4.

Moreover, the 100% range for NEDC is also 238.9 km, while the 80% range is 191.1 km. It indicates that the proposed model can achieve a longer range, which can benefit electric vehicles in terms of usability and practicality. In summary, the model with a fuzzy logic controller and optimization by brute-force algorithm for the NEDC with a maximum accumulative load of 3000W for the HVAC system has shown to be more effective in terms of range performance and can be a useful tool for improving the overall performance of electric vehicles.

In Figure 8, the actual SR achieved by the model using FLC and optimization by brute force is higher than the assumed limit, indicating that the driver is more satisfied with the driving range provided by the model. The dSoC is relatively low, indicating that the battery performs efficiently during the driving cycle. Overall, these results suggest that the model



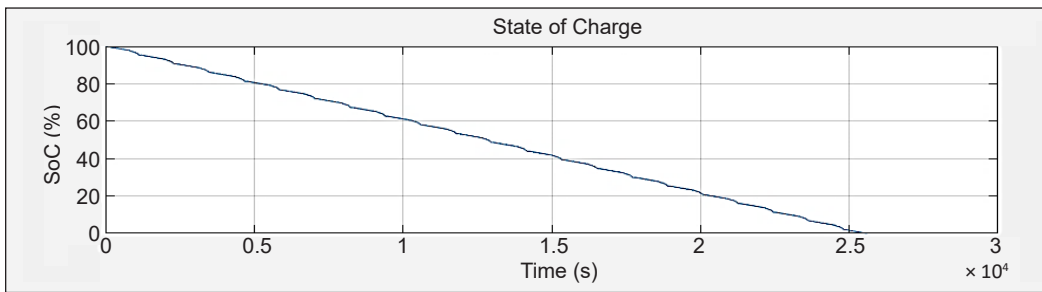


Figure 7. SoC for BEV using NDEC

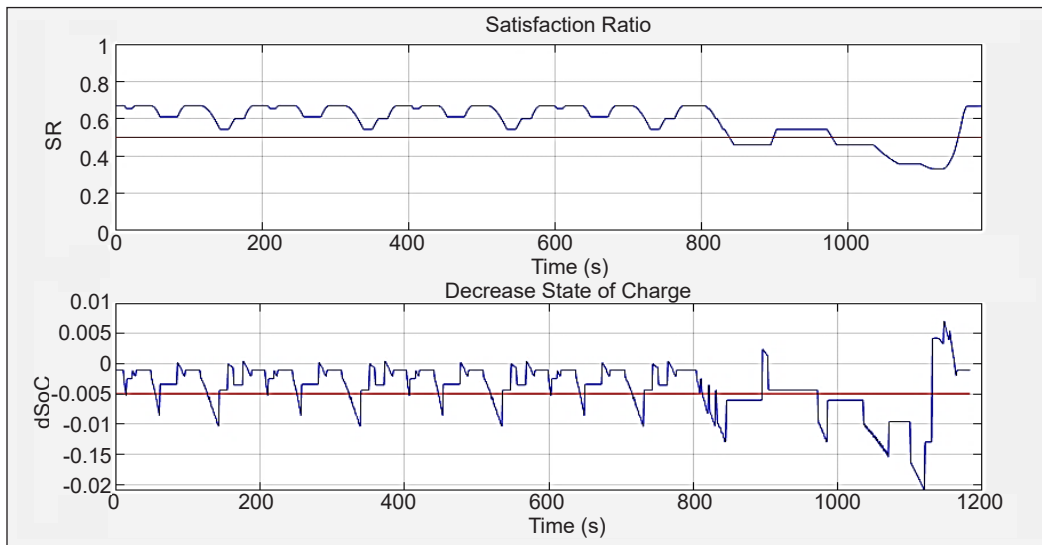


Figure 8. SR and dSoC for BEV using NDEC

using FLC and optimization by brute-force algorithm effectively improves both battery range and driver satisfaction.

Based on the results presented in Figures 9 and 10, it can be concluded that the BEV model using FLC and optimization by brute-force algorithm for the UDDS with a load has a better range compared to the basic model with load and the basic fuzzy model with load. The achieved SoC of 26058 seconds corresponds to 247.5 km for the full trip, which is better than the range achieved by the basic model with a load of about 200 km and the basic fuzzy model with a load of about 223 km, as shown in Table 4. Additionally, dSoC is relatively low and maintained in the threshold range. It indicates that the battery is performing efficiently and is able to maintain a stable state of charge throughout the cycle.

It is important to note that the distance traveled may vary depending on various factors, such as driving conditions, terrain, and temperature. The study also shows that the 100% range for the UDDS is 247.5 km, and the 80% range for UDDS is 198 km. The results

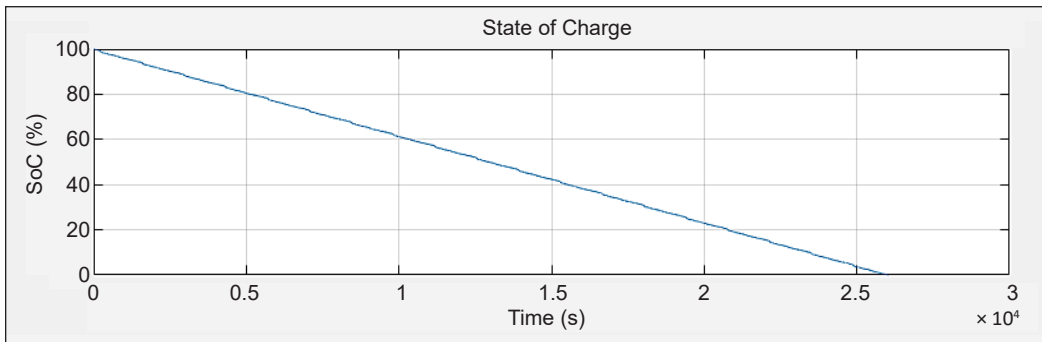


Figure 9. SoC for BEV using UDDS

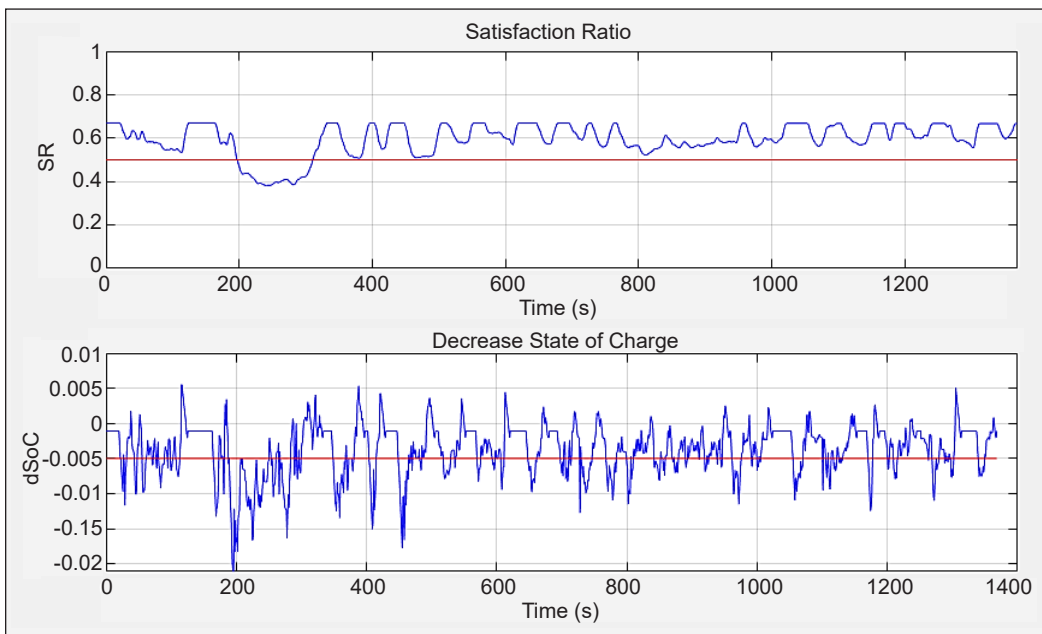


Figure 10. SR and dSoC for BEV using UDDS

show that the FLC and optimization by brute-force algorithm could potentially improve the range of the BEV model, which could be valuable information for developing more efficient and effective electric vehicles.

Figures 11 and 12 show the results of the BEV model using FLC and optimization by brute-force algorithm for the Japan 10-15 driving cycle mode with a load of about 3000 W for the HVAC system. The study reports that the SoC lasted for 32574 seconds, equivalent to 205.3 km for the full trip. A low and stable dSoC during a driving cycle is a positive sign for battery performance. It is important for the reliability and longevity of the battery, as well as for the performance of the vehicle that relies on it for power. A low and stable dSoC is a good indicator of efficient battery performance.

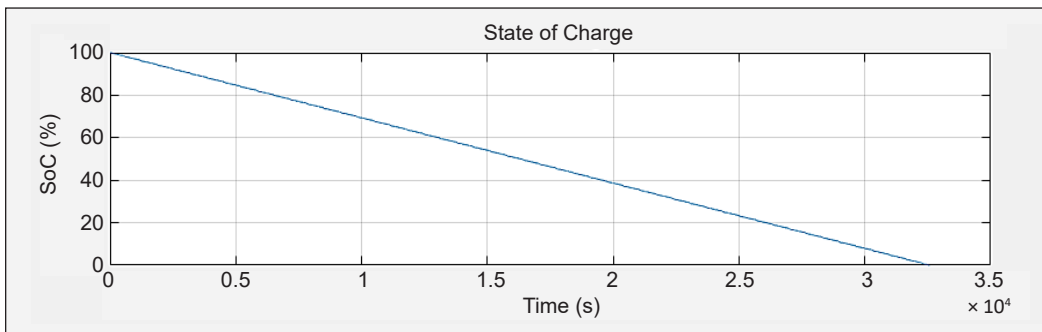


Figure 11. SoC for BEV using Japan 10-15

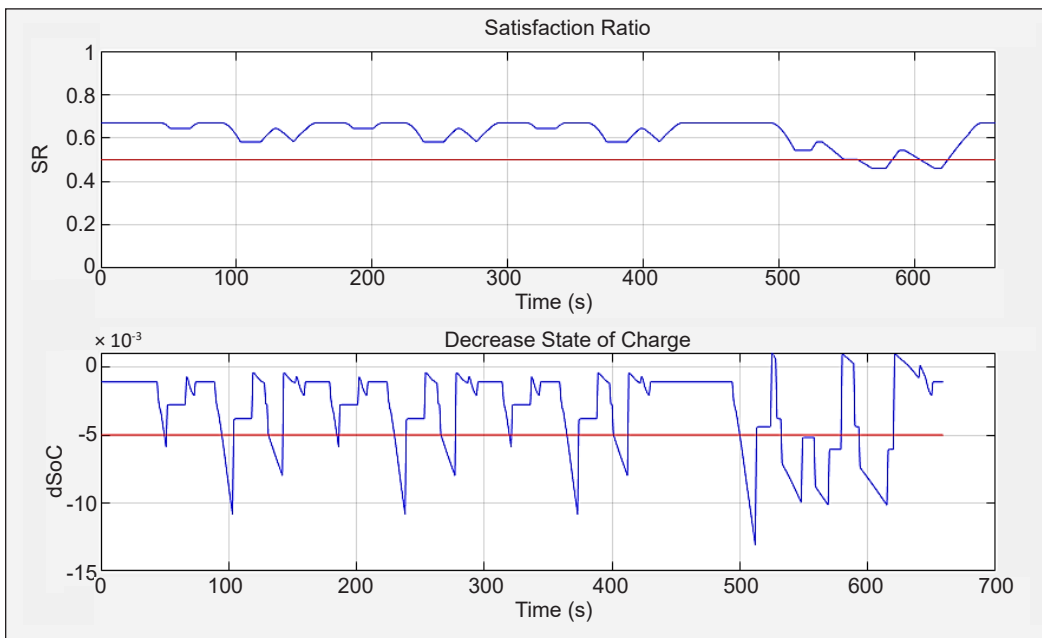


Figure 12. SR and dSoC for BEV using Japan 10-15

Based on the results presented in Table 4, it can be concluded that the model using FLC and optimization by brute-force algorithm for Japan 10-15 with load has a better range compared to the basic model with load for the Japan 10-15 mode and the basic fuzzy model with load for the Japan 10-15 mode. The 100% range for Japan 10-15 mode is reported to be 205.3 km, while the 80% range is 164.3 km. These findings suggest that the optimal model can achieve a longer range of about 205.3 km, which is better than the range achieved by the basic model with load for the Japan 10-15 mode, which is about 162.2 km, and the basic fuzzy model with load, which is about 183.3 km. It indicates that the proposed model can improve the range performance of electric vehicles in Japan’s 10-15 mode, which can benefit drivers in Japan. Therefore, using FLC and optimization by brute-force algorithm

can be considered a useful approach to improve the range performance of electric vehicles in Japan's 10-15 mode with load.

Overall, the study shows that using a fuzzy logic controller and optimization by brute force can significantly improve the range of battery-powered electric vehicles, as shown in Table 4. The results also suggest that the performance of the EMS can vary depending on the driving cycle used for testing. Implementing the fuzzy logic strategy and optimization demonstrates a clear improvement in power consumption for the HVAC system while preserving power capacity for motor torque and speed. The results show that the basic fuzzy EMS can improve power consumption by 11.7% to 12.4%, and the optimized fuzzy EMS can improve it by 23.2% to 26.6%. The optimal strategy for improving the range of the BEV with an auxiliary load system was the fuzzy logic controller and optimization by brute force, with the highest improvement observed in the NEDC mode. Additionally, the optimal strategy performed better than the basic BEV model with an auxiliary load system in all four driving cycles. These findings can be useful for designing and optimizing EMS for battery electric vehicles, ultimately leading to more efficient and practical electric vehicles.

Table 4  
Summary of results for the three EMS model

EMS	Performance	Driving Cycle		
		NEDC	UDDS	Japan 10-15
Basic BEV with HVAC Load	SoC(second)	20774	21060	25726
	Full Trip Distance (km)	193.9	200.0	162.2
	Full Consumption Rate (%)	34.8	36.3	44.2
BEV FL Model with HVAC load	SoC(second)	23214	23515	28925
	Full Trip Distance (km)	216.6	223.0	182.3
	SR (%)	90	90	90
	Fuzzy Enhancement Rate (%)	11.7	11.7	12.4
BEV FL Model + Optimization (brute-force algorithm) with HVAC load	SoC(second)	25605	26058	32574
	Full Trip Distance (km)	238.9	247.5	205.3
	SR (%)	65	65	65
	Optimization Enhancement Rate (%)	23.2	23.7	26.6

## COMPARISON OF RESULTS WITH PUBLISHED WORKS

Upon comparing the results of this study with previous studies, it is evident that this study has obtained significant improvements, especially in terms of driving range. Table 5 shows a comparison with the previous work.

The proposed solution can provide better results than most of the previous studies that focused on the EMS system because no previous studies have used the Fuzzy technique with BF in the BEV field and placed emphasis on achieving a balance between two conflicting objectives: reducing power consumption by the HVAC and satisfying the driver. The

Table 5

*Comparison between the performance of the proposed solutions and the previous work*

Source	Solution/Design	Driving cycle	Results
(Pan et al., 2021)	Fuzzy optimal EMS concerning the equivalent speed (FLC strategy combined with a GA optimal algorithm)	Custom with Slope	- 8.66% improvement in the driving range
(Hu et al., 2019)	generalized regression neural network (GRNN) and Dynamic programming – based energy management strategy (DPEMS) under typical driving	Custom	- 5.65 to 11.04% improvement in range and power-saving
(Masjosthusmann et al., 2012)	Four modular EMS (storage, drivetrain, load, consumption estimation)	Custom	- 15% improvement in range and power saving
Auxiliary power strategy by using a Fuzzy Logic Controller that is based on SoC and speed <b>(Proposed)</b>		NDEC	- 11.7%
		UDDC	- 11.7%
		Japan 10-15	- 12.4%
			Improvement in range and power-saving
Optimal auxiliary power strategy by using Hybrid Design of Fuzzy Logic Controller that is based on SoC and Speed and Brute force algorithm for Optimal FLC <b>(Proposed)</b>		NDEC	- 23.2%
		UDDC	- 23.7%
		Japan 10-15	- 26.6%
			Improvement in range and power-saving

challenge lies in reducing the power supplied to the HVAC system while maintaining driver satisfaction at an appropriate level. While most previous studies concentrated on enhancing power consumption or recharge efficiency, they did not address driver satisfaction.

This study introduces a novel measure called WPM, which establishes a relationship between the SR and the rate of dSoC. The optimal trade-off between these two conflicting measures can be attained using brute force techniques, which have not been utilized in prior studies. The results from the four proposed systems, tested on different driving cycles, clearly demonstrate that implementing fuzzy logic with the BF strategy can enhance the power efficiency of the HVAC system while preserving power capacity for motor torque and speed. However, previous studies did not incorporate the brute force technique with a Fuzzy Logic Controller to identify the best solution or establish a strategy for resetting BF at any point for BEVs. Furthermore, these studies did not propose a measurement technique similar to WPM.

## CONCLUSION

This study aims to propose an optimization algorithm that integrates the brute-force technique and the fuzzy logic controller. A basic fuzzy logic controller is designed and

integrated into the EMS to achieve this goal; an additional optimization technique is integrated to seek the optimal configuration of the fuzzy logic controller using a brute force algorithm. The fuzzy controller of this study is designed to control the auxiliary load consuming power based on the SoC and speed. The solution is based on the brute force function, the proposed optimization technique to find the best solution from a wide range of measures in which the decision is based on two or more conflicted measures. Brute force is a searching algorithm for all possible solutions in the solution space.

Overall, the study provides valuable insights into the design and optimization of EMS for battery electric vehicles, specifically improving their range. Using fuzzy logic controllers and optimization by brute force is an effective approach for achieving this goal, with significant improvements observed in all driving cycles tested. The study highlights the importance of considering different driving cycles for testing and evaluation, as well as the potential benefits of incorporating auxiliary load systems and optimizing the power consumption of the HVAC system. These findings can inform the development and optimization of EMS for battery electric vehicles, ultimately leading to more efficient and practical electric vehicles.

## ACKNOWLEDGEMENT

This work is financed by Universiti Putra Malaysia, PUTRA Grant Scheme under Project Title: Predictive Optimization for Energy Management System in a Battery Electric Vehicle Using Hybrid Artificial Intelligence (GP/2018/9591500).

## REFERENCES

- Dou, H., Zhang, Y., & Fan, L. (2021). Design of optimized energy management strategy for all-wheel-drive electric vehicles. *Applied Sciences*, *11*(17), 1-14. <https://doi.org/10.3390/app11178218>
- Eberle, U., & von Helmolt, R. (2010). Sustainable transportation based on electric vehicle concepts: A brief overview. *Energy & Environmental Science*, *3*(6), 689-699. <https://doi.org/10.1039/C001674H>
- Giakoumis, E. G. (2017). *Driving and Engine Cycles*. Springer International Publishing. <https://link.springer.com/book/10.1007/978-3-319-49034-2>
- Górriz, J. M., Ramírez, J., Ortíz, A., Martínez-Murcia, F. J., Segovia, F., Suckling, J., Leming, M., Zhang, Y. D., Álvarez-Sánchez, J. R., Bologna, G., Bonomini, P., Casado, F. E., Charte, D., Charte, F., Contreras, R., Cuesta-Infante, A., Duro, R. J., Fernández-Caballero, A., Fernández-Jover, E., ... & Ferrández, J. M. (2020). Artificial intelligence within the interplay between natural and artificial computation: Advances in data science, trends and applications. *Neurocomputing*, *410*, 237-270. <https://doi.org/10.1016/j.neucom.2020.05.078>
- Han, S., Zhang, F., & Xi, J. (2018). A real-time energy management strategy based on energy prediction for parallel hybrid electric vehicles. *IEEE Access*, *6*, 70313-70323. <https://doi.org/10.1109/ACCESS.2018.2880751>

- Hassanzadeh, M., & Rahmani, Z. (2022). A predictive controller for real-time energy management of plug-in hybrid electric vehicles. *Energy*, 249, Article 123633. <https://doi.org/10.1016/j.energy.2022.123663>
- Hu, J., Niu, X., Jiang, X., & Zu, G. (2019). Energy management strategy based on driving pattern recognition for a dual-motor battery electric vehicle. *International Journal of Energy Research*, 43(8), 3346-3364. <https://doi.org/10.1002/er.4474>
- Hu, X., Zheng, Y., Howey, D. A., Perez, H., Foley, A., & Pecht, M. (2020). Battery warm-up methodologies at subzero temperatures for automotive applications: Recent advances and perspectives. *Progress in Energy and Combustion Science*, 77, Article 100806. <https://doi.org/10.1016/j.peccs.2019.100806>
- Hussain, S., Ali, M. U., Park, G. S., Nengroo, S. H., Khan, M. A., & Kim, H. J. (2019). A real-time bi-adaptive controller-based energy management system for battery-supercapacitor hybrid electric vehicles. *Energies*, 12(4662), 1-24. <https://doi.org/10.3390/en12244662>
- Masjosthusmann, C., Köhler, U., Decius, N., & Büker, U. (2012). A vehicle energy management system for a battery electric vehicle. In *2012 IEEE Vehicle Power and Propulsion Conference* (pp. 339-344). IEEE Publishing. <https://doi.org/10.1109/VPPC.2012.6422676>
- Mohd, T. A. T. (2020). *Development of Optimal Energy Management Topology for Battery Electric Vehicle with Load Segmentation* [Doctoral dissertation]. Universiti Putra Malaysia, Malaysia. <http://psasir.upm.edu.my/id/eprint/92800/1/FK%20%202020%20104%20IR.pdf>
- Pan, C., Gu, X., Chen, L., Yi, F., & Zhou, J. (2021). Fuzzy optimal energy management for battery electric vehicles concerning equivalent speed. *International Transactions on Electrical Energy Systems*, 31(1), 1-15. <https://doi.org/10.1002/2050-7038.12527>
- Pham, C., & Månsson, D. (2018). Optimal energy storage sizing using equivalent circuit modelling for prosumer applications (Part II). *Journal of Energy Storage*, 18, 1-15. <https://doi.org/10.1016/j.est.2018.04.015>
- Tammi, K., Minav, T., & Kortelainen, J. (2018). Thirty years of electro-hybrid powertrain simulation. *IEEE Access*, 6, 35250-35259. <https://doi.org/10.1109/ACCESS.2018.2850916>
- Temiz, A. (2015). *Assessment of Impacts of Electric Vehicles on Low Voltage Distribution Networks in Turkey* [Master dissertation]. Middle East Technical University, Turkey. <http://etd.lib.metu.edu.tr/upload/12619200/index.pdf>
- Valentina, R., Viehl, A., Bringmann, O., & Rosenstiel, W. (2014). HVAC system modeling for range prediction of electric vehicles. In *2014 IEEE Intelligent Vehicles Symposium Proceedings* (pp. 1145-1150). IEEE Publishing. <https://doi.org/10.1109/IVS.2014.6856500>
- Zhang, F., Xi, J., & Langari, R. (2017). Real-time energy management strategy based on velocity forecasts using V2V and V2I communications. *IEEE Transactions on Intelligent Transportation Systems*, 18(2), 416-430. <https://doi.org/10.1109/TITS.2016.2580318>





## Mechanical Properties of Virgin and Recycled Polymer for Construction Pile Application

Hoo Tien Nicholas Kuan<sup>1</sup>, Yee Yong Lee<sup>2\*</sup>, Sim Nee Ting<sup>2</sup>, Chee Khoon Ng<sup>2</sup> and Mohd Khairul Afiq<sup>1</sup>

<sup>1</sup>Department of Mechanical Engineering, Faculty of Engineering, Universiti Malaysia Sarawak, 94300 Kota Samarahan, Sarawak, Malaysia

<sup>2</sup>Department of Civil Engineering, Faculty of Engineering, Universiti Malaysia Sarawak, 94300 Kota Samarahan, Sarawak, Malaysia

### ABSTRACT

Annual polymer waste generated in Malaysia has increased significantly to more than 1 million tonnes. The prolonged degradation periods required by diverse industrial polymer waste streams are a matter of significant concern, with some taking up to 1000 years to fully degrade. Pursuing a similar environmental concern, the use of bakau piles as supports for lightweight structures in Sarawak, including drainage systems, roads, sewerage, and other water-related structures, has become a matter of concern due to the deforestation of mangrove forests. Both bakau deforestation and polymer waste issues are significant environmental and global concerns. The idea of mitigating mangrove degradation and the non-biodegradable nature of polymer waste has led to the conceptualization of an alternative solution whereby recyclable thermoplastic polymer piles are utilized to supplant bakau piles in providing support for lightweight structures during civil engineering construction projects. Therefore, the study of polymer piles is conducted to examine their mechanical properties in the form of virgin (V) and recycled (R) thermoplastic polymers. In this

study, high-density polyethylene (HDPE), polypropylene (PP), and polyvinyl chloride (PVC) are considered, and the possibility of being utilized in pile application has been discussed. Based on the results, all virgin types of thermoplastic polymers (HDPE, PP, and PVC), 50%V:50%R for PP, PP(R), and PVC(R), respectively, exceed the bakau ultimate tensile strength. Thermoplastic polymer piles showed great potential to be

### ARTICLE INFO

#### Article history:

Received: 16 May 2023

Accepted: 12 September 2023

Published: 26 March 2024

DOI: <https://doi.org/10.47836/pjst.32.2.18>

#### E-mail addresses:

khtnicholas@unimas.my (Hoo Tien Nicholas Kuan)

yylee@unimas.my (Yee Yong Lee)

snting@unimas.my (Sim Nee Ting)

ckng@unimas.my (Chee Khoon Ng)

22020081@siswa.unimas.my (Mohd Khairul Afiq)

\* Corresponding author

the substitution for bakau piles to serve in the construction industry, with the recorded experimental tensile and compressive strength tests.

*Keywords:* Compression, mechanical properties, polymer, construction pile, tensile

---

## INTRODUCTION

The increasing volume of polymer waste produced by industries has been alarming, especially in polymer pollution. The available types of synthetic polymers in the market include polyvinyl chloride (PVC), polyethylene (PE), polycarbonate (PC), polyethylene terephthalate (PET), and polypropylene (PP). PVC is a polymer that consists of half chlorine by weight. PC and PET are the most commonly used thermoplastic polymers in the market and are known as polyester in the textile industry. PE and PP are part of the polyolefin family, but PE is slightly more rigid and heat-resistant. Their qualities and various characteristics make them appropriate for a wide range of uses in industries, including packaging, construction, home and sporting goods, cars, electronics, and agriculture. As a result of polymer materials' applications, 13.2% of polymer waste is generated per year, amounting to 53 kg of polymer waste per person per year or 1.59 million tons per year (Akenji et al., 2020). Municipal solid trash accounts for roughly two-thirds of total polymer trash, while the supply and industrial sectors account for the remaining third (Perugini et al., 2005).

Polymer pollution is becoming a huge environmental issue due to the large amounts generated, which endangers the environment and its population (Awoyera & Adesina, 2020). In addition, polymers need a long period to degrade, approximately 1000 years (Gerrard, 2020). The non-biodegradable nature of polymer waste generated over the years, compounded with the escalating amount of waste deposited in landfills worldwide, has become a pressing environmental issue. Polymer waste poses a significant threat to various facets of the environment, including oceanic health, human health, coastal regions, food safety and quality, as well as climate change. It brings a challenge to the polymer in construction to segregate, reuse and recycle polymer waste at the end of its life or alternatively combine it with natural fiber into a green polymer composite (Tan et al., 2017; Kuan et al., 2021). In line with this, biodegradable polymer is also introducing since the early 1980s due to the increasing volume of polymer waste, which is hard to recycle and has had a long life on the earth since its birth (Wang, 2022). However, due to their cost, biodegradable polymers are still unfavorable in the market. The recycling of polymer waste presents a viable solution to curb the mounting issue of polymer waste accumulation in landfills. In light of this, greater emphasis should be placed on recycling industrial polymer waste to mitigate the adverse environmental impact of polymer pollution caused by the accumulation of polymeric waste.

Polymer recycling is becoming a way to reduce environmental problems caused by the polymeric waste accumulation generated from day-to-day applications. Polymer recycling is one approach to decreasing pollution and resource depletion issues generated by polymeric waste aggregation from utilization in various sectors of the economy. Recycling is the final result of the intermediate stages of collection, sorted by polymer type and processing (Hawkins, 2018). Because only clean, homogenous polymers can produce the highest quality recycled polymer products in the existing secondary process, material recycling, and high-value chemical products in the current tertiary process, feedstock recycling (Curlee & Das, 1991; Hawkins, 1987). As a result, recycling polymer has the possibilities; meanwhile, the recovery and simple treatment of polymers from mixed, contaminated wastes into at least down-cycling products seems to be possible (Möllnitz et al., 2021).

Various approaches exist for the recycling of polymers, including mechanical recycling, chemical recycling, and reuse. The reuse of post-consumer packaging, such as glass bottles and jars, was a common practice in which items like milk and drink bottles were returned to be cleaned and used again. However, in the context of plastic packaging, reuse is not extensively adopted, primarily due to the single-use nature of plastic products. As a result, plastic items are typically discarded after their initial use. Meanwhile, the transformation/downgrading of waste plastic into a less demanding product via mechanical means such as screw extrusion, injection molding, blow molding, and compression molding, also known as mechanical recycling (Lamberti et al., 2020; Cui & Forssberg, 2003). As for chemical recycling, polymer waste is turned back into its oil/hydrocarbon component in the cases of polyolefin and monomers in the case of polyesters and polyamides, which can be used as raw materials for new polymer production and petrochemical industry, or directly into other useful materials (Lamberti et al., 2020; Sasse & Emig, 1998).

Bakau pile usage is one of the high-demand materials produced from the mangrove forest, pursuing a similar line of environmental concerns. According to JKR (2017), the bakau pile is generally designed as a friction pile in a light civil works structure where the load-bearing resistance is derived mainly from skin friction. In Sarawak, mangroves are harvested as bakau piles in light civil works, especially drainage, road, light water-related structures, and sewerage works. The construction industry's high demand for materials for construction activities has resulted in the overharvesting of mangroves. Consequently, the overuse of mangrove trees resulted in the indiscriminate destruction of mangroves along the coastline, leading to coastal erosion and other environmental issues. In addition, the escalation or destruction of mangroves impacts food security, biodiversity, and the lives of some of the most marginalized coastal populations in developing countries, with over 90% of the world's mangrove species (UNEP, 2014). Therefore, further study on using thermoplastic polymers to produce engineered construction piles is needed as an alternative to bakau piles or maybe to replace them.

Until about 15–20 years ago, the conventional materials for piling were timber, steel, and reinforced concrete. With the introduction of polymer materials and then composite polymeric material, the traditional materials for piling have changed dramatically (Dutta & Vaidya, 2003). The deterioration of materials, concrete oxidation, steel corrosion, degradation, and marine borer attacks on bakau or timber products are significant obstacles in pile construction and can be neglected by replacing polymer materials, raising pile durability, and lowering environmental effects. Dutta and Vaidya (2003) mentioned that PVC is the most popular and first commercially produced polymer, and it has been used as a sheet pile in pile construction. Even the 10-year-old PVC sheet piles in Louisiana showed no signs of cracks, blemishes, or deterioration (Dutta & Vaidya, 2003). Besides, current products include fiber-reinforced polymers (FRP) piles (Sakr et al., 2005), FRP sheet piles (Boscatto et al., 2011), concrete-filled polymer shells, recycled polymers reinforced with stiffer bar elements, and piles made entirely of recycled polymers (Robinson & Iskander, 2008). Many tests in regard to polymers in soil stated that utilization of polymers brings benefits to construction piles, such as an increase of interface friction between soil and polymer surface (Vineetha & Ganesan, 2014) and reduced soil erosion (Yakupoglu et al., 2019). The existing polymer pile application creates the possibility of replacing bakau pile materials with polymer, especially in light structures. Moreover, it prevents the overharvesting of mangroves due to the usage of traditional pile materials. The recyclable behaviour of polymers can also reduce the polymer waste embedded in landfills.

Increasing volumes of synthetic polymers are manufactured for various applications such as HDPE, PP, and PVC. In this study, mechanical recycling is adopted together with the usage of raw materials for comparison. Hence, three types of virgins, recycled polymers, which are HDPE, PP, and PVC, are used in the study. Despite being categorized as thermoplastics, each type possesses unique characteristics and applications, particularly their melting points and densities. The recycling of plastics refers to the processing of plastic waste into secondary raw material without significantly changing the chemical structure of the material. In order to obtain the most stable and sustainable combination while fulfilling its application in pile construction, the material characterization of the polymers and recycled polymers, which best emulate bakau piles, is carefully formulated in terms of the optimized mix proposed for this study.

## **MATERIAL AND METHODS**

### **Material**



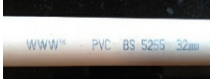



This study used three types of virgin and recycled polymers, HDPE, PP, and PVC, for testing. These are all thermoplastics; however, they have varying characteristics and uses, especially their melting temperatures and densities. The hot compression method was used to fabricate samples for all the polymers.

The hot press machine was used for laminating the virgin and recycled polymers at their respective melting temperatures and pressure to maintain the shape of the laminate and remove excess air bubbles due to the boiling of the polymer. It is to ensure a neat sample while avoiding the failure of fabrication of samples. The samples were fabricated according to ASTM D3039 for tensile testing and ASTM D695 for compression testing. The results were averaged over five sample measurements for each type of laminate.

There are three types of polymers, including recycled (R), virgin (V), and mixed 50%R:50%V in combination for polymer fabrication. All the respective raw materials for recycled polymers were collected for cleaning purposes, while virgin polymers were purchased from local suppliers. Other than that, recycled polymers were cut and ground into smaller sizes to feed into the mold. Prior to the hot press process, the prepared polymers would be weighed beforehand to ensure the laminate was in the desired size according to ASTM testing standards. Finally, suppose the laminate is without visible physical defects such as air bubbles, cracking, or warping. In that case, the laminate is considered successfully fabricated, and continuation with ASTM tensile and compression testing would be performed, respectively.

For the gathering of recycled polymers such as HDPE, PVC, and PP, recycled HDPE (RHDPE) was gathered from used detergent bottles, recycled PVC (RPVC) from used pipes, while recycled PP (RPP) was collected from used containers. All the polymers went through the hot-pressed method to form compression and tensile samples. Table 1 summarizes the materials used for sample fabrication.

Table 1  
Materials used for sample fabrication

Class	Polymer	Description	Image
Recycled	HDPE	Used Detergent Bottles	
	PP	Used Food Containers	
	PVC	Used PVC Pipes	
	HDPE	HDPE Sheets	
Virgin	PP	PP Sheets	
	PVC	PVC Sheets	

## Testing Procedure

Tensile testing and compression testing were conducted according to ASTM D3039 and ASTM D695 standards, respectively.

**Tensile Testing.** Tensile testing was conducted with a crosshead displacement rate of 3 mm/min. Based on the ASTM standards, the dimension of tensile samples is 3 mm in thickness, 25 mm in width, and 250 mm in length (Figure 1). This testing produced a stress-strain diagram, which is then used to determine tensile modulus. Ambient temperature and humidity were maintained as constant as possible throughout this test.

**Compression Test.** A compression test was conducted following the ASTM D695 standards to determine the strength and modulus of the polymer material. Compressive properties describe the behaviour of a material subjected to a compressive load. The specimen was positioned parallel to the surface between the compressive plates. The specimen was then compressed with a uniform load. The maximum load was recorded using the computer system and the collected data. The sizing of the block specimen was 12.7 mm × 12.7 mm × 25.4 mm (Figure 2).

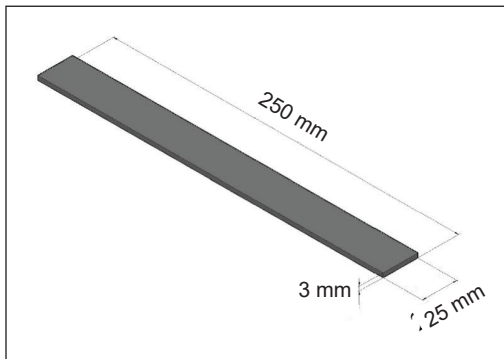


Figure 1. Tensile test sample 3D model

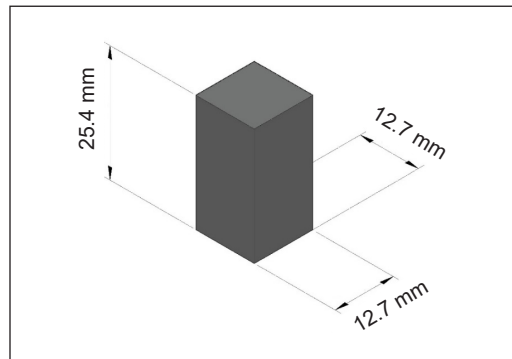


Figure 2. Compression test sample 3D model

## RESULTS AND DISCUSSION

### Tensile Testing

A material subjected to stretching or tension requires significant tensile strength. Tensile properties, such as the tensile strength and tensile modulus of the thermoplastic polymers, were determined. Figure 3 illustrates the comparison of the tensile strength among polymers.

Figure 3 compares the tensile strength of virgin polymers and their recycled counterparts, where results show that all virgin-class polymers demonstrate greater tensile strength values. For the 50%R:50%V samples, it varies among the polymer types. However, it is evident that the values are not on par with the virgin samples. For HDPE,

the 50%R:50%V samples have a slightly higher tensile strength at 21.05 MPa than the recycled samples at 18.31 MPa. For PP, the results indicate that the recycled samples possess higher tensile strength at 19.31 MPa, while the 50%R:50%V samples are only at 14.92 MPa. The weaker strength of recycled polypropylene could be attributed to the adverse impact of impurities or contaminants on its binding with the virgin counterpart. However, in comparison among polymers, PVC exhibits the highest tensile strength for its virgin and recycled samples. Generally, it is observed that virgin polymers display superior tensile strength properties in comparison to their recycled counterparts. This observation may be attributed to the fact that recycled polymers have undergone prior processing and have been subjected to post-consumer utilization. It can cause the recycled polymer to deteriorate in its mechanical characteristics, leading to diminished performance as it may have gone through various resultant effects, such as long exposure to heat, sunlight, chemical exposure, or overextended consumer usage.

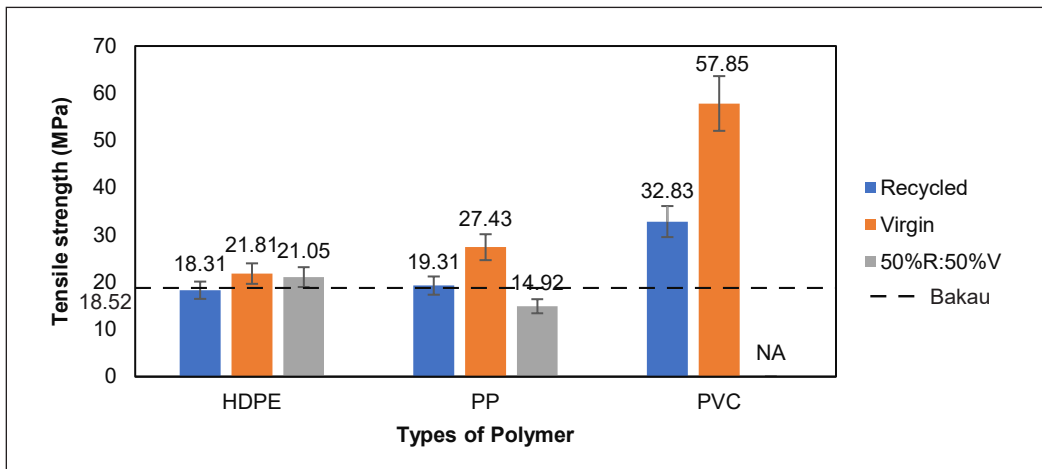


Figure 3. Comparison of the tensile strength among polymers

### Tensile Modulus

Due to the differences in strains among the samples and classes, it is only possible to compare the average values when comparing the tensile modulus. It differs among samples due to several factors, including but not limited to surrounding temperature, minute human errors, and sample defects. Hence, from Figure 4, the highest tensile modulus, which is 1336.88 MPa, is exhibited by the virgin PVC. In comparison among the polymers, the tensile modulus of HDPE is significantly lower among PP and PVC, regardless of class, where its virgin sample only achieved 208.66 MPa. Virgin PP can be seen to have a lower tensile modulus in comparison with its recycled and 50%R:50%V counterparts, which indicates virgin PP is less stiff. The increased stiffness of recycled PP that makes it more suitable for consumer usage may be attributed to small amounts of additives or stabilizers.

At the same time, 50%R:50%V PP exhibits higher tensile modulus in comparison to its virgin and recycled counterparts. It might be due to the possibility of either the virgin or recycled PP acting as filler material instead, similar to reinforced materials, increasing the tensile modulus. On the other hand, virgin PVC that does not have additives tends to perform better than recycled PVC in tensile modulus. This discrepancy can be attributed to the additives present in recycled PVC, which are often intended to improve its elastic properties and water absorption. Such modifications are particularly relevant in applications such as piping within housing projects.

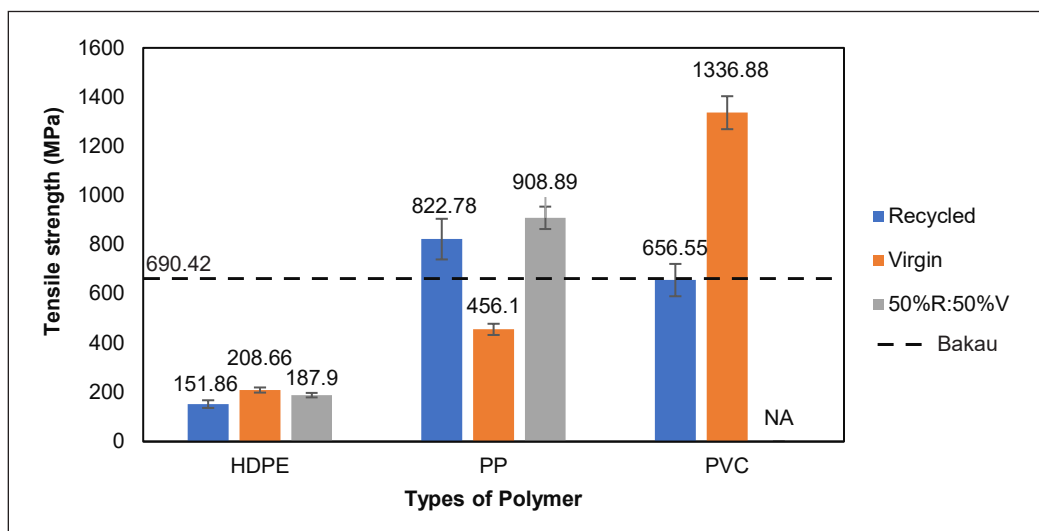


Figure 4. Comparison of the tensile modulus among polymers

### Compression Testing

Compression properties such as the compression strength and compression modulus of the thermoplastic polymers were determined. Table 3 presents the compression strength of different classifications of thermoplastic polymer. Meanwhile, Figure 5 illustrates the comparison of the compression strength among polymers.

In Figure 5, the recycled samples for HDPE and PP show slightly higher compressive strengths in comparison to the virgin samples. The underlying cause of enhanced compressive characteristics in recycled PP and HDPE can be additives or stabilizers. It stands in contrast to virgin PVC, where superior performance is observed. However, regardless of the class of polymers, PVC samples demonstrated overall better compressive strength performance. It is solely due to the chemical bonding of PVC, which involves the repeating monomer Vinyl Chloride ( $C_2H_3Cl$ ), which makes the density of PVC greater than both PP and HDPE. HDPE has a repeating monomer of Ethylene ( $C_2H_4$ ), while PP has a repeating monomer of Propene ( $C_3H_6$ ).



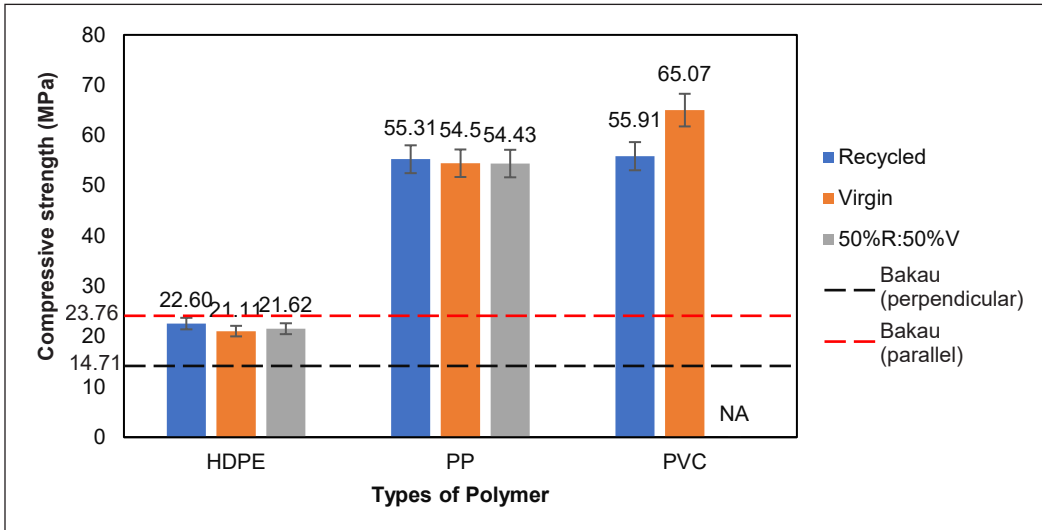


Figure 5. Comparison of the compressive strength among polymers

Due to the variability of strains among the samples and classes, the only way to compare compressive modulus is to compare average values. Figure 6 shows that virgin polymers excel in compressive modulus, which indicates that virgin polymers are much stiffer in compression compared to their counterparts. In addition, virgin PP has a greater compressive modulus of 728.16 MPa than virgin PVC, which is 637.82 MPa. Regardless of class, HDPE still performs lower in comparison to other tested polymers. The reason is that virgin polymers were not exposed to consumer-used environments, which is likely to maintain their polymer characteristics.

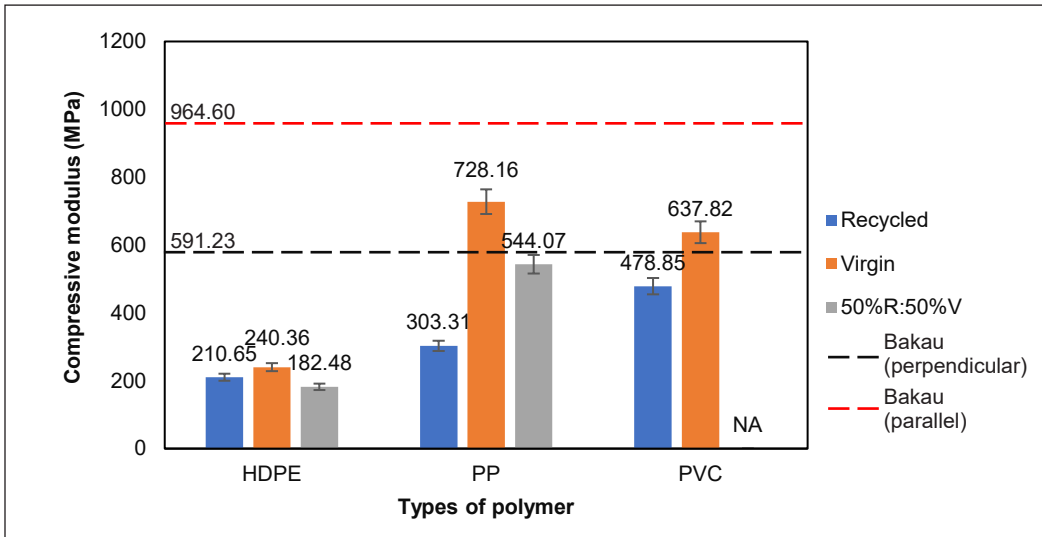


Figure 6. Comparison of the compressive modulus among polymers

### Tensile Stress-strain Analysis

Figure 7 demonstrates that virgin HDPE can withstand higher stress at a given strain compared to its counterparts. The curve displays a distinct sudden dip at 0.25 strain for the 50%R:50%V HDPE due to internal cracking, nucleating, or premature delamination during testing. It may be found that the incomplete ability of recycled and virgin HDPE is probably due to the effects of colorants, residual chemicals, and abs and orb ed fluids. However, for all classes of HDPE, even after 0.4 strain, the sample does not fail completely, which then proves the durability of HDPE.

From Figure 8, the low strain exhibited by virgin PP suggests its brittleness relative to other thermoplastic polymers. Tensile failure can be clearly seen in Figure 8 across the different classes of PP. The steepness of the curve for virgin PP suggests its stiffness compared to other classes of PP, particularly when compared to virgin PVC. The early failure of the 50%R:50%V PP sample suggests a possible incompatibility issue between the recycled and virgin PP materials. The incompatibility may be due to causes, and not limited to, prior manufacturing processes, water absorbed, minor defects and minute additives.

In Figure 9, virgin PVC is stiffer and can withstand greater strains than recycled PVC. A dip can also be observed in the

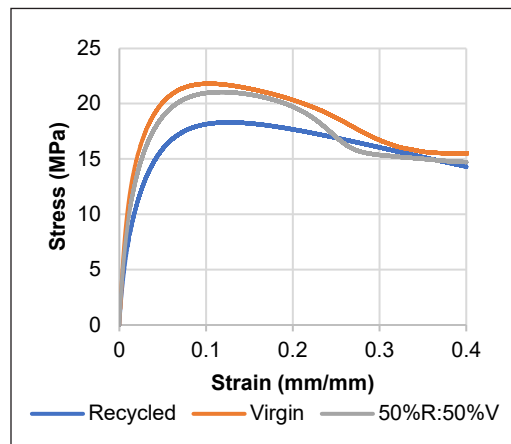


Figure 7. Tensile stress-strain curves for classes of HDPE

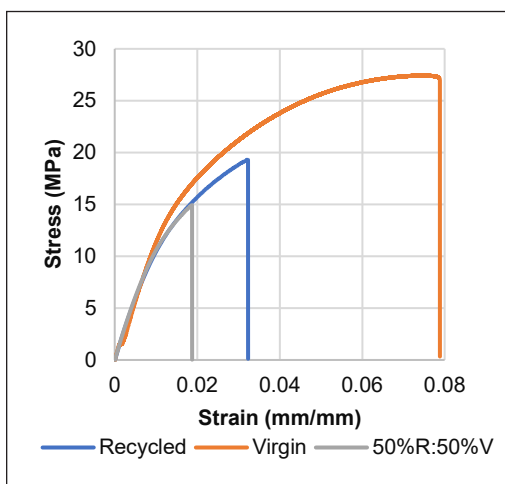


Figure 8. Tensile stress-strain curves for classes of PP

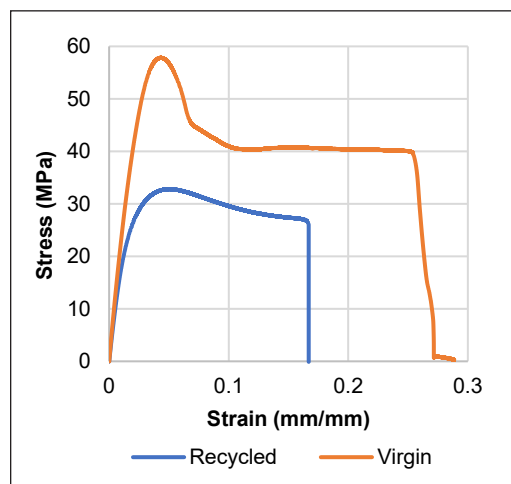


Figure 9. Tensile stress-strain curves for classes of PVC

curve of virgin PVC, indicating potential internal delamination, nucleation, or premature internal failure during testing. For 50%R:50%V PVC, the fabrication of samples could not be completed.

Meanwhile, as illustrated in Figure 10, the virgin PVC and recycled PVC did not seem to merge well. Several factors could possibly cause it, primarily the difference in melting temperatures of the two mentioned PVCs. Recycled PVC required a higher melting temperature with plasticizers and additives, resulting in an elevated melting point compared to virgin PVC. This incompatibility can be overcome only with heavy-duty chemical and mechanical manufacturing (You et al., 2022), which is highly strenuous. Instead, propositions of the addition of synthetic or natural reinforcing materials would increase the mechanical properties of polymers. Luck et al. (2022) stated that the use of seawater sea sand concrete (SWSSC) filled fiber reinforced polymer (FRP) tubes offers several benefits, including the prevention of resource shortages and corrosion resistance. Compressive strength and ductility improvements were also evident (Bazli et al., 2021). Furthermore, the utilization of fibers plays an important role in enhancing the mechanical properties of polymers. Jahan et al. (2012) experimented on glass and jute FRP and found that LDPE reinforced with either jute or glass fibers possess greater mechanical properties in comparison to standalone LDPE. Synthetic fibers offer high strength in a composite material, but their recyclability is challenging (Kamarudin et al., 2022). Hence, the utilization of SWSSC, natural and synthetic fibers, or hybrid fibers in reinforcing polymers can benefit future construction works.

From Figure 11, the stress-strain curves of the tested recycled, virgin, and 50%R:50%V samples for HDPE, PP, and PVC are compared. The 50%R:50%V PVC samples are not included because the fabrication of the samples was not successful, as seen in Figure 10.

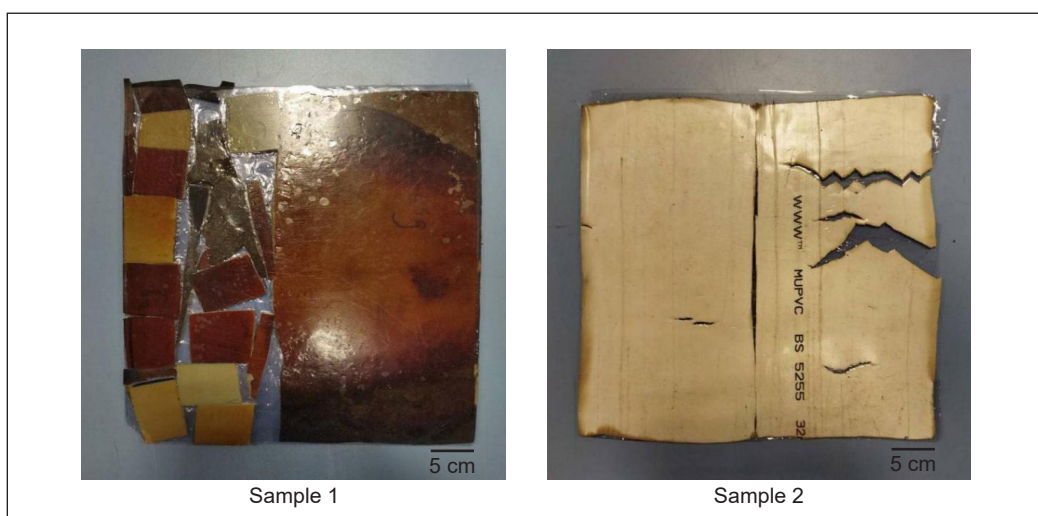


Figure 10. Failed 50%R:50%V PVC samples

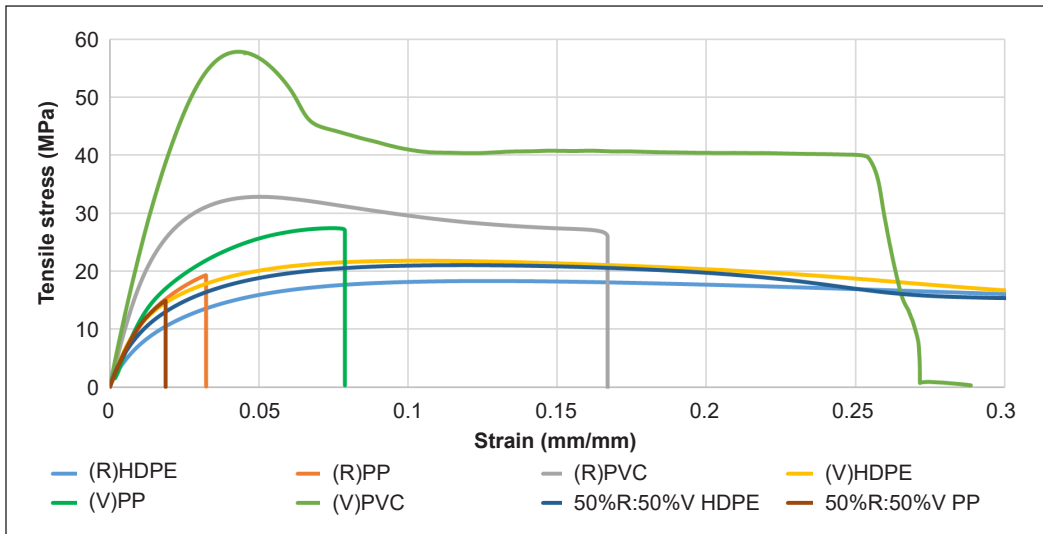


Figure 11. Comparison of tensile stress-strain curves

### Compressive Stress-strain Analysis

In Figure 12, HDPE experiences close values of compressive yield stress across the classes, as seen above. The dip observed in the curve for 50%R:50%V HDPE is likely due to the incompatibility between the recycled and virgin HDPE, potentially caused by the presence of colorants, residual chemicals, absorbed fluids, or similar factors. The failure of virgin HDPE samples is attributed to premature cracking or slipping caused by compressive stresses. The imperfect samples may also contribute to the slipping before densification, likely caused by the compression of the samples in a tilted manner. Rough observation can hypothesize that the stiffness of HDPE across classes is rather similar under compressive stresses.

From Figure 13, it can be observed that the maximum compressive stress for PP is similar among the different classes. A dip in the curve is observed for virgin PP, which may be attributed to its brittleness compared to other polymers, resulting in cracking. It is probably due to minor defects or small bubbles appearing in the samples. Another possibility is that the virgin PP does not have additives or stabilizers to aid its mechanical properties. It is also observed that all samples undergo densification. The curve for 50%R:50%V PP shows good performance, suggesting that the recycled and virgin PP blend well and have good lamination.

50%R:50%V PVC could not be fabricated due to the inability to achieve lamination without chemical treatment or mechanical manufacturing, as seen in Figure 10. Nonetheless, a comparison between recycled and virgin PVC was carried out. As shown in Figure 14, virgin PVC has a steeper curve, indicating greater stiffness compared to recycled PVC. The straight decrease of compressive stress observed in recycled PVC suggests failure

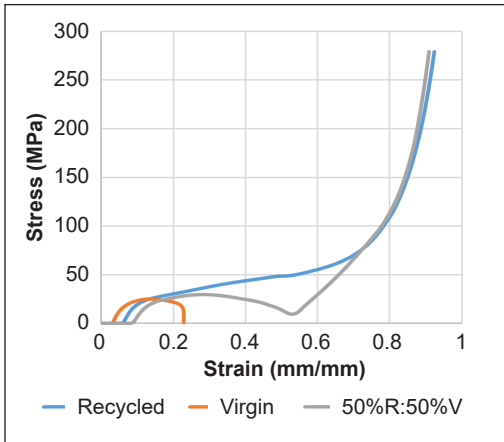


Figure 12. Compressive stress-strain curves for classes of HDPE

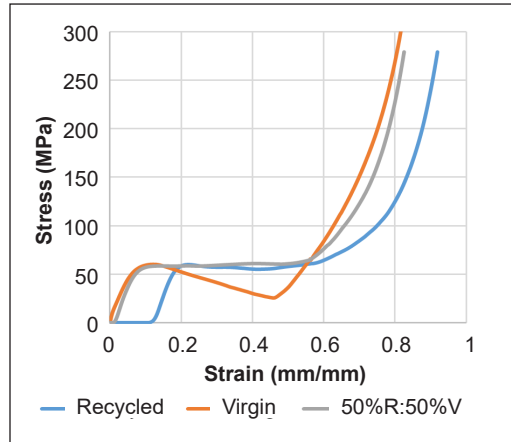


Figure 13. Compressive stress-strain curves for classes of PP

during testing, likely due to the brittleness of PVC under compressive stress, resulting in the delamination of samples.

Figure 15 compares the stress-strain curves of the tested recycled, virgin, and 50%R:50%V samples for HDPE, PP, and PVC. The 50%R:50%V PVC samples are not included because the fabrication of the samples was not successful, as seen in Figure 10. The exponential behaviour in the fracture region may be due to the large deformation by buckling.

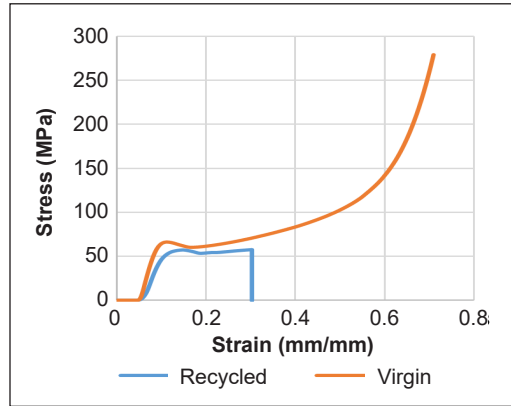


Figure 14. Compressive stress-strain curves for classes of PVC

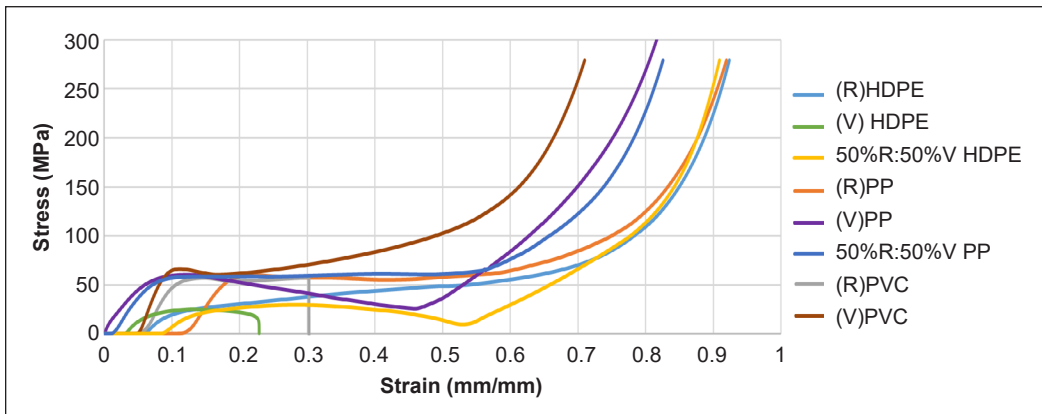


Figure 15. Comparison of compressive stress-strain curves

### Application of Plastic Pile

**Elastic Behaviour Under Serviceability Limits State Design.** When designing for a serviceability limit state, it is important to consider that permanent deformation should be avoided as it can cause occupants to feel insecure in the building. The different plastic materials investigated in this study had tensile elastic modulus values ranging from 151.86 to 1336.88 MPa and compressive elastic modulus values ranging from 182.48 to 728.16 MPa. Since the focus of the application is on the pile, a higher compressive elastic modulus is preferred. All the materials mostly exhibited tensile elastic strain ranging from 0.02 to 0.05, with a compressive elastic strain of 0.1.

The initial intention was to utilize plastic materials to create piles as a substitute for bakau piles in the construction industry. Table 2 summarizes the properties obtained from tensile stress-strain curves. From Table 2, the polymer with an elastic modulus that approaches bakau wood is PP (R), PVC (R), PVC (V), and 50% R:50%R PP, which exceeded the elastic modulus of bakau in the elastic region. Table 3 summarizes the properties obtained from compressive stress-strain curves. Table 3 shows that none of the

Table 2  
*Properties obtained from tensile stress-strain curves*

Materials	Young's Modulus, E (MPa)	Ultimate stress, MPa	Ultimate strain, $\epsilon$
HDPE (R)	151.86	18.31	> 0.3
HDPE (V)	208.66	21.81	> 0.3
PP (R)	822.78	19.31	0.02
PP (V)	456.10	27.43	0.08
PVC (R)	656.55	32.83	0.16
PVC (V)	1336.88	57.85	0.25
50%R:50%V HDPE	187.90	21.05	> 0.3
50%R:50%V PP	980.89	14.92	0.02
Bakau wood (Yunus, 2018)	690.42	18.52	-

Table 3  
*Properties obtained from compressive stress-strain curves*

Materials	Young's Modulus, E (MPa)	Ultimate stress (MPa)	Ultimate strain
HDPE (R)	210.65	22.60	> 0.80
HDPE (V)	240.36	21.11	0.21
PP (R)	303.31	55.31	> 0.80
PP (V)	728.16	54.50	> 0.80
PVC (R)	478.85	55.91	0.30
PVC (V)	637.82	65.07	> 0.70
50%R:50%V HDPE	182.48	21.62	> 0.80
50%R:50%V PP	544.07	54.43	> 0.80
Bakau wood (Yunus, 2018)	964.60 (parallel) 591.23 (perpendicular)	23.76 (parallel) 14.71 (perpendicular)	-

specimens exceeded the bakau's compressive elastic modulus parallel to the wood grain. However, PP (V) and PVC (V) exceeded their compressive elastic modulus perpendicular to the direction of the wood grain.

### **Plastic Behaviour During Ultimate Limit State Design**

The investigation of tensile and compression modulus at ultimate stress is crucial in pile design to avoid premature failure, such as the development of eccentric moments, which could reduce the pile capacity. Thus, it is important to examine these properties. All samples met the tensile ductility requirement except for PP, which set the benchmark at 0.10 strain.

All virgin types of polymer (HDPE, PP and PVC), 50%V:50%R PP, PP(R), and PVC (R) exceed the bakau's ultimate tensile strength. In terms of compression stress-strain behaviour in the ultimate limit state, all specimens exceeded ultimate strength (perpendicular to wood grain), and PP(V), PP(R), PVC(V), PVC (R) and 50% R: 50% V PP were higher than bakau's ultimate stress with parallel wood grain. Regardless of the wood grain arrangement, plastic piles could be substituted for bakau piles in the construction industry, with the recorded experimental tensile and compression strength tests. As mangrove ecosystems are declining at an alarming rate (Goldberg et al., 2020), the urge to recycle polymers into construction piles is needed to promote the sustainability of bakau. This further coincides with the Sustainable Development Goals (SDG) 12, responsible consumption and production (United Nations, 2022).

### **The Load Capacity of the Plastic Pile**

The compressive strength data was used to compute the total cross-section area based on the load capacity of the pile. Thus, the optimum cross-section area can be identified. The pile is assumed to be a polymer pile that replaces the timber pile, which has an average diameter of 75 mm due to the range of available timber. The unsupported length ( $L$ ) is assumed to be 3 m below the ground surface in soft soils. Utilizing Euler's equation, the critical axial loads and critical stress for respective polymers can be obtained, as shown in Table 4.

In Figure 16, it can be observed that all of the virgin polymer classes exhibit a high critical axial load, with PP having the highest at 673.38 kN. It suggests that PP is well-suited for use under axial loads. In general, the performance of the virgin samples is superior to that of the recycled and 50%R:50%V classes.

Figure 17 compares the critical stress for all polymers. Regardless of class, it is clear that PP will outperform HDPE and PVC. In the case of a polymer pile, virgin PP has a critical stress of 2976.66 MPa, virgin HDPE has 982.56 MPa, and virgin PVC has 2607.38 MPa.

Furthermore, the study also investigated the pile dimension and cross-sectional area across different types of polymer with respect to the buckling load capacity of a 3-meter length, where the effective length is taken as 3.3 m. The rule of thumb we use here is a

Table 4  
Critical axial load and critical stress of polymers

Polymer		Compressive Modulus (MPa)	Critical Axial Load (kN)	Critical Stress (MPa)
Recycled (R)	HDPE	210.65	861.12	194.80
	PP	303.31	1239.91	280.49
	PVC	478.85	1957.51	442.82
Virgin (V)	HDPE	240.36	982.56	222.27
	PP	728.16	2976.66	673.38
	PVC	637.82	2607.38	589.84
50%R:50%V	HDPE	182.48	745.98	168.75
	PP	544.07	2224.11	503.13
	PVC	NA	NA	NA

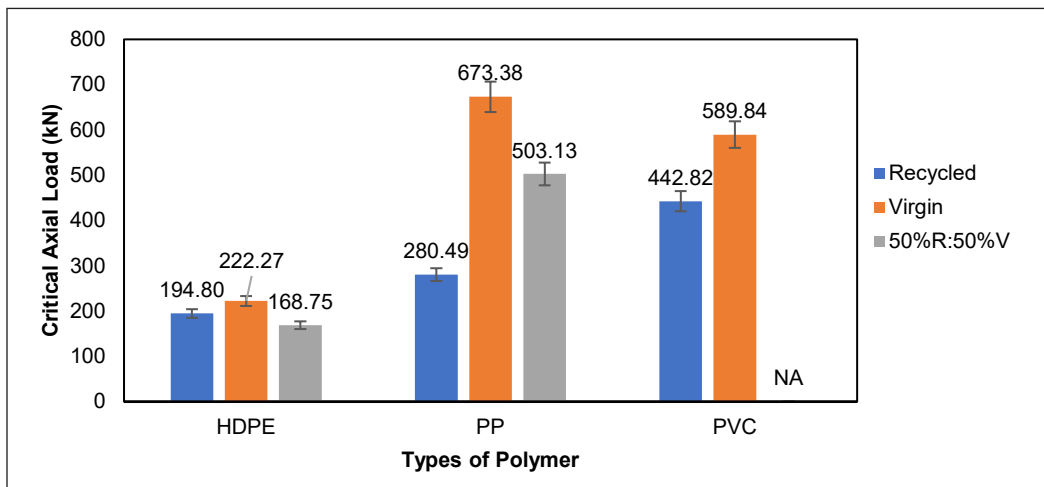


Figure 16. Critical axial load comparisons among classes of polymers

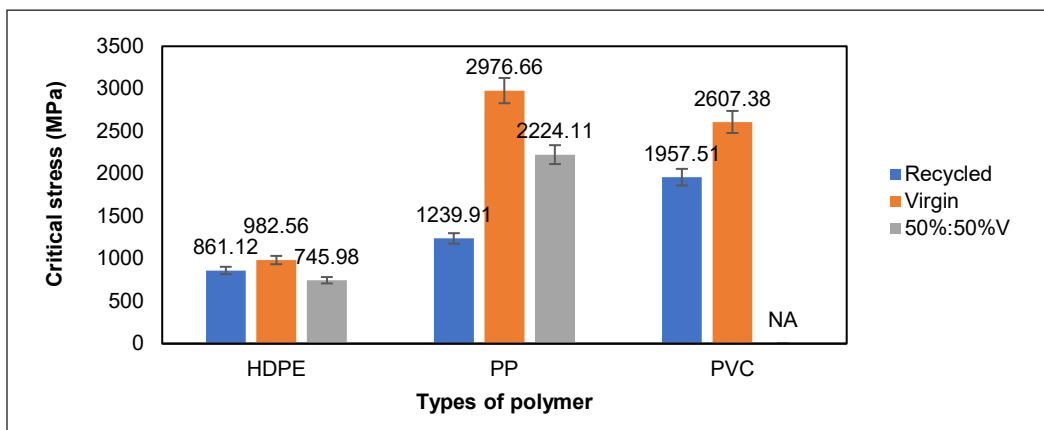
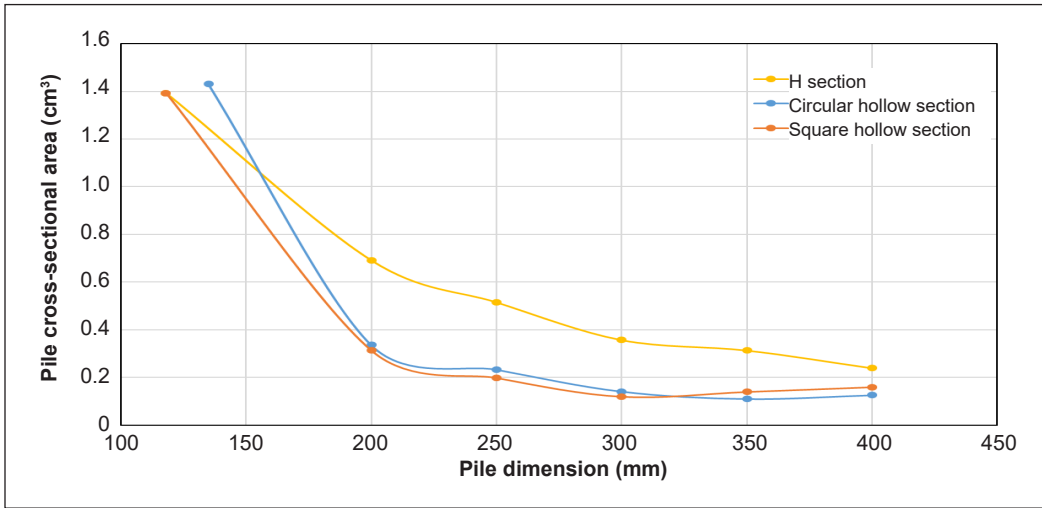
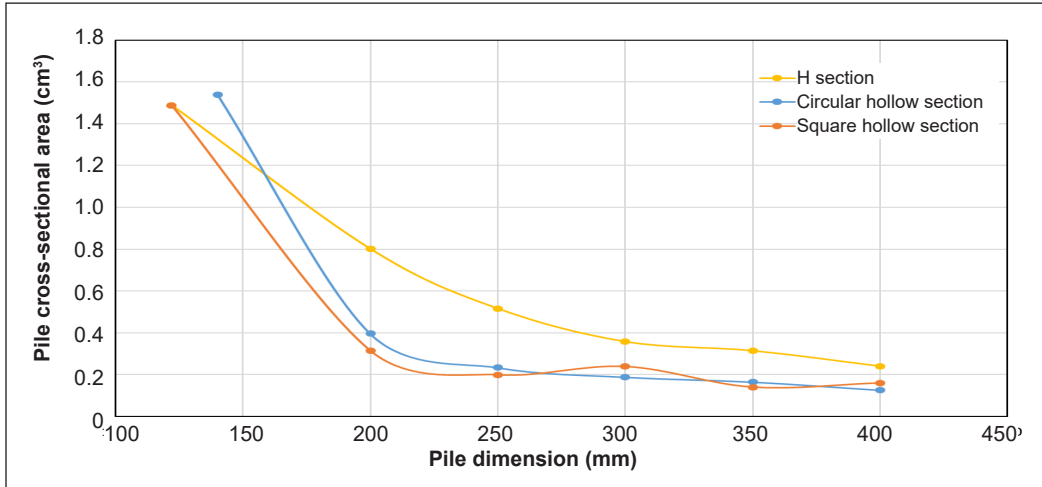


Figure 17. Critical stress comparisons among classes of polymers





(a)



(b)

Figure 18. Cross-sectional area vs pile dimension: (a) PP(V); and (b) PVC (V)

capacity of 1 metric ton per pile, simulating bakau pile capacity, with a typical safety factor of 1.3. Two polymers are being considered here: PP (V) and PVC (V), which have the highest compressive elastic modulus. Figure 18 shows that the section efficiency is the same across different types of polymers regardless of polymer type. The pile’s cross-sectional area decreases as the pile dimension increases. The feasible dimension for both circular and square hollow sections is 250 mm, as the larger dimension does not indicate a significant reduction in cross-sectional area. The H-section’s feasible dimension is 200 mm to ensure sufficient thickness to avoid local buckling, although a larger dimension can yield a smaller cross-sectional area.

## CONCLUSION

The mechanical properties of virgin and recycled polymers, namely HDPE, PVC, and PP, were investigated, and the possibility of being applied in pile application was discussed and summarized as follows. The elastic moduli that approach bakau wood are PP (R), PVC(R), PVC (V), and 50% R:50%R PP, which exceeded the elastic modulus of bakau in the elastic region. None of the specimens exceeded the compressive elastic modulus of bakau parallel to the wood grain, while PP (V) and PVC (V) exceeded their compressive elastic modulus perpendicular to the wood grain direction. Besides that, all virgin types of plastic (HDPE, PP and PVC), 50%V:50%R PP, PP(R), and PVC (R) exceeded the bakau's ultimate tensile strength. In terms of compression stress-strain behaviour in the ultimate limit state, all specimens exceeded ultimate strength (perpendicular to wood grain), and PP(V), PP(R), PVC(V), PVC (R) and 50% R: 50% V PP were higher than bakau's ultimate stress with parallel wood grain. Calculated critical stress subjected to polymer pile also showed that virgin PP exhibited a critical stress of 2976.66 MPa, while virgin HDPE had 982.56 MPa, and virgin PVC had 2607.38 MPa. The results of experimental tensile and compression strength tests indicate that polymer material has the potential to serve as a viable alternative to bakau piles in the construction industry, particularly in light structures. The buckling load analysis also shows that polymer piles can be shaped in circular hollow, square hollow, and H sections of 200 to 250 mm to carry a similar load in bakau piles. Polymer piles could replace traditional bakau piles, thereby addressing issues related to polymer wastes and mangrove deforestation while maintaining, if not enhancing, the structural integrity of lightweight structures in construction.

## ACKNOWLEDGEMENT

The authors acknowledge the Sarawak Research and Development Council (Sarawak RDC) through the Research Initiation Fund (RDCRG/RIF/2019/11) and Universiti Malaysia Sarawak for their financial support and research facilities.

## REFERENCES

- Akenji, L., Bengtsson, M., Hotta, Y., Kato, M., & Hengesbaugh, M. (2020). Chapter 21 - Policy responses to plastic pollution in Asia: Summary of a regional gap analysis. In T. M. Letcher (ed.), *Plastic Waste and Recycling* (pp. 531-567). Academic Press. <https://doi.org/10.1016/b978-0-12-817880-5.00021-9>
- American Society for Testing and Materials. (2014). *Standard test method for tensile properties of polymer matrix composite materials (ASTM D3039)*. [https://www.astm.org/d3039\\_d3039m-08.html](https://www.astm.org/d3039_d3039m-08.html)
- American Society for Testing and Materials. (2023). *Standard test method for compressive properties of rigid plastics (ASTM D695)*. <https://www.astm.org/d0695-23.html>

- Awoyera, P. O., & Adesina, A. (2020). Plastic wastes to construction products: Status, limitations and future perspective. *Case Studies in Construction Materials*, 12, Article e00330. <https://doi.org/10.1016/j.cscm.2020.e00330>
- Bazli, M., Heitzmann, M., & Hernandez, B. V. (2021). Hybrid fibre reinforced polymer and seawater sea sand concrete structures: A systematic review on short-term and long-term structural performance. *Construction and Building Materials*, 301, Article 124335. <https://doi.org/10.1016/j.conbuildmat.2021.124335>
- Boscato, G., Mottram, J. T., & Russo, S. (2011). Dynamic response of a sheet pile of fiber-reinforced polymer for waterfront barriers. *Journal of Composites for Construction*, 15(6), 974-984. [https://doi.org/10.1061/\(ASCE\)CC.1943-5614.0000231](https://doi.org/10.1061/(ASCE)CC.1943-5614.0000231)
- Cui, J., & Forssberg, E. (2003). Mechanical recycling of waste electric and electronic equipment: A review. *Journal of Hazardous Materials*, 99, 243-263. [https://doi.org/10.1016/S0304-3894\(03\)00061-X](https://doi.org/10.1016/S0304-3894(03)00061-X)
- Curless, T. R., & Das, S. (1991). *Plastic Wastes: Management, Control, Recycling, and Disposal*. Noyes Data Corp.
- Dutta, P. K., & Vaidya, U. (2003). *A Study of the Long-Term Applications of Vinyl Sheet Piles*. US Army Corps of Engineers, Engineer Research and Development Center.
- Gerrard, N. (2020). *The Construction Industry Rises to the Plastics Challenge*. <https://www.marsh.com/ph/industries/construction/insights/construction-industry-rise-to-the-plastic-challenge.html>
- Goldberg, L., Lagomasino, D., Thomas, N., & Fatoyinbo, T. (2020). Global declines in human-driven mangrove loss. *Global Change Biology*, 26(10), 5844-5855. <https://doi.org/10.1111/gcb.15275>
- Hawkins, W. L. (1987). Recycling of polymers. *Conservation and Recycling* 10(1), 15–19. [https://doi.org/10.1016/0361-3658\(87\)90003-8](https://doi.org/10.1016/0361-3658(87)90003-8)
- Jahan, A., Rahman, M. M., Kabir, H., Kabir, M. A., Ahmed, F., Hossain, M. A., & Gafur, M. A. (2012). Comparative study of physical and elastic properties of jute and glass fiber reinforced LDPE composites. *International Journal of Scientific and Technology Research*, 1(10), 68-72.
- JKR. (2017). *Guideline for Piling Works*. Jabatan Kerja Raya. <https://vdokumen.net/guideline-for-piling-works-epsmgjkrgov-cpka-jkr-malaysia-1172017-2-1-0.html>
- Kamarudin, S. H., Basri, M. S. M., Rayung, M., Abu, F., Ahmad, S., Norizan, M. N., Osman, S., Sarifuddin, N., Desa, M. S., Abdullah, U. H., Tawakkal, I. S. M. A., & Abdullah, L. C. (2022). A review on natural fiber reinforced polymer composites (NFRPC) for sustainable industrial applications. *Polymers*, 14(17), Article 3698. <https://doi.org/10.3390/polym14173698>
- Kuan, H. T. N., Tan, M. Y., Shen, Y., & Yahya, M. Y. (2021). Mechanical properties of particulate organic natural filler-reinforced polymer composite: A review. *Composites and Advanced Materials*, 30, 1-17. <https://doi.org/10.1177/26349833211007502>
- Lamberti, F. M., Román-Ramírez, L. A., & Wood, J. (2020). Recycling of bioplastics: Routes and benefits. *Journal of Polymers and the Environment*, 28, 2551-2571. <https://doi.org/10.1007/s10924-020-01795-8>
- Luck, J. D., Bazli, M., & Rajabipour, A. (2022). Bond between fibre-reinforced polymer tubes and sea water sea sand concrete: Mechanisms and effective parameters: Critical overview and discussion. *Fibers*, 10(1), Article 8. <https://doi.org/10.3390/fib10010008>

- Möllnitz, S., Feuchter, M., Duretek, I., Schmidt, G., Pomberger, R., & Sarc, R. (2021). Processability of different polymer fractions recovered from mixed wastes and determination of material properties for recycling. *Polymers*, 13(3), Article 457. <https://doi.org/10.3390/polym13030457>
- Perugini, F., Mastellone, M. L., & Arena, U. (2005). A life cycle assessment of mechanical and feedstock recycling options for management of plastic packaging wastes. *Environmental Progress*, 24(2), 137-154. <https://doi.org/10.1002/ep.10078>
- Robinson, B., & Iskander, M. (2008). Static and dynamic load tests on driven polymeric piles. In *GeoCongress 2008: Geosustainability and Geohazard Mitigation* (pp. 939-946). ASCE Publishing. [https://doi.org/10.1061/40971\(310\)117](https://doi.org/10.1061/40971(310)117)
- Sakr, M., El Naggari, M. H., & Nehdi, M. (2005). Interface characteristics and laboratory constructability tests of novel fiber-reinforced polymer/concrete piles. *Journal of Composites for Construction*, 9(3), 274-283. [https://doi.org/10.1061/\(asce\)1090-0268\(2005\)9:3\(274\)](https://doi.org/10.1061/(asce)1090-0268(2005)9:3(274))
- Sasse, F., & Emig, G. (1998). Chemical recycling of polymer materials. *Chemical Recycling of Polymer Materials*, 21, 777-789. [https://doi.org/10.1002/\(SICI\)1521-4125\(199810\)21:10%3C777::AID-CEAT777%3E3.0.CO;2-L](https://doi.org/10.1002/(SICI)1521-4125(199810)21:10%3C777::AID-CEAT777%3E3.0.CO;2-L)
- Tan, M. Y., Kuan, H. T. N., & Khan, A. A. (2017). Tensile properties of ground coffee waste reinforced polyethylene composite. In *Materials Science Forum* (Vol. 880, pp. 73-76). Trans Tech Publications Ltd.
- United Nations. (2022). *The Sustainable Development Goals Report 2022*. United Nations. <https://unstats.un.org/sdgs/report/2022/>
- UNEP. (2014). *Destruction of Carbon-Rich Mangroves Costs up to US\$42 billion in Economic Damages Annually*. UNEP Report. <https://www.unep.org/news-and-stories/press-release/destruction-carbon-rich-mangroves-costs-us42-billion-economic>
- Vineetha, V. J., & Ganesan, K. (2014). Interface friction between glass fibre reinforced polymer and gravel soil. *Advanced Materials Research*, 984-985, 707-710. <https://doi.org/10.4028/www.scientific.net/amr.984-985.707>
- Wang, X. H. (2022). Biodegradable polymers, history tells polymer science's fortune. *Chinese Journal of Polymer Science*, 40, 431-432. <https://doi.org/10.1007/s10118-022-2737-x>
- Yakupoglu, T., Rodrigo-Comino, J., & Cerdà, A. (2019). Potential benefits of polymers in soil erosion control for agronomical plans: A laboratory experiment. *Agronomy*, 9(6), Article 276. <https://doi.org/10.3390/agronomy9060276>
- You, J., Jiang, Z., Jiang, H., Qiu, J., Li, M., Xing, H., Xue, J., & Tang, T. (2022). A “plasticizing-foaming-reinforcing” approach for creating thermally insulating PVC/polyurea blend foams with shape memory function. *Chemical Engineering Journal*, 450, Article 138071. <https://doi.org/10.1016/j.cej.2022.138071>
- Yunus, M. (2018). Model test ultimate bearing capacity of bakau piles foundation on soft soil deposit. *EPI International Journal of Engineering*, 1(2), 94-99. <https://doi.org/10.25042/epi-ije.082018.15>

## Thermal Decomposition and Combustion Analysis of Malaysian Peat Soil Samples Using Coats Redfern Model-free Method

Dayang Nur Sakinah Musa<sup>1</sup>, Hamidah Jamil<sup>1</sup>, Mohd Zahirasri Mohd Tohir<sup>1,2\*</sup>, Syafie Syam<sup>3</sup> and Ridwan Yahaya<sup>4</sup>

<sup>1</sup>Department of Environment and Chemical Engineering, Faculty of Engineering, Universiti Putra Malaysia, 43400 UPM, Serdang, Selangor, Malaysia

<sup>2</sup>Department of Construction, Building Services and Structures, Universidad de Navarra, Pamplona, Spain

<sup>3</sup>Chemical and Materials Engineering Department, Faculty of Engineering-Rabigh Branch, King Abdulaziz University, Jeddah, Kingdom of Saudi Arabia

<sup>4</sup>Science and Technology Research Institute for Defence (STRIDE), Kajang, Selangor, Malaysia

### ABSTRACT

This research investigates the thermal decomposition behaviour of Malaysian peat soil through thermogravimetric analysis at varying heating rates. The study aims to analyse the thermal kinetics of decomposition for distinct peat soil types under inert and oxidative atmospheres while considering the role of available oxygen. The investigation encompasses virgin and agricultural peat, employing a non-isothermal thermogravimetric analysis technique to evaluate thermal decomposition characteristics and compute kinetic parameters using the Coats Redfern model-free approach. The pyrolysis profiles reveal three primary stages: moisture evaporation (30–180°C), organic component decomposition (200–500°C), and mineral decomposition (600–800°C). Virgin peat experiences a 43% mass loss during pyrolysis, while agricultural peat shows a 46% mass loss, emphasising insights into thermal behaviour and consistent decomposition patterns across peat types. Combustion profiles exhibit three main stages: dehydration (30–180°C), oxidative pyrolysis transforming organic matter into volatiles and char (200–300°C), and subsequent char oxidation (300–500°C). The

study determines average activation energy trends, measuring 14.87 kJ/mol for virgin peat and 5.37 kJ/mol for agricultural peat under an inert atmosphere, and 28.89 kJ/mol for virgin peat and 36.66 kJ/mol for agricultural peat under an oxidative atmosphere. The research introduces an innovative two-step reaction model elucidating peat thermal decomposition kinetics (excluding dehydration), including a

### ARTICLE INFO

#### Article history:

Received: 20 May 2023

Accepted: 02 October 2023

Published: 26 March 2024

DOI: <https://doi.org/10.47836/pjst.32.2.19>

#### E-mail addresses:

m.dayangnursakinah@gmail.com (Dayang Nur Sakinah Musa)

zbuckets1000@gmail.com (Hamidah Jamil)

zahirasri@upm.edu.my (Mohd Zahirasri Mohd Tohir)

s.syafie@gmail.com (Syafie Syam)

ridwan.yahaya@stride.gov.my (Ridwan Yahaya)

\* Corresponding author

discussion on the impact of oxygen availability on kinetic parameters. These findings essential peat fire smouldering modelling, contributing to peat combustion behaviour for effective strategies to reduce peat fire risks.

*Keywords:* Coats Redfern, combustion, peat, pyrolysis, thermal decomposition, thermogravimetric analysis

---

## INTRODUCTION

Peat is an important component representing a carbon-rich organic soil that contains at least 12% organic carbon (Rezanezhad et al., 2016), accompanied by a mineral content ranging from 20% to 35% (Turetsky et al., 2015). A brownish-black colour peat is formed through the partial decomposition of organic matter accumulated over thousands of years within oxygen-deprived, water-logged conditions derived from plant material (Lourenco et al., 2022). Precisely, peat is defined as soil containing no less than 65% organic matter and reaching a thickness of at least 50 cm (Adon et al., 2012; Lourenco et al., 2022).

Malaysian peatlands cover an area of about 2.6 Mha (Melling, 2015). Sarawak, one of two Malaysian states on the island of Borneo, possesses the largest extent of peat, over 1.6 Mha. They represent about 70% of all Malaysian peatlands (Melling, 2015) Emphasising tropical peat is of great significance due to its millennia-long peat accumulation, encompassing around 15%–19% of the total peat carbon and playing a role in 90% of carbon emissions from combustion (Azmi et al., 2021; Dommain et al., 2011; Sundari et al., 2012). However, the high carbon content in peat makes it easy to ignite (Rein, 2013), with the presence of oxygen and ignition sources (Melling, 2015). Especially when it is below its critical ignition point, the fire on the peat is called smouldering fire, which is a flameless and slow combustion process (Rein, 2013).

Peat is classified as a subsurface fuel beneath the ground's surface (Rein, 2013). During dry seasons, the peat's surface rapidly dries out, rendering it susceptible to easy ignition (Huang & Rein, 2014). Among the elements forming the fire triangle, fuels, oxygen, and ignition heat are the final elements needed for peat to catch fire. This heat can originate from various sources, including human activities, whether intentional or accidental, that act as potential ignition points (Fawzi et al., 2021). Examples include discarding lit cigarettes or neglecting to properly extinguish smouldering wood. Furthermore, external natural factors such as extremely hot weather, wind dispersion, or other influences can also contribute to ignition, leading to smouldering peat fires (Hu et al., 2018; Rein, 2013).

Smouldering combustion is the slow, low-temperature, flameless burning of porous fuels and is the most persistent type of combustion phenomenon (Rein, 2013). Upon ignition, smouldering peat fires possess the potential to persist for hours initially and then continue to smoulder over extended periods, spanning months to even years (Goldstein et al., 2020; Rein, 2013). Within controlled laboratory conditions, the persistence of smouldering peat

fires can extend over several weeks (Qin et al., 2022). This observation emphasises the need for further research on their thermal behaviour in this domain. The global impact of smouldering fires leads to forest degradation and localised haze occurrences with associated mortalities (Mezbahuddin et al., 2023; Othman et al., 2014). The main concern surrounding these events is their potential to desiccate the environment, disrupt natural ecosystems, and release harmful carbon emissions, ultimately contributing to haze formation. This particular setting provided the reasoning behind our research endeavour.

Smouldering occurs in the presence of ample oxygen; nonetheless, as the fire goes downward, the availability of oxygen is limited, and it may eventually disappear (Rein, 2013; Zhao et al., 2014). Consequently, at elevated temperatures and in the absence of oxygen, peat pyrolysis predominates the reaction. The smouldering peat fire emerges due to limited oxygen intake, resulting from the peat's organic materials undergoing pyrolysis (Kosyakov et al., 2020). Oxygen affects the peat's thermal decomposition process and subsequent smouldering combustion (Zhao et al., 2014). Various experimental studies have explored smouldering peat combustion under differing oxygen concentrations. For example, previous studies have examined the influence of different oxygen concentrations on the thermal decomposition of peat and the kinetics of thermal decomposition for peat samples within the atmosphere of Nitrogen and air, which are two of the most common atmospheres during the smouldering of peat fires (Chen et L., 2011; Zhao et al., 2014). These atmospheric conditions represent two common scenarios during peat smouldering. Another study examined three distinct peat types: two high-moor peat types collected in Edinburgh (Scotland) and Tomsk (Siberia), along with a transitional peat from Tomsk. Significantly different degradation patterns have been identified for the various peat forms of peat through a kinetic approach to estimate the sample temperature at high heating rates (Cancellieri et al., 2012).

This paper studies peat soil decomposition from two different locations in Malaysia using thermogravimetric analysis under oxidative and inert atmospheres. Peat properties influence its chemical reaction, including combustion and pyrolysis. Moisture content is one of the main factors contributing to the smouldering peat fire when the moisture decreases on the peat surface caused by evapotranspiration (Taufik et al., 2022; Prat et al., 2015). The peat soil types are characterised by their carbon content, and data for carbon and moisture are in Table 1. Model-free methods of Coats Redfern is used to calculate the activation energy of peat decomposition, and the two-step reaction model is applied. The role of oxygen on kinetic parameters is extensively discussed in this paper.

Table 1  
*Peat sample's carbon and moisture content*

Type of Peat	Carbon content (wt%)	Moisture content (wt%)
Virgin Peat	80.48	70.97
Agricultural Peat	68.27	76.66

## METHODOLOGY

The area for the sample collection has been identified around Selangor, Malaysia. The first sample, a virgin peat sample, was taken from Hutan Simpan Raja Musa, Selangor. The second agricultural peat sample was taken from a plantation site in Banting, Selangor.

Peat soil is distinctively characterised by its high carbon content, a primary marker of its identity. According to Ekono (1981), for soil to qualify as peat, it should possess a carbon content above 55% by weight percentage. Any value below this benchmark may indicate that the sample is not purely peat or could have been adulterated with other soil types. In the provided sample, the carbon content stands prominently at 80.48%, well above the standard value, affirming its status as peat soil. Other sample constituents include oxygen at 11.20%, aluminium at 2.69%, and silicon at 5.63%, with carbon being the predominant element, as expected for peat soils.

The sample was required to be weighed before ( $W_1$ ), and after ( $W_2$ ), the sample was dried in the oven to measure the moisture content. The weight of the sample before it dried contains the original moisture content of the sample ( $MC = ((W_1 - W_2) / W_2) \times 100\%$ ). Post-drying, the peat sample's weight indicated the absence of moisture. The sample was dried in the oven at 105°C for 24 hours, allowing water to evaporate and leaving only the dry content of the peat. The sample's moisture content was recorded, and the dried samples were sent to the Laboratory for thermalgravimetric analysis (TGA).

The tests were conducted under two conditions, air atmosphere and nitrogen atmosphere, for both virgin peat and agricultural peat samples. The heating rate was set to be 5, 10 and 20°C min<sup>-1</sup> and the temperature range from 30°C to 1000°C for virgin peat samples. Two runs were performed with the same experimental conditions, and the experiment's reproducibility was verified. The same conditions were applied for agricultural peat but with a heating rate of 10°C min<sup>-1</sup>.

The Coats-Redfern method is applied to calculate the pet decomposition activation energy ( $A_c$ ), and the two-step reaction model is applied (Ali et al., 2021). Every kinetic model obeys the same Arrhenius equation (Yan et al., 2019) and conversion rate equation as in Equations 1 and 2:

$$K(T) = A \exp\left(-\frac{E}{RT}\right) \quad (1)$$

$$\frac{da}{dt} = A e^{-E/RT} (1 - a)^n \quad (2)$$

where  $T$  = absolute temperature;  $R$  is the universal gas constant;  $A$  is the frequency or pre-exponential factor;  $E$  is the activation energy of the reaction;  $n$  is the order of reaction; and  $t$  is the time.



## RESULTS AND DISCUSSION

In a thermogravimetric analyser, the most valuable signal arising from a reaction is the curve derivative, DTG. This study employed DTG to pinpoint inflexion points on the TG curve, serving as a reference for calculating weight changes in each peat sample (Cancellieri et al., 2012). The activation energy ( $E_a$ ) represents the energy required for a reaction, indicating a component's reactivity level.

For this study,  $E_a$  and pre-exponential values were determined through the Coats Redfern method and the Microsoft Excel Solver. From TGA results, three regions were identified on each thermograph. These regions were defined by the approximate starting and ending points of the DTG curve, which visualises the thermal breakdown of the organic matter and the volatiles in the samples. The first region on the DTG curve, associated with the moisture and low boiling point of the organic matter in the sample, will not be further elaborated.

### Pyrolysis for Virgin Peat

Peat organic material falls under the biomass category (Kosyakov et al., 2020), allowing the application of the three-component reaction scheme to model organic material pyrolysis kinetics (Chen et al., 2011). In this study, peat pyrolysis unfolds in three main mass loss stages of mass loss: moisture evaporation (Stage 1), organic component decomposition (Stage 2), and mineral decomposition (Stage 3). Illustrated in Figure 1 are the experimental TG and derivative thermogravimetry (DTG) plots for virgin peat pyrolysis under Nitrogen at heating rates of 5, 10 and 20°C min<sup>-1</sup>.

Examining the DTG plot at a heating rate of 5°C min<sup>-1</sup> provides details about the thermal decomposition. Stage 2 occurred within the temperature range of about 250–500°C, which signifies the important phase of organic material transformation. As the temperature rises from 200°C, the decomposition rate of organic materials increases and reaches the first peak temperature at 378°C. Following this, the rate decreases slightly before reaching the secondary peak temperature at 400°C. After 500°C, the sample's mass decreases gradually, making the culmination of the organic materials decomposition process, accounting for 43% mass loss during this phase.

In the absence of oxygen, the organic material does not combust; instead, it decomposes into combustible gases and char, encompassing chemical compounds like cellulose, hemicellulose, and lignin (Rein et al., 2008). During this stage, the organic components of the peat undergo a transition into ash and charred fragments, and the resulting volatile substances are carried away by the flowing gas (Chen et al., 2011; Khoroshavin et al., 2012). At this stage, the impact of ash in the biomass char becomes significant in the context of the gasification procedure (Jayaraman & Gökalp, 2015). This observation highlights the complexity of peat decomposition but also the role of oxygen in dictating the organic material outcome.

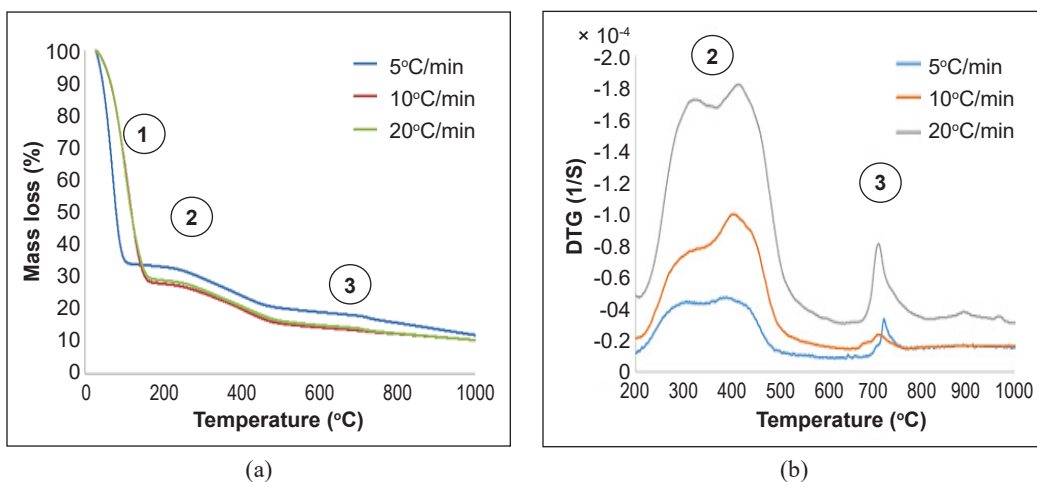


Figure 1. (a) TG and (b) DTG plots for virgin peat pyrolysis in Nitrogen at 5, 10 and 20°C min<sup>-1</sup>

The third stage of mass loss under the heating rate of 5°C min<sup>-1</sup> begins at 600°C and becomes more obvious between 660°C and 800°C. Such a high temperature facilitates the decomposition of peat materials, leading to a reduction in char production (Chen et al., 2011; Khelkhal et al., 2021). In Figure 1(b), the DTG curve illustrates a mass loss peak at about 780°C for a 5°C min<sup>-1</sup> heating rate. This finding aligns with the decomposition traits of certain minerals, such as calcium carbonate (Chen et al., 2011). The manifestation of this stage results in a total mass loss of 21%, providing a quantitative representation of the relationship between temperature and the decomposition process of the virgin peat. The calculated kinetic parameters for all heating rates of virgin peat in an inert atmosphere are tabulated in Table 2. The data offers comprehensive findings of the observed reaction and lays the groundwork for future studies into the kinetic complexities that influence peat's decomposition behaviour.

It was summarised that the pyrolysis kinetics of virgin peat were classified into moisture evaporation (Stage 1), organic component decomposition (Stage 2), and mineral

Table 2

*Kinetic parameters pyrolysis of virgin peat under different heating rates*

Heating Rate (°C min <sup>-1</sup> )	5	10	20
Ea <sub>2</sub> (kJ mol <sup>-1</sup> )	4.405	10.09	52.46
Ea <sub>3</sub> (kJ mol <sup>-1</sup> )	21.88	19.66	10.52
Average Ea (kJ mol <sup>-1</sup> )	13.14	14.87	31.49
A <sub>2</sub> (s <sup>-1</sup> )	-0.00030	-0.05058	215.1
A <sub>3</sub> (s <sup>-1</sup> )	0.03550	0.09343	-0.01841
n	2	2	2

Note. Subs 2 and 3 indicate the parameters at Stages 2 and 3, respectively

decomposition (Stage 3). Stage 2 at 250–500°C results in 43% mass involving organic material decomposing into combustible gases and char. The subsequent ash and chare are carried away by flowing gas in the third stage at 600–800°C, leading to significant peat material decomposing, reducing char production and resulting in a 21% mass loss. The data will offer insights into the behaviour of virgin peat under elevated temperature conditions, particularly in the context of smouldering peat fires.

**Pyrolysis of Agricultural Peat.** Figure 2 shows the experimental thermogravimetry (TG) and derivative thermogravimetry (DTG) plots depicting agricultural peat pyrolysis under a nitrogen atmosphere with a heating rate of 10°C min<sup>-1</sup>. Similar to virgin peat, agricultural peat also undergoes three primary mass loss stages for pyrolysis: moisture evaporation (Stage 1), organic component decomposition (Stage 2) and mineral decomposition (Stage 3).

DTG curve analysis reveals that Stage 2 transpires within a temperature range of about 270–530°C. As temperature rises from 200°C, the decomposition rate of organic materials increases, reaching its first peak temperature at 323°C. Subsequently, the rate experiences a minor decline, followed by a secondary peak temperature at 415°C. As the temperature exceeds 450°C, the gradual decrease in the sample's mass signifies the completion of the decomposition process for organic materials, resulting in an overall mass loss of 46% during this phase.

Moving to the third stage of mass loss, it initiates at 800°C and reaches its peak temperature at 915°C, leading to a total mass loss of 20%. These findings emphasise the complex condition of agricultural peat decomposition under diverse temperature conditions. The presence of certain mineral constituents within the peat could contribute

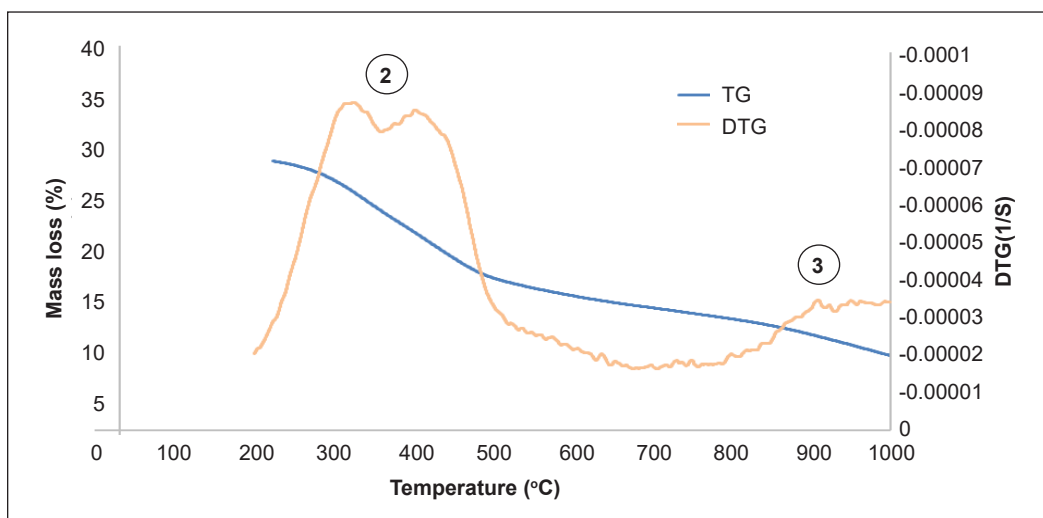


Figure 2. TG and DTG plots for agricultural peat pyrolysis in Nitrogen at a heating rate of 10°C min<sup>-1</sup>

to the decomposition behaviours. Table 3 presents the calculated kinetic parameters for agricultural peat under an inert atmosphere with a heating rate of  $10^{\circ}\text{C min}^{-1}$ , explaining the distinct thermal behaviour of the virgin peat under specified conditions.

The findings elucidate that agricultural peat shares resemblances with virgin peat, manifesting three distinct stages of mass loss throughout the pyrolysis process. Stage 2, unveiled through the DTG curve analysis, is notable within the temperature

span of  $270\text{--}530^{\circ}\text{C}$ . This stage showcases escalated decomposition rates as the temperature increases, leading to a substantial percentage mass loss of 46%. The third stage, which unfolds at higher temperatures, specifically starting at  $800^{\circ}\text{C}$  and reaching its peak at  $915^{\circ}\text{C}$ , brings about a significant 20% mass loss. These observations highlight the intricate thermal behaviour of agricultural peat during pyrolysis, contributing to a more comprehensive understanding of its decomposition characteristics.

**Comparison Pyrolysis of Virgin Peat and Agricultural Peat.** Figure 3 displays the DTG plots of virgin and agricultural peat under an inert atmosphere at a heating rate of  $10^{\circ}\text{C min}^{-1}$ . The graph shows that virgin peat exhibits a higher decomposition rate than agricultural peat within the same temperature range ( $200\text{--}500^{\circ}\text{C}$ ). This discrepancy is attributed to the higher carbon content in virgin peat. Consequently, the organic decomposition transpires more swiftly in virgin peat compared to agricultural peat, even when subjected to the same heating rate.

The study on the activation energy values for virgin and agricultural peat offers valuable insights into their respective thermal behaviours. Activation energy represents the minimum energy required to initiate a chemical reaction (Hänninen, 2017). The contrast between the average activation energy value was  $14.87\text{ kJ mol}^{-1}$  for virgin peat and  $5.37\text{ kJ mol}^{-1}$  for agricultural peat, underscoring a significant distinction in both peat types of reactivity. Particularly, the lower activation energy of agricultural peat suggests that the initiation of its pyrolysis might transpire at comparatively lower temperatures, indicative of a propensity for earlier decomposition. As evidenced by the results, the peak temperature in Stage 2 was  $405^{\circ}\text{C}$  for virgin peat and  $323^{\circ}\text{C}$  for agricultural peat. Generally, this peak temperature can be seen as the ignition temperature, which can be reached even with a relatively weak heat source. In light of this, it becomes evident that virgin peat could potentially present a heightened risk compared to agricultural peat due to its lower ignition

Table 3  
*Kinetic parameters pyrolysis of virgin peat under different heating rates*

Heating Rate ( $^{\circ}\text{C min}^{-1}$ )	10
$Ea_2$ ( $\text{kJ mol}^{-1}$ )	5.74
$Ea_3$ ( $\text{kJ mol}^{-1}$ )	5.00
Average $Ea$ ( $\text{kJ mol}^{-1}$ )	5.37
$A_2$ ( $\text{s}^{-1}$ )	-0.15318
$A_3$ ( $\text{s}^{-1}$ )	-0.00958
n	2

Note. Subs 2 and 3 indicate the parameters at Stages 2 and 3, respectively

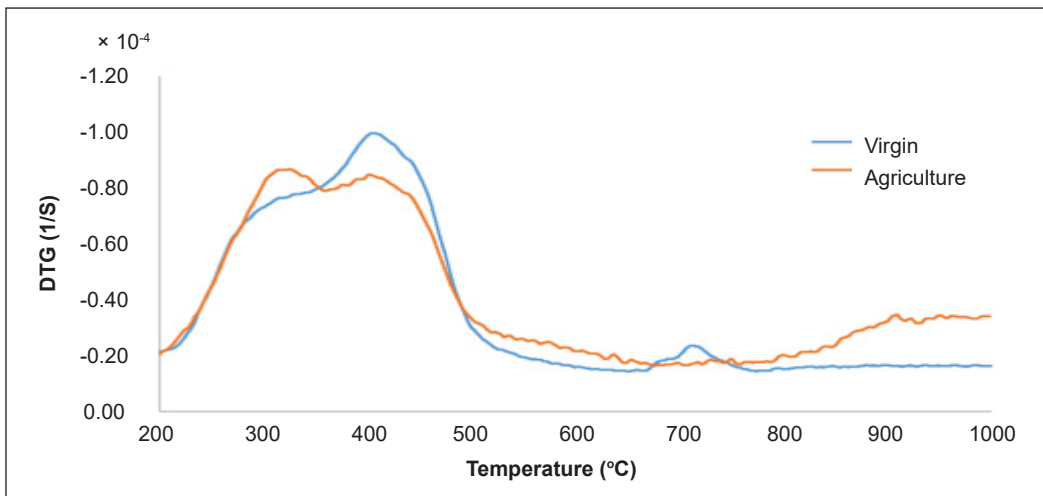


Figure 3. DTG curve of Virgin and Agricultural Peat under an inert atmosphere at  $10^{\circ}\text{C min}^{-1}$  heating rate

Table 4

*Kinetic parameters of virgin peat and agricultural peat under an inert atmosphere under  $10^{\circ}\text{C min}^{-1}$*

Parameters	$E_a$ ( $\text{kJ mol}^{-1}$ )	$A$ ( $\text{s}^{-1}$ )	$R^2$
Virgin Peat	14.87	-0.05058	0.9313
Agricultural Peat	5.37	-0.09128	0.9692

threshold. A comparison of kinetics can be found detailed in Table 4 for comprehensive reference and analysis.

The discussion focused on virgin and agricultural peat under an inert atmosphere. Upon observing the graph, it becomes apparent that virgin peat displays a higher decomposition rate than agricultural peat in the temperature range of  $200^{\circ}\text{C}$  to  $500^{\circ}\text{C}$ , indicative of its elevated carbon content, which poses a significant risk of environmental pollution. These findings imply faster organic decomposition in virgin peat, displaying an average activation energy of  $14.87 \text{ kJ mol}^{-1}$  than agricultural peat's  $5.37 \text{ kJ mol}^{-1}$ . Agricultural peat's lower activation energy suggests possible pyrolysis at lower temperatures, making it more susceptible to ignition. The ignition points occur in Stage 2, at  $405^{\circ}\text{C}$  for virgin peat and  $323^{\circ}\text{C}$  for agricultural peat.

### Combustion of Virgin Peat

Figure 4 depicts the TG and DTG plots for illustrating peat decomposition within the atmosphere of the air. These tests were conducted using  $5$ ,  $10$  and  $20^{\circ}\text{C min}^{-1}$  heating rates. The first region on the DTG curve indicates the process of dehydration and water elimination. This first stage, which occurs from room temperature to approximately  $180^{\circ}\text{C}$ , is linked to the dehydration of samples and requires no further elaboration. The second

region (Stage 2) is linked to the oxidation and removal of volatile matter within the samples. Following this, the third region (Stage 3) corresponds to the oxidation of residual char after the volatiles were removed from the samples (Varol et al., 2010).

At a heating rate of  $5^{\circ}\text{C min}^{-1}$ , Stage 2 occurred between  $200\text{--}300^{\circ}\text{C}$ , becoming notably obvious at  $270^{\circ}\text{C}$ . As the temperature rises from  $200^{\circ}\text{C}$ , the decomposition rate of organic materials increases, culminating in a prominent peak temperature at  $272^{\circ}\text{C}$  (Figure 4b). It signifies the decomposition of peat's organic components into volatiles, semi-volatiles, and char residues. The combustible components of the generated volatiles can then be oxidised by the influx of air, accompanied by substantial heat release (Kosyakov et al., 2020; Chen et al., 2011). In the second stage, the hemicellulose, cellulose, and lignin within the samples underwent decomposition. Subsequently, the third stage involved the combustion of structures possessing greater complexity and thermal stability, as well as char oxidation (Jayaraman et al., 2017b). As the temperature surpassed  $300^{\circ}\text{C}$ , a gradual decline in the virgin peat sample's mass was discerned, effectively encapsulating the culmination of the decomposition processes concerning organic and volatile constituents. A total mass loss of 44% resulted at this stage, bearing testimony to the extensive transformation during the combustion process. Biomass reactivity is linked to its light volatile content, while energy release is influenced by fixed carbon combustion (Jayaraman et al., 2017a).

Stage 3 is estimated to begin within the  $340\text{--}400^{\circ}\text{C}$  temperature range at a heating rate  $5^{\circ}\text{C min}^{-1}$ . At this stage, the peak occurs at  $350^{\circ}\text{C}$ , with a corresponding peak on the DTG graph. Here, the total mass loss reaches 27%. Beyond  $600^{\circ}\text{C}$ , the variations in the sample's mass alteration become imperceptible. According to Kosyakov et al. (2020), this pyrolysis range of  $200\text{--}600^{\circ}\text{C}$  resembles actual peat fire conditions. However, Chen et al. (2011)

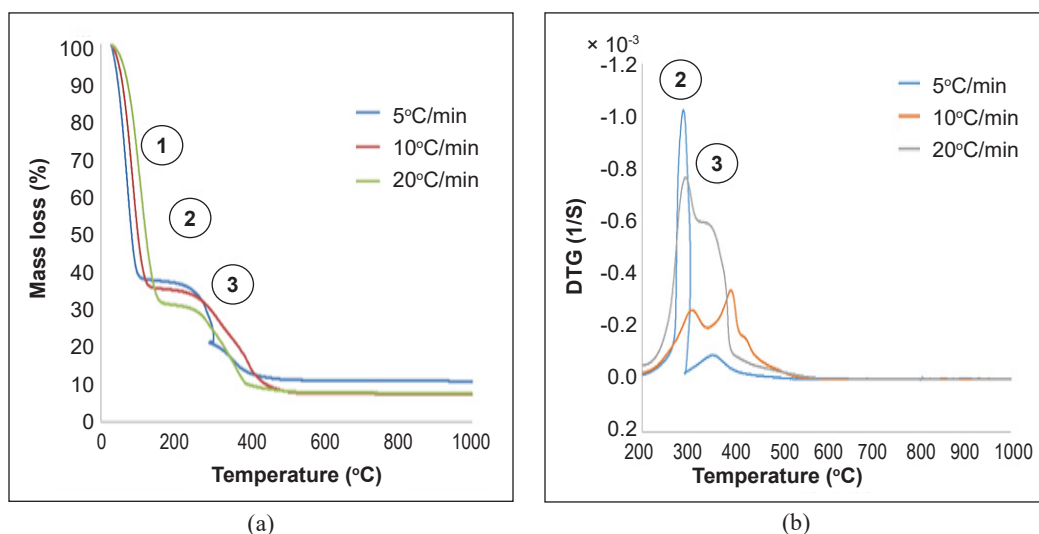


Figure 4. TG and DTG curves of virgin peat under an oxidative atmosphere at heating rates of 5, 10 and  $20^{\circ}\text{C min}^{-1}$

suggest that the phase of mineral decomposition is less discernible in an air environment. Table 5 presents the calculated kinetic parameters for all heating rates of virgin peat under an oxidative atmosphere. Additionally, the quality of the fitted lines was evaluated based on the  $R^2$  value assessment.

The findings regarding peat decomposition in an air atmosphere under heating rates of 5, 10, and 20°C min<sup>-1</sup> were summarised. The first stage signifies dehydration and water elimination up to 180°C. In the second stage, at a heating rate of 5°C min<sup>-1</sup>, oxidation and removal of volatile matter occur at 270°C, indicating the decomposition of peat's organic components. The third stage corresponds to char oxidation following volatile removal, commencing around 340–400°C, resulting in a 27% mass loss. This condition mirrors actual peat fire conditions, and these findings contribute to the understanding of peat combustion for the virgin peat, which is related to the forest reserve area.

Table 5  
*Kinetic parameters of virgin peat under different heating rates*

Heating Rate (°C min <sup>-1</sup> )	5	10	20
Ea <sub>2</sub> (kJ mol <sup>-1</sup> )	34.64	11.92	16.57
Ea <sub>3</sub> (kJ mol <sup>-1</sup> )	64.74	45.87	62.11
Average Ea (kJ mol <sup>-1</sup> )	49.69	28.89	39.34
A <sub>2</sub> (s <sup>-1</sup> )	4.708	0.06555	0.2631
A <sub>3</sub> (s <sup>-1</sup> )	1416	25.62	1118
n	2	2	2

*Note.* Subs 2 and 3 indicate the parameters at Stages 2 and 3, respectively

**Combustion of Agricultural Peat.** Figure 5 displays the thermogravimetry (TG) and derivative thermogravimetry (DTG) plots depicting the decomposition of agricultural peat within an oxygen environment, using heating rates of 10°C min<sup>-1</sup>. Similar to virgin peat, the decomposition of agricultural peat under oxygen exhibits three primary mass loss stages. The first stage occurs from room temperature up to about 150°C, which was attributed to the dehydration process of the peat samples.

Upon reviewing the DTG curve, Stage 2 occurred in the temperature range of approximately 270–350°C. As the temperature surpasses 200°C, the decomposition rate of organic materials escalates, culminating in a peak temperature of 326°C. Beyond 330°C, the sample's mass decreases, indicating the completion of the decomposition process for organic and volatiles. The total mass loss recorded at this stage is 30%.

The onset of the third stage of mass loss is estimated at 360°C, reaching its peak temperature at 398°C. Beyond 400°C, the sample's mass experiences a notable decline and achieves another minor peak at 430°C. The second appears to correspond to a maximum decomposition of hemicellulose. At this stage, less stable compounds created in the first stage, along with the cellulose and lignin, decompose due to heat, forming more complex

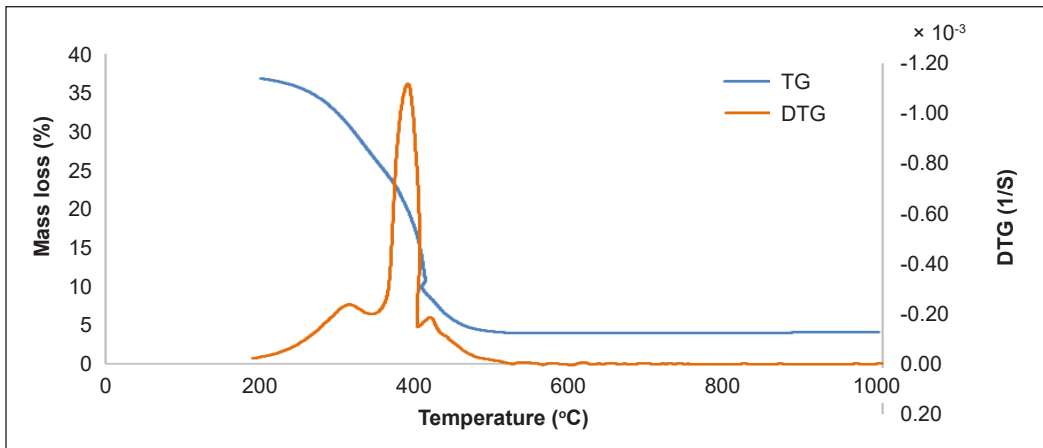


Figure 5. TG and DTG curves of agricultural peat under an oxidative atmosphere at heating rates of  $10^{\circ}\text{C min}^{-1}$

substances that need less heat to form (Khelkhal et al., 2022). The overall mass loss at this stage totals 44%. The kinetic parameters calculated for agricultural peat within an oxidative atmosphere are presented in Table 6.

The analysis of agricultural peat combustion is summarised in its decomposition at a rate of  $10^{\circ}\text{C min}^{-1}$ . It is important to highlight the presentation of kinetic parameters that illustrate the oxidative behaviour of agricultural peat. Similar to virgin peat, three stages occur in the mass loss process. The first stage involves peat sample dehydration at around  $150^{\circ}\text{C}$ . Stage 2 reveals an increase in organic decomposition, resulting in a 30% mass loss at a peak temperature of  $326^{\circ}\text{C}$ . Stage 3 demonstrates further mass loss corresponding to significant hemicellulose decomposition, accompanied by the decomposition of less stable compounds under heat, forming complex substances that require less heat. This finding underscores the importance of efficient thermal utilisation for agricultural peat samples, particularly as the mass loss in the third stage reaches 44%.

Table 6  
Kinetic parameters combustion of agricultural peat at  $10^{\circ}\text{C min}^{-1}$

Heating Rate ( $^{\circ}\text{C min}^{-1}$ )	10
$Ea_2$ ( $\text{kJ mol}^{-1}$ )	8.75
$Ea_3$ ( $\text{kJ mol}^{-1}$ )	64.58
Average $Ea$ ( $\text{kJ mol}^{-1}$ )	36.66
$A_2$ ( $\text{s}^{-1}$ )	-0.02706
$A_3$ ( $\text{s}^{-1}$ )	709.96
n	2

Note. Subs 2 and 3 indicate the parameters at Stages 2 and 3, respectively

**Comparison Combustion of Virgin Peat and Agricultural Peat.** Figure 6 illustrates the derivative thermogravimetry (DTG) of virgin and agricultural peat subjected to a heating rate of  $10^{\circ}\text{C min}^{-1}$  within an oxidative atmosphere. Based on the graph, agricultural peat displays a higher decomposition rate within the temperature range of  $350\text{--}420^{\circ}\text{C}$ . Notably, the DTG curve diverges between the Nitrogen and oxidative atmosphere due to the absence



of oxidation reactions in Nitrogen. Moreover, virgin peat's decomposition rate was lower than agricultural peat's under oxidative conditions.

By exploring the activation energy values, a differential pattern emerges between the two types of peat samples. The average activation energy value for virgin peat was  $28.89 \text{ kJ mol}^{-1}$ , while agricultural peat records a value of  $36.66 \text{ kJ mol}^{-1}$ . Higher activation energy values for agricultural peat suggest that agricultural peat requires more energy in comparison to virgin peat to undergo the same process. The activation energy of virgin peat indicated that it was easier for the peat to reach oxygen (Palamba et al., 2018). In simpler terms, virgin peat exhibits a higher flammability contrasted with agricultural peat. This contrast can be attributed to the higher carbon content in virgin peat. Comprehensive kinetic comparisons of the virgin peat and agricultural peat under an oxidative atmosphere are detailed in Table 7.

The combustion characteristics of virgin and agricultural peat, observed under a  $10^\circ\text{C min}^{-1}$  heating rate within an oxidative atmosphere, have been summarised to provide insights into peat fire behaviour. The importance of carbon content in combustion behaviour is also evident, as it indicates that virgin peat is more flammable than agricultural peat due to its reaction with oxygen. The higher activation energy observed in agricultural peat

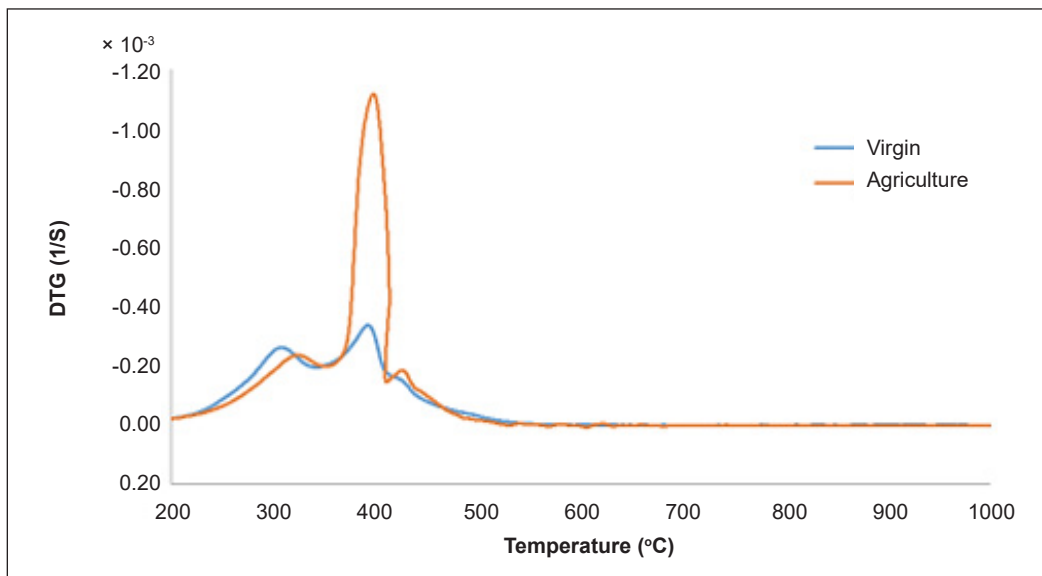


Figure 6. DTG curve of virgin and agricultural peat under an oxidative atmosphere at  $10^\circ\text{C min}^{-1}$  heating rate

Table 7

*Kinetic parameters of virgin peat and agricultural peat under an oxidative atmosphere at  $10^\circ\text{C min}^{-1}$*

Parameters	$E_a$ ( $\text{kJ mol}^{-1}$ )	$A$ ( $\text{s}^{-1}$ )	$R^2$
Virgin Peat	28.89	4.708	0.9405
Agricultural Peat	36.66	-0.02706	0.9444

suggests that it requires more energy compared to virgin peat for the same process. Virgin peat exhibits a slower decomposition rate than agricultural peat, with average activation energy values of 28.89 kJ mol<sup>-1</sup> for virgin peat and 36.66 kJ mol<sup>-1</sup> for agricultural peat. These findings imply that the higher flammability of virgin peat leads to increased carbon release during peat fire events compared to agricultural peat.

### Comparison of Pyrolysis and Combustion of Peat

As stated earlier, peat can break down in environments within inert or oxidative atmospheres, like in-ground fires. The presence of oxygen influences this decomposition process. Thus, this study compares the TG and DTG curves of peat decomposition in air and nitrogen atmospheres to see how oxygen plays a role in influencing the decomposition process. This study has redrawn the TG-DTG curves for nitrogen and air atmospheres of virgin peat under a heating rate of 10°C min<sup>-1</sup> to clarify the comparison. These can be found in Figures 1 and 4 and were redrawn in Figure 7.

Up to the temperature mark around 200°C, the two TG curves in Figure 7 closely match, indicating similar mass loss rates for peat decomposition in air and Nitrogen environments. This similarity arises because the initial mass loss is due to moisture evaporation, where the influence of oxygen is minimal. Therefore, the mass loss was mainly based on the heating rate rather than the moisture content of the sample (Jayaraman et al., 2020).

Within the temperature range of approximately 200–500°C, the mass loss rate is higher in the presence of air, and the starting temperature is lower compared to Nitrogen. It suggests that the reactions occurring in an oxidative atmosphere are more active within this temperature range. During this phase, a crucial decomposition process commences as

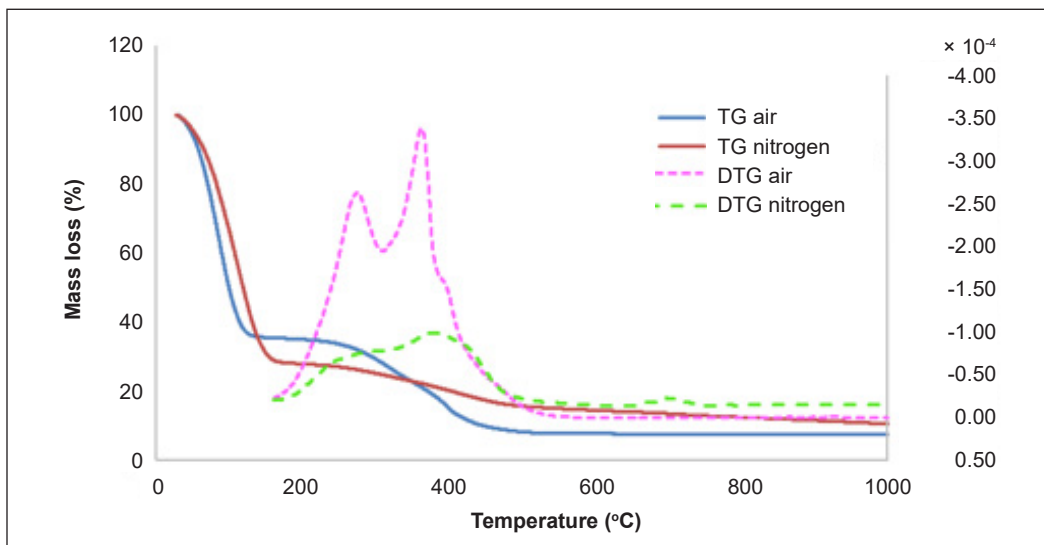


Figure 7. TG-DTG curve of virgin peat Nitrogen and air atmosphere at 10°C min<sup>-1</sup> heating rate

hemicellulose and cellulose decompose (Chen et al., 2011). In particular, oxygen availability leads to the combustion of volatile gases, thus intensifying the volatilisation rate.

Additionally, after reaching 600°C, nitrogen still allows the decomposition process to proceed, involving the decomposition of minerals in peat. However, this high-temperature effect is not noticeable in an oxidative atmosphere. At such high temperatures, oxygen does not significantly impact peat decomposition (Chen et al., 2011). Nevertheless, the presence of oxygen does result in the peak pyrolysis phase to lower temperatures and an earlier onset of the decomposition stage (Jayaraman & Gökalp, 2015). This complex interaction of temperature, oxygen, and decomposition processes is clarified through these observations.

Hence, the impact of oxygen on peat decomposition is examined in both inert and oxidative atmospheres, with specific relevance for environments such as in-ground fires. The study notes that mass loss rates primarily due to moisture evaporation, where oxygen's influence is minimal, occur around 200°C. Mass loss is subsequently expedited in the presence of air, with a slightly lower starting temperature within the 200–500°C range, indicating heightened reaction activity in an oxidative atmosphere. Beyond 600°C, nitrogen continues to support decomposition, including mineral breakdown, while oxidative atmospheres lack notable high-temperature effects. However, the presence of oxygen shifts peak pyrolysis to lower temperatures and advances the onset of decomposition. These findings emphasise the complex role of oxygen in peat decomposition, especially in the context of peat fire behaviour.

**Heating Rate Effect.** The thermal degradation patterns of virgin peat were examined at different heating rates of 5, 10 and 20°C min<sup>-1</sup> under both inert and oxidative atmospheres. Figures 1(b) and 4(b) showcase these profiles. Specifically, as the heating rate increased, the temperature range for thermal decomposition moved to a higher temperature zone. For example, the peak temperature for peat pyrolysis (Stage 2) was observed at 378°C, 405°C, and 415°C under heating rates of 5, 10 and 20°C min<sup>-1</sup>, respectively. One reason for the change in the DTG curve could be the poor heat conduction ability of peat, causing a lag in temperature distribution across its cross-section during heating.

Mishra and Mohanty (2018) have put forth an interesting proposition regarding the influence of heating rates on the temperature distribution within biomass particles. Their study suggests that at a lower heating rate, the temperature profile along the cross-section of biomass is assumed to be linear, as both the outer surface and the inner core of biomass gradually attain the same temperature over time. Recent studies have shown that lower heating rates enhance heat transfer within the particle surface (Mishra & Mohanty, 2018). Its heightened heat transfer efficiency at lower heating rates leads to more homogeneous temperatures within the peat samples, thus having implications for the kinetics and thermal behaviours during the pyrolysis or combustion process.

On the contrary, Gogoi et al. (2018) argue that a higher heating rate generally leads to less char formation during biomass pyrolysis. Moreover, the increased heating rate impacts the activation energy values of biomass decomposition reactions under an inert atmosphere (Gogoi et al., 2018). Besides, the completion of combustion was closely linked to the heating rate (Dong et al., 2023). Based on the result from Table 2 reveals that the average activation energy of virgin peat under an inert atmosphere was 13.14 kJ mol<sup>-1</sup>, 14.87 kJ mol<sup>-1</sup> and 31.49 kJ mol<sup>-1</sup> for heating rates of 5, 10 and 20°C min<sup>-1</sup>, respectively. Mishra and Mohanty (2018) propose that higher heating rates lead to a peak decomposition rate due to an increase in thermal energy. It will cause the ignition and combustion index to increase when the heating rate increases (Jayaraman et al., 2020)

In summary, this study examined the thermal degradation pattern of virgin peat under varying heating rates (5, 10 and 20°C min<sup>-1</sup>) in both inert and oxidative atmospheres. The altered DTG curve shape may arise from the poor heat conduction of virgin peat, resulting in temperature distribution delays during heating. The study also revealed the average activation energies for virgin peat under inert atmospheres, where higher heating rates induce peak decomposition rates due to increased thermal energy, impacting ignition and combustion indices. This research offers valuable insights into the complex relationship between heating rates, thermal behaviour, and peat combustion characteristics, contributing to a deeper understanding of peat fire behaviour under various conditions.

## CONCLUSION

In conclusion, this study delves into the thermal degradation of two distinct varieties of Malaysian peat soils and their associated kinetic parameters under varied experimental conditions, encompassing peat type, heating rates, and surrounding atmospheric composition. The samples analysed include virgin peat from a forest reserve and agricultural peat from a cultivated area, exhibiting different carbon contents due to potential elemental mixtures in agricultural peat. The research uncovers that the pyrolysis patterns of both peat types are similar, yet virgin peat displays a higher decomposition rate at Stage 2 due to its elevated carbon content. This higher carbon content leads to a greater heating value (Jayaraman et al., 2017b) and significantly influences the organic component decomposition process. Notably, virgin peat experiences a 43% mass loss during pyrolysis, while agricultural peat demonstrates a 46% mass loss, highlighting insights into thermal behaviour and consistent decomposition patterns across peat types.

Furthermore, the investigation unveils altered DTG curve shapes and activation energy trends, with 14.87 kJ mol<sup>-1</sup> for virgin peat and 5.37 kJ mol<sup>-1</sup> for agricultural peat under an inert atmosphere, and 28.89 kJ mol<sup>-1</sup> for virgin peat and 36.66 kJ mol<sup>-1</sup> for agricultural peat under an oxidative atmosphere. It deepens our understanding of the intricate relationships between heating rates, thermal behaviours, and peat combustion characteristics. By contrasting

the decomposition behaviours of virgin and agricultural peat under inert atmospheres, the differential influence of carbon content on their combustion characteristics becomes evident. Oxygen's presence significantly affects thermal decomposition and smouldering combustion, particularly pertinent to the deep soil layers with limited oxygen availability. The study underscores the higher flammability of virgin peat due to its elevated carbon content, impacting ignition points and decomposition rates, which in turn emphasises the need for tailored management strategies based on peat type to mitigate fire risks.

The significance of this research lies in Malaysia's vast peatland extent, approximately 2.5 million hectares, constituting 7.5% of the total land area and frequently encountering smouldering peat fire events. Despite existing research on peat soil thermal and kinetic decomposition, there remains a dearth of Malaysian peat soil studies. This study contributes to understanding and potentially simulating smouldering peat fires in Malaysia and holds relevance for global peatland management. The insights from investigating peat pyrolysis kinetics offer a comprehensive understanding of its behaviour under diverse conditions. The delineation of distinct mass loss stages, including moisture evaporation, organic component decomposition, and mineral breakdown, offers foundational knowledge. Moreover, the research highlights the paramount influence of heating rates on decomposition, influencing ignition, combustion, and flammability dynamics. By elucidating oxygen's role in peat decomposition, particularly in the context of ground fires, this research updates the potential research on management strategies to mitigate the environmental risks associated with peat fires.

## ACKNOWLEDGEMENTS

The authors acknowledge the financial support from the Ministry of Higher Education Malaysia via the Fundamental Research Grant Scheme (FRGS/1/2020/WAB03/UPM/02/1).

## REFERENCES

- Adon, R., Bakar, I., Wijeyesekera, D. C., & Zainorabidin, A. (2012). Overview of the sustainable uses of peat soil in Malaysia with some relevant geotechnical assessments. *International Journal of Integrated Engineering*, 4(4), 38-46.
- Azmi, N. A. C., Apandi, N. M., & Ahmad, A. S. (2021). Carbon emissions from the peat fire problem - A review. *Environmental Science and Pollution Research*, 28(14), 16948-16961. <https://doi.org/10.1007/s11356-021-12886-x>
- Cancellieri, D., Leroy-Cancellieri, V., Leoni, E., Simeoni, A., Kuzin, A. Y., Filkov, A. I., & Rein, G. (2012). Kinetic investigation on the smouldering combustion of boreal peat. *Fuel*, 93, 479-485. <https://doi.org/10.1016/j.fuel.2011.09.052>
- Chen, H., Zhao, W., & Liu, N. (2011). Thermal analysis and decomposition kinetics of Chinese forest peat under nitrogen and air atmospheres. *Energy and Fuels*, 25(2), 797-803. <https://doi.org/10.1021/ef101155n>

- Dommain, R., Couwenberg, J., & Joosten, H. (2011). Development and carbon sequestration of tropical peat domes in south-east Asia: Links to post-glacial sea-level changes and Holocene climate variability. *Quaternary Science Reviews*, 30(7-8), 999-1010. <https://doi.org/10.1016/j.quascirev.2011.01.018>
- Dong, H., Hu, X., Yu, A., Wang, W., Zhao, Q., Wei, H., Yang, Z., Wang, X., & Luo, C. (2023). Study on the mechanism of an enteromorpha-based compound inhibitor for inhibiting the spontaneous combustion of coal using in situ infrared spectroscopy and thermal analysis kinetics. *Journal of Environmental Chemical Engineering*, 11(2), Article 109577. <https://doi.org/10.1016/j.jece.2023.109577>
- Fawzi, N. I., Qurani, I. Z., & Darajat, R. (2021). Alleviating peatland fire risk using water management trinity and community involvement. In *IOP Conference Series: Earth and Environmental Science* (Vol. 914, No. 1, p. 012037). IOP Publishing. <https://doi.org/10.1088/1755-1315/914/1/012037>
- Gogoi, M., Konwar, K., Bhuyan, N., Borah, R. C., Kalita, A. C., Nath, H. P., & Saikia, N. (2018). Assessments of pyrolysis kinetics and mechanisms of biomass residues using thermogravimetry. *Bioresource Technology Reports*, 4, 40-49. <https://doi.org/10.1016/j.biteb.2018.08.016>
- Goldstein, J. E., Graham, L., Ansori, S., Vetruta, Y., Thomas, A., Applegate, G., Vayda, A. P., Saharjo, B. H., & Cochrane, M. A. (2020). Beyond slash-and-burn: The roles of human activities, altered hydrology and fuels in peat fires in Central Kalimantan, Indonesia. *Singapore Journal of Tropical Geography*, 41(2), 190-208. <https://doi.org/10.1111/sjtg.12319>
- Hänninen, K. I. (2017). A chemical mechanism for self-ignition in a peat stack. *Environment and Ecology Research*, 5(1), 6-12. <https://doi.org/10.13189/eer.2017.050102>
- Hu, Y., Fernandez-Anez, N., Smith, T. E. L., & Rein, G. (2018). Review of emissions from smouldering peat fires and their contribution to regional haze episodes. *International Journal of Wildland Fire*, 27(5), 293-312. <https://doi.org/10.1071/WF17084>
- Huang, X., & Rein, G. (2014). Smouldering combustion of peat in wildfires: Inverse modelling of the drying and the thermal and oxidative decomposition kinetics. *Combustion and Flame*, 161(6), 1633-1644. <https://doi.org/10.1016/j.combustflame.2013.12.013>
- Jayaraman, K., & Gökalp, I. (2015). Pyrolysis, combustion and gasification characteristics of miscanthus and sewage sludge. *Energy Conversion and Management*, 89, 83-91. <https://doi.org/10.1016/j.enconman.2014.09.058>
- Jayaraman, K., Kok, M. V., & Gokalp, I. (2017a). Combustion properties and kinetics of different biomass samples using TG-MS technique. *Journal of Thermal Analysis and Calorimetry*, 127(2), 1361-1370. <https://doi.org/10.1007/s10973-016-6042-1>
- Jayaraman, K., Kok, M. V., & Gokalp, I. (2017b). Thermogravimetric and mass spectrometric (TG-MS) analysis and kinetics of coal-biomass blends. *Renewable Energy*, 101, 293-300. <https://doi.org/10.1016/j.renene.2016.08.072>
- Jayaraman, K., Kök, M. V., & Gökalp, I. (2020). Combustion mechanism and model free kinetics of different origin coal samples: Thermal analysis approach. *Energy*, 204, Article 117905. <https://doi.org/10.1016/j.energy.2020.117905>

- Khelkhal, M. A., Lapuk, S. E., Buzyurov, A. V., Krapivnitskaya, T. O., Peskov, N. Yu., Denisenko, A. N., & Vakhin, A. V. (2022). Thermogravimetric study on peat catalytic pyrolysis for potential hydrocarbon generation. *Processes*, *10*(5), Article 974. <https://doi.org/10.3390/pr10050974>
- Khelkhal, M. A., Lapuk, S. E., Ignashev, N. E., Eskin, A. A., Glyavin, M. Y., Peskov, N. Y., Krapivnitskaia, T. O., & Vakhin, A. V. (2021). A thermal study on peat oxidation behavior in the presence of an iron-based catalyst. *Catalysts*, *11*(11), Article 1344. <https://doi.org/10.3390/catal11111344>
- Khoroshavin, L. B., Medvedev, O. A., Belyakov, V. A., & Bezzaponnaya, O. V. (2012). *Peat Fires and their Extinguishing*. ResearchGate. [https://www.researchgate.net/publication/324694093\\_PEAT\\_FIRES\\_AND\\_THEIR\\_EXTINGUISHING](https://www.researchgate.net/publication/324694093_PEAT_FIRES_AND_THEIR_EXTINGUISHING)
- Kosyakov, D. S., Ul'yanovskii, N. V., Latkin, T. B., Pokryshkin, S. A., Berzhonskis, V. R., Polyakova, O. V., & Lebedev, A. T. (2020). Peat burning - An important source of pyridines in the earth atmosphere. *Environmental Pollution*, *266*, Article 115109. <https://doi.org/10.1016/j.envpol.2020.115109>
- Lourenco, M., Fitchett, J. M., & Woodborne, S. (2022). Peat definitions: A critical review. *Progress in Physical Geography*, *47*(4), 506-520. <https://doi.org/10.1177/03091333221118353>
- Melling, L. (2015). Peatland in Malaysia. In *Tropical Peatland Ecosystems* (pp. 59-73). Springer. [https://doi.org/10.1007/978-4-431-55681-7\\_4](https://doi.org/10.1007/978-4-431-55681-7_4)
- Mezbahuddin, S., Nikonovas, T., Spessa, A., Grant, R. F., Imron, M. A., Doerr, S. H., & Clay, G. D. (2023). Accuracy of tropical peat and non-peat fire forecasts enhanced by simulating hydrology. *Scientific Reports*, *13*(1), 1-10. <https://doi.org/10.1038/s41598-022-27075-0>
- Mishra, R. K., & Mohanty, K. (2018). Pyrolysis kinetics and thermal behavior of waste sawdust biomass using thermogravimetric analysis. *Bioresource Technology*, *251*, 63-74. <https://doi.org/10.1016/j.biortech.2017.12.029>
- Othman, J., Sahani, M., Mahmud, M., & Ahmad, M. K. S. (2014). Transboundary smoke haze pollution in Malaysia: Inpatient health impacts and economic valuation. *Environmental Pollution*, *189*, 194-201. <https://doi.org/10.1016/j.envpol.2014.03.010>
- Palamba, P., Ramadhan, M. L., Pamitran, A. S., Prayogo, G., Kosasih, E. A., & Nugroho, Y. S. (2018). Drying Kinetics of Indonesian Peat. *International Journal of Technology*, *9*(5), Article 1006. <https://doi.org/10.14716/ijtech.v9i5.805>
- Prat, N., Belcher, C. M., Hadden, R. M., Rein, G., & Yearsley, J. M. (2015). A laboratory study of the effect of moisture content on the spread of smouldering in peat fires. *Flamma*, *6*(1), 35-38.
- Qin, Y., Musa, D. N. S., Lin, S., & Huang, X. (2022). Deep peat fire persistently smouldering for weeks: A laboratory demonstration. *International Journal of Wildland Fire*, *32*(1), 86-98. <https://doi.org/10.1071/wf22143>
- Rein, G. (2013). Smouldering fires and natural fuels. In *Fire Phenomena and the Earth System: An Interdisciplinary Guide to Fire Science* (pp. 15-33). John Wiley & Sons, Inc. <https://doi.org/10.1002/9781118529539.ch2>

- Rezanezhad, F., Price, J. S., Quinton, W. L., Lennartz, B., Milojevic, T., & Van Cappellen, P. (2016). Structure of peat soils and implications for water storage, flow and solute transport: A review update for geochemists. *Chemical Geology*, 429, 75-84. <https://doi.org/10.1016/j.chemgeo.2016.03.010>
- Sundari, S., Hirano, T., Yamada, H., Kusin, K., & Limin, S. (2012). Effect of groundwater level on soil respiration in tropical peat swamp forests. *Journal of Agricultural Meteorology*, 68(2), 121-134. <https://doi.org/10.2480/agrmet.68.2.6>
- Taufik, M., Widyastuti, M. T., Sulaiman, A., Murdiyarso, D., Santikayasa, I. P., & Minasny, B. (2022). An improved drought-fire assessment for managing fire risks in tropical peatlands. *Agricultural and Forest Meteorology*, 312, Article 108738. <https://doi.org/10.1016/j.agrformet.2021.108738>
- Turetsky, M. R., Benscoter, B., Page, S., Rein, G., Van Der Werf, G. R., & Watts, A. (2015). Global vulnerability of peatlands to fire and carbon loss. *Nature Geoscience*, 8, 11-14. <https://doi.org/10.1038/ngeo2325>
- Varol, M., Atimtay, A. T., Bay, B., & Olgun, H. (2010). Investigation of co-combustion characteristics of low quality lignite coals and biomass with thermogravimetric analysis. *Thermochimica Acta*, 510(1-2), 195-201. <https://doi.org/10.1016/j.tca.2010.07.014>
- Zhao, W., Chen, H., Liu, N., & Zhou, J. (2014). Thermogravimetric analysis of peat decomposition under different oxygen concentrations. *Journal of Thermal Analysis and Calorimetry*, 17(1), 489-497. <https://doi.org/10.1007/s10973-014-3696-4>



*Review Article*

## **Employment of Artificial Intelligence (AI) Techniques in Battery Management System (BMS) for Electric Vehicles (EV): Issues and Challenges**

**Marwan Atef Badran and Siti Fauziah Toha\***

*Department of Mechatronics Engineering, Faculty of Engineering, International Islamic University Malaysia, 53100, Gombak, Kuala Lumpur, Malaysia*

### **ABSTRACT**

Rechargeable Lithium-ion batteries have been widely utilized in diverse mobility applications, including electric vehicles (EVs), due to their high energy density and prolonged lifespan. However, the performance characteristics of those batteries, in terms of stability, efficiency, and life cycle, greatly affect the overall performance of the EV. Therefore, a battery management system (BMS) is required to manage, monitor and enhance the performance of the EV battery pack. For that purpose, a variety of Artificial Intelligence (AI) techniques have been proposed in the literature to enhance BMS capabilities, such as monitoring, battery state estimation, fault detection and cell balancing. This paper explores the state-of-the-art research in AI techniques applied to EV BMS. Despite the growing interest in AI-driven BMS, there are notable gaps in the existing literature. Our primary output is a comprehensive classification and analysis of these AI techniques based on their objectives, applications, and performance metrics. This analysis addresses these gaps and provides valuable insights for selecting the most suitable AI technique to develop a reliable BMS for EVs with efficient energy management.

*Keywords:* Artificial intelligence, battery management system, electric vehicle, lithium-ion battery, State of Charge

### ARTICLE INFO

*Article history:*

Received: 22 May 2023

Accepted: 02 October 2023

Published: 26 March 2024

DOI: <https://doi.org/10.47836/pjst.32.2.20>

*E-mail addresses:*

[marwan\\_69@yahoo.com](mailto:marwan_69@yahoo.com) (Marwan Atef Badran)

[tsfauziah@iium.edu.my](mailto:tsfauziah@iium.edu.my) (Siti Fauziah Toha)

\* Corresponding author

### **INTRODUCTION**

The phenomenon of global warming has evoked the concern of scholars and governments as well. Therefore, environmental protection has become a

priority of most countries worldwide. Especially when the climate is affected by air pollutants such as carbon dioxide released from fuel burning by various vehicles. In this context, EVs have emerged as clean energy-based alternatives with numerous advantages compared to traditional vehicles. They exhibit simplicity that leads to cost-effective maintenance, lower charging costs compared to fuel expenses, and the absence of noise and harmful emissions.

Nevertheless, EVs encounter several challenges, such as the limited driving range per full charge, the relatively long charging time, the cost of degraded battery replacement, and the heavy weight of the battery packs (Sanguesa et al., 2021). Consequently, the current industry trend is towards developing EVs to overcome the gas pollution of traditional cars (Jose et al., 2022). Hence, extra attention has been paid to rechargeable batteries, especially Lithium-ion ones, which are used in EVs as an environmentally friendly alternative.

In this regard, EV batteries have been extensively discussed in numerous studies in the literature from different aspects, such as the battery charge balance and battery aging (Laadjal & Cardoso, 2021). Therefore, researchers have made noticeable efforts to improve the performance of the Battery Management System (BMS) for efficient utilization of the EV battery pack.

The journey of the BMS from a unit of merely monitoring tasks to a multi-functional integrated unit was illustrated in Shen and Gao (2019). The study's authors discussed different battery models, such as thermal, electrical, and multi-physics modeling, besides the developments in BMS functions introduced by different manufacturers in this field. The research in these fields is still ongoing, including studies on heating methods for optimal battery pack heating in cold environments (Talele et al., 2023).

However, the increasing attention and recent advancements in the realm of Artificial Intelligence (AI) and machine learning (ML) have significantly influenced research and development efforts in developing novel techniques for estimating the states of EV batteries (Vidal et al., 2020). Hence, benefiting from the development in digitalization and the availability of reliable data sources, AI technology has been employed to solve complex computational problems that used to be challenging (Nagarale & Patil, 2020). However, some other non-AI techniques may be used to reduce the online calculations, especially when simple equations are adopted, yet it may lead to less, but acceptable, accuracy (Othman et al., 2022).

On the other hand, cloud-based predictive BMS was also introduced for the estimation of various battery states, including State of Charge (SOC) and State of Health (SOH) (Tran, Panchal, Khang et al., 2022). By taking advantage of the Internet of Things (IoT) and cloud computing, a digital twin BMS has been introduced in some studies to enhance the computation power, reliability, and storage capability (Li et al., 2020; Wang et al., 2022). The digital twin BMS is a virtual copy of the physical one but is located in the cloud. The

networked architecture of digital twin BMS improves its ability to perform various tasks such as fault detection, optimization and estimation of battery states. Furthermore, digital twin technology can play a crucial role in smart EVs, including autonomous navigation control, vehicle health monitoring and self-driving assistance (Bhatti et al., 2021). Hence, the utilization of online services for data training, fast computation, and model updating helps overcome the drawbacks of the traditional BMS.

In this study, the utilization of AI techniques in BMS of EV is reviewed. In particular, the study focused on the related publications in the past five years. The study provided some perspectives on the potential applications of AI techniques in the field of BMS. The study also illustrates the classification, benefits, and drawbacks of AI methods used for BMS.

## OVERVIEW OF BMS

The past decades have witnessed an increased demand for batteries as reliable energy storage for various applications, such as laptops, cell phones, and EVs. Compared to other types of rechargeable batteries, lithium-ion batteries have exhibited better performance, especially in terms of battery life, which has made them the favorite for EV manufacturers. Furthermore, it is considered a clean source of energy due to its non-toxic components and high level of safety (Liu et al., 2019).

However, the chemical nature of the battery, along with frequent charging and discharging, leads to battery aging and temperature issues that need to be handled. Therefore, a BMS should be utilized for monitoring, controlling and enhancing battery performance to prolong its lifespan (Gabbar et al., 2021). An overview of BMS will be illustrated, including its main functions, as well as a brief description of the main state indicators frequently mentioned in the literature. Furthermore, as part of this overview, we present Table 1, which offers a concise summary of typical technical specifications of battery cells as obtained from the reviewed papers. Table 1 serves as a reference point to illustrate the key characteristics of battery cells in the context of BMS functionality.

Table 1  
*Key technical specifications of battery cells in BMS applications*

Study	Battery Chemistry	Capacity	Nominal Voltage	Cut-Off Voltage	Maximum Discharging Current	Operating Temperature
Liu et al., 2020	Lithium-Nickel-Manganese-Cobalt-Oxide (LiNiMnCoO <sub>2</sub> )	2 Ah	3.6 V	2.5/ 4.2 V	20 A	-20°– 60°
Tran, Panchal, Chauhan et al., 2022	Lithium-Iron- Manganese-Phosphate (LiFeMnPO <sub>4</sub> )	25 Ah	3.2 V	2.2/ 3.65 V	75 A	-20°– 65°

Table 1 (continue)

Study	Battery Chemistry	Capacity	Nominal Voltage	Cut-Off Voltage	Maximum Discharging Current	Operating Temperature
Liu et al., 2018	Lithium-Iron- Phosphate (LiFePO4)	3.8 Ah	3.3 V	2.5/3.8 V	3.8 A	-20°– 60°
Kaur et al., 2021	Lithium Nickel Cobalt Manganese Oxide (LiNiCoMnO2)	3 Ah	3.7 V	2.7/4.2 V	3 Ah	-20°– 65°
Li et al., 2020	Lithium-Nickel-Cobalt-Aluminum-Oxide (Li-NCA)	3.4 Ah	3.6 V	2.65/4.2 V	8 Ah	-10°– 60°
Meng et al., 2019	Lithium-Nickel-Manganese-Cobalt (Li-NMC)	63 Ah	3.7 V	3/ 4.15 V	63 Ah	-20°– 60°
Baveja et al., 2023	Lithium-Iron-Phosphate (LiFePO4)	1.1 Ah	3.2 V	2/ 3.65 V	1.1 Ah	-20°– 60°

## BMS Functions

Different types of BMS may have various functions according to their complexity and functionality. However, BMS functions typically include monitoring, protection and optimization of battery performance (Andrea, 2010). For example, BMS can monitor different measurements of the battery cells, such as voltage, current and temperature. Those measurements are essential for another vital BMS function, which is the estimation of battery states, such as SOC, SOH and State of Power (SOP). Such information can be used to perform cell balancing tasks to protect the battery cells, maximize their performance, and control the system temperature.

Moreover, BMS needs to establish good communication with the battery pack and other related devices, as seen in Figure 1, which illustrates the general functions of BMS. However, the architecture of BMS may include other tasks based on its complexity.

## Cell Balancing

The battery pack of an EV is composed of several connected cells of similar characteristics. Nevertheless, different cells may have different behavior in terms of impedance, self-discharge, and temperature, which leads to an unbalanced charging situation. Hence, to handle this situation, BMS can use onboard or external components to control the charging flow so that cell balancing is achieved. Therefore, cell balancing is a vital function of MBS that helps to extend the battery life by controlling the charging process (Duraisamy & Kaliyaperumal, 2021).

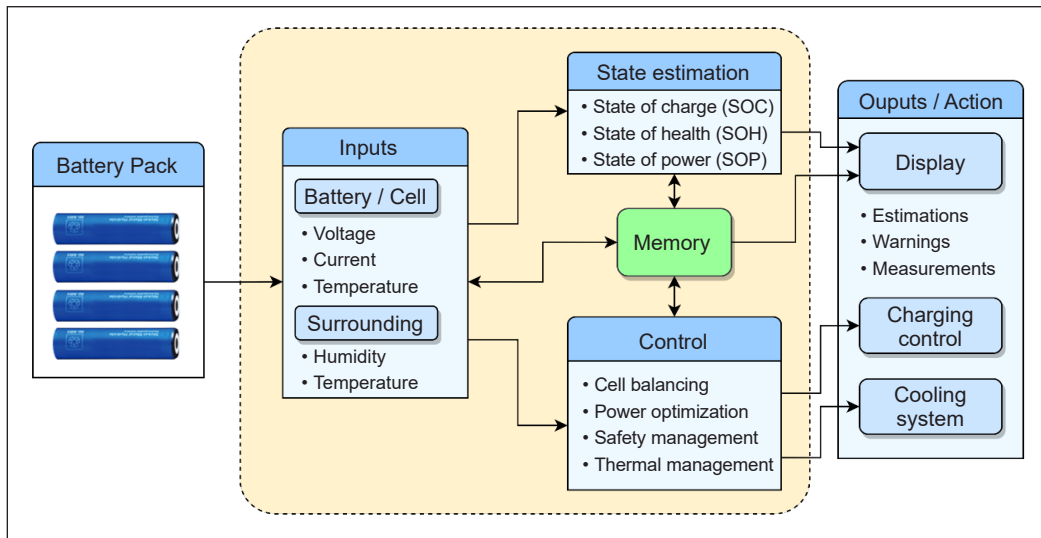


Figure 1. General functions of BMS (Zhang & Fan, 2020)

Cell balancing includes active and passive balancing, while the latter is more popular due to its low cost and simplicity. Theoretically, passive cell balancing can be achieved by a simple resistor or a power transistor, which dissipates the balancing energy as heat. On the other hand, energy is not wasted in active cell balancing; instead, it is transferred to the other cells within the battery pack (Andrea, 2010). However, the design of the cell balancing module can take a more complicated form, where it can provide thermal predictions for optimal battery thermal management systems (Baveja et al., 2023).

Generally, both passive and active cell balancing schemes have advantages and drawbacks, yet both techniques lead to a remarkable enhancement in battery performance (Omariba et al., 2019). However, optimal cell balancing can be achieved by adopting intelligent techniques, such as machine learning. This approach leads to extra advantages such as achieving higher SOC, reducing cell degradation, improving battery safety, and extending lifespan (Andrea, 2010). Furthermore, AI techniques can also be employed in other BMS functions to enhance performance.

## Battery States

Batteries have attracted the concern of developers and researchers due to their features as a clean source of energy that can be recharged and requires minimal maintenance. However, batteries are degradable products that wear out over time as a result of aging and repeated charging and discharging, which affect their efficiency and performance. Therefore, the battery state should always be monitored to ensure its safety and efficiency and to keep the EV under control. However, the battery states cannot be measured directly; instead, they can be estimated by utilizing other acquired measurements such as current, voltage and temperature.

With regard to BMS, there are several battery states to be considered, such as SOC, SOH and state of life. Such states have been widely utilized to avoid battery overcharging and over-discharging and, consequently, to prolong the battery life (Park et al., 2020). The following is a brief discussion of the most important battery state indicators, namely, SOC, SOH and SOP.

**State of Charge (SOC).** Like the fuel gauge in traditional vehicles, SOC is the battery state gauge of the remaining amount of energy inside a battery, which can be used to obtain other states of the battery, such as the state of safety and the state of function (Sanguesa et al., 2021). SOC indicator is mathematically defined as the ratio of battery charge level to its rated capacity and can be expressed as Equation 1 (Murnane & Ghazel, 2017):

$$SOC = \frac{C_{releasable}}{C_{rated}} \times 100\% \quad [1]$$

where,  $C_{releasable}$  is the amount of capacity that can be discharged when the battery is fully depleted, while  $C_{rated}$  is the measurement of charge and discharge currents with respect to the nominal capacity of the battery.

It can be noticed that many approaches for the enhancement of SOC prediction have been proposed by several studies related to BMS in the literature. However, it is noteworthy that apart from SOC prediction, the value of SOC can be improved during the driving process using different technologies, such as the Regenerative Braking System (RBS) (Ghazali et al., 2020).

**State of Health (SOH).** For a fully charged new battery, the maximum releasable capacity is almost the same as its rated capacity. However, as the battery degrades over time, its maximum capacity declines. This concept can serve as an indicator of the overall health of the battery; hence, the SOH indicator is defined as the ratio of maximum battery charge level to its rated capacity and can be expressed as Equation 2 (Murnane & Ghazel, 2017):

$$SOH = \frac{C_{max}}{C_{rated}} \times 100\% \quad [2]$$

where,  $C_{max}$  is the maximum capacity that can be discharged from a fully charged battery.

It should be noted that the value of  $C_{max}$  naturally decreases over time due to several factors, such as ambient temperature, cycle aging, and charging rate. Monitoring these factors is crucial for enhancing the SOH and prolonging battery life.

**State of Power (SOP).** For safety purposes, it is important to know how much power can be delivered by the battery at a specific time. That purpose can be achieved by the SOP indicator, which is defined as the ratio of battery peak power to its rated power and can be expressed as Equation 3 (Rahimifard et al., 2021):

$$SOP = \frac{P_{max}}{P_{rated}} \times 100\% \quad [3]$$

where,  $P_{max}$  is the maximum power that can be continually delivered by the battery over a given duration, while  $P_{rated}$  is the rated power as specified by the manufacturer.

The main advantage of SOP is that it helps to bind the charge or discharge power within certain limits; thus, the lifespan of the battery can be prolonged. However, SOP is highly dependent on the SOC in addition to other factors such as battery capacity, voltage, chemistry, and initial features.

### AI TECHNIQUES APPLIED IN BMS

AI has significantly influenced the advancement of EV technology in the past decade. Therefore, several AI techniques, such as Deep Learning (DL), have been applied in the technology of EVs for different purposes, including the control of self-driving vehicles and charging system optimization, as illustrated in Figure 2.

An analytical study by Lee (2020) demonstrates the effect of AI on EV technology based on patent data over more than three decades. The study concluded that AI has been

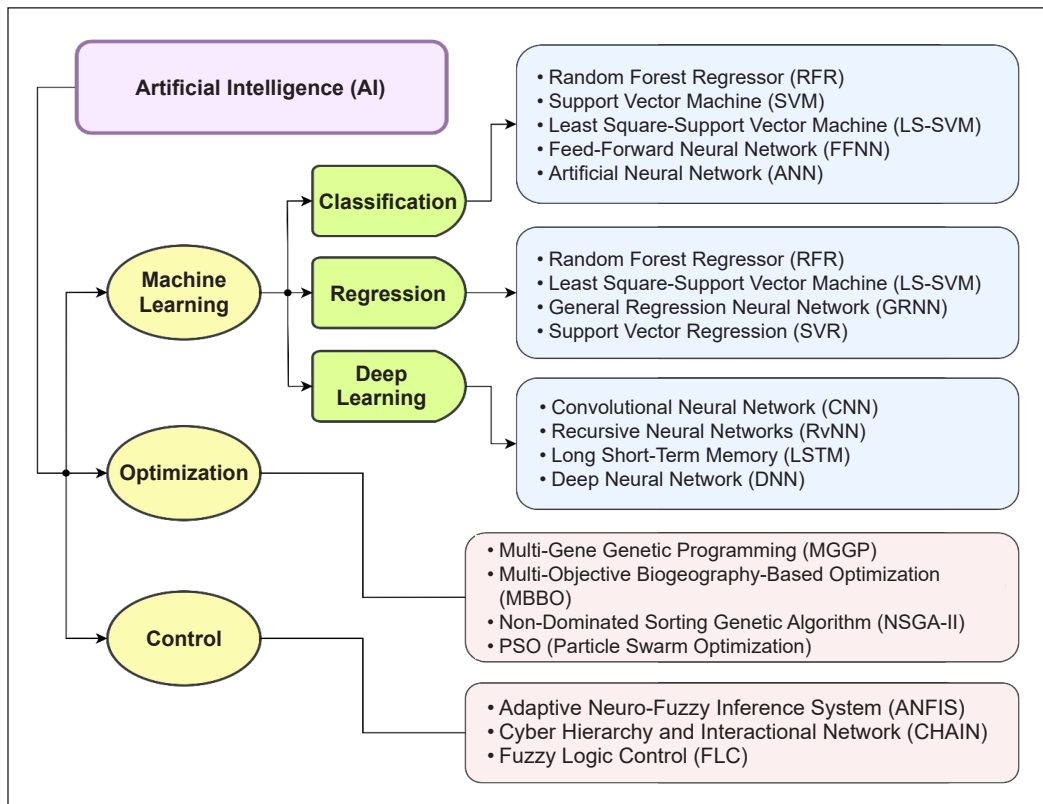


Figure 2. AI techniques in BMS applications (Ardeshiri et al., 2020)

employed to increase the driving range of EVs, enhance the automation of EVs, and encourage clean energy by adopting battery-based EVs. Furthermore, the study found that fuzzy and Neural Networks (NN) have been the most used AI algorithms in EV technology, which have influenced the charging time, the battery state prediction, and the optimization of the energy management system.

Recent research efforts on battery management technology have paid extra attention to AI algorithms aiming for smarter and more effective BMS. Therefore, various types of AI techniques have been proposed in the literature to enhance the efficiency and functionality of the BMS.

### Neural Networks

Neural Network (NN) is a biologically inspired algorithm that has been used for solving a variety of problems. In general, NN is composed of three layers: the input layer that accepts the initial data, a hidden layer that includes the computations, and the output layer that produces the result. However, the NN may contain one hidden layer or more, as illustrated in Figure 3.

Further insights into the diversity of neural network architectures can be obtained from Table 2, which summarizes key attributes of neural networks as observed in some relevant studies from our reviewed papers. These studies provide valuable examples of different configurations, including variations in inputs, hidden layers, and outputs.

In battery management, NN exhibited an accurate SOC estimation. Therefore, different NN methods were utilized in the

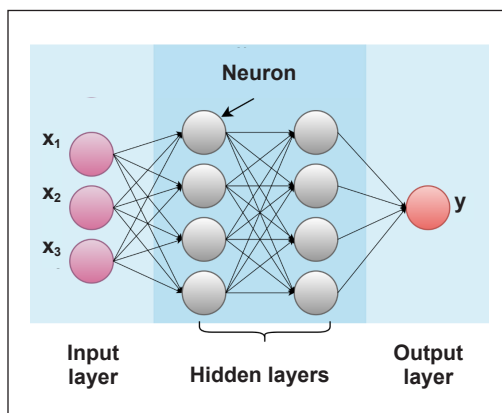


Figure 3. Neural network architecture (Karahoca, 2012)

Table 2  
Key attributes of Neural Networks applied in BMS

Study	Inputs	Hidden Layers	Output
Liang et al., 2018	Current and Temperature	9	Discharge Priority
Bonfitto, 2020	Current, Voltage and Temperature	2	SOC
How et al., 2020	Current, Voltage and Temperature	4	SOC
Zhao et al., 2020	Current, Voltage and Temperature	6	SOC
Purohit et al., 2021	Current and Time	1	SOC/ SOE/ PL
Chandran et al., 2021	Time, Current and Voltage	1	SOC
Duraisamy and Kaliyaperumal, 2021	Current, Voltage and Temperature	1	Resistor Switch



literature for SOC estimation under two main categories: Feed-Forward Neural Network (FFNN) and DL methods. The first has the advantage of a simple structure, while the latter has the ability to handle time-series data. Thus, a hybrid method of FFNN and DL may have the advantages of both methods. However, battery aging, temperature, and operating conditions should be considered to enhance the accuracy of SOC estimation when NN is applied (Cui et al., 2022).

In recent research, various types of Neural Networks have been utilized to improve the performance of BMS. The following is a brief demonstration of the researchers' efforts in that field.

**Feed-Forward Neural Network.** FFNN algorithm is the conventional type of NNs, which consists of three layers with several neurons in each one. This algorithm has been used to solve a wide range of problems using different optimization techniques. However, the efficiency of FFNN is affected by the quality of the trained data in terms of accuracy, precision, and flexibility. Therefore, prior data cleaning should be applied to the trained data to improve its quality (Hemeida et al., 2020).

Benefitting from its capabilities, Purohit et al. (2021) employed the FFNN algorithm in the realm of battery management to predict SOC, state of energy (SOE), and power loss (PL) of EV battery packs. The training algorithm was simulated using two-layer FFNN to estimate the battery pack states. The results showed higher accuracy of the proposed estimation method compared to other regression models. FFNN algorithm was also employed by Bonfitto (2020) to obtain a combined estimation of SOC and SOH battery states. FFNN was designed by training the collected datasets from laboratory environment experiments while real driving profiles were used for validation. The study results showed high accuracy in both SOC and SOH estimation.

While most researchers focused on the battery states at the individual battery level, Liang et al. (2018) considered the state of the battery module as a whole. The study proposed a methodology to evaluate the state of the battery module using its current and temperature values as inputs to overcome the difficulty of SOH estimation on the module level. For that purpose, Artificial Neural Network (ANN) models were used with three training algorithms, namely, Levenberg, Bayesian Regularization and Scaled Conjugate. The findings of the study indicated that the model with the best performance was obtained using the Levenberg algorithm.

**General Regression Neural Network.** The General Regression Neural Network (GRNN) method is a single-pass NN algorithm that can be used for solving regression problems. GRNN consists of four layers: input, hidden, summation, and division layer. Instead of iterative training, GRNN uses input and output data to approximate an arbitrary function between them (Azzeh et al., 2018).

Li and Zhao (2021) employed the GRNN algorithm to enhance the performance of EV BMS. The study proposed a cloud-based framework for battery management by utilizing big data and cyber-physical system technologies. The study used GRNN and a data cleaning technique to restore the missing data in the battery's cloud database under varying temperature conditions. The outcomes of the experiments revealed that the proposed method was stable and adaptable to the changes in battery temperature. The results also showed a minimum error in data restoring and SOC estimation. However, the proposed method is highly dependent on the quality and the speed of communication with the data in the cloud, which may not always be stable.

**Deep Neural Network.** Nowadays, Deep Neural Network (DNN) plays a main role in data modeling and analysis; thus, it can be used in BMS technology to enhance the prediction of the battery states. For example, data-driven modeling can use battery signals to achieve a reliable estimation of battery capacity without the need to know its internal features.

A data-driven DNN approach was utilized by Kara (2021) to predict the Remaining Useful Life (RUL) of lithium-ion batteries, which helps reduce maintenance costs and increase system efficiency and reliability. The proposed method combined Convolutional neural networks (CNN), Fully Connected Layer (FCL), and Long Short-Term Memory (LSTM) algorithms, while Particle Swarm Optimization (PSO) was applied to obtain the optimal parameters, such as a number of epochs and NN layers, to extract the spatial-temporal relationship from historical degradation data. The proposed model, which was tested on NASA's battery dataset, showed accurate results in terms of SOH and RUL prediction compared to the benchmark models. However, the proposed model may introduce high computational demand due to the hyperparameter optimization procedure, especially in the case of using a large training set.

DNN was also used by How et al. (2020) to develop a SOC estimation model, which was trained using the drive cycle of Dynamic Stress Test (DST). The study results revealed that increasing the number of hidden layers in the DNN model can noticeably improve the SOC estimation. However, the study found that four hidden layers were the optimal number that, if exceeded, would increase the error rate. According to the study results, the proposed model was found capable of estimating SOC values of various unseen drive cycles, including the Federal Urban Driving Schedule (FUDS), Beijing Dynamic Stress Test (BDST), and Supplemental Federal Test Procedure (SFTP) US06.

**Recursive Neural Network.** A Recursive Neural Network (RvNN) is a kind of deep learning network with an architecture in which the same weights are applied recursively on a structured input to get a structured prediction. RvNN can be seen as a generalized version of the Recurrent Neural Network (RNN) with a specific tree structure. It is a useful

technique for pattern recognition in a data set and for the prediction of structured outputs (Irsoy & Cardie, 2014).

A SOC prediction model for Lithium-ion Batteries was proposed by Zhao et al. (2020) based on RvNN. The proposed model aims to improve the representation of battery data and obtain hidden feature information in the battery vector. Consequently, the prediction performance of SOC will be improved. The study also proposed a prediction model based on CNNs and fed it with trained battery vectors. Simulation results of the study showed that the integration of the trained vectors with CNNs enhanced the performance of SOC prediction by a noticeable margin compared to the traditional estimation methods.

### Evolutionary Methods

In some cases, it is difficult to use conventional methods for developing the EV battery model, especially in the presence of nonlinear relations, complicated computations, or multi-objective optimization. In this case, evolutionary computation techniques can be considered a good alternative to deal with those challenges.

**Multi-Objective Biogeography-based Optimization.** When two or more objectives are needed to be achieved, Multi-Objective Optimization (MOO) is a good option for optimal solutions. The main advantage of the MOO algorithm is that it helps find a balance between contradictory objective functions and optimal trade-off solutions.

An example of the employment of an evolutionary algorithm in the field of BMS has been proposed by Liu et al. (2018), where a Multi-objective Biogeography-Based Optimization (M-BBO) algorithm was applied to derive the charging patterns that suit Lithium-ion batteries. The optimization technique in that study was fed with the following objectives: charging time, battery health and efficiency of energy conversion. On the other hand, the constraints were defined as voltage, current, temperature, and SOC of the battery. The authors used Pareto frontiers to find a trade-off between the charging speed and the efficiency of energy conversion so that a suitable charging pattern can be selected for different priorities.

**Multi-Gene Genetic Programming.** Multi-Gene Genetic Programming (MGGP) is a nonlinear system modeling technique that combines the advantages of Genetic Programming (GP) and classical regression and, thus, can be used to generate prediction models. Taking advantage of this feature, MGGP has been employed by Cui et al. (2020) to model the EV battery. The study has two objectives: to create a model for battery capacity and to find the optimized design of the battery enclosure. For that purpose, the study used a modified MGGP approach for training the experimental data to obtain the model of EV battery capacity. Then, the battery pack enclosure was optimized using the Non-dominated

Sorting Genetic Algorithm (NSGA-II) algorithm to achieve the study objectives, such as minimizing the mass and improving the performance of the heat dissipation of the battery packs. However, the optimum design of the battery pack enclosure cannot be generalized, as it is influenced by other factors such as vehicle design, size, and weight.

**Non-dominated Sorting Genetic Algorithm.** As mentioned, multi-objective optimization deals with problems of conflicting objectives, where a set of solutions is obtained, which may contain a non-dominated set of solutions. In this case, NSGA-II, the succeeding version of the NSGA algorithm, can be used to solve this multi-objective optimization problem. NSGA-II offers an enhanced mating mechanism based on crowding distance and uses an adapted dominance explanation without penalty functions to build the constraints (Hojjati et al., 2018).

The mentioned advantage of NSGA-II has been utilized by Meng et al. (2019) to improve the accuracy of battery SOH estimation. Considering the accuracy of SOH estimation and the measurement efficiency, multiple voltage ranges were optimized in the said study using the NSGA-II algorithm. The non-dominated solutions helped to increase the flexibility of the proposed method. Consequently, more choices would be available for SOH estimation at different stages of battery charging. The results of that study showed an accurate estimation of battery capacity using an optimal single voltage range. However, the proposed method cannot be generalized for different battery types since the optimal voltage ranges require prior information about the degradation process of the battery. Furthermore, the cycle aging of the battery was not considered in the study.

**Particle Swarm Optimization.** In addition to the wide range of applications, the well-known Particle Swarm Optimization (PSO) algorithm can also be used for battery SOH prediction, as introduced by Li et al. (2021). The authors performed data cleaning on real driving data before the data was optimized using PSO. The obtained results showed an accurate model of SOH prediction. However, battery aging has not been considered in that study, which may affect its performance when applied in reality.

**Genetic Particle Filter.** Particle Filter (PF) algorithm is a type of Monte Carlo method and recursive Bayesian estimation. In recent years, researchers have shown increasing interest in the ability of this algorithm to estimate the state of non-linear and non-Gaussian problems. However, using PF leads to a particle degeneracy problem, which can be solved by involving a Genetic Algorithm (GA) to change the small-weight particles into offspring particles (Qiu & Qian, 2018).

A prediction method based on Genetic Particle Filter (GPF) was introduced by Liu et al. (2020) for SOC and SOP estimation. The advantages of GA and PF were combined by

the proposed method to enhance the diversity of particles. The incremental current test was used in the study to identify the parameters of the proposed battery model, which was tested on the FUDS driving cycle. The outcomes of the experiments showed that the proposed genetic PF algorithm achieved better accuracy in SOC and SOP estimation compared to the traditional PF method.

### Regression Algorithms

Regression algorithms, such as Decision Trees (DT), are a type of supervised machine learning algorithm for classification and prediction applicable in a wide range of fields. The nodes in the decision tree perform a comparison test between independent variables and a constant in a top-down process to achieve the best attribute for solving the classification problems (López et al., 2022). The employment of different types of regression algorithms in BMS technology, as discussed in the reviewed papers, is illustrated in the following points:

**Least Square-Support Vector Machine.** Support Vector Machine (SVM) is an effective technique for solving problems such as non-linear classification and density estimation. Therefore, the SVM algorithm has been effectively used for classification purposes, such as image classification in OCR applications (Tan et al., 2022). On the other hand, the Least-Square Support Vector Machine (LS-SVM) is a variant of the traditional SVM technique, which can be used for classification, regression, and clustering, besides exhibiting high accuracy in solving optimization problems (Mitra et al., 2007).

Shu et al. (2020) proposed a uniform framework for SOH estimation and healthy features optimization of the Lithium-ion battery in EVs. The study utilized a fixed-size LS-SVM for SOH estimation, while GA was applied to determine the optimal charging voltage range and the optimal parameters of fixed-size LS-SVM. The experimental results showed that the proposed framework was robust and more accurate in terms of SOH estimation compared to traditional ML algorithms. However, the experiments in the study have been conducted at a fixed temperature, which is not the case in real life. Therefore, the proposed method in the study can be enhanced by considering the change in the surrounding temperature.

**Support Vector Regression.** Support Vector Regression (SVR) is a supervised ML technique that can solve regression problems by analyzing the relationship between a continuous dependent variable and the predictor variables. Furthermore, SVR has the ability to handle high-dimensional data as its optimization is represented by support vectors rather than the dimension of input data (Zhang & O'Donnell, 2020).

Xuan et al. (2020) employed the Principal Component Analysis (PCA) of battery features to study the effect of external factors, such as voltage, current, and temperature, on

the accuracy of SOC estimation. The study also proposed an SVR-based SOC prediction method with a classification of collected data and optimization of the training set size. The experimental results showed that the enhanced SVR algorithm outperformed the original SVR algorithm in terms of accuracy and computational speed. However, the evaluation of the proposed method did not include more complicated driving conditions.

**Random Forest Regressor.** Random Forest (RF) is an ensemble learning algorithm that can be used for solving classification and regression problems. In RF, a group of decisions is made to classify the dataset, while the final decision is taken based on the majority. Therefore, RF demonstrates better accuracy when applied to large datasets. Besides, it is an effective technique for estimating missing data (Awad & Khanna, 2015).

Utilizing RF advantages, Mawonou et al. (2021) employed the Random Forest Regressor (RFR) for data-driven aging prediction of EV lithium-ion batteries. The RF algorithm was trained on real-life EV data collected over several years to develop an aging predictor to accurately estimate the battery SOH.

**Multi ML Techniques.** Machine Learning (ML) is a general topic that includes numerous techniques with a wide range of applications. Many types of those techniques have been successfully implemented by several studies in BMS applications. In general, ML methods can be classified into three categories: supervised, unsupervised and reinforcement learning.

Basically, ML methods have been used in BMS for battery modeling; thus, the exact chemical process of the battery is not needed. Moreover, ML techniques have been used to perform other functions of BMS, such as estimating the battery states and predicting the battery aging and degradation (Ahmed et al., 2021). The following is a brief demonstration of several studies where multiple ML techniques have been employed in BMS applications.

Kaur et al. (2021) proposed three models of battery capacity estimation based on three network architectures: FFNN, CNN and LSTM. The evaluation of battery capacity estimation considered the impact of different variables, such as the model complexity and the sampling rate. The study results showed that LSTM was more accurate and flexible compared to FNN and CNN methods. Results also proved that using sparsely sampled signals as model input was more efficient than using densely sampled signals and reduced the computational cost. However, the study considered measurements from a set of two batteries to evaluate the model performance, while the validation could be more accurate if larger battery datasets were considered. Furthermore, the study did not consider the effect of other parameters, such as the ambient temperature, on SOH estimation.

Tran, Panchal, Chauhan, et al. (2022) included a comparison of four ML models, namely, Linear Regression, RF, K-Nearest Neighbors, and DT, for predicting thermal and electrical behaviors of Lithium-ion batteries under different ambient temperatures. The

training, validation, and testing of the models used the following input features: battery capacity, ambient temperature, battery current, historical battery voltage, and temperature to predict the battery voltage and temperature. Simulation results showed that the DL-based model was the most accurate of all models.

Another comparison of six ML models for Lithium-ion battery SOC estimation was presented by Chandran et al. (2021). The comparison included several ML algorithms, such as SVM, ANN, and Gaussian Process Regression (GPR). The study results showed that among the proposed ML methods, ANN and GPR demonstrated the best performance in terms of SOC estimation according to Mean Squared Error (MSE) and Root Mean Squared Error (RMSE) metrics. Moreover, the study denoted that the proposed method is valid for real-time SOC estimation after optimizing the hyperparameters of the GPR-linear model.

### Other AI Techniques

In addition to the previously mentioned AI techniques, several other techniques have been proposed in related literature studies on EV BMS, which will be described in this subsection.

**Fuzzy Logic Control.** Fuzzy Logic Control (FLC) is an intelligent algorithm that can be useful, especially when it is difficult to build a mathematical model of the system. The robust FLC is very useful for nonlinear and time-varying systems. Besides, it has the advantage of adaptation due to flexibility and easiness of changing the fuzzy rules (Ma et al., 2018).

Benefiting from its capability of dealing with such nonlinear systems, FLC was employed by Abulifa et al. (2019) to control the energy consumption of EV batteries. The study aimed to increase driving time by minimizing energy consumption, namely, when the Heating, Ventilation, and Air-Conditioning (HVAC) system is on. The proposed FLC was tested on NEDC and Japan10-15 driving cycles. The results showed that applying FLC increased the battery driving range between 10% and 20% compared to the uncontrolled strategy. However, the proposed design in the study is limited to a specific configuration and needs to be tested using different specifications and driving cycles.

Similarly, Kamal and Adouane (2018) applied FLC to minimize total energy consumption and reduce battery aging. The parameters of the fuzzy membership function were tuned using NNs to control power distribution between the internal combustion engine and the electric motor. FLC was employed to detect battery faults and to compensate for the faults of the voltage sensor and current actuator. Simulation results confirmed the ability of the proposed approach to achieve a suboptimal energy consumption when applied to vehicles of unknown driving cycles and its ability to compensate for the effects of battery faults.

However, fuzzy logic is dependent on human intelligence and expertise, which may vary from one person to another. Therefore, fuzzy membership functions of FLC usually need tuning for better performance.

**Cyber Hierarchy and Interactional Network.** Cyber Hierarchy and Interactional Network (CHAIN) is a framework that can provide multi-scale insights; thus, it is a suitable environment to develop efficient algorithms for battery state estimation, fault diagnosis, cell balancing, and other functions of BMS. In that context, a CHAIN framework of end-edge-cloud architecture was proposed by Yang et al. (2020) for developing a cloud-based BMS. The proposed framework included several functions, such as SOX estimation, cell balancing, and fault diagnosis. Such a cloud-based BMS provides multi-scale perceptions and allows the application of advanced algorithms to perform the system functions efficiently. The CHAIN framework was also proposed by Yang et al. (2021) to certify the stability and security of full battery lifespan to achieve optimal battery performance.

It can be noted that the CHAIN framework is a promising technology as it utilizes the high computing capabilities of the platform to solve complex algorithms. Thus, the performance of BMS is enhanced. However, like other cloud-based technologies, it is dependent on wireless communication and online services; thus, it is highly dependent on and affected by network availability and conditions. Therefore, an onboard control module may be considered as a backup solution for outage conditions.

In conclusion, the investigated AI techniques in this paper have been used for different purposes in BMS, such as regression, optimization, and state estimation. However, each technique may be more suitable for a particular application. Therefore, a summary of those techniques, including their advantages, disadvantages, and applications in BMS, is illustrated in Table 3.

Table 3  
*Advantages and disadvantages of various AI techniques used in EV BMS*

AI Technique	Application in BMS	Advantages	Disadvantages
<ul style="list-style-type: none"> <li>• <b>Neural Networks (FFNN, GRNN) (Hemeida et al., 2020; Purohit et al., 2021; Bonfitto, 2020; Liang et al., 2018; Azzeh et al., 2018; Li &amp; Zhao, 2021)</b></li> </ul>	<ul style="list-style-type: none"> <li>• SOC, SOH &amp; PL prediction</li> <li>• To estimate the orders of cell balancing.</li> <li>• To obtain the optimal charging current profile to decrease temperature and charging time.</li> <li>• To recover lost data in the battery's cloud database</li> </ul>	<ul style="list-style-type: none"> <li>• Ability to handle unorganized data</li> <li>• Its adaptive structure makes it applicable for different purposes</li> </ul>	<ul style="list-style-type: none"> <li>• Heavily relies on the size of training data</li> <li>• Affected by data suitability</li> </ul>
<ul style="list-style-type: none"> <li>• <b>Deep Learning (CNN, RvNN, LSTM) (Zhao et al., 2020; Kaur et al., 2021; Tran, Panchal, Chauhan et al., 2022)</b></li> </ul>	<ul style="list-style-type: none"> <li>• SOC prediction</li> <li>• RUL prediction</li> </ul>	<ul style="list-style-type: none"> <li>• Ability to handle complex data and relationships</li> <li>• Suiting parallel and distributed modes for fast training</li> </ul>	<ul style="list-style-type: none"> <li>• Requires high computational power</li> <li>• Requirement of huge amount of trained data</li> </ul>



Table 3 (continue)

AI Technique	Application in BMS	Advantages	Disadvantages
<ul style="list-style-type: none"> <li>• <b>Evolutionary Methods (MGGP, M-BBO, NSGA-II, PSO) (Cui et al., 2020; Liu et al., 2018; Meng et al., 2019; Li et al., 2021)</b></li> </ul>	<ul style="list-style-type: none"> <li>• To obtain the model of EV battery capacity by training the experimental data</li> <li>• To derive the charging patterns that suit Lithium-ion batteries</li> <li>• To enhance SOH estimation via optimal charge voltage range</li> <li>• To identify optimal battery pack features for better heat dissipation</li> </ul>	<ul style="list-style-type: none"> <li>• Reducing the search time for the optimal solution</li> <li>• Supporting multi-objective optimization</li> </ul>	<ul style="list-style-type: none"> <li>• Do not always achieve the best answer</li> <li>• Sometimes they get stuck in local optima</li> <li>• Require well-defined objective and constraint functions</li> </ul>
<ul style="list-style-type: none"> <li>• <b>Regression Algorithms (LS-SVM, SVR, RFR) (Shu et al., 2020; Xuan et al., 2020; Mawonou et al., 2021)</b></li> </ul>	<ul style="list-style-type: none"> <li>• SOC prediction</li> <li>• SOH estimation</li> </ul>	<ul style="list-style-type: none"> <li>• Better performance in higher dimensions</li> <li>• Optimal choice for linear/non-linear classes</li> <li>• No need for data normalization or scaling</li> <li>• The impact of missing values is negligible</li> <li>• Reduced error through aggregated tree inputs</li> </ul>	<ul style="list-style-type: none"> <li>• Slow when dealing with a larger dataset</li> <li>• Poor performance with overlapped classes</li> <li>• Sensitive to data change</li> <li>• Training decision trees is time-consuming</li> </ul>
<ul style="list-style-type: none"> <li>• <b>CHAIN (Yang et al., 2020)</b></li> </ul>	<ul style="list-style-type: none"> <li>• SOC, SOH prediction</li> <li>• Cell balancing</li> <li>• Thermal control</li> </ul>	<ul style="list-style-type: none"> <li>• Powerful computational performance</li> <li>• Offers multi-disciplinary digital solutions</li> </ul>	<ul style="list-style-type: none"> <li>• Requires a continuous internet connection</li> <li>• High-performance cloud computing increases the cost</li> </ul>
<ul style="list-style-type: none"> <li>• <b>FLC (Abulifa et al., 2019; Kamal &amp; Aduane, 2018)</b></li> </ul>	<ul style="list-style-type: none"> <li>• To minimize the energy consumption of EV battery</li> </ul>	<ul style="list-style-type: none"> <li>• Effective tool for solving nonlinear problems</li> <li>• Can be easily constructed and modified</li> </ul>	<ul style="list-style-type: none"> <li>• Limited to human knowledge and expertise</li> <li>• Membership functions require tuning to increase accuracy</li> </ul>
<ul style="list-style-type: none"> <li>• <b>PCA (Xuan et al., 2020)</b></li> </ul>	<ul style="list-style-type: none"> <li>• To study the effect of current, voltage and temperature on SOC estimation</li> </ul>	<ul style="list-style-type: none"> <li>• Saving time by removing correlated features in a dataset</li> <li>• Improves visualization by transforming data from high to low dimensions</li> </ul>	<ul style="list-style-type: none"> <li>• Data normalization is required before performing</li> <li>• Combination of features makes it difficult to understand the major components</li> </ul>

A critical review of BMS research reveals significant gaps. While AI, especially Neural Networks, is widely used for SOC estimation, more robustness testing is needed under dynamic conditions, like varying temperatures and real-world driving profiles. Integration with advanced battery tech, e.g., solid-state batteries, lacks attention. Adapting AI to these technologies is unexplored. Additionally, BMS and IoT integration for real-time monitoring and predictive maintenance remains underexplored.

Lastly, assessing AI-driven BMS scalability across diverse applications needs more research. A holistic approach, encompassing cybersecurity, materials science, and data analytics, is essential for evolving battery management.

## CONCLUSION

In this paper, the employment of AI techniques in EV BMS was reviewed. The study explored the state of the art in the field of AI-based BMS as indicated in the literature over the past few years. Various types of AI techniques, such as neural networks, regression algorithms, and evolutionary methods, were demonstrated in this study, with more focus on their applications in BMS development.

It was noted that most reviewed papers employed supervised machine learning methods, either for classification or regression purposes. Meanwhile, a smaller number of researchers applied AI techniques for optimization or control purposes. It was also observed that recent studies have given more attention to the fast-growing technologies in the fields of IoT, communications, and cloud computing. Therefore, several studies have proposed cloud-based approaches to enhance the efficiency of BMS and obtain faster and more accurate results.

Finally, here are key recommendations to improve BMS performance and identify further research opportunities:

- Enhance Lithium-ion battery performance simulation by incorporating factors like temperature, humidity, and noise during data acquisition.
- Consider onboard control modules as a robust alternative to cloud-based technology, particularly in areas with unstable internet connections.
- Continue researching the physical optimization of battery pack topology for improved power consumption, cell balancing, and ease of control.

## ACKNOWLEDGEMENTS

This work was supported by the Research Management Centre (RMC) and International Islamic University Malaysia (IIUM). We are grateful for the support enabling us to conduct this research.

## REFERENCES

- Abulifa, A. A., Soh, A. C., Hassan, M. K., Ahmad, R. M. K. R., & Radzi, M. A. M. (2019). Energy management system in battery electric vehicle based on fuzzy logic control to optimize the energy consumption in HVAC system. *International Journal of Integrated Engineering*, 11(4), 11-20. <https://doi.org/10.30880/ijie.2019.11.04.002>
- Ahmed, M., Zheng, Y., Amine, A., Fathiannasab, H., & Chen, Z. (2021). The role of artificial intelligence in the mass adoption of electric vehicles. *Joule*, 5(9), 2296-2322. <https://doi.org/10.1016/j.joule.2021.07.012>
- Andrea, D. (2010). *Battery Management Systems for Large Lithium Battery Packs*. Artech House.
- Ardeshiri, R., Balagopal, B., Alsabbagh, A., Ma, C., & Chow, M. (2020). Machine learning approaches in battery management systems: State of the art: Remaining useful life and fault detection. In *2020 2nd IEEE International conference on industrial electronics for sustainable energy systems (IESES)* (Vol. 1, pp. 61-66). IEEE Publishing. <https://doi.org/10.1109/ieses45645.2020.9210642>
- Awad, M., & Khanna, R. (2015). *Efficient learning machines: Theories, concepts, and applications for engineers and system designers*. Springer nature. <https://doi.org/10.1007/978-1-4302-5990-9>
- Azzeh, M., Nassif, A. B., & Banitaan, S. (2018). Comparative analysis of soft computing techniques for predicting software effort based use case points. *IET Software*, 12(1), 19-29. <https://doi.org/10.1049/iet-sen.2016.0322>
- Baveja, R., Bhattacharya, J., Panchal, S., Fraser, R., & Fowler, M. (2023). Predicting temperature distribution of passively balanced battery module under realistic driving conditions through coupled equivalent circuit method and lumped heat dissipation method. *Journal of Energy Storage*, 70, Article 107967. <https://doi.org/10.1016/j.est.2023.107967>
- Bhatti, G., Mohan, H., & Singh, R. R. (2021). Towards the future of smart electric vehicles: Digital twin technology. *Renewable and Sustainable Energy Reviews*, 141, Article 110801. <https://doi.org/10.1016/j.rser.2021.110801>
- Bonfitto, A. (2020). A method for the combined estimation of battery state of charge and state of health based on artificial neural networks. *Energies*, 13(10), Article 2548. <https://doi.org/10.3390/en13102548>
- Chandran, V., Patil, C. K., Karthick, A., Ganeshaperumal, D., Rahim, R., & Ghosh, A. (2021). State of charge estimation of lithium-ion battery for electric vehicles using machine learning algorithms. *World Electric Vehicle Journal*, 12(1), Article 38. <https://doi.org/10.3390/wevj12010038>
- Cui, X., Panda, B., Chin, C. M. M., Sakundarini, N., Wang, C. T., & Pareek, K. (2020). An application of evolutionary computation algorithm in multidisciplinary design optimization of battery packs for electric vehicle. *Energy Storage*, 2(3), Article e158. <https://doi.org/10.1002/est2.158>
- Cui, Z., Wang, L., Li, Q., & Wang, K. (2022). A comprehensive review on the state of charge estimation for lithium-ion battery based on neural network. *International Journal of Energy Research*, 46(5), 5423-5440. <https://doi.org/10.1002/er.7545>
- Duraisamy, T., & Kaliyaperumal, D. (2021). Machine learning-based optimal cell balancing mechanism for electric vehicle battery management system. *IEEE Access*, 9, 132846-132861. <https://doi.org/10.1109/access.2021.3115255>

- Gabbar, H. A., Othman, A. M., & Abdussami, M. R. (2021). Review of battery management systems (BMS) development and industrial standards. *Technologies*, 9(2), Article 28. <https://doi.org/10.3390/technologies9020028>
- Ghazali, A. K., Hassan, M. K., Radzi, M. A. M., & As'array, A. (2020). Integrated braking force distribution for electric vehicle regenerative braking system. *Pertanika Journal of Science & Technology*, 28(S2), 173-182. <https://doi.org/10.47836/pjst.28.s2.14>
- Hemeida, A. M., Hassan, S. A., Mohamed, A. A. A., Alkhalaf, S., Mahmoud, M. M., Senjyu, T., & El-Din, A. B. (2020). Nature-inspired algorithms for feed-forward neural network classifiers: A survey of one decade of research. *Ain Shams Engineering Journal*, 11(3), 659-675. <https://doi.org/10.1016/j.asej.2020.01.007>
- Hojjati, A., Monadi, M., Faridhosseini, A., & Mohammadi, M. (2018). Application and comparison of NSGA-II and MOPSO in multi-objective optimization of water resources systems. *Journal of Hydrology and Hydromechanics*, 66(3), 323-329. <https://doi.org/10.2478/johh-2018-0006>
- How, D. N., Hannan, M. A., Lipu, M. S. H., Sahari, K. S., Ker, P. J., & Muttaqi, K. M. (2020). State-of-charge estimation of Lithium-Ion battery in electric vehicles: A deep neural network approach. *IEEE Transactions on Industry Applications*, 56(5), 5565-5574. <https://doi.org/10.1109/tia.2020.3004294>
- Irsoy, O., & Cardie, C. (2014). Deep recursive neural networks for compositionality in language. In Z. Ghahramani, M. Welling, C. Cortes, N. Lawrence & K. Q. Weinberger (Eds.), *Advances in Neural Information Processing Systems 27* (pp. 1-9). DBLP Publishing.
- Jose, P. S., Jose, P., Wessley, G., & Rajalakshmy, P. (2022). Environmental impact of electric vehicles. In *E-Mobility* (pp. 31-42). Springer. [https://doi.org/10.1007/978-3-030-85424-9\\_2](https://doi.org/10.1007/978-3-030-85424-9_2)
- Kamal, E., & Adouane, L. (2018). Hierarchical energy optimization strategy and its integrated reliable battery fault management for hybrid hydraulic-electric vehicle. *IEEE Transactions on Vehicular Technology*, 67(5), 3740-3754. <https://doi.org/10.1109/tvt.2018.2805353>
- Kara, A. (2021). A data-driven approach based on deep neural networks for lithium-ion battery prognostics. *Neural Computing and Applications*, 33(20), 13525-13538. <https://doi.org/10.1007/s00521-021-05976-x>
- Karahoca, A. (2012). *Advances in data mining knowledge discovery and applications*. BoD—Books on Demand.
- Kaur, K., Garg, A., Cui, X., Singh, S., & Panigrahi, B. K. (2021). Deep learning networks for capacity estimation for monitoring SOH of Li-ion batteries for electric vehicles. *International Journal of Energy Research*, 45(2), 3113-3128. <https://doi.org/10.1002/er.6005>
- Laadjal, K., & Cardoso, A. J. M. (2021). Estimation of lithium-ion batteries state-condition in electric vehicle applications: Issues and state of the art. *Electronics*, 10(13), Article 1588. <https://doi.org/10.3390/electronics10131588>
- Lee, M. (2020). An analysis of the effects of artificial intelligence on electric vehicle technology innovation using patent data. *World Patent Information*, 63, Article 102002. <https://doi.org/10.1016/j.wpi.2020.102002>
- Li, S., & Zhao, P. (2021). Big data driven vehicle battery management method: A novel cyber-physical system perspective. *Journal of Energy Storage*, 33, Article 102064. <https://doi.org/10.1016/j.est.2020.102064>

- Li, W., Rentemeister, M., Badeda, J., Jöst, D., Schulte, D., & Sauer, D. U. (2020). Digital twin for battery systems: Cloud battery management system with online state-of-charge and state-of-health estimation. *Journal of Energy Storage*, 30, Article 101557. <https://doi.org/10.1016/j.est.2020.101557>
- Li, X., Wang, T., Wu, C., Tian, J., & Tian, Y. (2021). Battery pack state of health prediction based on the electric vehicle management platform data. *World Electric Vehicle Journal*, 12(4), Article 204. <https://doi.org/10.3390/wevj12040204>
- Liang, X., Bao, N., Zhang, J., Garg, A., & Wang, S. (2018). Evaluation of battery modules state for electric vehicle using artificial neural network and experimental validation. *Energy Science & Engineering*, 6(5), 397-407. <https://doi.org/10.1002/ese3.214>
- Liu, K., Li, K., Ma, H., Zhang, J., & Peng, Q. (2018). Multi-objective optimization of charging patterns for lithium-ion battery management. *Energy Conversion and Management*, 159, 151-162. <https://doi.org/10.1016/j.enconman.2017.12.092>
- Liu, K., Li, K., Peng, Q., & Zhang, C. (2019). A brief review on key technologies in the battery management system of electric vehicles. *Frontiers of Mechanical Engineering*, 14(1), 47-64. <https://doi.org/10.1007/s11465-018-0516-8>
- Liu, X., Zheng, C., Wu, J., Meng, J., Stroe, D. I., & Chen, J. (2020). An improved state of charge and state of power estimation method based on genetic particle filter for lithium-ion batteries. *Energies*, 13(2), Article 478. <https://doi.org/10.3390/en13020478>
- López, O. A. M., López, A. M., & Crossa, J. (2022). *Multivariate statistical machine learning methods for genomic prediction*. Springer Nature. <https://doi.org/10.1007/978-3-030-89010-0>
- Ma, Y., Duan, P., Sun, Y., & Chen, H. (2018). Equalization of lithium-ion battery pack based on fuzzy logic control in electric vehicle. *IEEE Transactions on Industrial Electronics*, 65(8), 6762-6771. <https://doi.org/10.1109/tie.2018.2795578>
- Mawonou, K. S., Eddahech, A., Dumur, D., Beauvois, D., & Godoy, E. (2021). State-of-health estimators coupled to a random forest approach for lithium-ion battery aging factor ranking. *Journal of Power Sources*, 484, Article 229154. <https://doi.org/10.1016/j.jpowsour.2020.229154>
- Meng, J., Cai, L., Stroe, D. I., Luo, G., Sui, X., & Teodorescu, R. (2019). Lithium-ion battery state-of-health estimation in electric vehicle using optimized partial charging voltage profiles. *Energy*, 185, 1054-1062. <https://doi.org/10.1016/j.energy.2019.07.127>
- Mitra, V., Wang, C. J., & Banerjee, S. (2007). Text classification: A least square support vector machine approach. *Applied soft computing*, 7(3), 908-914. <https://doi.org/10.1016/j.asoc.2006.04.002>
- Murnane, M., & Ghazel, A. (2017). A closer look at state of charge (SOC) and state of health (SOH) estimation techniques for batteries. *Analog devices*, 2, 426-436.
- Nagarale, S. D., & Patil, B. P. (2020). A review on AI based predictive battery management system for e-mobility. *TEST Engineering & Management*, 83, 15053-15064.
- Omariba, Z. B., Zhang, L., & Sun, D. (2019). Review of battery cell balancing methodologies for optimizing battery pack performance in electric vehicles. *IEEE Access*, 7, 129335-129352. <https://doi.org/10.1109/access.2019.2940090>

- Othman, B. M., Salam, Z., & Husain, A. R. (2022). A computationally efficient adaptive online state-of-charge observer for Lithium-ion battery for electric vehicle. *Journal of Energy Storage*, 49, Article 104141. <https://doi.org/10.1016/j.est.2022.104141>
- Park, S., Ahn, J., Kang, T., Park, S., Kim, Y., Cho, I., & Kim, J. (2020). Review of state-of-the-art battery state estimation technologies for battery management systems of stationary energy storage systems. *Journal of Power Electronics*, 20(6), 1526-1540. <https://doi.org/10.1007/s43236-020-00122-7>
- Purohit, K., Srivastava, S., Nookala, V., Joshi, V., Shah, P., Sekhar, R., Panchal, S., Fowler, M., Fraser, R., Tran, M. K., & Shum, C. (2021). Soft sensors for state of charge, state of energy, and power loss in formula student electric vehicle. *Applied System Innovation*, 4(4), Article 78. <https://doi.org/10.3390/asi4040078>
- Qiu, Z., & Qian, H. (2018). Adaptive genetic particle filter and its application to attitude estimation system. *Digital Signal Processing*, 81, 163-172. <https://doi.org/10.1016/j.dsp.2018.06.015>
- Rahimifard, S., Ahmed, R., & Habibi, S. (2021). Interacting multiple model strategy for electric vehicle batteries state of charge/health/power estimation. *IEEE Access*, 9, 109875-109888. <https://doi.org/10.1109/access.2021.3102607>
- Sanguesa, J. A., Torres-Sanz, V., Garrido, P., Martinez, F. J., & Marquez-Barja, J. M. (2021). A review on electric vehicles: Technologies and challenges. *Smart Cities*, 4(1), 372-404. <https://doi.org/10.3390/smartcities4010022>
- Shen, M., & Gao, Q. (2019). A review on battery management system from the modeling efforts to its multiapplication and integration. *International Journal of Energy Research*, 43(10), 5042-5075. <https://doi.org/10.1002/er.4433>
- Shu, X., Li, G., Shen, J., Lei, Z., Chen, Z., & Liu, Y. (2020). A uniform estimation framework for state of health of lithium-ion batteries considering feature extraction and parameters optimization. *Energy*, 204, Article 117957. <https://doi.org/10.1016/j.energy.2020.117957>
- Talele, V., Morali, U., Patil, M. S., Panchal, S., & Mathew, K. (2023). Optimal battery preheating in critical subzero ambient condition using different preheating arrangement and advance pyro linear thermal insulation. *Thermal Science and Engineering Progress*, 42, Article 101908. <https://doi.org/10.1016/j.tsep.2023.101908>
- Tan, K. K. H., Wong, Y. W., & Nugroho, H. (2022). Image classification for edge-cloud setting: A comparison study for OCR application. *Pertanika Journal of Science & Technology*, 30(2), 1157 - 1170. <https://doi.org/10.47836/pjst.30.2.17>
- Tran, M. K., Panchal, S., Chauhan, V., Brahmabhatt, N., Mevawalla, A., Fraser, R., & Fowler, M. (2022). Python-based scikit-learn machine learning models for thermal and electrical performance prediction of high-capacity lithium-ion battery. *International Journal of Energy Research*, 46(2), 786-794. <https://doi.org/10.1002/er.7202>
- Tran, M. K., Panchal, S., Khang, T. D., Panchal, K., Fraser, R., & Fowler, M. (2022). Concept review of a cloud-based smart battery management system for lithium-ion batteries: Feasibility, logistics, and functionality. *Batteries*, 8(2), Article 19. <https://doi.org/10.3390/batteries8020019>
- Vidal, C., Malysz, P., Kollmeyer, P., & Emadi, A. (2020). Machine learning applied to electrified vehicle battery state of charge and state of health estimation: State-of-the-art. *IEEE Access*, 8, 52796-52814. <https://doi.org/10.1109/access.2020.2980961>

- Wang, Y., Xu, R., Zhou, C., Kang, X., & Chen, Z. (2022). Digital twin and cloud-side-end collaboration for intelligent battery management system. *Journal of Manufacturing Systems*, 62, 124-134. <https://doi.org/10.1016/j.jmsy.2021.11.006>
- Xuan, L., Qian, L., Chen, J., Bai, X., & Wu, B. (2020). State-of-charge prediction of battery management system based on principal component analysis and improved support vector machine for regression. *IEEE Access*, 8, Article 164693-164704. <https://doi.org/10.1109/access.2020.3021745>
- Yang, S., He, R., Zhang, Z., Cao, Y., Gao, X., & Liu, X. (2020). CHAIN: Cyber hierarchy and interactional network enabling digital solution for battery full-lifespan management. *Matter*, 3(1), 27-41. <https://doi.org/10.1016/j.matt.2020.04.015>
- Yang, S., Zhang, Z., Cao, R., Wang, M., Cheng, H., Zhang, L., Jiang, Y., Li, Y., Chen, B., Ling, H., Lian, Y., We, B., & Liu, X. (2021). Implementation for a cloud battery management system based on the CHAIN framework. *Energy and AI*, 5, Article 100088. <https://doi.org/10.1016/j.egyai.2021.100088>
- Zhang, F., & O'Donnell, L. J. (2020). Support vector regression. In *Machine Learning* (pp. 123-140). Academic Press. <https://doi.org/10.1016/b978-0-12-815739-8.00007-9>
- Zhang, M., & Fan, X. (2020). Review on the state of charge estimation methods for electric vehicle battery. *World Electric Vehicle Journal*, 11(1), Article 23. <https://doi.org/10.3390/wevj11010023>
- Zhao, F., Li, Y., Wang, X., Bai, L., & Liu, T. (2020). Lithium-ion batteries State of Charge prediction of electric vehicles using RNNs-CNNs neural networks. *IEEE Access*, 8, 98168-98180. <https://doi.org/10.1109/access.2020.2996225>





# Optimal Constrained Groove Pressing Process Parameters Applying Modified Taguchi Technique and Multi-Objective Optimization

Muni Tanuja Anantha<sup>1,2\*</sup>, Sireesha Koneru<sup>1</sup>, Saritha Pyatla<sup>2</sup>, Parameshwaran Pillai Thiruvambalam Pillai<sup>3</sup>, Tanya Buddi<sup>4</sup> and Nageswara Rao Boggarapu<sup>1</sup>

<sup>1</sup>Department of Mechanical Engineering, Koneru Lakshmaiah Education Foundation, Green Fields, Vaddeswaram, Guntur-522502, Andhra Pradesh, India

<sup>2</sup>Department of Mechanical Engineering, ANURAG University, Ghatkesar, Hyderabad-500088, Telangana, India

<sup>3</sup>Department of Mechanical Engineering, University College of Engineering, BIT Campus, Tiruchirappalli-620 024, Tamil Nadu, India

<sup>4</sup>Department of Mechanical Engineering, GRIET, Bachupally, Kukatpally, Hyderabad-500090, Telangana, India

## ABSTRACT

Most engineering problems are complicated, and developing mathematical models for such problems requires understanding the phenomena through experiments. It is well known that as processing parameters with assigned levels increase, so does the number of experiments. By minimizing the number of experiments, Taguchi's method of experimental design will help to furnish the idea of full factorial experimental design. Taguchi's method is more appropriate for single-objective optimization problems and needs modifications while dealing with multi-objective optimization problems. Aluminum alloys are in great demand in today's automotive and aerospace sectors due to their low density, good corrosion resistance, and excellent machinability. The material is subjected to a

constrained groove pressing (CGP) process to obtain microstructural grain refinement with enhanced mechanical behavior. This paper considers AA6061 material having major alloys such as silicon and magnesium. For this work, 3 CGP process parameters (viz., displacement rate, plate thickness and number of passes) are assigned 3 levels to each parameter, acquired the test data, viz., grain size ( $g_s$ ), micro hardness ( $h_s$ ), and tensile strength ( $\sigma_{ult}$ ) based on  $L_9$  orthogonal array of Taguchi.

## ARTICLE INFO

### Article history:

Received: 22 May 2023

Accepted: 09 October 2023

Published: 26 March 2024

DOI: <https://doi.org/10.47836/pjst.32.2.21>

### E-mail addresses:

thanu.dhanu@gmail.com (Muni Tanuja Anantha)

sireekoneru@gmail.com (Sireesha Koneru)

sarithamech@anurag.edu.in (Saritha Pyatla)

paramesh551@yahoo.com (Parameshwaran Pillai Thiruvambalam Pillai)

tanyab@griet.ac.in (Tanya Buddi)

bnrao52@kluniversity.in (Nageswara Rao Boggarapu)

\* Corresponding author

Using a modified version of Taguchi's methodology, it is possible to estimate the range of grain size ( $g_s$ ), micro hardness ( $h_s$ ), and tensile strength ( $\sigma_{ult}$ ) for effective combinations of the CGP processing parameters and validate the results with existing test data. A more dependable and simpler multi-objective optimization procedure is used to choose the optimal CGP processing parameters.

*Keywords:* AA6061, displacement rate, grain size, micro hardness, number of passes, plate thickness, tensile strength

---

## INTRODUCTION

The ability of the severe plastic deformation technique to successfully reduce the microstructure to nanoscale levels has attracted much attention in the fields of material science and engineering (Segal, 1995; Cherukuri & Srinivasan, 2006). Constrained groove pressing (CGP) and Accumulative roll bonding (ARB) are the two primary SPD techniques that are typically used to produce nanostructured sheets (Tsuji et al., 2003; Omotoyinbo & Oladele, 2010). Shin et al. (2002) provided the first detailed explanation of the CGP process, which includes multiple corrugating and flattening phases. During CGP, the work sample undergoes cyclic shear deformation using flat and asymmetrically grooved dies. In this method, an inclined section of the workpiece between the grooves undergoes pure shear deformation because the thickness of the work sample and the distance between the upper and lower dies are similar (Horita et al., 2001; Akin & Fedai, 2018). Figure 1 represents the detailed procedure of the CGP process. By including more CGP passes, the workpiece is subjected to higher stresses. Aluminum, Low 'C' steel, and copper alloys, when subjected to CGP, demonstrated considerable improvements in sheet metal's mechanical characteristics, as well as microstructural alterations (Lowe & Valiev, 2004; Kurzydowski et al., 2004). The potentiality of processing using SPD for different the composites' special patterns was noted, and Equal channel angular pressing (ECAP), High-Pressure Torsion (HPT), Multi-axial forging (MAF), and additional SPD methods were examined (Kulagin et al., 2019; Husaain et al., 2017). The SPD methods were used to continuously draw low-carbon steel (Zavdoveev et al., 2021).

Using SPD techniques, ultra-fine grain structured metals and alloys have been created (Sauvage et al., 2012). The early stages of SPD development included HPT and ECAP processing methods (Sabirov et al., 2013). Later, a variety of SPD techniques were created, like ARB (accumulative roll bonding), CHPT (continuous high-pressure torsion), RCS (repeated corrugation and straightening), and CGP procedures (Khodabakhshi et al., 2011; Saritha et al., 2020). For sheet metals, ECAP, RCS, ARB, and CGP techniques are used (Mueller & Mueller, 2007; Saritha et al., 2018; Hu et al., 2018). Repeated corrugating and flattening phases are part of CGP. Specimens are highly strained by enforcing more CGP

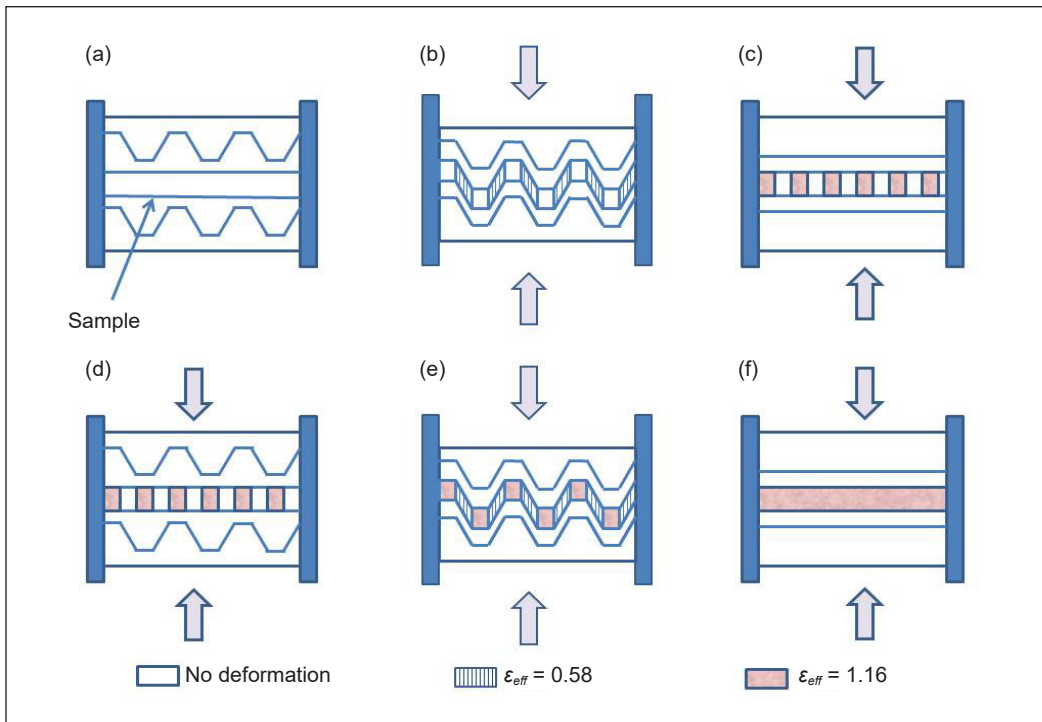


Figure 1. Detailed illustration of the CGP process

passes (Nazari & Honarpisheh, 2018). Several investigations were made on materials undergoing CGP (Nazari & Honarpisheh, 2019; Khodabakhshi et al., 2010; Kumar & Vedrtam, 2021). Post-deformation annealing and cryo-rolling of Al-Mg alloys undergoing the CGP process enhanced the strength, ductility, and fracture toughness (Tanuja et al., 2022; Khandani et al., 2020). To determine the optimal die geometry (like the angle of the groove, the width of the groove, and the friction coefficient), a modified Taguchi technique with the data from the elastoplastic finite element analysis was used (Anantha et al., 2023a; Anantha et al., 2023b; Sahiti et al., 2017). Engineering optimization problems are solved using the Taguchi technique (Siddesha & Shanharaja, 2014; Rao et al., 2008; Singaravelu et al., 2009; Parameshwaranpillai et al., 2011). The strain homogeneity and the impact of processing parameters are examined using various techniques (Bharathi et al., 2016; Kumar, 2017; Ross, 1989; Pillai et al., 2018).

A hybrid experimental-numerical method was adopted for designing a suitable die through the groove pressing-cross route process (Googarchin et al., 2019; Hayes, 2000). An artificial neural network (ANN) and a two-objective genetic algorithm (GA) are used to seek an optimal solution (Ghorbanhosseini & Fereshteh-sanice, 2019). Girish et al. (2019) used AA6061 material with magnesium and silicon as major alloying elements. They considered displacement rate ( $\dot{\delta}$ ), plate thickness ( $t$ ) and number of passes ( $v_p$ ) as

the 3 process parameters and assigned 3 levels to each parameter. They conducted 27 experiments for the possible combination of three process parameters and three assigned levels and reported the grain size ( $g_s$ ), micro hardness ( $h_s$ ) and tensile strength ( $\sigma_{ult}$ ) measurements. Taguchi grey relational analysis was performed on the measured data to identify the optimal set of process variables that leads to ultra-fine grain structure with better mechanical characteristics.

For the 3 process parameters and the assigned 3 levels to each parameter, Taguchi’s design of experiments recommends an  $L_9$  orthogonal array (OA) to conduct 9 tests and obtain optimal solutions. The Taguchi method is well suited for optimizing a single objective output response and requires modifications to handle the problems of multi-objective output responses. This paper utilizes a modified approach of Taguchi with the simple technique of multi-objective optimization considering the data of 9 tests as per the  $L_9$  OA to obtain the optimal solution and the estimated range of responses ( $g_s, h_s, \sigma_{ult}$ ) for all 27 combinations of processing parameters ( $\delta, v_p, t$ ). Empirical relationships are developed and validated for  $g_s, h_s$  and  $\sigma_{ult}$  in terms of  $\delta, t$  and  $v_p$ .

## MATERIALS AND METHODS

Girish et al. (2019) conducted tests on AA 6061 (whose mechanical properties and chemical composition are given in Table 1) to select a set of optimal process parameters  $\delta, v_p, t$  for improving the mechanical properties ( $g_s, h_s, \sigma_{ult}$ ) of the sheet metal through the CGP process. Most researchers used Minitab as a computational tool and under-utilized the potential of Taguchi’s experiment design. For the 3 process parameters with 3 levels, Taguchi’s  $L_9$  OA is appropriate for obtaining optimal solutions and generating the data of output responses for all the possible 27 sets of process parameters. A modified Taguchi approach is followed here to generate the complete information from the 9 tests and also the expected range of output responses. A simple multi-objective optimization procedure is presented to trace the optimal process parameters.

Table 1  
*Mechanical properties and chemical composition of the material*

Mechanical Properties								
	Young’s modulus (GPa)		68					
	Yield strength (MPa)		145					
	Tensile strength (MPa)		241					
	Hardness (HV)		107					
	Poisson’s ratio		0.33					
Chemical composition								
Element	Magnesium	Silicon	Copper	Chromium	Zinc	Manganese	Titanium	Aluminum
wt %	0.93	0.62	0.28	0.17	0.21	0.06	0.10	Bal

## Analysis

In order to improve the mechanical properties, the process parameters need to be combined optimally; three levels are assigned to each experimental parameter, as represented in Table 2. The displacement rate ( $\dot{\delta}$ ) varies from 1 to 2 mm/min, and the thickness ( $t$ ) ranges from 3 to 5 mm, with the number of passes ( $v_p$ ) varying from 1 to 5.

Table 2  
Levels assigned to the experimental parameters

Input Parameters	1 <sup>st</sup> Level	2 <sup>nd</sup> Level	3 <sup>rd</sup> Level
Displacement rate, $\dot{\delta}$ (mm/min)	1	1.5	2
Number of passes, $v_p$	1	3	5
Thickness, $t$ (mm)	3	4	5
Fictitious, $\varepsilon$	$\varepsilon_1$	$\varepsilon_2$	$\varepsilon_3$

Table 3 shows the  $L_9$  orthogonal array of Taguchi, which is considered for three parameters of the experimentation process ( $N_p = 3$ ), each assigned with three levels ( $N_l = 3$ ) using Equation 1 (Ross, 1989) to reduce the 27 possible combinations of the process parameters.

$$N_{Tag} = 1 + N_p \times (N_l - 1) \quad [1]$$

According to Equation 1,  $N_{Tag} = 7$ , and the optimal solution results for a set of 9 test data are presented in Table 3.  $N_{Tag} = 9$ ;  $N_p = 4$  and  $N_l = 3$ . As in (Dharmendra et al., 2019; Dharmendra et al., 2020; Satyanarayana et al., 2021), a fictitious parameter ( $\varepsilon$ ) is presented in Table 2.

In Table 3, the experimental findings for grain size ( $g_s$ ), hardness ( $h_s$ ), and tensile strength ( $\sigma_{ult}$ ) have been presented. The outcomes of ANOVA are presented in Table 4. The findings demonstrate that the number of passes ( $v_p$ ) had a maximum impact on grain size ( $g_s$ ) as well as on hardness ( $h_s$ ), with a contribution of 87.2% and 79.7%, respectively. Thickness ( $t$ ) greatly influences tensile strength ( $\sigma_{ult}$ ), contributing 51.9%. The contribution of  $\dot{\delta}$  and  $t$  on  $g_s$  are 3.6% and 8.6%, respectively, whereas 4.6% and 15% for  $h_s$  and 0.2% and 46.6% for  $\sigma_{ult}$ . Total % contributions of  $\dot{\delta}$ ,  $t$  and  $v_p$  and  $\varepsilon$  is 100. The % error of the grand mean of the output responses is considered as the % contribution of the parameter  $\varepsilon$ .

Modified Taguchi method (Dharmendra et al., 2019; Dharmendra et al., 2020; Satyanarayana et al., 2021) can provide the estimate range for the mechanical properties (viz., grain size ' $g_s$ ', micro hardness ' $h_s$ ' and tensile strength ' $\sigma_{ult}$ ') for the specified set of process parameters as input variables viz., displacement rate ( $\dot{\delta}$ ), number of passes ( $v_p$ ) and thickness ( $t$ ), which will help design the process to know the possible scatter for the repeated experiments. On representing  $\hat{\phi}$  as a performance indicator and applying the additive law (Ross, 1989),  $\hat{\phi}$  is predicted for the levels of the process parameters from Equation 2.

Table 3

Mechanical properties, viz., grain size ( $g_s$ ), tensile strength ( $\sigma_{ult}$ ) and micro hardness ( $h_s$ ), having levels of the parameters as per  $L_9$  OA (orthogonal array)

Test Run	Parameter levels				Mechanical properties		
	$\dot{\delta}$	$v_p$	$t$	$\varepsilon$	$g_s$ ( $\mu\text{m}$ )	$h_s$ (HV)	$\sigma_{ult}$ (MPa)
1	1	1	1	1	7.7	44.48	94.820
2	1	2	2	2	6.4	45.50	109.81
3	1	3	3	3	4.0	47.98	96.000
4	2	1	2	3	7.2	44.38	96.920
5	2	2	3	1	5.0	45.45	91.100
6	2	3	1	2	4.2	52.78	114.70
7	3	1	3	2	6.4	42.33	78.690
8	3	2	1	3	6.3	47.91	104.51
9	3	3	2	1	3.8	52.23	121.94
Grand mean					5.667	47.004	100.943

Table 4

Findings from Analysis of Variance (ANOVA) regarding mechanical properties ( $g_s$ ,  $h_s$ , and  $\sigma_{ult}$ )

Input Parameters	1 <sup>st</sup> Mean	2 <sup>nd</sup> Mean	3 <sup>rd</sup> Mean	SOS (Sum of squares)	Contribution (%)
Grain size, $g_s$ ( $\mu\text{m}$ )					
$\dot{\delta}$	6.033	5.466	5.500	0.606	3.60
$v_p$	7.100	5.900	4.000	14.66	87.2
$t$	6.066	5.800	5.133	1.386	8.20
$\varepsilon$	5.500	5.667	5.833	0.166	1.00
Micro hardness, $h_s$ (HV)					
$\dot{\delta}$	45.986	47.536	47.490	4.664	4.60
$v_p$	43.730	46.286	50.996	81.53	79.7
$t$	48.390	47.370	45.253	15.36	15.0
$\varepsilon$	47.386	46.870	46.756	0.676	0.70
Tensile strength, $\sigma_{ult}$ (MPa)					
$\dot{\delta}$	100.210	100.906	101.713	3.3960	0.20
$v_p$	90.143	101.806	110.880	648.36	46.6
$t$	104.676	109.556	88.596	721.70	51.9
$\varepsilon$	102.620	101.066	99.143	18.199	1.30

$$\bar{\phi} = \bar{\phi}_g + \sum_{i=1}^{n_p} (\bar{\phi}_i - \bar{\phi}_g) = \sum_{i=1}^{n_p} \bar{\phi}_i - (n_p - 1)\bar{\phi}_g \quad [2]$$

$\bar{\phi}_i$  is the mean value of  $\phi$  from the table of the ANOVA for the 'i' level of process parameters, and  $\bar{\phi}_g$  is referred to as the grand mean of  $\phi$  for experimental runs. The subscript 'i' = 1, 2, 3, and 4, in this case, stands for  $\dot{\delta}$ ,  $t$ ,  $v_p$ ,  $\varepsilon$ , respectively. The test results are compared to the estimates of ' $g_s$ ', ' $h_s$ ', and ' $\sigma_{ult}$ ' as shown in Table 5 for the nine test

runs of Taguchi’s  $L_9$  orthogonal array. In Equation 2, the variables  $N_p = 4$  and  $N_p = 3$  provide estimates for  $g_s$ ,  $h_s$  and  $\sigma_{ult}$  with fictitious parameter ( $\varepsilon$ ). Taguchi method considers  $N_p = 3$  to identify the optimal set of process parameters from the levels of optimal mean values in the ANOVA table and to estimate the output response using the additive law (Equation 2).

Equation 2 can be used to determine the range of estimates with the consideration of maximum and minimum mean values of ‘ $g_s$ ’, ‘ $h_s$ ’ and ‘ $\sigma_{ult}$ ’ and for ‘ $\varepsilon$ ’. The mechanical property estimates in Table 5 using ‘ $\varepsilon$ ’ (i.e.,  $N_p = 4$  in Equation 2) have an exact match with the test results, whereas Taguchi’s method with  $N_p = 3$  in Equation 2 showed deviation from the test data. For the various levels of  $\delta$ ,  $v_p$  and  $t$ , the corrections for  $g_s$  with estimates are -0.166 and 0.167  $\mu\text{m}$ ; the corrections for  $h_s$  estimates are -0.248 and 0.382 HV; and the corrections for  $\sigma_{ult}$  estimates are -1.8 and 1.68 MPa. The test results in Tables 5 to 7 are within/close to the estimated range of  $g_s$ ,  $h_s$  and  $\sigma_{ult}$ .

Table 5  
Comparison of test data with estimates of grain size,  $g_s$  ( $\mu\text{m}$ ) for AA6061

Test Run	Parameter levels				Test	Estimate Equation 2			Estimated range	
	$\delta$	$v_p$	$t$	$\varepsilon$		$N_p = 3$	R.E. (%)	$N_p = 4$	Lower- bound	Upper- bound
1	1	1	1	1	7.7	7.866	-2.2	7.7	7.700	8.033
2	1	2	2	2	6.4	6.400	0.0	6.4	6.233	6.566
3	1	3	3	2	4.0	3.833	4.2	4.0	3.666	4.000
4	2	1	2	3	7.2	7.033	2.3	7.2	6.866	7.200
5	2	2	3	1	5.0	5.166	-3.3	5.0	5.000	5.333
6	2	3	1	2	4.2	4.200	0.0	4.2	4.033	4.366
7	3	1	3	2	6.4	6.400	0.0	6.4	6.233	6.566
8	3	2	1	3	6.3	6.133	2.6	6.3	5.966	6.300
9	3	3	2	1	3.8	3.966	-4.4	3.8	3.800	4.133

Table 6  
Comparison of test data with estimates of micro hardness,  $h_s$  (HV) for AA6061

Test Run	Parameter levels				Test	Estimate Equation 2			Estimated range	
	$\delta$	$v_p$	$t$	$\varepsilon$		$N_p = 3$	R.E. (%)	$N_p = 4$	Lower- bound	Upper- bound
1	1	1	1	1	44.48	44.098	0.9	44.48	43.850	44.480
2	1	2	2	2	45.50	45.634	-0.3	45.50	45.387	46.017
3	1	3	3	2	47.98	48.228	-0.5	47.98	47.980	48.610
4	2	1	2	3	44.38	44.628	-0.6	44.38	44.380	45.010
5	2	2	3	1	45.45	45.068	0.8	45.45	44.820	45.450
6	2	3	1	2	52.78	52.914	-0.3	52.78	52.667	53.297
7	3	1	3	2	42.33	42.464	-0.3	42.33	42.217	42.847
8	3	2	1	3	47.91	48.158	-0.5	47.91	47.910	48.540
9	3	3	2	1	52.23	51.848	0.9	52.33	51.60	52.230

Table 7

Comparison of test data with obtained estimates for tensile strength,  $\sigma_{ult}$  (MPa) for AA6061

Test Run	Parameter levels				Test	Estimate Equation 2			Estimated range	
	$\dot{\delta}$	$v_p$	$t$	$\varepsilon$		$N_p = 3$	R.E. (%)	$N_p = 4$	Lower- bound	Upper- bound
1	1	1	1	1	94.820	93.143	1.8	94.820	91.340	94.81
2	1	2	2	2	109.81	109.69	0.1	109.81	107.89	111.4
3	1	3	3	2	96.000	97.800	-1.9	96.000	96.000	99.47
4	2	1	2	3	96.920	98.720	-1.9	96.920	96.920	100.4
5	2	2	3	1	91.100	89.423	1.7	91.000	87.620	91.09
6	2	3	1	2	114.70	114.58	0.1	114.70	112.78	116.2
7	3	1	3	2	78.690	78.567	0.2	78.690	76.770	80.23
8	3	2	1	3	104.51	106.31	-1.7	104.51	104.51	108.0
9	3	3	2	1	121.94	120.26	1.4	121.94	118.46	121.9

Nine test runs are performed in accordance with Taguchi's  $L_9$  OA approach; Equation 2 assigns the estimates of  $g_s$ ,  $h_s$ , and  $\sigma_{ult}$  for all 27 combinations of input variables viz., displacement rate ( $\dot{\delta}$ ), number of passes ( $v_p$ ) and thickness ( $t$ ). These 27 input variable combinations are arranged sequentially ( $\dot{\delta}_i, v_{pj}, t_k$ ),  $k = 1$  to 3,  $j = 1$  to 3,  $i = 1$  to 3). The sequence numbers (1,5,9,11,15,16,21,22,26) represent the 9 test runs considered in the  $L_9$  orthogonal array of Taguchi represented in Table 3. Test outcomes of the work (Girish et al., 2019) and the generated lower and upper bounds of  $g_s$ ,  $h_s$ , and  $\sigma_{ult}$  from Equation 2 are displayed in Figures 2(a) to 2(c).

Taking into account the mean values of ANOVA in Table 4 for  $g_s$ ,  $h_s$  and  $\sigma_{ult}$ , the constructed empirical relations using input variables ( $\dot{\delta}$ ,  $v_p$  and  $t$ ) are as in Equations 3 to 5.

$$g_s = 5.8333 - 0.26667\xi_1 + 0.3\xi_1^2 - 1.55\xi_2 - 0.35\xi_2^2 - 0.4667\xi_3 - 0.2\xi_3^2 \quad [3]$$

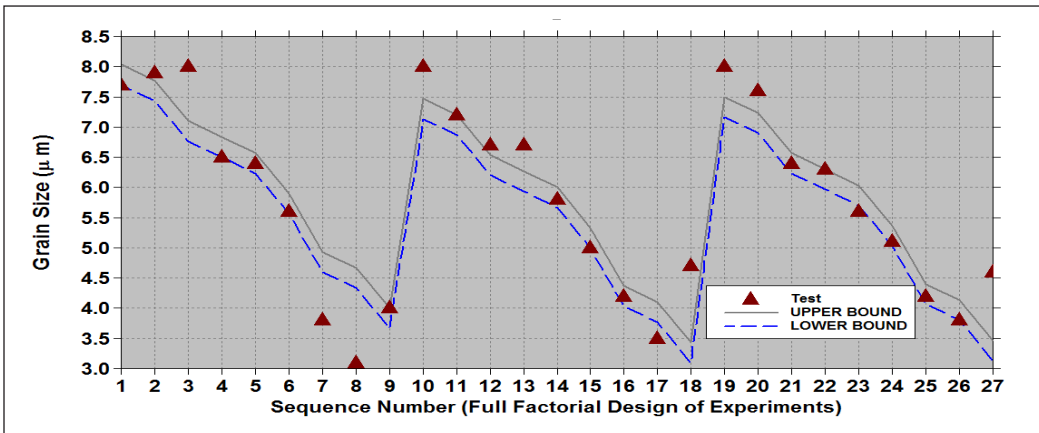
$$h_s = 47.1844 + 0.751667\xi_1 - 0.79833\xi_1^2 + 3.63333\xi_2 + 1.076667\xi_2^2 - 1.56833\xi_3 - 0.54833\xi_3^2 \quad [4]$$

$$\sigma_{ult} = 110.3833 + 0.751667\xi_1 + 0.055\xi_1^2 + 10.36833\xi_2 - 1.295\xi_2^2 - 8.04\xi_3 - 12.92\xi_3^2 \quad [5]$$

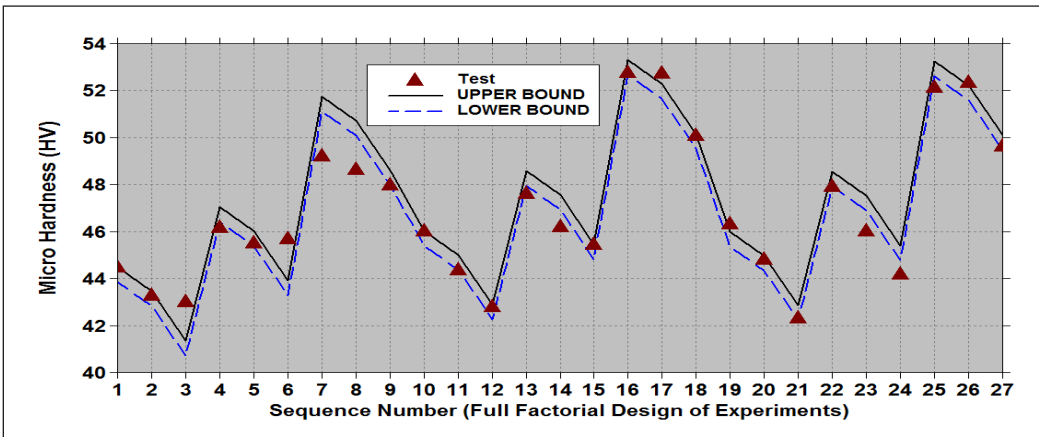
Here,  $\xi_1 = 2\dot{\delta} - 3$ ;  $\xi_2 = 0.5v_p - 1.5$ ; and  $\xi_3 = t - 4$ .

Applying Equation 2 and the constructed empirical Equations 3 to 5, the estimates of  $g_s$ ,  $h_s$  and  $\sigma_{ult}$  shown in Figures 3(a) to 3(c) provide a good comparison. The estimated lower bound of  $g_s$ ,  $h_s$  and  $\sigma_{ult}$  are attained by making corrections -0.1667 $\mu\text{m}$ , -0.248 HV, and -1.8MPa to  $g_s$ ,  $h_s$  and  $\sigma_{ult}$  in Equations 3 to 5, the application of corrections yields upper bound estimates as 0.167  $\mu\text{m}$ , 0.382 HV and 1.68MPa in Equations 3 to 5.

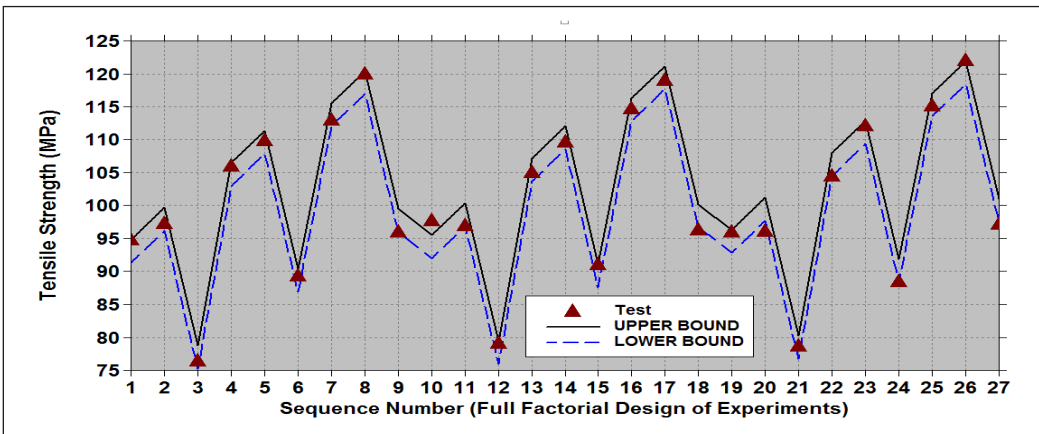




(a)

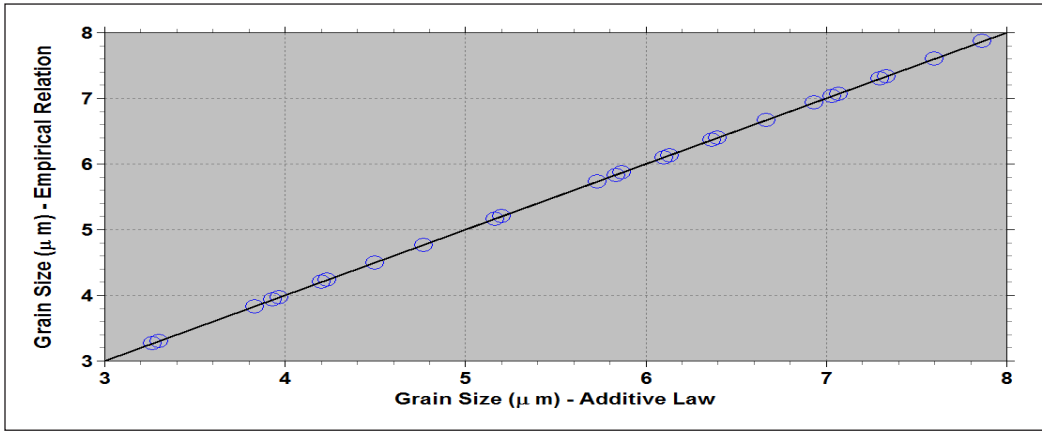


(b)

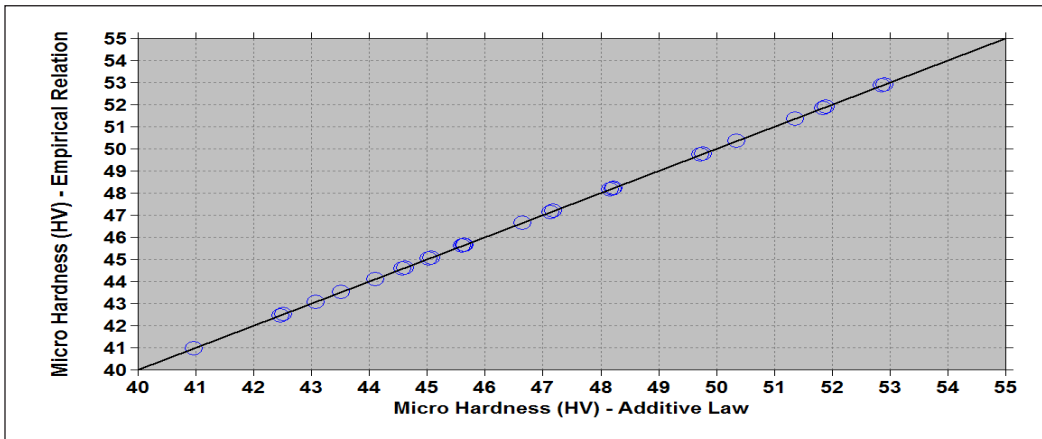


(c)

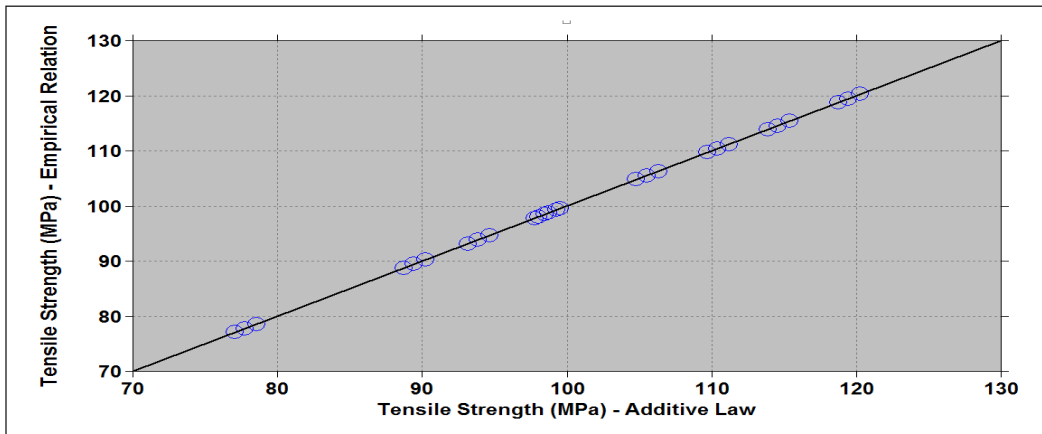
Figure 2. (a) Estimates of grain size,  $g_s$  ( $\mu\text{m}$ ) for AA6061 with test data (Girish et al., 2019); (b) Estimates of micro hardness,  $h_s$  (HV) for AA6061 with test data (Girish et al., 2019); (c) Estimates of tensile strength,  $\sigma_{ult}$  (MPa) for AA6061 with test data (Girish et al., 2019)



(a)



(b)



(c)

Figure 3. (a) Comparison of estimates of grain size  $g_s$  ( $\mu\text{m}$ ) using Equations 2 and 3, (b) Comparison of estimates of micro hardness,  $h_s$  (HV) for AA6061 using Equations 2 and 4, (c) Comparison of estimates of tensile strength,  $\sigma_{ult}$  (MPa) for AA6061 using the Equations 2 and 5

## RESULTS AND DISCUSSION

### Optimal Solution

For achieving the minimum grain size ( $g_s$ ), a set of input parameters ( $\dot{\delta}_2 v_{p3} t_3$ ) (where the level of the input variable is indicated by subscripts) are listed in ANOVA Table 4. A different set of parameters ( $\dot{\delta}_2 v_{p3} t_1$ ) was identified for achieving maximum micro hardness ( $h_s$ ). Another set of parameters ( $\dot{\delta}_3 v_{p3} t_1$ ) was identified for achieving maximum tensile strength ( $\sigma_{ult}$ ). Table 8 gives the output responses viz., grain size ( $g_s$ ), micro hardness ( $h_s$ ), and tensile strength ( $\sigma_{ult}$ ) for the various input variable optimal sets that have been found. To obtain the minimum grain size ( $g_s$ ), maximum micro hardness ( $h_s$ ), and maximum tensile strength ( $\sigma_{ult}$ ), a multi-objective optimization analysis can be used to determine the best set of optimal input variables.

For single-objective optimization problems, the Taguchi method is more appropriate (Mohamed et al., 2015). In the case of multiple responses optimization, the utility concept based on Taguchi is utilized (Tong et al., 1997; Gaitonde et al., 2009; Akin & Fedai, 2018; Lonavath & Boda, 2023; Anantha et al., 2023a). Applying Taguchi method concepts, a reliable multi-objective optimization technique has been used. This approach defines a single function  $\zeta$  with weighing factors ( $\omega_1, \omega_2$  and  $\omega_3$ , which satisfies  $\omega_1 + \omega_2 + \omega_3 = 1$ ) and the output responses ( $g_s, h_s$  and  $\sigma_{ult}$ ) in Equation 6.

$$\zeta = \omega_1 \left( \frac{g_s}{g_{s \max}} \right) + \omega_2 \left( 1 - \frac{h_s}{h_{s \max}} \right) + \omega_3 \left( 1 - \frac{\sigma_{ult}}{\sigma_{ult \max}} \right) \quad [6]$$

Table 8  
Output responses for the identified optimal set of input variables through single objective optimization

Optimal Set	Input Variables			Output Responses		
	Displacement rate, ' $\dot{\delta}$ ' (mm/min)	Number of passes, ' $v_p$ '	Thickness, ' $t$ ' (mm)	Grain size, ' $g_s$ ' ( $\mu\text{m}$ )	Micro hardness, ' $h_s$ ' (HV)	Tensile strength, ' $\sigma_{ult}$ ' (MPa)
In the case of minimum grain size, $g_s$						
$\dot{\delta}_2 v_{p3} t_3$	1.5	5	5	3.1–3.433 (4.7) <sup>+</sup>	49.53 – 50.16 (50.08)	96.7–100.2 (96.25)
In the case of maximum micro hardness, $h_s$						
$\dot{\delta}_2 v_{p3} t_1$	1.5	5	3	4.0333– 4.36667 (4.2)	52.667–53.297 (52.78)	112.78–116.2 (114.7)
In the case of maximum tensile strength, $\sigma_{ult}$						
$\dot{\delta}_3 v_{p3} t_1$	2	5	3	4.0667–4.4 (4.2)	52.62–53.25 (52.13)	113.58–117.1 (115.18)

Note. + Results in parenthesis are from tests

Minimization of  $\zeta$  provides the minimum  $g_s$ , maximum  $h_s$  and  $\sigma_{ult}$  assigning equal weighing factors to a set of input variables:  $\omega_1 = \omega_2 = \omega_3 = 1/3$ . Here,  $g_{s\ max} = 8.033\ \mu\text{m}$ ;  $h_{s\ max} = 53.297\ \text{HV}$ ; and  $\sigma_{ult\ max} = 121.94\ \text{MPa}$ . Values of  $\zeta$  are produced using the data in Table 3 and presented the data in Table 9. ANOVA is carried out on  $\zeta$  as given in Table 10.

To achieve the minimum  $\zeta$ , the optimal input variables are  $\delta_2 v_{p3} t_2$ . This optimal set of input variables corresponds to a displacement rate of 1.5 mm/min; number of passes as 5; and sheet thickness as 4 mm. The range of output responses for the optimal input variables, as determined by Equations 3 to 5 are: grain size,  $g_s = 3.76 - 4.1\ \mu\text{m}$ ; micro hardness,  $h_s = 51.647 - 52.277\ \text{HV}$ , and the tensile strength,  $\sigma_{ult} = 117.66 - 121.1\ \text{MPa}$ . The test results for the optimal input variables are as follows: grain size = 3.5  $\mu\text{m}$ ; and tensile strength = 119.01 MPa and micro hardness = 52.73 HV. The % Contribution of the number of passes on the grand mean of the output responses is high. Figures 4(a) to 4(c) illustrate the variation of output responses depending on the number of passes for the ideal input variables, displacement rate = 1.5 mm/min, and thickness = 4 mm.

Table 9

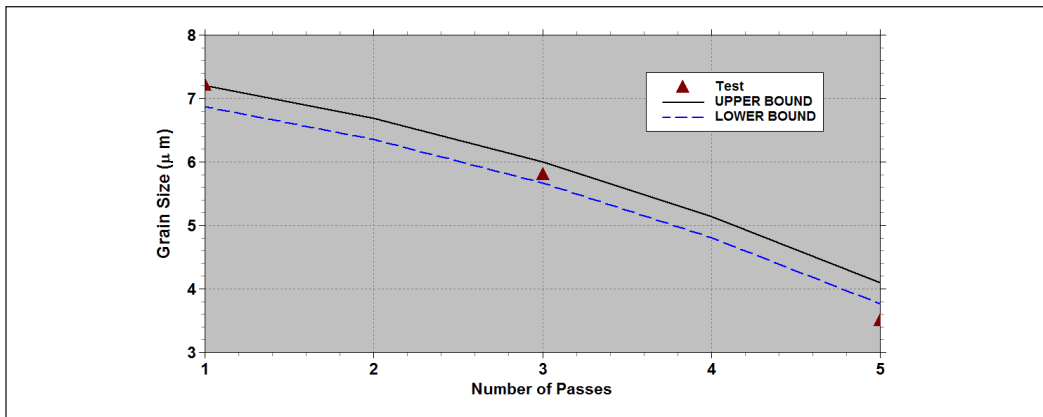
Single objective function ( $\zeta$ ) in Equation 6 from the mechanical properties, viz., grain size ( $g_s$ ), micro hardness ( $h_s$ ) and tensile strength ( $\sigma_{ult}$ ) with levels of the process parameters based on  $L_9$  OA (orthogonal array)

Test Run	Parameter levels			Normalized output responses			Objective function, $\zeta$ Eq.(6)
	$\delta$	$v_p$	$t$	$\frac{g_s}{g_{s\ max}}$	$1 - \frac{h_s}{h_{s\ max}}$	$1 - \frac{\sigma_{ult}}{\sigma_{ult\ max}}$	
1	1	1	1	0.95850	0.19821	0.28601	0.48091
2	1	2	2	0.79668	0.17135	0.11046	0.35950
3	1	3	3	0.49792	0.11081	0.27021	0.29298
4	2	1	2	0.89626	0.20092	0.25815	0.45177
5	2	2	3	0.62240	0.17264	0.33853	0.37786
6	2	3	1	0.52282	0.00978	0.06312	0.19857
7	3	1	3	0.79668	0.25907	0.54962	0.53513
8	3	2	1	0.78423	0.11243	0.16678	0.35448
9	3	3	2	0.47302	0.02042	0	0.16448

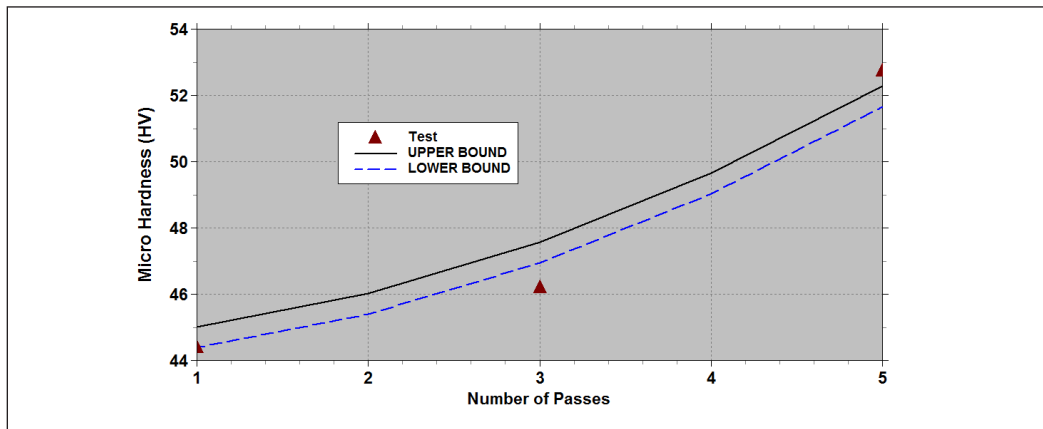
Table 10

Results of ANOVA on the single objective function, from  $\zeta$  Table 9

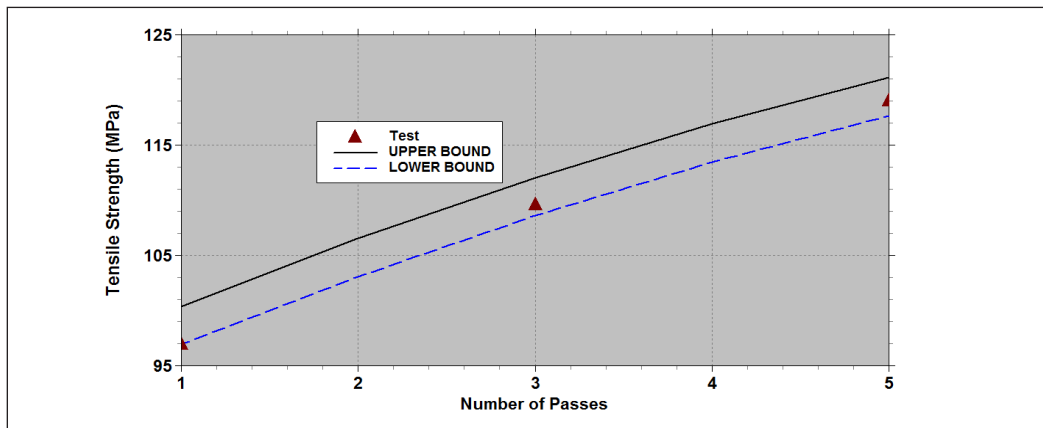
Input parameters	1 <sup>st</sup> Mean	2 <sup>nd</sup> Mean	3 <sup>rd</sup> Mean
$\delta$	0.377798	<b>0.342738</b>	0.351364
$v_p$	0.489272	0.363947	<b>0.218681</b>
$t$	0.344657	<b>0.325254</b>	0.401989



(a)



(b)



(c)

Figure 4. (a) Grain size versus number of passes for the optimal input variables, displacement rate = 1.5 mm/min; and thickness = 4 mm; (b) Micro hardness versus number of passes for the optimal input variables, displacement rate = 1.5 mm/min; and thickness = 4 mm; (c) Tensile strength versus number of passes for the optimal input variables, displacement rate = 1.5 mm/min; and thickness = 4 mm

## CONCLUSION

Aluminum alloys are in high demand in the aerospace and automobile sectors because of their low density, high resistance to corrosion and machinability. The mechanical properties can be improved by refining the grain structure using constrained groove pressing (CGP).

Developing mathematical models for such complex problems needs experimentation to understand the phenomena. However, it is known that the time-consuming experiments will be expensive due to the requirement of large numbers by increasing the processing parameters with assigned levels. Modified Taguchi's design of experiments with a simple multi-objective optimization procedure adopted in this study to obtain optimal process parameters with a minimum number of experiments and the data with expected range for the full factorial design of experiments—empirical relationships developed and validated for the output responses in terms of process parameters for AA6061.

The mechanical properties of AA6061 were enhanced by refining the grain structure using CGP. Taguchi's  $L_9$  orthogonal array (OA) is selected for the 3 CGP process parameters (viz., displacement rate,  $\dot{\delta}$ ; plate thickness,  $t$ ; and number of passes,  $v_p$ ) and assigned 3 levels to each parameter. ANOVA analysis was performed from the acquired data (viz., grain size,  $g_s$ ; micro hardness,  $h_s$ ; and tensile strength,  $\sigma_{ult}$ ) of 9 tests. The % contribution of each CGP parameter is evaluated on the grand mean of  $g_s$ ,  $h_s$  and  $\sigma_{ult}$ . Following are the highlights of the present study.

- ANOVA results indicate that a number of passes ( $v_p$ ) has a maximum influence on grain size ( $g_s$ ) with a contribution of 87.2% and on micro hardness ( $h_s$ ) with a contribution of 79.7%, whereas thickness ( $t$ ) has a maximum impact on tensile strength ( $\sigma_{ult}$ ) having a contribution of 51.9%.
- The displacement rate is 1.5mm/min; the number of passes is 5 and the thickness is 5mm, which are the optimal CGP process variables to achieve minimum grain size ( $g_s$ ).
- The displacement rate is 1.5mm/min; the number of passes is 5, and the thickness is 3mm, which are the optimal CGP process variables to achieve maximum micro hardness ( $h_s$ ).
- The displacement rate is 2mm/min; the number of passes is 5, and the thickness is 3mm, which are the optimal CGP process variables to achieve maximum tensile strength ( $\sigma_{ult}$ ).
- The displacement rate is 1.5mm/min; the number of passes is 5, and the thickness of 4 mm is the optimal CGP process variable to achieve minimum grain size ( $g_s$ ), maximum micro hardness ( $h_s$ ), and maximum tensile strength ( $\sigma_{ult}$ ).

## ACKNOWLEDGEMENTS

The authors thank the Koneru Lakshmaiah Education Foundation, Green Fields, Vaddeswaram, Guntur-522502, Andhra Pradesh, India, for providing the facility to carry out the research study. The authors are also grateful to the handling editor and the reviewers for their valuable comments, which helped improve the quality of this manuscript.

## REFERENCES

- Akin, H. K., & Fedai, Y. (2018). Optimization of machining parameters in face milling using multi-objective Taguchi technique. *Tehnički Glasnik*, 12(2), 104-108. <https://doi.org/10.31803/tg-20180201125123>
- Anantha, M. T., Buddi, T., & Boggarapu, N. R. (2023a). Multi-objective optimization basing modified Taguchi method to arrive the optimal die design for CGP of AZ31 magnesium alloy. *International Journal on Interactive Design and Manufacturing*, 1-10. <https://doi.org/10.1007/s12008-022-01176-6>
- Anantha, M. T., Buddi, T., & Boggarapu, N. R. (2023b). Utilisation of fuzzy logic and genetic algorithm to seek optimal corrugated die design for CGP of AZ31 magnesium alloy. *Advances in Materials and Processing Technologies*, 1-15. <https://doi.org/10.1080/2374068X.2023.2192135>
- Bharathi, P., Priyanka, T. G. L., Rao, G. S., & Rao, B. N. (2016). Optimum WEDM process parameters of SS304 using taguchi method. *International Journal of Industrial and Manufacturing Systems Engineering*, 1(3), 69-72.
- Cherukuri, B., & Srinivasan, R. (2006). Properties of AA6061 processed by multi-axial compressions/ forging (MAC/F). *Materials and Manufacturing Processes*, 21(5), 519-525. <https://doi.org/10.1080/10426910500471649>
- Dharmendra, B. V., Kodali, S. P., & Rao, B. N. (2019). A simple and reliable Taguchi approach for multi-objective optimization to identify optimal process parameters in nano-powder-mixed electrical discharge machining of INCONEL800 with copper electrode. *Heliyon*, 5(8), Article e02326. <https://doi.org/10.1016/j.heliyon.2019.e02326>
- Dharmendra, B. V., Kodali, S. P., & Boggarapu, N. R. (2020). Multi-objective optimization for optimum abrasive water jet machining process parameters of Inconel718 adopting the Taguchi approach. *Multidiscipline Modeling in Materials and Structures*, 16(2), 306-321. <https://doi.org/10.1108/MMMS-10-2018-0175>
- Gaitonde, V. N., Karnik, S. R., & Davim, J. P. (2009). Multiperformance optimization in turning of free-machining steel using taguchi method and utility concept. *Journal of Materials Engineering and Performance*, 18(3), 231-236. <https://doi.org/10.1007/s11665-008-9269-6>
- Ghorbanhosseini, S., & Fereshteh-sanice, F. (2019). Multi-objective optimization of geometrical parameters for constrained groove pressing of aluminium sheet using a neural network and the genetic algorithm. *Journal of Computational Applied Mechanics*, 50(2), 275-281. <https://doi.org/10.22059/jcamech.2018.267948.335>
- Girish, B. M., Siddesh, H. S., & Satish, B. M. (2019). Taguchi grey relational analysis for parametric optimization of severe plastic deformation process. *SN Applied Sciences*, 1(8). <https://doi.org/10.1007/s42452-019-0982-6>

- Googarchin, H. S., Teimouri, B., & Hashemi, R. (2019). Analysis of constrained groove pressing and constrained groove pressing-cross route process on AA5052 sheet for automotive body structure applications. *Proceedings of the Institution of Mechanical Engineers, Part D: Journal of Automobile Engineering*, 233(6), 1436-1452. <https://doi.org/10.1177/0954407018785734>
- Hayes, J. S. (2000). Effect of grain size on tensile behaviour of a submicron grained Al-3 wt-%Mg alloy produced by severe deformation. *Materials Science and Technology*, 16(11-12), 1259-1263. <https://doi.org/10.1179/026708300101507479>
- Horita, Z., Fujinami, T., & Langdon, T. G. (2001). The potential for scaling ECAP: Effect of sample size on grain refinement and mechanical properties. *Materials Science and Engineering A*, 318(1-2), 34-41. [https://doi.org/10.1016/S0921-5093\(01\)01339-9](https://doi.org/10.1016/S0921-5093(01)01339-9)
- Hu, H., Qin, X., Zhang, D., & Ma, X. (2018). A novel severe plastic deformation method for manufacturing AZ31 magnesium alloy tube. *International Journal of Advanced Manufacturing Technology*, 98(1-4), 897-903. <https://doi.org/10.1007/s00170-018-2179-3>
- Husaain, Z., Ahmed, A., M. Irfan, O., & Al-Mufadi, F. (2017). Severe plastic deformation and its application on processing titanium: A review. *International Journal of Engineering and Technology*, 9(6), 626-431. <https://doi.org/10.7763/ijet.2017.v9.1011>
- Khandani, S. T., Faraji, G., & Torabi, H. (2020). Development of a new integrated severe plastic deformation method. *Materials Science and Technology*, 36(4), 468-476. <https://doi.org/10.1080/02670836.2019.1710926>
- Khodabakhshi, F., Kazeminezhad, M., & Kokabi, A. H. (2010). Constrained groove pressing of low carbon steel: Nano-structure and mechanical properties. *Materials Science and Engineering A*, 527(16-17), 4043-4049. <https://doi.org/10.1016/j.msea.2010.03.005>
- Khodabakhshi, F., Kazeminezhad, M., & Kokabi, A. H. (2011). Mechanical properties and microstructure of resistance spot welded severely deformed low carbon steel. *Materials Science and Engineering A*, 529(1), 237-245. <https://doi.org/10.1016/j.msea.2011.09.023>
- Kulagin, R., Beygelzimer, Y., Bachmaier, A., Pippin, R., & Estrin, Y. (2019). Benefits of pattern formation by severe plastic deformation. *Applied Materials Today*, 15, 236-241. <https://doi.org/10.1016/j.apmt.2019.02.007>
- Kumar, D. R. (2017). Optimum drilling parameters of coir fiber-reinforced polyester composites. *American Journal of Mechanical and Industrial Engineering*, 2(2), 92-97. <https://doi.org/10.11648/j.ajmie.20170202.15>
- Kumar, S., & Vedrtam, A. (2021). Experimental and numerical study on effect of constrained groove pressing on mechanical behaviour and morphology of aluminium and copper. *Journal of Manufacturing Processes*, 67, 478-486. <https://doi.org/10.1016/j.jmapro.2021.05.008>
- Kurzydłowski, K. J., Garbac, H., & Richert, M. (2004). Effect of severe plastic deformation on the microstructure and mechanical properties of Al and Cu. *Reviews on Advanced Materials Science*, 8(2), 129-133.
- Lonavath, S. N., & Boda, H. (2023). Consequences of the rotational speed and profile of tool pin in microstructure and mechanical properties of AA8011/ZrO<sub>2</sub> composite produced by FSW. *International Journal on Interactive Design and Manufacturing*, 1-13. <https://doi.org/10.1007/s12008-023-01295-8>



- Lowe, T. C., & Valiev, R. Z. (2004). The use of severe plastic deformation techniques in grain refinement. *JOM*, 56(10), 64-68. <https://doi.org/10.1007/s11837-004-0295-z>
- Mohamed, M. A., Manurung, Y. H. P., & Berhan, M. N. (2015). Model development for mechanical properties and weld quality class of friction stir welding using multi-objective Taguchi method and response surface methodology. *Journal of Mechanical Science and Technology*, 29(6), 2323-2331. <https://doi.org/10.1007/s12206-015-0527-x>
- Mueller, K., & Mueller, S. (2007). Severe plastic deformation of the magnesium alloy AZ31. *Journal of Materials Processing Technology*, 187-188, 775-779. <https://doi.org/10.1016/j.jmatprotec.2006.11.153>
- Nazari, F., & Honarpisheh, M. (2018). Analytical model to estimate force of constrained groove pressing process. *Journal of Manufacturing Processes*, 32, 11-19. <https://doi.org/10.1016/j.jmapro.2018.01.015>
- Nazari, F., & Honarpisheh, M. (2019). Analytical and experimental investigation of deformation in constrained groove pressing process. *Proceedings of the Institution of Mechanical Engineers, Part C: Journal of Mechanical Engineering Science*, 233(11), 3751-3759. <https://doi.org/10.1177/0954406218809738>
- Omotoyinbo, J. A., & Oladele, I. O. (2010). The effect of plastic deformation and magnesium content on the mechanical properties of 6063 aluminium alloys. *Journal of Minerals and Materials Characterization and Engineering*, 09(06), 539-546. <https://doi.org/10.4236/jmmce.2010.96038>
- Parameshwaranpillai, T., Lakshminarayanan, P. R., & Rao, B. N. (2011). Taguchi's approach to examine the effect of drilling induced damage on the notched tensile strength of woven GFR-epoxy composites. *Advanced Composite Materials*, 20(3), 261-275. <https://doi.org/10.1163/092430410X547083>
- Pillai, J. U., Sanghrajka, I., Shunmugavel, M., Muthuramalingam, T., Goldberg, M., & Littlefair, G. (2018). Optimisation of multiple response characteristics on end milling of aluminium alloy using Taguchi-Grey relational approach. *Measurement: Journal of the International Measurement Confederation*, 124, 291-298. <https://doi.org/10.1016/j.measurement.2018.04.052>
- Rao, B. S., Rudramoorthy, R., Srinivas, S., & Rao, B. N. (2008). Effect of drilling induced damage on notched tensile and pin bearing strengths of woven GFR-epoxy composites. *Materials Science and Engineering A*, 472(1-2), 347-352. <https://doi.org/10.1016/j.msea.2007.03.023>
- Ross, P. J. (1989). *Taguchi techniques for quality engineering*. McGraw-Hill.
- Sabirov, I., Murashkin, M. Y., & Valiev, R. Z. (2013). Nanostructured aluminium alloys produced by severe plastic deformation: New horizons in development. *Materials Science and Engineering A*, 560, 1-24. <https://doi.org/10.1016/j.msea.2012.09.020>
- Sahiti, M., Reddy, M. R., Joshi, B., & Rao, B. N. (2017). Application of taguchi method for optimum weld process parameters of pure aluminum. *American Journal of Mechanical and Industrial Engineering*, 1(3), 123-128. <https://doi.org/10.11648/j.ajmie.20160103.25>
- Saritha, P., Raju, P. R., Reddy, R. V., & Snehalatha, S. (2018). Mechanical behavior of hybrid composites. *International Journal of Mechanical Engineering and Technology*, 9(9), 71-76.
- Saritha, P., Satyadevi, A., & Raju, P. R. (2020). Tribological behavior of metal matrix composites. *Journal of Advanced Research in Dynamical and Control Systems*, 12(2), 2335-2341. <https://doi.org/10.5373/JARDCS/V12I2/S20201280>

- Satyanarayana, G., Narayana, K. L., & Rao, B. N. (2021). Incorporation of Taguchi approach with CFD simulations on laser welding of spacer grid fuel rod assembly. *Materials Science and Engineering B: Solid-State Materials for Advanced Technology*, 269, Article 115182. <https://doi.org/10.1016/j.mseb.2021.115182>
- Sauvage, X., Wilde, G., Divinski, S. V., Horita, Z., & Valiev, R. Z. (2012). Grain boundaries in ultrafine grained materials processed by severe plastic deformation and related phenomena. *Materials Science and Engineering A*, 540, 1-12. <https://doi.org/10.1016/j.msea.2012.01.080>
- Segal, V. M. (1995). Materials processing by simple shear. *Materials Science and Engineering A*, 197(2), 157-164. [https://doi.org/10.1016/0921-5093\(95\)09705-8](https://doi.org/10.1016/0921-5093(95)09705-8)
- Shin, D. H., Park, J. J., Kim, Y. S., & Park, K. T. (2002). Constrained groove pressing and its application to grain refinement of aluminum. *Materials Science and Engineering A*, 328(1), 98-103. [https://doi.org/10.1016/S0921-5093\(01\)01665-3](https://doi.org/10.1016/S0921-5093(01)01665-3)
- Siddesha, H. S., & Shantharaja, M. (2014). Optimization of cyclic constrained groove pressing parameters for tensile properties of Al6061/sic metal matrix composites. *Procedia Materials Science*, 5, 1929-1936. <https://doi.org/10.1016/j.mspro.2014.07.515>
- Singaravelu, J., Jeyakumar, D., & Rao, B. N. (2009). Taguchi's approach for reliability and safety assessments in the stage separation process of a multistage launch vehicle. *Reliability Engineering and System Safety*, 94(10), 1526-1541. <https://doi.org/10.1016/j.ress.2009.02.017>
- Tanuja, A. M., Kumar, A., & Rao, B. N. (2022). Review on the application of CGP to improve AZ31 Mg alloy properties. In *Applications of Computational Methods in Manufacturing and Product Design: Select Proceedings of IPDIMS 2020* (pp. 237-246). Springer Nature. [https://doi.org/10.1007/978-981-19-0296-3\\_21](https://doi.org/10.1007/978-981-19-0296-3_21)
- Tong, L. I., Su, C. T., & Wang, C. H. (1997). The optimization of multi-response problems in the Taguchi method. *International Journal of Quality and Reliability Management*, 14(4), 367-380. <https://doi.org/10.1108/02656719710170639>
- Tsuji, N., Saito, Y., Lee, S. H., & Minamino, Y. (2003). ARB (accumulative roll-bonding) and other new techniques to produce bulk ultrafine grained materials. *Advanced Engineering Materials*, 5(5), 338-344. <https://doi.org/10.1002/adem.200310077>
- Zavdoveev, A., Baudin, T., Pashinska, E., Kim, H. S., Brisset, F., Heaton, M., Poznyakov, V., Rogante, M., Tkachenko, V., Klochkov, I., & Skoryk, M. (2021). Continuous severe plastic deformation of low-carbon steel: Physical-mechanical properties and multiscale structure analysis. *Steel Research International*, 92(3), Article 2000482. <https://doi.org/10.1002/srin.202000482>

## Inorganic Material of Magnesium Nitrate $Mg(NO_3)_2$ Film as Q-Switcher in the C-Band Region

Noor Umami Hazirah Hani Zalkepali<sup>1</sup>, Muwafaq Mohammed Bakr Alsaady<sup>1</sup>, Mustafa Mudhafar<sup>2</sup>, Nik Noor Haryatul Eleena Nik Mahmud<sup>1</sup>, Nur Ainnaa Mardhiah Muhammad<sup>1</sup>, Ain Zamira Muhammad Zamri<sup>1</sup> and Noor Azura Awang<sup>1\*</sup>

<sup>1</sup>Photonics Devices and Sensors Research Center (PDSR), Department of Physics and Chemistry, Faculty of Applied Sciences and Technology, Universiti Tun Hussein Onn Malaysia, 84600 Pagoh, Johor, Malaysia

<sup>2</sup>Department of Pharmaceutical Chemistry, College of Pharmacy, University of Ahl Al Bayt, 56001, Karbala, Iraq

### ABSTRACT

A novel inorganic material of Magnesium Nitrate ( $Mg(NO_3)_2$ ) thin film is successfully investigated in the C-band region. The Q-switcher is  $Mg(NO_3)_2$  thin film. The solvent casting method has been applied to prepare  $Mg(NO_3)_2$  thin film before being positioned within the fiber ferrule duo to act as a Q-switcher. Thereby, the modulation depth and the saturation intensity of the  $Mg(NO_3)_2$  thin film exhibit at 32.40% and 0.07 MW/cm<sup>2</sup>, respectively. It is possible to produce a steady Q-switched pulse fiber laser with a maximum pump power of 403.00 mW, a repetition rate of 72.56 kHz, and a pulse width of 3.00  $\mu$ s. In addition, the tunable Q-switched pulse fiber laser is also examined using a figure-of-eight cavity design incorporating a tunable bandpass filter (TBF). Consequently, the operating wavelength is changed in the range of 1528 nm to 1552 nm, even while the pump power remains the same at 403.00 mW. During this time, the pulse width and repetition rate shifted from 2.10  $\mu$ s to 4.10  $\mu$ s and altered from 67.90 kHz to 35.80 kHz, respectively. Consequently, the  $Mg(NO_3)_2$  thin film has the opportunity to be an effective saturable absorber for generating pulsed fiber lasers and can be applied in optical communications applications.

### ARTICLE INFO

#### Article history:

Received: 02 April 2023

Accepted: 12 September 2023

Published: 26 March 2024

DOI: <https://doi.org/10.47836/pjst.32.2.22>

#### E-mail addresses:

noorummi@uthm.edu.my (Noor Umami Hazirah Hani Zalkepali)  
mofaq.alsaady@gmail.com (Muwafaq Mohammed Bakr Alsaady)  
almosawy2014@gmail.com (Mustafa Mudhafar)  
eleena2994@gmail.com (Nik Noor Haryatul Eleena Nik Mahmud)  
gw210036@student.uthm.edu.my (Nur Ainnaa Mardhiah Muhammad)  
hw210016@student.uthm.edu.my (Ain Zamira Muhammad Zamri)  
norazura@uthm.edu.my (Noor Azura Awang)

\* Corresponding author

**Keywords:** Magnesium nitrate, pulse fiber laser, Q-switched, saturable absorber

## INTRODUCTION

Numerous Q-switched pulse fiber laser applications have been widely applied in medicine, telecommunications, range findings, material processing, and sensing due to high pulse energy and peak power (Chen et al., 2013; Ahmad et al., 2015; Ahmad, Albaqawi et al., 2020). Based on the Pauli blocking principle, saturable absorbers (SA) are key elements in generating Q-switched pulse fiber lasers. In the laser cavity, high losses prevent any lasing and allow the construction of population inversion at higher energy states. When the gain is higher than the losses in the laser cavity, narrow pulse durations and high intensity of Q-switched pulse are generated (Degnan, 1995). The techniques to develop a Q-switched pulse fiber laser are active and passive. An active approach requires external modulators such as acousto-optic modulators (Cuadrado-Laborde et al., 2007; Delgado-Pinar et al., 2006) and electro-optic modulators (El-Sherif & King, 2003; Zhao et al., 2006), which have the drawbacks of high maintenance cost, bulky and expensive. On the other hand, a passive approach, by integrating a tiny piece of SA in the laser cavity, is more desirable among researchers. In addition, the advantages of using SA to generate pulse fiber lasers are their flexibility, simplicity, inexpensive design, and less consideration of dispersion, nonlinearity, and compactness.

Semiconductor saturable absorber mirrors (SESAMs) were the first discovery of SA by Keller et al. (1996). They were widely used in the 90s, exhibiting a narrow bandwidth operation, limiting the broader tunable Q-switched operation (Okhotnikov et al., 2004). The challenges of utilizing SESAMs as SAs are bandwidth limitations and fabrication complexity. Hence, this motivates the other researchers to discover other potential materials to apply as SA. Two-dimensional (2D) nanomaterials as SA have been reported, such as graphene, carbon nanotube, topological insulators (TIs), transition metal dichalcogenides (TMDs), and black phosphorus (BP). However, these materials have drawbacks, such as graphene having a low percentage modulation depth of 1.3% per layer with zero bandgaps (Sun et al., 2016) and carbon nanotube, as SA has limited bandwidth and chirality control (Sun et al., 2012).

Furthermore, the use of TIs as SA, such as bismuth selenide ( $\text{Bi}_2\text{Se}_3$ ), antimony telluride ( $\text{Sb}_2\text{Te}_3$ ), and bismuth telluride ( $\text{Bi}_2\text{Te}_3$ ), has a problem throughout the age of dominating bulk conduction. Its susceptibility to pollution in the air environment makes operation more challenging and restricts the uses of several devices due to the unique surface conditions of TI (Kim et al., 2014). Besides that, molybdenum disulfide ( $\text{MoS}_2$ ), tungsten disulfide ( $\text{WS}_2$ ), molybdenum diselenide ( $\text{MoSe}_2$ ), and tungsten diselenide ( $\text{WSe}_2$ ) are a few examples of TMD. These substances are indirect semiconductors in bulky states made of hexagonal metal atoms sandwiched between two chalcogenide layers. They have limitations in mid-infrared applications because of their bandgap of more than 1.0 eV (Xia et al., 2014). BP is polarization-dependent and a hydrophilic substance that can easily interact with water; it

has certain limitations, including harrowing production and handling requirements (Island et al., 2015). Additionally, BP is not sufficiently stable, especially atomic BP, which is highly vulnerable to oxidative destruction in environmental settings.

Khaleel et al. (2019) have recently utilized magnesium oxide (MgO) as SA to generate a mode-locked pulse. From their study, the fixed repetition rate of 3.5 MHz is achieved at 156 mW pump power with a pulse duration of 5.6 ps and signal-to-noise ratio (SNR) of 50 dB. Moreover, the inorganic substance MgO had a direct band gap of (7.3 eV). Before now, it has been employed in several industrial, medicinal, and scientific-practical applications because of its affordable price, high breakdown field, high-temperature stability, and environmentally favorable characteristics (Płóciennik et al., 2016). Furthermore, due to its unique and alluring optical elements, such as its high optical transparency, high nonlinear optical susceptibility, strong breakdown field, and quick recovery time, MgO has recently attracted some interest in the field of ultrafast optics (Płóciennik et al., 2016; Faragl et al., 2014; Mia et al., 2017). Besides that, Morshed et al. (2017) employed magnesium diboride (MgB<sub>2</sub>) to generate Q-switched by obtaining a pulse duration between 200 to 1700 ns based on a ytterbium-doped fiber laser. However, the pulse duration is changed between 200 to 1200 ns to reduce the dispersion effects after integrating the acousto-optic modulator in the cavity (Morshed et al., 2017). Thus, this motivates us to apply other inorganic materials of Mg as SA, which is integrated with the materials in the Figure-eight-cavity design to generate Q-switched.

In this research, the novel material of Mg(NO<sub>3</sub>)<sub>2</sub> film is successfully fabricated and synthesized as SA by the solvent casting approach by incorporating polyvinyl alcohol (PVA). The Mg(NO<sub>3</sub>)<sub>2</sub> film has modulation depth and saturation intensity of 32.40% and 0.07 MW/cm<sup>2</sup>, respectively. Furthermore, a Q-switched pulse fiber laser using Mg(NO<sub>3</sub>)<sub>2</sub> film as a Q-switcher is experimentally generated by exhibiting a maximum repetition rate of 72.56 kHz and a narrow pulse width of 3.00 μs. The maximum pulse energy and average output power of the Q-switched pulse are 6.20 nJ and 0.45 mW, respectively. Moreover, at the fixed pump power of 403.00 mW, the wavelength can be modified from 1528 nm to 1552 nm due to altering the knob of TBF, which gives the tuning range of 24.00 nm.

## MATERIALS AND METHODS

### Preparation of Magnesium Nitrate Film

The technique of producing SA, known as the solvent-cast method, calls for using a polymer as the host material. Polymer materials come in a wide variety of forms, some of which include polymethylmethacrylate (PMMA), polyvinyl alcohol (PVA), polycarbonate, and polyimide. The fact that the solvent-cast method utilizes a one-of-a-kind drying process that dries a liquid on a surface without subjecting the material to any further mechanical or thermal stress is the primary benefit of this technique.

The material and polymer mixture must be transferred to a petri container before being utilized as SA. The mixture is allowable to dry to produce a film layer with room temperature conditions in a dry cabinet. Using a polymer composite can minimize the scattering and improve the homogeneous dispersion of the solution.

Thus, the  $\text{Mg}(\text{NO}_3)_2$  film is prepared using solvent casting, as demonstrated in Figure 1. The  $\text{Mg}(\text{NO}_3)_2$  was purchased from Nanochemazone with a molecular weight of 148.313 g/mol, and the purity of the material was  $\geq 99\%$ . Firstly, 1 g of the polyvinyl alcohol (PVA), also known as a synthetic polymer, water-soluble, and 100 ml of deionized water are mixed to dissolve the PVA by applying a magnetic stirrer in the beaker. Then, 10 mg of  $\text{Mg}(\text{NO}_3)_2$  are dissolved in 5 ml PVA solution to create an  $\text{Mg}(\text{NO}_3)_2$  solution. Then, the  $\text{Mg}(\text{NO}_3)_2$  solution undergoes ultrasonication for 90 minutes and centrifugation for 10 minutes to obtain  $\text{Mg}(\text{NO}_3)_2$ -PVA suspension with stable solution. The  $\text{Mg}(\text{NO}_3)_2$ -PVA suspension is placed in a 14.4  $\text{cm}^3$  petri container. Within 48 hours, the solution is permitted to dry in a dry cabinet to form  $\text{Mg}(\text{NO}_3)_2$  film. Next, a Q-switcher is produced when a film is cut off and positioned within the fiber ferrule duo.

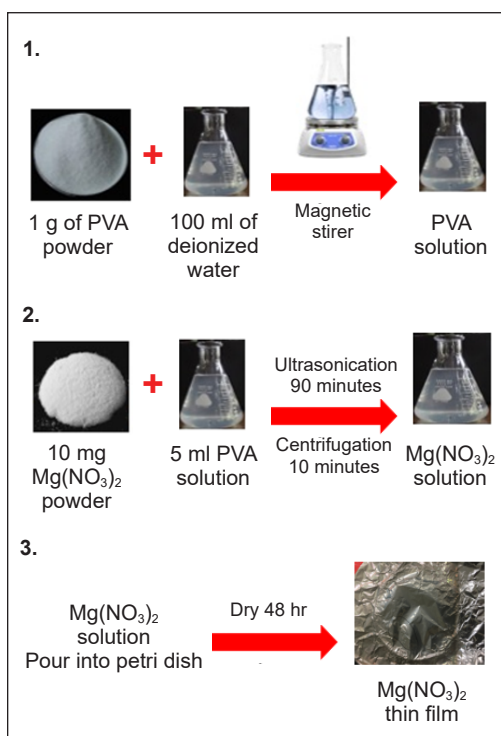


Figure 1. The solvent casting method for preparing  $\text{Mg}(\text{NO}_3)_2$

### Characterization of Magnesium Nitrate Film

Figures 2(a) and (b) indicate the surface morphology of  $\text{Mg}(\text{NO}_3)_2$  film with different magnifications of  $\times 100$  and  $\times 10000$ , respectively, which is examined with the assistance of a Field Emission Scanning Electron Microscope. The surface morphology of  $\text{Mg}(\text{NO}_3)_2$  film depicts a peak and a valley on either side, potentially arising from a small alteration in the film's thickness. Furthermore, the lack of aggregates is apparent. The Energy Dispersive X-ray exhibits the elements of magnesium, oxygen, nitrogen, and carbon, as demonstrated in Figures 2(c) and (d). The carbon parts appear during the characterization because the film is attached to the stage holder. However, the weight percentage of carbon elements is 3.1%, which is lower than magnesium, oxygen, and nitrogen, with weight percentages of 8.7%, 78.4%, and 9.8%, respectively.

The UV-Vis spectrophotometer is employed to capture the absorption spectrum of the  $\text{Mg}(\text{NO}_3)_2$  film, which extends from 200 nm to 800 nm, as depicted in Figure 2(e). An evident peak signifies the occurrence of  $\text{Mg}(\text{NO}_3)_2$  in the sample at 295 nm wavelength. Based on the measured absorption spectrum, the optical bandgap of  $\text{Mg}(\text{NO}_3)_2$  film is recognized through the Tauc relation as Equation 1:

$$\alpha h\nu = A (h\nu - E_g)^n \quad [1]$$

where  $\alpha$  is the absorption coefficient,  $h$  is Planck's constant,  $\nu$  is the photon's frequency,  $A$  is constant,  $n$  is a type of transition; in this study,  $n=2$ , and  $E_g$  is the energy band gap. Determining the bandgap of a film of  $\text{Mg}(\text{NO}_3)_2$  involves the extrapolation of the linear segment of the absorption edge towards the x-axis. The Tauc curve depicted in Figure 2(f) at  $y = 0$  reveals that the optical band gap of the  $\text{Mg}(\text{NO}_3)_2$  film is 4.80 eV. The analysis of the structural characteristics of  $\text{Mg}(\text{NO}_3)_2$  film using Bruker-2D Phaser X-ray diffraction (XRD) in the range of  $10^\circ$ – $80^\circ$  is depicted in Figure 2(g). The main peaks are noticed, which are located at  $15^\circ$ ,  $25^\circ$ ,  $27^\circ$ ,  $28^\circ$ ,  $30^\circ$ ,  $33^\circ$ , and  $43.8^\circ$ . The findings appear consistent with those of other studies (Sulaiman et al., 2013). The high intensities and narrow peaks of the  $\text{Mg}(\text{NO}_3)_2$  film are observed in the specified peaks, and it is determined that this is because the  $\text{Mg}(\text{NO}_3)_2$  film had a high crystallinity and minimum surface energy.

On the other hand, it is determined that other peaks that had been noticed are caused by the substrate as well as other defects (Oztas et al., 2012). Figure 2(h) revealed the Fourier transform infrared spectroscopy (FTIR) analysis of the  $\text{Mg}(\text{NO}_3)_2$  film, conducted utilizing a Perkin Elmer FTIR Spectrometer LR 64912C; N3896 outfitted with universal Attenuated Total Reflectance (ATR) sample stage and spectrum express FTIR software V1.3.2 Perkin Elmer LX100877-1. The FTIR spectrum of the sample displays a distinctive absorption band at  $3351 \text{ cm}^{-1}$ , attributed to the O-H stretching band, N=O bending at  $1645 \text{ cm}^{-1}$ , and a mixture of N-O stretching and bending of N=O at  $1351 \text{ cm}^{-1}$ . Furthermore, the observation of bands at  $819 \text{ cm}^{-1}$  implies the existence of a bidentate type of  $\text{NO}_3^-$  ion when interacting with  $\text{Mg}^{2+}$  (Chang & Irish, 1973).

The balance twin detector is constructed to examine the nonlinear absorption characteristics of  $\text{Mg}(\text{NO}_3)_2$  films. "modulation depth" refers to the most significant degree of change in the SA absorption. It is possible to excite it by emitting light of a specific wavelength. Regarding the construction of pulse fiber lasers, modulation depth is one of the most important criteria. A reasonably large modulation depth SA can achieve a short pulse width and effective self-starting functioning due to the robust pulse-shaping capacity that the absorber possesses. An arrangement of twin detectors has a home mode mode-locked pulse laser source, attenuator, optical coupler (OC) with a ratio of 50:50, and two optical power meters (OPM), as illustrated in Figure 3(a). A mode-locked pulse is applied to measure the optical power loss of  $\text{Mg}(\text{NO}_3)_2$  with operating wavelength, repetition rate, and

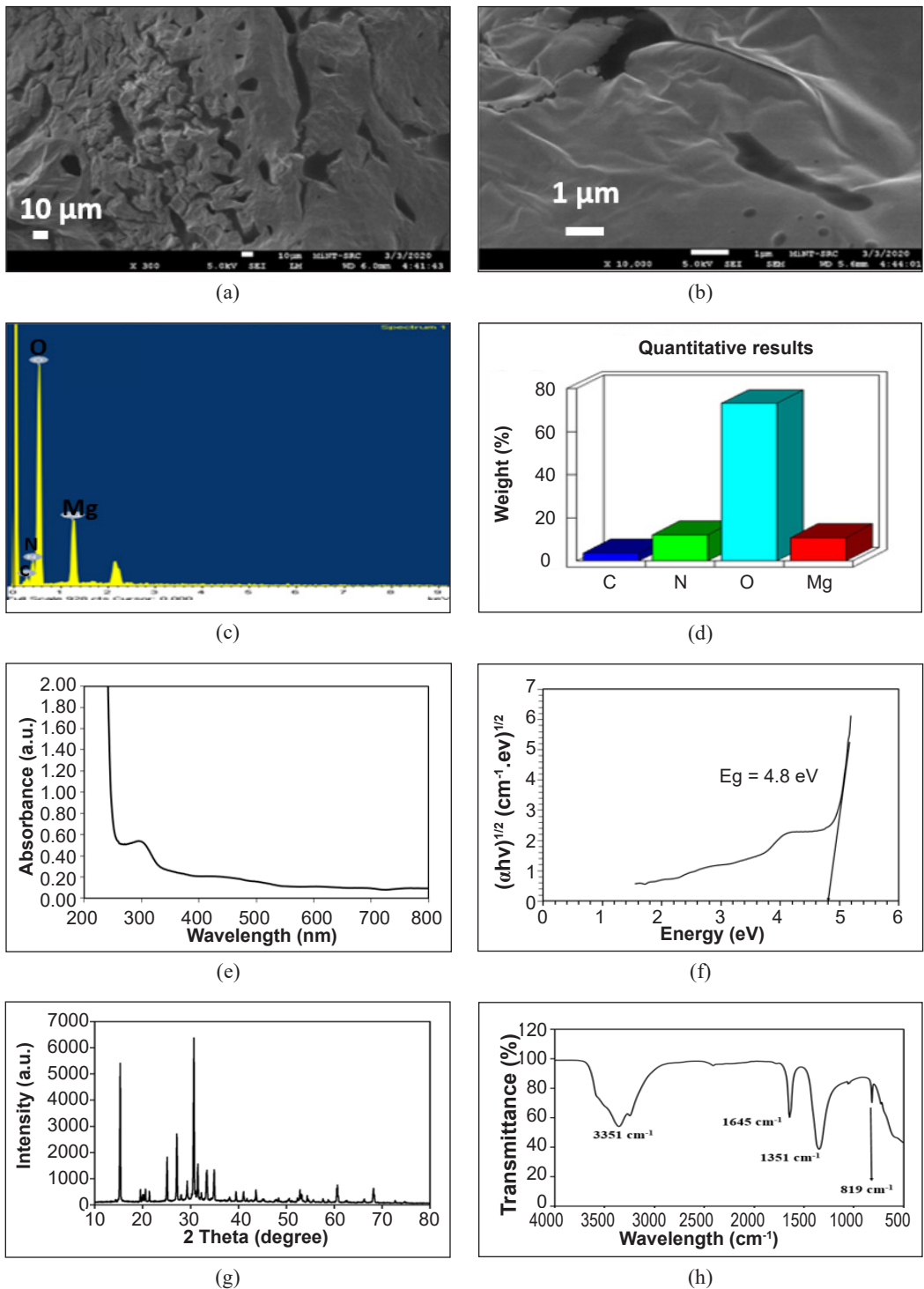


Figure 2.  $Mg(NO_3)_2$  film: (a) and (b) the surface morphology; (c) EDX spectrum; (d) weight percentage of elements; (e) absorption spectrum; (f) energy band gap; (g) XRD pattern; and (h) FTIR spectrum



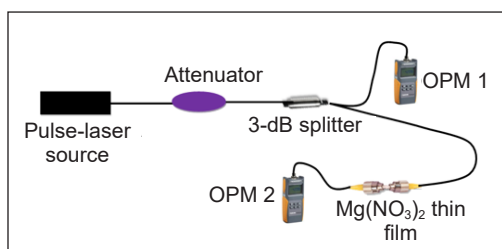
pulse width of 1570 nm, 38.73 MHz, and 640 fs, respectively. In order to generate the graph depicted in Figure 3(b), the following saturation model Equation 2 is utilized so that it can be fitted to the experimental data.

$$\alpha(I) = \frac{\alpha_s}{1+I/I_{sat}} + \alpha_{ns} \quad [2]$$

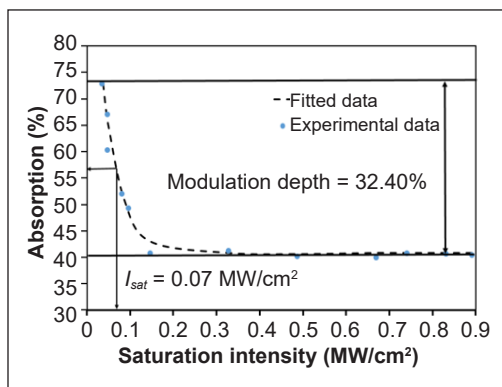
Where  $\alpha$  is absorption,  $\alpha_{ns}$  is non-saturable loss,  $\alpha_s$  is saturable absorption,  $I$  is intensity, and  $I_{sat}$  is saturation intensity. The modulation depth, non-saturable absorption, and saturation intensity of  $\text{Mg}(\text{NO}_3)_2$  film are 32.40%, 40.14%, and 0.07  $\text{MW}/\text{cm}^2$ , respectively. The comparatively large modulation depth is indicative of the strong pulse-shaping capabilities of the SA, which ultimately results in short pulse duration and dependable self-starting of the Q-switched operation. Applying the SA to the experimental setup, the light photons are absorbed by electrons in the valence band, which stimulates them toward the conduction band. It is how the nonlinear behavior of the SA can be described. It is expected that the energy of any photons absorbed will be equal to the bandgap. Because the  $\text{Mg}(\text{NO}_3)_2$  film has a structure consisting of energy bands, a significant number of electrons can be excited once the high power intensity is used. In the conduction band, the absorption of photons is significantly diminished because of the prevalence of electrons present. Figure 3(c) illustrates the insertion loss of the  $\text{Mg}(\text{NO}_3)_2$  film to measure how much the signal power is diminished after passing through the SA. The insertion loss of  $\text{Mg}(\text{NO}_3)_2$  film is 2.8 dB.

### Design of Figure-of-eight

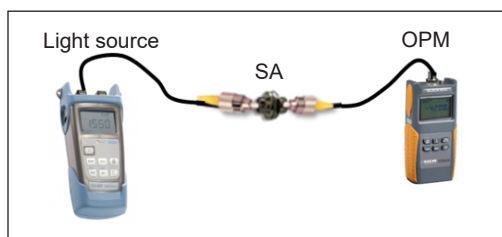
Figure 4 depicts the cavity design known as the figure-of-eight incorporating the  $\text{Mg}(\text{NO}_3)_2$  film. The schematic design consists of a nonlinear amplifying mirror (NALM) (first loop)



(a)



(b)



(c)

Figure 3. (a) Arrangement of twin detector method; (b) The nonlinear absorption of  $\text{Mg}(\text{NO}_3)_2$  film; and (c) The illustration of insertion loss of  $\text{Mg}(\text{NO}_3)_2$  film

and an optical isolator with an output optical coupler (unidirectional ring cavity) (second loop). A 50% optical coupler connects the two loops of Figure-of-eight. The first rings constructed for NALM consist of an EDF M-5 as gain media with 2 m length, wavelength division multiplexing (WDM) with a 980/1550 nm ratio, and  $Mg(NO_3)_2$  film as SA. The small pieces of  $Mg(NO_3)_2$  film are cut with the size of  $1.74 \text{ mm}^2$  and attached to the fiber ferrules, then sandwiched between two fiber ferrules to form an SA. The area is measured using an optical microscope, as shown in Figure 4(b). The matching gel is dropped on the fiber ferrules to minimize light's back reflections and guarantee that the  $Mg(NO_3)_2$  film is wholly attached to the fiber ferrule's functional area. The EDF M-5 has specifications such as absorption coefficients of 6.43 dB/m at a wavelength of 1530 nm, a coating diameter of  $240.3 \text{ }\mu\text{m}$ , core concentricity of  $0.26 \text{ }\mu\text{m}$ , a cut-off wavelength of 949 nm, a numerical aperture of 0.23, mode field diameter of  $5.8 \text{ }\mu\text{m}$  and fiber diameter of  $124.9 \text{ }\mu\text{m}$ . The propagation of the electric fields determines the laser pulse evolution in the NALM. Upon passing through the coupler, the electric fields are divided into two distinct components of varying intensities, propagating in opposite directions within the cavity (Han et al., 2020).  $E_3$  and  $E_4$  determine the electric fields circulated in the NALM in the clockwise (CW) and counterclockwise (CCW) directions, as presented in Figure 5.

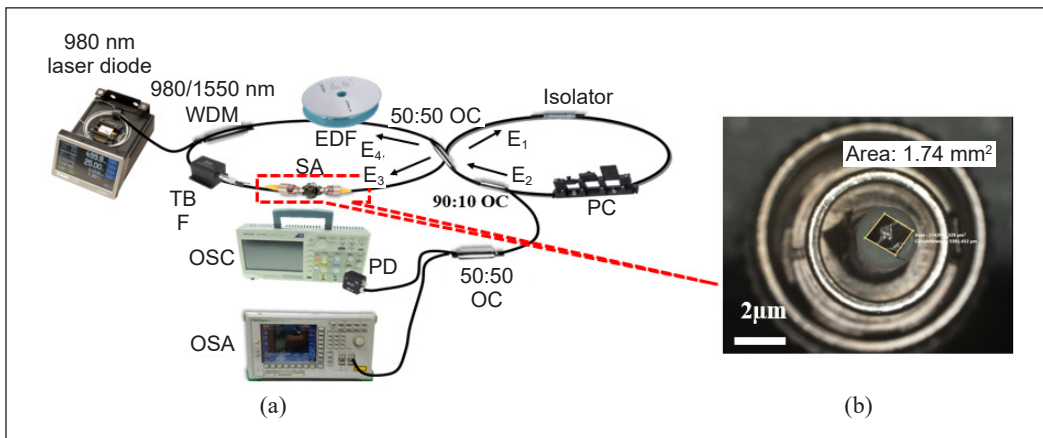


Figure 4. (a) Experimental design of tunable Q-switched pulse fiber laser using  $Mg(NO_3)_2$  film; and (b) A small piece of SA is attached to the fiber ferrule

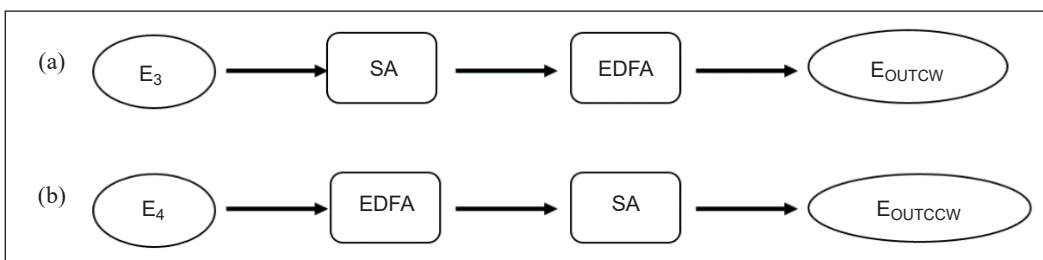


Figure 5. Schematic representation of NALM: (a) clockwise; and (b) counterclockwise direction

## RESULTS AND DISCUSSION

A passive method is implemented to generate a Q-switched pulse fiber laser, and this is accomplished by incorporating a figure-of-eight cavity design into which a film of  $\text{Mg}(\text{NO}_3)_2$  has been incorporated. After the  $\text{Mg}(\text{NO}_3)_2$  film has been inserted, it is possible to observe the self-starting Q-switched pulse fiber laser functioning at 154.30 mW of pump power. Due to the high transmission loss impact caused by the  $\text{Mg}(\text{NO}_3)_2$  embedded with PVA to produce a film, the Q-switched threshold is slightly higher than it would have been otherwise. Raising the pump power to 403.00 mW will allow for generating a steady Q-switched pulse.

The Q-switched spectrum has a center wavelength of 1553 nm, with an output power of -7.9 dBm and a resolution of 1.0 nm, as shown in Figure 6(a). Several peaks can be seen in the optical spectrum as a result of mode competition and a greater cavity length in the figure-of-eight designs. This competition mode is created due to a uniform gain broadening in EDF. Besides, in the context of electromagnetic fields in cavities, such as a figure-eight resonator, competition between multiple peaks refers to the phenomenon where different resonant modes within the cavity are vying for energy, and their frequencies influence each other. This competition arises due to the interaction and coupling between these modes, and it can lead to shifts in the resonant frequencies and changes in the mode shapes. However, it can be mitigated with the help of the inhomogeneous loss features of nonlinear polarization rotation (NPR), which causes intensity-dependent loss for various frequencies. Consequently, the equilibrium between the inhomogeneous loss generated by NPR and the mode competition effect of the EDF can result in stable multiple peak oscillations at room temperature with a uniform power distribution among the wavelengths (Feng et al., 2006).

Further increasing the pump power above 403.00 mW shows an irregular Q-switched pulse, and the pulse is stable when the pump power is between 154.30 mW and 403.00 mW. This phenomenon indicated that the  $\text{Mg}(\text{NO}_3)_2$  film did not experience damage SA. It affects the unstable Q-switched caused by the oversaturation of the  $\text{Mg}(\text{NO}_3)_2$  film when exposed to a high incident intensity. The process in the  $\text{Mg}(\text{NO}_3)_2$  film is related to two-photon absorption, which has been initiated because of the high optical intensity. Therefore, the absorption coefficient increases as pump power continuously rises. As a result, the Q-switched procedure is unable to continue when the pump power is above 403.00 mW. The  $\text{Mg}(\text{NO}_3)_2$  film in the laser cavity is eliminated to observe the condition of the Q-switched pulse. The findings indicate that only continuous waves appear on the OSC and OSA, which proves that the Q-switched pulse fiber laser can be generated with the help of  $\text{Mg}(\text{NO}_3)_2$  film.

Figure 6(b) illustrates a steady Q-switched pulse train operating with a maximum pump power of 403.00 mW. The repetition rate of 72.56 kHz relates to a period of 13.78  $\mu\text{s}$  and

a pulse width of  $3.00 \mu\text{s}$ . Additionally, the pulse trains maintained a constant intensity distribution with no discernible variation or amplitude modulation. It demonstrates the pulse regime's stability and capacity to function at different repetition rates and pulse widths. Then, the stability of the pulse is investigated from the OSC, as illustrated in Figure 6(c). The resolution bandwidth and span from the OSC are  $300 \text{ kHz}$  and  $300 \text{ Hz}$ , respectively. The fundamental frequency is precisely synchronized with the Q-switched pulse repetition rate of  $72.56 \text{ kHz}$ . Regarding the signal-to-noise ratio (SNR), the fundamental frequency has a value of  $63.59 \text{ dB}$ . The SNR is more significant than  $50.00 \text{ dB}$ , better or comparable to those reported by Q-switched pulse fiber laser by platinum (Yuzaila et al., 2019) and indium tin oxide (Zalkepali et al., 2019). Hence, these show that the Q-switched laser is steady, which might be appropriate for real-world uses.

When tuning the pump power, the Q-switched pulse fiber laser's repetition rate rises continuously from  $35.36 \text{ kHz}$  to  $72.56 \text{ kHz}$ . In the meantime, as seen in Figure 7(a), the pulse width dramatically declined, starting from  $4.24 \mu\text{s}$  to  $3.00 \mu\text{s}$ , because more photons are cycled inside the figure-of-eight cavity due to increasing pump power, saturating the  $\text{Mg}(\text{NO}_3)_2$  film. Hence, by enhancing the modulation depth of  $\text{Mg}(\text{NO}_3)_2$  film and shortening the fiber laser cavity design, the pulse width of the Q-switched pulse may be further reduced.

Figure 7(b) illustrates the patterns in average output power with a steady rise from  $0.03 \text{ mW}$  to  $0.45 \text{ mW}$  between working pump power of  $154.30 \text{ mW}$  and  $403.00 \text{ mW}$ . The same goes for Q-switched pulse energy, steadily increasing against the pump power from  $0.88 \text{ nJ}$  to  $6.20 \text{ nJ}$ . Both values are consistent with the Q-switched pulse

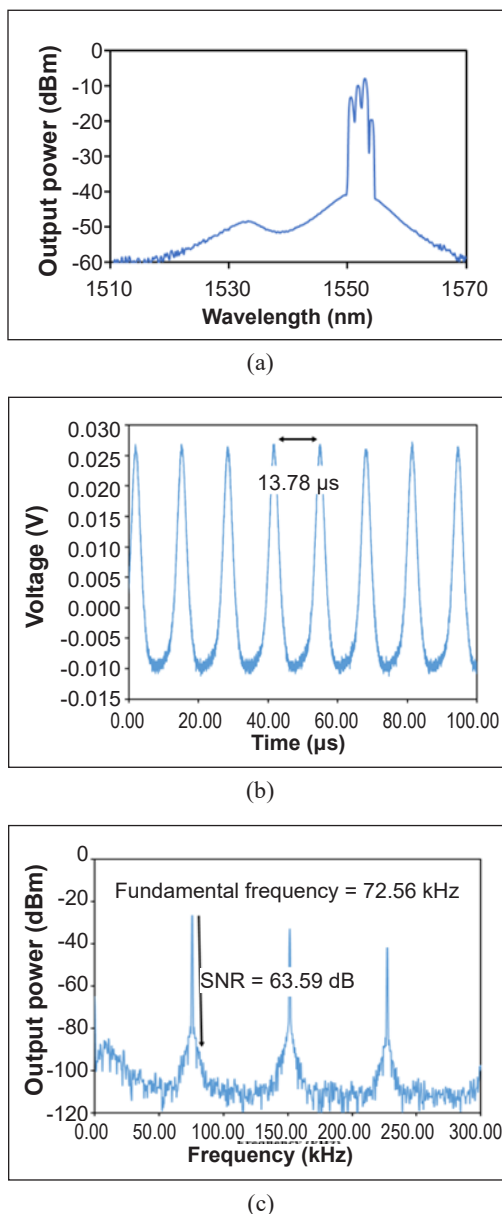


Figure 6. Q-switched pulse fiber laser: (a) optical spectrum; (b) pulse train; and (c) fundamental frequency at a pump power of  $403.00 \text{ mW}$

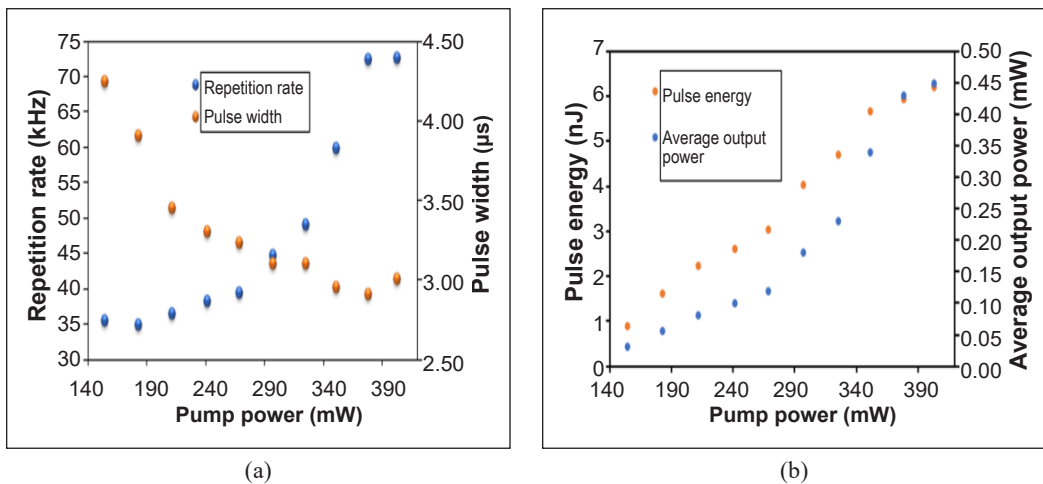


Figure 7. The relationship of: (a) repetition rate and pulse width; and (b) pulse energy and average output power by varying the pump power

fiber laser's usual properties. The proposed research shows no stable mode-locked pulse operation with this SA. These outcomes might be explained by the SA's significant inset loss or small modulation depth. For instance, the mode-locking process in the fiber laser will not be achieved when the SA cannot compensate for the output-induced disturbance or the dispersion-induced temporal broadening (Mao et al., 2016; Feng et al., 2016).

The stable Q-switched pulse at the pump power of 403.00 mW is observed for the wavelength tunability by integrating TBF inside the cavity design. The continuously tunable wavelength of the Q-switched pulse is obtained from 1528 nm to 1552 nm with a tuning range of 24 nm, as depicted in Figure 8(a). Parameters of repetition rate and pulse width are plotted, as displayed in Figure 8(b), against the lasing wavelength. The repetition rate varies significantly between 35.36 kHz and 72.56 kHz as the laser's wavelength is adjusted between 1528 and 1552 nm. It explains that the intracavity laser is more powerful, and  $\text{Mg}(\text{NO}_3)_2$  film bleaching occurs more quickly under quicker population inversion/depletion at a larger-gain EDF wavelength, resulting in a higher repetition rate. The pulse width can range between 2.10  $\mu\text{s}$  to 4.10  $\mu\text{s}$  depending on the tuning range. Beyond the tuning wavelength, no Q-switched pulse is observed, indicating the limitation of stable wavelength tunability.

In this research, various SAs have been compared in Table 1 with Q-switched parameters. The highest repetition rate, smallest pulse width, highest pulse energy and operation, tunable wavelength, and SNR are examined and compared for the Q-switched features. Compared to  $\text{MgO}$ ,  $\text{MgB}_2$ ,  $\text{WTe}_2$ ,  $\text{Al}_3$ ,  $\text{TiO}_2$ , and ITO, our work's SNR value is more outstanding, demonstrating that our suggested SA has superior stability and performance in producing the Q-switched pulse fiber laser. Although the  $\text{WTe}_2$  has a more

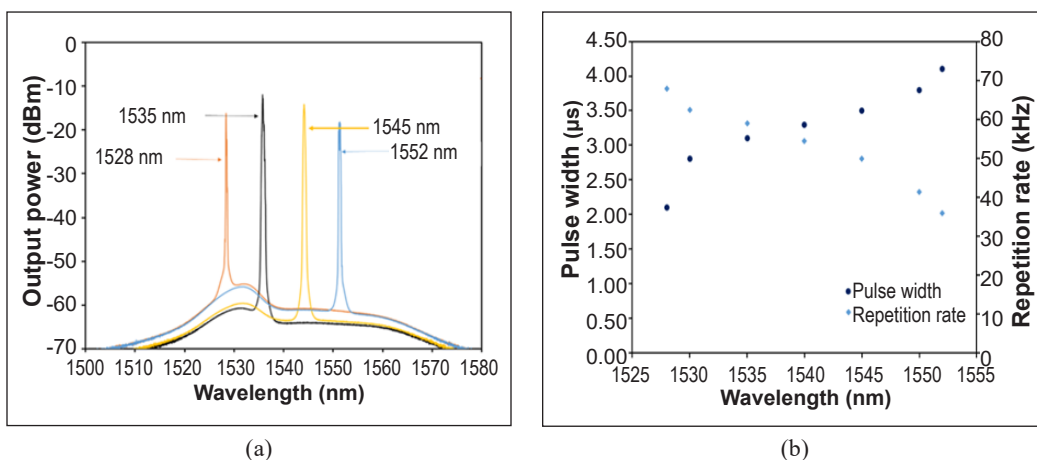


Figure 8. (a) The tunable Q-switched pulse fiber laser; and (b) the relationship of repetition rate and pulse width at a fixed pump power of 403.00 mW

significant tuning range, it still has a broader pulse width than other SA. As a result, the suggested SA effectively produces the tunable Q-switched pulse fiber laser.

The present study found that the absence of a mode-locked spectrum can be attributed to several factors within the laser cavity and the preparation of the  $\text{Mg}(\text{NO}_3)_2$  as an SA. One significant contributing factor is the elongated length of the laser cavity, which poses a challenge in attaining a mode-locked spectrum. Hence, optimizing the cavity length to enable efficient operation in a mode-locked regime is crucial. Furthermore, the initial presence of high cavity loss poses a challenge in achieving the necessary power level for successful mode-locked operation. The potential cause of this cavity loss can be attributed to various factors, including the characteristics of the SA itself, the fiber ferrule adapter, and other components incorporated into the figure-eight cavity design. The successful attainment of mode-locked operation necessitates the synchronization of phases across numerous longitudinal modes.

## CONCLUSION

In conclusion, a novel inorganic  $\text{Mg}(\text{NO}_3)_2$  film material is successfully investigated as a Q-switcher. The  $\text{Mg}(\text{NO}_3)_2$  film is synthesized using solvent casting. Based on the analysis of the nonlinear absorption, the modulation depth is 32.40%, and the saturation intensity is  $0.07 \text{ MW/cm}^2$ . The higher repetition rate of 72.56 kHz is performed at a stable Q-switched pulse fiber laser using 403.00 mW pump power, displaying the shortest pulse of  $3.00 \mu\text{s}$ . Furthermore, incorporating TBF in a figure-of-eight cavity design at 403.00 mW pump power allows the Q-switched pulse fiber laser wavelength to be adjusted from 1528 nm to 1552 nm. Consequently, it provides tuning results for a pulse width of  $2.10 \mu\text{s}$  to  $4.10 \mu\text{s}$ . Meanwhile, the repetition rate ranges from 67.90 kHz to 35.80 kHz. Therefore, the

Table 1  
*The comparison of previous saturable absorbers with this work*

Types of SA	Modulation depth (%)	Saturation Intensity (MW/cm <sup>2</sup> )	Operational / Tunable Wavelength (nm)	Tuning range (nm)	Repetition rate (kHz)	Pulse width ( $\mu$ s)	Pulse energy (nJ)	Average output power (mW)	SNR (dB)	Ref.
MgO	32.4	16.00	1569.1/NA	NA	350000.00	0.0000056	2.17	3.5	50.00	Khaleel et al., 2019
MgB <sub>2</sub>	NA	NA	1070/NA	NA	50.00	0.92	NA	NA	NA	Morshed et al., 2017
WTe <sub>2</sub>	20.0	0.025	1494/1459-1513	54	36.50	3.70	16.5	0.60	42.00	Ahmad, Ismail et al., 2020
Alq <sub>3</sub>	8.1	3.000	1563.3/1520-1563.3	43.3	71.00	2.12	37.0	2.63	53.00	Salam et al., 2021
TiO <sub>2</sub>	19.1	0.040	1532-1570	38	83.30	0.08	0.41	NA	45.00	Ahmad et al., 2019
ITO	NA	NA	1562.07/1540-1570	30	94.34	3.22	30.29	2.86	58.93	Zalkepli et al., 2021
Mg(NO <sub>3</sub> ) <sub>2</sub>	1.5	0.450	1562.37 / 1528-1552	24	72.56	3.00	6.20	0.45	63.59	This work

$Mg(NO_3)_2$  film may have the opportunity to be implemented in an application involving optical communications. Furthermore, the ultrashort pulse fiber laser can be obtained by optimizing the preparation of  $Mg(NO_3)_2$  film and figure-of-eight cavity design.

## ACKNOWLEDGEMENTS

Communication of this research is made possible through monetary assistance from Universiti Tun Hussein Onn Malaysia (UTHM) and the UTHM Publisher's Office via Publication Fund E15216. This work was supported by the Ministry of Higher Education, Government of Malaysia, under the project Fundamental of Research Grant Scheme (FRGS) FRGS/1/2019/WAB05/UTHM/02/4 (Grant No: K170).

## REFERENCES

- Ahmad, H., Albaqawi, H.S., Yusoff, N., Bayang, L., Kadir, M. Z. B. A., & Yi, C.W. (2020). Tunable passively Q-switched erbium-doped fiber laser based on  $Ti_3C_2Tx$  MXene as saturable absorber. *Optical Fiber Technology*, 58, Article 102287. <https://doi.org/10.1016/j.yofte.2020.102287>
- Ahmad, H., Ismail, N. N., Aidit, S. N., Yusoff, N., & Zulkifli, M. Z. (2020). Tunable S+/S band Q-switched thulium-doped fluoride fiber laser using tungsten ditelluride (WTe<sub>2</sub>). *Results in Physics*, 17, Article 103124. <https://doi.org/10.1016/j.rinp.2020.103124>
- Ahmad, H., Reduan, S. A., Ruslan, N. E., Lee, C. S. J., Zulkifli, M. Z., & Thambiratnam, K. (2019). Tunable Q-switched erbium-doped fiber laser in the C-band region using nanoparticles ( $TiO_2$ ). *Optics Communications*, 435, 283-288. <https://doi.org/10.1016/j.optcom.2018.11.035>
- Ahmad, H., Soltanian, M.R.K., Narimani, L., Amiri, I.S., Khodaei, A., & Harun, S.W. (2015). Tunable S-band Q-switched fiber laser using  $Bi_2Se_3$  as the saturable absorber. *IEEE Photonics Journal*, 7(3), 1-8. <https://doi.org/10.1109/JPHOT.2015.2433020>
- Chang, T. G., & Irish, D. E. (1973). Raman and infrared spectra study of magnesium nitrate-water systems. *The Journal of Physical Chemistry*, 77(1), 52-57. <https://doi.org/10.1021/j100620a011>
- Chen, Y., Zhao, C., Chen, S., Du, J., Tang, P., Jiang, G., Zhang, H., Wen, S., & Tang, D. (2013). Large energy, wavelength widely tunable, topological insulator Q-switched erbium-doped fiber laser. *IEEE Journal of Selected Topics in Quantum Electronics*, 20(5), 315-322. <https://doi.org/10.1109/JSTQE.2013.2295196>
- Cuadrado-Laborde, C., Delgado-Pinar, M., Torres-Peiró, S., Díez, A. & Andrés, M.V. (2007). Q-switched all-fibre laser using a fibre-optic resonant acousto-optic modulator. *Optics Communications*, 274(2), 407-411. <https://doi.org/10.1016/j.optcom.2007.02.032>
- Degnan, J. J. (1995). Optimization of passively Q-switched lasers. *IEEE Journal of Quantum Electronics*, 31(11), 1890-1901. <https://doi.org/10.1109/3.469267>
- Delgado-Pinar, M., Zalvidea, D., Díez, A., Pérez-Millán, P., & Andrés, M. V. (2006). Q-switching of an all-fiber laser by acousto-optic modulation of a fiber Bragg grating. *Optics Express*, 14(3), 1106-1112. <https://doi.org/10.1364/OE.14.001106>



- El-Sherif, A. F., & King, T. A. (2003). High-energy, high-brightness Q-switched  $Tm^{3+}$ -doped fiber laser using an electro-optic modulator. *Optics Communications*, *218*(4-6), 337-344. [https://doi.org/10.1016/s0030-4018\(03\)01200-8](https://doi.org/10.1016/s0030-4018(03)01200-8)
- Faragl, M. A., El-Okr, M., Mahani, R. M., Turky, G. M., & Afify, H. H. (2014). Investigation of dielectric and optical properties of MgO thin films. *International Journal of Advancement in Engineering, Technology and Computer Sciences*, *1*(1), 1-9.
- Feng, T., Mao, D., Cui, X., Li, M., Song, K., Jiang, B., Lu, H., & Quan, W. (2016). A filmy black-phosphorus polyimide saturable absorber for Q-switched operation in an erbium-doped fiber laser. *Materials*, *9*(11), Article 917. <https://doi.org/10.3390/ma9110917>
- Feng, X., Tam, H. Y., & Wai, P. K. A. (2006). Stable and uniform multiwavelength erbium-doped fiber laser using nonlinear polarization rotation. *Optics Express*, *14*(18), 8205-8210. <https://doi.org/10.1364/OE.14.008205>
- Han, Y., Guo, Y., Gao, B., Ma, C., Zhang, R., & Zhang, H. (2020). Generation, optimization, and application of ultrashort femtosecond pulse in mode-locked fiber lasers. *Progress in Quantum Electronics*, *71*, Article 100264. <https://doi.org/10.1016/j.pquantelec.2020.100264>
- Island, J. O., Steele, G. A., van der Zant, H. S., & Castellanos-Gomez, A. (2015). Environmental instability of few-layer black phosphorus. *2D Materials*, *2*(1), Article 011002. <https://doi.org/10.1088/2053-1583/2/1/011002>
- Keller, U., Weingarten, K. J., Kartner, F. X., Kopf, D., Braun, B., Jung, I. D., Fluck, R., Honninger, C., Matuschek, N., & Der Au, J. A. (1996). Semiconductor saturable absorber mirrors (SESAM's) for femtosecond to nanosecond pulse generation in solid-state lasers. *IEEE Journal of selected topics in Quantum Electronics*, *2*(3), 435-453. <https://doi.org/10.1109/2944.571743>
- Khaleel, W. A., Sadeq, S. A., Alani, I. A. M., & Ahmed, M. H. M. (2019). Magnesium oxide (MgO) thin film as saturable absorber for passively mode locked erbium-doped fiber laser. *Optics & Laser Technology*, *115*, 331-336. <https://doi.org/10.1016/j.optlastec.2019.02.042>
- Kim, N., Lee, P., Kim, Y., Kim, J. S., Kim, Y., Noh, D. Y., Yu, S. U., Chung, J., & Kim, K. S. (2014). Persistent topological surface state at the interface of  $Bi_2Se_3$  film grown on patterned graphene. *ACS Nano*, *8*(2), 1154-1160. <https://doi.org/10.1021/nn405503k>
- Mao, D., She, X., Du, B., Yang, D., Zhang, W., Song, K., Cui, X., Jiang, B., Peng, T., & Zhao, J. (2016). Erbium-doped fiber laser passively mode locked with few-layer  $WSe_2/MoSe_2$  nanosheets. *Scientific Reports*, *6*(1), Article 23583. <https://doi.org/10.1038/srep23583>
- Mia, M. N. H., Pervez, M. F., Hossain, M. K., Rahman, M. R., Uddin, M. J., Al Mashud, M. A., Ghosh, H. K., & Hoq, M. (2017). Influence of Mg content on tailoring optical bandgap of Mg-doped ZnO thin film prepared by sol-gel method. *Results in physics*, *7*, 2683-2691. <https://doi.org/10.1016/j.rinp.2017.07.047>
- Morshed, M., Hattori, H. T., Haque, A., & Olbricht, B. C. (2017). Magnesium diboride ( $MgB_2$ ) as a saturable absorber for a ytterbium-doped Q-switched fiber laser. *Applied Optics*, *56*(27), 7611-7617. <https://doi.org/10.1364/AO.56.007611>
- Okhotnikov, O., Grudinina, A., & Pessa, M. (2004). Ultra-fast fibre laser systems based on SESAM technology: New horizons and applications. *New Journal of Physics*, *6*(1), Article 177. <https://doi.org/10.1088/1367-2630/6/1/177>

- Oztas, M., Bedýr, M., Sur, S., & Öztürk, Z. (2012). Influence of an aqueous/ethanolic solution on the structural and electrical properties of polycrystalline ZnS films. *Chalcogenide Letters*, 9(6), 249-256.
- Plóciennik, P., Guichaoua, D., Zawadzka, A., Korcala, A., Strzelecki, J., Trzaska, P., & Sahraoui, B. (2016). Optical properties of MgO thin films grown by laser ablation technique. *Optical and Quantum Electronics*, 48, 1-12. <https://doi.org/10.1007/s11082-016-0536-8>
- Salam, S., Nizamani, B., Yasin, M., & Harun, S. W. (2021). C-band tunable Q-switched fiber laser based on Alq<sub>3</sub> as a saturable absorber. *Results in Optics*, 2, Article 100036. <https://doi.org/10.1016/j.rio.2020.100036>
- Sulaiman, M., Rahman, A. A., & Mohamed, N. S. (2013). Structural, thermal and conductivity studies of magnesium nitrate–alumina composite solid electrolytes prepared via sol-gel method. *International Journal of Electrochemical Science*, 8, 6647-6655.
- Sun, Z., Hasan, T., & Ferrari, A. C. (2012). Ultrafast lasers mode-locked by nanotubes and graphene. *Physica E: Low-dimensional Systems and Nanostructures*, 44(6), 1082-1091. <https://doi.org/10.1016/j.physe.2012.01.012>
- Sun, Z., Martinez, A., & Wang, F. (2016). Optical modulators with 2D layered materials. *Nature Photonics*, 10(4), 227-238. <https://doi.org/10.1038/nphoton.2016.15>
- Xia, F., Wang, H., & Jia, Y. (2014). Rediscovering black phosphorus as an anisotropic layered material for optoelectronics and electronics. *Nature Communications*, 5(1), Article 4458. <https://doi.org/10.1038/ncomms5458>
- Yuzaille, Y. R., Awang, N. A., Zalkepali, N. U. H. H., Zakaria, Z., Latif, A. A., Azmi, A. N., & Hadi, F. A. (2019). Pulse compression in Q-switched fiber laser by using platinum as saturable absorber. *Optik*, 179, 977-985. <https://doi.org/10.1016/j.ijleo.2018.11.057>
- Zalkepali, N. U. H. H., Awang, N. A., Yuzaille, Y. R., Zakaria, Z., Latif, A. A., Ali, A. H., & Mahmud, N. N. H. E. N. (2019). Indium tin oxide thin film based saturable absorber for Q-switching in C-band region. *Journal of Physics: Conference Series IOP Publishing*, 1371(1), Article 012018. <https://doi.org/10.1088/1742-6596/1371/1/012018>
- Zalkepali, N. U. H. H., Awang, N. A., Yuzaille, Y. R., Zakaria, Z., Latif, A. A., Ali, A. H., & Mahmud, N. N. H. E. (2021). Tunable indium tin oxide thin film as saturable absorber for generation of passively Q-switched pulse erbium-doped fiber laser. *Indian Journal of Physics*, 95, 733-739. <https://doi.org/10.1007/s12648-020-01738-y>
- Zhao, S., Zhao, J., Li, G., Yang, K., Sun, Y., Li, D., An, J., Wang, J. & Li, M. (2006). Doubly Q-switched laser with electric-optic modulator and GaAs saturable absorber. *Laser Physics Letters*, 3(10), 471-473. <https://doi.org/10.1002/lapl.200610038>

*Review Article*

## **Bead Geometry Control in Wire Arc Additive Manufactured Profile — A Review**

**Zarirah Karrim Wani and Ahmad Baharuddin Abdullah\***

*School of Mechanical Engineering, Universiti Sains Malaysia, 14300 Nibong Tebal, Pulau Pinang, Malaysia*

### **ABSTRACT**

Wire arc additive manufacturing (WAAM) is a well-established additive manufacturing method that produces 3D profiles. A better deposition efficiency can be achieved by understanding the parameters that may influence the geometry of the bead. This paper provides a review that focuses on the factors that may influence the formation of the 3D profile. The included factors are the flow pattern of the molten pool after deposition, the built structure and orientation, the heat input and cooling conditions, the welding parameters, and other uncertainties. This review aims to facilitate a better understanding of these factors and achieve the optimum geometry of the 3D parts produced. According to the literature, the behavior of molten pools is identified as one of the major factors that can impact the deposition efficiency of a bead and govern its geometry. The review indicated that the flow behavior of the molten pool and the geometry of the deposited bead are significantly affected by most welding parameters, such as torch angle, wire travel speed, filler feed rate, and cooling conditions. Furthermore, this paper incorporates the technology utilized for comprehending the behaviors of the molten pool, as it constitutes an integral component

of the control strategy. It has been concluded that automated planning and strategy are necessary to ensure efficient deposition by controlling those factors. The integration of artificial intelligence could bring benefits in planning to address the variation and complexity of shapes.

### **ARTICLE INFO**

*Article history:*

Received: 19 April 2023

Accepted: 12 September 2023

Published: 26 March 2024

DOI: <https://doi.org/10.47836/pjst.32.2.23>

*E-mail addresses:*

zarirah@usm.my (Zarirah Karrim Wani)

mebaha@usm.my (Ahmad Baharuddin Abdullah)

\* Corresponding author

*Keywords:* Bead geometry, deposition efficient, molten pool, wire arc additive manufacturing

## INTRODUCTION

Wire Arc Additive Manufacturing (WAAM) has been highlighted as a metal 3D printing method that holds immense promise for large-scale (Ermakova et al., 2020; Laghi et al., 2021) 3D printing applications across a wide range of sectors. WAAM employs arc welding methods that are also used in gas tungsten arc welding (GTAW), gas metal arc welding (GMAW), or plasma arc welding (PAW). WAAM, on the other hand, stands out due to its far superior computer control. WAAM's key features are material and feedstock, software, power supply, and understanding of these aspects. WAAM, in particular, can work with a wide variety of metals as long as they are in the form of wire. Metals include stainless steel, nickel-based alloys, titanium alloys, and aluminum alloys. Furthermore, WAAM is compatible with any metal that can be welded and utilizes a heat source for melting the wire. The wire melts and is subsequently deposited onto the substrate in the form of a molten pool. Once cooled to room temperature, it undergoes solidification and forms into a bead. The process is repeated, layer by layer, until a 3D profile with a specific geometry is formed. The geometry of the bead depends on various process factors, including current, voltage, travel speed, wire feed rate, torch angle, and the distance between the torch and substrate.

WAAM offers various advantages, including a high deposition rate, which can provide significant benefits for production and throughput (Lin et al., 2021; Liu et al., 2020; Rodrigues et al., 2019). A wide range of materials can be used for WAAM in wire form (Rodrigues et al., 2019). The material properties in WAAM parts are improved through supplemental considerations, including heat input and the cooling process (Su et al., 2019). Producing metal 3D parts, which requires an established manufacturing process such as the welding process, is also beneficial in terms of reasonable cost (Li, Chen et al., 2018; Liu et al., 2020; Shen et al., 2020). Despite the benefits, WAAM has shortcomings, such as high residual stress and distortion, low part accuracy and surface roughness (Paskual et al., 2018), and near net shape, which requires an additional finishing process like machining (Wu et al., 2018b). Residual stress and distortion commonly occur due to excessive energy input, high deposition rate, and large temperature gradient in wire-fed additive manufacturing (AM) processes. The most difficult challenge in WAAM is heat management because the process requires metal in wire form to be melted. The geometry of the deposited material is determined by the behavior of molten material in a pool. This behavior is influenced by heat, mass transfer, and cooling.

Gas Metal Arc Welding (GMAW) is the most commonly used energy source in WAAM because GMAW-based additive manufacturing has several advantages, the most important of which is lower cost (Chernovol et al., 2020; Giarollo et al., 2022; Navarro et al., 2021; Van Thao, 2020). In addition, the technique offers a high deposition rate (Chaturvedi et al., 2021; Nagasai et al., 2021; Paskual et al., 2018; Shen et al., 2020; Van Thao, 2020) and high welding efficiency, that is, material and energy (Giarollo et al., 2022; Grebmalai

& Warinsiriruk, 2020; Henckell et al., 2020; Paskual et al., 2018; Reisgen et al., 2020). GMAW is more suitable for medium and large components (Feucht et al., 2021; Gierth et al., 2020; Pandey, 2019; Waldschmitt, 2019). Other important features of GMAW are multi-material (Hauser, Reisch, Seebauer et al., 2021; Karayel & Bozkurt, 2020; Leicher et al., 2020) and improved material properties like impact strength (Nagasai et al., 2021; Waqas et al., 2018) but less in terms of dimensional accuracy (Rosli et al., 2019; Wang et al., 2022).

The paper commences by providing a comprehensive explanation of fundamental WAAM knowledge, including the molten pool, bead geometry, and the behaviors of different WAAM welding and process parameters that result in efficient material deposition. The efficacy is measured based on the geometrical representation of the profile, which includes height, width, and volume. It is assumed that the integrity issue has been resolved. It is important to understand the behavior of the molten pool during deposition to achieve a good bead geometry for a thin wall structure. This understanding enables shorter building times or higher welding efficiency.

## BEAD GEOMETRY

The geometry of beads is a crucial aspect of WAAM, as it impacts the quality of the parts, their structural integrity, and overall performance. In WAAM, a welding bead is a deposited layer of molten metal laid down by the welding process to construct a three-dimensional object. Like other welding processes, a welding bead is created in WAAM when the welding wire is melted and fused with the underlying base material. However, in the context of WAAM, these beads are deposited layer by layer to gradually construct a complex part or component. Figure 1 depicts a schematic diagram of the typical geometry of a bead. The welding bead cross-section can determine the bead height, width, radius, and degree of contact angle. The parameters set during the deposition process determine the size and geometry of the welding bead. Bead geometry includes shaping individual beads, ensuring bead consistency, managing the overlapping of multiple beads, controlling thin wall formation, and achieving accurate solid structures. Figure 2 depicts an example of geometry produced by the WAAM process.

Single bead shaping involves the control of the shape and dimensions of individual beads as they are deposited layer by layer. Properly shaping a single bead contributes to the accuracy of part dimensions and surface finish. Optimize process parameters (arc voltage, wire feed rate, and travel speed) for precise bead shaping. According

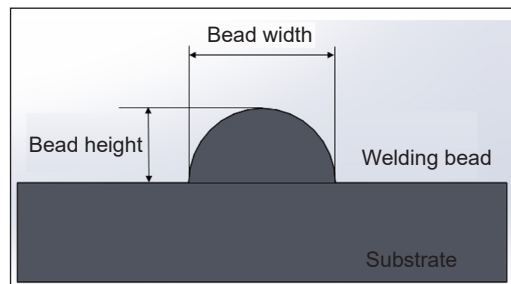


Figure 1. Schematic diagram of a weld bead

to Venkatarao’s (2021) research, the depth of the weld bead is primarily determined by current and torch angles, while the breadth and height are influenced by wire feed speed and welding speed (Venkatarao, 2021). When different torch angles are used, the bead results are comparable. For instance, when a 90° torch angle is used, the influence of arc force at a 60° angle has a lesser effect on the molten pool and depth of metal deposition. In comparison to single-bead shaping, multi-bead shaping necessitates greater attention due to the importance of effectively managing the interaction between adjacent beads as they overlap to achieve a bond that is seamless and robust. Properly overlapping multiple beads prevents the occurrence of gaps or voids between the beads, thereby ensuring a continuous and robust build. To achieve proper multi-bead overlapping, selecting appropriate overlap strategies (full or partial) based on part specifications and optimizing the overlap amount and pattern for uniform fusion and minimum gaps is necessary. Maintain consistent spacing between overlapping beads, and by adjusting the travel speed and direction, produce a seamless transition between beads.

In modern times, the prediction of bead geometry size can be achieved through applications such as the artificial neural network (Karmuhilan & Sood, 2018). The diagram of this approach is shown in Figure 3. Panchagnula and Simhambhatla (2018) also introduced a mathematical model that predicts the geometry of subsequent layers based on the height

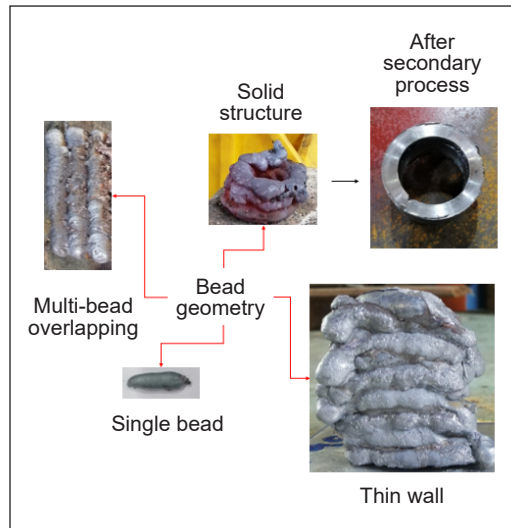


Figure 2. Example of bead geometry produced by WAAM

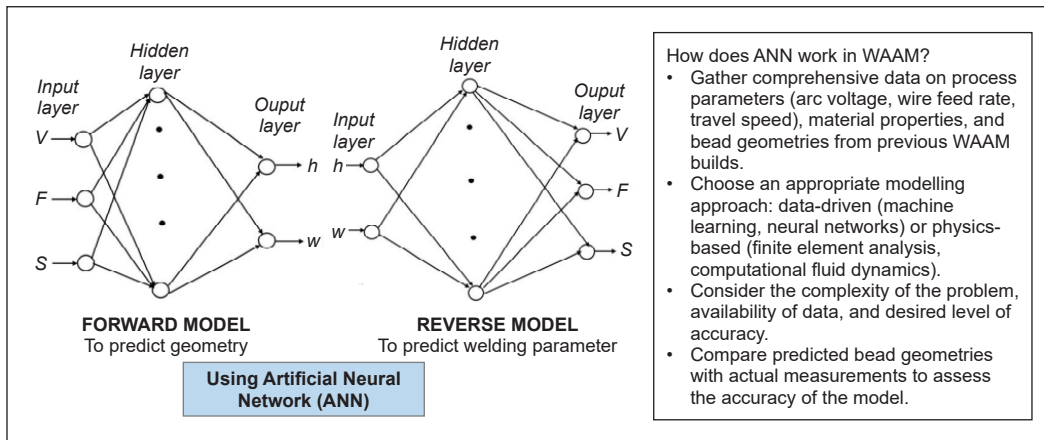


Figure 3. ANN model in predicting bead geometry (Karmuhilan & Sood, 2018)

and width of the first layer. The mathematical model can also demonstrate the relationship between the parameters and bead geometry (Panchagnula & Simhambhatla, 2018). Li, Ma et al. (2018) discovered that the stability of the formed bead is also important in the fabrication of large parts using weave beads. According to Dinovitzer et al. (2019), the geometry and microstructure of welding beads were determined to be the most affected by travel speed and current. In addition to single and multi-bead, printing a thin wall structure also necessitates meticulous control of deposition parameters to avoid distortion, warping, or collapse of said structure. It is recommended that the process parameters be fine-tuned to balance heat input and prevent warping to achieve a good bead geometry for a thin wall structure. By utilizing preheating or controlled environments, one can minimize thermal stresses.

One can achieve accurate deposition of thin walls by opting for smaller layer heights. It is essential to maintain bead consistency in thin walls for structural integrity. The user is interested in controlling the placement and dimensions of beads to accurately replicate the intended design of a solid structure. One is suggested to have an accurate bead deposition to ensure the final part meets design specifications and functional requirements. Employing precise CAD/CAM software makes it easier to produce an accurate part design and bead path planning, as shown in Figure 4. It is important to define a path for the depositing process because the backward fluid flow and swelling of metal in the molten pool can explain the uneven bead geometry and the length of the beginning region is positively related to the sloped shape at its end and the length of the molten pool (Jafari et al., 2021). Implementing iterative testing and optimization based on data from part inspection and using in-process monitoring (thermal imaging, sensors) to detect and correct deviations also aids in accuracy control. According to Jafari et al. (2021), shielding gas is also a significant factor affecting the weld bead's physical appearance. Improper shielding can lead to irregular bead profiles and diminished dimensional accuracy. Arc Striking (AS) and Arc Extinguishing (AE) are important considerations in Wire Arc Additive Manufacturing

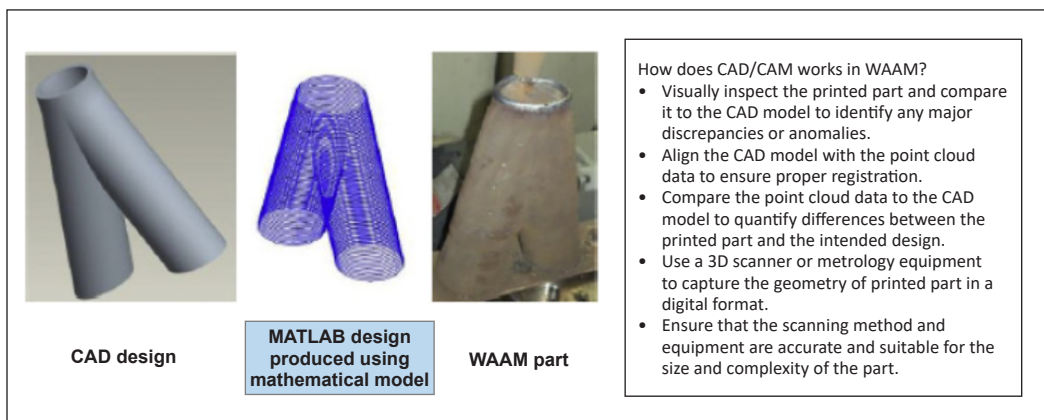


Figure 4. CAD/CAM verification shaping for geometry accuracy in WAAM (Jafari et al., 2021)

(WAAM). They are crucial in achieving precise bead geometry and maintaining process stability. These conditions can lead to variations in bead shape, dimensions, and overall part quality.

Tang et al. (2019) discovered that these two conditions result in limitations on the control of bead geometry in WAAM, and they also lead to low precision of the bead. The goal is to ensure uniformity in bead dimensions, shape, and material properties across multiple layers and throughout printing. The beads' consistency impacts the overall mechanical properties and the structural integrity of the printed part. The geometry of beads plays a crucial role in the surface finish, formation of defects, and mechanical properties of parts produced using WAAM processes. Figure 5 summarizes the influence of bead geometry on the surface finish and mechanical properties, with various effects listed. According to research conducted by Han et al. (2018), installing a controller that utilizes a rule-based engine eliminates height variation in multilayer depositing styles (Han et al., 2018). The surface polish improves accuracy and smoothness, which results in fewer or no defects being discovered inside the deposited bead and built wall. Excessive material deposition or insufficient fusion between adjacent beads can result in a rough surface finish due to too much overlap or improper spacing between beads. A smoother surface finish can be achieved by spreading out the molten material and minimizing irregularities through the controlled oscillation of the welding torch during deposition. The geometry of the bead indirectly affects the mechanical characteristics through the deposition of the produced bead. The welding parameters used during the depositing process affect the mechanical properties. Table 1 displays the impact of bead geometry on mechanical properties, surface finish, or defects based on the available research.

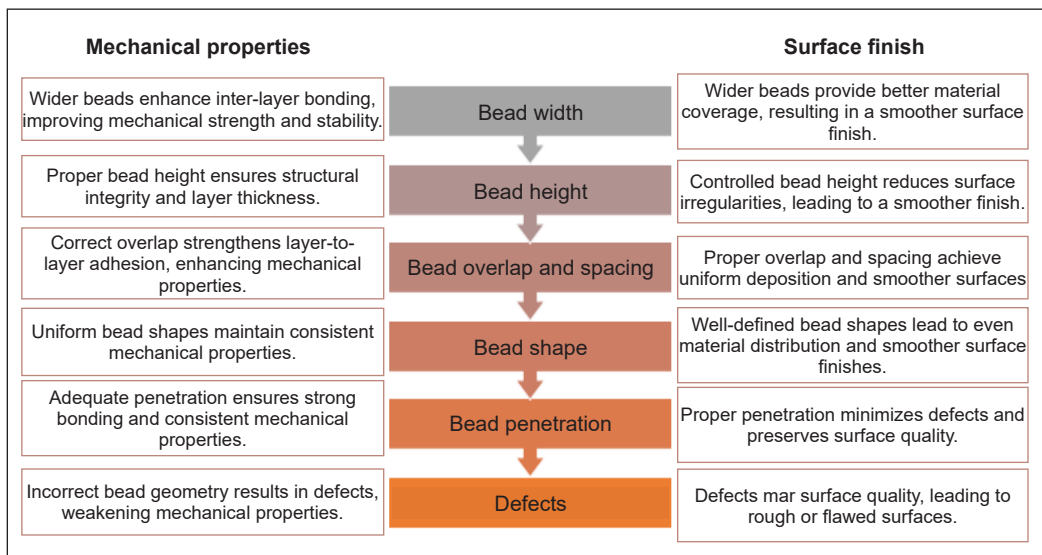


Figure 5. Summary of bead geometry effect on surface finish and mechanical properties



Table 1

*Influence of bead geometry on mechanical properties, surface roughness or defects*

Reference	Welding technique	Filler material (wire diameter)	Effect of the bead geometry on:		
			Mechanical properties	Surface finish	Defect
Xiong et al., 2018	GMAW	H08Mn2Si (1.2 mm)		/	
Liu et al., 2019	compulsively constricted WAAM (CC-WAAM)	ER70S-G (1.2 mm)	/	/	/
Dinovitzer et al., 2019	TIG	HASTELLOX alloy (NA)		/	/
Su et al., 2019	CMT	ER5356 alloy (1.2 mm)	/		/
Aldalur et al., 2020	GMAW	ER70S-6 mild steel (1.2 mm)	/	/	
Yuan et al., 2020	CMT	ER70S-6 (0.9 mm)			/
Zeng et al., 2020	TIG	NiTi wire (0.7 mm)			/
Vora et al., 2023	GMAW	SS-309L (1.2 mm)	/		/
Ni et al., 2023	GMAW	ER70S-6 (1.2 mm)		/	/

## BEAD GEOMETRY CONTROL

The control of bead geometry is a crucial aspect of WAAM. It entails the management of the shape, dimensions, and quality of each bead deposited during the additive manufacturing process. Precise control of bead geometry is essential to ensure the accuracy of the part, mechanical properties, and overall performance. Effective bead geometry control can be achieved by utilizing optimized parameter control, advanced CAD/CAM software, consistent layer height control, optimal overlap strategies, proper shielding gas, conducting material testing, and continuously analyzing data. Mu et al. (2021), who implemented an online layer-by-layer controller under various welding conditions to improve the deposition accuracy of the WAAM process, is just one example of the numerous approaches taken by previous researchers to improve the deposition accuracy of the WAAM process. The deposited profile is measured with a laser scanner and compared to the CAD model during the process. Errors are then compensated by generating a new set of welding parameters for the subsequent layer. In their measurement, Wang et al. (2020) utilized the same device and adopted the response surface optimization method to obtain accurate bead geometry. They considered the width, layer height, penetration, accumulated area, penetration area, aspect ratio, and dilution ratio.

In another case, the utilization of the dual pulsing combination of both high and low-frequency pulsing is employed to observe the effects on the weld bead geometry and heat-affected zone of Gas Tungsten Arc Welding (GTAW) (Benakis et al., 2020; Manokruang et al., 2021). Machine learning was employed to create a fully intelligent WAAM system,

as demonstrated by Ding et al. (2021) and Tang et al. (2019). In their study, Ding et al. (2021) discovered that integrating three crucial modules, namely the data generation module, the model creation module, and the welding parameter generation module, led to notable enhancements in product quality and reductions in manufacturing costs. These cost reductions encompassed aspects such as raw material usage and manual labor. Tang et al. (2019) focused on determining abnormality by examining the arc-striking and arc-extinguishing areas of the bead. Using a burning-back method, they optimized the weld bead on both ends.

## MOLTEN POOL FLOW BEHAVIOUR

A molten weld pool is a dime-sized weld volume where the filler metal has reached its melting point and is beginning to solidify. In their study, Tang et al. (2019) found that several physical properties influence a molten pool. These properties include droplet transfer, gravity, arc force, heat radiation, and conduction. The flow of liquid inside the weld-molten pool contributes to the dynamic nature of these properties. The flow direction of the molten pool varies at the arc strike, middle point, and arc extinguishing area due to different forming conditions, which results in a variation of weld geometry. Controlling these parameters may lead to the achievement of optimal bead geometry. Controlling heat accumulation in Gas Tungsten WAAM is difficult, which makes achieving good geometry and stable metal transfer challenging (Wu et al., 2018a). Figure 6 shows a schematic diagram of the molten pool from different perspectives. As the travel directional movement increases, the heat dissipation over the substrate becomes broader.

As mentioned earlier, droplets from the welding wire create the welding bead, which varies in size based on the heat dissipation determined by the setting parameter. Raising the arc force increases the droplet impact force on the molten pool even more. The heat dissipation modes from the beginning, during the built-in thin-wall part, and the overlapping welding bead are all detailed in Figure 7, which also shows the heat dissipation. As the material begins to solidify, primary and secondary penetration pushes to the back of the molten pool and creates the crown (Ou et al., 2018). In this context, the crown refers to the formed welding bead on top of the substrate.

The most frequent cause of a molten pool with poor uniformity and final appearance is a combination of high temperature and

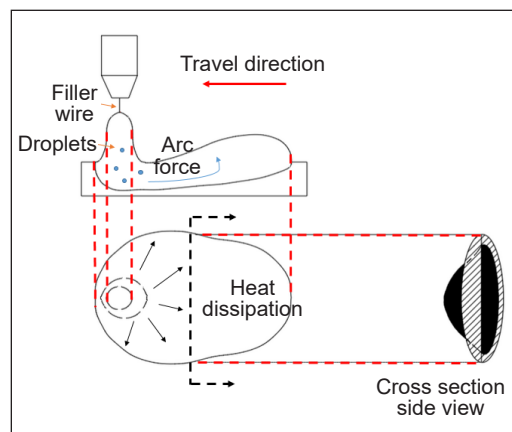


Figure 6. The schematic of weld molten pool in WAAM

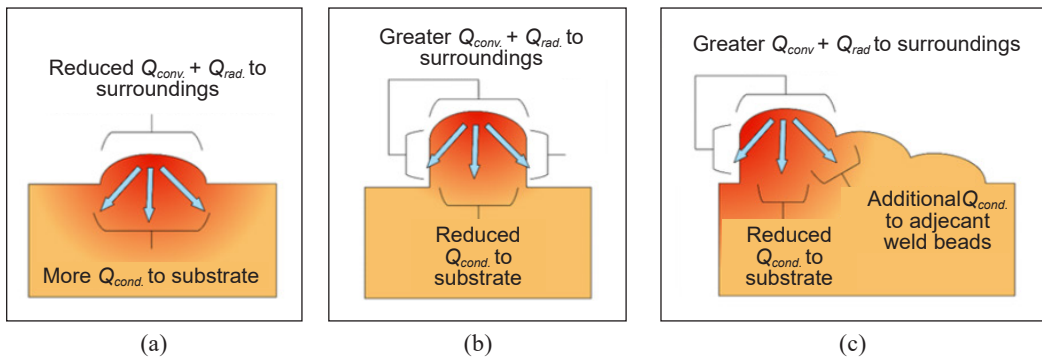


Figure 7. Schematic diagram of the heat dissipation modes: (a) at the beginning of WAAM; (b) during the build of a thin wall part; and (c) for a part with overlapping weld beads. (Cunningham et al., 2018)

deposition rate. The appearance of the welding bead is affected by heat accumulation during the movement of the welding torch, which causes the shape to vary as the molten pool cools (Cunningham et al., 2018). Multilayer deposited welding beads exhibit a semi-elliptical shape for each layer segregation (Bai et al., 2018; Dinovitzer et al., 2019; Jia et al., 2020). In order to achieve a near-net shape and good material utilization, it is necessary to regularly control the temperature during the WAAM process. In multilayer welding, it is necessary to appropriately maintain or define the distance between the welding torch and each successive layer. The molten pool on the first layer differs from that on the subsequent layer because the amplitude of the heat flow decreases as the number of deposited layers increases, resulting in heat accumulation. Several methods for reducing heat accumulation include an inter-pass idle period, active cooling, and in situ active cooling or in situ heating.

By utilizing indirect arc and force constriction, Compulsive Constricted WAAM also aids in the resolution of heat accumulation and low precision (Guo et al., 2020; Liu et al., 2019). Hejripour et al. (2018) expanded on the research by considering fluid flow and mass transfer. Heat conduction models are progressively replacing more realistic models that account for convective heat transfer. Errors in the setting of depositing parameters (such as current, voltage, welding speed, filler feed rate and torch angle) result in various issues within the molten pool. These errors cause defects like porosity, cracks, and small pores.

### Monitoring Technology

Skills and techniques are required to carry out the precise setting and monitoring of the depositing process. Table 2 summarizes research on monitoring molten pool behavior, temperature gradient, flow control, and geometry determination using various types of technology. Adaptability to a high-temperature environment and the ability to closely monitor changes in temperature and the flow of a molten pool are among the most important technological criteria.

Table 2

*Summary of methods used in the molten pool studies in recent research*

Reference	Year	Technology used	Observation
<b>Hu and Kovacevic, 2003</b>	2003	A closed-loop control system based on the infrared image	Acquire infrared images of the molten pool real-time, control of the heat input and size of the molten pool
<b>Zeinali and Khajepour, 2010</b>	2010	Charge Couple Device (CCD) camera	Obtain the molten pool height and feedback control
<b>Hofman et al., 2012</b>	2012	Complementary Metal Oxide Semiconductor (CMOS) camera	Obtain the width of the melt pool during a laser AM process, and a Proportional Integral (PI) controller was then used to control the width of the pool during deposition
<b>Clijsters et al., 2014</b>	2014	High-speed near-infrared (NIR) thermal CMOS camera and a photodiode	Obtaining the geometry of the molten pool and the photodiode is used to get the molten pool size
<b>Bai et al., 2018</b>	2018	Process camera (Xiris XVC-1000e)	Obtain images for the characteristic dimensions of deposited bead and molten pool
<b>Su and Chen, 2019</b>	2019	High-speed camera (CR600X2)	Effect of torch angle on the dynamic behavior of the weld pool
<b>Halisch et al., 2020</b>	2020	A high-speed camera and high dynamic range two-colored pyrometric camera (Pyrocam)	Obtain melt pool size measurement in GMAW
<b>Cadiou et al., 2020</b>	2020	High-speed camera (Keyence VM-600M)	Visualize the melt pool and its interaction with the filler wire
<b>Xiong et al., 2020</b>	2020	Novel virtual binocular vision sensing system including a single camera and a biprism	Monitoring the molten pool geometry
<b>Liu et al., 2020</b>	2021	Fluke TI400 thermographic infrared camera	Measuring the temperatures during the depositions
<b>Mu et al., 2021</b>	2021	Laser scanner	Improve the accuracy and flexibility of the deposited bead.

### Built Strategy and Bead Orientation

Planning for an appropriate process Variables such as bead orientation, support structure, number of layers, tool path, and process parameters play a significant role in the production of parts (Ríos et al., 2018). During the profile design phase, the orientation and direction of each layer must be clearly defined (Qin et al., 2021). Bead orientation in welding refers to how a bead is arranged during welding. Vazquez et al. (2021) referred to it as build strategy. In the case of a single layer, the beads may be arranged either side by side or overlapping, as demonstrated by Vazquez et al. (2021). They tilted the torch 20° away from the vertical position to create a bead that had a 50% overlap with its adjacent bead. The bead can be arranged alternately, in line, or perpendicularly for multiple layers, as shown

in Figure 8 (a), (b), and (c), respectively. In their study, Cunningham et al. (2018) found that the arrangement of beads can impact heat dissipation, ultimately leading to improved dimensional control.

The orientation may vary depending on the welder's experience in previous decades. The current practice is to automate the appropriate orientation for creating a part, determined by part production criteria. The output varies in physical appearance, width, and height because the molten pool behavior determines the bead orientation specification. For example, if the welding direction is reversed between each layer, the difference in deposition height is modest. However, if the orientation is not changed for the subsequent layering process, the height becomes irregular, with the starting point being higher than the ending point (Shen et al., 2020). Qin et al. (2021) recommend considering several factors related to building orientation to achieve optimal building orientation. These factors include part property, part accuracy, surface quality, support structure, built time, built cost, post-processing time, and post-processing cost. Bead orientation is a critical decision because it affects the formation of the developed profile.

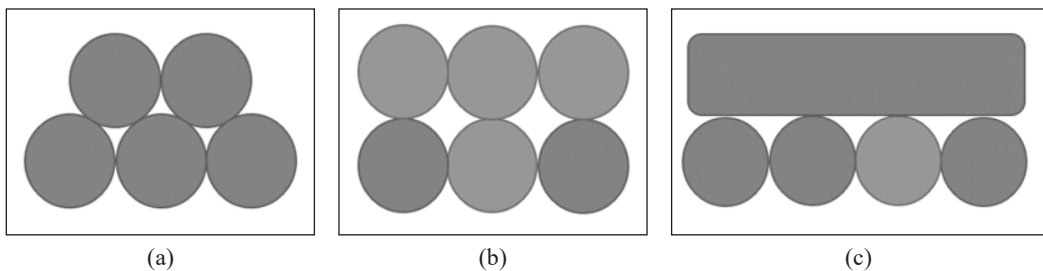


Figure 8. Different bead formations with the same orientation: (a) alternate; (b) in-line; and (c) perpendicular

## WELDING PARAMETERS

The properties and geometry of welds are significantly affected by numerous parameters. The parameters that are commonly referred to when producing a 3D part with WAAM can be divided into two categories: process parameters. These process parameters include welding current, filler feed rate, welding voltage, and welding travel speed. The other category is design parameters, which include cooling rate, material types, build strategy, and deposition path. Since these variables can be altered over a broad range, they are regarded as the most important adjustments in every welding process. The ideal welding bead should possess a consistent width, exhibiting uniform and well-worn ripples integrated into the substrate. In addition, it is important that the welding bead does not burn as a result of excessive heat. In order to determine the optimum bead parameter, it is necessary to conduct a comprehensive examination of each WAAM process. The process includes pre- and post-welding processes, such as designing, machine setup, welding, and cooling.

Parameter optimization and process improvement during the engineering phase can be accomplished by creating a process database for the described processes (Chaudhary et al., 2021).

The welding bead size in height and width is influenced by other factors such as welding torch position, torch angle, flux composition, gas control, and power supply. The parameters must be configured correctly before beginning the welding process because they are linked. In order to experiment, it is necessary to determine the parameters for the WAAM. It can be done by referring to welding preferences, existing research, expert experiences, or gathered data. Many researchers discuss the process parameters, as improper process parameters can lead to the formation of a welding bead of low quality (Halisch et al., 2020). Chaudhary et al. (2021) emphasized the impact of voltage, welding speed, and filler feed rate on penetration depth, bead width, and reinforcement height in their study. The width of the bead was observed to increase significantly with voltage and wire feed rate, but it decreases as the welding speed increases. Even though wire feed rate has a strong beneficial effect on reinforcement, the height of reinforcement decreases significantly with welding speed and marginally with voltage. In order to produce homogeneous material properties in WAAM, it is necessary to control the size of the melt pool (Halisch et al., 2020). The deposition experiments conducted by Ji et al. (2022) also revealed that ultrasonic devices can expand the size of the molten pool.

Temperature dissipation can be measured using various methods, such as pyrometers, thermocouples, and thermal cameras (Pan et al., 2018). The molten zone is where the pool flow occurs, and the direction of its flow during the WAAM process leads to the formation of the welding bead. A preliminary relationship was established between current and droplet diameters to forecast droplet size. According to Jia et al. (2020), the droplets were found to have a minor impact on the behaviors of the molten pool, which led to stable shapes of the molten pool. The X-ray method can observe droplet transfer in the WAAM process (Huang et al., 2022). Current and voltage are the most influential factors on molten pool flow and welding bead (Mai et al., 2021). The other parameters include the distance of the torch from the substrate, the angle of the torch, the speed of welding, the rate of filler feed, and the method of cooling. In the current study, the parameters of interest are displayed in Table 3. Each parameter has distinct effects on mechanical properties, surface finish, and defect formation in parts produced through WAAM. The key is to find the right balance for each parameter based on material characteristics, process requirements, and desired outcomes. Achieving the desired mechanical properties and surface finish and minimizing defects in the final WAAM parts requires careful experimentation, optimization, and continuous monitoring. The radar chart depicted in Figure 9 displays each parameter's significance in producing a satisfactory WAAM part.

Table 3  
Welding parameters to be controlled in the WAAM process

Parameters	Effect	Welding Technique	Materials	Reference
Voltage	Controlled voltage: Width of the structure becomes uniform	GMAW	Mild steel	Abe et al., 2020
Current	High current flow: Instability and overflow of the molten pool	GMAW	Copper coated steel	Xiong et al., 2015)
Torch angle	Different torch angles: Change fluid flow stress and pattern flow of the weld pool	GTAW	SS304 stainless steel	Parvez et al., 2013
	Different torch angles: Different sizes of deposited beads	NA	NA	Gao et al., 2017
Welding speed	Speed increase: Fusion zone size decrease	NA	H13 tool steel	Ou et al., 2018
Filler feed rate	Constant filler feed rate: Double-wire surface morphology is better than single-wire process	CMT	Al-Cu-Sn alloy	Wang et al., 2019
	High filler feed rate speed: Overflowing molten pool	Tandem GMAW-WAAM	NA	Shi et al., 2019
Cooling	The cooling system helps to maintain the size of the molten pool.	GMAW	NA	Reisgen et al., 2020

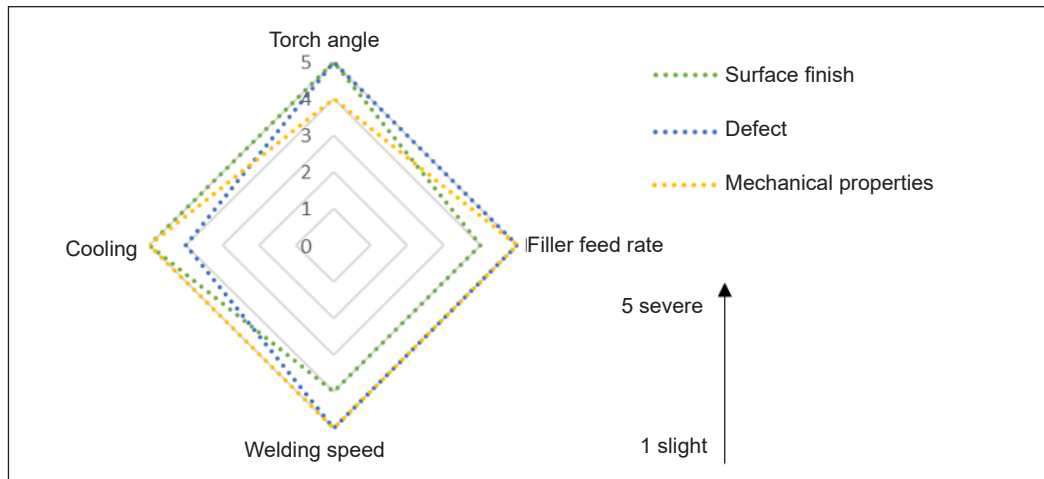


Figure 9. Effect of welding parameters on mechanical properties, surface finish and defects on deposited bead

### Torch Angle

Torch angle is an important parameter that can significantly influence the quality of the deposited material and the overall printing process. The torch angle refers to the angle at which the welding torch is positioned relative to the workpiece surface during the deposition of each layer. Typically, a welding torch is moved by a gantry, which can be a

machine or a Kuka robot arm. In the case of a simple or straight-line profile, it is customary for the welding torch angle to be perpendicular to the substrate. On the other hand, the position of the torch is determined by the part to be manufactured. The angle of the torch affects both the direction and angle of the heat input into the material. Since heat input is a crucial variable that influences the behavior of pool flow, alterations in torch angle have a noteworthy effect on the dynamics of the weld pool, encompassing the flow of the molten pool and the geometry of the bead. As the heat input increases, the contact area between the substrate and the welding metal also increases.

In their study, Lee et al. (2020) found that a small contact angle results in low heat input. The maximal heat flow from conduction and convection was located at the head of the electrode tip in accordance with the welding direction. As a result, the greatest total heat flux is symmetric along the center of the arc. When the torch angle decreases, the heat flux from conduction and convection also decreases, which leads to a shallow weld pool. The angle of the torch influences both the rate of melting and the size of the weld pool. Incorrect torch angles can lead to uneven heat distribution, resulting in residual stresses within the part. The stresses mentioned may impact mechanical properties, resulting in distortion, warping, or cracking. The shape of the weld, the generation of porosity, and the flow of the weld pool are all affected by different torch angles. Additionally, the deposited beads exhibit varying flaws depending on the torch angle (Bai et al., 2018). Moving in the same deposition direction, the space between the torch and the substrate may vary depending on the angle set. As a result, the space for heat accumulation and the molten pool produced may change.

According to Bai et al. (2018), it is suggested that a torch with a range of 0–10° can be adjusted from its vertical position in the deposition direction. This adjustment can produce well-formed deposited beads with reduced porosity and other flaws. The mobility of liquid metal causes hydrogen bubbles and molecules from the solidification front in the molten pool to travel together (Chen et al., 2020). The generated structures may fluctuate if the interlayer temperature is too low or too high for a particular lead angle. In order to avoid fluctuation effects, it is recommended to push the WAAM technique with a slightly inclined lead angle (Hauser, Reisch, Breese et al., 2021). Selecting the optimal torch angle in WAAM requires striking a balance between achieving the desired part geometry, ensuring good interlayer adhesion, minimizing distortion, and optimizing build speed. As the optimal angle can vary based on factors such as the material, part geometry, and equipment setup, it is essential to conduct systematic testing and optimization to determine the optimal torch angle for a particular WAAM application.

## **Welding Speed**

The welding speed in WAAM refers to the rate at which the welding torch or arc travels along the substrate while depositing material to build up a part. This crucial process



parameter directly affects the deposition rate, part quality, and overall efficiency of the additive manufacturing process. The welding speed in WAAM is typically measured in units of length per unit of time, such as millimeters per minute. The optimal welding speed depends on several factors, such as the material being deposited, the wire feed rate, the torch configuration, the part geometry, and the desired quality of the printed part. The speed at which welding occurs is an important factor that influences the quality of the weld—a faster throughput results in a faster welding speed. However, the maximum achievable welding speed is limited for a variety of reasons when it comes to producing a quality weld. The welding torch moves at a speed that the user sets to create a 3D profile. Defects such as porosity, humping, and cracking may occur when an insufficient welding speed is used. The defect known as the humping bead, for instance, is caused by partial solidification occurring in the rear of the bead. When the deposition speed is slow, ineffective heat is supplied to the molten pool.

Welding speeds that are either too fast or too slow may lead to fluctuations in the flow and size of the molten pool, as well as the geometry of the welding bead. Fast welding can cause the weld pool to become excessively large and run ahead of the arc. Additionally, the arc might not have sufficient time to fully melt the substrate, leading to a thin and narrow weld, exhibiting inadequate fusion and penetration. As the welding speed increases, the higher heating frequency raises the substrate temperature while decreasing the heat flux. On the other hand, slow welding speeds may result in excessive bead formation and the arc forming directly above the center of the molten weld pool. The increase in welding speed leads to an increase in weld penetration. The increase in welding speed leads to an increase in weld penetration. The arc causes the penetration of depth; if the penetration is too close to the leading edge of the weld pool, the metal transfer droplets will strike portions of the substrate immediately. The determination of the appropriate welding speed for a specific WAAM application involves the process of experimentation and optimization. Manufacturers and researchers frequently conduct test builds at various speeds to discover the optimal range that offers the finest blend of part quality, deposition rate, and process stability. It is important to consult material-specific guidelines, equipment manufacturer recommendations, and expertise in the field to make informed decisions about welding speed in WAAM.

### **Filler Feed Rate**

The filler feed rate in WAAM refers to the rate at which the filler material, typically in the form of a wire, is fed into the welding process during the additive manufacturing process. The electric arc melts the filler material and is then deposited onto the workpiece to build up the desired part layer by layer. The filler feed rate, a critical process parameter in WAAM, can impact various aspects of the additive manufacturing process and the quality of the

printed parts. It is necessary to adjust the feed rates based on the specific welding setups and wire compositions to achieve optimal melting efficiency. Proper feed rate control helps ensure that the filler material is completely melted. A higher filler feed rate typically results in a faster deposition rate, accelerating the build process. However, a high feed rate can lead to issues, such as inadequate melting and fusion of the filler material, which results in poor layer bonding and compromised part quality. According to Ou et al. (2018), the wire feed rate and wire diameter do not significantly affect the heat transfer from the molten pool to the substrate.

However, it was discovered by Xiong et al. (2018) that the stability of the molten pool decreased, and a low-quality welding bead resulted when the filler feed rate was increased. Maintaining a consistent and stable feed rate is essential to achieve a stable welding arc and consistent deposition. Fluctuations in the feed rate may result in irregular deposition and defects. Optimizing material usage and minimizing waste is achieved by balancing the feed rate, welding speed, and other process parameters. Increasing the feed rate allows greater mixing in the additive layer, preventing the filler from melting properly (Paskual et al., 2018). In their study, Hejripour et al. (2018) discovered that the travel speed and feed rate impact mass transport, heat transfer, and fluid flow in different substrates. In order to determine the optimal filler feed rate for a specific WAAM application, it is necessary to conduct experiments and optimize various factors, including welding speed. Manufacturers and researchers frequently conduct tests on builds at different rates to ascertain the optimal combination of part quality, deposition rate, and process stability. When defining filler feed rate selections in WAAM, it is important to consider material-specific concerns, equipment manufacturer guidelines, and field expertise.

## Cooling

Implementing a cooling system in WAAM can result in different outcomes that affect both the fabrication process and the properties of the deposited material. The specific outputs of implementing a cooling system depend on various factors, including the cooling method employed, the material utilized, process parameters, and the desired properties of the final part. Cooling, which affects the microstructure, mechanical properties, and overall quality of the printed parts, is an important aspect of any additive manufacturing process, including WAAM. In the WAAM process, the deposited metal layers undergo rapid heating and cooling. Proper part cooling is essential for controlling the thermal gradient and reducing the risk of thermal distortion, cracking, and residual stress buildup. Part cooling can be achieved through various methods, such as fans, water-based cooling systems, or controlled ambient conditions. The cooling effect in WAAM has been extensively studied because it reduces the time required for producing a 3D part. Cooling strategies can be integrated into the planning of the toolpath. Designing toolpaths that incorporate controlled cooling

periods makes it possible to regulate the temperature distribution within the part during the deposition process. There are two types of cooling in WAAM, namely free cooling and active cooling (Le et al., 2020).

Natural air is utilized for free cooling, while a cooling system is specifically designed for active cooling. Researchers discussed the cooling effect in molten pool flow to reduce thermal accumulation during the WAAM process. Some of the former cooling systems discussed are cold metal transfer (Scotti et al., 2020; Teixeira et al., 2021; Zhong et al., 2021), the thermoelectric cooling device (Li, Chen et al., 2018), water cooling tank (Kozamernik et al., 2020; Montevecchi et al., 2018), air-jet cooling (Hackenhaar et al., 2020; Montevecchi et al., 2021), and integrated water-cooling channel's substrate (Ogino et al., 2018). Each type of cooling system has a distinct effect on the flow of the molten pool. Heat conduction models have been utilized to predict the shape of weld pools, temperature ranges, and cooling rates of solidified structures. Ogino et al. (2018) created a multilayer 3D model to investigate deposited strategy and cooling conditions in terms of heat input and arc pressure. In their study, Hauser, Reisch, Breese et al. (2021) discovered a relationship between the cooling effect and both the gas flow rate and porosity defect. Specifically, they observed that a higher gas flow rate leads to faster hardening of molten pools, primarily due to enhanced convective cooling. Additionally, this increased gas flow rate also results in the formation of more pores. It is critical to use the proper cooling method because insufficient cooling can disrupt the flow of the molten pool. According to Rodrigues et al. (2019), air cooling can destabilize the arc, and liquid cooling may necessitate additional liquid circulation. Proper cooling aids in attaining uniform solidification and minimizes surface irregularities, thereby resulting in a smoother surface finish.

Adding a post-weld cooling gas improves bead geometry accuracy, improving layer geometry and mechanical properties. This improvement is achieved through grain refinement and the attainment of homogeneous hardness. The width and height of the welding bead vary due to the additional cooling effect. A welding bead with a cooling effect produces a larger bead and aids in grain size refinement compared to one without a cooling effect. It is important to note that WAAM processes can vary depending on the specific equipment, materials, and applications. Cooling strategies, as such, may need to be tailored to the specific requirements of each use case. Proper cooling can result in better part quality, fewer defects, and enhanced mechanical properties in parts produced through WAAM. However, careful planning and tailoring of the implementation of a cooling system are necessary to meet the specific requirements of the WAAM process, material properties, and part design. The optimization of the choice of cooling method, the intensity of cooling, and the placement of cooling devices should be done to achieve the desired outcomes while also avoiding potential challenges such as excessive cooling rates or uneven cooling distribution.

The parameters discussed in this review impact the flow of the molten pool, as well as the geometry and size of the welding bead, either directly or indirectly. However, the research has gaps in considering other factors during developing the WAAM technique for molten pool flow to achieve smooth welding bead geometry and size. Studying other aspects is necessary to optimize specific bead geometry based on requirements. It is important not to focus solely on the addressed parameter but to be proficient in addressing all problems. Various factors, including the physical configuration of the welding table, the surface condition of the substrate, the position of the nozzle, and the presence of nozzle accessories, such as the contact tip and tip holder, can influence the molten pool flow. When the distance between the substrate and the welding torch is adjusted improperly, the contact tip and tip holder adversely affect the welding bead, causing it to clog. The process could benefit from a study that would lengthen the nozzle's useful life. Future WAAM experiments should consider incorporating a reference table. Having such a reference would assist new research in achieving good bead geometry, as opposed to initiating and conducting all experiments from scratch to determine the optimal parameters for wire feed rate, voltage, current, and travel speed. The existing research primarily focuses on a specific material, and some parameters only apply to that specific material and machine. Therefore, the reference tables should include, at the very least, the machine type, range of setup parameters, and material type. Orientation and built strategy should also be well discussed in relation to the other welding parameters.

## CONCLUSION

The flow of molten pools and the geometry of beads are inextricably linked, and controllability improves process efficiency. A good molten pool flow will lead to an excellent deposited bead in shape, size, and quality. The parameters that influence bead geometry and molten pool flow are generally similar. During the review, the following issues were discovered:

1. The space of the molten pool changes depending on the position of the welding torch. Applying a slight welding angle to the direction of welding movement results in a more stable flow of the molten pool and produces a high-quality weld bead.
2. If the welding travel speed is not configured correctly, the flow of the molten pool and the formation of the weld pool are improper. As the welding travel speed increases, the welding bead becomes thinner and narrower, leading to less penetration.
3. An unstable pool flow may occur due to a higher wire feed rate, as the molten pool has not yet formed while the filler wire continues to be dispensed. Poor welding bead geometry is typically produced due to an unstable filler feed rate, which results in inadequate melting of the filler material.

4. Recently, cooling methods have been widely introduced to shorten cooling time. Although the cooling effect slightly influences the molten pool flow and the bead geometry, it assists the WAAM process in reducing the number of defective parts produced.
5. The demands for bi-metal WAAM may pose more challenges as the material behavior may differ and require greater attention.

Based on the review, a few recommendations can be made for improving the quality and efficiency of the deposited bead, such as the following:

1. Implementing automated systems like machine learning and artificial intelligence aims to control bead geometry. It is done to meet the requirements of profile complexity and process repeatability.
2. It is crucial to have reliable and efficient optimization tools for tackling various parameters in the unique applications of part repair, where the part profile may not be standard.

## ACKNOWLEDGEMENT

The authors thank Universiti Sains Malaysia (USM) for the technical and providing facilities for this experiment to be conducted successfully. The authors also gratefully acknowledge USM for being supported under the research project RUI Grant and Short-Term Grant (Grant No: 1001/PMEKANIK/8014031 and 304/PMEKANIK/6315332).

## REFERENCES

- Abe, T., Kaneko, J., & Sasahara, H. (2020). Thermal sensing and heat input control for thin-walled structure building based on numerical simulation for wire and arc additive manufacturing. *Additive Manufacturing*, 35, Article 101357. <https://doi.org/10.1016/j.addma.2020.101357>
- Aldalur, E., Veiga, F., Suárez, A. R., Bilbao, J., & Lamikiz, A. (2020). High deposition wire arc additive manufacturing of mild steel: Strategies and heat input effect on microstructure and mechanical properties. *Journal of Manufacturing Processes*, 58, 615-626. <https://doi.org/10.1016/j.jmapro.2020.08.060>
- Bai, X., Colegrove, P. A., Ding, J., Zhou, X., Diao, C., Bridgeman, P., Hönnige, J., Zhang, H., & Williams, S. (2018). Numerical analysis of heat transfer and fluid flow in multilayer deposition of PAW-based wire and arc additive manufacturing. *International Journal of Heat and Mass Transfer*, 124, 504-516. <https://doi.org/10.1016/j.ijheatmasstransfer.2018.03.085>
- Benakis, M., Costanzo, D., & Patran, A. (2020). Current mode effects on weld bead geometry and heat affected zone in pulsed wire arc additive manufacturing of Ti-6-4 and Inconel 718. *Journal of Manufacturing Processes*, 60, 61-74. <https://doi.org/10.1016/j.jmapro.2020.10.018>
- Cadiou, S., Courtois, M., Carin, M., Berckmans, W., & Masson, P. (2020). 3D heat transfer, fluid flow and electromagnetic model for cold metal transfer wire arc additive manufacturing (Cmt-Waam). *Additive Manufacturing*, 36, Article 101541. <https://doi.org/10.1016/j.addma.2020.101541>

- Chaturvedi, M., Scutelnicu, E., Rusu, C. C., Mistodie, L. R., Mihailescu, D., & Subbiah, A. V. (2021). Wire arc additive manufacturing: Review on recent findings and challenges in industrial applications and materials characterization. *Metals*, *11*(6), Article 939. <https://doi.org/10.3390/met11060939>
- Chaudhary, C. S., Kashish, & Khanna, P. (2021). Effect of welding parameters on the weld bead profile of submerged arc welded low carbon steel plates. *IOP Conference Series: Materials Science and Engineering*, *1126*(1), Article 012022. <https://doi.org/10.1088/1757-899x/1126/1/012022>
- Chen, S., Chi, Y., Zhang, P., & Shi, Y. (2020). Mechanism to reduce the porosity during argon arc welding of aluminum alloys by changing the arc angle. *Metals*, *10*(9), Article 1121. <https://doi.org/10.3390/met10091121>
- Chernovol, N., Lauwers, B., & Van Rymenant, P. (2020). Development of low-cost production process for prototype components based on Wire and Arc Additive Manufacturing (WAAM). *Procedia CIRP*, *95*, 60-65. <https://doi.org/10.1016/j.procir.2020.01.188>
- Clijsters, S., Craeghs, T., Buls, S., Kempen, K., & Kruth, J. (2014). In situ quality control of the selective laser melting process using a high-speed, real-time melt pool monitoring system. *The International Journal of Advanced Manufacturing Technology*, *75*(5-8), 1089-1101. <https://doi.org/10.1007/s00170-014-6214-8>
- Cunningham, C., Flynn, J. M., Shokrani, A., Dhokia, V., & Newman, S. T. (2018). Invited review article: Strategies and processes for high quality wire arc additive manufacturing. *Additive Manufacturing*, *22*, 672-686. <https://doi.org/10.1016/j.addma.2018.06.020>
- Ding, D., He, F., Yuan, L., Pan, Z., Wang, L., & Ros, M. (2021). The first step towards intelligent wire arc additive manufacturing: An automatic bead modelling system using machine learning through industrial information integration. *Journal of Industrial Information Integration*, *23*, Article 100218. <https://doi.org/10.1016/j.jii.2021.100218>
- Dinovitzer, M., Chen, X., Laliberté, J., Huang, X., & Frei, H. (2019). Effect of wire and arc additive manufacturing (WAAM) process parameters on bead geometry and microstructure. *Additive Manufacturing*, *26*, 138-146. <https://doi.org/10.1016/j.addma.2018.12.013>
- Ermakova, A., Mehmanparast, A., Ganguly, S., Razavi, J., & Berto, F. (2020). Investigation of mechanical and fracture properties of wire and arc additively manufactured low carbon steel components. *Theoretical and Applied Fracture Mechanics*, *109*, Article 102685. <https://doi.org/10.1016/j.tafmec.2020.102685>
- Feucht, T., Waldschmitt, B., Lange, J., & Erven, M. (2021). 3D-printing with steel: Additive manufacturing of a bridge *in situ*. *Ce/Papers*, *4*(2-4), 1695-1701. <https://doi.org/10.1002/cepa.1475>
- Gao, F., Zhao, W., Gao, Q., Zhang, M., Sun, E., Liu, Z., & Jiang, P. (2017). Study on the influencing factors in the forming process of arc additive manufacturing. *Development & Application of Materials*, *2*, 59-63.
- Giarollo, D. F., Mazzaferro, C. C. P., & Mazzaferro, J. A. E. (2022). Comparison between two heat source models for wire-arc additive manufacturing using GMAW process. *Journal of the Brazilian Society of Mechanical Sciences and Engineering*, *44*, 1-13. <https://doi.org/10.1007/s40430-021-03307-8>
- Gierth, M., Henckell, P., Ali, Y., Scholl, J., & Bergmann, J. P. (2020). Wire arc additive manufacturing (WAAM) of aluminum alloy AlMg5Mn with energy-reduced gas metal arc welding (GMAW). *Materials*, *13*(12), Article 2671. <https://doi.org/10.3390/ma13122671>

- Greebmalai, J., & Warinsiriruk, E. (2020). Multi-heat input technique for aluminum WAAM using DP-GMAW process. In *AIP Conference Proceedings* (Vol. 2279, No. 1). AIP Publishing. <https://doi.org/10.1063/5.0022954>
- Guo, M., Jia, C., Zhou, J., Liu, W., & Wu, C. (2020). Investigating the generation process of molten droplets and arc plasma in the confined space during compulsively constricted WAAM. *Journal of Materials Processing Technology*, 275, Article 116355. <https://doi.org/10.1016/j.jmatprotec.2019.116355>
- Hackenhaar, W., Mazzaferro, J. A. E., Montevecchi, F., & Campatelli, G. (2020). An experimental-numerical study of active cooling in wire arc additive manufacturing. *Journal of Manufacturing Processes*, 52, 58-65. <https://doi.org/10.1016/j.jmapro.2020.01.051>
- Halisch, C., Radel, T., Tyralla, D., & Seefeld, T. (2020). Measuring the melt pool size in a wire arc additive manufacturing process using a high dynamic range two-colored pyrometric camera. *Welding in the World*, 64(8), 1349-1356. <https://doi.org/10.1007/s40194-020-00892-5>
- Han, Q., Li, Y., & Zhang, G. (2018). Online control of deposited geometry of multi-layer multi-bead structure for wire and arc additive manufacturing. In *Transactions on Intelligent Welding Manufacturing: Volume 1 No. 1 2017* (pp. 85-93). Springer. [https://doi.org/10.1007/978-981-10-5355-9\\_7](https://doi.org/10.1007/978-981-10-5355-9_7)
- Hauser, T., Reisch, R. T., Breese, P., Lutz, B., Pantano, M., Nalam, Y., Bela, K., Kamps, T., Volpp, J., & Kaplan, A. (2021). Porosity in wire arc additive manufacturing of aluminium alloys. *Additive Manufacturing*, 41, Article 101993. <https://doi.org/10.1016/j.addma.2021.101993>
- Hauser, T., Reisch, R. T., Seebauer, S., Parasar, A., Kamps, T., Casati, R., Volpp, J., & Kaplan, A. (2021). Multi-material wire arc additive manufacturing of low and high alloyed aluminium alloys with *in-situ* material analysis. *Journal of Manufacturing Processes*, 69, 378-390. <https://doi.org/10.1016/j.jmapro.2021.08.005>
- Hejripour, F., Valentine, D. T., & Aidun, D. K. (2018). Study of mass transport in cold wire deposition for wire arc additive manufacturing. *International Journal of Heat and Mass Transfer*, 125, 471-484. <https://doi.org/10.1016/j.ijheatmasstransfer.2018.04.092>
- Henckell, P., Gierth, M., Ali, Y., Reimann, J., & Bergmann, J. P. (2020). Reduction of energy input in wire arc additive manufacturing (WAAM) with gas metal arc welding (GMAW). *Materials*, 13(11), Article 2491. <https://doi.org/10.3390/ma13112491>
- Hofman, J., Pathiraj, B., Van Dijk, J., Lange, D., & Meijer, J. (2012). A camera based feedback control strategy for the laser cladding process. *Journal of Materials Processing Technology*, 212(11), 2455-2462. <https://doi.org/10.1016/j.jmatprotec.2012.06.027>
- Hu, D., & Kovacevic, R. (2003). Sensing, modeling and control for laser-based additive manufacturing. *International Journal of Machine Tools & Manufacture*, 43(1), 51-60. [https://doi.org/10.1016/s0890-6955\(02\)00163-3](https://doi.org/10.1016/s0890-6955(02)00163-3)
- Huang, J., Li, Z., Yu, S., Yu, X., & Fan, D. (2022). Real-time observation and numerical simulation of the molten pool flow and mass transfer behavior during wire arc additive manufacturing. *Welding in the World*, 66(3), 481-494. <https://doi.org/10.1007/s40194-021-01214-z>
- Jafari, D., Vaneker, T. H., & Gibson, I. (2021). Wire and arc additive manufacturing: Opportunities and challenges to control the quality and accuracy of manufactured parts. *Materials & Design*, 202, Article 109471. <https://doi.org/10.1016/j.matdes.2021.109471>

- Ji, F., Qin, X., Hu, Z., Xiong, X., Ni, M., & Wu, M. (2022). Influence of ultrasonic vibration on molten pool behavior and deposition layer forming morphology for wire and arc additive manufacturing. *International Communications in Heat and Mass Transfer*, *130*, Article 105789. <https://doi.org/10.1016/j.icheatmasstransfer.2021.105789>
- Jia, C., Liu, W., Chen, M., Guo, M., Wu, S., & Chen, W. (2020). Investigation on arc plasma, droplet, and molten pool behaviours in compulsively constricted WAAM. *Additive Manufacturing*, *34*, Article 101235. <https://doi.org/10.1016/j.addma.2020.101235>
- Karayel, E., & Bozkurt, Y. (2020). Additive manufacturing method and different welding applications. *Journal of Materials Research and Technology*, *9*(5), 11424-11438. <https://doi.org/10.1016/j.jmrt.2020.08.039>
- Karmuhilan, M., & Sood, A. K. (2018). Intelligent process model for bead geometry prediction in WAAM. *Materials Today: Proceedings*, *5*(11), 24005-24013. <https://doi.org/10.1016/j.matpr.2018.10.193>
- Kozamernik, N., Bračun, D., & Klobčar, D. (2020). WAAM system with interpass temperature control and forced cooling for near-net-shape printing of small metal components. *The International Journal of Advanced Manufacturing Technology*, *110*(7-8), 1955-1968. <https://doi.org/10.1007/s00170-020-05958-8>
- Laghi, V., Palermo, M., Gasparini, G., Girelli, V. A., & Trombetti, T. (2021). On the influence of the geometrical irregularities in the mechanical response of Wire-and-Arc Additively Manufactured planar elements. *Journal of Constructional Steel Research*, *178*, Article 106490. <https://doi.org/10.1016/j.jcsr.2020.106490>
- Le, V. T., Si, D., & Hoang, Q. H. (2020). Effects of cooling conditions on the shape, microstructures, and material properties of SS308L thin walls built by wire arc additive manufacturing. *Materials Letters*, *280*, Article 128580. <https://doi.org/10.1016/j.matlet.2020.128580>
- Lee, H., Kim, J., Pyo, C., & Kim, J. (2020). Evaluation of bead geometry for aluminum parts fabricated using additive Manufacturing-Based Wire-Arc welding. *Processes*, *8*(10), Article 1211. <https://doi.org/10.3390/pr8101211>
- Leicher, M., Kamper, S., Treutler, K., & Wesling, V. (2020). Multi-material design in additive manufacturing - Feasibility validation. *Welding in the World*, *64*(8), 1341-1347. <https://doi.org/10.1007/s40194-020-00887-2>
- Li, F., Chen, S., Shi, J., Zhao, Y., & Tian, H. (2018). Thermoelectric Cooling-Aided bead geometry regulation in wire and Arc-Based additive manufacturing of thin-walled structures. *Applied Sciences*, *8*(2), Article 207. <https://doi.org/10.3390/app8020207>
- Li, Z., Ma, G., Zhao, G., Yang, M., & Xiao, W. (2018). Weave bead welding based wire and arc additive manufacturing technology. In *Recent Advances in Intelligent Manufacturing: First International Conference on Intelligent Manufacturing and Internet of Things and 5th International Conference on Computing for Sustainable Energy and Environment, IMIOT and ICSEE 2018, Proceedings, Part I 5* (pp. 408-417). Springer. [https://doi.org/10.1007/978-981-13-2396-6\\_38](https://doi.org/10.1007/978-981-13-2396-6_38)
- Lin, Z., Song, K., & Yu, X. (2021). A review on wire and arc additive manufacturing of titanium alloy. *Journal of Manufacturing Processes*, *70*, 24-45. <https://doi.org/10.1016/j.jmapro.2021.08.018>
- Liu, J., Xu, Y., Yu, G., Hou, Z., & Chen, S. (2020). Wire and arc additive manufacturing of metal components: A review of recent research developments. *The International Journal of Advanced Manufacturing Technology*, *111*(1-2), 149-198. <https://doi.org/10.1007/s00170-020-05966-8>



- Liu, W., Jia, C., Guo, M., & Gao, J. (2019). Compulsively constricted WAAM with arc plasma and droplets ejected from a narrow space. *Additive Manufacturing*, 27, 109-117. <https://doi.org/10.1016/j.addma.2019.03.003>
- Mai, D. S., Doan, T. K., & Paris, H. (2021). Wire and arc additive manufacturing of 308L stainless steel components: Optimization of processing parameters and material properties. *Engineering Science and Technology, an International Journal*, 24(4), 1015-1026. <https://doi.org/10.1016/j.jestch.2021.01.009>
- Manokruang, S., Vignat, F., Museau, M., & Limousin, M. (2021). Process parameters effect on weld beads geometry deposited by wire and arc additive manufacturing (WAAM). In *Advances on Mechanics, Design Engineering and Manufacturing III: Proceedings of the International Joint Conference on Mechanics, Design Engineering & Advanced Manufacturing, JCM 2020* (pp. 9-14). Springer International Publishing. [https://doi.org/10.1007/978-3-030-70566-4\\_3](https://doi.org/10.1007/978-3-030-70566-4_3)
- Montevecchi, F., Venturini, G., Grossi, N., Scippa, A., & Campatelli, G. (2018). Heat accumulation prevention in wire-arc-additive-manufacturing using air jet impingement. *Manufacturing Letters*, 17, 14-18. <https://doi.org/10.1016/j.mfglet.2018.06.004>
- Mu, H., Pan, Z., Li, Y., He, F., Polden, J., & Xia, C. (2021). MIMO model predictive control of bead geometry in wire arc additive manufacturing. In *2021 IEEE 11th Annual International Conference on CYBER Technology in Automation, Control, and Intelligent Systems (CYBER)* (pp. 169-174). IEEE Publishing. <https://doi.org/10.1109/cyber53097.2021.9588331>
- Nagasai, B. P., Malarvizhi, S., & Balasubramanian, V. (2021). Mechanical properties of wire arc additive manufactured carbon steel cylindrical component made by gas metal arc welding process. *Journal of the Mechanical Behavior of Materials*, 30(1), 188-198. <https://doi.org/10.1515/jmbm-2021-0019>
- Navarro, M., Matar, A., Diltemiz, S. F., & Eshraghi, M. (2021). Development of a low-cost wire arc additive manufacturing system. *Journal of Manufacturing and Materials Processing*, 6(1), Article 3. <https://doi.org/10.3390/jmmp6010003>
- Ni, M., Zhou, Y., Hu, Z., Qin, X., Xiong, X., & Ji, F. (2023). Forming optimization for WAAM with weaving deposition on curved surfaces. *International Journal of Mechanical Sciences*, 252, Article 108366. <https://doi.org/10.1016/j.ijmecsci.2023.108366>
- Ogino, Y., Asai, S., & Hirata, Y. (2018). Numerical simulation of WAAM process by a GMAW weld pool model. *Welding in the World*, 62(2), 393-401. <https://doi.org/10.1007/s40194-018-0556-z>
- Ou, W., Mukherjee, T., Knapp, G., Wei, Y., & DebRoy, T. (2018). Fusion zone geometries, cooling rates and solidification parameters during wire arc additive manufacturing. *International Journal of Heat and Mass Transfer*, 127, 1084-1094. <https://doi.org/10.1016/j.ijheatmasstransfer.2018.08.111>
- Pan, Z., Ding, D., Cuiuri, D., Li, H., & Norrish, J. (2018). Arc welding processes for additive manufacturing: A review. *Transactions on intelligent welding manufacturing*, 1(1), 3-24. [https://doi.org/10.1007/978-981-10-5355-9\\_1](https://doi.org/10.1007/978-981-10-5355-9_1)
- Panchagnula, J. S., & Simhambhatla, S. (2018). Manufacture of complex thin-walled metallic objects using weld-deposition based additive manufacturing. *Robotics and Computer-Integrated Manufacturing*, 49, 194–203. <https://doi.org/10.1016/j.rcim.2017.06.003>

- Pandey, P. K. (2019). Manufacturing of large metallic components through wire and arc additive manufacturing (WAAM) (Master thesis). Indian Institute of Technology Hyderabad, India. [https://raiith.iith.ac.in/5599/1/Mtech\\_Thesis\\_TD1428\\_2019.pdf](https://raiith.iith.ac.in/5599/1/Mtech_Thesis_TD1428_2019.pdf)
- Parvez, S., Abid, M., Nash, D., Fawad, H., & Galloway, A. (2013). Effect of torch angle on arc properties and weld pool shape in stationary GTAW. *Journal of Engineering Mechanics*, *139*(9), 1268-1277. [https://doi.org/10.1061/\(asce\)em.1943-7889.0000553](https://doi.org/10.1061/(asce)em.1943-7889.0000553)
- Paskual, A., Álvarez, P. G., & Suárez, A. R. (2018). Study on arc welding processes for high deposition rate additive manufacturing. *Procedia CIRP*, *68*, 358-362. <https://doi.org/10.1016/j.procir.2017.12.095>
- Qin, Y., Qi, Q., Shi, P., Scott, P. J., & Jiang, X. (2021). Status, issues, and future of computer-aided part orientation for additive manufacturing. *The International Journal of Advanced Manufacturing Technology*, *115*(5-6), 1295-1328. <https://doi.org/10.1007/s00170-021-06996-6>
- Reisgen, U., Sharma, R., Mann, S. M., & Oster, L. (2020). Increasing the manufacturing efficiency of WAAM by advanced cooling strategies. *Welding in the World*, *64*(8), 1409-1416. <https://doi.org/10.1007/s40194-020-00930-2>
- Ríos, S., Colegrove, P. A., Martina, F., & Williams, S. (2018). Analytical process model for wire + arc additive manufacturing. *Additive Manufacturing*, *21*, 651-657. <https://doi.org/10.1016/j.addma.2018.04.003>
- Rodrigues, T. A., Duarte, V. R., Miranda, R. M. M., Santos, T. G., & Oliveira, J. (2019). Current status and perspectives on Wire and Arc Additive Manufacturing (WAAM). *Materials*, *12*(7), Article 1121. <https://doi.org/10.3390/ma12071121>
- Rosli, N. A., Alkahari, M. R., Ramli, F. R., Mat, S., & Yusof, A. A. (2019). Influence of process parameters on dimensional accuracy in GMAW based additive manufacturing. In *Proceedings of Mechanical Engineering Research Day 2019* (pp. 7-9). CARE Publishing.
- Scotti, F. M., Teixeira, F. R., Da Silva, L. J., De Araújo, D. B., Reis, R. P., & Scotti, A. (2020). Thermal management in WAAM through the CMT Advanced process and an active cooling technique. *Journal of Manufacturing Processes*, *57*, 23-35. <https://doi.org/10.1016/j.jmapro.2020.06.007>
- Shen, H., Deng, R., Liu, B., Tang, S., & Li, S. (2020). Study of the mechanism of a stable deposited height during GMAW-Based additive manufacturing. *Applied Sciences*, *10*(12), Article 4322. <https://doi.org/10.3390/app10124322>
- Shi, J., Li, F., Chen, S., Zhao, Y., & Tian, H. (2019). Effect of in-process active cooling on forming quality and efficiency of tandem GMAW-based additive manufacturing. *The International Journal of Advanced Manufacturing Technology*, *101*(5-8), 1349-1356. <https://doi.org/10.1007/s00170-018-2927-4>
- Su, C., & Chen, X. (2019). Effect of depositing torch angle on the first layer of wire arc additive manufacture using cold metal transfer (CMT). *Industrial Robot-an International Journal*, *46*(2), 259-266. <https://doi.org/10.1108/ir-11-2018-0233>
- Su, C., Chen, X., Gao, C., & Wang, Y. (2019). Effect of heat input on microstructure and mechanical properties of Al-Mg alloys fabricated by WAAM. *Applied Surface Science*, *486*, 431-440. <https://doi.org/10.1016/j.apsusc.2019.04.255>

- Tang, S., Wang, G., Huang, C., & Zhang, H. (2019). Investigation and control of weld bead at both ends in WAAM. In *2019 International Solid Freeform Fabrication Symposium* (pp. 693-702). University of Texas at Austin. <https://doi.org/10.26153/tsw/17307>
- Teixeira, F. R., Scotti, F. M., Reis, R. P., & Scotti, A. (2021). Effect of the CMT advanced process combined with an active cooling technique on macro and microstructural aspects of aluminum WAAM. *Rapid Prototyping Journal*, *27*(6), 1206-1219. <https://doi.org/10.1108/rpj-11-2020-0285>
- Van Thao, L. E. (2020). A preliminary study on gas metal arc welding-based additive manufacturing of metal parts. *VNUHCM Journal of Science and Technology Development*, *23*(1), 422-429.
- Vázquez, L., Rodriguez, M. N., Rodriguez, I., & Álvarez, P. (2021). Influence of post-deposition heat treatments on the microstructure and tensile properties of Ti-6Al-4V parts manufactured by CMT-WAAM. *Metals*, *11*(8), Article 1161. <https://doi.org/10.3390/met11081161>
- Venkatarao, K. (2021). The use of teaching-learning based optimization technique for optimizing weld bead geometry as well as power consumption in additive manufacturing. *Journal of Cleaner Production*, *279*, Article 123891. <https://doi.org/10.1016/j.jclepro.2020.123891>
- Vora, J., Pandey, R., Dodiya, P., Patel, V., Khanna, S., Vaghasia, V., & Chaudhari, R. (2023). Fabrication of multi-walled structure through parametric study of bead geometries of GMAW-based WAAM process of SS309L. *Materials*, *16*(14), Article 5147. <https://doi.org/10.3390/ma16145147>
- Waldschmitt, B. (2019). *Additive Manufacturing of a Bridge* (Doctoral dissertation). Technische Universität Darmstadt, Darmstadt.
- Wang, C., Bai, H., Ren, C., Fang, X., & Lu, B. (2020). A comprehensive prediction model of bead geometry in wire and arc additive manufacturing. *Journal of Physics: Conference Series*, *1624*(2), Article 022018. <https://doi.org/10.1088/1742-6596/1624/2/022018>
- Wang, S., Gu, H., Wang, W., Li, C., Ren, L., Wang, Z., Zhai, Y., & Ma, P. (2019). Study on microstructural and mechanical properties of an AL-CU-SN alloy wall deposited by double-wire arc additive manufacturing process. *Materials*, *13*(1), Article 73. <https://doi.org/10.3390/ma13010073>
- Wang, Z., Zimmer-Chevret, S., Léonard, F., & Abba, G. (2022). Improvement strategy for the geometric accuracy of bead's beginning and end parts in wire-arc additive manufacturing (WAAM). *The International Journal of Advanced Manufacturing Technology*, *118*(7-8), 2139-2151. <https://doi.org/10.1007/s00170-021-08037-8>
- Waqas, A., Qin, X., Xiong, J., Chao, Y., & Fan, L. (2018). Impact toughness of components made by GMAW based additive manufacturing. *Procedia Structural Integrity*, *13*, 2065-2070. <https://doi.org/10.1016/j.prostr.2018.12.207>
- Wu, B., Ding, D., Cuiuri, D., & Li, H. J. (2018a). Effects of heat accumulation on microstructure and mechanical properties of Ti6Al4V alloy deposited by wire arc additive manufacturing. *Additive Manufacturing*, *23*, 151-160. <https://doi.org/10.1016/j.addma.2018.08.004>
- Wu, B., Ding, D., Cuiuri, D., Li, H. J., Xu, J., & Norrish, J. (2018b). A review of the wire arc additive manufacturing of metals: properties, defects and quality improvement. *Journal of Manufacturing Processes*, *35*, 127-139. <https://doi.org/10.1016/j.jmappro.2018.08.001>

- Xiong, J., Li, Y., Li, R., & Yin, Z. (2018). Influences of process parameters on surface roughness of multi-layer single-pass thin-walled parts in GMAW-based additive manufacturing. *Journal of Materials Processing Technology*, 252, 128-136. <https://doi.org/10.1016/j.jmatprotec.2017.09.020>
- Xiong, J., Liu, Y., & Yin, Z. (2020). Passive vision measurement for robust reconstruction of molten pool in wire and arc additive manufacturing. *Measurement*, 153, Article 107407. <https://doi.org/10.1016/j.measurement.2019.107407>
- Xiong, J., Zhang, G., & Zhang, W. (2015). Forming appearance analysis in multi-layer single-pass GMAW-based additive manufacturing. *The International Journal of Advanced Manufacturing Technology*, 80(9-12), 1767-1776. <https://doi.org/10.1007/s00170-015-7112-4>
- Yuan, L., Pan, Z., Ding, D., He, F., Van Duin, S., Li, H. J., & Li, W. (2020). Investigation of humping phenomenon for the multi-directional robotic wire and arc additive manufacturing. *Robotics and Computer-Integrated Manufacturing*, 63, Article 101916. <https://doi.org/10.1016/j.rcim.2019.101916>
- Zeinali, M., & Khajepour, A. (2010). Height control in laser cladding using adaptive sliding mode technique: Theory and experiment. *Journal of Manufacturing Science and Engineering-Transactions of the ASME*, 132(4), Article 041016. <https://doi.org/10.1115/1.4002023>
- Zeng, Z., Cong, B., Oliveira, J., Ke, W., Schell, N., Peng, B., Qi, Z., Ge, F., Zhang, W., & Ao, S. (2020). Wire and arc additive manufacturing of a Ni-rich NiTi shape memory alloy: Microstructure and mechanical properties. *Additive Manufacturing*, 32, Article 101051. <https://doi.org/10.1016/j.addma.2020.101051>
- Zhong, Y., Zheng, Z., Li, J., & Wang, C. (2021). Fabrication of 316L nuclear nozzles on the main pipeline with large curvature by CMT wire arc additive manufacturing and self-developed slicing algorithm. *Materials Science and Engineering: A*, 820, Article 141539. <https://doi.org/10.1016/j.msea.2021.141539>

# Application of the Ultrasonic Method to Produce Starch Nanoparticles from Cassava Starch

Beni Hidayat\*, Vida Elsyana and Sheniah Glori Simorangkir

*Agricultural Technology Department, Politeknik Negeri Lampung, 35141, Bandar Lampung, Lampung, Indonesia*

## ABSTRACT

Starch nanoparticles have the potential to be developed as a cassava starch derivative. The research aims to obtain the optimal process conditions (ultrasonic process time and starch concentration) to produce starch nanoparticles with the best characteristics. The treatment variables used in this study were the duration of the ultrasonication process (30, 60, and 90 minutes) and the starch concentration (1%, 2%, and 3%). The results showed that the ultrasonication process time and starch concentration affected the yield, particle size and distribution, polydispersity index, optical characteristics (transmittance), and clarity score of starch nanoparticles. Ultrasonic process time of 90 minutes and starch concentration of 3% will produce starch nanoparticle products with a yield of 13.68%, particle size  $\leq 100$  nm of 23.6%, average particle size of 230.8 nm with polydispersity index of 0.581, transmittance value of 61.27%, and a solution clarity score of 3.80 (not clear). Tapioca-based SNPs can be developed solely with ultrasonic method to simplify the process.

*Keywords:* Cassava starch, starch nanoparticles, ultrasonic

## ARTICLE INFO

### *Article history:*

Received: 28 April 2023

Accepted: 09 October 2023

Published: 26 March 2024

DOI: <https://doi.org/10.47836/pjst.32.2.24>

### *E-mail addresses:*

[beni\\_lpg@polinela.ac.id](mailto:beni_lpg@polinela.ac.id) (Beni Hidayat)

[vida@polinela.ac.id](mailto:vida@polinela.ac.id) (Vida Elsyana)

[sheniaglori@gmail.com](mailto:sheniaglori@gmail.com) (Sheniah Glori Simorangkir)

\* Corresponding author

## INTRODUCTION

Starch is a natural, renewable, biodegradable polymer many plants use to store energy. Starch is the second most abundant biomass in nature and is found in staple crop commodities such as rice, corn, wheat, cassava, and potatoes (BeMiller & Whistler, 2009). The primary potential source of starch in Indonesia is cassava starch obtained from cassava extraction (Zukryandry et al., 2022). Based on data

from the Food and Agriculture Organization (FAO) in 2012, Indonesia is the world's third exporter of tapioca, followed by Thailand and Vietnam (Hidayat et al., 2021). According to BPS-Statistics of Lampung Province (2022), Indonesia's cassava production in 2021 will be 19,341,233 tons, and Lampung Province, with a production of 6,683,758 tons, is the main producer of cassava in Indonesia (34.5%).

Starch nanoparticles (SNPs) have the potential to be developed as a tapioca derivative product. SNPs are nano-sized starch derivative products (one billionth of a meter, 10-9 meters) with a size range of 1–100 nm (EFSA Scientific Committee, 2011). The process of modifying starch into starch nanoparticle products has many advantages, including increasing stability, chemical reactivity, flowability, opacity, and mechanical strength (Zhu et al., 2007), improving the sensory characteristics of the product (Sharma et al., 2013), and enhancing encapsulation ability for bioactive components (Ezhilarasi et al., 2013).

Despite their potential, the development of SNPs based on tapioca is relatively limited and is mostly developed from corn starch (Le-Corre et al., 2010; Kim et al., 2013; Kumari et al., 2020) and rice starch (Zuo et al., 2012). Compared to corn and rice starch, cassava starch (tapioca) is a more economical source in Indonesia. The development of SNPs based on tapioca will increase the added value of the tapioca industry.

The manufacture of SNPs can be carried out using various methods, namely, acid hydrolysis (Le-Corre et al., 2010), enzymatic hydrolysis (Le-Corre et al., 2010), high-pressure homogenization (Liu et al., 2016), gamma irradiation (Garcia et al., 2011; Lamanna et al., 2013), a combination of acid hydrolysis and ultrasonication (Kim et al., 2013; Goncalves et al., 2014), and ultrasonication (Haaj et al., 2013). The research results by Haaj et al. (2013) showed that SNP products could be prepared solely with the ultrasonic method, simplifying the manufacturing process.

According to Jambrak et al. (2010), the ultrasonication process to produce SNPs can be carried out using an ultrasonic probe or a bath system. Compared to an ultrasonic system bath, using an ultrasonic system probe will be more effective with a shorter processing time (Bonto et al., 2021) and produce SNP products with better characteristics (Haaj et al., 2013). This study aims to obtain optimal process conditions (ultrasonic process time and starch concentration) to produce cassava starch-based starch nanoparticles with the best characteristics (yield, distribution and particle size, transmittance, and clarity).

## **MATERIALS AND METHODS**

### **Equipment**

The main tools used are Ultrasonication probe Biomaisen type MSUCD 650, UV-Vis single beam spectrophotometer Aelab type AE-S60-4U, and Particle Size Analyzer (PSA) Malvern Zetasizer Nano ZS type.

## Starch Nanoparticle (SNP) Formation

The formation of SNPs from cassava starch was modified from the method of Haaj et al. (2013) by preparing 50 ml of cassava starch solution with concentrations according to treatment (1%, 2%, and 3%). The probe temperature is set below 40°C, kept constant by adding ice, and the process frequency is set at 20 kHz. The probe used has a diameter of 6 cm with an ultrasonic power of 650 W. The ultrasonication process is then carried out with the duration of the ultrasonication process according to the treatment (30, 60, and 90 min). The solution resulting from the sonification process was then filtered using 1-micron Whatman filter paper and tested for yield and characteristics.

## Yield Analysis

The yield is the percentage of the dry weight of the SNP product divided by the initial weight of the starch raw material, with the following Equation 1:

$$\text{Yield (\%)} = \frac{\text{mass of SNP (gram)}}{\text{mass of initial starch (gram)}} \times 100\% \quad (1)$$

## Analysis of Particle Size

The distribution and size of SNPs were analyzed using a particle size analyzer (PSA) with the dynamic light scattering (DLS) method that utilizes infrared scattering. The SNP solution sample was put into the PSA cuvette. Infrared scattering was fired at the sample so that the sample would react to produce Brownian motion (random motion of the particles). The tool then analyzes this random motion, where the smaller the particle size, the faster the movement.

In addition to the distribution and size of SNPs, the polydispersity Index (PI) value, a measure of molecular mass distribution in the sample, could also be obtained. The PI value indicates the level of confidence in the size of the particles dispersed in a solution. The smaller the polydispersity value, the better the particle size distribution confidence level in the starch solution. Conversely, if the polydispersity value is higher, then the particles present in the sample are not uniform and unstable and would quickly flocculate.

## Transmittance Analysis

Samples of SNP solution resulting from the sonication process of various treatments were put into the spectrophotometer cuvette. Analysis was conducted by placing a cuvette into a UV-Vis spectrophotometer with a 450–800 nm wavelength range. The results obtained were then recorded in the form of transmittance percentage values.

## Clarity Analysis

Observation of the clarity of the SNP solution was carried out after being left for 2 hours (Haaj et al., 2013). The sensory test was carried out using 10 panelists using a hedonic score of 1–5 (score 1 = very unclear; score 2 = not clear; score 3 = not clear enough; score 4 = clear; score 5 = very clear).

## RESULT AND DISCUSSION

### Yield of Starch Nanoparticles

The yield of SNPs at various ultrasonic process times and starch concentrations is presented in Table 1. The test results in Table 1 show that the ultrasonication process, with a duration of 90 minutes and 3% starch concentration, will produce SNP products with higher yields (13.68%) than other treatments. The higher yield of this SNP indicates that increasing the ultrasonication process time to 90 minutes and increasing the starch concentration to 3% will cause the breakdown of starch molecules into nano-sized to become more intensive. The yield of SNPs using the ultrasonic method (13.68%) is relatively the same as the acid hydrolysis method (15%) but lower than the combined acid and ultrasonic hydrolysis method, which can reach 78% (Kim et al., 2013).

The longer the ultrasonic process, the more intensive the degradation process of starch molecules. According to Czechowska-Biskup et al. (2005), the ultrasonic application will cause the degradation of starch molecules caused by mechanochemical effects. The more intensive the starch degradation process, the smaller the granule size.

The increase in SNP yields up to 3% starch concentration, indicating that up to 3% starch solution concentration, the starch degradation process was still occurring intensively. A different opinion was conveyed by Haaj et al. (2013), which stated that the ultrasonication process without chemical treatment was effective at low concentrations (1%–2%). The conditioning of starch in the form of an aqueous solution, not a suspension, is based on the

Table 1  
*Yield of SNP at various ultrasonication process times and starch concentrations (mean  $\pm$  SD, n = 3)*

Treatment	SNP yield (%)
Processing time 30 minutes, starch concentration 1%	11.94 $\pm$ 0.02
Processing time 30 minutes, starch concentration 2%	13.18 $\pm$ 0.20
Processing time 30 minutes, starch concentration 3%	13.33 $\pm$ 0.18
Processing time 60 minutes, starch concentration 1%	12.02 $\pm$ 0.11
Processing time 60 minutes, starch concentration 2%	13.37 $\pm$ 0.17
Processing time 60 minutes, starch concentration 3%	13.56 $\pm$ 0.21
Processing time 90 minutes, starch concentration 1%	12.32 $\pm$ 0.23
Processing time 90 minutes, starch concentration 2%	13.66 $\pm$ 0.24
Processing time 90 minutes, starch concentration 3%	13.68 $\pm$ 0.05



results of Czechowska-Biskup et al. (2005), which showed that the process of degradation of starch molecules was more effective in aqueous/solution conditions.

### Distribution and Particle Size of SNP

Distribution, particle size, and PI of SNPs at various ultrasonic process times and starch concentrations are presented in Table 2 and Figure 1. The results in Figure 1 show the percentage of SNP particle size at various particle sizes continuously using a particle size analyzer (PSA). In contrast, the results in Table 2 show the particle size in various particle size groups ( $\leq 100$  nm, 101-1000 nm, and  $> 1000$  nm).

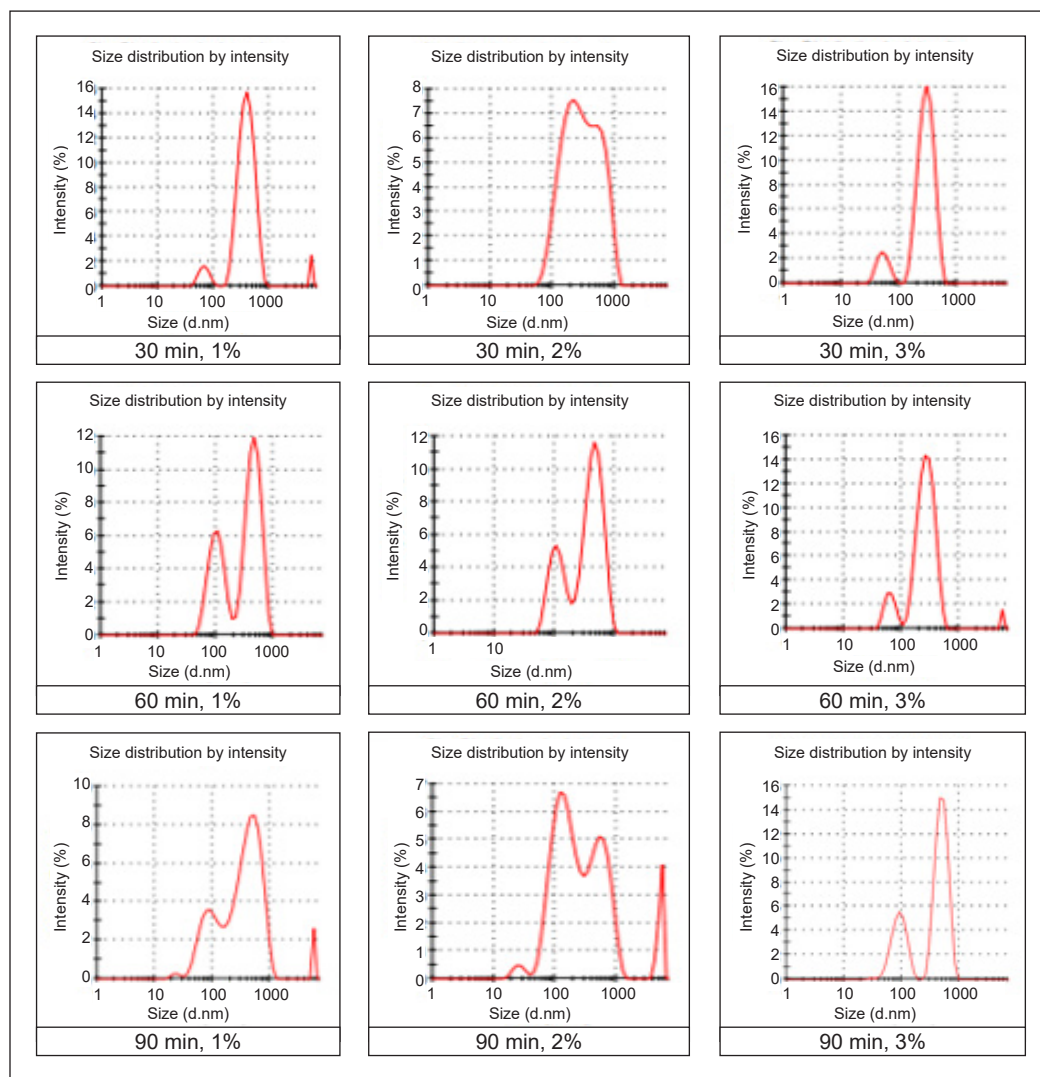


Figure 1. Distribution of various SNP sizes at various ultrasonication process times and starch concentrations

Table 2

*Particle size distribution per size group and polydispersity index of SNPs at various ultrasonication process times and starch concentrations*

Treatment	SNP Particle Size			Average (nm)	Polydispersity index
	≤ 100 nm (%)	101 – 1000 nm (%)	> 1000 nm (%)		
Processing time 30 minutes, starch concentration 1%	6.30	93.70	0.00	501.50	0.47
Processing time 30 minutes, starch concentration 2%	7.60	91.50	0.90	419.90	0,47
Processing time 30 minutes, starch concentration 3%	11.00	89.00	0.00	470.20	0.46
Processing time 60 minutes, starch concentration 1%	12.00	86.40	1.60	429.60	0.51
Processing time 60 minutes, starch concentration 2%	16.70	83.30	0.00	355.00	0.47
Processing time 60 minutes, starch concentration 3%	22.90	77.10	0.00	333.70	0.34
Processing time 90 minutes, starch concentration 1%	20.10	76.80	3.10	430.30	0.50
Processing time 90 minutes, starch concentration 2%	22.30	69.70	8.00	422.90	0.58
Processing time 90 minutes, starch concentration 3%	23.60	76.40	0.00	230.80	0.58

Most SNPs are 101 to 1000 nm in size showing, that the sonication process is quite effective in reducing the size of starch particles (Figure 1). According to Boufi et al. (2018) and Zuo et al. (2012), the ultrasonic method was able to damage and reduce the size of starch granules. The research results in Table 2 also show the presence of particles with a diameter of more than 1000 nm with a small intensity. Particles with a size of more than 1000 nm are thought to be starch particles that have agglomerated into a larger size. According to Jambrak et al. (2010), with changes in temperature and longer storage time, nanoparticles can agglomerate into larger sizes.

The results in Table 2 show that the ultrasonic process of starch with a concentration of 1%–3% for 30–90 minutes will produce SNP products with a diameter range of 230.80 nm to 501.50 nm and a PI value range of 0.34–0.58 nm. The lowest PI was shown in the sonication time of 60 minutes with a starch concentration of 3% with a PI of 0.34 and an average particle size of 333.70 nm. The low PI indicates that the particle size dispersion of SNP is homogeneous and evenly distributed. A PI value greater than 0.70 indicates a very wide distribution of particle sizes so that sedimentation is likely to occur.

The results showed that the ultrasonication process, with a duration of 90 minutes and 3% starch concentration, would produce SNP products with a particle size of less than 100 nm, which was higher (23.6%) than the other treatments. The results also showed that

the longer the sonification process and the higher the starch concentration, the higher the percentage of SNP particles less than 100 nanometers in size. It indicates that ultrasonication can break down starch granules into smaller sizes. The phenomenon of acoustic cavitation by ultrasonic waves causes starch particles to break into nano-sized pieces (Czechowska-Biskup et al., 2005). The increase in the percentage of SNP particle size in line with the increase in concentration up to 3% also shows that at a starch concentration of up to 3%, the cavitation process, which causes the breakdown of starch granules into nano-sized, still occurs effectively. The increase in the cavitation process, in line with the increase in starch concentration in the formation of SNPs, was also reported by Jambrak et al. (2010).

### Starch Nanoparticles Transmittance Values

The transmittance value of SNPs at various ultrasonic process times and starch concentrations are presented in Table 3 and Figure 2. The results show that the ultrasonication process, with a duration of 30 minutes and 1% starch concentration, will produce SNP products with the highest transmittance values (86.38%). Conversely, the ultrasonication process time of 90 minutes and 3% starch concentration will produce SNP products with the lowest transmittance value (61.27%).

Ultrasonic process time of 90 minutes and concentration of 30% (Table 2, Figure 2) will produce SNPs with the lowest transmittance value compared to other treatments. The

Table 3

*Transmittance values of SNPs at various ultrasonic process times and starch concentrations (mean  $\pm$  SD, n =3)*

Treatment	Transmittance (%) at wavelength (nm)					Average transmittance (%)
	450	500	600	700	800	
Processing time 30 minutes, starch concentration 1%	85.31 $\pm$ 0.08	85.62 $\pm$ 0.04	86.78 $\pm$ 0.13	86.60 $\pm$ 0.65	88.34 $\pm$ 0.16	86.53 $\pm$ 0.20
Processing time 30 minutes, starch concentration 2%	75.17 $\pm$ 0.11	76.55 $\pm$ 0.13	77.37 $\pm$ 0.44	77.96 $\pm$ 0.42	80.16 $\pm$ 0.05	77.44 $\pm$ 0.14
Processing time 30 minutes, starch concentration 3%	66.72 $\pm$ 0.32	67.47 $\pm$ 0.64	69.27 $\pm$ 0.23	69.97 $\pm$ 0.34	72.00 $\pm$ 1.63	69.09 $\pm$ 0.52
Processing time 60 minutes, starch concentration 1%	82.37 $\pm$ 0.64	82.30 $\pm$ 0.36	83.25 $\pm$ 0.43	83.20 $\pm$ 0.19	83.83 $\pm$ 0.55	82.99 $\pm$ 0.34
Processing time 60 minutes, starch concentration 2%	69.65 $\pm$ 1.06	70.78 $\pm$ 0.40	72.58 $\pm$ 0.64	73.71 $\pm$ 0.18	76.88 $\pm$ 0.40	72.72 $\pm$ 0.30
Processing time 60 minutes, starch concentration 3%	62.74 $\pm$ 0.38	63.56 $\pm$ 0.51	64.76 $\pm$ 0.40	64.72 $\pm$ 0.13	66.48 $\pm$ 0.27	64.45 $\pm$ 0.15
Processing time 90 minutes, starch concentration 1%	78.97 $\pm$ 0.48	78.51 $\pm$ 0.30	78.16 $\pm$ 0.12	78.12 $\pm$ 0.43	78.47 $\pm$ 0.27	78.45 $\pm$ 0.29
Processing time 90 minutes, starch concentration 2%	64.91 $\pm$ 0.48	65.86 $\pm$ 0.65	67.27 $\pm$ 0.19	68.40 $\pm$ 0.28	70.22 $\pm$ 0.24	67.33 $\pm$ 0.31
Processing time 90 minutes, starch concentration 3%	58.29 $\pm$ 0.25	59.41 $\pm$ 0.41	61.09 $\pm$ 0.11	62.23 $\pm$ 0.23	64.23 $\pm$ 0.10	61.05 $\pm$ 0.22

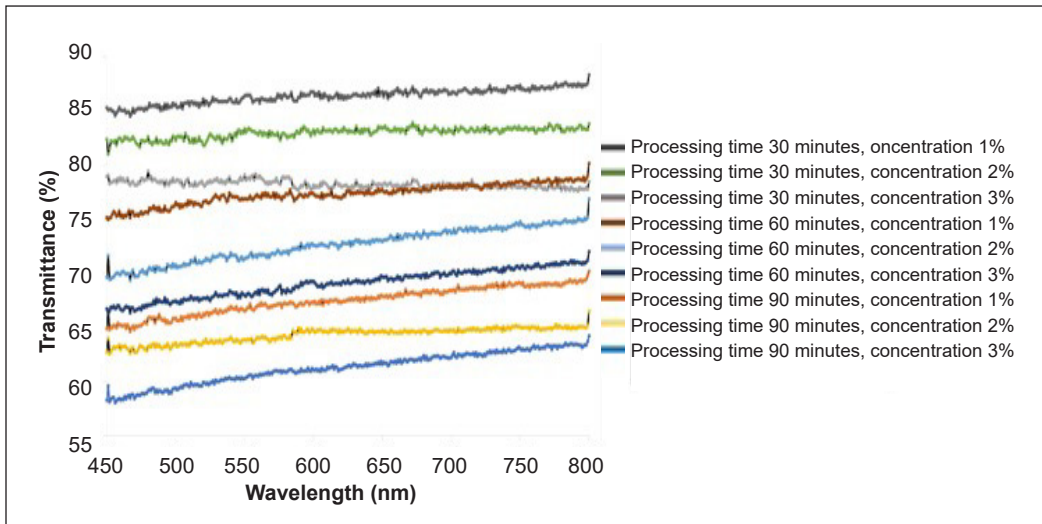


Figure 2. SNP transmittance curves for various ultrasonication process times and starch concentrations

lower transmittance value of the SNP is strongly related to the size of the SNP particles. The smaller the SNP particle size is, the more difficult it is for the starch particles to precipitate and the lower the transmittance value is. On the other hand, the larger the SNP particle size is, the faster the particles settle and the greater the transmittance value is. Changes in the transmittance of SNPs and a decrease in particle size were also reported by Bel Haaj et al. (2013) on SNP formation in corn starch. According to Haaj et al. (2013), SNPs with a size of more than 10  $\mu\text{m}$  will precipitate quickly.

### Starch Nanoparticles Clarity Score

The clarity scores of SNPs at various lengths of the ultrasonication process are presented in Table 4 and Figure 3. The results show that the 90-minute ultrasonication process and 3% starch concentration will produce SNPs with the lowest level of clarity compared to other treatments. The lower clarity of the SNP is strongly related to the size of the SNP particles and their solubility. The smaller the SNP particle size, the lower the clarity of the SNP solution because the nano-sized SNP particles will dissolve and have difficulty settling even though they have been left for 2 hours. The increase in SNP solubility with the smaller particle size is mainly related to the increase in the porosity of starch granules (Sujka, 2017). Changes in the level of clarity of SNP solutions, along with a decrease in particle size, were also reported by Jambrak et al. (2010) and Kim et al. (2013) on SNP formation in corn starch.

The decrease in the clarity score is also directly proportional to the decline in the transmittance value. The smaller the particle size, the lower the transmittance value and the clarity score. If a solution is passed by light, there will be a scattering of dissolved

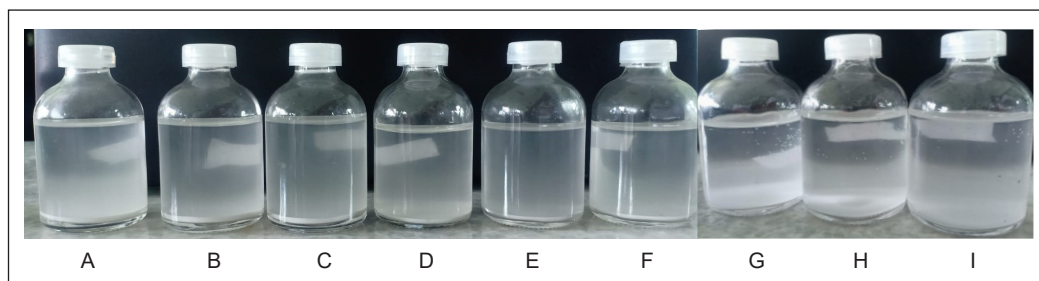
particles, which causes a reduction in transparency. It is closely related to the size of the particles dispersed in the solution. In solutions containing nano-sized granules, these are soluble so that the scattering effect becomes more significant, reducing the transmittance value of the solution and its clarity score.

Table 4

*SNP clarity scores at various ultrasonic process times and starch concentrations (mean  $\pm$  SD, n = 10)*

Treatment	SNP clarity score (%)
Processing time 30 minutes, starch concentration 1%	3.80 $\pm$ 0.13
Processing time 30 minutes, starch concentration 2%	3.60 $\pm$ 0.20
Processing time 30 minutes, starch concentration 3%	3.10 $\pm$ 0.27
Processing time 60 minutes, starch concentration 1%	2.90 $\pm$ 0.22
Processing time 60 minutes, starch concentration 2%	2.80 $\pm$ 0.08
Processing time 60 minutes, starch concentration 3%	2.70 $\pm$ 0.07
Processing time 90 minutes, starch concentration 1%	2.40 $\pm$ 0.13
Processing time 90 minutes, starch concentration 2%	2.20 $\pm$ 0.09
Processing time 90 minutes, starch concentration 3%	2.10 $\pm$ 0.21

Score description: 1 = very unclear; 2 = not clear; 3 = not clear enough; 4 = clear; 5 = very clear



*Figure 3. Clarity of SNP solutions at various ultrasonic process times and starch concentrations (A = 30 min, 1%; B = 30 min, 2%; C = 30 min, 3%; D = 60 min, 1%; E = 60 min, 2%; F = 60 min, 3%; G = 90 min, 1%; H = 90 min, 2%; I = 90 min, 3%)*

## CONCLUSION

Ultrasonic process time and starch concentration affect the yield, particle size and distribution, polydispersity index, optical characteristics (transmittance), and SNP clarity score. Ultrasonic process time of 90 minutes and starch concentration of 3% will produce SNP products with a yield of 13.68%, particle size  $\leq$  100 nm of 23.6%, average particle size of 230.8 nm with polydispersity index of 0.581, transmittance value of 61.27%, and a solution clarity score of 3.80 (not clear).

Tapioca-based SNPs can be developed solely with ultrasonic method to simplify the process. Further research is needed to improve the yield of SNPs based on tapioca.

## ACKNOWLEDGEMENTS

The author thanks the Directorate of Research and Community Service, Ministry of Education, Culture, Research and Technology of the Republic of Indonesia, for funding this research through the Higher Education Excellence Applied Research scheme in 2021.

## REFERENCES

- BeMiller, J., & Whistler, R. (2009). *Starch: Chemistry and Technology* (3rd ed.). Academic Press.
- Bonto, A. P., Tiozon, R. N., Sreenivasulu, N., & Camacho, H. (2021). Impact of ultrasonic treatment on rice starch and grain functional properties: A review. *Ultrasonic Sonochemistry*, 71, Article 105383. <https://doi.org/10.1016/j.ultsonch.2020.105383>
- Boufi, S., Haaj, S. B., Magnin, A., Pignon, F., & Mortha, G. (2018). Ultrasonic assisted production of starch nanoparticles: Structural characterization and mechanism of disintegration. *Ultrasonic Sonochemistry*, 41, 327-336. <http://dx.doi.org/10.1016/j.ultsonch.2017.09.033>
- BPS-Statistics of Lampung Province. (2022). *Lampung Province in Figure 2021*. <https://lampung.bps.go.id/publication/2021/02/26/443c020eb6a33a394e6d3df4/provinsi-lampung-dalam-angka-2021.html>
- Czechowska-Biskup, R., Rokita, B., Lotfy, S., Ulanski, P., & Rosiak, J. M. (2005). Degradation of chitosan and starch by 360-kHz ultrasound. *Carbohydrate Polymers*, 60, 175-184. <https://doi.org/10.1016/j.carbpol.2004.12.001>
- EFSA Scientific Committee. (2011). Guidance on the risk assessment of the application of nanoscience and nanotechnologies in the food and feed chain. *EFSA Journal*, 9(5), Article 2140. <https://doi.org/10.2903/j.efsa.2011.2140>
- Ezhilarasi, P. N., Karthik, P., Chhanwal, N., & Anandharamakrishnan, C. (2013). Nanoencapsulation techniques for food bioactive components: A review. *Food and Bioprocess Technology*, 6, 628-647. <https://doi.org/10.1007/s11947-012-0944-0>
- Garcia, N. L., Ribbon, L., Dufresne, A., Aranguren, M., & Goyanes S. (2011). Effect of glycerol on the morphology of nanocomposites made from thermoplastic starch and starch nanocrystals. *Carbohydrate Polymers*, 84(1), 203-210. <https://doi.org/10.1016/j.carbpol.2010.11.024>
- Goncalves, P. M., Norena, C. P. Z., Silveira, N. P., & Brandelli, A. (2014). Characterization of starch nanoparticles obtained from *Araucaria angustifolia* seeds by acid hydrolysis and ultrasound. *LWT - Food Science and Technology*, 58, 21-27. <https://dx.doi.org/10.1016/j.lwt.2014.03.015>
- Haaj, S. B., Magnin, A., Pétrier, C., & Boufi, S. (2013). Starch nanoparticles formation via high power ultrasonication. *Carbohydrate Polymers*, 92, 1625-1632. <https://doi.org/10.1016/j.carbpol.2012.11.022>
- Hidayat, B., Hasanuddin, U., Nurdjanah, S., Yuliana, N., Muslihudin, M., & Akmal, S. (2021). Application of partial gelatinization autoclaving-cooling process to increase the resistant starch content of fermented cassava pulp flour-based composite flour. *Asian Journal of Agriculture and Biology*, 2021(3), 1-10. <https://doi.org/10.35495/ajab.2020.09.483>

- Jambrak, A. N., Herceg, Z., Šubarić, D., Babić, J., Brncić, M., Brncić, S. R., Bosiljkov, T., Cvek, D., Tripalo, B., & Boufi, S. (2010). Ultrasound effect on physical properties of corn starch. *Carbohydrate Polymers*, 79, 91-100. <https://dx.doi.org/10.1016/j.carbpol.2009.07.051>
- Kim, H. Y., Park, D. J., Kim, J. Y., & Lim, S. T. (2013). Preparation of crystalline starch nanoparticles using cold acid hydrolysis and ultrasonication. *Carbohydrate Polymer*, 98, 295-301. <https://dx.doi.org/10.1016/j.carbpol.2013.05.085>
- Kumari, S., Yadav, B. S., & Yadav, R. B. (2020). Synthesis and modification approaches for starch nanoparticles for their emerging food industrial applications: A review. *Food Research International*, 128, Article 108765. <https://doi.org/10.1016/j.foodres.2019.108765>
- Lamanna, M., Morales, N. J., Garcia, N. L., & Goyanes, S. (2013). Development and characterization of starch nanoparticles by gamma radiation: Potential application as starch matrix filler. *Carbohydrate Polymers*, 97, 90-97. <https://dx.doi.org/10.1016/j.carbpol.2013.04.081>
- Le-Corre, D., Bras, J., & Dufresne, A. (2010). Starch nanoparticles: A review. *Biomacromolecules*, 11(5), 1139-1153.
- Liu, C., Qin, Y., Li, X., Sun, Q., Xiong, L., & Liu, Z. (2016). Preparation and characterization of starch nanoparticles via self-assembly at moderate temperature. *International Journal of Biological Macromolecules*, 84, 354-360. <https://dx.doi.org/10.1016/j.ijbiomac.2015.12.040>
- Sharma, M., Kadam, D. M., Chadha, S., Wilson, R. A., & Gupta, R. K. (2013). Influence of particle size on physical and sensory attributes of mango pulp powder. *International Agrophysics*, 27(3), 323-328. <https://doi.org/10.2478/intag-2013-0001>
- Sujka, M. (2017). Ultrasonik modification of starch - Impact on granules porosity. *Ultrasonic Sonochemistry*, 37(2017), 424-429. <https://doi.org/10.1016/j.ultsonch.2017.02.001>
- Zhu, H. P., Zhou, Z. Y., Yang, R. Y., & Yu, A. B. (2007). Discrete particle simulation of particulate systems: Theoretical developments. *Chemical Engineering Science*, 62(13), 3378-3396. <https://doi.org/10.1016/j.ces.2006.12.089>
- Zukryandry, Hidayat, B., & Muslihudin. (2022). Timing of extraction with ultrasonic bath system to improve the yield and chemical characteristic of cassava starch. *IOP Conference Series: Earth and Environmental Science*, 1012, Article 012016. <https://doi.org/10.1088/1755-1315/1012/1/012016>
- Zuo, Y. Y. J., Hebraud, P., Hemar, Y., & Ashokkumar, M. (2012). Quantification of high-power ultrasound induced damage on potato starch granules using light microscopy. *Ultrasonics Sonochemistry*, 19, 421-426. <https://doi.org/10.1016/j.ultsonch.2011.08.006>





*Review Article*

## **A Review: Current Trend of Immersive Technologies for Indoor Navigation and the Algorithms**

**Muhammad Shazmin Sariman, Maisara Othman\*, Rohaida Mat Akir, Abd Kadir Mahamad and Munirah Ab Rahman**

*Department of Electronic Engineering, Faculty of Electrical and Electronic Engineering, Universiti Tun Hussein Onn Malaysia, 86400 Parit Raja, Batu Pahat, Johor, Malaysia*

### **ABSTRACT**

The term “indoor navigation system” pertains to a technological or practical approach that facilitates the navigation and orientation of individuals within indoor settings, such as museums, airports, shopping malls, or buildings. Over several years, significant advancements have been made in indoor navigation. Numerous studies have been conducted on the issue. However, a fair evaluation and comparison of indoor navigation algorithms have not been discussed further. This paper presents a comprehensive review of collective algorithms developed for indoor navigation. The in-depth analysis of these articles concentrates on both advantages and disadvantages, as well as the different types of algorithms used in each article. A systematic literature review (SLR) methodology guided our article-finding, vetting, and grading processes. Finally, we narrowed the pool down to 75 articles using SLR. We organized them into several groups according to their topics. In these quick analyses, we pull out the most important concepts, article types, rating criteria, and the positives and negatives of each piece. Based on the findings of this review, we can

conclude that an efficient solution for indoor navigation that uses the capabilities of embedded data and technological advances in immersive technologies can be achieved by training the shortest path algorithm with a deep learning algorithm to enhance the indoor navigation system.

#### **ARTICLE INFO**

*Article history:*

Received: 27 July 2023

Accepted: 20 November 2023

Published: 26 March 2024

DOI: <https://doi.org/10.47836/pjst.32.2.25>

*E-mail addresses:*

[muhdshazmin98@gmail.com](mailto:muhdshazmin98@gmail.com) (Muhammad Shazmin Sariman)

[maisara@uthm.edu.my](mailto:maisara@uthm.edu.my) (Maisara Othman)

[rohaida@uthm.edu.my](mailto:rohaida@uthm.edu.my) (Rohaida Mat Akir)

[kadir@uthm.edu.my](mailto:kadir@uthm.edu.my) (Abd Kadir Mahamad)

[munira@uthm.edu.my](mailto:munira@uthm.edu.my) (Munirah Ab Rahman)

\* Corresponding author

*Keywords:* Augmented reality, deep learning, indoor navigation, mixed reality, shortest path, virtual reality

## INTRODUCTION

In current navigation systems, electronic devices are used to determine the user's location, find the most direct route, and, in certain cases, automatically direct vehicles to their destinations. The science and technology of spotting a sailboat, airplane, or other types of vehicles and directing them to a specific location are known as navigation (Kunhoth et al., 2020). In today's world, most navigational aids depend on satellite signals transmitted by the global positioning system (GPS). While GPS works perfectly outside, it is difficult to use inside due to several factors, such as reduced signal strength, dim lighting, and complicated environments. Recent discussions have brought up potential new directions for the development of indoor navigation, including the use of image-based and Wi-Fi-based systems. GPS is ineffective for determining the location inside a building due to the absence of a line of sight (NLoS), weak signal strength, and reduced accuracy (Syazwani et al., 2022). Although GPS performs admirably in open areas, its performance in urban canyons is notoriously poor because of the signal reflections of NLOS satellites (Z. Liu et al., 2022).

There are numerous applications for indoor navigation systems, such as in universities, complex malls, bus stations, train stations, airports, libraries, and museums. Furthermore, specific navigation applications for humans and people with visual impairments benefit from internal navigation systems. Unlike exterior areas, indoor areas are more difficult to navigate due to the absence of reliable GPS signals and physical obstacles like walls, stairs, and furniture. Different obstacles are present in interior environments, increasing the difficulty of implementing navigation systems.

The fundamental components of a human indoor navigation system consist of three elements, namely the indoor positioning system (IPS) module, the navigation module, and the human-machine interaction (HMI) module. The system for indoor positioning is designed to approximate the user's location. At the same time, the navigation element determines which routes are the most efficient to take from the user's present location to the destination they have in mind. The Human Machine Interface (HMI) module makes engaging with the system easier and allows users to give commands. The efficiency of GPS-based indoor positioning is limited; hence, alternative methods such as those based on computer vision (Lee et al., 2022), pedestrian dead reckoning (PDR) (Jiang et al., 2022), and radio frequency (RF) (Syazwani et al., 2022) signals are employed for indoor positioning.

Various technologies can be utilized for indoor positioning, including but not limited to Wi-Fi (Chan et al., 2023), Bluetooth (Babakhani et al., 2021), *radio frequency identification* (Chumkamon et al., 2008), ZigBee (Dong et al., 2018), ultra-wideband (Sarkar et al., 2021), and a geomagnetic field (Yeh et al., 2020). These technologies require specific equipment, resulting in a high implementation cost. Wi-Fi boasts a notable advantage despite potential drawbacks due to its widespread integration and prevalence across various devices. The popularity of ultra-wideband (UWB) technology in high-precision indoor positioning

systems can be attributed to its advantages over narrowband-based technologies such as Bluetooth and Wi-Fi. UWB offers a wide variety of benefits, including a high data transfer rate, low transmission energy, a short signal transmission length, and deep penetration (Che et al., 2023).

One of the most important aspects of indoor navigation is that it may be applied in a variety of different contexts involving people (Abdallah et al., 2022). However, there is a significant challenge when the concept is applied to multiple rooms and obstacles in the indoor environment. The layout of an indoor navigation system's user interface is critical. Most electronic navigation systems still use a conventional interface; thus, users must actively compare on-screen arrows with their surroundings to identify the right position. For example, with indoor mapping tools, students may easily find their way to class or any other location on campus. However, if they are new to the campus, they may soon feel lost among the maze of buildings and departments in a typical university.

The use of augmented reality (AR), virtual reality (VR), and mixed reality (MR) technologies for indoor navigation presents a promising area of research that provides diverse opportunities for improving navigation in interior environments. Industry-wide adoption of AR indoor navigation is increasing (Verma et al., 2020). Technology firms have started investing in AR due to its appealing features and compatibility with other devices. Currently, AR can be used in many different environments, such as in the classroom, the workplace, a museum, a factory, a store, or a museum shop. Furthermore, AR has been rigorously tested and investigated, and indoor navigation is just one of its applications. By using image recognition technology to calculate the location and angle of the acquired image actuarially, AR enables the virtual world on the screen to blend with and interact with real-world situations.

The application of VR for indoor navigation is currently a thriving field of research and development. Indoor navigation utilizing VR is an active research and development topic. It entails using VR technology to assist users in navigating and orienting themselves within indoor environments. Virtual reality is a scenario generated by a computer that simulates a realistic experience. Popular online maps provide primarily two-dimensional views of the tops of buildings—the interiors of a location become difficult to envision. Indoor navigation utilizing VR technology solves the issue of visualizing the interior infrastructure of vast, complex structures (Khan et al., 2020).

The term MR denotes a continuum that encompasses both VR and AR. This technology integrates elements of reality with virtual objects or surroundings to generate a blended experience for individuals. This technology is more user-friendly, adaptable, and productive compared to more conventional methods of navigating within a building. Even though this technology is still in its infancy, it is already abundantly evident that it will flourish in the years to come (El-Sheimy & Li, 2021).

The implementation of algorithms is vital for navigating inside buildings. Indoor navigation systems depend on algorithms as their primary component because they provide precise mapping and localization, efficient path planning, and real-time adaptation. Algorithms are a very important component in making interior navigation accurate, efficient, and user-friendly. Although various alternative algorithms have been used for indoor navigation, the ones discussed in this article are the shortest path and deep learning algorithms. The problem of discovering the shortest way or route between an origin point and an endpoint is frequently referred to as the issue of the shortest path. In most cases, the challenge of the shortest path is represented through graphs. A graph is an example of an abstract mathematical entity comprising many collections of vertices and edges. Edges connect two adjacent vertices. It is possible to walk along the edges of a graph by moving from one vertex to another. A graph's edges provide a path for walking from one vertex to another. The presence or absence of the ability to walk along the edges in both directions distinguishes between a directed graph and an undirected graph. There are several different algorithms designed to solve the issue of the shortest path, including but not limited to Dijkstra's algorithm (P. Liu et al., 2022), the Bellman-Ford algorithm (Parimala et al., 2021), the A\* algorithm (Rachmawati & Gustin, 2020), the D\* algorithm (Alves et al., 2019), and the Floyd-Warshall algorithm (Ramadiani et al., 2018).

Deep learning is a specialization within the larger area of machine learning. It uses an artificial neural network (ANN) architecture to spot patterns and calculate feature extraction. Many studies have proposed combining a variety of indoor navigation techniques and algorithms. Most analyses investigated the use of various shortest-path algorithms. Location awareness and remembering navigation (LARN) and flexible path planning (FPP) are among the algorithms used for indoor navigation systems.

The evolution of technology for navigation inside buildings is faced with several significant challenges, including imprecise positioning (Nessa et al., 2020), intricate and ever-changing surroundings (Varma & Anand, 2021), restricted scalability and adaptability (Zlatanova et al., 2013), obstructions within indoor spaces and signal interference (El-Sheimy & Li, 2021), and limited connectivity (Trybała & Gattner, 2021). In order to tackle these obstacles, a blend of technological advancements, algorithmic enhancements, data management tactics, and user-focused design methodologies is necessary. Ongoing research and progress in positioning technologies, machine learning, and data fusion techniques are directed toward surmounting these obstacles and enhancing indoor navigation systems' precision, user-friendliness, and dependability.

Additionally, deep learning techniques allow for indoor navigation that is accurate and responsive to adjustments in the surrounding environment, such as the presence of obstacles or changes in lighting conditions (Shahbazian et al., 2023). These factors can affect the accuracy and reliability of the algorithm, especially if it has not been trained in a wide

range of environments and scenarios. Another challenge is the computational complexity of deep learning algorithms, which may require significant computing resources and time to train and optimize. It can be a significant barrier for researchers with limited access to computing resources, as well as for real-time applications where speed and efficiency are critical. Finally, there is also a need for standardized evaluation metrics and benchmarks to compare the performance of different deep-learning algorithms for indoor navigation systems. Currently, there is a lack of consensus on the most appropriate metrics and benchmarks, making it difficult to compare and replicate results across different studies.

One of the common problems in recent research on indoor navigation using deep learning algorithms is the absence of identified training information. In order to properly learn and generalize patterns and correlations between features, deep learning algorithms require enormous amounts of labeled data to work. However, obtaining labeled data for indoor navigation can be challenging and time-consuming, as it requires manually labeling the floor plans, indoor maps, and trajectories of users. Next, this article discusses the most recent developments in immersive technologies such as AR, VR, and MR. In addition to that, this research emphasized the algorithm that has been implemented in the indoor navigation system. Deep learning and shortest path algorithms are the two categories into which the algorithms have been divided due to the use of a number of different technological innovations and techniques. The goal of shortest-path algorithms is to identify the most direct route between two nodes in a network, while the objective of deep learning is to learn and anticipate complicated patterns.

## **CURRENT TRENDS OF IMMERSIVE TECHNOLOGIES IN INDOOR NAVIGATION**

Indoor navigation systems are rapidly incorporating immersive technologies such as VR, AR, and MR to improve the user experience and deliver navigation solutions that are both more user-friendly and immersive. Augmented reality superimposes digital information over a user's view of the physical world, enabling users to get real-time visual signals and directional information (Rehman & Cao, 2017). Augmented reality wayfinding applications have the capability to superimpose navigational instructions, arrows, or markers over the user's vision of the indoor space, directing the user to their desired location.

VR's immersive and participatory nature makes it a viable option for interior navigation. When used indoors, traditional GPS navigation might be difficult because of the reduced availability and accuracy of satellite signals. Virtual reality can help with these issues by simulating indoor navigation and constructing virtual representations of indoor spaces (B. Liu et al., 2021).

Mixed reality allows users to engage with virtual and physical objects. With this technology, it is possible to create the illusion that the virtual and physical worlds coexist.

Virtual markers, routes, or annotations can be superimposed over the user's environment to serve as interactive navigation instructions and directions when using an MR device like Microsoft HoloLens or Magic Leap One for interior navigation (B. Liu et al., 2022).

## **INDOOR NAVIGATION USING AUGMENTED REALITY**

Augmented reality indoor navigation systems provide users with a more natural and immersive experience by fusing digital information with the physical world (Verma et al., 2020). By superimposing digital data (e.g., visual cues, directions, or annotations) onto a user's perspective of the real world, AR provides a more enriching experience. For example, Saeliw et al. (2022) developed an AR-based mall navigation utilizing AR Core, which directs visitors to the exhibition's location and provides them with the opportunity to experience and enjoy the virtual things in the mall.

Furthermore, according to Yang and Sanjie (2017), the system that is being proposed will make use of devices with cameras, such as smartphones, to deliver position information by scanning AR markers that have been placed in the environment. It will ultimately assist users in being more aware of where they are. Chidsin et al. (2021) proposed a marker-free system for AR-based indoor navigation. The suggested system utilized the red-green blue-depth (RGB-D) camera to monitor the surroundings, and the technology known as simultaneous localization and mapping (SLAM) was utilized to generate a point cloud map (Lee et al., 2017). An indoor navigation system was implemented with the help of the Internet of Things devices available in the building and AR technology to direct people out of the building in the event of a fire.

Rehman and Cao (2017) proposed an AR-based indoor localization application with the goal of assisting people in navigating around areas that are entirely indoors. The software may be installed on a wide variety of computers, mobile phones, as well as wearable computers. Yoon and Lee (2023) proposed an idea for AR logistics software that can be used on smartphones. The application would lead the user to the appropriate logistical area at a building site. The logistical program was coded in Unity 3D, based on the AR Foundation foundation for AR, as well as the ZXing library, which is used to recognize QR codes. Saeliw et al. (2022) address a reasonable alternative, architecture, and how technology has advanced to construct an indoor navigation system application using AR for shopping malls.

## **INDOOR NAVIGATION USING VIRTUAL REALITY**

VR technology can be effectively utilized to innovate indoor positioning systems. Yuan et al. (2023) implemented an indoor fire evacuation simulated in virtual reality using a navigation grid's corner points. The VR simulation of the evacuation of the interior fire crowd was implemented on the basis of the dynamic layout of the route taken by firefighters evacuating

from a building with many exits. Khan et al. (2020) proposed an indoor navigation system for stadiums using WebVR technology and offering users an experience that is wholly immersive and compelling. With the assistance of 360-degree photos, the “virtual shortest path” to the location of interest is presented.

In addition, VR equipment can furnish fully immersive learning environments and provide interactive learning opportunities for teams working together in a shared space. By using VR, the unattractiveness and lack of interest in conventional teaching approaches can be overcome. Guo et al. (2020) recommended using a method to evacuate a large group of people using virtual reality simulations in the event of an indoor fire with several exits. For many years, the field of health sciences has focused on improving interior navigation methods for people who are blind or have other visual impairments. Real and Araujo (2021) developed a tool for validating navigation instructions and another tool for user training for the PERCEPT system.

In conclusion, VR can make indoor navigation easier, which is especially beneficial in complicated places like airports, malls, and stadiums. The widespread adoption of VR technology has the potential to completely alter the environment of indoor navigation.

## **INDOOR NAVIGATION USING MIXED REALITY**

The application of MR technology, which enhances the existing physical environment by displaying digital holograms and supplying supplementary details, shows promise for use in indoor navigation. An appropriate strategy has the potential to enhance the development of MR-based indoor navigation applications as well as related research. For example, B. Liu et al. (2021) provided user studies with an overview of magnetic resonance MR technology, equipment, and the design of MR-based indoor navigation systems.

In addition, MR will also provide a better experience for the user based on real-time navigation. Chung et al. (2021) used a gadget called Microsoft HoloLens to construct a head-mounted museum navigation system by merging several technologies, such as MR, gesture recognition, and location awareness.

Next, MR can be employed for indoor rescue operations by providing rescuers real-time data about the inside environment and the position of people needing rescue. This system employs augmented indoor maps and MR to improve the speed and effectiveness of rescue teams reacting to and dealing with unexpected hazards (Chae et al., 2023).

It is one of the studies that used MR for indoor navigation (B. Liu et al., 2021). The system was created, developed, and put into operation with virtual semantic landmarks in interior spaces based on MR. Additionally, users were evaluated to investigate whether such markers can aid in the acquisition of spatial information when navigating.

Microsoft HoloLens was used to analyze the inside environment and give data to be used as an indoor navigation aid (B. Liu et al., 2021). HoloLens is an AR helmet that uses

MR technology to provide users with holographic images that blend with the context of their surroundings.

MR-based indoor navigation systems can give users accurate and reliable help when navigating indoor environments. However, additional research is required to make position monitoring more accurate and to design user interfaces that are easy to use and intuitive. Table 1 shows the summary work of immersive technologies for indoor navigation.

Table 1  
Summary work of immersive technologies of indoor navigation

Type of Immersive Technology	Year	Title/Project Name	Strengths	Weaknesses
AR	2022	FIND: Mall navigation using augmented reality (Rochadiani et al., 2022)	<ul style="list-style-type: none"> <li>i. Attract more visitors</li> <li>ii. Easy to use</li> </ul>	<ul style="list-style-type: none"> <li>i. High cost</li> <li>ii. No direction arrow</li> </ul>
AR	2017	Indoor navigation for the visually impaired using AR markers (Yang & Saniie, 2017)	<ul style="list-style-type: none"> <li>i. Highly accurate</li> <li>ii. The system provides voice instruction</li> </ul>	<ul style="list-style-type: none"> <li>i. Users must be trained to use the AR marker system effectively</li> </ul>
AR	2021	AR-based navigation using RGB-D camera and hybrid map (Chidsin et al., 2021)	<ul style="list-style-type: none"> <li>i. Real-time navigation</li> <li>ii. Easy to use</li> </ul>	<ul style="list-style-type: none"> <li>i. High-cost</li> <li>ii. No audio instruction</li> </ul>
AR	2017	Indoor navigation system for evacuation route in case of fire by using environment and location data (Lee et al., 2017)	<ul style="list-style-type: none"> <li>i. Increased safety</li> <li>ii. Quick evacuation</li> </ul>	<ul style="list-style-type: none"> <li>i. High-cost</li> <li>ii. The system may estimate a person's location incorrectly</li> </ul>
AR	2017	Augmented reality-based indoor navigation: A comparative analysis of handheld devices vs. Google Glass (Rehman & Cao, 2017)	<ul style="list-style-type: none"> <li>i. Low cost</li> <li>ii. User-friendly</li> </ul>	<ul style="list-style-type: none"> <li>i. Limited battery life</li> <li>ii. Wearable devices and smartphones failed the memory tests</li> </ul>
AR	2023	Development of a Construction-Site Work Support System Using BIM-Marker-Based Augmented Reality (Yoon & Lee, 2023)	<ul style="list-style-type: none"> <li>i. Low cost</li> <li>ii. Low implementation effort</li> </ul>	<ul style="list-style-type: none"> <li>i. Obstacles in constructing paths have not yet been considered</li> </ul>
AR	2021	Research direction for Android-based indoor navigation solution for shopping malls through augmented reality-EasyMap (Rubio-Sandoval et al., 2021)	<ul style="list-style-type: none"> <li>i. User-friendly</li> <li>ii. Real-time navigation</li> </ul>	<ul style="list-style-type: none"> <li>i. High-cost</li> <li>ii. Limited coverage</li> </ul>



Table 1 (continue)

Type of Immersive Technology	Year	Title/Project Name	Strengths	Weaknesses
VR	2023	Application of navigation grid corner point algorithm in virtual reality simulation images of indoor fire evacuation (Yuan et al., 2023)	<ul style="list-style-type: none"> <li>i. Virtual reality can solve the situation of multiple indoor exits and dynamic environmental factors</li> <li>ii. Quick evacuation</li> </ul>	<ul style="list-style-type: none"> <li>i. Cannot predict others' evacuation routes or completely comprehend the current situation's threats</li> </ul>
VR	2020	Indoor navigation in stadium using virtual reality (Khan et al., 2020)	<ul style="list-style-type: none"> <li>i. WebVR offers an immersive experience with a 360-degree image view</li> </ul>	<ul style="list-style-type: none"> <li>i. Security issue</li> </ul>
VR	2020	A virtual reality simulation method for crowd evacuation in a multi-exit indoor fire environment (Guo et al., 2020)	<ul style="list-style-type: none"> <li>i. Real-time</li> </ul>	<ul style="list-style-type: none"> <li>i. The user's VR experience is seamless only when the frame rate is stable over 60 fps</li> </ul>
VR	2017	Ves: A Mixed-Reality Development Platform Of Navigation Systems For the Blind And Visually Impaired (Real & Araujo, 2021)	<ul style="list-style-type: none"> <li>i. Improve the user's experience in the actual world by letting them explore and learn before they arrive</li> </ul>	<ul style="list-style-type: none"> <li>i. The system lacks an interface for orientation and mobility instructors to alter the environment by specifying points of interest and exploratory activities</li> </ul>
MR	2022	Designing mixed reality-based indoor navigation for user studies (B. Liu et al., 2021)	<ul style="list-style-type: none"> <li>i. Helps researchers construct a research-oriented MR-based indoor navigation system in more generic situations</li> </ul>	<ul style="list-style-type: none"> <li>i. MR technology struggles to map transparent objects and display holograms in bright lighting conditions</li> </ul>
MR	2021	Development of a head-mounted mixed-reality museum navigation system (Chung et al., 2021)	<ul style="list-style-type: none"> <li>i. Real-time</li> <li>ii. Increase the efficiency of navigation</li> </ul>	<ul style="list-style-type: none"> <li>i. The system is limited to being used at Tamsui Oxford College of Aletheia University only</li> </ul>
MR	2023	Design of a mixed reality system for simulating indoor disaster rescue (Chae et al., 2023)	<ul style="list-style-type: none"> <li>i. Efficient at making rescues work more rapidly</li> </ul>	<ul style="list-style-type: none"> <li>i. The system compatibility is only for one device</li> </ul>
MR	2021	Spatial knowledge acquisition with virtual semantic landmarks in mixed reality-based indoor navigation (B. Liu et al., 2021)	<ul style="list-style-type: none"> <li>i. Enhance incidental spatial information development, although consumers believe better holograms would benefit them more</li> </ul>	<ul style="list-style-type: none"> <li>i. The device is heavy</li> </ul>

Table 1 (continue)

Type of Immersive Technology	Year	Title/Project Name	Strengths	Weaknesses
MR	2022	Designing Mixed Reality-Based Indoor Navigation for User Studies (B. Liu et al., 2021)	<ul style="list-style-type: none"> <li>i. High accuracy</li> <li>ii. Have a navigator to help users</li> </ul>	<ul style="list-style-type: none"> <li>i. These approaches might not always be effective in real life due to logistical or technological limitations</li> </ul>

### INDOOR NAVIGATION ALGORITHM

A literature review on indoor navigation systems has been conducted in this part of the article. It summarizes the research done in this area in the past. According to the published research, a considerable number of researchers have utilized different algorithms, such as Dijkstra (Z. Liu et al., 2021), A\*(Wang et al., 2022), Bellman-Ford (Tamimi, 2015), Floyd Warshall (Ramadiani et al., 2018), Node2vec (Grover & Leskovec, 2016), recurrent neural networks (RNN) (Hoang et al., 2019), convolutional neural networks (CNN) (Gong et al., 2021), deep neural networks (DNN) (Oh & Kim, 2021) and artificial neural networks (ANN) (Jamil & Kim, 2019) to navigate inside buildings.

The classification of indoor navigation algorithms is depicted in Figure 1. By using a variety of technologies, the algorithms have been segmented into two categories: deep learning and shortest-path algorithms. Most prior research has concentrated on the shortest path and deep learning algorithms separately, whereas no studies have investigated both algorithms together.

The shortest path algorithm is a fundamental technique for identifying the most efficient route between two points in a graph. This route is determined by finding the

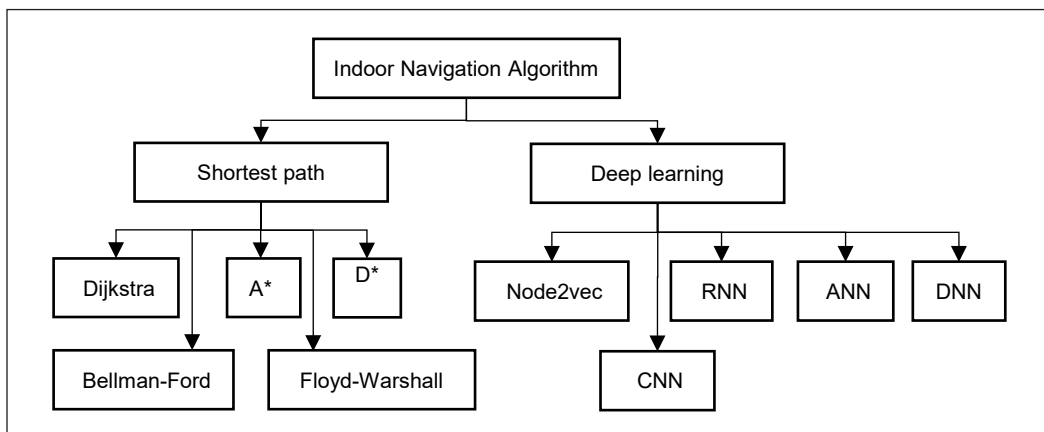


Figure 1. Indoor navigation algorithm taxonomy

smallest distance between the two locations. The graph represents the layout of the indoor environment in the context of indoor navigation. The graph nodes present specific places (e.g., rooms, corridors, or intersections), while the edges present the connections that link these locations (Rizi et al., 2018).

Using multiple deep learning techniques allows for performance to be improved based on prior experience. It will assist in improving accuracy and finding more ideal paths, depending on the experience gained. For example, Al-habashna et al. (2022) proposed a technique that can extract the received signal strength indicator (RSSI) from user equipment (UEs) and then utilize it to develop a fingerprint database using the information. The RSSI data of the UEs is then sent into a deep learning algorithm, which generates an estimate of the locations of the UEs within the building. Ge et al. (2022) developed a platform for collecting environmental sensing data and used environmental data for machine learning on location awareness in a building to improve location awareness.

Woensel et al. (2020) applied deep learning techniques with knowledge-based algorithms and instruments to accurately determine the precise position of an individual and its semantic relation to the determined location. Wu et al. (2020) applied image classification in deep learning to achieve the positioning function, and an algorithm was used to determine the most effective route to your destinations. The calculation results were then presented in the form of an interior navigation system.

Bakale et al. (2020) suggested deep learning to identify objects in the provided indoor scene and then used reinforcement learning to find a path. The suggested solution has provided the navigation path for approximately 2 minutes and 10 seconds.

## THE TYPES OF ALGORITHMS FOR INDOOR NAVIGATION

The articles surveyed and presented in the Indoor Navigation Algorithm section demonstrate that the current research has concentrated on both algorithms, which determine where a person is located using deep learning and the shortest distance between two points. Table 2 shows the types of shortest-path algorithms for indoor navigation, and Table 3 presents the types of deep-learning algorithms.

Table 2  
*The shortest path algorithm for indoor navigation*

Title/Project Name	Year	Algorithms	Results
Design and Implementation of the Optimization Algorithm in the Layout of Parking Lot Guidance (Z. Liu et al., 2021)	2021	Dijkstra	Determined the source node's lowest total weight (distance)
An improved Dijkstra-based algorithm for resource-constrained shortest path (P. Liu et al., 2022)	2022	Dijkstra	Determined the shortest path

Table 2 (continue)

Title/Project Name	Year	Algorithms	Results
Reliability study on the adaptation of Dijkstra’s algorithm for gateway KLIA2 indoor navigation (Samah et al., 2020)	2020	Dijkstra	Determined the shortest route from the current location to the point of origin
Analysis of Dijkstra’s algorithm and A* algorithm in shortest path problem (Rachmawati & Gustin, 2020)	2020	Dijkstra and A*	Dijkstra and A* have different loop counts depending on the number of points (nodes) in the graph
Indoor navigation using A* algorithm (Kasim et al., 2016)	2016	A*	A* uses a statistical function to find a better path, while Dijkstra's method just looks at all possible routes
The EBS-A* algorithm: An improved A* algorithm for path planning (Wang et al., 2022)	2022	A*	EBS-A* algorithm reduced the critical nodes by 91.89%, right-angle turns by 100%, and path planning efficiency by 278%
Analysis of path planning algorithms for service robots applied in indoor environments (Jia, 2023)	2019	A*	The A* search is a more straightforward option and can improve traditional path planning algorithm
Indoor Navigation with Human Assistance for Service Robots Using D*Lite (Alves et al., 2019)	2018	D*	D*Lite can quickly and effectively replan a new path.
Bellman-Ford algorithm for solving the shortest path problem of a network under a picture fuzzy environment (Parimala et al., 2021)	2021	Bellman-Ford	The Bellman-Ford algorithm solves the shortest path issue under uncertainty in fuzzy image environments
A study on the Bellman-Ford shortest path algorithm using a global positioning system (Rai, 2022)	2022	Bellman-Ford	Dijkstra's algorithm and Bellman-Ford algorithm determine the graph's shortest path and optimize GPS
Floyd-Warshall algorithm to determine the shortest path based on Android (Ramadiani et al., 2018)	2018	Floyd-Warshall	Floyd-Warshall algorithm finds the fastest and shortest path between two nodes, whereas the program finds the path of more than two nodes
Comparison Studies for Different Shortest Path Algorithms (Tamimi, 2015)	2015	Dijkstra’s, A*, Bellman-Ford and Floyd-Warshall	All of these algorithms are useful in different situations (e.g., the Floyd-Warshall algorithm functions as an adaptive and a multi-source shortest-path algorithm)

Table 3  
The deep learning algorithm for indoor navigation

Title/Project Name	Year	Algorithms	Results
Node2vec: Scalable feature learning for networks (Grover & Leskovec, 2016)	2016	Node2vec	Node2vec is flexible and can handle changes

Table 3 (continue)

Title/Project Name	Year	Algorithms	Results
An improved collaborative filtering algorithm based on node2vec (Liang & Tang, 2018)	2018	Node2vec	Node2vec, graph attention networks, and multi-layer perceptrons find pivots with path lengths close to the shortest alternative route
A convolutional neural network feature detection approach to autonomous quadrotor indoor navigation (Garcia et al., 2019)	2019	CNN	CNN-based recognition of objects makes it easy to distinguish between a building structure and a person
Indoor positioning algorithm based on improved convolutional neural network (Zhou et al., 2022)	2022	CNN	The CNN algorithm is extremely reliable
Indoor localization with Wi-Fi fingerprinting using convolutional neural network (Jang & Hong, 2018)	2018	CNN	The CNN-based model is quicker and less time-complex than the current technique
Design and development of an indoor navigation system using a denoising autoencoder-based convolutional neural network for visually impaired people (Jothi & Sabeenian, 2022)	2022	CNN	DAECNN outperforms other previous classification methods.
DeepNav : A scalable and plug-and-play indoor navigation system based on visual CNN (Gong et al., 2021)	2021	CNN	DeepNav can be set up fast and has an average mistake in location of 2.3 m
DeepLoc : A deep neural network-based indoor positioning framework (S. Liu et al., 2021)	2021	DNN	DeepLoc can help enhance the accuracy of localization and achieve better efficiency
Deep neural network-based Wi-Fi/pedestrian dead reckoning indoor positioning system using adaptive robust factor graph model (Wang et al., 2020.)	2019	DNN	The DNN-based system is more reliable and accurate under different motion movements
The indoor positioning system using fingerprint method-based deep neural network the indoor positioning system using fingerprint method based deep neural network (Malik et al., 2019)	2019	DNN	The effectiveness of a DNN is proportional to the sum of its hidden layer sizes
Applying deep neural network (DNN) for robust indoor localization in multi-building environments (Adege et al., 2018.)	2018	DNN	DNN is capable of accurately localizing Wi-Fi users in wireless environments that are both hierarchical and complex
Wi-Fi-based indoor positioning system using deep neural network (Giney et al., 2020)	2020	DNN	DNN works better than other machine-learning algorithms
Deep neural network for indoor positioning based on channel impulse response (Dao & Salman, 2022)	2020	DNN	DCNN reduces the optimal ADE by half compared to the situation without optimal AP locations

Table 3 (continue)

Title/Project Name	Year	Algorithms	Results
DNN-based Wi-Fi positioning in 3GPP indoor office environment (Oh & Kim, 2021)	2021	DNN	DNN has a high accuracy for indoor localization
A deep autoencoder and RNN model for indoor localization with variable propagation loss (Espindola et al., 2021)	2023	RNN	RNN model improves the positioning accuracy
Bluetooth direction finding using recurrent neural network (Babakhani et al., 2021)	2021	RNN	RNN method produces fewer errors with higher accuracy
Centimeter-level indoor Localization using channel State Information with Recurrent Neural Networks (Yu et al., 2020)	2020	RNN	RNN estimate values more accurately than tree-based approaches
Recurrent neural networks for accurate RSSI indoor localization (Hoang et al., 2019)	2019	RNN	LSTM framework performs better than feedforward neural network with 0.75 m average localization error and 80% of mistakes under 1 m
Towards the implementation of recurrent neural network schemes for Wi-Fi fingerprint-based indoor positioning (Hsieh et al., 2018)	2018	RNN	RNN and LSTM algorithms predict sensor floor with excellent accuracy
Wireless fingerprinting uncertainty prediction based on machine learning (Li et al., 2019)	2019	ANN	ANN can predict wireless fingerprinting uncertainty and adaptive measurement noises in integrated localization EKF work
Artificial neural networks for navigation systems: a review of recent research (Jwo et al., 2023)	2023	ANN	The full ANN research was examined for integrating the INS with GNSS and using ANNs in navigation systems
Improving the accuracy of the alpha-beta filter algorithm using an ANN-based learning mechanism in indoor navigation system (Jamil & Kim, 2019)	2019	ANN	An ANN-based learning module was developed to improve the prediction accuracy of the alpha-beta filter algorithm as a case study.

## DISCUSSION AND ANALYSIS OF SHORTEST-PATH ALGORITHMS

Indoor navigation is a challenging task that requires efficient algorithms to find the shortest path between two points. Based on Table 2, several studies have proposed different algorithms to address this issue. Dijkstra's algorithm is one of the most commonly used algorithms for indoor navigation (Z. Liu et al., 2021; P. Liu et al., 2022; Rachmawati & Gustin, 2020; Samah et al., 2020). It determines the shortest path between graph nodes. Other algorithms have addressed Dijkstra's shortcomings. The researchers decided on Dijkstra's and A\* algorithms because they provide the quickest route to their objective. It has been demonstrated that modifying Dijkstra's algorithm can provide the shortest route for indoor navigation, starting from the current place and ending at the desired site.

A\* algorithm uses a statistical function to determine a better path, while Dijkstra's algorithm considers all feasible routes (Kasim et al., 2016). EBS-A\* algorithm reduced the number of important nodes by 91.89 %, the number of right-angle turns by 100 %, and the efficiency of path planning by 278 %. In addition, the shortest path problem that arises in environments with fuzzy images can be resolved with the help of the Bellman-Ford method (Parimala et al., 2021). Dijkstra's algorithm and the Bellman-Ford algorithm, which optimizes GPS and finds the shortest path through the graph, are utilized in the process (Rai, 2022). The Floyd-Warshall method determines the quickest and shortest path between any two nodes, while the algorithm determines the path between any number of nodes (Ramadiani et al., 2018). Dijkstra's, A\*, Bellman-Ford and Floyd-Warshall algorithms are useful in different situations. For instance, the Floyd-Warshall algorithm can perform the duties of both adaptive and multi-source shortest-path algorithms (Tamimi, 2015).

In conclusion, indoor navigation algorithms have been proposed to identify the shortest way to the selected destination. Dijkstra's algorithm is the most widely used, whereas the A\*, Bellman-Ford, and Floyd-Warshall algorithms have been presented to solve their weaknesses. Hybrid algorithms that mix techniques can also increase the shortest path accuracy (Alani et al., 2020).

## **DISCUSSION AND ANALYSIS OF DEEP LEARNING ALGORITHM**

The ability of CNN to learn and identify visual features included within maps or floor layouts shows that it offers great promise. Garcia et al. (2019) performed CNN-based detection and localization of the structural characteristics of a corridor on an off-board platform, where the method independently guided a quadrotor through hallways with intersections and dead ends. Zhou et al. (2022) introduced the CNN-LOC system, which provides precise and reliable indoor localization via Wi-Fi fingerprint and CNN. Otherwise, CNN-based Wi-Fi fingerprint systems demonstrated their capability to provide a higher level of accuracy compared to deep learning-based multi-floor-multi-building classifiers currently in use (Jang & Hong, 2018). Jothi and Sabeenian (2022) utilized a denoising auto-encoder based on the convolutional neural network (DAECNN) to determine the current position of the users. Gong et al. (2021) presented DeepNav, a new indoor navigation system that relies solely on visual CNN to perform large-scale navigation. In order to facilitate rapid deployment, DeepNav uses a deployment strategy that only requires a single pilot.

Node2vec is a method for algorithmic learning used for representational purposes on graphs. It learns a continuous classification model for the nodes of any graph, which may then be used for a variety of other machine-learning tasks further down the line (Grover & Leskovec, 2016). In optimizing a neighborhood-preserving objective, the Node2vec framework can discover low-dimensional representations for the nodes that make up a graph (Liang & Tang, 2018).

It is possible to use deep neural networks (DNN) for indoor navigation by first training them to understand and categorize various aspects of indoor surroundings, such as partitions, entrances, and furniture, and then employing these data to estimate the user's current location and direct them to the destination of their choosing. S. Liu et al. (2021) presented a system based on DNNs (DeepLoc) to enable Wi-Fi fingerprint location. In addition, a DNN-based Wi-Fi/PDR indoor positioning system that uses a highly adaptive and robust factor-graph model was suggested for the indoor placement of smartphones to obtain a system that is more reliable and accurate under a variety of motion gestures (Wang et al., 2020).

In Malik et al. (2019), the DNN algorithm was suggested to enhance the fingerprint technique implemented in the IPS. Next, to accomplish precise localization in Wi-Fi situations, researchers suggested using DNNs (Adege et al., 2018.). Giney et al. (2020) used DNN and more traditional machine learning algorithms for categorizing 22-square grids representing different places.

Additionally, researchers have developed a deep CNN to predict the position of a moving robot. One of the input parameters of this network is a measurement of the channel's impulse response (Dao & Salman., 2022). Furthermore, DNN was suggested for application in the location positioning process within an indoor office environment by the 3rd generation partnership project (3GPP) (Oh & Kim, 2021).

Recurrent neural networks are well-suited to handle time-series data, typically in indoor navigation, as the user's location and motions change continuously throughout the navigation session. For example, Espindola et al. (2021) used a deep autoencoder and an RNN to develop a new method of indoor localization optimized for situations with varying propagation losses.

Babakhani et al. (2021) produced a design for the angle of arrival (AoA) estimation that uses a robust and fast signal processing method and a tiny RNN model to improve performance by approaching AoA estimation as a time-series problem. Yu et al. (2020) applied RNN for indoor localization. The suggested approach uses channel state information (CSI) data as features and considers the user's trajectory and the signal-to-noise ratio.

Furthermore, RNN has been proposed for Wi-Fi fingerprinting and indoor localization. The approach considers the relationship between a number of RSSI measurements and treats the user's movement as a single problem (Hoang et al., 2019). Hsieh et al. (2018) analyzed the effectiveness of RNN as a method of deep learning that could be applied in an indoor location system, particularly for the Wi-Fi fingerprinting dataset.

In conclusion, indoor navigation algorithms have become an essential tool for the user inside the building to find the right path to the desired destination accurately. Deep learning and shortest path algorithms are two of the most popular algorithms used for indoor navigation. Deep learning algorithms use various data sources to create detailed maps of buildings and locate a person, while shortest path algorithms find the quickest



route between two points within a building. By using these algorithms, indoor navigation systems can provide accurate and efficient navigation within large buildings.

## CONCLUSION

In the past six years, research into indoor navigation has been consistently active. This paper conducts an in-depth analysis of related articles, focusing on their strengths and weaknesses, as well as analyzing the algorithm types that have been implemented. The use of algorithms for indoor navigation has become an indispensable component in daily life. Shortest path and deep learning algorithms have become two of the most prominent types of algorithms used for indoor navigation. Deep learning algorithms use a variety of data sources to produce precise maps of buildings and locate a person. In contrast, shortest path algorithms determine the most direct path between two spots within a building in the smallest amount of time. With the assistance of these algorithms, indoor navigation systems can deliver precise and time-saving navigation around enormous structures.

The article is divided into the appropriate classifications and outlines several appealing alternatives for the continuation of future research. Indoor navigation is a difficult task involving complicated maps, advertising, and directional cues. Extended reality (XR) technologies, which include VR, AR, and MR, have the potential to revolutionize the process of navigating indoor spaces by giving consumers an experience that is both comprehensive and accessible.

In future work, by looking at this research gap, it is anticipated that this research will enable a new exploration of combining deep learning into the shortest path method by utilizing XR technology. This investigation will also help the XR developers choose the suitable algorithm they want to implement in the product for development and commercialization.

## ACKNOWLEDGEMENTS

This research was supported by Universiti Tun Hussein Onn Malaysia (UTHM) through *Geran Penyelidikan Pascasiswazah (GPPS)* (Vote No. Q217). Communication of this research is made possible through monetary assistance by UTHM and the UTHM Publisher's Office via Publication Fund E15216.

## REFERENCES

- Abdallah, A. A., Jao, C. S., Kassas, Z. M., & Shkel, A. M. (2022). A pedestrian indoor navigation system using deep-learning-aided cellular signals and zupt-aided foot-mounted Imus. *IEEE Sensors Journal*, 22(6), 5188-5198. <https://doi.org/10.1109/jsen.2021.3118695>
- Adege, A., Lin, H. P., Tarekegn, G., & Jeng, S. S. (2018). Applying deep neural network (DNN) for robust indoor localization in multi-building environment. *Applied Sciences*, 8(7), Article 1062. <https://doi.org/10.3390/app8071062>

- Al-habashna, A., Wainer, G., & Aloqaily, M. (2022). Simulation modelling practice and theory machine learning-based indoor localization and occupancy estimation using 5G ultra-dense networks. *Simulation Modelling Practice and Theory*, 118, Article 102543. <https://doi.org/10.1016/j.simpat.2022.102543>
- Alani, S., Baseel, A., Hamdi, M. M., & Rashid, S. A. (2020). A hybrid technique for single-source shortest path-based on a\* algorithm and ant colony optimization. *IAES International Journal of Artificial Intelligence (IJ-AI)*, 9(2), Article 356. <https://doi.org/10.11591/ijai.v9.i2.pp356-363>
- Alves, R., De Morais, J. S., & Lopes, C. R. (2019). Indoor navigation with human assistance for service robots using D\*Lite. In *2018 IEEE International Conference on Systems, Man, and Cybernetics (SMC)* (pp. 4106-4111). IEEE Publishing. <https://doi.org/10.1109/SMC.2018.00696>
- Babakhani, P., Merk, T., Mahlig, M., Sarris, I., Kalogiros, D., & Karlsson, P. (2021). Bluetooth direction finding using recurrent neural network. In *2021 International Conference on Indoor Positioning and Indoor Navigation (IPIN)* (pp. 1-7). IEEE Publishing. <https://doi.org/10.1109/IPIN51156.2021.9662611>
- Bakale, V. A., Kumar V S, Y., Roodagi, V. C., Kulkarni, Y. N., Patil, M. S., & Chickerur, S. (2020). Indoor navigation with deep reinforcement learning. In *2020 International Conference on Inventive Computation Technologies (ICICT)* (pp. 660-665). IEEE Publishing. <https://doi.org/10.1109/iciict48043.2020.9112385>
- Chae, Y. J., Lee, H. W., Kim, J. H., Hwang, S. W., & Park, Y. Y. (2023). Design of a mixed reality system for simulating indoor disaster rescue. *Applied Sciences*, 13(7), Article 4418. <https://doi.org/10.3390/app13074418>
- Chan, P. Y., Chao, J. C., & Wu, R. B. (2023). A Wi-Fi-based passive indoor positioning system via entropy-enhanced deployment of Wi-Fi sniffers. *Sensors*, 23(3), Article 1376. <https://doi.org/10.3390/s23031376>
- Che, F., Ahmed, Q. Z., Lazaridis, P. I., Sureephong, P., & Alade, T. (2023). indoor positioning system (IPS) using ultra-wide bandwidth (UWB) for industrial internet of things (IIoT). *Sensors*, 23(12), Article 5710. <https://doi.org/10.3390/s23125710>
- Chidsin, W., Gu, Y., & Goncharenko, I. (2021). AR-based navigation using RGB-D camera and hybrid map. *Sustainability*, 13(10), Article 5585. <https://doi.org/10.3390/su13105585>
- Chumkamon, S., Tuvaphanthaphiphat, P., & Keeratiwintakorn, P. (2008). A blind navigation system using RFID for indoor environments. In *2008 5th International Conference on Electrical Engineering/Electronics, Computer, Telecommunications and Information Technology* (Vol. 2, pp. 765-768). IEEE Publishing. <https://doi.org/10.1109/ECTICON.2008.4600543>
- Chung, H. L., Chin, K. Y., & Wang, C. S. (2021). Development of a head-mounted mixed reality museum navigation system. In *2021 IEEE 4th International Conference on Knowledge Innovation and Invention (ICKII)* (pp. 111-114). IEEE Publishing. <https://doi.org/10.1109/ICKII51822.2021.9574731>
- Dao, V. L., & Salman, S. M. (2022). Deep neural network for indoor positioning based on channel impulse response. In *2022 IEEE 27th International Conference on Emerging Technologies and Factory Automation (ETFA)* (pp. 1-8). IEEE Publishing. <https://doi.org/10.1109/etfa52439.2022.9921735>
- Dong, Z. Y., Xu, W. M., & Zhuang, H. (2018). Research on zigbee indoor technology positioning based on RSSI. *Procedia Computer Science*, 154, 424-429. <https://doi.org/10.1016/j.procs.2019.06.060>

- El-Sheimy, N., & Li, Y. (2021). Indoor navigation: State of the art and future trends. *Satellite Navigation*, 2(1), 1-23. <https://doi.org/10.1186/s43020-021-00041-3>
- Espindola, A., Viegas, E. K., Traleski, A., Pellenz, M. E., & Santin, A. O. (2021). A deep autoencoder and RNN model for indoor localization with variable propagation loss. In *2021 17th International Conference on Wireless and Mobile Computing, Networking and Communications (WiMob)* (pp. 391-396). IEEE Publishing. <https://doi.org/10.1109/wimob52687.2021.9606346>
- Garcia, A., Mittal, S. S., Kiewra, E., & Ghose, K. (2019). A convolutional neural network feature detection approach to autonomous quadrotor indoor navigation. In *2019 IEEE/RSJ International Conference on Intelligent Robots and Systems (IROS)* (pp. 74-81). IEEE Publishing. <https://doi.org/10.1109/iros40897.2019.8968222>
- Ge, H., Sun, Z., Chiba, Y., & Koshizuka, N. (2022). Accurate indoor location awareness based on machine learning of environmental sensing data. *Computers and Electrical Engineering*, 98, Article 107676. <https://doi.org/10.1016/j.compeleceng.2021.107676>
- Gong, J., Ren, J., & Zhang, Y. (2021). DeepNav: A scalable and plug-and-play indoor navigation system based on visual CNN. *Peer-to-Peer Networking and Applications*, 14, 3718-3736. <https://doi.org/10.1007/s12083-021-01216-0>
- Grover, A., & Leskovec, J. (2016). Node2vec: Scalable feature learning for networks. In *Proceedings of the 22nd ACM SIGKDD International Conference on Knowledge Discovery and Data Mining* (pp. 855-864). ACM Publishing. <https://doi.org/10.1145/2939672.2939754>
- Giney, S., Erdogan, A., Aktas, M., & Ergun, M. (2020). Wi-Fi based indoor positioning system with using deep neural network. In *2020 43rd International Conference on Telecommunications and Signal Processing (TSP)* (pp. 225-228). IEEE Publishing. <https://doi.org/10.1109/tsp49548.2020.9163548>
- Guo, Y., Zhu, J., Wang, Y., Chai, J., Li, W., Fu, L., Xu, B., & Gong, Y. (2020). A virtual reality simulation method for crowd evacuation in a multiexit indoor fire environment. *ISPRS International Journal of Geo-Information*, 9(12), Article 750. <https://doi.org/10.3390/ijgi9120750>
- Hoang, M. T., Yuen, B., Dong, X., Lu, T., Westendorp, R., & Reddy, K. (2019). Recurrent neural networks for accurate RSSI indoor localization. *IEEE Internet of Things Journal*, 6(6), 10639-10651. <https://doi.org/10.1109/JIOT.2019.2940368>
- Hsieh, H. Y., Prakosa, S. W., & Leu, J. S. (2018). Towards the implementation of recurrent neural network schemes for WiFi fingerprint-based indoor positioning. In *2018 IEEE 88th Vehicular Technology Conference (VTC-Fall)* (pp. 1-5). IEEE Publishing. <https://doi.org/10.1109/vtcfall.2018.8690989>
- Jamil, F., & Kim, D. (2019). Improving accuracy of the alpha-beta filter algorithm using an ANN-based learning mechanism in indoor navigation system. *Sensor*, 19(18), Article 3946. <https://doi.org/10.3390/s19183946>
- Jang, J. W., & Hong, S. N. (2018). Indoor localization with WiFi fingerprinting using convolutional neural network. In *2018 Tenth International Conference on Ubiquitous and Future Networks (ICUFN)* (pp. 753-758). IEEE Publishing. <https://doi.org/10.1109/icufn.2018.8436598>
- Jia, S. (2023). Analysis of path planning algorithms for service robots applied in indoor environments. *Highlights in Science, Engineering and Technology*, 52, 192-201. <https://doi.org/10.54097/hset.v52i.8888>

- Jiang, C., Chen, Y., Chen, C., Jia, J., Sun, H., Wang, T., & Hyyppa, J. (2022). Implementation and performance analysis of the PDR/GNSS integration on a smartphone. *GPS Solutions*, 26(3), Article 81. <https://doi.org/10.1007/s10291-022-01260-0>
- Jothi, J. A. G., & Sabeenian, A. N. R. S. (2022). Design and development of an indoor navigation system using denoising autoencoder based convolutional neural network for visually impaired people. *Multimedia Tools and Applications*, 81(3), 3483-3514. <https://doi.org/10.1007/s11042-021-11287-z>
- Jwo, D. J., Biswal, A., & Mir, I. A. (2023). Artificial neural networks for navigation systems: A review of recent research. *Applied Sciences*, 13(7), Article 4475. <https://doi.org/10.3390/app13074475>
- Khan, S., Patil, A., Kadam, G., & Jadhav, A. (2020). Indoor navigation in stadium using virtual reality. *ITM Web of Conferences*, 32, Article 03002. <https://doi.org/10.1051/itmconf/20203203002>
- Kasim, S., Xia, L. Y., Wahid, N., Fudzee, M. F. M., Mahdin, H., Ramli, A. A., Suparjoh, S., & Salamat, M. A. (2016). Indoor navigation using a\* algorithm. In *Recent Advances on Soft Computing and Data Mining: The Second International Conference on Soft Computing and Data Mining (SCDM-2016), Bandung, Indonesia, August 18-20, 2016 Proceedings Second* (pp. 598-607). Springer International Publishing. [https://doi.org/10.1007/978-3-319-51281-5\\_60](https://doi.org/10.1007/978-3-319-51281-5_60)
- Kunhoth, J., Karkar, A. G., Al-Maadeed, S., & Al-Ali, A. (2020). Indoor positioning and wayfinding systems: A survey. *Human-centric Computing and Information Sciences*, 10(1), 1-41. <https://doi.org/10.1186/s13673-020-00222-0>
- Lee, J., Jin, F., Kim, Y., & Lindlbauer, D. (2022). User preference for navigation instructions in mixed reality. In *2022 IEEE Conference on Virtual Reality and 3D User Interfaces (VR)* (pp. 802-811). IEEE Publishing. <https://doi.org/10.1109/VR51125.2022.00102>
- Lee, S., Park, S., Kim, S., Lee, S. H., Lee, S., Member, S., & Park, S. (2017.) Indoor navigation system for evacuation route in case of fire by using environment and location data. In *2020 IEEE International Conference on Consumer Electronics-Taiwan (ICCE-Taiwan)* (pp. 1-2). IEEE Publishing. <https://doi.org/10.1016/j.autcon.2016.08.043.P>
- Li, Y., Gao, Z., He, Z., Zhuang, Y., Radi, A., Chen, R., & El-Sheimy, N. (2019). Wireless fingerprinting uncertainty prediction based on machine learning. *Sensors*, 19(2), Article 324. <https://doi.org/10.3390/s19020324>
- Liang, L., & Tang, R. (2018). An improved collaborative filtering algorithm based on Node2vec. In *Proceedings of the 2018 2nd International Conference on Computer Science and Artificial Intelligence* (pp. 218-222). ACM Publishing. <https://doi.org/10.1145/3297156.3297219>
- Liu, B., Ding, L., & Meng, L. (2021). Spatial knowledge acquisition with virtual semantic landmarks in mixed reality-based indoor navigation. *Cartography and Geographic Information Science*, 48(4), 305-319. <https://doi.org/10.1080/15230406.2021.1908171>
- Liu, P., Li, Y., Ai, S., Luo, C., & Yang, C. (2022). An improved dijkstra-based algorithm for resource constrained shortest path. In *2022 9th International Conference on Dependable Systems and Their Applications (DSA)* (pp. 368-373). IEEE Publishing. <https://doi.org/10.1109/DSA56465.2022.00056>
- Liu, S., Ren, Q., Li, J., & Xu, H. (2021). DeepLoc: Deep neural network-based indoor positioning framework. In *2021 IEEE 23rd Int Conf on High Performance Computing & Communications; 7th Int Conf on Data Science & Systems; 19th Int Conf on Smart City; 7th Int Conf on Dependability in Sensor, Cloud & Big*

- Data Systems & Application (HPCC/DSS/SmartCity/DependSys)* (pp. 1735-1740). IEEE Publishing. <https://doi.org/10.1109/hpcc-dss-smartcity-dependsys53884.2021.00255>
- Liu, Z., Li, D., Yang, Y., Chen, X., Lv, X., & Li, X. (2021). Design and implementation of the optimization algorithm in the layout of parking lot guidance. *Wireless Communications and Mobile Computing, 2021*, 1-6. <https://doi.org/10.1155/2021/6639558>
- Liu, Z., Liu, J., Xu, X., & Wu, K. (2022). *DeepGPS*: Deep learning enhanced GPS positioning in urban canyons. *IEEE Transactions on Mobile Computing, 23*(1), 376-392. <https://doi.org/10.1109/tmc.2022.3208240>
- Malik, R. F., Gustifa, R., Farissi, A., Stiawan, D., Ubaya, H., Ahmad, M. R., & Khirbeet, A. S. (2019). The indoor positioning system using fingerprint method based deep neural network. *IOP Conference Series: Earth and Environmental Science, 248*, Article 012077. <https://doi.org/10.1088/1755-1315/248/1/012077>
- Nessa, A., Adhikari, B., Hussain, F., & Fernando, X. N. (2020). A survey of machine learning for indoor positioning. *IEEE Access, 8*, 214945-214965. <https://doi.org/10.1109/ACCESS.2020.3039271>
- Oh, S. H., & Kim, J. G. (2021). DNN based WiFi positioning in 3GPP indoor office environment. In *2021 International Conference on Artificial Intelligence in Information and Communication (ICAIIIC)* (pp. 302-306). IEEE. <https://doi.org/10.1109/ICAIIIC51459.2021.9415207>
- Parimala, M., Broumi, S., Prakash, K., & Topal, S. (2021). Bellman–Ford algorithm for solving shortest path problem of a network under picture fuzzy environment. *Complex and Intelligent Systems, 7*(5), 2373-2381. <https://doi.org/10.1007/s40747-021-00430-w>
- Rachmawati, D., & Gustin, L. (2020). Analysis of Dijkstra's algorithm and A\* algorithm in shortest path problem. *Journal of Physics: Conference Series, 1566*, Article 012061. <https://doi.org/10.1088/1742-6596/1566/1/012061>
- Rai, A. (2022). A study on Bellman Ford algorithm for shortest path detection in global positioning system. *International Journal for Research in Applied Science and Engineering Technology, 10*(5), 2118-2126. <https://doi.org/10.22214/ijraset.2022.42720>
- Ramadiani, Bukhori, D., Azainil, & Dengen, N. (2018). Floyd-warshall algorithm to determine the shortest path based on android. *IOP Conference Series: Earth and Environmental Science, 144*, Article 012019. <https://doi.org/10.1088/1755-1315/144/1/012019>
- Real, S., & Araujo, A. (2021). Ves: A mixed-reality development platform of navigation systems for blind and visually impaired. *Sensors, 21*(18), Article 6275. <https://doi.org/10.3390/s21186275>
- Rehman, U., & Cao, S. (2017). Augmented-reality-based indoor navigation: A comparative analysis of handheld devices versus google glass. *IEEE Transactions on Human-Machine Systems, 47*(1), 140-151. <https://doi.org/10.1109/THMS.2016.2620106>
- Rizi, F. S., Schloetterer, J., & Granitzer, M. (2018). Shortest path distance approximation using deep learning techniques. In *2018 IEEE/ACM International Conference on Advances in Social Networks Analysis and Mining (ASONAM)* (pp. 1007-1014). IEEE Publishing. <https://doi.org/10.1109/asonam.2018.8508763>
- Rochadiani, T. H., Atmojo, W. T., Bari, M., Kristina, E., Renaldi, & Setiawan, A. (2022). Find: Mall navigation using augmented reality. In *2022 8th International Conference on Virtual Reality (ICVR)* (pp. 110-115). IEEE Publishing. <https://doi.org/10.1109/icvr55215.2022.9847949>

- Rubio-Sandoval, J. I., Martinez-Rodriguez, J. L., Lopez-Arevalo, I., Rios-Alvarado, A. B., Rodriguez-Rodriguez, A. J., & Vargas-Requena, D. T. (2021). An indoor navigation methodology for mobile devices by integrating augmented reality and semantic web. *Sensors*, *21*(16), Article 5435. <https://doi.org/10.3390/s21165435>
- Saeliw, A., Hualkasin, W., & Puttinaovarat, S. (2022a). Indoor navigation application in shopping mall based on augmented reality (AR). *TEM Journal*, *11*(3), 1119-1127. <https://doi.org/10.18421/TEM113-17>
- Samah, K. A. F. A., Sharip, A. A., Musirin, I., Sabri, N., & Salleh, M. H. (2020). Reliability study on the adaptation of Dijkstra's algorithm for gateway KLIA2 indoor navigation. *Bulletin of Electrical Engineering and Informatics*, *9*(2), 594-601. <https://doi.org/10.11591/eei.v9i2.2081>
- Sarkar, T., Ghosh, A., Chakraborty, S., Singh, L. L., & Chattopadhyay, S. (2021). A new insightful exploration into a low profile ultra-wide-band (UWB) microstrip antenna for DS-UWB applications. *Journal of Electromagnetic Waves and Applications*, *35*(15), 2001-2019. <https://doi.org/10.1080/09205071.2021.1927855>
- Shahbazian, R., Macrina, G., Scalzo, E., & Guerriero, F. (2023). Machine learning assists IOT localization: A review of current challenges and future trends. *Sensors*, *23*(7), Article 3551. <https://doi.org/10.3390/s23073551>
- Syazwani, C. J. N., Wahab, N. H. A., Sunar, N., Ariffin, S. H. S., Wong, K. Y., & Aun, Y. (2022). Indoor positioning system: A review. *International Journal of Advanced Computer Science and Applications*, *13*(6), 477-490. <https://doi.org/10.14569/IJACSA.2022.0130659>
- Tamimi, A. A. (2015). Comparison studies for different shortest path algorithms. *International Journal Of Computers & Technology*, *14*(8), 5979-5986. <https://doi.org/10.24297/ijct.v14i8.1857>
- Trybała, P., & Gattner, A. (2021). Development of a building topological model for indoor navigation. *IOP Conference Series: Earth and Environmental Science*, *684*, Article 012031. <https://doi.org/10.1088/1755-1315/684/1/012031>
- Varma, P. S., & Anand, V. (2021). Indoor localization for IoT applications: Review, challenges and manual site survey approach. In *2021 IEEE Bombay Section Signature Conference (IBSSC)* (pp. 1-6). IEEE Publishing. <https://doi.org/10.1109/IBSSC53889.2021.9673236>
- Verma, P., Agrawal, K., & Sarasvathi, V. (2020). Indoor navigation using augmented reality. In *Proceedings of the 2020 4th International Conference on Virtual and Augmented Reality Simulations* (pp. 58-63). ACM Publishing. <https://doi.org/10.1145/3385378.3385387>
- Wang, H., Lou, S., Jing, J., Wang, Y., Liu, W., & Liu, T. (2022). The EBS-A\* algorithm: An improved A\* algorithm for path planning. *PLoS ONE*, *17*(2), Article e0263841. <https://doi.org/10.1371/journal.pone.0263841>
- Wang, Y., Li, Z., Gao, J., & Zhao, L. (2020). Deep neural network-based Wi-Fi/pedestrian dead reckoning indoor positioning system using adaptive robust factor graph model. *IET Radar, Sonar & Navigation*, *14*(1), 36-47. <https://doi.org/10.1049/iet-rsn.2019.0260>
- Woensel, W. Van, Roy, P. C., Sibte, S., Abidi, R., & Raza, S. (2020). Indoor location identification of patients for directing virtual care: An AI approach using machine learning and knowledge-based methods. *Artificial Intelligence In Medicine*, *108*, Article 101931. <https://doi.org/10.1016/j.artmed.2020.101931>

- Wu, J. H., Huang, C. T., Huang, Z. R., Chen, Y. B., & Chen, S. C. (2020). A rapid deployment indoor positioning architecture based on image recognition. In *2020 IEEE 7th International Conference on Industrial Engineering and Applications (ICIEA)* (pp. 784-789). IEEE. <https://doi.org/10.1109/iciea49774.2020.9102083>
- Yang, G., & Saniie, J. (2017). Indoor navigation for visually impaired using AR markers. In *2017 IEEE International Conference on Electro Information Technology (EIT)* (pp. 1-5). IEEE Publishing. <https://doi.org/10.1109/eit.2017.8053383>
- Yeh, S. C., Hsu, W. H., Lin, W. Y., & Wu, Y. F. (2020). Study on an indoor positioning system using earth's magnetic field. *IEEE Transactions on Instrumentation and Measurement*, *69*(3), 865-872. <https://doi.org/10.1109/TIM.2019.2905750>
- Yoon, J. W., & Lee, S. H. (2023). Development of a construction-site work support system using BIM-marker-based augmented reality. *Sustainability*, *15*(4), Article 3222. <https://doi.org/10.3390/su15043222>
- Yu, J., Saad, H. M., & Buehrer, R. M. (2020). Centimeter-level indoor localization using channel state information with recurrent neural networks. In *2020 IEEE/ION Position, Location and Navigation Symposium (PLANS)* (pp. 1317-1323). IEEE Publishing. <https://doi.org/10.1109/plans46316.2020.9109805>
- Yuan, J., Chen, R., & Yu, P. (2023). Application of navigation grid corner point algorithm in virtual reality simulation images of indoor fire evacuation. *Internet of Things*, *22*, Article 100716. <https://doi.org/10.1016/j.iot.2023.100716>
- Zhou, T., Ku, J., Lian, B., & Zhang, Y. (2022). Indoor positioning algorithm based on improved convolutional neural network. *Neural Computing and Applications*, *34*(9), 6787-6798. <https://doi.org/10.1007/s00521-021-06112-5>
- Zlatanova, S., Sithole, G., Nakagawa, M., & Zhu, Q. (2013). Problems in indoor mapping and modelling. *International Archives of the Photogrammetry, Remote Sensing and Spatial Information Sciences - ISPRS Archives*, *40*(4W4), 63-68. <https://doi.org/10.5194/isprsarchives-XL-4-W4-63-2013>





**REFEREES FOR THE PERTANIKA  
JOURNAL OF SCIENCE & TECHNOLOGY**

**Vol. 32 (2) Mar. 2024**

The Editorial Board of the Pertanika Journal of Science and Technology wishes to thank the following:

Abam Fidelis  
*(MOUUAU, Nigeria)*

Jayaraman Kandasamy  
*(IIT, India)*

Amir M. Mortazavian  
*(SBMU, Iran)*

Jiangqi Long  
*(Wenzhou University, China)*

Anand Paul  
*(KNU, South Korea)*

Jinjin Yan  
*(Haerbin Engineering University, China)*

Andi Nur Cahyo  
*(IRRI, Indonesia)*

Joshua M. Pearce  
*(Western University, Canada)*

Bukhari Manshoor  
*(UTHM, Malaysia)*

Kai Blin  
*(DTU, Denmark)*

Chong Wu Yi  
*(UM, Malaysia)*

Katarzyna Sosnowska  
*(UMB, Poland)*

Chukwu Ogbonnaya  
*(FUTMinna, Nigeria)*

Lee Yeong Huei  
*(Curtin University, Malaysia)*

Dinna N. Mohd Nizam  
*(UMS, Malaysia)*

Mo Kim Hung  
*(UM, Malaysia)*

Douglas Law  
*(UMK, Malaysia)*

Mohamad Zhafran Hussin  
*(UiTM, Malaysia)*

Farid Mulana  
*(USK, Indonesia)*

Mohammed Alias Yusof  
*(UPNM, Malaysia)*

Gokhan Basar  
*(OKÜ, Türkiye)*

Mohd Hendra Hairi  
*(UTeM, Malaysia)*

Gopinath Halder  
*(NITDGP, India)*

Mohd Khair Hassan  
*(UPM, Malaysia)*

Hamed Hamishehkar  
*(TBZMED, Iran)*

Mohd Khairul Nizam Mohd Zuhan  
*(UTHM, Malaysia)*

Harshavardhana Natarajan  
*(SRMIST, India)*

Mohd Rosdzimin Abdul Rahman  
*(UPNM, Malaysia)*

Haslina Md. Sarkan  
*(UTM, Malaysia)*

Mourad Abdelkrim  
*(UKMO, Algeria)*

Hedzlin Zainuddin  
*(UiTM, Malaysia)*

Noor Akhmazillah Mohd Fauzi  
*(UTHM, Malaysia)*

Hussein Adel Mahmood  
*(UPM, Malaysia)*

Nozieana Khairuddin  
*(UPM, Malaysia)*

Nur Farhayu Ariffin  
(UMP, Malaysia)

Pradeep Jangir  
(RRVPN, India)

Sahazati Md Rozali  
(UTeM, Malaysia)

Satyam Panchal  
(University of Waterloo, Canada)

Sharifah Sakinah Syed Alwi  
(UPM, Malaysia)

Sher Afghan Khan  
(IIUM, Malaysia)

Sharifah Fathiyah Sy Mohamad  
(UMP, Malaysia)

Siti Aekbal Salleh  
(UiTM, Malaysia)

Sofia A. Costa Lima  
(University of Porto, Portugal)

Syahrun Nizam Md Arshad  
(UNIMAP, Malaysia)

Taranath N L  
(Alliance University, India)

Wenjun Liu  
(BUPT, China)

Xiaohong Jiao  
(Yanshan University, China)

Yahui Guo  
(CCNU, China)

Yuvarajan Devarajan  
(Vel Tech, India)

Zengxi Pan  
(UOW, Australia)

Zulhilmy Sahwee  
(UniKL, Malaysia)

Zulkarnain Ahamad Noorden  
(UTM, Malaysia)

---

BUPT – Beijing University of Posts and Telecommunications  
CCNU – Central China Normal University  
DTU – Danmarks Tekniske Universitet  
FUTMinna – Federal University of Technology Minna  
IIT – Indian Institute of Technology  
IIUM – International Islamic University Malaysia  
IRRI – Indonesian Rubber Research Institute  
KNU – Kyungpook National University  
MOUAU – Michael Okpara University of Agriculture  
NITDGP – National Institute of Technology Durgapur  
OKU – Osmaniye Korkut Ata Üniversitesi  
RRVPN – Rajasthan Rajya Vidyut Prasaran Nigam Ltd  
SBMU – Shahid Beheshti University of Medical Sciences  
SRMIST – SRM Institute of Science and Technology  
TBZMED – Tabriz University of Medical Sciences  
UiTM – Universiti Teknologi MARA  
UKMO – University of Kasdi Merbah Ouargla

UM – Universiti Malaya  
UMB – Uniwersytet Medyczny w Białymstoku  
UMK – Universiti Malaysia Kelantan  
UMP – Universiti Malaysia Pahang  
UMS – Universiti Malaysia Sabah  
UniKL – Universiti Kuala Lumpur  
UNIMAP – Universiti Malaysia Perlis  
UOW – University of Wollongong  
UPM – Universiti Putra Malaysia  
UPNM – Universiti Pertahanan Nasional Malaysia  
USK – Syiah Kuala University  
UTeM – Universiti Teknikal Malaysia Melaka  
UTHM – Universiti Tun Hussein Onn Malaysia  
UTM – Universiti Teknologi Malaysia  
Vel Tech – Vel Tech Rangarajan Dr. Sagunthala R&D Institute of Science and Technology

---

While every effort has been made to include a complete list of referees for the period stated above, however if any name(s) have been omitted unintentionally or spelt incorrectly, please notify the Chief Executive Editor, *Pertanika* Journals at [executive\\_editor.pertanika@upm.edu.my](mailto:executive_editor.pertanika@upm.edu.my)

Any inclusion or exclusion of name(s) on this page does not commit the *Pertanika* Editorial Office, nor the UPM Press or the university to provide any liability for whatsoever reason.

<i>Review Article</i>	
Bead Geometry Control in Wire Arc Additive Manufactured Profile — A Review	917
<i>Zarirah Karrim Wani and Ahmad Baharuddin Abdullah</i>	
Application of the Ultrasonic Method to Produce Starch Nanoparticles from Cassava Starch	943
<i>Beni Hidayat, Vida Elsyana and Sheniah Glori Simorangkir</i>	
<i>Review Article</i>	
A Review: Current Trend of Immersive Technologies for Indoor Navigation and the Algorithms	955
<i>Muhammad Shazmin Sariman, Maisara Othman, Rohaida Mat Akir, Abd Kadir Mahamad and Munirah Ab Rahman</i>	

Utilization of Aluminum Dross as a Cement Replacement Material for Sustainable Concrete Development <i>Nur Hidayah Mohd Zahari, Ali Salmiaton, Shafreeza Sobri, Noor Azline Mohd Nasir and Nor Shafizah Ishak</i>	761
Structural Deformation and Displacement of a Disc Winding due to Standard Switching Impulse Voltage via Finite Element Method <i>Nurul Farahwahida Md Yasid, Norhafiz Azis, Jasronita Jasni, Mohd Fairouz Mohd Yousof, Mohd Aizam Talib and Avinash Srikanta Murthy</i>	781
Integrating Fuzzy Logic and Brute Force Algorithm in Optimizing Energy Management Systems for Battery Electric Vehicles <i>Abdulhadi Abdulsalam Abulifa, Azura Che Soh, Mohd Khair Hassan, Raja Kamil and Mohd Amran Mohd Radzi</i>	797
Mechanical Properties of Virgin and Recycled Polymer for Construction Pile Application <i>Hoo Tien Nicholas Kuan, Yee Yong Lee, Sim Nee Ting, Chee Khoon Ng and Mohd Khairul Afiq</i>	819
Thermal Decomposition and Combustion Analysis of Malaysian Peat Soil Samples Using Coats Redfern Model-free Method <i>Dayang Nur Sakinah Musa, Hamidah Jamil, Mohd Zahirasri Mohd Tohir, Syafie Syam and Ridwan Yahaya</i>	839
<i>Review Article</i>	
Employment of Artificial Intelligence (AI) Techniques in Battery Management System (BMS) for Electric Vehicles (EV): Issues and Challenges <i>Marwan Atef Badran and Siti Fauziah Toha</i>	859
Optimal Constrained Groove Pressing Process Parameters Applying Modified Taguchi Technique and Multi-Objective Optimization <i>Muni Tanuja Anantha, Sireesha Koneru, Saritha Pyatla, Parameshwaran Pillai Thiruvambalam Pillai, Tanya Buddi and Nageswara Rao Boggarapu</i>	883
Inorganic Material of Magnesium Nitrate $Mg(NO_3)_2$ Film as Q-Switcher in the C-Band Region <i>Noor Ummi Hazirah Hani Zalkepali, Muwafaq Mohammed Bakr Alsaady, Mustafa Mudhafar, Nik Noor Haryatul Eleena Nik Mahmud, Nur Ainnaa Mardhiah Muhammad, Ain Zamira Muhammad Zamri and Noor Azura Awang</i>	901

Microencapsulation of <i>Citrus Hystrix</i> Essential Oil by Gelatin B/Chitosan Complex Coacervation Technique	599
<i>Siti Afiqah 'Aisyah Murtadza, Nurul Asyikin Md Zaki, Junaidah Jai, Fazlena Hamzah, Nur Suhanawati Ashaari, Dewi Selvia Fardhyanti, Megawati and Nadya Alfa Cahaya Imani</i>	
<i>Review Article</i>	
Current Insight on <i>Siraitia grosvenorii</i> Flavonoids Extraction Process and its Bioactivity Characteristic: A Review	623
<i>Zhao Jing, Douglas Law, Ahmed Najm, Cheah Yew Hoong and Shazrul Fazry</i>	
Loss-of-Life Analyses Based on Modified Arrhenius and Relative Aging Rate for Non-Thermally Upgraded Paper in Oil-Immersed Transformer	647
<i>Najiyah Saleh, Norhafiz Azis, Jasronita Jasni, Mohd Zainal Abidin Ab Kadir and Mohd Aizam Talib</i>	
Performance of Waste Cooking Oil Esterification for Biodiesel Production Using Various Catalysts	669
<i>Indah Thuraya Herman, Khairuddin Md Isa, Naimah Ibrahim, Saiful Azhar Saad, Tuan Amran Tuan Abdullah, Mohd Aizudin Abd Aziz and Muhammad Auni Hairunnaja</i>	
Smart Hydroponic Farming System Integrated with LED Grow Lights	685
<i>Primadiyanti Nirbita, Kah-Yoong Chan, Gregory Soon How Thien and Chu-Liang Lee</i>	
Biochemical and Agronomic Responses of Soybean ( <i>Glycine max</i> L. Merrill) to Spent and Deoiled Bleaching Earth of NPK Fertilization on Filler Basis	703
<i>Muhammad Parikesit Wisnubroto, Eka Tarwaca Susila Putra and Budiastuti Kurniasih</i>	
Physical Properties of Full-ripe Dabai ( <i>Canarium odontophyllum</i> miq. Variety Song) at Different Fractions	725
<i>Nur Afiqah Hani Abdul Rashid, Rosnah Shamsudin, Siti Hajar Ariffin, Wan Nor Zanariah Zainol@Abdullah and Puteri Nurain Megat Ahmad Azman</i>	
Microencapsulation of <i>Acalypha indica</i> Linn. Extracts Using Chitosan-Polycaprolactone Blends	741
<i>Maizatul Akmal Johari, Fathilah Ali, Azlin Suhaida Azmi, Hazleen Anuar, Jamarosliza Jamaluddin and Rosnani Hasham</i>	

**Content**

Foreword <i>Mohd Sapuan Salit</i>	i
Analysis Study of Thermal and Exergy Efficiency in Double-Layers Porous Media Combustion Using Different Sizes of Burner: A Comparison <i>Nazmi Che Ismail, Mohd Zulkifly Abdullah, Nurul Musfirah Mazlan, Khairil Faizi Mustafa, Mohd Syakirin Rusdi and Roslan Kamarudin</i>	481
<i>Review Article</i> Bacterial Secondary Metabolite Activation Through Epigenetic Modifiers: A Systematic Review <i>Joana Noor Rashidah Rosli, Sharifah Aminah Syed Mohamad, Anis Low Muhammad Low and Suhaidi Ariffin</i>	495
Baby Weight and Length Measurement System with Data Storage Using MySQL Database <i>Rifqi Kamaddin Sholeh Lubis, Rahmat Rasyid and Meqorry Yusfi</i>	509
<i>Review Article</i> Integration of Unmanned Aerial Vehicle and Multispectral Sensor for Paddy Growth Monitoring Application: A Review <i>Nur Adibah Mohidem, Suhami Jaafar and Nik Norasma Che'Ya</i>	521
A Comparison of Results from Two Multi-Criteria Decision-Making Methods for Solar Photovoltaic Plant Site Location: Case Study Rio De Janeiro <i>Marco Pereira de Souza, Luis Claudio Bernardo Moura, Carlos Alberto Nunes Cosenza, Silvio de Macedo Amaral, Rodrigo Pestana Cunha Telles, Manuel Oliveira Lemos Alexandre, Silvio Barbosa, Bruno de Sousa Elia, Maria Fernanda Zelaya Correia, Antonio Carlos de Lemos Oliveira, Rodrigo Ventura da Silva and Thais Rodrigues Pinheiro</i>	551
Modelling and Optimisation of Cooling-Slope Parameters of Magnesium AZ91D Using Improvement Multi-Objective Jaya Approach for Predicted Feedstock Performance <i>Rahaini Mohd Said, Roselina Salleh@Sallehuddin, Norhaizan Mohamed Radzi, Wan Fahmin Faiz Wan Ali and Mohamad Ridzuan Mohamad Kamal</i>	573



Pertanika Editorial Office, Journal Division,  
Putra Science Park,  
1st Floor, IDEA Tower II,  
UPM-MTDC Center,  
Universiti Putra Malaysia,  
43400 UPM Serdang,  
Selangor Darul Ehsan  
Malaysia

<http://www.pertanika.upm.edu.my>  
Email: [executive\\_editor.pertanika@upm.edu.my](mailto:executive_editor.pertanika@upm.edu.my)  
Tel. No.: +603- 9769 1622

**PENERBIT**  
**UPM**  
UNIVERSITI PUTRA MALAYSIA  
**P R E S S**

<http://www.penerbit.upm.edu.my>  
Email: [penerbit@upm.edu.my](mailto:penerbit@upm.edu.my)  
Tel. No.: +603- 9769 8851

